THE LIFETIME OF METHANE BUBBLES THROUGH SEDIMENT AND WATER COLUMN

EDITED BY: Regina Katsman, Miriam Römer and Andreas Lorke

PUBLISHED IN: Frontiers in Earth Science and Frontiers in Environmental Science

frontiers Research Topics

frontiers

ISSN 1664-8714
ISBN 978-2-83250-015-6
DOI 10.3389/978-2-83250-015-6

About Frontiers

Frontiers is more than just an open-access publisher of scholarly articles: it is a pioneering approach to the world of academia, radically improving the way scholarly research is managed. The grand vision of Frontiers is a world where all people have an equal opportunity to seek, share and generate knowledge. Frontiers provides immediate and permanent online open access to all its publications, but this alone is not enough to realize our grand goals.

Frontiers Journal Series

The Frontiers Journal Series is a multi-tier and interdisciplinary set of open-access, online journals, promising a paradigm shift from the current review, selection and dissemination processes in academic publishing. All Frontiers journals are driven by researchers for researchers; therefore, they constitute a service to the scholarly community. At the same time, the Frontiers Journal Series operates on a revolutionary invention, the tiered publishing system, initially addressing specific communities of scholars, and gradually climbing up to broader public understanding, thus serving the interests of the lay society, too.

Dedication to Quality

Each Frontiers article is a landmark of the highest quality, thanks to genuinely collaborative interactions between authors and review editors, who include some of the world's best academicians. Research must be certified by peers before entering a stream of knowledge that may eventually reach the public - and shape society; therefore, Frontiers only applies the most rigorous and unbiased reviews.
Frontiers revolutionizes research publishing by freely delivering the most outstanding research, evaluated with no bias from both the academic and social point of view. By applying the most advanced information technologies, Frontiers is catapulting scholarly publishing into a new generation.

What are Frontiers Research Topics?

Frontiers Research Topics are very popular trademarks of the Frontiers Journals Series: they are collections of at least ten articles, all centered on a particular subject. With their unique mix of varied contributions from Original Research to Review Articles, Frontiers Research Topics unify the most influential researchers, the latest key findings and historical advances in a hot research area! Find out more on how to host your own Frontiers Research Topic or contribute to one as an author by contacting the Frontiers Editorial Office: frontiersin.org/about/contact

THE LIFETIME OF METHANE BUBBLES THROUGH SEDIMENT AND WATER COLUMN

Topic Editors:
Regina Katsman, University of Haifa, Israel
Miriam Römer, University of Bremen, Germany
Andreas Lorke, University of Koblenz and Landau, Germany

Citation: Katsman, R., Römer, M., Lorke, A., eds. (2022). The Lifetime of Methane Bubbles Through Sediment and Water Column. Lausanne: Frontiers Media SA. doi: 10.3389/978-2-83250-015-6

Table of Contents

frontiers | Frontiers in Earth Science

TYPE Editorial
PUBLISHED 10 August 2022
DOI 10.3389/feart.2022.993293

OPEN ACCESS

EDITED AND REVIEWED BY
Sabine Schmidt,
Centre National de la Recherche Scientifique (CNRS), France

*CORRESPONDENCE
Regina Katsman,
rkatsman@univ.haifa.ac.il

SPECIALTY SECTION
This article was submitted to Marine Geoscience,
a section of the journal
Frontiers in Earth Science

RECEIVED 13 July 2022
ACCEPTED 19 July 2022
PUBLISHED 10 August 2022

CITATION
Katsman R, Römer M and Lorke A (2022), Editorial: The lifetime of methane bubbles through sediment and water column.
Front. Earth Sci. 10:993293.
doi: 10.3389/feart.2022.993293

Editorial: The lifetime of methane bubbles through sediment and water column

Regina Katsman[1]*, Miriam Römer[2] and Andreas Lorke[3]

[1]Dr. Moses Strauss Department of Marine Geosciences, Leon H. Charney School of Marine Science, University of Haifa, Haifa, Israel, [2]MARUM - Center for Environmental Sciences and Department of Geosciences at the University of Bremen, Bremen, Germany, [3]Institute for Environmental Sciences, University of Koblenz-Landau, Landau, Germany

KEYWORDS

bubbles, methane, gassy sediment, global warming, sediment destabilization

Editorial on the Research Topic
The lifetime of methane bubbles through sediment and water column

Gassy sediments of inland waters and oceans are abundant over the Earth. They host methane (CH_4), a potent greenhouse gas with a warming potential 27 times greater than CO_2 over a 100-years time span, whose concentration in the atmosphere has been rising by 1% per year over the last century (Forster et al., 2021).

CH_4 bubbles are discrete bodies of immiscible gas in a surrounding medium (Boudreau, 2012). Their lifetime starts from nucleation under supersaturated conditions in sediment and proceeds by their growth and subsequent migration in sediment and water column driven by buoyancy. The bubbles are diffusion-fed from the surrounding field of dissolved CH_4 in sediment fuelled by microbial or thermogenic decomposition of organic matter, or by gas hydrate dissociation (Kvenvolden, 1988; Martens et al., 1998; Boudreau, 2012).

CH_4 bubble presence affects the structural integrity, load-bearing capabilities, and effective physical and mechanical properties of sediments (Wheeler, 1990). They are a source of a permanent concern due to their potential destabilization of coastal and aquatic infrastructure.

CH_4 emission from the aquatic sediments to the water column is often dominated by ebullition. CH_4 bubble pathways and thus carbon fluxes from the aquatic sediments into the water column are highly variable in time and space, suggesting their dependence on the ambient conditions: e.g., changing hydrostatic and even atmospheric pressure, temperature or particulate matter flux to sediment, which become increasingly important in the context of global warming and sea level rise. Gaseous CH_4 often liberates *via* spatially distributed small- and large-scale outlets: seeps, vents, mud volcanoes, and pockmarks, serving as hot spots of CH_4 emission. However, there is a large uncertainty in the emission estimates.

Despite the growing knowledge, there are still fundamental open questions regarding all aspects of the bubble lifecycle. The thirteen papers comprising this Research Topic

reflect the interdisciplinary nature of research on CH_4 bubble evolution in sediments and in the water column of inland waters and oceans. The contributions provide novel research results and methods for understanding the relevant processes, their temporal dynamics and spatial variability across different scales of the system. The order of the articles below follows the bubble lifecycle sequence.

Carty and Daigle studied the changes in geomechanical properties of the seafloor sediment in response to methane hydrate dissociation. Using a statistical model, they estimated organic carbon content in sediments along the U.S. Atlantic margin and used a one-dimensional sediment burial and methanogenesis model to simulate hydrate and gas formation at selected locations over a 120,000 years glacial cycle. In drained sediments, no failure was found to occur during hydrate dissociation. However, in undrained sediments, the criterion for shear failure is quickly met, even with low (e.g., between 0.2% and 1%) hydrate concentrations.

Madhusudhan et al. explore methane hydrate formation from CH_4 gas in water saturated sand by high-resolution synchrotron imaging. Hydrate develops at the outer bubble surface, which leads to a reduction in bubble size, bubble connectivity, and in origination of nano- to micro-sized bubbles. Effective medium rock physics modelling including a resonance effect shows that using an actual bubble size distribution rather than the uniform bubble size of the equivalent gas volume, produces more accurate geophysical gas estimates.

Painuly and Katsman studied a CH_4 bubble growth mechanism under the wave action, using a single-bubble mechanical/solute transport numerical model. Early and multiple sediment fracturing by the growing bubble manifested themselves at reduced overburden loads at wave troughs, amplified at shallow water depth. Bubbles matured in a shorter time in presence of waves, controlled by a larger wave amplitude to equilibrium water depth ratio and by a shorted wave period.

Marcon et al. (a) characterized spatio-temporal pattern in sediment gas content and its controls in a drinking water reservoir in Brazil. They used echo-sounding surveys to characterize the gassy sediment, and acoustic methodology for ebullition measurements in the water column. Correlations of sediment gas content with water depth, sediment thickness, and organic matter content were best reproduced by a trained artificial neural network model. The largest gas content was found in the shallower upstream part of the reservoir, accompanied by highest and continuous ebullition rates. In the deeper downstream part, elevated above the average gas content and intermittent ebullition dynamics were observed.

Yatsuk et al. report results of gas geochemical studies of seafloor sediments of the East Siberian Sea from three expeditions (2008, 2016, 2020). Increased concentrations of CH_4 and hydrocarbon gases encountered at some stations indicate a predominance of thermogenically derived gases. The stable isotopic composition of carbon was determined for CH_4, C_2H_6, and CO_2 in gases desorbed from marine sediments. The suggested hydrocarbon classification system outlines eight regional gas sources.

Rovere et al. describe their finding of dozens of flares in the southeastern Tyrranian Sea, originating in a hybrid volcanic-sedimentary basin. CH_4 and CO_2 release corresponds to areas of subsurface doming and diapirism that could be related to seafloor hydrothermal vent complexes fed by igneous intrusions. Their results indicate that magmatic activity has been the main driver of fluid flow in this area.

Silva et al. investigated the oil and gas release from a destroyed oil platform in the Gulf of Mexico. Atmospheric CH_4 measurements above the plumes revealed a ~6 times greater concentration than baseline. After installation of a containment device preventing oil release, the measurements showed only slightly elevated CH_4 concentrations although bubbles were still observed to rise. Oil was suggested as a greater source of CH_4 to the atmosphere than associated gas bubbles.

The study by Marcon et al. (b) focusses on gas emission variability using continuous long-term sonar monitoring offshore Vancouver Island. The results show that the diurnal and semi-diurnal tides influence the timing of the onset and cessation of bubble emissions, but the tides do not seem to modulate the vigor of the active gas emissions.

Turco et al. present a quantitative assessment of total CH_4 release on the Hikurangi Margin, off New Zealand. Using a split beam echosounder, the CH_4 fluxes at five seep sites releasing CH_4 bubbles were estimated at 8.66 and 27.21 kg $\times 10^6$ kg of CH_4 per year. The results were extrapolated on an existing gas seep database and reveal between 2.7×10^8 and 9.32 kg $\times 10^8$ kg of CH_4 released into the water column at the Hikurangi Margin each year.

Zhao et al. analysed continuous, high-frequency ebullition time series from a boreal pit lake during the open-water season. 22 out of the 24 ebullition events that were observed during the 4-month period occurred during low atmospheric pressure. The authors provide empirical equations that incorporate a pressure threshold to model the time-series of ebullition events and demonstrate good agreement between the observed and predicted ebullition fluxes.

Riedel et al. provide a synthesis of the research conducted over 20 years at a highly investigated seep area at Barkley Canyon, offshore Vancouver Island, characterized by thermogenic gas seepage and Structure II and Structure-H gas hydrate mounds. This site is situated on a remnant of a rotated fault block that had slipped off the canyon wall, and the location of the gas hydrate mounds is controlled by a combination of fault-focused fluid migration from a deeper reservoir and fluid

seepage along more permeable strata within the rotated slope block.

Veloso-Alarcón et al. calibrated lander-based hydroacoustic measurements of bubble flow rates using optical information and investigated the spatial and temporal variability of gas flow rates at a seep area offshore Oregon, United States. Optical measurements were obtained from a stereo camera and provided information on bubble size distributions and rising speeds, to quantify bubble flow rates within the ensonified area of a horizontally oriented multibeam echo sounder (~1700 m^2). The explored bubble streams revealed a modulation of the gas flux by near-bottom-currents associated with the tidal regime.

Snyder et al. report on gas plumes in the Tartar Strait, northernmost Japan Sea, and analysed their interaction with water masses and the degree of their contribution to greenhouse gas emissions. Their results point on a key role of the Amur River discharge in determining shallow, subsurface and even intermediate water circulation in the Tatar Strait. The atmospheric CH_4 fluxes demonstrated no enrichment compared to a reference site estimated in 2019, while fluxes above the plumes were much higher in 2015.

Author contributions

All authors listed have made a substantial, direct, and intellectual contribution to the work and approved it for publication.

Conflict of interest

The authors declare that the research was conducted in the absence of any commercial or financial relationships that could be construed as a potential conflict of interest.

Publisher's note

References

Boudreau, B. P. (2012). The physics of bubbles in surficial, soft, cohesive sediments. *Mar. Pet. Geol.* 38, 1–18. doi:10.1016/j.marpetgeo.2012.07.002

Forster, P., Storelvmo, T., Armour, K., Collins, W., Dufresne, J.-L., Frame, D.; IPCC, et al. (2021). "The earth's energy budget, climate feedbacks, and climate sensitivity," in *Climate change 2021: The physical science basis. Contribution of working group I to the sixth assessment report of the intergovernmental panel on climate change [Masson-Delmotte, V.* Editors P. Zhai, A. Pirani, S. L. Connors, C. Péan, S. Berger, N. Caud, et al. (Cambridge, United Kingdom and New York, NY, USA: Cambridge University Press), 923–1054. doi:10.1017/9781009157896.009

Kvenvolden, K. A. (1988). Methane hydrate - a major reservoir of carbon in the shallow geosphere? *Chem. Geol.* 71, 41–51. doi:10.1016/0009-2541(88)90104-0

Martens, C. S., Albert, D. B., and Alperin, M. J. (1998). Biogeochemical processes controlling methane in gassy coastal sediments - Part 1. A model coupling organic matter flux to gas production, oxidation and transport. *Cont. Shelf Res.* 18, 1741–1770. doi:10.1016/s0278-4343(98)00056-9

Wheeler, S. J. (1990). Movement of large gas bubbles in unsaturated fine grained sediments. *Mar. Geotechnol.* 9 (2), 113–129. doi:10.1080/10641199009388234

frontiers in Earth Science

ORIGINAL RESEARCH
published: 02 March 2022
doi: 10.3389/feart.2022.834047

Estimates of Methane Release From Gas Seeps at the Southern Hikurangi Margin, New Zealand

Francesco Turco[1,2], Yoann Ladroit[2,3,4], Sally J. Watson[2]*, Sarah Seabrook[2], Cliff S. Law[2,5], Gareth J. Crutchley[6], Joshu Mountjoy[2], Ingo A. Pecher[7], Jess I. T. Hillman[8], Susi Woelz[2] and Andrew R. Gorman[1]*

[1]Department of Geology, University of Otago, Dunedin, New Zealand, [2]National Institute of Water and Atmospheric Research (NIWA), Wellington, New Zealand, [3]ENSTA Bretagne Rue François Verny, Brest, France, [4]Institute for Marine and Antarctic Studies, University of Tasmania, Battery Point, TAS, Australia, [5]Department of Marine Sciences, University of Otago, Dunedin, New Zealand, [6]GEOMAR Helmholtz Centre for Ocean Research Kiel, Kiel, Germany, [7]School of Environment, University of Auckland, Auckland, New Zealand, [8]GNS Science, Avalon, New Zealand

OPEN ACCESS

Edited by:
Miriam Römer,
University of Bremen, Germany

Reviewed by:
Adam Skarke,
Mississippi State University, United States
Zhilei Sun,
Qingdao Institute of Marine Geology (QIMG), China

***Correspondence:**
Francesco Turco
francesco.turco@niwa.co.nz
Sally J. Watson
Sally.Watson@niwa.co.nz

Specialty section:
This article was submitted to Marine Geoscience, a section of the journal Frontiers in Earth Science

Received: 12 December 2021
Accepted: 04 February 2022
Published: 02 March 2022

Citation:
Turco F, Ladroit Y, Watson SJ, Seabrook S, Law CS, Crutchley GJ, Mountjoy J, Pecher IA, Hillman JIT, Woelz S and Gorman AR (2022) Estimates of Methane Release From Gas Seeps at the Southern Hikurangi Margin, New Zealand. Front. Earth Sci. 10:834047. doi: 10.3389/feart.2022.834047

The highest concentration of cold seep sites worldwide has been observed along convergent margins, where fluid migration through sedimentary sequences is enhanced by tectonic deformation and dewatering of marine sediments. In these regions, gas seeps support thriving chemosynthetic ecosystems increasing productivity and biodiversity along the margin. In this paper, we combine seismic reflection, multibeam and split-beam hydroacoustic data to identify, map and characterize five known sites of active gas seepage. The study area, on the southern Hikurangi Margin off the North Island of Aotearoa/New Zealand, is a well-established gas hydrate province and has widespread evidence for methane seepage. The combination of seismic and hydroacoustic data enable us to investigate the geological structures underlying the seep sites, the origin of the gas in the subsurface and the associated distribution of gas flares emanating from the seabed. Using multi-frequency split-beam echosounder (EK60) data we constrain the volume of gas released at the targeted seep sites that lie between 1,110 and 2,060 m deep. We estimate the total deep-water seeps in the study area emission between 8.66 and 27.21 $\times 10^6$ kg of methane gas per year. Moreover, we extrpolate methane fluxes for the whole Hikurangi Margin based on an existing gas seep database, that range between 2.77×10^8 and 9.32×10^8 kg of methane released each year. These estimates can result in a potential decrease of regional pH of 0.015–0.166 relative to the background value of 7.962. This study provides the most quantitative assessment to date of total methane release on the Hikurangi Margin. The results have implications for understanding what drives variation in seafloor biological communities and ocean biogeochemistry in subduction margin cold seep sites.

Keywords: gas seeps, methane flux, Hikurangi Margin, hydroacoustics, water column imaging

INTRODUCTION

Methane forms in marine sediments that are rich in organic matter through either microbial methanogenesis or thermogenic processes (Schoell, 1988). Methane formation occurs at different depths in the subsurface but, because of the buoyancy of the gas, it migrates upwards through pathways that include permeable carrier sedimentary units, faults, or densely fractured regions (Cook and Malinverno, 2013; Crutchley et al., 2015; Nole et al., 2016; Hillman et al., 2017; Hoffmann et al., 2019; Hillman et al., 2020). When these pathways connect to the surface, gas bubbles escape the seafloor as gas seeps, which can range from diffusive sporadic and localized emanations of bubbles to widespread, vigorous gas seeps, occurring in different geological contexts, from the coastal environments to deep ocean regions (Judd, 2004; Duarte et al., 2007; Watson et al., 2020). In shallow waters—up to 800 mbsl, the gas bubbles can reach the sea surface and release greenhouse gases into the atmosphere (Schmale et al., 2005), having direct implications for climate. In deeper seas, however, most of the gas that is released at the seabed dissolves into the ocean without reaching the sea surface, causing localized methane-induced seawater acidification over long time scales (Law et al., 2010; Biastoch et al., 2011; Garcia-Tigreros et al., 2021).

Seismic and acoustic methods are useful tools to identify, map and characterize free gas accumulations in the subsurface (e.g., Judd and Hovland, 1992; Kim et al., 2020), evidence for past and present seepage at the seafloor (e.g., Stott et al., 2019) and gas release into the water column (e.g., Colbo et al., 2014; Böttner et al., 2020). In the subsurface, the presence of gas in the pore-space significantly affects the elastic properties of the bulk sediment, primarily by reducing the bulk seismic velocities and generating a contrast in acoustic impedance. The detection, mapping and characterization of subsurface gas reservoirs are parts of the traditional hydrocarbon exploration workflow (Yilmaz, 2001). Low seismic velocities, often associated with fluid migration through geological structures such as chimneys, conduits, and faults, can be an indicator of free gas in the sediments.

In the ocean, columns of rising gas bubbles (also called flares for the typical shape they assume in hydroacoustic imaging) are less dense than seawater and thus represent strong acoustic reflectors, as they generate sharp localized changes in the acoustic impedance of the water column. Calculating methane fluxes at a seep site is challenging, as it requires ground-truth information about bubble size distribution, chemical composition, density, bubble coating, and ascending speed (Leblond et al., 2014). Typically, gas bubbles released at the seafloor tend to have a radius in the range of 1–15 mm (Veloso et al., 2015), resonating at frequencies from a few hundred Hz to ~12 kHz, depending on depth and size (Weidner et al., 2019). Single-frequency sonar systems have been successfully used for the identification of seep sites and for water column imaging for decades (e.g., Merewether et al., 1985; Hornafius et al., 1999; Nikolovska et al., 2008). However, these instruments cannot be used to determine the size distribution of the bubble population.

A common approach for the estimation of gas fluxes is coupling acoustic imaging of the gas bubbles with optical point-source measurements from towed camera systems (Higgs et al., 2019), remotely operated vehicles (Naudts et al., 2010), bubble observation modules (Bayrakci et al., 2014) or bubble traps (Römer et al., 2012). Although these point-source measurements provide the most accurate observation of bubble parameters, they require long deployment durations and a restricted field of view of less than ~15 m. Moreover, they are also limited to measurements at the seafloor, and cannot provide a way to track the changes in bubble size distribution as they rise through the water column. Broadband hydroacoustic methods provide a more efficient tool to directly estimate bubble parameters by insonifying large areas of the oceans using a range of frequencies (e.g., Veloso et al., 2015; Colbo et al., 2014; Dupré et al., 2015; von Deimling et al., 2011; Li et al., 2020).

The highest concentration of cold seep sites worldwide has been observed along convergent margins, (Saffer and Tobin, 2011; Suess, 2020; Watson et al., 2020). In these regions, gas flares observed at the seabed and other shallow gas migration features are often connected to subsurface methane reservoirs through gas conduits (e.g., Meldahl et al., 2001; Petersen et al., 2010; Krabbenhoeft et al., 2013; Crutchley et al., 2021). On the seafloor, gas seeps are the most common manifestations of ongoing subsurface fluid flow (Judd and Hovland, 2009). The gases that are expelled from gas seeps on continental margins are primarily composed of methane, leaving major questions open on: 1) the amount of methane reaching the ocean surface (McGinnis et al., 2006; Shakhova et al., 2010; Fu et al., 2020), 2) the connectivity of seeps to deeper hydrocarbon systems (Crutchley et al., 2021), 3) the role of gas hydrate dissociation (Reagan et al., 2011), 4) how gas flux rates change over time and the potential influence of seismicity on subsurface fluid flow (Bassett et al., 2014; Bonini, 2019; Legrand et al., 2021). The southern Hikurangi Margin, off the North Island of Aotearoa/New Zealand, reveals evidence of widespread methane seepage (Greinert et al., 2001; Barnes et al., 2010; Watson et al., 2020). The accretionary wedge here consists of a series of thrust-related ridges striking NE-SW, composed of compressed and deformed sediments, probably turbidites and ancient trench-fill deposits (Kroeger et al., 2015; Lewis et al., 1998). Seismic data show evidence of concentrated gas hydrate accumulations in the core regions of many thrust ridges in this region, indicating the preferential migration of free gas along permeable strata towards the core of anticlinal structures (Crutchley et al., 2019; Turco et al., 2020; Wang et al., 2017a; Schwalenberg et al., 2010; Kroeger et al., 2021). Estimation of gas fluxes at gas seeps on the Hikurangi Margin has so far relied on *in situ* optical measurements of gas bubbles (Naudts et al., 2010; Higgs et al., 2019) combined with single-beam acoustic data.

In this paper, we use a combination of seismic and acoustic data to characterize five known sites of active gas seepage on the southern Hikurangi Margin. The interpretation of seismic amplitudes provides a means to identify regions of free gas accumulations within the sediments. Qualitative analysis of multibeam data collected over 3 years allows the spatial extent of the region of active venting at the seafloor to be mapped, while

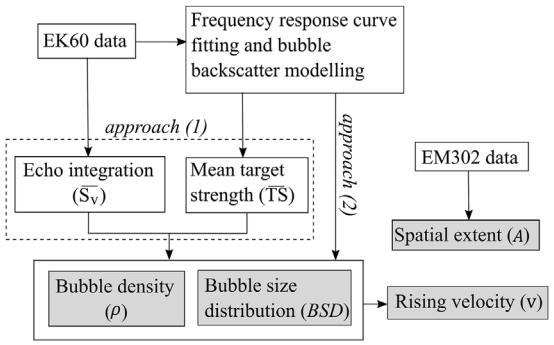

FIGURE 1 | Illustration of the workflow to estimate gas fluxes from MBES (EM302) and single-beam (EK60) backscatter data. Approach (1) is based on the manual curve fitting of the normalized frequency response of the 18 and 38 kHz channels of the EK60 data, while approach (2) is based on a linear inversion of the non-normalized frequency response. S_v, mean volume backscattering strength computed for each cell; $\overline{TS}$, mean target strength computed for the whole acoustic flare; ρ, density of bubbles; *BSD*, bubble size distribution; v, bubble rising velocity; A, spatial extent of acoustic anomaly.

also imaging the acoustic flares in the water column and analyzing their variability over time. Split-beam echo sounder data are used to extract important parameters for the quantification of gas bubbles in the water from the backscattered acoustic energy, which are then used to calculate gas fluxes at the cold seep locations.

DATA AND METHODS

Acoustic Data Processing

The identification and mapping of gas seeps in deep waters was achieved through the analysis of acoustic data (**Figure 1**). Bathymetric and water column data were acquired during three scientific voyages onboard the R/V Tangaroa (**Figure 2**): TAN1808 (September-October 2018), TAN1904 (July 2019) and TAN2012 (November 2020).

Swath bathymetry and acoustic backscatter of mid-water reflectors were collected with a hull-mounted Kongsberg EM302 multibeam echo-sounder during the three voyages. The EM302 echo sounder operates at a nominal frequency of 30 kHz and with a swath of ~120°. The use of the multibeam data was twofold: 1) to accurately locate gas seeps on the seafloor and 2) to calculate the area of seepage at the seafloor. For the former objective, the data were processed using the National Institute of Water and Atmospheric Research (NIWA) custom-built software *Espresso* with the following steps: seafloor detection filtering, removal of the outermost noisy beams (>45°), removal of bad pings, filtering side lobe artefacts and muting the first 5 m of data above the automatically picked seafloor, to avoid misinterpreting

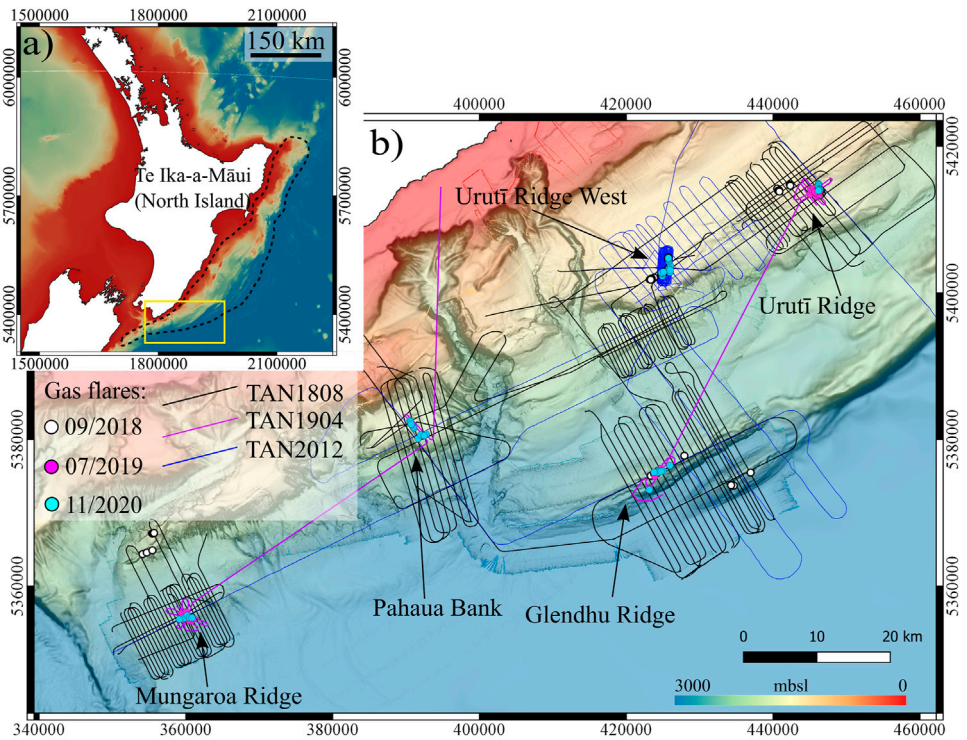

FIGURE 2 | (A) Overview of the Hikurangi subduction Margin of New Zealand (dashed black line) and the study area (yellow rectangle). **(B)** expansion of the study area on the southern Hikurangi Margin: white, cyan and magenta dots are gas flares identified from the MBES data from the three R/V Tangaroa voyages (TAN1808, TAN1904, TAN2012). The five target areas are mentioned in the text. Map coordinates are in metres of New Zealand Transverse Mercator 2000 (New Zealand Geodetic Datum 2000).

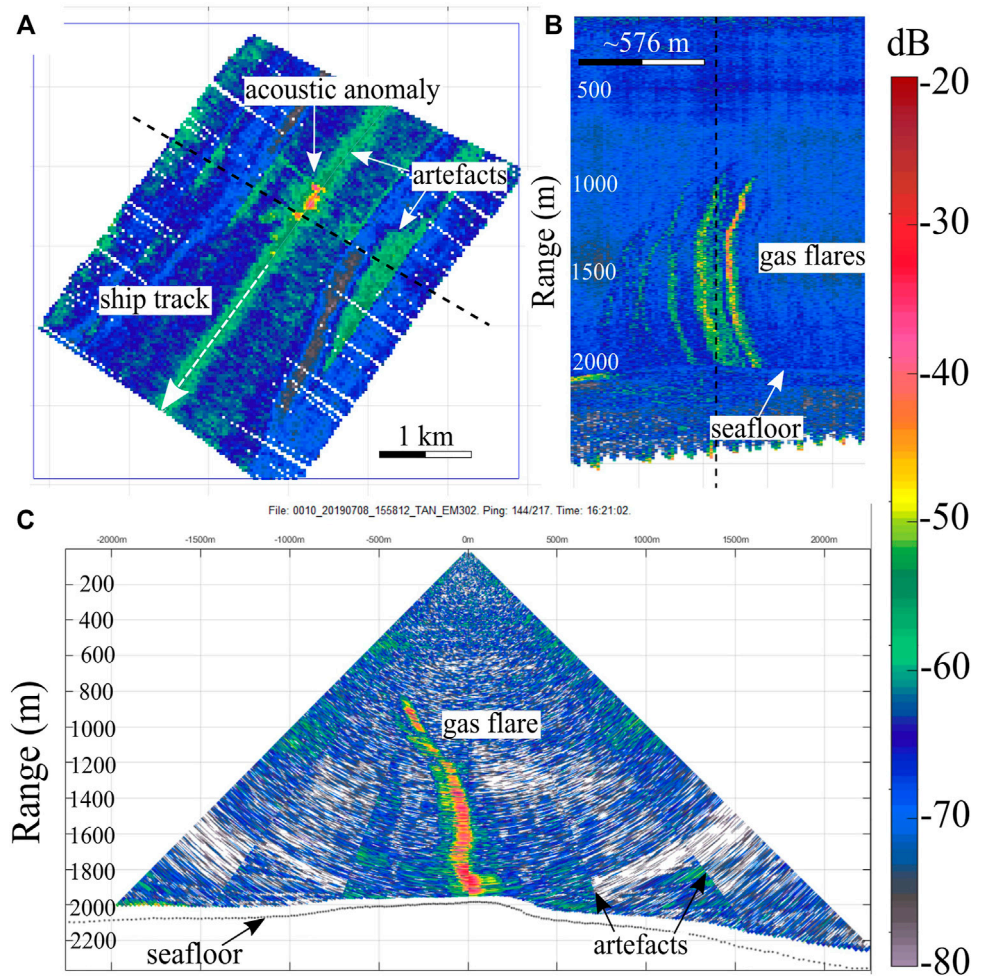

FIGURE 3 | Backscatter intensity images of the Glendhu seep field (see **Figure 2** for location) from multibeam data. **(A)** echo integrated map (resolution 20 × 20 m); **(B)** range stacked view along the profile shown in a); **(C)** fan view at the location indicated by the dashed black line in **(A)**.

the smearing of the beams at the seafloor as gas bubbles (Schimel et al., 2020). The correct pinpoint (as well as could be determined) of seepage at the seafloor was facilitated by the fan visualization of MBES data (**Figure 3**). To calculate the total area of gas seepage in proximity of the seafloor, the processed data were vertically summed over a window between 5 and 20 m above the seabed - a process known as echo integration (MacLennan et al., 2002). The output of this process is a georeferenced image of volume backscatter intensity with a horizontal spatial resolution of 15 m × 15 m, that allowed mapping the spatial extent of the acoustic anomaly in the water column.

A suite of 5 Simrad EK60 echo sounders were used to obtain calibrated acoustic measurements of the water column during TAN1904 and TAN2012 voyages. The data were acquired over the five targeted areas based on existing multibeam coverage. These split-beam systems were calibrated using a standard 38.1 mm tungsten sphere hung under the vessel, following standard procedures (Demer et al., 2015). Given the relatively great water depth of most targeted flares (>1,000 mbsl), only the 18 and the 38 kHz echo sounders had sufficient range to image the full vertical extent of the gas bubbles. The two-way beam angle of the EK60 echo sounder is 11° for the 18 kHz system and 7° for the 38 kHz one. We extracted and processed the data recorded for the targeted gas flares using the open-source software package ESP3 (Ladroit et al., 2020). The data were processed to only extract the acoustic signal associated with gas venting. The processing included seafloor echo detection and removal, bad ping removal and de-noising (De Robertis and Higginbottom, 2007). Once acoustic flares were identified and extracted, we carried out frequency analysis on the pre-processed split-beam data and compared the frequency response to theoretical bubble backscatter models to estimate the bubble size distribution (*BSD*) of the entire flare (**Figure 1**). Finally, we echo integrated the processed 18 kHz data using cells 25 m high and 10 m wide, in order to retrieve a mean volume backscattering strength ($\overline{S_v}$) response for each cell.

Estimation of Gas Fluxes

Existing theoretical models to predict the acoustic backscattering cross-section (σ_{bs}) of underwater bubbles differ in terms of

parameters such the bubble size distribution (*BSD*), bubble morphology, the frequency range of the acoustic signal and the environment characteristics. For the scope of this work, we adopt the model proposed by Ainslie and Leighton (2009). For a more complete overview of the definitions and terminology used in underwater acoustics and adopted in this work the reader is referred to, e.g., MacLennan et al. (2002).

The workflow to estimate gas fluxes at the seep locations is illustrated in **Figure 1**. To estimate the *BSD* and density, we followed two approaches, one based on the normalized frequency response of the 18 and 38 kHz channels of the EK60 data, and one based on the non-normalized frequency response, similarly to the approach used by Li et al. (2020).

In the first approach (1), gas flares were isolated using the 18 kHz data, and they were echo integrated using a variable cell size ranging from 25–50 m in height and 5–10 m in width. The echo integration process yields a mean volume backscattering strength ($\overline{S_v}$) for each cell of the acoustic flare. The frequency analysis of the gas plume from both the 18 and 38 kHz channels, normalized relatively to the 38 kHz S_v values, provides frequency-dependent S_v values that the theoretical backscatter model curves aim to match. The curve-matching procedure was achieved through manual tuning of the mean bubble radius and bubble size distribution. When the match is considered satisfactory, i.e., when the residuals between the observed and the theoretical S_v are below a chosen threshold for each water depth, the resulting *BSD* is considered representative of the entire flare, and the mean backscattering cross-section is computed following:

$$\overline{\sigma_{bs}} = \frac{\int_0^{a_{max}} BSD(a)\sigma_{bs}(a)da}{\int_0^{a_{max}} BSD(a)da}, \tag{1}$$

where *BSD* is the bubble size distribution, and a the bubble radius. σ_{bs} is given byAinslie and Leighton (2009):

$$\sigma_{bs} = \frac{4\pi a^2}{\left(\frac{\omega_1^2}{\omega^2} - 1\right)^2 + \delta^2}, \tag{2}$$

where ω is the frequency of the active source of the acoustic signal, ω_1 is the resonance frequency of the bubble and δ is a dimensionless frequency-dependant damping constant. To retrieve the density of bubbles per volume unit, the mean volume backscattering strength $\overline{S_v}$ value of each cell of the echo integrated flare is compared to the representative mean target strength ($\overline{TS}$) value of the whole flare. **Eq. 3** relates the mean backscattering cross-section representative of the entire flare $\overline{\sigma_{bs}}$ (in m^{-1}, or expressed in decibels by $\overline{TS}$) to the mean volume backscattering coefficient of a given cell of the echogram $\overline{s_v}$ (m^2, or $\overline{S_v}$ in decibels), following:

$$\rho = \frac{\overline{s_v}}{\overline{\sigma_{bs}}}, \tag{3}$$

Then, ρ is averaged across cells located at the same water depth, hence a mean density of bubbles is estimated for each horizontal slice of the gas flare ($\bar{\rho}$).

The second approach (2) to retrieve *BSD* and $\bar{\rho}$ for each flare consists of a linear inversion technique that aims to minimize the difference between the modelled and the observed non-normalized volume scattering strengths at each depth of the acoustic flare. The forward modelled data are computed following the theoretical backscatter model by Ainslie and Leighton (2009), and the optimization is achieved through a conjugate gradient technique. The model parameters that are inverted are bubble size, bubble size distribution parameters (for a fixed distribution type) and density of bubbles per volume unit. These parameters are initialized using the results from the first approach and updated iteratively during the inversion. 100 iterations were performed on each flare, and the inversion was carried out twice, once assuming a log-normal type bubble size distribution (Veloso et al., 2015), and once assuming a Weibull type distribution (Dey and Kundu, 2012).

Once the *BSD* and $\bar{\rho}$ are known, the gas flux is estimated for the entire flare (which could represent a field of seeps) following **Eq. 4**:

$$flux = A\,\bar{\rho} \int_0^{a_{max}} \frac{4}{3}\pi a^3 BSD(a)\, v(a)\, da, \tag{4}$$

where A is the spatial extent of the acoustic anomaly in the proximity of the seafloor as interpreted from the processed MBES data, $\bar{\rho}$ is the mean density of bubbles in the water in m^{-3}, v(a) is the mean rising velocity of the gas bubbles, *BSD* is the bubble size distribution and a is the bubble radius. The bubble rise velocity valuesare based on the work by Leifer and Patro (2002) and consider the two endmembers clean and coated bubbles, where the latter model represents gas bubbles which are coated with oil or hydrate (Fu et al., 2020).

In the next section, the estimated gas fluxes are presented as ranges of values. The major source of variability in the flux estimations comes from the use of coated versus clean bubbles models: because clean bubbles rise faster than coated bubbles, changes in v have a linear effect on the fluxes (**Eq. 4**). Hydrate-coated bubbles have been observed at some of the seep sites analyzed in this paper (Sarah Seabrook, personal communication). However, due to the scarcity of observational data, we use both models to provide a range of possible gas flux estimates.The secondary source of uncertainty in the estimations is related to the approach used for the calculation of the *BSD* and density (**Figure 1**). These parameters impact both the mean rising velocity–which depends on the bubble size, and the volume of gas calculated at the seafloor.

Because of the lack of *in situ* chemical measurements at the locations of seepage, we assume that 100% of the gas released at the seeps is CH_4.

Seismic Data

High resolution seismic reflection data were acquired during the TAN1808 research cruise (**Figure 2**). A GI gun and a 600 m long streamer of 48 channels were used for the acquisition (Crutchley et al., 2018). The seismic data processing is described in detail by Turco et al. (2020) and included geometry application,

TABLE 1 | Overview of seeps observations based on MBES data.

Seep site	Number of acoustic flares (2018/2019/2020)	Flare height from seafloor (m) (2018/2019/2020)
Mungaroa Ridge	4/6/5	1,300/1,290/1,300
Glendhu Ridge	5/8/8	1150 210/1,200
Pahaua Bank	9/4/13	900/930/930
Urutī Ridge	17/14/9	390/470/460
Urutī Ridge West	11/n.a./18	500/n.a./600

Butterworth filtering (corner frequencies of 7, 14, 150, and 200 Hz), constant high-dip noise removal through FK filtering, corrections for spherical divergence correction (1,500 m/s), CDP sorting and NMO correction (1,500 m/s), stacking and post-stack Kirchhoff time migration. Due to the presence of gas hydrates within the sediments, we used a seismic velocity of 1700 m/s, based on the velocity analysis by Turco et al. (2020) to depth convert the seismic sections. The dominant frequency of the processed seismic data is 95 Hz, and the vertical resolution is approximately 4–5 m.

RESULTS

Identification of Gas Seeps

Gas seep sites are identified in the multibeam data by anomalously high acoustic backscatter in the water column with respect to the surrounding region. High backscatter values in the water could also indicate the presence of schools of fish, thermo-cline layering or artefacts. Given the ambiguity in interpreting vertically summed (echo integrated) backscatter intensity maps, we analysed horizontally stacked sections and fan-view images of backscatter intensity (**Figures 3B,C**, respectively) in the vicinity of the acoustic anomalies, to confidently interpret gas flares where regions of high backscatter intensity propagate from the seafloor upwards, as expected from a rising aggregate of gas bubbles. We analysed three datasets from different voyages that surveyed the same target areas (**Figure 2**). This approach ensures that we accurately pinpoint the location of gas venting at the seafloor and gives a temporal dimension to the study. In the study area, we identified a total of 129 individual gas flares: 46 from TAN1808, 32 from TAN1904 and 53 from TAN2012 datasets (**Table 1**). Most of these flares are located approximately at the same point on the seafloor in the three datasets; however, the difference in data quality and acquisition parameters does not allow a more detailed comparison between the three datasets. It is important to note that the flares observed in the acoustic data are presumably formed by multiple bubble outlets sited in an area that is smaller than the insonified seabed area. The lateral resolution of the MBES data at the seafloor depends on several factors such as beamwidth, water depth, survey speed and swath coverage. For our study area, the lateral resolution varies between 25 and 50 m. The five regions of focused gas seepage are: Urutī Ridge, Urutī Ridge West, Pahaua Bank, Glendhu Ridge and Mungaroa Ridge (**Figure 4**). Mungaroa Ridge is an informal name, which has not been officially gazetted by the New Zealand Graphic Board—Ngā Pou Taunaha o Aotearoa. The shallowest seeps occur at Urutī Ridge West at ~1,100 mbsl, while the deepest one is the Honeycomb Ridge seep, located in ~2,400 m water depth. There is no acoustic evidence that any of the analysed gas flares reaches the sea surface in the study area.

Gas Fluxes and Seismic Observations

In this section, we present the results of gas flux estimations for the five target areas (**Figure 5**) and analyse the local geological structure of these sites.

At each seep site, we selected one representative flare from the SBES data (shown in **Figures 7**–**10**). The selection was driven by data quality, representativeness of the flare for the entire seep field, and vicinity to the location of the seismic line. The selected flares were used to estimate bubble size parameters and bubble density, which were considered to be representative of all the seeps located in the same field.

The flux estimates provided in the following sections represent an average of the linear inversion method (Approach 2), while the comparison of the results of the manual curve fitting (Approach 1) is shown in **Figure 5** and in **Table 2**, together with the details of the parametrization of gas flares for each of the target sites.

The average thickness of the gas hydrate stability zone (GHSZ) varies according to the water depth and the geological context, from ~360 m at Urutī Ridge (1,200 mbsl) to ~630 m at Mungaroa Ridge (2,100 mbsl). Despite being visible throughout the five study areas, bottom-simulating reflections (BSR) associated with gas hydrate occurrence are discontinuous and cannot be observed directly below the locations of gas seepage. In **Figures 7**–**11**, the vertical and horizontal scales of the EK60 echograms showing the gas flares are approximately equal to the scales of the seismic image. It is important to note that the acoustic images of the water column show the apparent resolution of the EK60 data: the true horizontal resolution depends on the beamwidth and varies with depth following:

$$r = r^{*} - 2d\tan\left(\frac{\theta}{2}\right), \tag{4a}$$

Where r is the horizontal resolution, r^{*} is the apparent resolution, d is the water depth and θ is the beam aperture angle (**Figure 6**). Seismic velocity of 1700 m/s (Turco et al., 2020) was used to depth convert the seismic sections, whereas the echograms were depth-converted on-the-fly during data acquisition using sound velocity profiles. The dominant frequency of the processed seismic data is 95 Hz, and the vertical resolution is approximately 4–5 m. The acquisition and processing parameters of the seismic data are provided by Crutchley et al. (2018) and Turco et al. (2020), respectively.

Urut Ridge

The main Urutī Ridge seep field is located slightly seaward of the bathymetric high of the anticlinal ridge. The seepage occurs over ~4 km^2 of the seafloor, in water depths from 1,175 m to 1,300 m, and tens of flares can be identified from the acoustic data (17 flares identified in the 2018 datasets, 14 flares in 2019 and 9 in

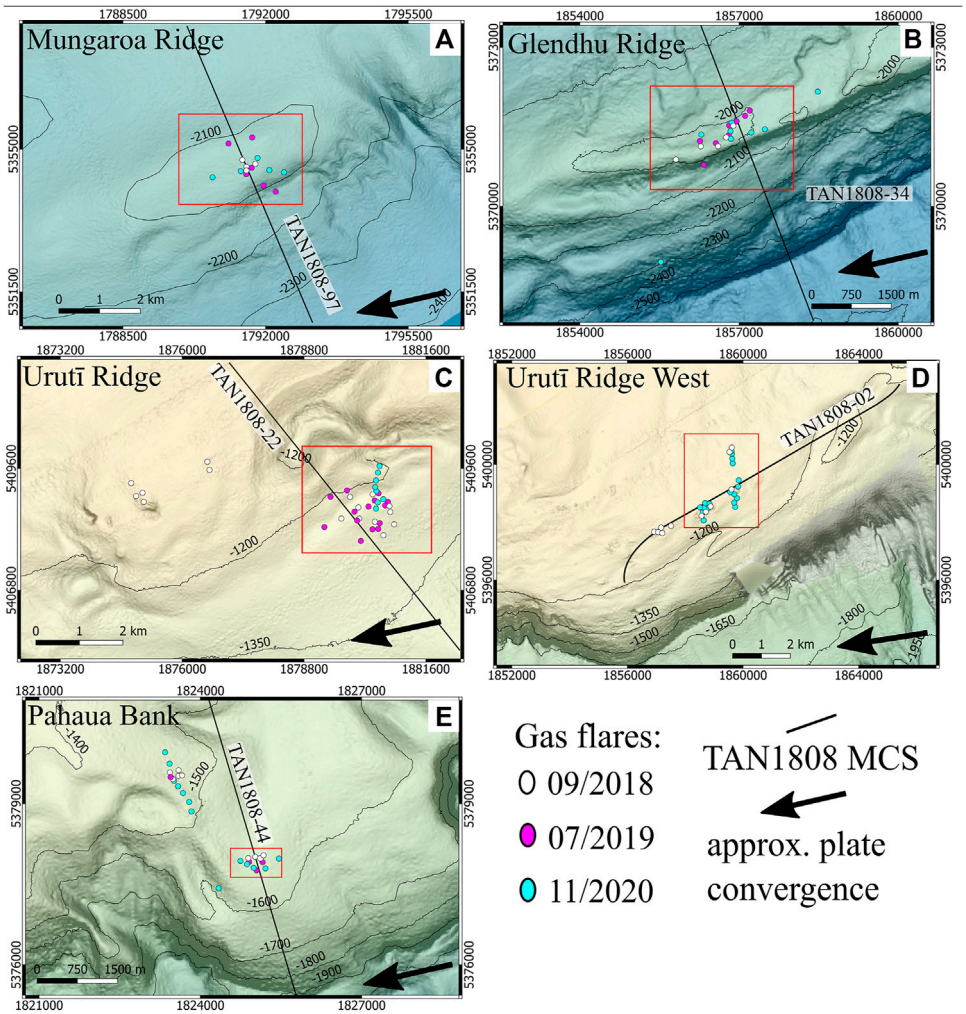

FIGURE 4 | Distribution of the gas flares identified in the five target areas: **(A)** Mungaroa Ridge; **(B)** Glendhu Ridge; **(C)** Urutī Ridge; **(D)** Urutī Ridge West; **(E)** Pahaua Bank. The approximate direction of plate convergence is extracted from the MORVEL online tool (Argus et al., 2011). MCS, multi-channel seismic data.

2020). The same flares were imaged in all surveys. Most acoustic flares reach ~700 m water depth, and the total area of high acoustic anomaly at 20 m above the seafloor measures 0.43 km^2. The easternmost flares imaged in the TAN2012 dataset seem to be aligned roughly NS, which is sub-perpendicular to the direction of plate convergence in this part of the margin. The main flare was selected from the total population of flares of this region to estimate the density of bubbles per cubic metre. Gas flux estimates for the entire seep field at Urutī Ridge range between 1.28 and 3.55 × 10^6 kg/year. The seismic profile shown in **Figure 7** runs perpendicular to the strike of the main anticlinal structure, and it crosses the seabed location of two major gas flares used for flux estimations. A broad extent of ~1 km of the shallow subsurface shows high-amplitude negative polarity reflections that reveal the presence of free gas in the sediments. The sedimentary sequence below this region is characterized by a general decrease in seismic amplitudes (seismic blanking) and disrupted reflections. The blanking zone in the overlying stratigraphic sequence is bounded in depth by a seismic unconformity that marks the top of a highly reflective unit of steeply dipping strata that form the seaward limb of the Urutī Ridge anticline. The amplitude of the BSR is higher to the NW and to the SE of the flare site, it fades out in the core region of the anticline, and it is not observed in the region of enhanced reflectivity on the seaward limb of the anticline.

Glendhu Ridge

Glendhu Ridge is a thrust-related elongated structural feature with four-way closure that lies close to the present-day deformation front. The anticlinal structure of the ridge is imaged in the seismic profiles and has been analysed in detail by Turco et al. (2020). There is no BSR below the seep location at the top of the ridge, similar to what is observed at Urutī Ridge (**Figure 7**). The main gas venting field is located right on the bathymetric crest of the ridge, at a water depth of about 2000 m, where 6–8 main acoustic flares can be identified from the multibeam data. The seeps are roughly aligned ENE-WSW, parallel to the long-axis of the four-way closure and sub-

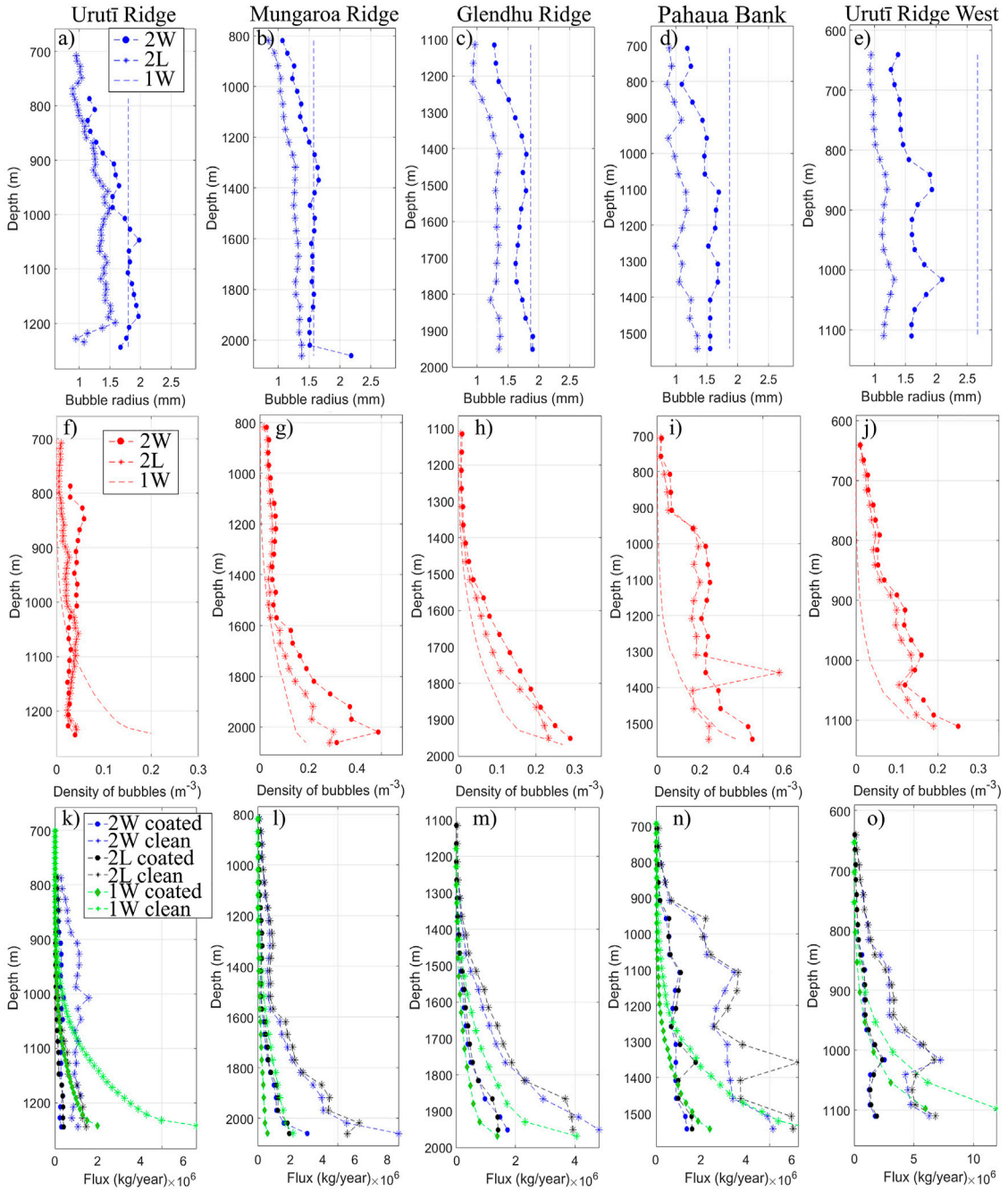

FIGURE 5 | Results of methane flux estimations for the five seep locations. **(A–E)** show the variations of the mean bubble radius versus depth; **(F–J)** show the mean density of bubbles and **(K–O)** show the mean methane fluxes calculated at depth with the clean and coated ascending velocity models. 2 W: linear inversion with Weibull distribution; 2 L: linear inversion with log-normal distribution; 1 W: manual curve fitting with Weibull distribution.

parallel to the vector of plate convergence (**Figure 4B**). For the parametrization of this gas seep field, we used the main acoustic flare visible in **Figure 8**, which rises from the seafloor for roughly 1,200 m reaching a depth of ~780 mbsl. The area of acoustic anomaly at this site is 0.17 km^2, yielding total gas flux estimates of 1.57 and 4.34 × 10^6 kg/year, considering coated and clean bubbles, respectively.

Pahaua Bank

Pahaua Bank is a submarine ridge located on the mid-slope portion of the accretionary wedge, at water depths of 1,450–1,570 m. There are two regions of gas seepage at the seafloor: the northernmost group of gas seeps includes at least seven distinct flares aligned NNW-SSE, perpendicular to the direction of plate convergence (**Figure 4E**). The southernmost

TABLE 2 | Details of bubble size parameters, density of bubbles, mean gas fluxes and seep water depth for the five target areas.

Seep	Mean bubble radius in mm (2 W)-(2 L)-(1 W)	Density of bubbles in m^{-3} (2 W)-(2 L)-(1 W)	Mean flux in kg/year linear inversion (coated/clean)*	Seafloor depth in m	Difference method 1 vs. 2 (clean/coated)
Mungaroa Ridge	2.18–1.38—1.57	0.316–0.288–0.189	$2.52/7.19 \times 10^6$	2060	+69%/+76%
Glendhu Ridge	1.90–1.35–1.87	0.288–0.232–0.268	$1.57/4.34 \times 10^6$	1950	+7%/+11%
Pahaua Bank	1.56–1.35–1.87	0.450–0.244–0.374	$1.47/5.58 \times 10^6$	1,550	−20%/−60%
Urutī Ridge West	1.60–1.15–2.67	0.25–0.190–0.129	$1.82/6.54 \times 10^6$	1,110	−82%/−210%
Urutī Ridge	1.67–1.08–2.25	0.039–0.042–0.128	$1.28/3.55 \times 10^6$	1,240	−410%/−450%

Column 2 and 3 show the results of the two approaches to estimate bubble parameters: (2 W): linear inversion with Weibull distribution; (2 L): linear inversion with log-normal distribution; (1 W): manual curve fitting with Weibull distribution. All values are calculated at the seafloor. Column 6 shows the difference between the manual curve fitting method and the linear inversion approach.

**The fluxes presented in this table are the averaged fluxes calculated using the linear inversion results only (2L and 2 W methods).*

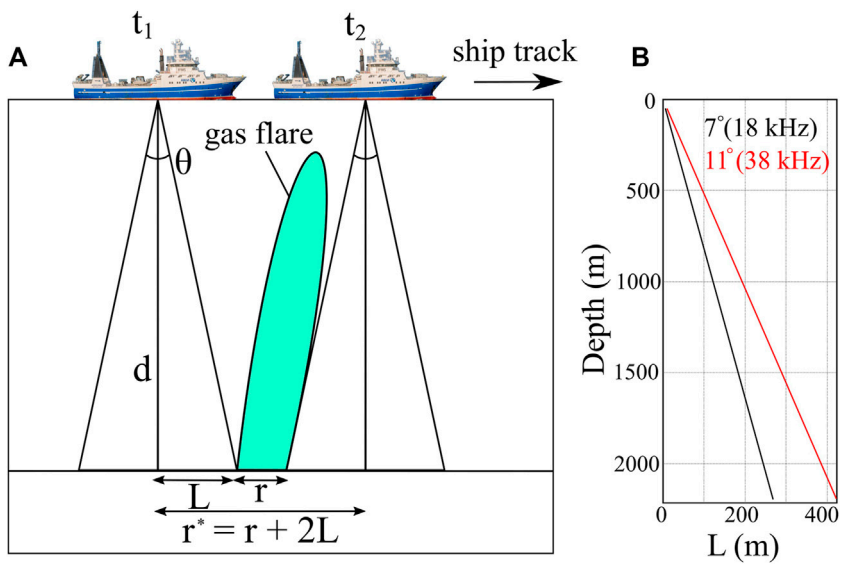

FIGURE 6 | (A) Graphical illustration of the lateral resolution of the acoustic images of the single-beam (EK60) data. **(B)** Plot showing the dependence of the lateral resolution (L) on water depth and beam angle.

group consists of at least six flares rising from 1,560 m. In both groups, the acoustic signature of the rising bubbles reaches the depth of ~750 mbsl. The total area of acoustic anomaly close to the seafloor measures 0.21 km^2. One flare from the southernmost group was used for bubble size and density parametrization, yielding gas flux estimates between 1.47 and 5.58×10^6 kg/year for this site. The seismic data reveal a ~400 m long, strong reflection with negative polarity right below the seabed at the location of gas seepage, indicative of widespread free gas in the shallow sediments (**Figure 8C**). Below the free gas accumulation, a column-shaped region of localised seismic blanking extends downwards towards the base of the GHSZ, in a region of disrupted reflections in the vicinity of an apparent BSR shoaling.

Urut Ridge West

This is the shallowest of the analysed seep fields, and it lies in a region of relatively flat bathymetry at ~1,140 m water depth. Urutī Ridge West is a SW-NE trending anticline that represents the southern extension of Urutī Ridge. The seismic profile shown in **Figure 9** runs parallel to the strike of the anticline, and crosses two areas of gas seepage. The sedimentary sequence is characterised by relatively flat and parallel strata. The thickness of the GHSZ at Urutī Ridge West is ~0.5 s, or ~450 m using an estimated seismic velocity of 1800 m/s. While the BSR appears as a distinct negative polarity reflection adjacent to the seep locations, it is characterised by a series of lower amplitude reflections in the central part of the seismic profile, and it is not imaged beneath the regions of gas expulsion. High amplitude reflections with the same polarity as the seafloor probably point to the presence of concentrated gas hydrates or authigenic carbonates in the shallow sediments, while column-shaped regions of seismic blanking suggest upward fluid migration from the base of gas hydrate stability (BGHS) towards the seafloor. Similar to the Urutī Ridge eastern flares

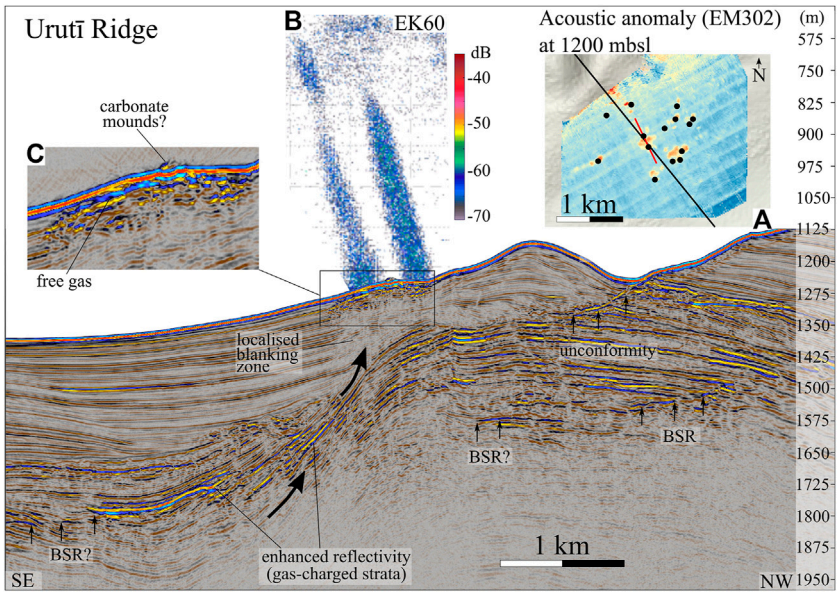

FIGURE 7 | Overview of the Urutī Ridge seep site: the interpreted TAN1808-22 seismic profile is shown in the main panel. The bold black arrows represent the direction of fluid flow as interpreted from the seismic data and explained in the text. BSR, bottom simulating reflection. **(A)** Map view of the Urutī Ridge seeps (red box in **Figure 4C**), showing the acoustic backscatter anomaly in the echo integrated MBES (EM302) data in proximity of the seafloor. The location of the TAN1808-22 seismic line and of the single-beam data (EK60) are indicated by the black and the red lines, respectively. The black dots represent the location of the main gas flares. The hydroacoustic data were collected during the TAN1904 voyage. **(B)** Echogram of two gas flares as imaged by the 18 kHz channel in the single-beam data. The horizontal scale is the same as the seismic panel. **(C)** Expanded view of the seismic data showing the shallow region beneath the cold seeps.

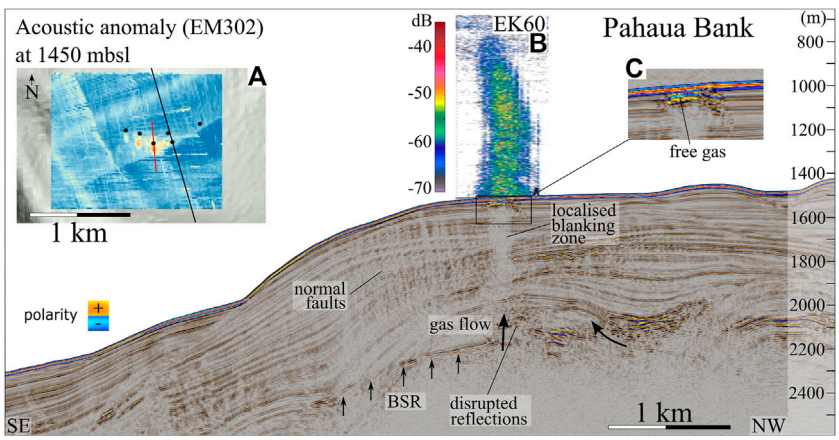

FIGURE 8 | Overview of the Pahaua Bank seep site: the interpreted TAN1808-44 seismic profile is shown in the main panel. The bold black arrows represent the direction of fluid flow as interpreted from the seismic data and explained in the text. BSR: bottom simulating reflection. **(A)** Map view of the Pahaua Bank seeps (red box in **Figure 4E**), showing the acoustic backscatter anomaly in the echo integrated MBES (EM302) data in proximity of the seafloor. The location of the TAN1808-44 seismic line and of the single-beam data (EK60) are indicated by the black and the red lines, respectively. The black dots show the locations of the main gas flares. The hydroacoustic data were collected during the TAN1904 voyage. **(B)** Echogram of a gas flare as imaged by the 18 kHz channel in the single-beam data. The horizontal scale is the same as the seismic panel. **(C)** Expanded view of the seismic data showing the shallow region beneath the cold seeps, where free gas accumulation is inferred by the negative polarity reflection.

and to the Pahaua Bank northern flares, the gas flares at Urutī Ridge West are aligned roughly perpendicularly to the direction of plate convergence. The 18 imaged flares can be grouped into four clusters (**Figure 4D**), and they rise ~500 m from the seafloor. One flare was selected to estimate bubble parameters (see **Table 2**). With a total area ~0.45 km^2 of acoustic anomaly, the gas flux estimates for the Urutī Ridge West venting field lie between 1.82 and 6.54 × 10^6 kg/year.

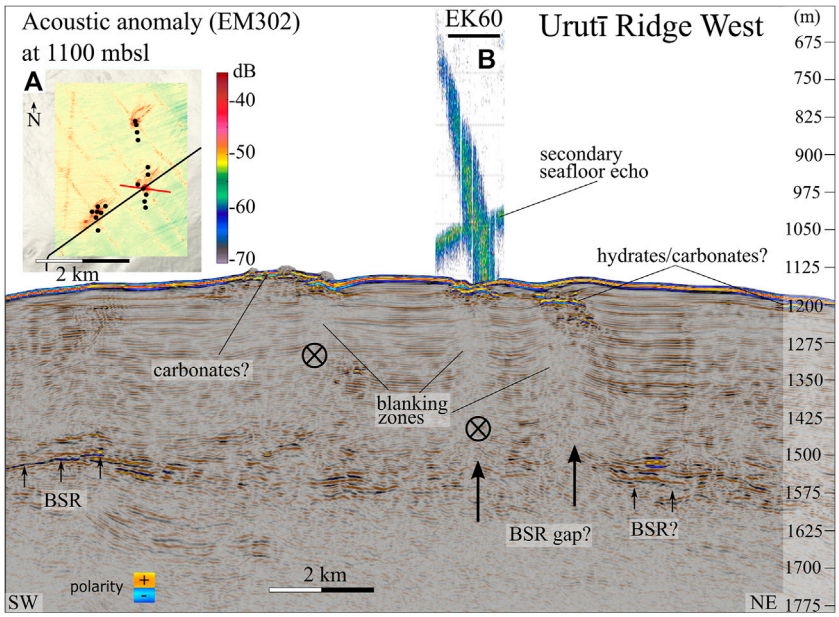

FIGURE 9 | Overview of the Urutī Ridge West seep site: the interpreted TAN1808-02 seismic profile is shown in the main panel. The black arrows show the direction of fluid flow as interpreted from the seismic data and explained in the text. The black crossed circles represent the direction of fluid flow going into the page. BSR: bottom simulating reflection. **(A)** Map view of the Urutī Ridge West seeps (red box in **Figure 4D**), showing the acoustic backscatter anomaly in the echo integrated MBES (EM302) data in proximity of the seafloor. The location of the TAN 1808-02 seismic line and of the single-beam data (EK60) are indicated by the black and the red lines, respectively. The black dots show the locations of the main gas flares. The hydroacoustic data were collected during the TAN2012 voyage. **(B)** Echogram of a gas flare as imaged by the 38 kHz channel in the single-beam data. The horizontal scale is the same as the seismic panel.

Mungaroa Ridge

The Mungaroa seep field (**Figure 10**) is the deepest analysed in this study, with its main gas flare located at 2080 mbsl at the top of Mungaroa Ridge, a thrust-related four-way closure that lies at the toe of the accretionary wedge. Crutchley et al. (2021) investigated the gas hydrate system and fuid flow processes at Mungaroa Ridge in detail, using seismic reflection and multibeam data. They interpreted a gas-water contact pointing to a thick free gas column beneath the BGHS (**Figure 10**). This gas column is sufficiently thick to cause hydraulic fracturing through the gas hydrate stability zone, which is evidenced by a vertical chimney structure connecting the gas reservoir to the seafloor gas flare. Despite the existence of normal faults beneath the ridge, Crutchley et al. (2021) noted that they are not exploited for focused gas flow into the hydrate stability zone. We surveyed the region of gas seepage at the seafloor of Mungaroa Ridge during the three R/V Tangaroa voyages. From these data, we observed six flares rising from the seabed up to roughly 600 mbsl, making them the highest flares observed in the region (~1,400 m high). The estimated methane fluxes at this site range from 2.52 to 7.18 $\times$ 10^6 kg/year.

DISCUSSION

The quantitative study of water column acoustic backscatter data combined with observations of subsurface geological structures has allowed a detailed characterisation of the five targeted cold seep areas on the southern Hikurangi Margin.

Sources of Uncertainty for Flux Estimations

There are several sources of uncertainty in the resulting estimations of gas fluxes at the seafloor.

The major source of uncertainty comes from the theoretical model used to predict bubble rising velocities. Because of the lack of quantitative observational data in the study area, we opted for using both clean and coated bubble models (Leifer and Patro, 2002) for our flux estimates.

Another type of uncertainty to be considered is related to instrumental parameters, that account for uncertainties of calibration, sound-velocity profiles and absorption rates. The calculated uncertainty for the SBES absolute backscatter measurements is ~0.2 dB. The uncertainty of the absolute S_v backscatter data will propagate on through the calculation of both *BSD* parameters and density of bubbles and will eventually affect flux estimations. However, due to the relatively high precision of the echo-sounders, we deem the effect of instrumental uncertainty negligible compared to the other sources of variability described in this and in the next section.

For the MBES data, usually 1–2% of the water depth is considered a conservative uncertainty in terms of positioning of soundings. Considering the deepest flare at Mungaroa Ridge (2080 mbsl) the highest uncertainty related to the spatial extent of the acoustic anomalies in the MBES data is of ~1,600 m^2. This translates in $\pm 2 \times 10^4$ and $\pm 3.01 \times 10^5$ kg/year of methane considering coated and clean bubble models, respectively.

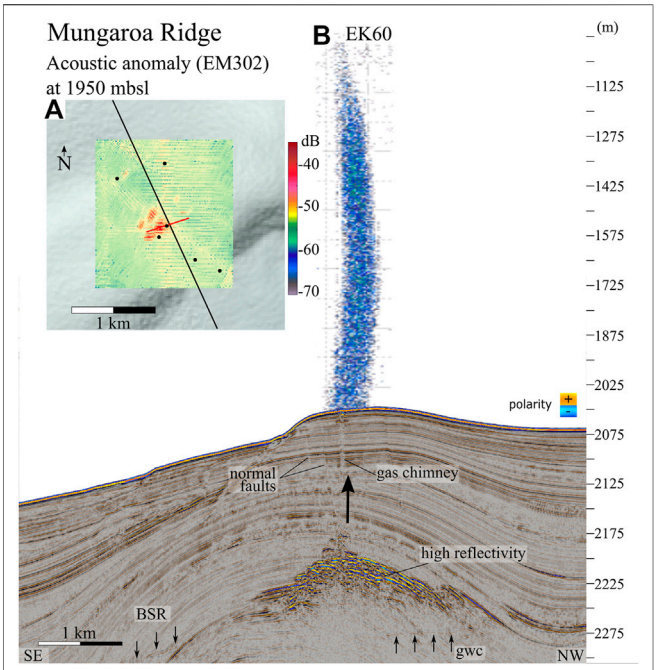

FIGURE 10 | Overview of the Mungaroa Ridge seep site: the interpreted TAN 1808-97 seismic profile is shown in the main panel (interpretation after Crutchley et al., 2021). The bold black arrow shows the direction of fluid flow as interpreted from the seismic data and explained in the text. BSR: bottom simulating reflection; gwc: gas-water contact. **(A)** Map view of the Mungaroa Ridge seeps (red box in **Figure 4A**), showing the acoustic backscatter anomaly in the echo integrated MBES (EM302) data in proximity of the seafloor. The location of the TAN1808-97 seismic line and of the single-beam data (EK60) are indicated by the black and the red lines, respectively. The black dots represent the locations of the main gas flares. The hydroacoustic data were collected during the TAN2012 voyage. **(B)** Echogram of a gas flare as imaged by the 38 kHz channel in the single-beam data.

Uncertainties related to the estimations of bubble parameters, such as mean radius, bubble density and bubble size distribution, are addressed in detail in the next section.

Constraints on Bubble Size Distributions

Quantification of gas flux is dependent on observations of bubble parameters. Ideally, optical measurements such as video observation, bubble size measuring, and sampling of the seep fluids provide the most accurate measures of the bubble size distribution function, their rising velocity, and the chemical gas composition, enabling the determination of realistic values of gas flow rates (e.g., von Deimling et al., 2011; Higgs et al., 2019; Wang et al., 2016; Weber et al., 2014).

Due to the lack of optical observations of the seeps analysed in this study, no measurements of *BSD* are available, and we adopt a variation of the method proposed by Veloso et al. (2015) to estimate the *BSD* from the split-beam EK60 data. To test the validity of the results, we analyse the dependence of the estimated methane fluxes on different *BSD* functions: we first parametrise the *BSD* by assuming log-normal and Weibull probability density functions (PDF), and then compare the inverted results (**Figure 11**). The choice of these PDFs was made based on published seep studies, which have suggested several distribution functions to describe bubble size data including normal (Römer et al., 2012), log-normal (Veloso et al., 2015; Wang et al., 2016; Li et al., 2020), and Weibull (Dey and Kundu, 2012).

The modelled S_v depends on both the *BSD* and the density of bubbles (e.g., MacLennan et al., 2002). If the *BSD* parameters are over corrected during the curve matching procedure, the density of bubbles will be underestimated, so that the final impact on the calculation of gas fluxes is minimal. This can be observed, for example, in the inversion results for the Mungaroa Ridge flare at 2060 mbsl (**Figure 10**), where the mean bubble radius of the *BSD* modelled assuming a Weibull distribution increases above 2 mm, the density of bubbles for the corresponding depth shows a sharp decrease. The number of bubbles smaller than 0.5 mm is probably overestimated by the Weibull PDF, and the log-normal curves are more likely to represent the real *BSD* at these seep sites.

The use of two different approaches to estimate bubble parameters allows us to quantify the degree of agreement between the two methods. The fluxes estimated assuming a constant *BSD* for the entire flare and based on the normalised S_v response (Approach 1–manual curve fitting method) show a general smooth trend with depth (**Figures 5K–O**). This trend can be explained by the fact that in this approach a mean $\overline{S_v}$ is calculated by averaging the echo integrated backscatter volume strength of the cells located at the same depth. Through this approach, we obtain one mean bubble radius per site rather than a profile of radii changing with depth. Because of the stronger response of bigger bubbles close to the emission site this method will also tend to overestimate the mean of the *BSD*, as the overall response of the flare is dominated by this area, as observed in **Figures 5A–E**. Despite this approximation, the manual curve fitting approach is a useful method that can be used to obtain informed starting models for the linear inversion method. Because of its deterministic nature, the second approach (linear inversion) requires the existence of a solid starting model in order to converge to a global minimum. This method provides a more reliable tool to track changes of physical parameters of the bubbles in the water column. The fluxes calculated through the linear inversion method (both assuming Weibull and log-normal distributions) show more variability in the calculated density of bubbles and fluxes, despite a general increase with depth (e.g., **Figure 5**). **Table 2** summarizes the differences in the results of the two approaches. The differences between flux estimates calculated using a constant *BSD* for the entire flare (approach 1) and the fluxes obtained through the linear inversion process (approach 2) can be over 400%. For these reasons, we deem the flux estimates calculated through linear inversion more reliable (**Table 2**), and use those to extrapolate margin-wide flux estimates.

Source of Gas and Seismic Manifestation of Fluid Flow

The southern Hikurangi Margin is a well-established province of gas hydrate occurrence, focussed fluid migration and gas seepage (e.g., Barnes et al., 2010; Crutchley et al., 2019; Kroeger et al.,

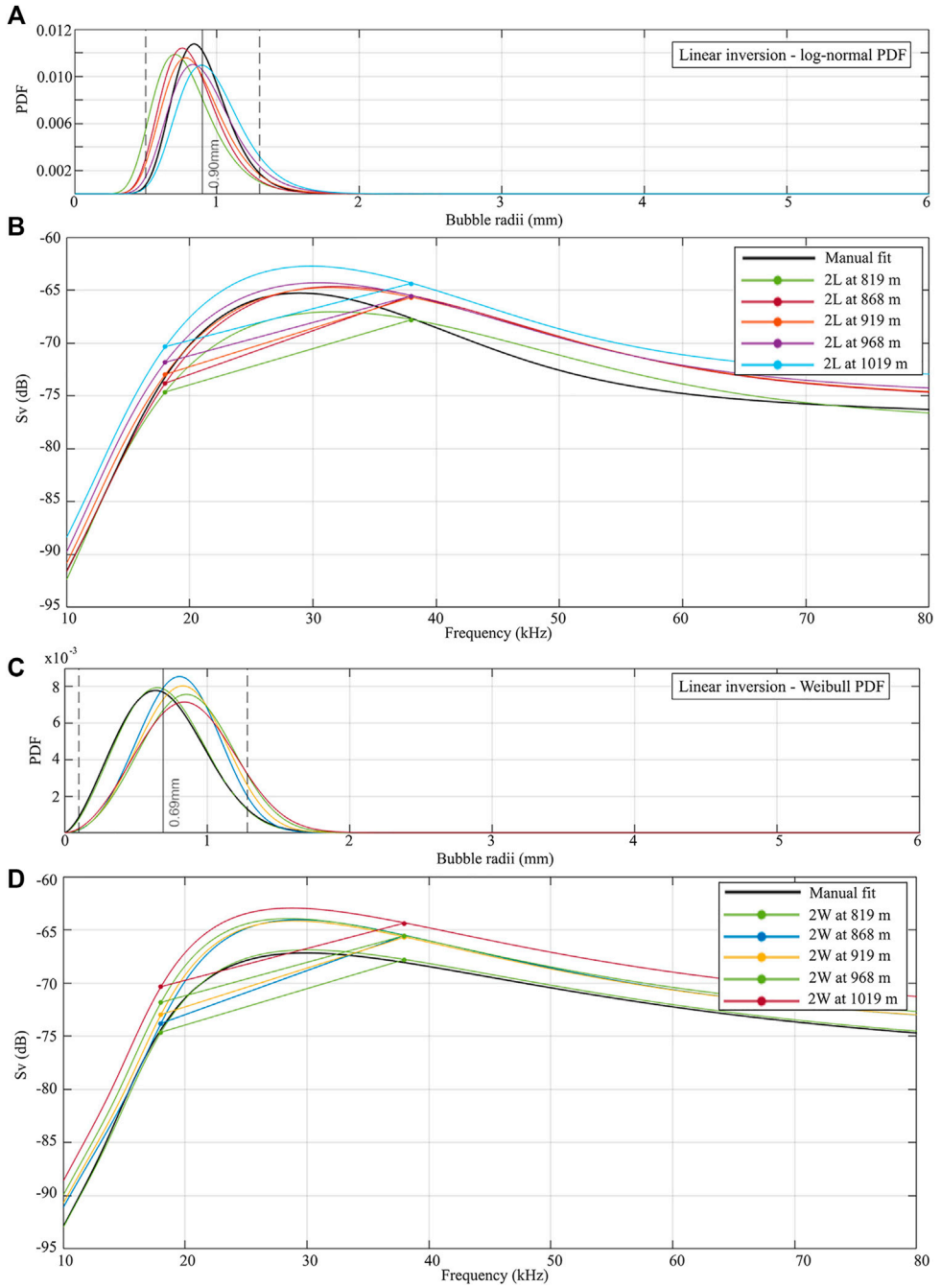

FIGURE 11 | Bubble size distributions estimated from linear inversion of the split-beam data at the Mungaroa Ridge gas flare, imposing log-normal **(A)** and Weibull **(C)** distributions. Each curve is representative of a 50 m high horizontal slice of the gas flare, and is color coded according to the water depth. **(B)** and **(D)** show the theoretical frequency response curves at each horizontal slice of the gas flare, and the dots represent the observed S_v at the same water depth for the 18 and the 38 kHz channels.

2019; Watson et al., 2020). Consistent with most subduction margins, the analysis of gases emitted at the seafloor suggests a predominantly microbial origin of methane over a thermogenic origin (Greinert et al., 2001; Faure et al., 2010). The co-location of high-resolution seismic reflection images and water column imaging (EK60 data) enables us to compare the sub-seafloor with the water column at gas seep locations.

At all the flare sites observed in this study, we found evidence of gas migrating from beneath the base of the GHSZ to the seafloor. In the case of Mungaroa Ridge, a large free gas reservoir

in the core region of the anticline has been interpreted by Crutchley et al. (2021) as the source that supplies gas to the main seep observed at the seafloor. Here, Crutchley et al. (2021) suggest that over-pressured gas causes hydraulic fracturing of the overlying sediments leading to the formation of the vertical gas chimney imaged in the seismic data (**Figure 10**). The presence of such large and interconnected free gas accumulations is not observed at the other target sites of this study. However, highly reflective strata are imaged directly beneath the base of the GHSZ at Urutī and Glendhu ridges, as well as at Pahauau Bank. The enhanced reflectivity is likely to be caused by the strong impedance contrast between fine-grained low-permeability layers and sandy gas-charged sedimentary units, as interpreted by Turco et al. (2020) at Glendhu Ridge. Stratigraphically driven fluid migration along permeable dipping strata has been suggested to be the main mechanism for upward fluid flow in many anticline-related ridges on the Hikurangi Margin (e.g., Crutchley et al., 2019; Wang et al., 2017a; Turco et al., 2020; Barnes et al., 2010; Kroeger et al., 2021). Urutī Ridge is a good example of this process, where highly reflective strata appear to be transporting gas from depth upward into the GHSZ (**Figure 6**). At Urutī Ridge, Urutī Ridge West, Pahaua Bank ,and Glendhu Ridge, fluid migration through the GHSZ is also identified by areas of decreased amplitude (seismic blanking) and disrupted stratigraphic reflections beneath the seeps (**Figures 6**–**9**). Seismic blanking is often caused by strong signal attenuation at the seafloor or within the shallow sub-seafloor, caused by the presence of highly reflective interfaces. Such interfaces could come from authigenic carbonates or gas hydrate accumulations (e.g., Bohrmann et al., 1998). The disruption of reflections can be due to the scattering of seismic energy caused by the presence of gas (Judd and Hovland, 1992) or by physical disruption of layering caused by focused gas migration (e.g., Davis 1992; Gorman et al., 2002). While free-gas occurrence is likely to cause most of the seismic blanking observed beneath the seep sites, the presence of autigenic carbonates on the seafloor might contribute to the loss of seismic energy transmission in high-frequency data. In summary, the seismic images show a diversity of manifestations of free gas in the sub-seafloor, ranging from gas-water contacts at the base of a free gas reservoir (Mungaroa Ridge; **Figure 10**) through layer-parallel gas migration (e.g., Urutī Ridge; **Figure 6**) to vertical gas migration facilitated by hydraulic fracturing (Flemings et al., 2003; e.g., Pahaua Bank and Mungaroa Ridge; **Figures 8**, **10**).

Temporal Variability of the Seeps

There are many mechanisms that control the activity of different types of gas seeps. Consequently, the time scales over which the activity of cold seeps fluctuates can span from minutes to millennia. For example, Feseker et al. (2014) document the eruption of a deep-sea mud volcano that triggered large methane and CO_2 emissions over a period of minutes. Pressure changes at the seafloor caused by tides have been shown to impact the flow rate of shallow and deep-sea gas seeps (Boles et al., 2001; Römer et al., 2016; Riedel et al., 2018), while seasonal sea-bottom temperature variations can cause cold seeps to hibernate during the cold months, trapping gas in the sediments that is released in pulses during warmer months (Berndt et al., 2014; Ferré et al., 2020). On the other hand, natural seismicity (Franek et al., 2017) and ocean warming (Baumberger et al., 2018) are potential triggers for significant release of methane from the sediments, especially in hydrate provinces.

Our study represents an opportunity to analyse the variability of methane emissions on the southern Hikurangi Margin over a three-year period. Although quantitative estimates were calculated only once for each gas flare, from either the 2019 or from the 2020 datasets, from the qualitative analysis of multibeam and split-beam data, no substantial difference could be observed in the activity of the main seeps at the time of each survey (**Figure 12**). In fact, the spatial extent of the acoustic anomaly close to the seafloor remains constant for the five target areas in the three datasets, as does the height of the acoustic flares.

In addition to acoustic observations, it is known from authigenic carbonates (for example on Urutī Ridge) that many of the seep sites have been active for thousands of years (e.g., Jones et al., 2010; Liebetrau et al., 2010). Likewise, there is evidence for stable methane seepage over intermediate timescales from tube worms (*Lamellibrachia spp.*) up to 2 m long sampled at Mungaroa, Urutī and Glendhu ridges (TAN1904 Voyage Report, NIWA). Tube worms of this species require at least 200 years to reach such lengths (Fisher et al., 1997; Cordes et al., 2007).

While the combination of acoustic observation and bio-geological sampling might indicate a constant seepage activity throughout this time, we cannot rule out that methane fluxes vary over seasonal or shorter cycles. For simplitity, we assume a constant discharge rate for the flux estimates presented in this work. Understanding and monitoring the temporal variability of a field of cold seeps is relevant to several scientific and socio-economic issues. At a national scale, one of the most direct implications is related to regional ecosystem management. Cold seeps are increasingly recognized as centres of local biogeochemical cycling and oases for many animals with recent studies finding that commercially important fisheries species are associated with seep habitats and consume methane derived carbon from chemosynthetic production in seep systems (Grupe et al., 2015; Levin et al., 2016; Seabrook et al., 2019; Turner et al., 2019).

Margin-Wide Estimates of Seafloor Methane Flux

To refine our understanding of the global carbon budget, it is important to study the potential implications of seabed gas release on a regional scale. To this end, the relevance of margin-wide studies on natural methane seeps has increased in the past decade: Pohlman et al. (2011) found that up to 28% of the total dissolved organic carbon derives from fossil methane, while Garcia-Tigreros et al. (2021) conclude that aerobic oxidation of CH_4 has a greater influence on ocean chemistry in regions where methane concentrations are locally elevated. Based on the analysis of more than 300 gas seeps, Riedel et al. (2018) estimate a combined average *in-situ* flow rate of about 88 × 10^6 kg/year for the Cascadia Margin. Sahling et al. (2014)

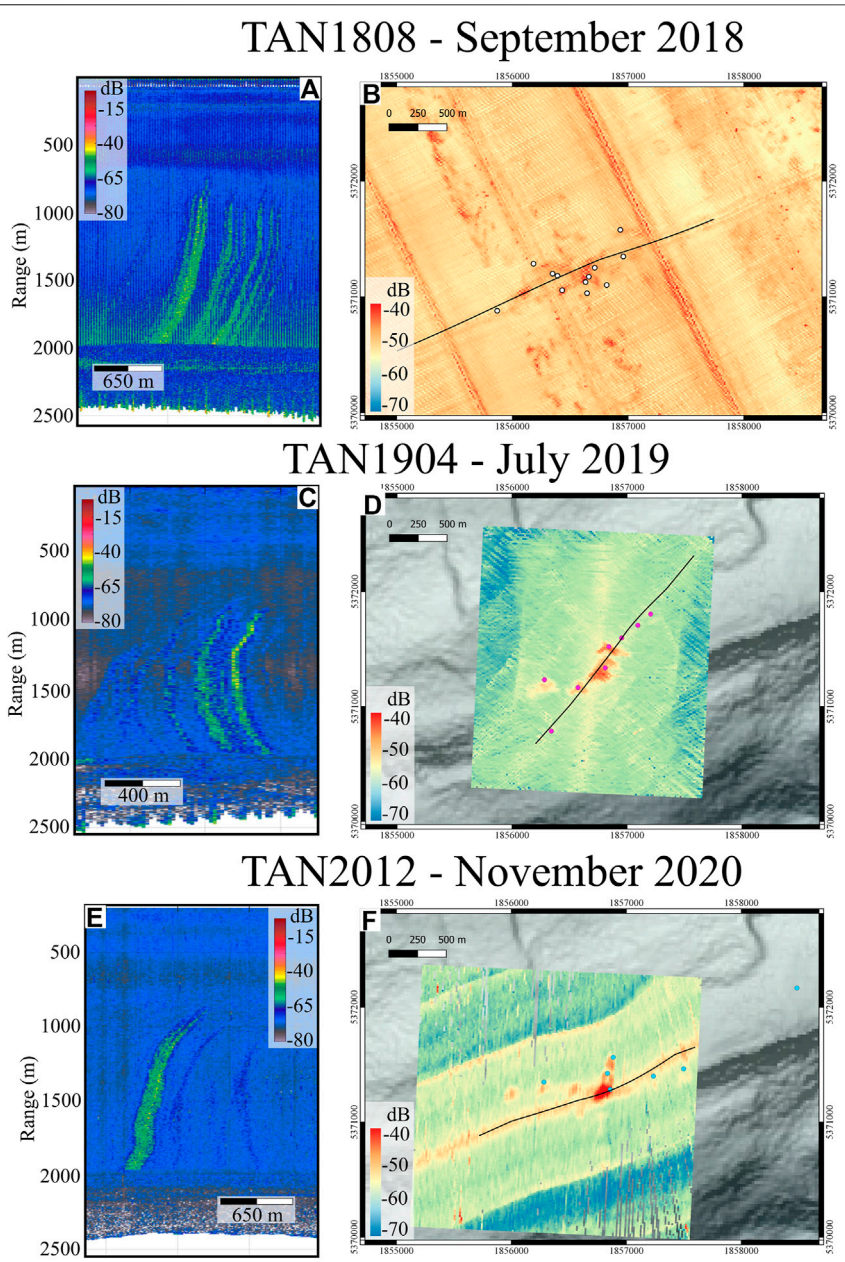

FIGURE 12 | Evolution of the Glendhu Ridge seep site over the years. The panels on the left **(A,C,E)** show range stacked views of MBES (EM302) data of the gas flares on the top of Glendhu Ridge from TAN1808, TAN1904, and TAN2012 datasets, respectively. The panels on the right **(B,D,F)** show the acoustic backscatter anomaly in the echo integrated MBES data in proximity of the seafloor. The black lines represent the ship track shown in the left panels. The coordinate system is UTM Zone 60 S (WGS84 datum).

calculate the gas flux on the western margin of Svalbard to be between 0.11 and 1.89 × 10^6 kg/year, while the combined methane leakage from the seafloor on the US Atlantic Margin is estimated to range between 1.5 and 90 × 10^4 kg/year (Skarke et al., 2014). About 0.13–1.01 × 10^6 kg of methane per year have been estimated to leak from gas seep fields on the Makran Margin offshore Pakistan (Römer et al., 2012).

The distribution of gas seeps on the Hikurangi Margin has been investigated in detail by Watson et al. (2020), who identified 1,457 gas flares from water column data, spanning from East Cape to Kekerengu Bank, off Kaikōura peninsula, in an area of approximately 51,215 km^2 (**Figure 2A**). If we consider the flux estimates presented in this paper for the five analyzed seep fields, and we divide them by the number of flares observed at each site, we obtain average methane fluxes per flare between 1.9 × 10^5 and 6.4 × 10^5 kg/year, considering coated bubbles and clean bubbles models, respectively. Multiplying by the number of observed flares from Watson et al. (2020), we can extrapolate a total

flux ranging between 2.77×10^8 and 9.32×10^8 kg of methane released each year on the whole Hikurangi Margin. These estimates correspond to, respectively, ~67 and ~233% of the total amount of methane that was released in 2019 from land sources in New Zealand (i.e., 4.121×10^8 kg/year New Zealand Ministry for Environment—Manatū Mō Te Taiao, www.environment.govt.nz). It is worth pointing out that these estimates might represent an underestimation of the real methane flux occurring on the margin, because they are based solely on acoustic evidence of focused fluid flow (i.e., gas bubbles in the water), and do not take into account diffusive fluid seepage, which is also inferred to occur on the Hikurangi Margin (Watson et al., 2020). On the other hand, assuming a constant methane discharge at the seep sites over seasonal or shorter cycles might lead to an overestimation of annual gas fluxes. Similarly, the assumption that all flares in the same seep field have identical bubble parameters is an approximation that can result in overestimating methane discharge at smaller seeps. To better assess the methane fluxes, long term observational data and chemical sampling at the analysed sites might be required.

Potential Implications for Ocean pH and Local Deoxygenation

From the acoustic imaging of the water column, no evidence was found that methane bubbles reach the sea surface at any of the analysed flares. Considering the depth of the seep sites reported here, two different processes will interact to prevent the CH_4 emitted at the seafloor from reaching the atmosphere: 1) the methane contained in the bubbles will dissolve into the water driven by the low concentration of CH_4 in the ocean (Wiesenburg and Guinasso, 1979), and2) dissolved CH_4 is converted into CO_2 in the water column by abiotic and biotic forces (McGinnis et al., 2006). Although bubble-stripping and methane oxidation reduce the amount of CH_4 released into the atmosphere, these processes can significantly impact local marine habitats and ocean chemistry.

As the majority of the CH_4 emitted by cold seeps remains in deep waters, aerobic oxidation is a primary sink for the methane, as well as a source of CO_2. This CO_2 production needs to be considered with respect to acidification of deep water (Archer et al., 2009; Biastoch et al., 2011), particularly as seeps represent a more direct source in deep water than the transfer of anthropogenic carbon via deep water formation and transport. Large-scale methane release has resulted in ocean acidification in earths geological past (Zachos et al., 2005), but assessments of the current contribution of methane seeps indicate a relatively minor impact on deep water pH (Garcia-Tigreros and Kessler, 2018). However, this source may become significant in response to warming and associated destabilisation of methane hydrates in regions such as the Arctic (Biastoch et al., 2011).

In the current study we estimated the regional contribution to deep waters on the Hikurangi Margin by scaling up the methane release estimated from the bubble plumes to the total number of flares identified in the acoustic data (Watson et al., 2020). Assuming this methane loading was uniformly distributed within the bottom 100 m of water overlying the sediment for the entire margin, from East Cape to the Kaikoura peninsula, provided an estimate of total input of 2.77×10^8 and 9.32×108 kg methane/year, based upon the clean and coated bubbles models, respectively. If 100% of this methane is oxidised to CO_2 then the resulting change in the carbonate system, calculated using measured bottom water dissolved inorganic carbon, total alkalinity, temperature, and salinity (C. Law, pers. comm.) in the *CO_2sys* programme (Hunter, 2015), would result in a decrease in pH_T of 0.048–0.144 relative to the background value of 7.962. These estimates are conservative, and suggest a relatively minor impact to a significant decrease in regional pH, with the upper estimate exceeding the surface ocean pH decrease arising from anthropogenic CO_2 emissions to date (Orr et al., 2005), and comparable to 50% of the projected pH decrease in New Zealand waters by the end of this century (Law et al., 2018). A reduction in pH of this magnitude could have significant impacts on benthic calcifying organisms, particularly as the Hikurangi Margin gas seeps are within the regional depth range of the Aragonite Saturation Horizon (Bostock et al., 2015), below which solid carbonate becomes thermodynamically unstable. However, this estimate of pH decrease should be regarded as an upper limit, as dilution and transport of methane in and out of the region are not considered in this estimate. Refined estimates of pH change require direct measurement of dissolved methane and regional modelling of methane distribution and dispersion using ROMS (Hadfield et al., 2007).

The aerobic oxidation of methane (methanotrophy) by free-living and symbiont-associated bacteria occurs in the seafloor and water column around sites of gas release (Steinle et al., 2015; Sweetman et al., 2017; Levin, 2018). Although not analysed in this study, the aerobic oxidation of methane to CO_2 can also cause localized deoxygenation at a regional scale, impacting ecosystem health and species distribution (Boetius and Wenzhöfer, 2013; Breitburg et al., 2018). Throughout the global ocean there has been an oxygen loss of at least 2% over the past 50–100 years, with well understood linkages of ocean warming reducing oxygen solubility and ocean ventilation (Dickens, 2001; Levin, 2018). However, the influence of features that influence dissolve oxygen at regional scales, such as methane seeps, remains unclear. In addition to the direct effect of methanotrophy, some evidence suggests that seeps with strong bubble plumes, such as observed at some of sites reported here, can draw nutrient and hydrocarbon rich water towards the surface, stimulating primary production and eventually drawing down oxygen as well (Levin, 2018). The potential scale of this process could be significant, as seen in the aftermath of the Deepwater Horizon oil spill in the Gulf of Mexico, where a major reduction of oxygen was measured ad microbial communities released from the spill (Kessler et al., 2011). The downstream ecological and biogeochemical impacts of the release of large volumes of methane by the Hikurangi Margin seeps, as detailed in this study, warrants further scientific attention to understand the implications of future change.

CONCLUSION

The combination of seismic and hydroacoustic data analysis allowed the characterisation of five cold seep sites on the southern Hikurangi Margin in terms of geological setting and gas flux estimates. Seismic imaging of the geological structures underlying the seep sitesprovided insights into the origin of the gas in the subsurface. Hydroacoustic data collected over 3 years allowed mapping of the backscatter anomalies near the seafloor at the sites of seepage and pinpointing the location of the main gas flares on the seabed. A total of 43, 33, and 53 individual flares were identified from the TAN1808, TAN1904, and TAN2012 datasets, respectively.

The use of the multi-frequency split-beam echosounder allowed estimates of the gas flux rates at the five target sites to be made. The five cold seep fields analysed in this study on the southern Hikurangi Margin of New Zealand lie in water depths ranging from 1,110 to 2060 m, and emit, combined, between 8.66 and 27. 21×10^6 kg of gas per year. The extrapolated methane flux for the whole Hikurangi Margin range between 2.77×10^8 and 9.32×10^8 kg of methane released each year. These estimates are based on acoustic evidence of focused fluid flow, and do not take into account diffusive seafloor seepage.

The results of this study provide the most quantitative assessment to date of total methane release on the Hikurangi Margin, filling gaps of unknown methane sources and better constraining models of ocean acidification and deoxygenation. Moreover, the fluxes presented here can be used as a proxy to monitor changes in the flux rates over the mid-to long term associated with ocean warming.

DATA AVAILABILITY STATEMENT

The raw data supporting the conclusions of this article will be made available by the authors, without undue reservation.

AUTHOR CONTRIBUTIONS

FT: conceptualization, literature review, acoustic, and seismic data acquisition (TAN1808–TAN2012), acoustic data processing, software developing for flux estimates, writing. YL: gas bubble project leader, supervision in the methodology, software developing for acoustic data analysis, and processing, data curation. SW: gas bubble project leader, writing–review, supervision, seismic, and acoustic data acquisition (TAN1808). CL: took care of the ocean acidification implications and estimates on pH change, writing–review. GJC: gas hydrate seismic project leader, conceptualization of manuscript, especially discussion, seismic and acoustic data acquisition and processing (TAN1808), writing–review. SS: contribution to writing biogeochemical implication of the study, acoustic data acquisition (TAN1904). JM: supervision, seismic and acoustic data acquisition (TAN1808), supervision, project management and facilities. CL: contribution to calculating CO_2 for ocean acidification, acquisition of acoustic data (TAN1904). IP: gas bubble project co-leader, acoustic data acquisition (TAN2012), writing–review. JITH: gas hydrate project leader, seismic and acoustic data acquisition (TAN1808), writing–review. SW: seismic data acquisition and processing (TAN1808), acoustic data acquisition (TAN2012). AG: supervision, provided facilities and funding.

FUNDING

Part of this work has been carried out within the HYDEE research programme, funded by the New Zealand's Ministry for Business, Innovation and Employment, contract no. C05X1708, and is included a Ph.D. thesis from the University of Otago (Turco, 2021). Part of the funding came from the Smart Idea project Broadband acoustic characterization of free gases in the ocean water, contract nr. C01X1915.

REFERENCES

Ainslie, M. A., and Leighton, T. G. (2009). Near Resonant Bubble Acoustic Cross-Section Corrections, Including Examples from Oceanography, Volcanology, and Biomedical Ultrasound. *J. Acoust. Soc. Am.* 126 (5), 2163–2175. doi:10.1121/1.3180130

Archer, D., Buffett, B., and Brovkin, V. (2009). Ocean Methane Hydrates as a Slow Tipping point in the Global Carbon Cycle. *Proc. Natl. Acad. Sci. U S A.* 106 (49), 20596–20601. doi:10.1073/pnas.0800885105

Argus, D. F., Gordon, R. G., and DeMets, C. (2011). Geologically Current Motion of 56 Plates Relative to the No-Net-Rotation Reference Frame. *Geochem. Geophys. Geosystems* 12 (11).

Barnes, P. M., Lamarche, G., Bialas, J., Henrys, S., Pecher, I., Netzeband, G. L., et al. (2010). Tectonic and Geological Framework for Gas Hydrates and Cold Seeps on the Hikurangi Subduction Margin, New Zealand. *Mar. Geology.* 272 (1-4), 26–48. doi:10.1016/j.margeo.2009.03.012

Bassett, D., Sutherland, R., and Henrys, S. (2014). Slow Wavespeeds and Fluid Overpressure in a Region of Shallow Geodetic Locking and Slow Slip, Hikurangi Subduction Margin, New Zealand. *Earth Planet. Sci. Lett.* 389, 1–13. doi:10.1016/j.epsl.2013.12.021

Baumberger, T., Embley, R. W., Merle, S. G., Lilley, M. D., Raineault, N. A., and Lupton, J. E. (2018). Mantle-derived Helium and Multiple Methane Sources in Gas Bubbles of Cold Seeps along the Cascadia Continental Margin. Geochemistry, Geophysics. *Geosystems* 19 (11), 4476–4486. doi:10.1029/2018gc007859

Bayrakci, G., Scalabrin, C., Dupré, S., Leblond, I., Tary, J.-B., Lanteri, N., et al. (2014). Acoustic Monitoring of Gas Emissions from the Sea_oor. Part II: a Case Study from the Sea of Marmara. *Mar. Geophys. Res.* 35 (3), 211–229. doi:10.1007/s11001-014-9227-7

Berndt, C., Feseker, T., Treude, T., Krastel, S., Liebetrau, V., Niemann, H., et al. (2014). Temporal Constraints on Hydrate-Controlled Methane Seepage off Svalbard. *Science* 343 (6168), 284–287. doi:10.1126/science.1246298

Biastoch, A., Treude, T., Rüpke, L. H., Riebesell, U., Roth, C., Burwicz, E. B., et al. (2011). Rising Arctic Ocean Temperatures Cause Gas Hydrate Destabilization and Ocean Acidi_cation. *Geophys. Res. Lett.* 38 (8). doi:10.1029/2011GL047222

Boetius, A., and Wenzhöfer, F. (2013). Seafloor Oxygen Consumption Fuelled by Methane from Cold Seeps. *Nat. Geosci* 6 (9), 725–734. doi:10.1038/ngeo1926

Bohrmann, G., Greinert, J., Suess, E., and Torres, M. (1998). Authigenic Carbonates from the Cascadia Subduction Zone and Their Relation to Gas Hydrate Stability. *Geol* 26 (7), 647–650. doi:10.1130/0091-7613(1998)026<0647:acftcs>2.3.co;2

Boles, J., Clark, J., Leifer, I., and Washburn, L. (2001). Temporal Variation in Natural Methane Seep Rate Due to Tides, Coal Oil Point Area, California. *J. Geophys. Res. Oceans* 106 (C11), 27077–27086. doi:10.1029/2000jc000774

Bonini, M. (2019). Seismic Loading of Fault-Controlled Fluid Seepage Systems by Great Subduction Earthquakes. *Sci. Rep.* 9 (1), 11332. doi:10.1038/s41598-019-47686-4

Bostock, H. C., Tracey, D. M., Currie, K. I., Dunbar, G. B., Handler, M. R., Mikaloff Fletcher, S. E., et al. (2015). The Carbonate Mineralogy and Distribution of Habitat-Forming Deep-Sea Corals in the Southwest pacific Region. *Deep Sea Res. Oceanographic Res. Pap.* 100, 88–104. doi:10.1016/j.dsr.2015.02.008

Böttner, C., Haeckel, M., Schmidt, M., Berndt, C., Vielstädte, L., Kutsch, J. A., et al. (2020). Greenhouse Gas Emissions from marine Decommissioned Hydrocarbon wells: Leakage Detection, Monitoring and Mitigation Strategies. *Int. J. Greenhouse Gas Control.* 100, 103119. doi:10.1016/j.ijggc.2020.103119

Breitburg, D., Levin, L. A., Oschlies, A., Grégoire, M., Chavez, F. P., Conley, D. J., et al. (2018). Declining Oxygen in the Global Ocean and Coastal Waters. *Science* 359 (6371). doi:10.1126/science.aam7240

Colbo, K., Ross, T., Brown, C., and Weber, T. (2014). A Review of Oceanographic Applications of Water Column Data from Multibeam Echosounders. *Estuarine, coastal shelf Sci.* 145, 41–56. doi:10.1016/j.ecss.2014.04.002

Cook, A. E., and Malinverno, A. (2013). Short Migration of Methane into a Gas Hydrate Bearing Sand Layer at Walker Ridge, Gulf of Mexico. Geochemistry, Geophysics. *Geosystems* 14 (2), 283–291. doi:10.1002/ggge.20040

Cordes, E. E., Bergquist, D. C., Redding, M. L., and Fisher, C. R. (2007). Patterns of Growth in Cold-Seep Vestimenferans Including Seepiophila Jonesi: a Second Species of Long-Lived Tubeworm. *Mar. Ecol.* 28 (1), 160–168. doi:10.1111/j.1439-0485.2006.00112.x

Crutchley, G., Fraser, D., Pecher, I., Gorman, A., Maslen, G., and Henrys, S. (2015). Gas Migration into Gas Hydrate-Bearing Sediments on the Southern Hikurangi Margin of New Zealand. *J. Geophys. Res. Solid Earth* 120 (2), 725–743. doi:10.1002/2014jb011503

Crutchley, G. J., Kroeger, K. F., Pecher, I. A., Gorman, A. R., and Watson, S. (2019). How Tectonic Folding Influences Gas Hydrate Formation: New Zealand's Hikurangi Subduction Margin. *Geology* 47 (1), 39–42.

Crutchley, G. J., Mountjoy, J., Hillman, J., Turco, F., Watson, S., Flemings, P., et al. (2021). Upward-doming Zones of Gas Hydrate and Free Gas at the Bases of Gas Chimneys, New Zealand's Hikurangi Margin. *J. Geophys. Res. Solid Earth*, e2020JB021489. doi:10.1029/2020jb021489

Crutchley, G. J., Mountjoy, J. J., Davy, B. D., Hillman, J. I. T., Watson, S., Stewart, L., et al. (2018). Gas Hydrate Systems of the Southern Hikurangi Margin, Aotearoa, New Zealand. TAN1808 Voyage Report, RV Tangaroa 8-Sep – 5 Oct 2018. *Lower Hutt (Nz) GNS Sci.*, 83p. Avaialble at: https://doi-org.ezproxy.otago.ac.nz/10.21420/73WW-1W83.

Davis, A. M. (1992). Shallow Gas: an Overview. *Continental Shelf Res.* 12 (10), 1077–1079. doi:10.1016/0278-4343(92)90069-v

De Robertis, A., and Higginbottom, I. (2007). A post-processing Technique to Estimate the Signal-To-Noise Ratio and Remove Echosounder Background Noise. *ICES J. Mar. Sci.* 64 (6), 1282–1291. doi:10.1093/icesjms/fsm112

Demer, D. A., Berger, L., Bernasconi, M., Bethke, E., Boswell, K., Chu, D., et al. (2015). Calibration of Acoustic Instruments.

Dey, A. K., and Kundu, D. (2012). Discriminating between the Weibull and Log-normal Distributions for Type-II Censored Data. *Statistics* 46 (2), 197–214. doi:10.1080/02331888.2010.504990

Dickens, G. (2001). On the Fate of Past Gas: What Happens to Methane Released from a Bacterially Mediated Gas Hydrate Capacitor? *Geochem. Geophys. Geosystems* 2 (1). doi:10.1029/2000gc000131

Duarte, H., Pinheiro, L. M., Teixeira, F. C., and Monteiro, J. H. (2007). High-resolution seismic imaging of gas accumulations and seepage in the sediments of the Ria de Aveiro barrier lagoon (Portugal). *Geo-Marine Lett.* 27 (2), 115–126. doi:10.1007/s00367-007-0069-z

Dupré, S., Scalabrin, C., Grall, C., Augustin, J.-M., Henry, P., engör, A. C., et al. (2015). Tectonic and Sedimentary Controls on Widespread Gas Emissions in the Sea of Marmara: Results from Systematic, Shipborne Multibeam echo Sounder Water Column Imaging. *J. Geophys. Res. Solid Earth* 120 (5), 2891–2912. doi:10.1002/2014jb011617

Faure, K., Greinert, J., von Deimling, J. S., McGinnis, D. F., Kipfer, R., et al. (2010). Methane Seepage along the Hikurangi Margin of New Zealand: Geochemical and Physical Data from the Water Column, Sea Surface and Atmosphere. *Mar. Geology.* 272 (1-4), 170–188. doi:10.1016/j.margeo.2010.01.001

Ferré, B., Jansson, P. G., Moser, M., Serov, P., Portnov, A., Graves, C. A., et al. (2020). Reduced Methane Seepage from Arctic Sediments during Cold Bottom-Water Conditions. *Nat. Geosci.* 13 (2), 144–148. doi:10.1038/s41561-019-0515-3

Feseker, T., Boetius, A., Wenzhöfer, F., Blandin, J., Olu, K., Yoeger, D., et al. (2014). Eruption of a Deep-Sea Mud Volcano Triggers Rapid Sediment Movement. *Nat. Commun.* 5 (1). doi:10.1038/ncomms6385

Fisher, C., Urcuyo, I., Simpkins, M., and Nix, E. (1997). Life in the Slow Lane: Growth and Longevity of Cold-Seep Vestimentiferans. *Mar. Ecol.* 18 (1), 83–94. doi:10.1111/j.1439-0485.1997.tb00428.x

Flemings, P. B., Liu, X., and Winters, W. J. (2003). Critical Pressure and Multiphase Flow in Blake Ridge Gas Hydrates. *Geol* 31 (12), 1057–1060. doi:10.1130/g19863.1

Franek, P., Plaza-Faverola, A., Mienert, J., Buenz, S., Ferré, B., and Hubbard, A. (2017). Microseismicity Linked to Gas Migration and Leakage on the Western Svalbard Shelf. Geochemistry, Geophysics. *Geosystems* 18 (12), 4623–4645. doi:10.1002/2017gc007107

Fu, X., Waite, W. F., and Ruppel, C. D. (2020). Hydrate Formation on Marine Seep Bubbles and the Implications for Water Column Methane Dissolution. *AGU Fall Meet. Abstr.* Vol. 2020, OS016–0006. doi:10.1029/2021jc017363

Garcia-Tigreros, F., and Kessler, J. D. (2018). Limited Acute Influence of Aerobic Methane Oxidation on Ocean Carbon Dioxide and pH in Hudson Canyon, Northern US Atlantic Margin. *J. Geophys. Res. Biogeosciences* 123 (7), 2135–2144. doi:10.1029/2018jg004384

Garcia-Tigreros, F., Leonte, M., Ruppel, C. D., Ruiz-Angulo, A., Joung, D. J., Young, B., et al. (2021). Estimating the Impact of Seep Methane Oxidation on Ocean pH and Dissolved Inorganic Radiocarbon along the US Mid-Atlantic Bight. *J. Geophys. Res. Biogeosciences* 126 (1), e2019JG005621. doi:10.1029/2019jg005621

Gorman, A. R., Holbrook, W. S., Hornbach, M. J., Hackwith, K. L., Lizarralde, D., and Pecher, I. (2002). Migration of Methane Gas through the Hydrate Stability Zone in a Low-Flux Hydrate Province. *Geol* 30 (4), 327–330. doi:10.1130/0091-7613(2002)030<0327:momgtt>2.0.co;2

Greinert, J., Bohrmann, G., and Suess, E. (2001). Gas Hydrate-Associated Carbonates and Methane-Venting at Hydrate Ridge: Classi_cation, Distribution and Origin of Authigenic Lithologies. *Geophys. Monograph-American Geophys. Union* 124, 99–114. doi:10.1029/gm124p0099

Grupe, B. M., Krach, M. L., Pasulka, A. L., Maloney, J. M., Levin, L. A., and Frieder, C. A. (2015). Methane Seep Ecosystem Functions and Services from a Recently Discovered Southern California Seep. *Mar. Ecol.* 36, 91–108. doi:10.1111/maec.12243

Hadfield, M. G., Rickard, G. J., and Uddstrom, M. J. (2007). A Hydrodynamic Model of Chatham Rise, New Zealand. *New Zealand J. Mar. Freshw. Res.* 41 (2), 239–264. doi:10.1080/00288330709509912

Higgs, B., Mountjoy, J., Crutchley, G. J., Townend, J., Ladroit, Y., Greinert, J., et al. (2019). Seep-bubble Characteristics and Gas _ow Rates from a Shallow-Water, High-Density Seep _eld on the Shelf-To-Slope Transition of the Hikurangi Subduction Margin. *Mar. Geology.* 417, 105985. doi:10.1016/j.margeo.2019.105985

Hillman, J. I., Cook, A. E., Daigle, H., Nole, M., Malinverno, A., Meazell, K., et al. (2017). Gas Hydrate Reservoirs and Gas Migration Mechanisms in the Terrebonne Basin, Gulf of Mexico. *Mar. Pet. Geology.* 86, 1357–1373. doi:10.1016/j.marpetgeo.2017.07.029

Hillman, J. I., Crutchley, G. J., and Kroeger, K. F. (2020). Investigating the Role of Faults in Fluid Migration and Gas Hydrate Formation along the Southern Hikurangi Margin, New Zealand. *Mar. Geophys. Res.* 41 (1), 1–19. doi:10.1007/s11001-020-09400-2

Hoffmann, J. J., Gorman, A. R., and Crutchley, G. J. (2019). Seismic Evidence for Repeated Vertical Fluid Flow through Polygonally Faulted Strata in the Canterbury Basin, New Zealand. *Mar. Pet. Geology.* 109, 317–329. doi:10.1016/j.marpetgeo.2019.06.025

Hornafius, J. S., Quigley, D., and Luyendyk, B. P. (1999). The World's Most Spectacular marine Hydrocarbon Seeps (Coal Oil Point, Santa Barbara Channel, California): Quanti_cation of Emissions. Journal of Geophysical Research:. *Oceans* 104 (C9), 20703–20711. doi:10.1029/1999jc900148

Hunter, K. (2007). *A.: XLCO2 – Seawater CO2 Equilibrium Calculations Using Excel Version 2New Zealand*. Dunedin: University of Otago. available at http://neon.otago.ac.nz/research/mfc/people/keith_hunter/software/swco2/(last access February 24, 2015).

Jones, A. T., Greinert, J., Bowden, D., Klaucke, I., Petersen, C. J., Netzeband, G., et al. (2010). Acoustic and Visual Characterisation of Methane-Rich Seabed Seeps at Omakere Ridge on the Hikurangi Margin, New Zealand. *Mar. Geology.* 272 (1-4), 154–169. doi:10.1016/j.margeo.2009.03.008

Judd, A. G. (2004). Natural Seabed Gas Seeps as Sources of Atmospheric Methane. *Environ. Geology.* 46 (8), 988–996. doi:10.1007/s00254-004-1083-3

Judd, A., and Hovland, M. (2009). *Seabed Fluid Flow: The Impact on Geology, Biology and the marine Environment*. Cambridge University Press.

Judd, A., and Hovland, M. (1992). The Evidence of Shallow Gas in marine Sediments. *Continental Shelf Res.* 12 (10), 1081–1095. doi:10.1016/0278-4343(92)90070-z

Kessler, J. D., Valentine, D. L., Redmond, M. C., Du, M., Chan, E. W., Mendes, S. D., et al. (2011). A Persistent Oxygen Anomaly Reveals the Fate of Spilled Methane in the Deep Gulf of Mexico. *Science* 331 (6015), 312–315. doi:10.1126/science.1199697

Kim, Y.-J., Cheong, S., Chun, J.-H., Cukur, D., Kim, S.-P., Kim, J.-K., et al. (2020). Identification of Shallow Gas by Seismic Data and AVO Processing: Example from the Southwestern continental Shelf of the Ulleung Basin, East Sea, Korea. *Mar. Pet. Geology.* 117, 104346. doi:10.1016/j.marpetgeo.2020.104346

Krabbenhoeft, A., Bialas, J., Klaucke, I., Crutchley, G., Papenberg, C., and Netzeband, G. L. (2013). Patterns of Subsurface Fluid Flow at Cold Seeps: The Hikurangi Margin, O_shore New Zealand. *Mar. Pet. Geology.* 39 (1), 59–73. doi:10.1016/j.marpetgeo.2012.09.008

Kroeger, K., Crutchley, G. J., Kellett, R., and Barnes, P. (2019). A 3-D Model of Gas Generation, Migration, and Gas Hydrate Formation at a Young Convergent Margin (Hikurangi Margin, New Zealand). Geochemistry, Geophysics,. *Geosystems* 20 (11), 5126–5147. doi:10.1029/2019gc008275

Kroeger, K. F., Crutchley, G. J., Hillman, J. I., Turco, F., and Barnes, P. M. (2021). Gas Hydrate Formation beneath Thrust Ridges: A Test of Concepts Using 3D Modelling at the Southern Hikurangi Margin, New Zealand. *Mar. Pet. Geology.* 135, 105394. doi:10.1016/j.marpetgeo.2021.105394

Kroeger, K., Plaza-Faverola, A., Barnes, P., and Pecher, I. (2015). Thermal Evolution of the New Zealand Hikurangi Subduction Margin: Impact on Natural Gas Generation and Methane Hydrate Formation. A Model Study. *Mar. Pet. Geology.* 63, 97–114. doi:10.1016/j.marpetgeo.2015.01.020

Ladroit, Y., Escobar-Flores, P. C., Schimel, A. C. G., and O'Driscoll, R. L. (2020). ESP3: An Open-Source Software for the Quantitative Processing of Hydro-Acoustic Data. *SoftwareX* 12, 100581. doi:10.1016/j.softx.2020.100581

Law, C., Nodder, S. D., Mountjoy, J. J., Orpin, A., Pilditch, C. A., Marriner, A., et al. (2010). Geological and Biogeochemical Characteristics of a New Zealand Deep-Water, Methane-Rich Cold Seep. *Mar. Geology.* 272 (1-4), 189–208. doi:10.1016/j.margeo.2009.06.018

Law, C. S., Rickard, G. J., Mikaloff-Fletcher, S. E., Pinkerton, M. H., Behrens, E., Chiswell, S. M., et al. (2018). Climate Change Projections for the Surface Ocean Around New Zealand. *New Zealand J. Mar. Freshw. Res.* 52 (3), 309–335. doi:10.1080/00288330.2017.1390772

Leblond, I., Scalabrin, C., and Berger, L. (2014). Acoustic Monitoring of Gas Emissions from the Seafloor. Part I: Quantifying the Volumetric _ow of Bubbles. *Mar. Geophys. Res.* 35 (3), 191–210. doi:10.1007/s11001-014-9223-y

Legrand, D., Iglesias, A., Singh, S., Cruz-Atienza, V., Yoon, C., Dominguez, L., et al. (2021). The Influence of Fluids in the Unusually High-Rate Seismicity in the Ometepec Segment of the Mexican Subduction Zone. *Geophys. J. Int.* 226 (1), 524–535. doi:10.1093/gji/ggab106

Leifer, I., and Patro, R. K. (2002). The Bubble Mechanism for Methane Transport from the Shallow Sea Bed to the Surface: A Review and Sensitivity Study. *Continental Shelf Res.* 22 (16), 2409–2428. doi:10.1016/s0278-4343(02)00065-1

Levin, L. A., Baco, A. R., Bowden, D. A., Colaco, A., Cordes, E. E., Cunha, M. R., et al. (2016). Hydrothermal Vents and Methane Seeps: Rethinking the Sphere of Influence. Frontiers in Marine Science, 3, 72.T. E. (1998). The Dammed Hikurangi Trough: a Channel-Fed Trench Blocked by Subducting Seamounts and Their Wake Avalanches (New Zealand France GeodyNZ Project). *Basin Res.* 10 (4), 441–468.

Lewis, K. B., Collot, J. Y., and Lallem, S. E. (1998). The Dammed Hikurangi Trough: A Channel-Fed Trench Blocked by Subducting Seamounts and Their Wake Avalanches (New Zealand–France Geodynz Project). *Basin Res.* 10 (4), 441–468.

Levin, L. A. (2018). Manifestation, Drivers, and Emergence of Open Ocean Deoxygenation. *Annu. Rev. Mar. Sci.* 10, 229–260. doi:10.1146/annurev-marine-121916-063359

Li, J., Roche, B., Bull, J. M., White, P. R., Leighton, T. G., Provenzano, G., et al. (2020). Broadband Acoustic Inversion for Gas Flux Quantification. *Appl. a methane plume Scanner Pockmark, Cent. North Sea. J. Geophys. Res. Oceans* 125 (9), e2020JC016360. doi:10.1029/2020jc016360

Liebetrau, V., Eisenhauer, A., and Linke, P. (2010). Cold Seep Carbonates and Associated Cold-Water Corals at the Hikurangi Margin, New Zealand: New Insights into Fluid Pathways, Growth Structures and Geochronology. *Mar. Geology.* 272 (1-4), 307–318. doi:10.1016/j.margeo.2010.01.003

McGinnis, D. F., Greinert, J., Artemov, Y., Beaubien, S., and Wüest, A. (2006). Fate of Rising Methane Bubbles in Stratified Waters: How Much Methane Reaches the Atmosphere? *J. Geophys. Res. Oceans* 111 (C9). doi:10.1029/2005jc003183

MacLennan, D. F., Fernandes, P. G., and Dalen, J. (2002). A Consistent Approach to Definitions and Symbols in Fisheries Acoustics *ICES J. Marine Sci.* 59 (2), 365–369.

Meldahl, P., Heggland, R., Bril, B., and de Groot, P. (2001). Identifying Faults and Gas Chimneys Using Multiattributes and Neural Networks. *The leading edge* 20 (5), 474–482. doi:10.1190/1.1438976

Merewether, R., Olsson, M. S., and Lonsdale, P. (1985). Acoustically Detected Hydrocarbon Plumes Rising from 2-km Depths in Guaymas Basin, Gulf of California. *J. Geophys. Res. Solid Earth* 90 (B4), 3075–3085. doi:10.1029/jb090ib04p03075

Naudts, L., Greinert, J., Poort, J., Belza, J., Vangampelaere, E., Boone, D., et al. (2010). Active Venting Sites on the Gas-Hydrate-Bearing Hikurangi Margin, O_ New Zealand: Di_usive-Versus Bubblereleased Methane. *Mar. Geology.* 272 (1-4), 233–250. doi:10.1016/j.margeo.2009.08.002

Nikolovska, A., Sahling, H., and Bohrmann, G. (2008). Hydroacoustic Methodology for Detection, Localization, and Quanti_cation of Gas Bubbles Rising from the Seafloor at Gas Seeps from the Eastern Black Sea. *Geochem. Geophys. Geosystems* 9 (10). doi:10.1029/2008gc002118

Nole, M., Daigle, H., Cook, A. E., and Malinverno, A. (2016). Short-range, Overpressure-Driven Methane Migration in Coarse-Grained Gas Hydrate Reservoirs. *Geophys. Res. Lett.* 43 (18), 9500–9508. doi:10.1002/2016gl070096

Orr, J. C., Fabry, V. J., Aumont, O., Bopp, L., Doney, S. C., Feely, R. A., et al. (2005). Anthropogenic Ocean Acidification over the Twenty-First century and its Impact on Calcifying Organisms. *Nature* 437 (7059), 681–686. doi:10.1038/nature04095

Petersen, C. J., Bünz, S., Hustoft, S., Mienert, J., and Klaeschen, D. (2010). High Resolution P-Cable 3D Seismic Imaging of Gas Chimney Structures in Gas Hydrated Sediments of an Arctic Sediment Drift. *Mar. Pet. Geology.* 27 (9), 1981–1994. doi:10.1016/j.marpetgeo.2010.06.006

Pohlman, J. W., Bauer, J. E., Waite, W. F., Osburn, C. L., and Chapman, N. R. (2011). Methane Hydrate-Bearing Seeps as a Source of Aged Dissolved Organic Carbon to the Oceans. *Nat. Geosci.* 4 (1), 37–41. doi:10.1038/ngeo1016

Reagan, M. T., Moridis, G. J., Elliott, S. M., and Maltrud, M. (2011). Contribution of Oceanic Gas Hydrate Dissociation to the Formation of Arctic Ocean Methane Plumes. *J. Geophys. Res. Oceans* 116 (C9). doi:10.1029/2011jc007189

Riedel, M., Scherwath, M., Römer, M., Veloso, M., Heesemann, M., and Spence, G. D. (2018). Distributed Natural Gas Venting Offshore along the Cascadia Margin. *Nat. Commun.* 9 (1), 3264. doi:10.1038/s41467-018-05736-x

Römer, M., Riedel, M., Scherwath, M., Heesemann, M., and Spence, G. D. (2016). Tidally Controlled Gas Bubble Emissions: A Comprehensive Study Using Long-Term Monitoring Data from the NEPTUNE Cabled Observatory O_shore Vancouver Island. Geochemistry, Geophysics,. *Geosystems* 17 (9), 3797–3814. doi:10.1002/2016gc006528

Römer, M., Sahling, H., Pape, T., Bohrmann, G., and Spieÿ, V. (2012). Quantification of Gas Bubble Emissions from Submarine Hydrocarbon Seeps at the Makran continental Margin (Offshore Pakistan). *J. Geophys. Res. Oceans* 117 (C10). doi:10.1029/2011jc007424

Saffer, D. M., and Tobin, H. J. (2011). Hydrogeology and Mechanics of Subduction Zone Forearcs: Fluid _ow and Pore Pressure. *Annu. Rev. Earth Planet. Sci.* 39, 157–186. doi:10.1146/annurev-earth-040610-133408

Sahling, H., Römer, M., Pape, T., Bergès, B., dos Santos Fereirra, C., Boelmann, J., et al. (2014). Gas Emissions at the continental Margin West of Svalbard: Mapping, Sampling, and Quantification. *Biogeosciences* 11, 6029–6046. doi:10.5194/bg-11-6029-2014

Schimel, A. C. G., Brown, C. J., and Ierodiaconou, D. (2020). Automated Filtering of Multibeam Water-Column Data to Detect Relative Abundance of Giant Kelp (Macrocystis Pyrifera). *Remote Sensing* 12 (9), 1371. doi:10.3390/rs12091371

Schmale, O., Greinert, J., and Rehder, G. (2005). Methane Emission from High-Intensity marine Gas Seeps in the Black Sea into the Atmosphere. *Geophys. Res. Lett.* 32 (7). doi:10.1029/2004gl021138

Schoell, M. (1988). Multiple Origins of Methane in the Earth. *Chem. Geology.* 71 (1-3), 1–10. doi:10.1016/0009-2541(88)90101-5

Schwalenberg, K., Haeckel, M., Poort, J., and Jegen, M. (2010). Evaluation of Gas Hydrate Deposits in an Active Seep Area Using marine Controlled Source Electromagnetics: Results from Opouawe Bank, Hikurangi Margin, New Zealand. *Mar. Geology.* 272 (1-4), 79–88. doi:10.1016/j.margeo.2009.07.006

Seabrook, S., De Leo, F. C., and Thurber, A. R. (2019). Flipping for Food: the Use of a Methane Seep by Tanner Crabs (Chionoecetes Tanneri). *Front. Mar. Sci.* 6, 43. doi:10.3389/fmars.2019.00043

Shakhova, N., Semiletov, I., Salyuk, A., Yusupov, V., Kosmach, D., and Gustafsson, O. (2010). Extensive Methane Venting to the Atmosphere from Sediments of the East Siberian Arctic Shelf. *Science* 327 (5970), 1246–1250. doi:10.1126/science.1182221

Skarke, A., Ruppel, C., Kodis, M., Brothers, D., and Lobecker, E. (2014). Widespread Methane Leakage from the Sea Floor on the Northern US Atlantic Margin. *Nat. Geosci* 7 (9), 657–661. doi:10.1038/ngeo2232

Steinle, L., Graves, C. A., Treude, T., Ferré, B., Biastoch, A., Bussmann, I., et al. (2015). Water Column Methanotrophy Controlled by a Rapid Oceanographic Switch. *Nat. Geosci* 8 (5), 378–382. doi:10.1038/ngeo2420

Stott, L., Davy, B., Shao, J., Co_n, R., Pecher, I., Neil, H., et al. (2019). CO2 Release from Pockmarks on the Chatham Rise-Bounty Trough at the Glacial Termination. *Paleoceanography and Paleoclimatology* 34 (11), 1726–1743. doi:10.1029/2019pa003674

Suess, E. (2020). Marine Cold Seeps: Background and Recent Advances. Hydrocarbons, Oils and Lipids. *Divers. Origin, Chem. Fate* 163, 747–767. doi:10.1007/978-3-319-90569-3_27

Sweetman, A. K., Thurber, A. R., Smith, C. R., Levin, L. A., Mora, C., Wei, C. L., et al. (2017). Major Impacts of Climate Change on Deep-Sea Benthic Ecosystems. *Elementa: Sci. Anthropocene* 5. doi:10.1525/elementa.203

Turco, F. (2021). *Geophysical Characterization of Gas Hydrate Systems on the Southern Hikurangi Margin of New Zealand*. PhD thesis (Dunedin: University of Otago).

Turco, F., Crutchley, G. J., Gorman, A. R., Mountjoy, J. J., Hillman, J. I., and Woelz, S. (2020). Seismic Velocity and Re_ectivity Analysis of Concentrated Gas Hydrate Deposits on the Southern Hikurangi Margin (New Zealand). *Mar. Pet. Geology.* 120 (104572), 164. doi:10.1016/j.marpetgeo.2020.104572

Turner, P. J., Thaler, A. D., Freitag, A., and Collins, P. C. (2019). Deep-sea Hydrothermal Vent Ecosystem Principles: Identification of Ecosystem Processes, Services and Communication of Value. *Mar. Pol.* 101, 118–124. doi:10.1016/j.marpol.2019.01.003

Veloso, M., Greinert, J., Mienert, J., and De Batist, M. (2015). A New Methodology for Quantifying Bubble _ow Rates in Deep Water Using Splitbeam Echosounders: Examples from the Arctic Offshore NW-Svalbard. Limnology and Oceanography:. *methods* 13 (6), 267–287. doi:10.1002/lom3.10024

von Deimling, J. S., Rehder, G., Greinert, J., McGinnnis, D., Boetius, A., et al. (2011). Quantification of Seep-Related Methane Gas Emissions at Tommeliten, North Sea. *Continental Shelf Res.* 31 (7-8), 867–878. doi:10.1016/j.csr.2011.02.012

Wang, B., Socolofsky, S. A., Breier, J. A., and Seewald, J. S. (2016). Observations of Bubbles in Natural Seep Ares at MC 118 and GC 600 Using *In Situ* Quantitative Imaging. *J. Geophys. Res. Oceans* 121 (4), 2203–2230. doi:10.1002/2015jc011452

Wang, H., Crutchley, G., and Stern, T. (2017a). Gas Hydrate Formation in Compressional, Extensional and Un-faulted Structural Settings. Examples from New Zealand's Hikurangi Margin. *Mar. Pet. Geology.* 88, 69–80. doi:10.1016/j.marpetgeo.2017.08.001

Watson, S. J., Mountjoy, J. J., Barnes, P. M., Crutchley, G. J., Lamarche, G., Higgs, B., et al. (2020). Focused Fluid Seepage Related to Variations in Accretionary Wedge Structure, Hikurangi Margin, New Zealand. *Geology* 48 (1), 56–61. doi:10.1130/g46666.1

Weber, T. C., Mayer, L., Jerram, K., Beaudoin, J., Rzhanov, Y., and Lovalvo, D. (2014). Acoustic Estimates of Methane Gas _ux from the Seabed in a 6000 Km2 Region in the Northern Gulf of Mexico. Geochemistry, Geophysics. *Geosystems* 15 (5), 1911–1925. doi:10.1002/2014gc005271

Weidner, E., Weber, T. C., Mayer, L., Jakobsson, M., Chernykh, D., and Semiletov, I. (2019). A Wideband Acoustic Method for Direct Assessment of Bubble-Mediated Methane Flux. *Continental Shelf Res.* 173, 104–115. doi:10.1016/j.csr.2018.12.005

Wiesenburg, D. A., and Guinasso, N. L., Jr (1979). Equilibrium Solubilities of Methane, Carbon Monoxide, and Hydrogen in Water and Sea Water. *J. Chem. Eng. Data* 24 (4), 356–360. doi:10.1021/je60083a006

Yilmaz, Ö. (2001). Seismic Data Analysis: Processing, Inversion, and Interpretation of Seismic Data. *Soc. Explor. Geophys.*.

Zachos, J. C., Röhl, U., Schellenberg, S. A., Sluijs, A., Hodell, D. A., Kelly, D. C., et al. (2005). Rapid Acidification of the Ocean during the Paleocene-Eocene thermal Maximum. *Science* 308 (5728), 1611–1615. doi:10.1126/science.1109004

Conflict of Interest: The authors declare that the research was conducted in the absence of any commercial or financial relationships that could be construed as a potential conflict of interest.

frontiers in Earth Science

ORIGINAL RESEARCH
published: 09 March 2022
doi: 10.3389/feart.2022.852786

Hydrothermal Vent Complexes Control Seepage and Hydrocarbon Release on the Overriding Plate of the Tyrrhenian-Ionian Subduction System (Paola Basin)

Marzia Rovere[1]*, *Alessandra Mercorella*[1], *Fabiano Gamberi*[1] and *Fabrizio Zgur*[2]

[1]Istituto di Scienze Marine, Consiglio Nazionale Delle Ricerche, Bologna, Italy, [2]Osservatorio Geofisico Sperimentale, Sgonico, Trieste, Italy

Active fluid seeps have been described in a wide range of geological environments and geodynamic contexts, which include continental shelves of non-volcanic passive margins and accretionary wedges. Fluids seeping in hybrid volcanic-sedimentary basins, characterized by the presence of magmatic intrusive complexes, have always received less attention. We detected and imaged dozens of distinct gas flares, as high as 700 m, on the continental slope of the Paola Basin in the southeastern Tyrrhenian Sea, at 550–850 m water depth. The sedimentary basin is surrounded by Pleistocene active and inactive volcanoes and volcanic-intrusive complexes, which formed in the back-arc basin of the Calabrian subduction zone, in response to subduction-induced mantle flow. Gas flares develop above pockmarks, craters and mud flows that form over and along the scarps of mound structures and correspond to seismic zones of free gas accumulation in the sub-seafloor. Here, methane-derived siderite shows enrichment in $\delta^{13}C$ and $\delta^{18}O$ isotopes likely related to methanogenesis and intermittent venting of deep-sourced CO_2. Multichannel seismic reflection data showed that the gas flares develop in correspondence of doming and diapirism apparently originating from the top of the Messinian evaporites and nearby magmatic sills, that are present in the lower part of the Plio-Quaternary succession. These diapiric structures can be related to seafloor hydrothermal vent complexes fed by the igneous intrusions. Our data suggest that the vent complexes acted as fluid migration pathways and gas conduits, which at times are bounded by deep-rooted normal faults, leading to post-explosive near-surface microbial activity and seep carbonate formation. Fluids being mobilised by magmatism in the study area include: hydrocarbons and hydrothermal fluids generated at depth, interstitial water expelled during formation of polygonal faults. The close spatial correlation between seafloor seep manifestations, fluid migration pathways in the sub-surface involving part of the Messinian units and igneous features indicates that magmatic activity has been the main driver of fluid flow and can have a long-term effect in the southern Tyrrhenian Sea.

Keywords: gas flares, hydrothermal vent complex, Messinian evaporites, Mediterranean Sea, methane-derived carbonates

OPEN ACCESS

Edited by:
Miriam Römer,
University of Bremen, Germany

Reviewed by:
Srikumar Roy,
University College Dublin, Ireland
Claudio Argentino,
UiT The Arctic University of Norway, Norway

***Correspondence:**
Marzia Rovere
marzia.rovere@cnr.it

Specialty section:
This article was submitted to Marine Geoscience, a section of the journal Frontiers in Earth Science

Received: *11 January 2022*
Accepted: *08 February 2022*
Published: *09 March 2022*

Citation:
Rovere M, Mercorella A, Gamberi F and Zgur F (2022) Hydrothermal Vent Complexes Control Seepage and Hydrocarbon Release on the Overriding Plate of the Tyrrhenian-Ionian Subduction System (Paola Basin). Front. Earth Sci. 10:852786. doi: 10.3389/feart.2022.852786

INTRODUCTION

The release of carbon-bearing gases from the seafloor into the water column is generally classified into: high-temperature hydrothermal vent complexes (HTVC), releasing gas rich in inorganic carbon dioxide (CO_2), typically produced by thermo-metamorphism of limestones or magma-mantle degassing (e.g. the Guaymas Basin, Berndt et al., 2016); low-temperature cold seep systems, releasing mainly biotic methane (CH_4) and other hydrocarbons, produced by microbial or thermogenic degradation of organic matter in sedimentary basins (e.g., the Cascadia margin, Riedel et al., 2018).

In many cases, however, magmatic intrusions and volcanic plumbing systems occur within sedimentary basins resulting in hybrid systems with both CO_2-rich geothermal fluids and CH_4-rich biotic gas (microbial or thermogenic) sourced from the organic-rich sediments (Procesi et al., 2019).

The importance of hybrid geological systems, hosting both volcano-hydrothermal and sedimentary components, was first recognized by Svensen et al. (2003), who noted that deep sedimentary basins affected by circulation of magmatic fluids or by the intrusion of igneous rocks, may result in the migration of a combination of fluids, hot water and gases, accompanied by precipitation of authigenic carbonates.

Evidence is growing that intrusive magmatic bodies, such as sills, can influence the long-term migration of fluids from the deep subsurface to form HTVCs that can be reutilized as focused areas of fluid flow (Lawrence and Cartwright, 2010; Rollet et al., 2012; Roelofse et al., 2021). This influence is largely due to permeability contrasts between the intrusion and the host sediment or to interconnected open fractures and faults within and around intrusions acting as conduits for migrating fluids (Omosanya et al., 2018). Large-scale fractures and fault can provide discontinuities with increased sediment permeability, that can represent further conduits for fluid and gas transport in seep sedimentary environments (e.g., Plaza-Faverola et al., 2015), allowing hydrocarbon-rich fluids from greater depth to reach shallow sediments and the sediment-water interface. Furthermore, also salt diapirs have been connected to seepage of gas to the seabed in different geological contexts (Serié et al., 2012; de Mahiques et al., 2017; Madof, 2018; Müller et al., 2018).

Sedimentary basins in geodinamically active regions, such as back-arc basins, host deep and permeable fault and fracture systems that can act as pathways for the migration of deep crustal or mantle gases (CO_2-rich) favouring their mixing with shallower sedimentary (CH_4-rich) gases. In these basins, the tectonic extensional regime can also allow for the emplacement of sills and/or magma intrusions, not necessarily leading to active volcanic centers. Sills typically penetrate only the bottom of the sedimentary formations (De Ritis et al., 2019).

Past hybrid systems are common, both on land and in the offshore: in the large igneous provinces of the Karoo Basin in South Africa (Svensen et al., 2006), offshore northeast Greenland (Reynolds et al., 2017), in the Vøring and Møre Basins of the North Sea (Omosanya et al., 2018), offshore NW Australia (Magee et al., 2016). However, modern hybrid systems remain overlooked, although are important because: i. they may lead to production of hydrocarbons from enhanced thermal maturity of sedimentary rocks (Sydnes et al., 2019); ii. depending on the water depth, can be natural sources of greenhouse gas to the atmosphere (McGinnis et al., 2006); iii. are potential drivers of past climate change (Svensen et al., 2004; Iyer et al., 2013).

An extensive hydroacoustic mapping campaign including water column recording, sub-bottom sediment profiling and multichannel seismic acquisition has been conducted in the Paola Basin, in the back-arc domain of the southern Tyrrhenian Sea. This contribution aims at showing how flares, indicative of gas bubble release, are widespread in the water column, and what is their relationships with seismic features indicative of subsurface gas, and morphologic elements suggestive of seafloor venting. We also discuss the origin of the fluids in the frame of the tectonic and volcanic regime of the Tyrrhenian back-arc area in the context of its subduction-related geodynamic setting.

Study Area

The Paola Basin lies at the rear of the Calabrian Arc, in the upper plate of the northwestward dipping Tyrrhenian-Ionian subduction system, which includes the back-arc domain of the SE Tyrrhenian Sea, volcanic seamounts, the Aeolian Islands volcanic arc and the fore-arc region of the Calabrian accretionary wedge (**Figure 1A**). The basin formed since the late Miocene, as a result of compressional (Pepe et al., 2010) and strike-slip (Milia et al., 2009) tectonics, in an overall extensional regime.

The Paola Basin area is flanked to the north and west by active and inactive volcanoes. In the north, the area is characterized by the presence of magmatic intrusions that locally reach the seafloor forming the Diamante and Enotrio volcanic edifices and the flat-topped Ovidio Seamount (Würtz and Rovere, 2015, **Figure 1B**). Altogether, these form a volcanic-intrusive complex characterized by a deep-rooted, magma feeding system, formed in consequence of the ascent of subduction-induced mantle flow originated in the northwestern edge of the retreating ionian slab (De Ritis et al., 2019). The volcanoes are not presently active even if hydrothermal activity occurs, as the emplacement and cooling of the magma occurred sometime during the Brunhes Chron (De Ritis et al., 2019).

The Alcione Seamount is a ~1,000 m-high conical volcano located on an almost flat seafloor on the lower slope of the Paola Basin (Marani and Gamberi, 2004) and is characterized by absence or very weak hydrothermal activity (Lupton et al., 2011). The Lametini Seamounts are two conical edifices on top of which Fe-Mn crusts characterized by a very low Fe/Mn ratio and high Cu-content indicative of hydrothermal venting were dredged (Rossi et al., 1980) (**Figure 1B**).

A 60-km-long anticline (Paola Ridge, **Figure 1A**) bounds westward the Paola Basin syncline (Gamberi and Rovere, 2010). Here, cold seep-like structures were discovered with

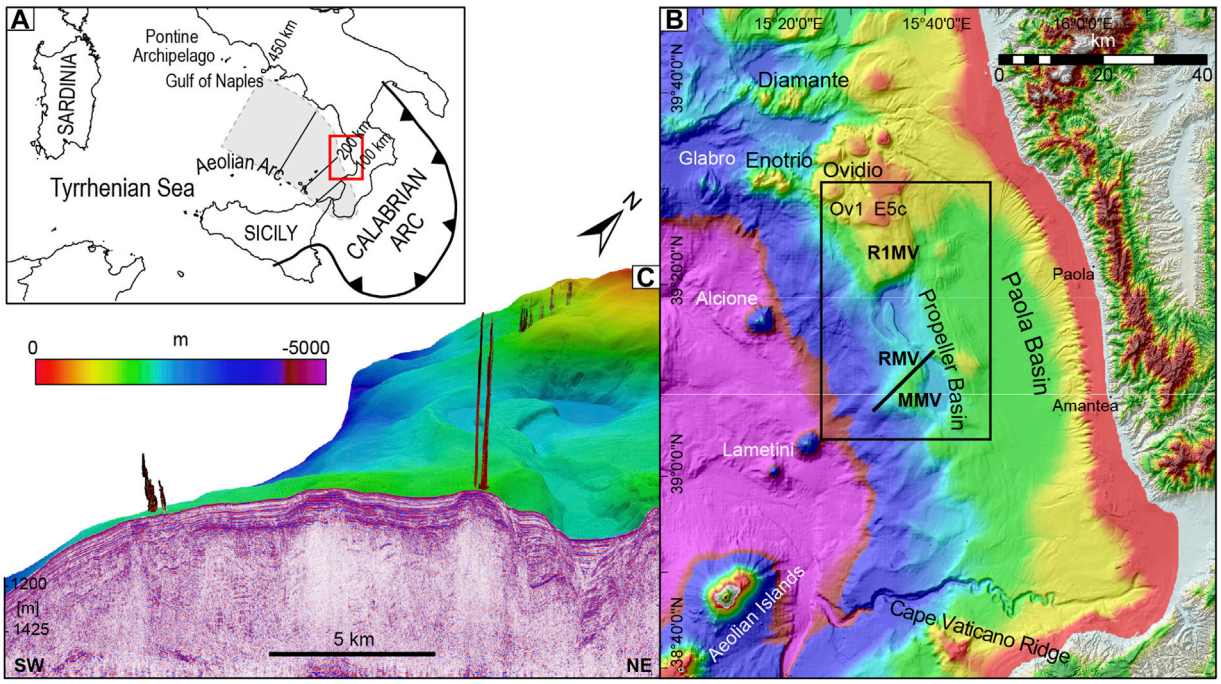

FIGURE 1 | (A) Sketch of the geodynamic setting of the southern Tyrrhenian Sea and Calabrian Arc with the outlines of the depths (from Chiarabba et al., 2008) of the northwestward dipping slab of the Tyrrhenian-Ionian subduction system. The red rectangle is the focus area imaged in **(B)**. **(B)** Bathymetry of the Paola Basin and the surrounding areas, the black rectangle outlines the study area of **Figure 2**. **(C)** 3D scene of the gas flares in the water column superimposed to a multichannel seismic reflection (MCS) profile whose track line is located in **(B)**.

full-ocean depth multibeam and backscatter data at 500–800 m water depth. Higher resolution acquisitions and seafloor sampling were carried out in 2011 (Rovere et al., 2014). The most prominent structures in the area are represented by three mound structures (RMV, MMV and R1MV, **Figure 1B**) which make up the Paola Ridge and stand 200–400 m above the Propeller Basin located landward (**Figure 1B**). Active gas venting at the seafloor was detected via multibeam echosounder at RMV location (Rovere et al., 2014), while oxy-hydroxides (goethite), sulfides (pyrite, marcasite and sphalerite) and siderites were collected in the sub-seafloor of all mounds (Rovere et al., 2015). Siderites precipitated in burrows and hardgrounds in the shallower sedimentary succession showing enrichment in $\delta^{13}C$ (3–10 V-PDB ‰) and $\delta^{18}O$ (8–9 V-PDB ‰) isotopes, which are compatible with their precipitation in the methanogenic zone (Rovere et al., 2015) during periods of lower gas discharges under prolonged anoxic conditions and intermittent venting of deep-sourced CO_2 (Franchi et al., 2017).

NW-SE and NNW-SSE-oriented normal faults, which can be regarded as the marine prolongation of the fault zones that dissect the Calabrian Arc from SE to NW, were suggested to be the most probable mechanism for the emplacement of the mud mobile structures and primary conduits for upward fluid migration (Rovere et al., 2014). It was further noted that the mound structures rise in coincidence with extensional faults that offset the Messinian evaporites, suggesting that pre-Messinian source rocks, mobilized along discrete belts of active tectonic deformation, were controlling the seepage of fluids in the study area (Gamberi and Rovere, 2010).

MATERIALS AND METHODS

The data for this study were acquired during the R/V Urania cruise MarBeep in 2014. The track lines in **Figure 2A** show the multichannel seismic reflection survey (MCS) and the location of the CROP M36 and other vintage seismic reflection data used for the seismostratigraphic correlations in the study area.

Hydroacoustic Data

The acoustic detection of the water column flares was performed using Kongsberg EM710 (100 kHz, 1° × 1°) and EM302 (30 kHz, 1° × 2°) multibeam systems (MBES) that were both hull-mounted on board the R/V Urania. Bathymetric data were also collected and integrated the seafloor coverage achieved during the previous campaign carried out in 2011 (Rovere et al., 2014). Sound velocity profiles were obtained with a Seabird-Scientific SBE 911 plus CTD unit mounted on a rosette carrying 24 Niskin bottles and were applied both in real-time acquisition and post-processing. Bathymetric and seafloor reflectivity data were post-processed using the suite CARIS HIPS & SIPS.

Water column data were extracted mainly from EM302 data after quality check and processed with the QPS Fledermaus (version 7.8, including the FMMidwater module) software package which allows for manual flare identification and geo-

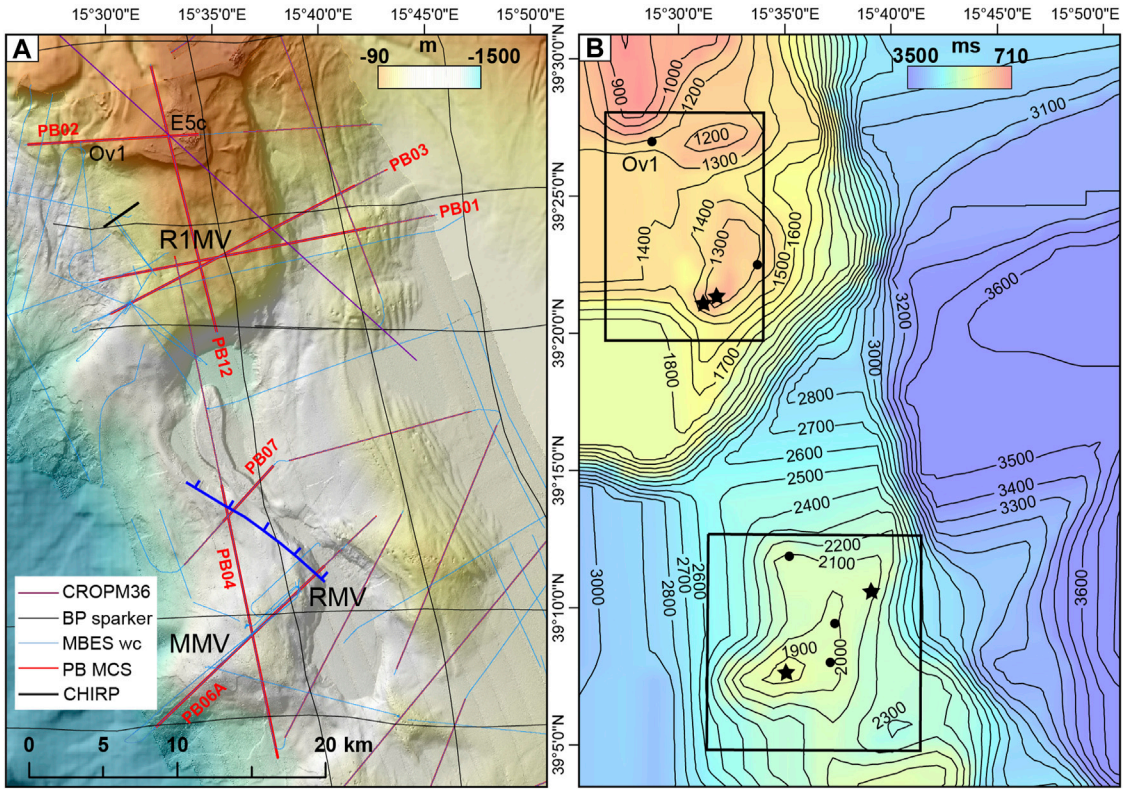

FIGURE 2 | (A) High resolution bathymetry of the Paola Ridge with track lines of the MCS and sparker data used to reconstruct the depth of the top of the Messinian units (MES) in **(B)**. The traces of water column acoustic recording by multibeam echosounders are presented and the portion of MCS profiles displayed in **Figures 3**–**8**, **11** are marked in bold. **(B)** The depth of the Messinian reflector (MES) is displayed in ms TWT with superimposed contour lines every 100 ms. Stars and circles indicate culmination of diapirs originated from updoming of the Messinian units with and without gas flares, respectively. The two rectangles outline the northern and southern sectors shown in **Figures 9**, **10**.

picking of flare sources. A normalization filter was applied to identify background noise values (dB) and apply signal-to-noise level thresholds (see Rovere et al., 2020 for a complete description of the processing routine). Water column plume features (flares) were manually extracted and exported as ASCII points, including longitude, latitude, depth of the feature and signal amplitude (dB) corrected with sound velocity profiles. The georeferenced seep data were imported into the Fledermaus software to explore virtual 3D scenes containing digital elevation models of the seafloor and sub-seafloor (**Figure 1C**). Geographical visualization and statistical analysis were performed using ESRI ArcMap 10.8. The relative height of the flares was obtained using the spatial analyst tool "extract multi value points" applied to the raster obtained from the bathymetric data acquired simultaneously with the water column.

Bottom waters were collected with a box-corer from the two most energetic gas discharging locations (R1MV and RMV), one of which already identified and imaged (Rovere et al., 2014). Water samples were taken immediately and bubble free after retrieval using a silicon tube. Samples were directly transferred into 250 ml pre-evacuated glass flasks and were acidified with 2 ml 37% HCl. The bottles were sealed with a Teflon-coated butyl rubber seal and were closed with aluminum crimp caps. Five additional near-bottom water samples were collected by means of the rosette sampler alongside the two most energetic structures. Dissolved gas concentrations were determined applying headspace analysis and gas chromatography techniques described in Franchi et al. (2017).

Seismic Reflection Data

Multichannel seismic reflection profiles (MCS, **Figure 2A**) were acquired by a single 60 in^3 mini Sercel GI-gun set in Harmonic Mode (30 Generator +30 Injector) with a shot interval of 9.375 m at 2000 psi. The data were collected by a 300 m long, 96 channels Geometrics GeoEel digital streamer with a trace distance of 3.125 m. Both the gun and the streamer were towed at 1.5 m below sea level to minimize the ghost effect on the emitted spectrum (centered well above 200 Hz), thus preserving the high frequencies needed to better resolve the shallower targets. During the acquisition four Digicourse birds were used to keep the streamer at a constant depth. The acquisition setting allowed a compromise between penetration in 700–800 m water depth and resolution, which can be regarded as metric along the vertical axes, if assuming a λ/4 criterion, with an actual 1.56 m lateral distance between the traces in the stack section. With this configuration, resulting in an effective horizontal sampling of

1.56 m in the stacked section, the maximum attainable fold coverage was 16 traces/CDP. The polarity of the seismic data was recorded as minimum-phase reverse SEG Standard. A conventional processing was applied by means of the Schlumberger Vista package; the sequence consisted of shot gather editing, large band pass filtering, velocity analyses, velocity based spherical divergence compensation, NMO correction, stack in common midpoint domain. The stack sections were eventually time migrated.

MCS profiles were further treated for image visualization with the Geosuite AllWorks software in which an A.G.C. window length of 250 ms was added to enhance the deeper reflections. The Petrel E&P Software Platform was used to extract the Root Mean Square (RMS) amplitude (iterative) attribute and to detect bright spots.

Vintage sparker profiles were made available by the Institute of Marine Sciences as paper profiles that were scanned to high resolution raster image (TIFF) and converted into georeferenced SEGY format using the Matlab routine IMAGE2SEGY (Farran, 2008).

The reflector corresponding to the top of the Messinian units (MES) was mapped on available MCS and sparker profiles and interpolated with spherical kriging with 1 km radius; contours were extracted as isobaths expressed in ms TWT (**Figure 2B**).

The seismic data are presented in TWT, as an accurate depth conversion is not feasible due to the lack of boreholes and a proper velocity model. However, some features are described in distance-depth and the thickness of sediment and volcanic deposits were derived from time to depth conversion using velocities of 1,500 and 2,100 m/s for respectively the water column and the Plio-Quaternary deposits, for consistency with De Ritis et al. (2019).

Sub-bottom echosounder profiles were used to image shallow sedimentary structures and map gas indicators with a Teledyne Benthos CHIRP-III system. The system is comprised of a 16 hull-mounted transducer array with a 2–20 kHz sweep-modulated bandwidth and 4 kW power per-channel, which allows a vertical resolution of about 50 cm. Data were post-processed for trace equalization and band-pass filtering with the software Geosuite All Works. Calculations for converting from two-way-traveltime to depth used a sound velocity of 1,500 m/s.

Indicators of Gas and Magmatic Features in Marine Geophysical Data

In seismic reflection data, bright spots and high-amplitude anomalies, seismic attenuation, velocity pull-down events, flat spots and chimneys are indicative of the presence of gas in the sediment and fluid contact (Müller et al., 2018). In our seismic data, gas-induced bright spots have the characteristic "peak-over-trough" pattern, in which a high-amplitude trough follows a high amplitude peak (a decrease in acoustic impedance, negative amplitude anomaly). On the contrary, the trough-over-peak reflections or positive amplitude anomalies represent a transition to a harder material (increase in acoustic impedance) generally associated with the occurrence of denser sediments, hardgrounds, precipitated authigenic carbonates, gas hydrates or the seabed.

Furthermore, in seep environments pull-up events may be caused by the presence of rocks with higher seismic velocity than the strata above, such as authigenic carbonates (Madof, 2018).

Magmatic sills can be interpreted based on their high amplitude character, showing as localized brightening of positive amplitude reflections similar to the seabed reflector (Omosanya et al., 2018). In terms of geometry and lateral continuity within the host strata, sills are imaged in seismic reflection data as saucer-shaped or sheet-like, high-amplitude reflections with abrupt lateral terminations within the host-rock strata (Roelofse et al., 2021).

Hydrothermal vent complexes are imaged on seismic sections as pipe-like, vertical zones of low amplitude and chaotic reflections in the conduits, terminating as dome, eye-shaped or crater morphologies at their summits (Omosanya et al., 2018). The interior of the vents vary between chaotic seismic reflections and clear reflections that terminate within the vents as a result of the disruption of the originally stratified sedimentary rock during fluid expulsion (Roelofse et al., 2021).

In side-scan sonar and multibeam backscatter data, the recognition of seep sites on the seafloor is often favoured by the detection of anomalously high acoustic seafloor reflectivity, caused by enhanced acoustic impedance contrast related to: sharp changes in the seafloor morphology (pockmarks, mud volcanoes); precipitation of authigenic carbonates at the seafloor; bubbles or gas hydrates in the sediment (Naudts et al., 2008).

RESULTS AND DISCUSSION

Seismostratigraphic Interpretation

The seismic stratigraphic analysis allowed the reconstruction of the depositional architecture of the stratigraphic units of the late Miocene and Pliocene-Quaternary, as well as the identification of magmatic intrusions. However, due to the lack of boreholes in the study area and adjoining sectors, a precise temporal framework for our seismostratigraphic reconstruction is not achievable. Some major seismic reflections can be assessed with confidence by correlation with CROP line M36, which passes above the volcanic structure E5c (after De Ritis et al., 2019) and crosses several MCS profiles presented in this study (**Figure 2A**).

In addition, a regional reflector associated with the top of the evaporites deposited during the late Messinian Salinity Crisis (MSC) is recognized by analogy with basins in the Western and Central Mediterranean, where it coincides with the top of the trilogy of units of the MSC (Dal Cin et al., 2016; Camerlenghi et al., 2020). The Lower Unit (LU) is inferred to be composed of gypsum and clastics, but is not visible in our data due to the poor energy of our source. The Mobile Unit (MU) is mostly a seismically transparent unit characterized by an upper folded boundary corresponding to evaporites filling the basins and onlapping into the lower continental slopes. The Upper Unit (UU) forms a distinct seismic facies, consisting of a package of high-amplitude parallel and continuous reflections, interpreted as

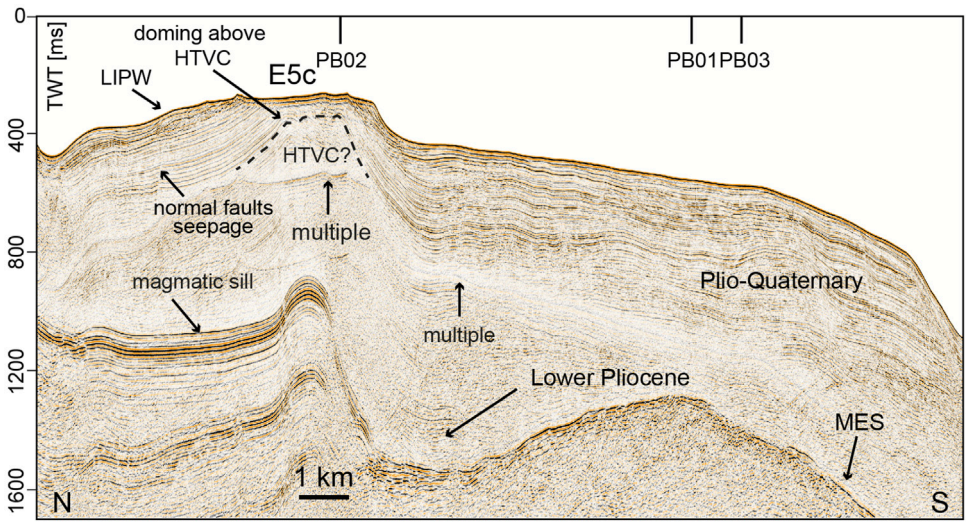

FIGURE 3 | Seismic reflection profile PB12 showing the vertically-stacked magmatic sills and the southward change in seismic facies of the upper Messinian units (MES). Location in **Figure 2A**.

an alternation of anhydrite or gypsum and marl layers. The erosion of these latter two units can be marked by the Margin Erosion Surface (MES), which is widespread on the continental slope of the Western Sardinian margin, where Messinian units are generally absent (Geletti et al., 2014). The MES can correspond with the regional M reflector recognized as the top of the Messinian units or regional unconformity in the Tyrrhenian Sea (e.g., De Ritis et al., 2019). This reflector is often located below the maximum penetration of our MCS data (e.g., **Figure 3**) and its depth surface has been mapped mostly with vintage sparker data (**Figure 2B**).

The overlaying Plio-Quaternary sedimentary succession is characterized by layered, mostly continuous, medium-to high-frequency and moderate to high-amplitude reflections. The Lower Pliocene is generally characterized by semi-transparent reflections (**Figure 3**).

In the northern study area a seismic facies characterized, internally, by high frequency and variable amplitude reflectors with sigmoid external geometry interpreted as "Lowstand Infralittoral Prograding Wedge" (LIPW) formed during pre-Last Glacial Maximum relative sea level lowstands has been identified by analogy with De Ritis et al. (2019) (**Figures 3**, **4A**).

Volcanic seismic features exhibit a mound-shaped or an eye-shaped geometry, with a flat base and convex top, discontinuous and chaotic internal reflectors, which can be interpreted as laccoliths and magmatic intrusions reaching the sea floor. Volcanic chimneys and seepage of fluids along vertical faults are widespread in the shallower sediments (**Figure 4A**). Similarly to the laccoliths, they are confined in the northernmost part of the Paola Basin, indicating that the ascent of magma wanes moving away from the northern volcanic-bearing sector of the study area.

The interpretation of magmatic sills is a problematic task in our data. In particular, the acoustic imaging of sills and the distinction between repeated sills and multiples beneath the first high amplitude sill reflection event (**Figure 3**) is challenging. However, the presence of sills is envisaged at this site in the lower-resolution CROP M36 line, on which, the same feature is interpreted as a magmatic sill associated with a conduit (see **Figure 4** in De Ritis et al., 2019). It is however, noteworthy to say that the seismic facies and striking folding of the reflectors corresponding with the magmatic sill are reminiscent of the acoustic response of the Messinian UU. In the Western Sardinia margin, the Messinian UU can be intercalated by (salt) lenses characterized by a more transparent facies (Geletti et al., 2014), with an overall seismic facies similar to what we observe in our case study (**Figure 3**). However, the presence of the Messinian UU in the upper and mid slope of the study area, where only marginal evaporites consisting of gypsum are believed to be present (Bertoni and Cartwright, 2015), is here considered unlikely. Additional high-resolution seismic data would be necessary to investigate this possible occurrence. Other sheet-like reflections characterized by high-amplitude that cross-cut the host-rock strata may be interpreted as sill remnants, severely disrupted or eroded by the observed diapirism of Messinian or pre-Messinian units (**Figure 4B**). Chaotic reflections and seismic attenuation stem from the sill and form a large vertical conduit below a 1.5 km wide eye-shaped feature characterized by an inner chaotic seismic facies with an external wall, which cuts surrounding clear reflections (**Figure 4A**). Bright spots are visible downslope from the conical edifice of Ov1, that overall can be interpreted as a volcanic feature (**Figure 4C**).

Proceeding farther south, in the non-volcanic sector of the study area, doming and diapirism of sediment below the MES reflector of the Messinian units remain significant (**Figure 2B**). In correspondence of the mound structure R1MV, the diapir gives rise to a prominent conduit which reaches 50 m below the seabed (**Figure 5A**), where bright spots and chimneys are connected to the presence of free gas in the shallow sediment (**Figure 5C**). The small chimney ascending to the seabed is barely visible also in the CHIRP profile (**Figure 5D**). Mass-transport deposits (MTDs) are

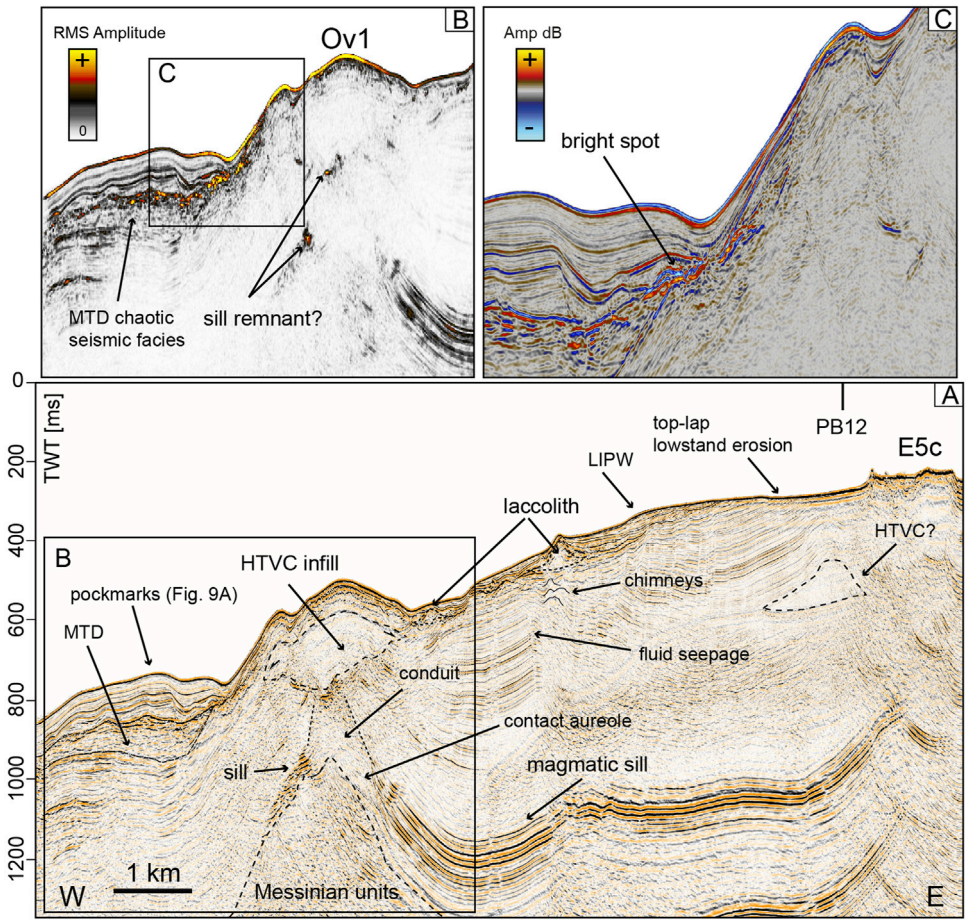

FIGURE 4 | (A) Seismic reflection profile PB02 showing the volcanic edifices of Ov1 and E5c with the hydrothermal vent complex (HTVC) located below Ov1 and the inferred extinct HTVC below E5c. The diapirism of Messinian units is also traced highlighting a conduit feeding the HTVC. Base and top of an MTD located downslope of Ov1 are outlined. **(B)** RMS Iterative amplitude extracted from the profile portion outlined in **(A)** showing possible remnants of a magmatic sill and the MTD chaotic facies. **(C)** Close-up of the seismic line outlined in **(B)**, where bright spots are indicated. Location in **Figure 2A**.

located both at the seabed (**Figure 5D**) and 130 m below the seafloor along the western slope of the mound structure (**Figure 5B**) suggesting a repeating pattern of discharge. A chimney is visible ascending from the top of the MTD, suggesting that gas-charged sediment is present within the MTD, although the latter appears to be sealed by positive amplitude anomalies, indicative of harder material (**Figure 5B**). Plio-Quaternary reflections pinch out against the diapir walls but are disrupted by crater-like reflections followed upward by chimney-like reflections (**Figure 5A**). Locally, the diapirism and associated conduits can reach to the seabed where the high amplitude reflectors are directly connected to the seabed (**Figure 6A**), and where acoustic flares have been detected in the MBES water column data. Sill remnants are possibly present also at these locations (**Figures 5A**, **6B**), while bright spots are quite evident (**Figure 6C**), also in the unfiltered shot gathers (**Figure 6D**).

Farther south, the depth of MES is always below the maximum penetration of our MCS data, however, the isobaths map highlights that the MES is shallower (**Figure 2B**) in correspondence of two mounded structures of very low relief (**Figure 7A**). Seismic attenuation is pervasive below scattered through-over-peak reflections that correspond to an impedance acoustic contrast, evidence of a harder layer located 150–160 m below the seabed (**Figure 7B**). Where these positive anomalies are more continuous, pockmarks are not present at the seafloor. The mound structures are not connected with gas flares in the water column, but are characterized by pockmarks and a crater on the seafloor (**Figure 7B**). Bright spots are present, but are buried below 25–50 m of sediment (**Figure 7C**). A saucer-shape reflection, that may resemble a magmatic sill, is present in the lower part of the Plio-Quaternary (**Figure 7A**).

In correspondence of the mound structure RMV, where the highest gas flare has been recorded, acoustic blanking is relevant (**Figure 8A**), while below the MMV structure a diapiric-like feature is imaged especially by RMS amplitude (**Figure 8B**). Acoustic blanking predominates where the acoustic impedance contrast likely indicates the presence of layers comprised of harder material (**Figure 8B**). Here, the observed scattered positive anomalies (**Figure 8D**) and pull-up events

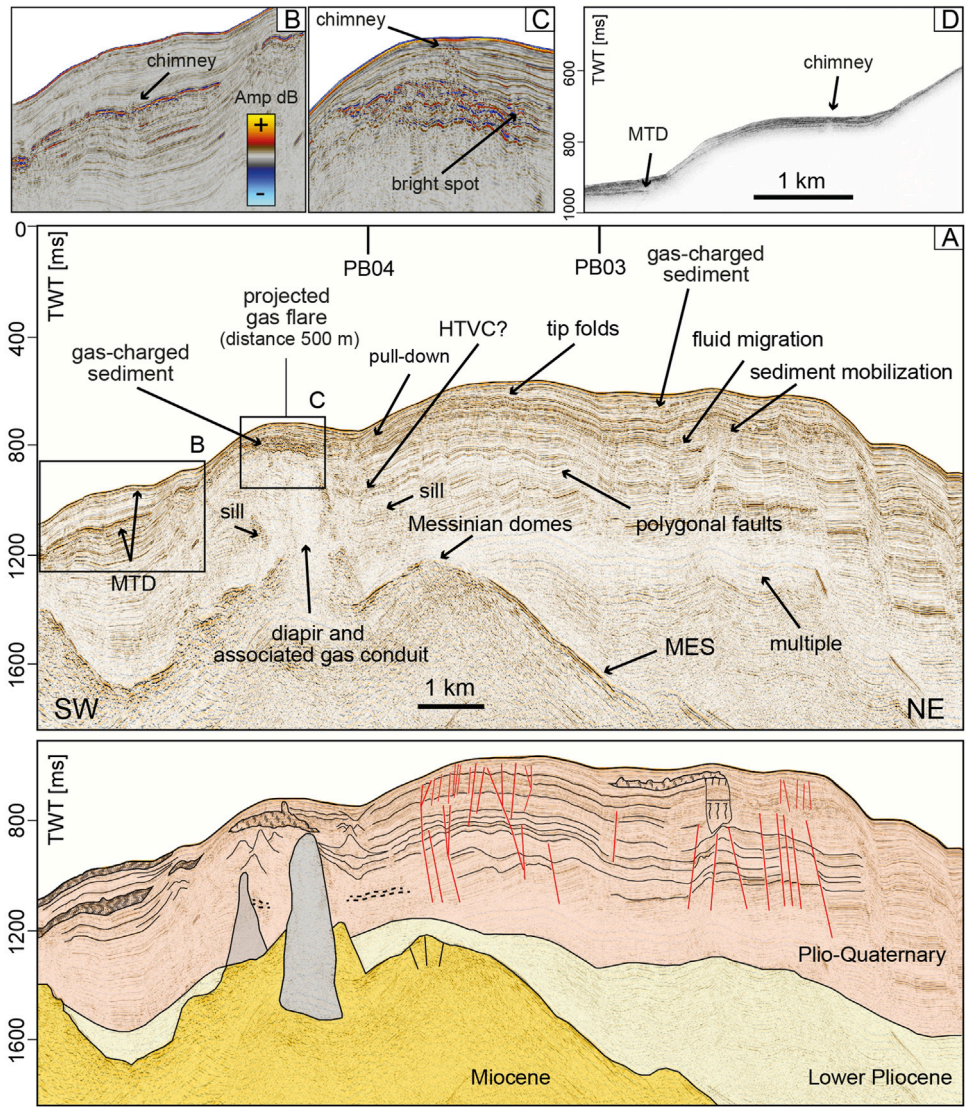

FIGURE 5 | (A) Seismic reflection profile PB01 and its line drawing (lower panel), showing the diapirism of the Messinian units below a projected gas flare in the water column. Close-up panels of seismics showing: **(B)** a chimney above an MTD; **(C)** a chimney emanating from bright spots located 50 m below the seabed. **(D)** CHIRP seismic profile showing the high amplitude character of the shallow reflections, a gas chimney and a shallow-seated MTD. Locations in **Figure 2A**.

(**Figure 8A**) are probably connected with the methane-derived carbonates that were actually collected by sediment coring. Bright spots are located near the seafloor where the gas flares are present (**Figures 8C,E**); in the mound structure where no flares were detected (same of **Figure 7A**) the bright spots are just 10 m below the seafloor (**Figure 8D**). In correspondence of MMV, faults radiate at the summit of the diapiric conduit outlined by seismic attenuation (**Figure 8C**).

Subsurface Gas Indications

Due to increased impedance contrasts, resulting from enriched free gas content in the pore-space, gas in the subsurface becomes visible in CHIRP profiles as enhanced reflectors resulting in high amplitudes of the seabed reflector and few meters below and acoustic blanking underneath (**Figure 5D**). A map of these areas of enhanced high-amplitude in the shallow sediment succession (1–10 m below the seabed) is shown in **Figures 9B**, **11B**. Mapping of high-amplitude reflections indicates that their occurrence is concentrated in the southern sector, around MMV and RMV, suggesting that these areas are influenced by higher gas concentrations. Subsurface acoustic blanking in CHIRP profiles is observed also as few-meters wide vertical chimneys reaching within 3–4 m from the seafloor (**Figure 5D**). Since they correspond with gas flares in the water column, or their projection at distances <500 m, and correlate with similar features in MCS data (**Figure 5B**), they are interpreted as gas pockets. Another type of high amplitude reflections, consisting of narrow vertical lineations, a few meters long, is frequently

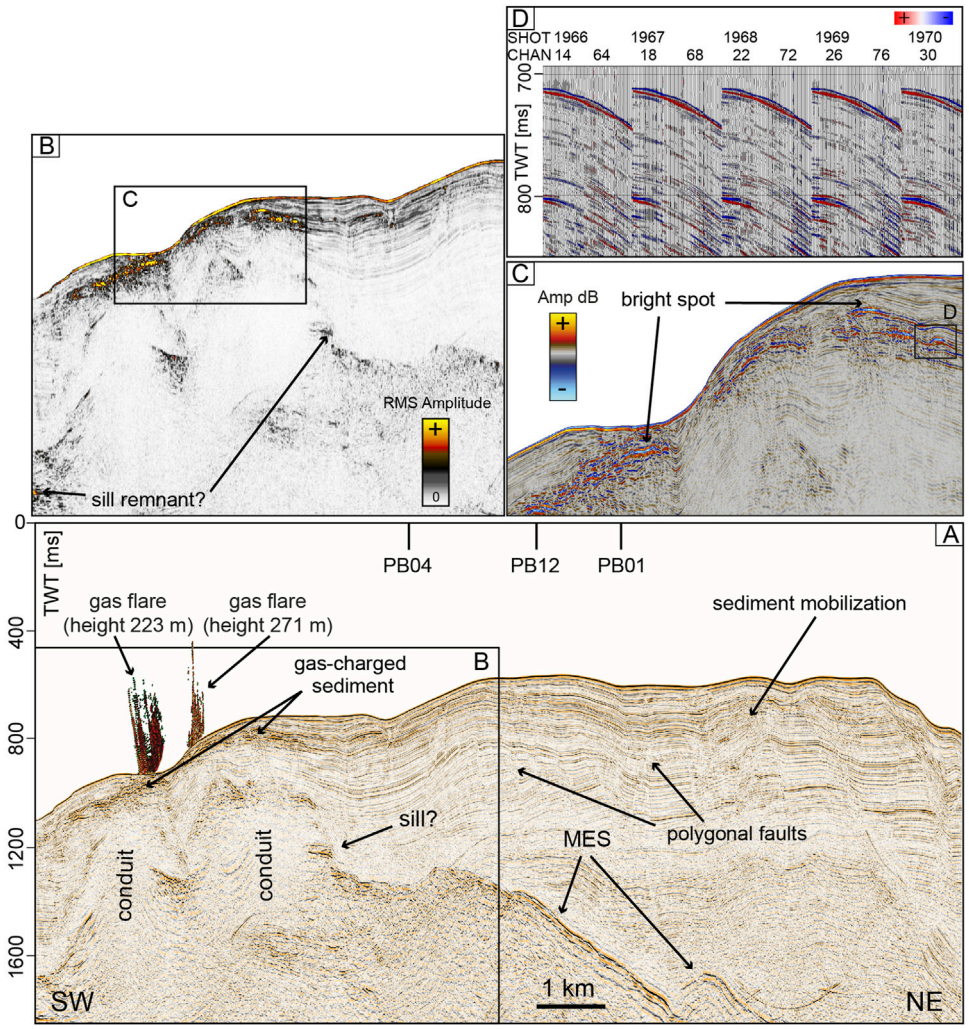

FIGURE 6 | (A) Seismic reflection profile PB03 showing diapirism and conduits below two gas flares in the water column. **(B)** RMS Iterative amplitude extracted from the profile portion outlined in **(A)** and showing bright spots, and possible remnants of a magmatic sill. **(C)** Inset outlined in **(B)** where bright spots are indicated. **(D)** 5 consecutive shot records along profile PB03 at trace 2,739 and 800 ms where a bright spot is present. A large ormsby band pass filter (10–20/500–1,000 Hz) was applied to remove the background noise. Location in **Figure 2A**.

observed close to the seafloor and connects gas chimneys with flares in the water column (vertical bright spots) (**Figures 9A**, **11A**). Vertical bright spots mostly corresponds with areas of pervasive landslide headwall scars (**Figure 9A**) in the northern sector of the study area, or pockmarks in the southern sector (**Figure 11A**).

Gas Flare Occurrence

Gas emissions were detected and identified as flares in water column echograms of the MBES. Due to the limited coverage of the swath needed for water column observations, the total area covered for water column flare imaging by swath coverage was restricted to 2,476 km^2 (**Figure 2A**). These data were loaded in the QPS Fledermaus Midwater tool using the stacked view as initial guide for possible venting, and the fan-view for detailed detection of gas emissions (**Figures 9D**, **11D**). When a flare was identified, its acoustic signal was traced to the seafloor through subsequent fan-images and its geographic location was picked at the central point. The MBES data allow also defining flare locations when offset from the central ship track. However, in this case, identifying the outlet at the seafloor can be problematic due to background noise, especially when flares are not standing out clearly above the seafloor and weather conditions are not ideal. Depending on water depths, bubble size distribution, bubble rise rates, and possible turbulent flows, some frequencies may be better suited for detecting gas in the water column, and EM302 30 kHz acoustic data were the most efficient to detect the gas flares.

In total, 15 water column anomalies were recorded in the study area (**Table 1**). This represents a minimum value, since some distinct flares may appear clustered because their spacing is smaller than half of the MBES footprint used to detect the

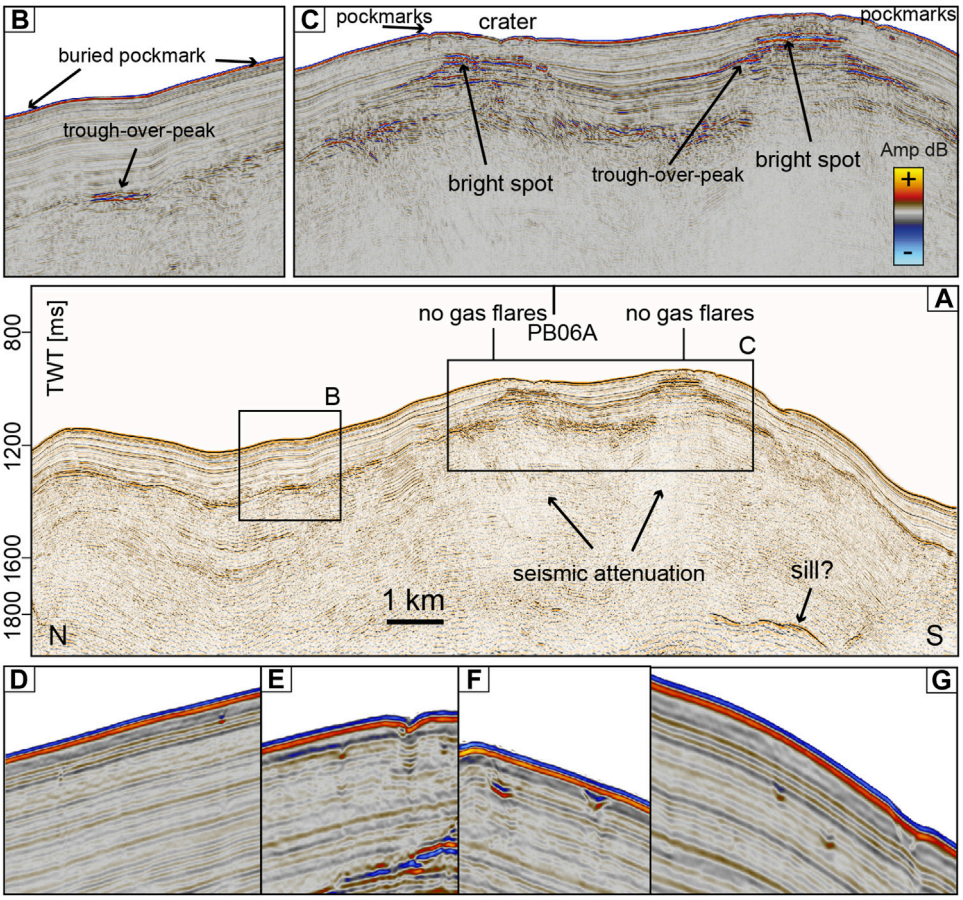

FIGURE 7 | (A) Seismic reflection profile PB04 crossing the area between RMV and MMV and showing seismic attenuation underneath bright spots and scattered trough-over-peak events located 100–150 m below the seabed. Close-up panels of seismics in correspondence of: **(B)** trough-over-peak events; **(C)** bright posts connected with the presence of pockmarks and free gas few meters below the seabed. Location in **Figure 2A**. **(D–G)** Examples of buried pockmarks.

flares (**Figure 9D**). Flare observations were classified according to their appearance being certainly caused by gas bubble emissions. Relatively weak anomalies or with shapes, deviant from a continuous linear feature connected to the seafloor, were therefore discarded; however, their number was negligible compared to the columnar shapes. So far manual identification and extraction, with quality check on, is the common methodology used (Römer et al., 2021), although some attempts for automation have been achieved to distinguish gas flares from fish schools (Minelli et al., 2021). However, the study area is not renowned for fishing grounds, therefore the occurrence of fish schools was unlikely or very limited. As some areas were studied multiple times, flare observations were partly repeated and flare numbers have been corrected for double counting. Double detection during different survey times suggests that most flares are spatially and temporally stable, this is further constrained by the observation of the same flare, characterized by similar height, recorded at RMV in 2011 (Rovere et al., 2014) and 2014 (this study).

Flares were detected at seafloor depths of 548–862 m. Flares appear in heights from less than 20 m in the outlets surrounding the main flares and end mostly within the water column, the only exception being the two flares identified on top of RMV that reach very shallow water depths. Flare height determination is generally limited by the swath geometry, and the upper parts of the highest flares detected at RMV are probably cut off about 15–25 m below the sea surface (**Figure 11D**). However, no natural ebullition at the sea surface was observed during the surveys and there is no reason to suggest that gas exchange with the atmosphere is active at least in calm weather conditions and during the summer season, when both the 2011 and the 2014 surveys have been conducted (August and June).

The flares are always located directly above bright spots and stacked bright spots connected to the seabed or very close to it in the MCS profiles (**Figures 6**, **8**).

Seafloor Morphology and Backscatter in Relation to Gas Flares

Bathymetric mapping of the study area revealed that flare locations are systematically related to specific morphological seafloor elements (e.g., mounds, pockmarks, and linear scarps)

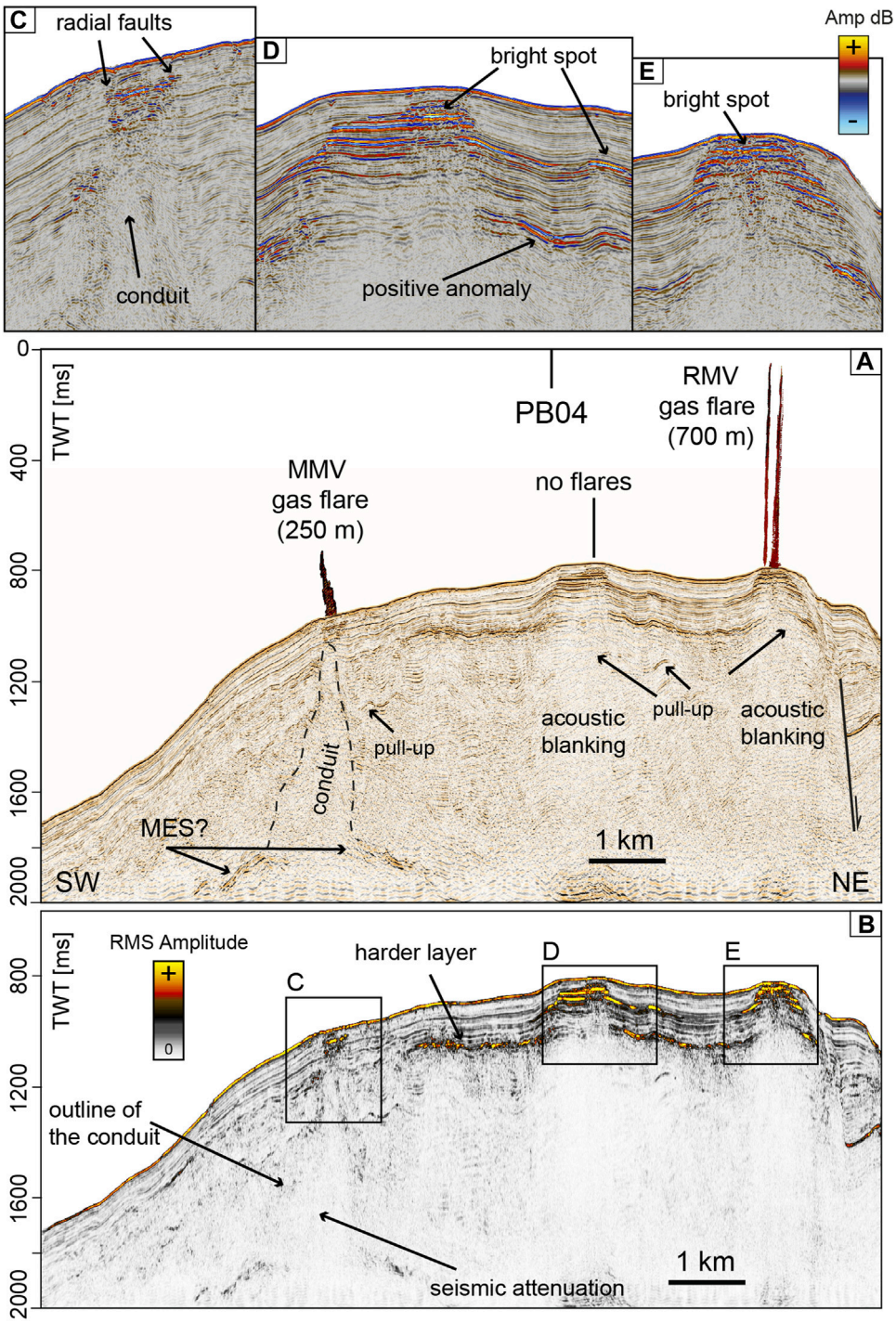

FIGURE 8 | (A) Seismic reflection profile PB06A passing above RMV and MMV where gas flares have been detected. **(B)** RMS Iterative amplitude extracted from the whole profile highlighting a continuous reflection connected to an impedance acoustic contrast due to a harder layer located 100–150 m below the seabed. Close-up panels of seismic in correspondence of: **(C)** MMV; **(D)** the mounded structure not connected to gas flares; **(E)** RMV. Location in **Figure 2A**.

(**Figures 9A**,C, **11A**,C) or seafloor backscatter anomalies (methane-derived carbonate precipitation and fluidized mud at the seafloor) that are usually associated with gas seepage (**Figures 9B**, **11B**). The flares align almost N–S along the seaward slope of the Paola Ridge (**Figure 2A**), the only exception being the flares in correspondence of the RMV. This mound structure is located more landward and is confined by a NE-dipping normal fault, which uplifts the mound with respects to the adjoining Propeller

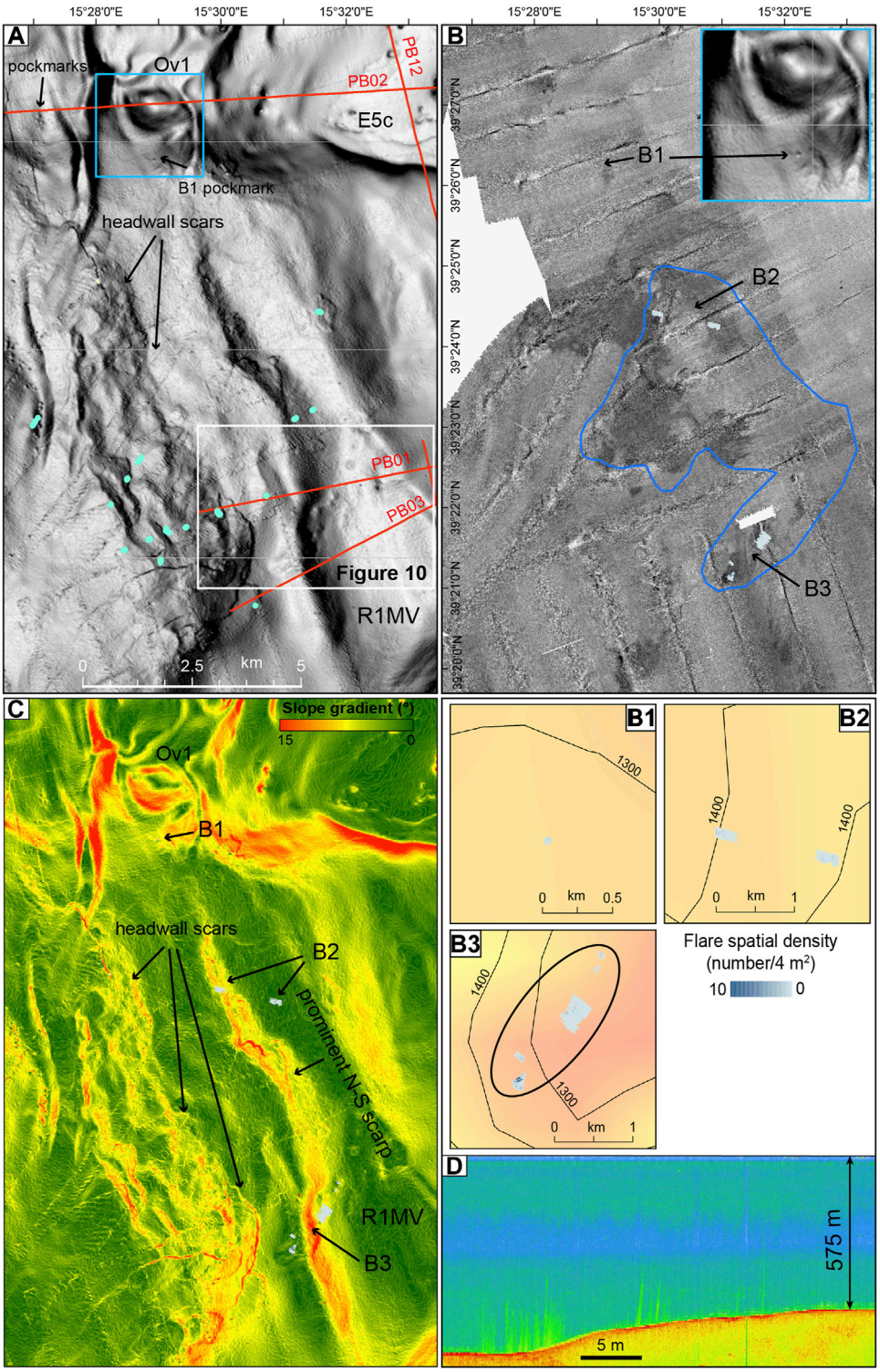

FIGURE 9 | (A) High-resolution MBES bathymetry of the northern sector of the study area with track lines of the MCS data (red), vertical bright spots identified in CHIRP profiles (small baby-blue circles). **(B)** MBES backscatter of the seafloor, the area of shallow high-amplitude reflectors in CHIRP profiles is outlined in blue. **(B1–B3)** are enlargements of flare density superimposed to the depth of the Messinian reflector. Zoom in of the pockmark located on the southern flank of Ov1 is framed in the upper right corner. **(C)** Slope gradient calculated from the MBES bathymetry showing the presence of headwall scars and the N–S scarp connecting Ov1 with the areas of R1MV flares. **(D)** Stacked view of gas flares detected in the water column by the MBES EM302 corresponding with the ellipsis in **(B3)**. The area is outlined in **Figure 2B**.

TABLE 1 | Summary of location, height and water depth at which the flares have been identified in MBES water column echograms.

Location	Structure	Water depth range (m)	Area of plume (m^2)	Max height (m)	Isolated plume	Cluster of plumes	Impacted area (km^2)
northern sector	Volcanic Flank	548	1968	154	Yes		
	Continental Slope	561–629	40,514	227		Yes	0.75
			37,312	238		Yes	
	R1MV	575–706	4,164	297	Yes		1.7
			3,445	90	Yes		
			106,,261	205		Yes	
			10,454	177	Yes		
			16,041	271		Yes	
			8,458	223		Yes	
southern sector	MMV	813–862	9,586	246	Yes		0.2
			9,937	146	Yes		
			17,217	115		Yes	
			27,854	145	Yes		
	RMV	722–736	28,868	597			0.08
			45,905	696			

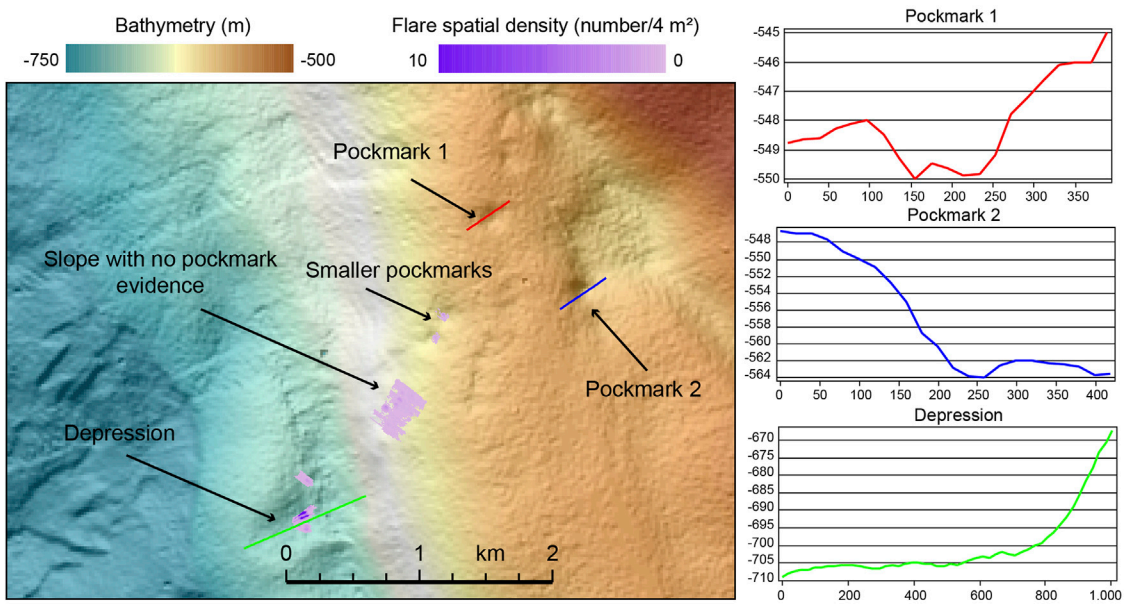

FIGURE 10 | Zoom in of the area of pockmarks and gas flares outlined in white in **Figure 9A**. On the right, bathymetric profiles of larger pockmarks, where no gas flares have been detected, and of the depression where gas flares are more concentrated. Note that flares are located above smaller pockmarks.

Basin (**Figure 8A**) and is particularly evident to the north (**Figure 13**).

The northernmost isolated flare rises above a pockmark located on the southern steepest flank (7–10° gradient slope) of Ov1, a 100-m-high almost conical mound which may be interpreted as an HTVC (**Table 1**, **Figure 9B1**). A sediment core collected on top of Ov1 recovered less than 1 meter of sediment, consisting of conglomerates and carbonate hardgrounds. On the western flank of Ov1, pockmarks are present but limited in number (**Figure 9A**), the largest being 100 m wide, and are probably related to fluid seepage through fractures from the buried MTDs located downslope (**Figure 4A**). The presence of MTDs characterized by bright spots and chimneys, indicative of the presence of free-gas in the sediment and seepage, may be related to past hydrothermal activity and gas discharge.

Other flares develop along a prominent scarp that connects the Ov1 HTVC with R1MV (**Table 1**), and forms a N–S oriented, 12-km-long feature consisting of a series of structural terraces originating a topographically complex slope sector (**Figures 9A,C**). The tallest flares (223–271 m) develop on a small depression (**Figure 10**), downslope from the scarp that makes up the western flank of R1MV (**Figures 9C, B3**). Here, flares are not obviously associated with pockmarks that are <5 m deep, and

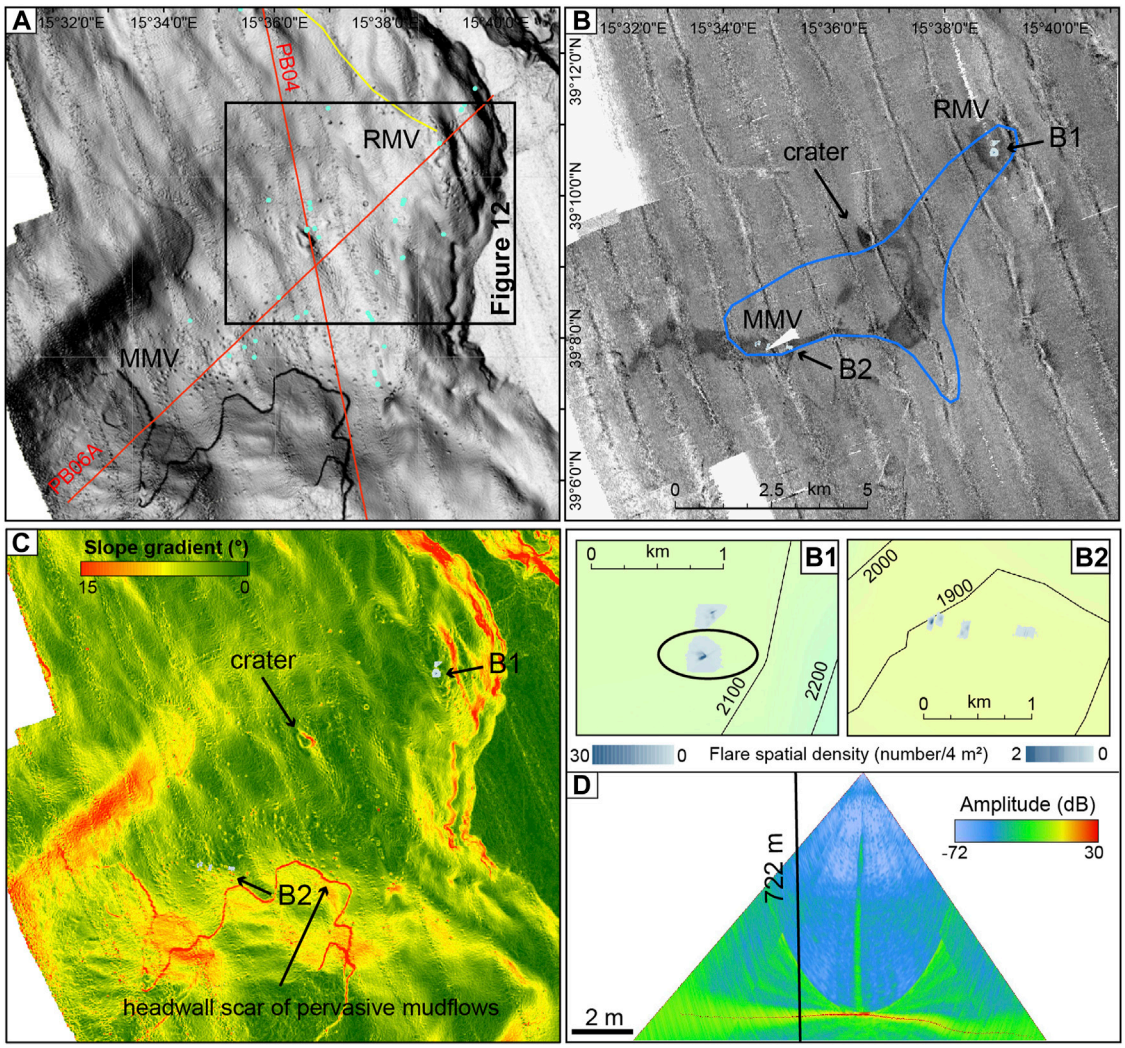

FIGURE 11 | (A) High-resolution MBES bathymetry of the southern sector of the study area with track lines of the MCS data (red), vertical bright spots identified in CHIRP profiles (small baby-blue circles). **(B)** MBES backscatter of the seafloor, the area of shallow high-amplitude reflectors in CHIRP profiles is outlined in blue. **(B1, B2)** are enlargements of flare density above MMV and RMV superimposed to the depth of the Messinian reflector. **(C)** Slope gradient calculated from the MBES bathymetry showing the overall mounded structure comprising MMV and RMV. **(D)** Fan view of the gas flare detected in the water column above RMV by the MBES EM302 corresponding with the ellipsis in **(B1)**. The area is outlined in **Figure 2B**.

averagely 100 m in diameter (**Figure 10**). Flares develop above the smaller pockmarks, a depression and the slope (**Figure 10**).

Gas flares are connected with areas of highest seafloor backscatter and high-amplitude shallow reflections in CHIRP profiles (**Figure 9B**); however, along the northern sector of the study area, the high seafloor backscatter is also indicative of the presence of several landslide headwall scars and erosion at the seafloor that contribute to the character of the acoustic response. Therefore, in this case, the seafloor backscatter is not an exhaustive tool to distinguish areas characterized by fluid seepage and presence of gas on or close to the seabed. Furthermore, a further contribution to the high backscatter can come from the widespread shallow-seated MTDs, possibly related to the discharge of fluidized mud and mudflows from R1MV, as testified by CHIRP profiles (**Figure 5D**). This setting is similar to that of MTDs located downslope of the HTVC of Ov1, where amplitude anomalies are associated with fluidized sediment and gases (**Figure 4C**), and may correspond to eruptive phases, which have now ceased. In addition, the presence of carbonate hardgrounds, in general not associated with active venting (e.g., Svensen et al., 2003), points to the extinction of the main hydrothermal vent activity, on top of Ov1. However, there might be still residual thermal effect reflected by the release of gas through fractures and along the flanks of the edifice.

Moving southward, MMV and RMV sit on a large almost rounded (13.5 × 11.5 km) mound 300 m high. There are no significant morphological differences between MMV and RMV, in terms of height and size, however RMV appears to be fault-controlled. Above MMV, several clusters of gas flares (**Table 1**)

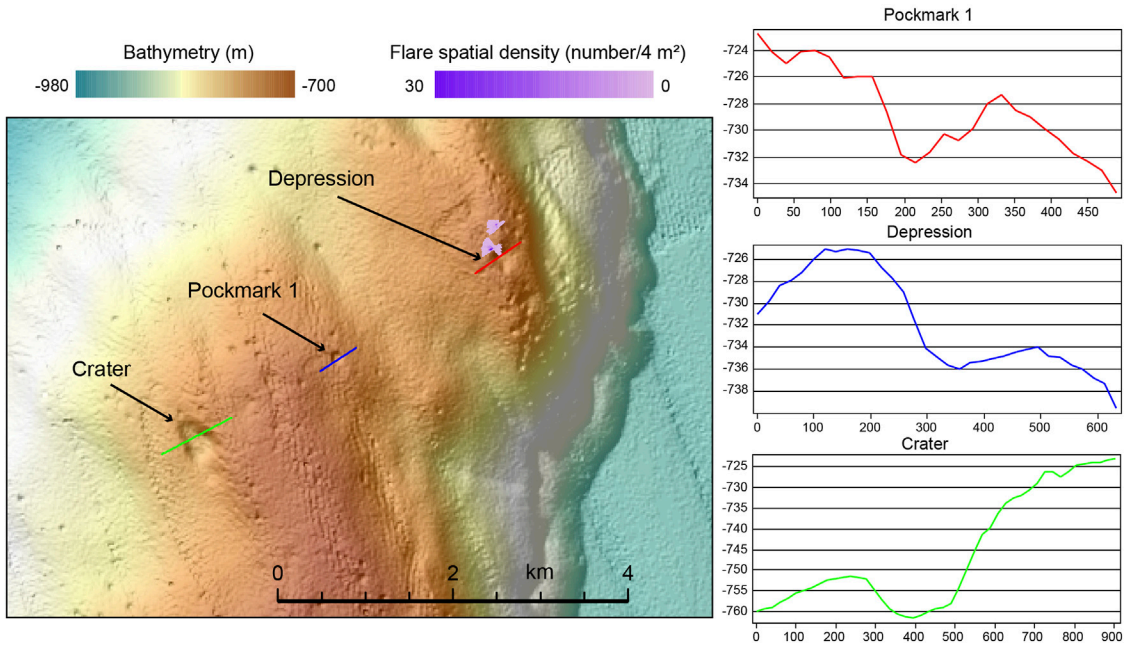

FIGURE 12 | Zoom in of the area of pockmarks and gas flares outlined in black in **Figure 11A**. On the right, bathymetric profiles of an average pockmark and the crater, where no gas flares have been detected, and of the depression where gas flares are more concentrated on top of RMV.

are associated with evenly distributed pockmarks with diameter of about 50 m and average depth of a few meters (**Figures 11A, B2**). The western flank of MMV is characterized by a belt of landslide headwall scars, which might coincide with shallow-seated mudflows (**Figure 11C**). MMV and RMV are morphologically separated by the largest depression observed in the study area. The latter is a 250 m wide and 10 m deep, crater hosted in a subtle saddle (< 40 m deep) between MMV and RMV, not associated with any gas flares (**Figures 11A**, C, **12**). On top of RMV the two highest gas flares detected in the study area (700 m against a water column of 736 m) develop above pockmarks and a depression, which has dimensions similar to the crater (**Figure 12**).

Also in the southern sector of the study area, the gas flares always coincide with high seafloor backscatter areas, which are however larger than those affected by gas discharge in the water column. Although slope gradient at the mounds flanks may enhance seafloor reflectivity, the very high backscatter of the crater may be a further evidence of the presence of gas in the first 25–50 m of the sub-seabed. This is further supported by bright spots in MCS data (**Figure 7C**), that may be related with a past outburst that formed the crater.

In other seep areas, steeper dipping and higher mounds are indicative of recent or prolonged growth of structures, whereas, lower-relief and gentler topography are associated with older features (e.g., Serié et al., 2012). In the study area, the differences in the morphology of the mounds are not so significant, and therefore may not be indicative of their different development stages and seepage activity. Furthermore, the seafloor reflector does not show significant variations in seismic amplitude with depth and topography, suggesting that the seafloor is everywhere covered by the same type of sediment, with the only exception coinciding with the erosional seafloor downslope R1MV.

Dissolved Gases in the Water Column and Bottom Waters

Gas samples from two box-cores collected on RMV (flare B1) and R1MV (flare B3) revealed a chemical composition dominated by CO_2 (up to 98.73% by vol.) and subordinately by N_2 (up to 1.26% by vol.) and methane (< 0.06% by vol.). The carbon and oxygen isotopic ratios of CO_2 are −1.8 and −1.1 (V-PDB ‰) and −2.4 and −4.4 (V-PDB ‰), respectively. Data collected with the Niskin bottles carry negligible CH_4 and other hydrocarbon content, probably due to the difficulty in controlling the lowering of the rosette sampler inside the flares and reaching close to the bottom. The chemical composition of the Niskin samples is similar to present-day seawater, whereas the alkalinity is slightly higher (Franchi et al., 2017).

Spatial Distribution of Flares in Relation with Diapirs, Faults, Magmatic Sills and Mineral Deposition

All flares detected are found in correspondence of subsurface of diapirs apparently originating from upward folding of the top Messinian units and diapirism connected to gas conduits directed to the seabed. The highest abundance of flares occurs around the diapir observed below R1MV (**Figure 6A**), while the highest gas flares were detected in connection with acoustic blanking

connected with up warping of the Messinian units (not imaged by our MCS data) below RMV and doming and diapirism below MMV (**Figure 8A**).

Gas chimneys or conduits, that represent the path of vertically migrating gas into shallow reservoir sediments below bright spots, and that are located above salt domes has been detected in various geological contexts, such as: the German North Sea (Müller et al., 2018); the upper continental slope of the Santos Basin offshore Brazil (de Mahiques et al., 2017), where Miocene diapirs are associated with fields of pockmarks on the seabed; the Angola offshore (Serié et al., 2012), where a cluster of gas hydrate pingoes is attributed to a gas migration system along the flanks of a salt diapir. In the Mediterranean Basin, Messinian evaporites deposited in thick sedimentary successions in the deepest sub-basin depocenters as a consequence of the MSC. Although salt diapirs and domes are normally implicated in shaping the thermal and dynamic fluid circulation and seepage, this straightforward relationships is not always observed in the Mediterranean. In the Nile deep-sea fan, not all mud volcanoes are linked to the presence of thick Messinian evaporites (Bertoni and Cartwright, 2015). Even in the Levantine Basin, diapirism of Messinian salt and focused fluid flow reaching the seabed in the form of chimneys, which cross the thick basinal Messinian evaporites and originate in the pre-Messinian units, are not directly linked with mud volcanoes (Hübscher et al., 2009; Bowman, 2011). In the Western Mediterranean, the largest Messinian diapiric structures form in the Plio-Quaternary depocentres, where the sediment overburden is larger (Geletti et al., 2014) and the buoyancy difference between indurated gypsum and overlying soft deep-sea muds favours the initiation of diapirism (Dal Cin et al., 2016). Less frequently, in these deep basins, salt diapirs cause intense deformation in the upper Plio-Quaternary, breach through the sea bottom and give rise to prominent surface fluid flow. On the contrary, in the slope context of the study area, where only gypsum deposits are present, which makes quite a different lithological and dissolution pattern compared to halite, diapiric structures concentrate where the thickness of the Plio-Quaternary is reduced in connection with up warping of the MES reflector (**Figures 5A**, **6A**).

Furthermore, in the Western Mediterranean, salt deformation was intense during the Lower Pliocene, whereas in the Paola Basin, a more prolonged phase of up-rising and deformation of the diapiric structures, not necessarily connected with passive diapirism of evaporites, is indicated by pinch-out terminations of the upper Quaternary units (**Figure 5A**). This may be explained with a tectonic control over the emplacement of the diapirism in the Paola Basin, which prevail over sedimentary processes. On the other hand, the presence of massive free gas in the very shallow subsurface and vigorous and steady gas flares in the water column, as above R1MV and RMV, requires high fluid flux which is usually associated with a supply of thermogenic fluids by a deep-rooted plumbing system (e.g., Plaza-Faverola et al., 2015). In our case study, this plumbing system likely exploits normal faults, which are not obviously imaged in our MCS data because of the intense acoustic masking. This notwithstanding, a normal fault along the western boundary of the Propeller Basin is

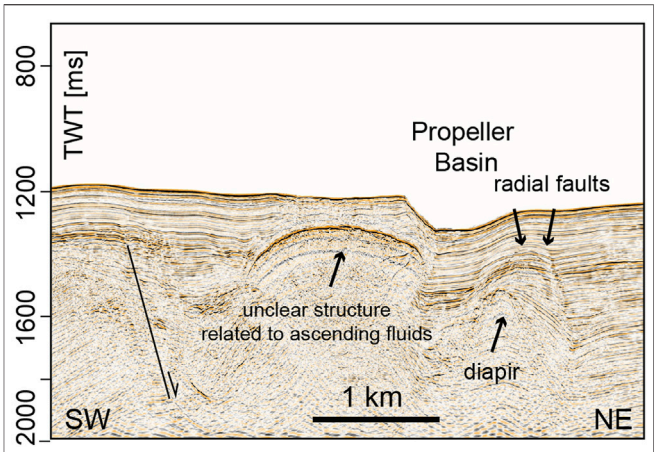

FIGURE 13 | Seismic reflection profile PB07 showing the normal faults that can be traced along the Propeller Basin. Location in **Figure 2A**.

imaged (**Figure 13**). Above the conduits, radial faults are often present, especially on top of MMV (**Figure 8C**). The conduits below R1MV and MMV, that are associated with gas flares in the water column, align along the westward slope of the Paola Ridge which is tectonically controlled by normal faults (Gamberi and Rovere, 2010) and experienced subsidence during Pliocene to Quaternary times (Pepe et al., 2010).

In addition, polygonal faults are observed in the upper Plio-Quaternary to the east of the gas flares area of R1MV, they are related to unfocused fluid flow probably by the early expulsion of pore waters in the fine-grained sediments of the Plio-Quaternary. Only few of these faults have a subtle manifestation at the seafloor, indicating recent activity (**Figure 5A**). In the Western Mediterranean, polygonal faulting directly above the thick stratified evaporite sequence may have formed in response to water release from the underlying evaporites, due to gypsum-anhydrite conversion. The gypsum-anhydrite diagenetic reaction is temperature and depth-dependent (Bertoni and Cartwright, 2015). Therefore, given the relatively shallow-burial depth in the R1MV area, the likely presence of only gypsum in the Messinian units, a high geothermal gradient/heat flow should be invoked for addressing the diffuse fluid seepage along the polygonal faulting area east of R1MV.

The presence of magmatic sills in the Plio-Quaternary succession of the study area (**Figures 4A**, **5A**) may represent the explanation for the additional thermal gradient needed for the observed intense fluid flow and gas venting in connection with up warping of thin Messinian evaporites in the study area. The upward folding of the Messinian units and seal bypass can be therefore associated with fracturing caused by the hot igneous intrusions, that are interconnected or lie just above the sealing succession (**Figures 4A**, **5A**), as in other contexts such as the Rockall Basin in the NE Atlantic (Cartwright et al., 2007). The heating of the colder and wetter Plio-Quaternary sediments may have resulted in boiling of pore water, rapid maturation of organic matter in the sill aureole and overpressure around the sill with the formation of the fracture network along which

gaseous hydrocarbons, water and magmatic material escaped to the seabed and formed eye-shaped or domed HTVCs (**Figure 4A**), where material is extruded into the seafloor and may resemble a mud volcano system (e.g., Iyer et al., 2013; Roelofse et al., 2021).

The assessment of the presence of sills in our MCS data remains problematic, although subtle evidence of magmatic sills may be detected in the lower part of the Plio-Quaternary (**Figures 5A**, **6B**, **7A**). The subtle evidence of magmatic sills may be due to: lack of seismic signal penetration; acoustic masking caused by the transparent facies of the diapirs and gas conduits (**Figure 8A**); fractures that may form for either thermal contraction during cooling, metamorphism in the contact aureole and rapid loss of hydrothermal fluids from the surrounding sediments (e.g., Cartwright et al., 2007; **Figure 4A**).

Seismic acoustic masking has been interpreted as gas chimneys or gas-charged fluid migration conduits also in areas not in connection with salt domes (Plaza-Faverola et al., 2015; Waage et al., 2019). A minor fraction of free gas in the pore space of sediments is sufficient to produce signal blanking in form of chimneys that can be thus regarded as gas-charged fluid migration pathways. On the other hand, acoustic masking and seismic attenuation can be due to the shadow effect by a sharp impedance contrast when short offsets are used in the acquisition of the seismic data, such as in the system used for this study. The acoustic masking zones underneath RMV and the other mounds in the southern sector of the study area crosscut the entire Plio-Quaternary succession (**Figure 7A**). The masking zones are located below scattered high-amplitude positive anomalies located 150–170 m below the seafloor, intercalated with bright spots and seismic pull-up events that may be associated with authigenic minerals (**Figures 6A,B**). This is confirmed by the fact that, where no high-impedance contrast is visible, the conduit rising to the seabed is well imaged by RMS amplitude, such as below MMV (**Figure 8B**). The scattered character of bright spots in the mounds, where no gas flares have been recorded (**Figures 7C**, **8D**), may further suggest that the lower-impedance contrast is caused by gas within the pore space and fractures rather than gas bubbling at the seabed surface. On the contrary, the positive anomalies may be related to the presence of authigenic carbonates or other types of deeper mineralizations that hamper the seepage towards the seabed. The isotopic signature of the authigenic siderites (δ^{13}C 3–10 V-PDB ‰, δ^{18}O 8–9 V-PDB ‰) collected in the sub-seafloor of R1MV, RMV and MMV (< 10 m) indicate a precipitation in the methanogenic zone (Rovere et al., 2015). Therefore, the seep-carbonate horizons may be fed by the migration of thermogenic methane and hydrocarbons from deeper levels below the Messinian units, or by maturation of the organic matter favoured by the thermal anomaly connected to the magmatic sill as, for example, in the Guaymas Basin (e.g., Simoneit et al., 1988). In the area of the crater separating MMV and RMV, where gas flares are absent, a bowl-shaped deep reflection can be interpreted as a magmatic sill connected with the development of HTVCs that are not presently active. Here, fluids migrated through the lower part of the hydrothermal vent complex, which acted as a vertical zone of high-permeability, enhanced fracturing of the host sediment and circulation of fluids. However, the fractures that develop during the initial stages of hydrothermal activity within the metamorphic contact aureole are highly subject to mineralization and clogging by cementation (Cartwright et al., 2007). Therefore, it is here suggested that the majority of the HTVCs in the southern sector of the study area formed in consequence of an initial gas-dominated explosive phase, but soon became inactive due to their pervasive mineralization. The thermal effect continued to promote the maturation of organic matter and deposition of methane-derived siderites that in turn progressively acted as major barrier for fluid seepage to the seafloor (**Figure 7A**). Where gas venting have been observed in the water column, either the hydrothermal activity is still prevalent or precipitation of methane-derived carbonates is not sufficient to prevent prolonged gas migration.

Flares and Hydrothermal Vent Complexes, Geodynamic Implications

Magmatic activity in sedimentary basins has a critical impact on fluid migration as hot intrusive rocks elevate the local geothermal gradient. The main temperature effect of magmatic sills is believed to last only few thousand years (Roelofse et al., 2021). However, normal faulting, which is quite common in hybrid sedimentary-volcanic systems, causes downward displacement of hanging wall sediments that are initially colder. This process results in the thermal instability of the basin, which may regain its steady state only after a long period, in the order of a few millions years (e.g., Sydnes et al., 2019). There are cases, such as the offshore of eastern Australia, where an Eocene phase of magmatism feeding hydrothermal vent complexes has been linked to the formation of buried mud volcanoes and is believed to still influence the occurrence of seep-related features at the seafloor (Rollet et al., 2012). Therefore, we interpret the Paola Basin as a site where magmatic intrusions, which remain challenging to image in our data but are likely present based of numerous linked observations, have provided the necessary thermal gradient to maintain an effective hydrothermal system.

In hybrid sedimentary-volcanic systems, inorganic CO_2 concentrations generally exceed 50 vol%, whereas CH_4 concentrations are generally lower (roughly > 1–2 vol%). Their surface manifestations, like muddy craters or bubbling pools, may be similar to, and thus may be confused with, pure sedimentary gas manifestations (hydrocarbon seeps), such as mud volcanoes (Procesi et al., 2019). According to a global review (Procesi et al., 2019), the δ^{13}C-CO_2 carbon isotope signature, related to decarbonation reactions (thermo-metamorphism) and magma-mantle degassing at high temperatures (> 250°C) varies from −8‰ to +2‰. These values are in agreement with those recorded at the two gas venting sites sampled above R1MV and RMV (−1.8 and −1.1 V-PDB ‰), implying that there must be a contribution from deep magmatic and metamorphic systems to the gas released at the seabed in the Paola Basin, although a certain contamination from seawater CO_2 cannot be excluded in our isotopic signal, due to the sampling of gas bubbles from the box

core. It must be added that the presence of an evaporitic sequence, although thin, such as the top Messinian unit, modifies pressure and temperature regime, adding a forcing to the sediment burial and fluid history of the basin, including complex feedbacks of diagenesis and dissolution. Furthermore, the diapirs originating from the Messinian units are connected through extensional faults to the deep-rooted plumbing systems. This setting enhances fluid migration of both abiotic CH_4, formed by deep magmatic and post-magmatic high-temperature reactions and biotic thermogenic CH_4 related to thermal reactions on organic matter, which is reflected in the precipitation of isotopically heavy carbonates.

The timing of the onset of fluid seepage in the study area must be better constrained. In the Mediterranean area, fluid flow systems formed around the Messinian time, and were sourced from the pre-MSC under saturated fluids and overpressured sediments, below the thick gypsum-halite sequences (Bertoni and Cartwright, 2015). The absence of paleo-pockmarks or limited presence of pockmarks buried by a thin (> 5°m) veneer of sediment (**Figures 7B,D–G**) and evidence of pinch-out terminations against the diapiric structures in the upper Plio-Quaternary sediment (**Figure 5**) point to a post-MSC activity of the seepage in the study area. In general, fluid flow dated after the MSC seems more dependent on the local geodynamic and depositional settings (Bertoni and Cartwright, 2015); therefore, a Pleistocene age would be more coherent with the establishment of magmatism in the area.

As a matter of fact, the geodynamic history of the Tyrrhenian Sea started at 10 Ma with the opening of the basin. The eastward migration and intensification of the rifting, between 10 and 5 Ma as a consequence of the slab roll-back, triggered seafloor spreading in the Vavilov back-arc basin and the formation of subduction-related volcanism. Between 5 and 0.6 Ma, the rifting migrated further to the southeast and seafloor spreading started in the Marsili back-arc basin, with the emplacemeant of oceanic crust (see Malinverno, 2012 and references therein). Around the same time (0.6 Ma), STEP (Subduction-Transform-Edge-Propagator) faults, associated with lateral lithospheric tearing, are believed to have formed (Cocchi et al., 2017; De Ritis et al., 2019) in the eastern Tyrrhenian domain. The STEP faults acted as the main conduit for upwelling of the isotherms due to mantle melts upraising from the edge of the slab along the lithospheric tear. Therefore, these inferred STEP faults would have controlled the magma uprising that fed the Palinuro volcanic complex (west of Glabro, outside of the area depicted in **Figure 1B**) and the Diamante-Enotrio-Ovidio volcanic-intrusive complex (**Figure 1B**). At present, the upwelling of subduction-induced mantle flow has stopped in the Diamante-Enotrio-Ovidio volcanic-intrusive complex, while the subduction-related volcanism continues in the Aeolian Arc (De Ritis et al., 2019). This reconstruction seems compatible with magmatism of Pleistocene age in the area located south of the Ovidio complex, which may have enhanced the fluid circulation in the Paola Basin, in a complex feedback system, including the top of Messinian units.

The hydrothermal vent complexes that develop along the eastern side of the Tyrrhenian domain deserve better understanding. There are indeed striking morphological and geochemical similarities with volcanic-hydrothermal systems located in shallow waters along the margin. For example, the morphology of seabed and nature of the gas is similar to active seabed doming and gas discharge in the Gulf of Naples (**Figure 1A**), where He and CO_2 are sourced from mantle melts and decarbonation reactions of crustal rocks (Passaro et al., 2016). Other large fluid-escape depressions and seafloor mounds have been observed on the continental shelf of the Pontine Archipelago (**Figure 1A**), where hydrothermal sulfides collected on the seabed and sub-seabed point to the possible degassing of magma similar to the one feeding the latest volcanic activity occurred on the islands in the Middle Pleistocene (Conte et al., 2020). Hydrothermal fluids discharged at this location are CO_2-rich and show a mantle-derived signature indicating that cooling magmas are still releasing enough thermal energy to feed an active hydrothermal system (Italiano et al., 2019). An example in water depths closer to our case study, is the fault-controlled system of deep-hydrothermal circulation discovered on the Cape Vaticano Ridge (**Figure 1B**). Here, δ^3He enriched bottom waters are related to magmatic intrusions generated from mantle-wedge partial melting above the Tyrrhenian-Ionian subducting slab and melt upward migration (Loreto et al., 2019). Therefore, submarine hydrothermal systems and vent complexes along the eastern side of the Tyrrhenian domain remain overlooked especially in deeper waters, where geophysical and geochemical data are sparse. The study of surface expressions of fluid circulation, such as near-seabed seepage and fluid discharge in the water column, would enable to better understanding their relationships with the deep processes associated with slab-subduction, slab tearing and mantle-wedge partial melting.

CONCLUSION AND OUTLOOK

Multichannel seismic investigations and detection of the acoustic backscatter of the water column by multibeam systems were carried out jointly in an area of intense gas seepage and venting in the water column, located in the Paola Basin, at the junction between the back-arc extensional domain and the fore-arc of the Calabrian accretionary wedge, in the southeastern Tyrrhenian Sea.

Using a ship-based multibeam echosounder we detected 15 clusters of flares that are indicative for free gas releases from the seafloor, which are mostly related to seafloor pockmarks, landslide headwall scars and fault scarps. The multichannel seismic reflection survey was designed to achieve the highest resolution in the shallower part of the sub-seafloor, where free gas accumulations and seep conduits were the primary target of our investigation. However, the seismics obtained also the imaging of deeper faults and Messinian units, which were already suggested to be related to the deeper-plumbing system of the seeps (Gamberi and Rovere, 2010; Rovere et al., 2014). Flares are related to acoustic blanking in MCS, high-amplitude

reflections in sediment profiler echograms, and high seafloor backscatter/reflectivity, all of which are indicative of pervasive free gas concentrations in the sediments. The results of these surveys allowed to define the depths of the free gas zones, which are located a few meters below the seabed.

Flares are not randomly distributed but show a relation to locations of magmatic sills, subsurface doming and diapirism at the top of the Messinian units. Possible Miocene fault-controlled hydrocarbon plays (and source rocks) are responsible for charging the mounded complexes with free gas through the faulted network and the overlying chimneys and conduits formed by hydrothermal vent complexes fed by magmatic sills intruded within the Plio-Quaternary deposits. Naturally seeping gas reaches the seafloor along sub-vertical faults, which have formed concurrently or soon after the establishment of diapirism. The main phase of magmatism occurred in the Pleistocene but fluid flow is a long-term process that continues after cessation of magmatism. Geochemical analysis of the dissolved gas, performed at the sea surface, confirm a deep, metamorphic origin of the gas, possibly provided by the magmatic and intrusive complexes surrounding the Paola Basin.

The transient nature of seepage or its absence must be better investigated with repeated surveys with the same acoustical tools, and validation of the acoustically defined features with *in-situ* measurements. The fact that gas flares are not ubiquitous above the sub-surface diapirs and small shallow sediment chimneys may indicate that the absence of water column anomalies is not fixed in time. A thicker seal of sediment and layers of hydrocarbon seep-related methane-derived carbonates may hinder gas release at specific locations, being the evidence that explosive hydrothermal activity, which released large quantities of gas and formed craters at the seafloor, may have ceased in the recent past (few thousand years ago).

Additional sampling of gas is further required because very little is known about long-term variations in the gas flux and venting over days to weeks and months, seasonal cycles and decades. The variability of gas fluxes might be controlled not only by fluid flow rates mediated by microbial processes but also by physical changes in bottom pressure in connection with tides, bottom currents, storms, swell, or earthquakes (e.g. Riedel et al., 2018). Furthermore, varying temperature within reasonable limits at flare sites may change the flow-rate by up to 5% and we only have data from two surveys carried out during the summer season. At the very least, despite our study did not systematically investigate the temporal variability, current observations do indicate that flares are stable over times of hours and days.

More importantly, targeted gas samplings, at the seafloor pressure conditions, and further analysis such as isotopic ratios of helium, carbon, and $^{4}He/^{20}Ne$ are required to unravel the true nature of the fluids released from the seafloor. A certain dissolution of CH_4 in the water column (700–800˚m) is expected, since the vertical transport of dissolved methane is highly restricted by the density stratification of the water column and strong summer thermoclines can limit the vertical gaseous transport. At least on continental shelves, summer thermoclines have been demonstrated to constrain methane transport to the mixed layer and the atmosphere (Schneider et al., 2011). Therefore, gas exchange leads to fast dissolution of methane out of the bubbles during their ascent in the water column. How much methane is released in form of gas bubbles and dissolved in pore water from the seafloor can be overlooked due to the sampling method used in this survey. Dedicated sampling efforts with ROVs, calibration of the acoustic methods with *in situ* flow measurements, and repeated imaging of the same regions during different tides, seasons and years are therefore necessary to assessing flow-rates in the study area.

Some hydroacoustic flares were observed to reach close to the sea surface, thus part of the released gas through seepage may contribute to the atmospheric inventory, but this has to be confirmed by further investigations. Seeps slowly release hydrogen sulfide, methane and other hydrocarbon-rich fluids in the water column, however uncertainties remain regarding the quantity of free methane that is emitted from deep-water seeps into the water column, with several authors showing that, at least in gas hydrates scenarios, most of the methane emitted per year within the gas hydrate stability zone remains trapped in the deep ocean (Römer et al., 2012). In our hybrid volcanic-sedimentary case scenario where fast venting of possible mixed hydrothermal and hydrocarbon gases is observed, a first qualitative assessment of the gas released, even if not constrained in terms of quantities, provide a possible case study for the release of greenhouse gases into the atmosphere. Long-term monitoring and repeated observations also at the sea surface to detect localized exchange with the atmosphere would allow for evaluation of the variability of gas emissions and provide evidence for the controlling mechanisms in our study area.

In summary, understanding the geographical distribution of gas venting sites along the eastern Tyrrhenian continental margin, constraining better their relation with the thickness and facies of Messinian units, hydrocarbon seeps, magmatic intrusions and hydrothermal vent complexes fed by mantle melting and monitoring their long-term variability are key to unravel the feedbacks of the sedimentary, tectonic and volcanic processes occurring at the margin. In addition, hydrocarbon formation and oceanographic processes that influence the distribution and burial of organic matter deposited on the seabed are important controlling factors that must be studied in more detail also for petroleum prospecting targets. Magmatic activity in sedimentary basins may indeed turn an otherwise unprospective area into a geothermal energy and hydrocarbon field (Roelofse et al., 2021). The igneous activity may have induced seal bypass systems, by breaching the Miocene regional seal across the study area and may have enhanced late-stage hydrocarbon generation and expulsion, with the formation of unconventional reservoirs.

DATA AVAILABILITY STATEMENT

The multibeam datasets generated for this study can be found in the bathymetry viewing and download service at https://portal.emodnet-bathymetry.eu/ of EMODnet Digital Bathymetry (DTM). https://doi.org/10.12770/bb6a87dd-e579-4036-abe1-e649cea9881a. Multichannel seismic data and water column echograms can be made available upon request to the corresponding author. The Institute of Marine Sciences of the National Research Council in Bologna (http://www.ismar.cnr.it/) can be enquired for accessing the digitalization of the Sparker database (SDB) at responsabile@bo.ismar.cnr.it.

AUTHOR CONTRIBUTIONS

MR provided funding acquisition as well as cruise preparation and management for R/V Urania cruise Marbeep 2014. MR, AM, and FG carried out on board hydroacoustic data collection, sediment and water sampling. AM took care about the hydroacoustic data processing, curation, and archiving. FZ acquired and processed MCS data. MR interpreted the hydroacoustic and MCS data. All authors contributed to the interpretation of the overall results. MR took the lead in writing the manuscript.

FUNDING

This research was funded by the Ritmare Project (www.ritmare.it), SP4 WP1 AZ3, including open access fees.

ACKNOWLEDGMENTS

We warmly thank the crew of the R/V Urania and the scientific party on board the MarBeep 2014 campaign for their contribution to the success of the cruise. Scientific party: MR (chief-party), FG (co-chief), Elisa Leidi, AM (navigation), Andrea Gallerani, Fabio Savelli (sediment sampling), FZ, Lorenzo Sormani, Lorenzo Facchin, Gianpaolo Visnovic (multichannel seismic acquisition), Bruna Petani, Eugenio Rastelli, Andrea Fioretti (biological sampling), Heba Rashed, Luciano Giannini, Yuri Galletti (water sampling), Fabio Canziani, Filippo Villi (trainees). We are also grateful to the Institute of Marine Sciences of the National Research Council in Bologna, Italy (http://www.ismar.cnr.it/), for providing and making accessible the digitalization of the Sparker database (SDB) comprising BP profiles. Filomena Loreto and Valentina Ferrante are particularly thanked for inspiring the initiative. Schlumberger and University of Bologna are thanked for the provision of Petrel software.

REFERENCES

Berndt, C., Hensen, C., Mortera-Gutierrez, C., Sarkar, S., Geilert, S., Schmidt, M., et al. (2016). Rifting under Steam-How Rift Magmatism Triggers Methane Venting from Sedimentary Basins. *Geology* 44, 767–770. doi:10.1130/G38049.1

Bertoni, C., and Cartwright, J. (2015). Messinian Evaporites and Fluid Flow. *Mar. Pet. Geology.* 66, 165–176. doi:10.1016/j.marpetgeo.2015.02.003

Bowman, S. A. (2011). Regional Seismic Interpretation of the Hydrocarbon Prospectivity of Offshore Syria. *GeoArabia* 16, 95–124. doi:10.2113/geoarabia160395

Camerlenghi, A., Del Ben, A., Hübscher, C., Forlin, E., Geletti, R., Brancatelli, G., et al. (2020). Seismic Markers of the Messinian Salinity Crisis in the Deep Ionian Basin. *Basin Res.* 32, 716–738. doi:10.1111/bre.12392

Cartwright, J., Huuse, M., and Aplin, A. (2007). Seal Bypass Systems. *Bulletin* 91, 1141–1166. doi:10.1306/04090705181

Chiarabba, C., De Gori, P., and Speranza, F. (2008). The Southern Tyrrhenian Subduction Zone: Deep Geometry, Magmatism and Plio-Pleistocene Evolution. *Earth Planet. Sci. Lett.* 268, 408–423. doi:10.1016/j.epsl.2008.01.036

Cocchi, L., Passaro, S., Tontini, F. C., and Ventura, G. (2017). Volcanism in Slab Tear Faults Is Larger Than in Island-Arcs and Back-Arcs. *Nat. Commun.* 8 (1), 1451. doi:10.1038/s41467-017-01626-w

Conte, A. M., di Bella, L., Ingrassia, M., Perinelli, C., and Martorelli, E. (2020). Alteration and Mineralization Products of the Zannone Giant Pockmark (Zannone Hydrothermal Field, central Tyrrhenian Sea). *Minerals* 10, 581. doi:10.3390/min10070581

Dal Cin, M., del Ben, A., Mocnik, A., Accaino, F., Geletti, R., Wardell, N., et al. (2016). Seismic Imaging of Late Miocene (Messinian) Evaporites from Western Mediterranean Back-Arc Basins. *Pet. Geosci.* 22, 297–308. doi:10.1144/petgeo2015-096

de Mahiques, M. M., Schattner, U., Lazar, M., Sumida, P. Y. G., and Souza, L. A. P. d. (2017). An Extensive Pockmark Field on the Upper Atlantic Margin of Southeast Brazil: Spatial Analysis and its Relationship with Salt Diapirism. *Heliyon* 3, e00257. doi:10.1016/j.heliyon.2017.e00257

De Ritis, R., Pepe, F., Orecchio, B., Casalbore, D., Bosman, A., Chiappini, M., et al. (2019). Magmatism along Lateral Slab Edges: Insights from the Diamante-Enotrio-Ovidio Volcanic-Intrusive Complex (Southern Tyrrhenian Sea). *Tectonics* 38, 2581–2605. doi:10.1029/2019TC005533

Farran, M. (2008). IMAGE2SEGY: Una aplicación informática para la conversión de imágenes de perfiles sísmicos a ficheros en formato SEG Y. *Geo-Temas* 10, 1215–1218.

Franchi, F., Rovere, M., Gamberi, F., Rashed, H., Vaselli, O., and Tassi, F. (2017). Authigenic Minerals from the Paola Ridge (Southern Tyrrhenian Sea): Evidences of Episodic Methane Seepage. *Mar. Pet. Geology.* 86, 228–247. doi:10.1016/j.marpetgeo.2017.05.031

Gamberi, F., and Rovere, M. (2010). Mud Diapirs, Mud Volcanoes and Fluid Flow in the Rear of the Calabrian Arc Orogenic Wedge (southeastern Tyrrhenian Sea). *Basin Res.* 22, 452–464. doi:10.1111/j.1365-2117.2010.00473.x

Geletti, R., Zgur, F., del Ben, A., Buriola, F., Fais, S., Fedi, M., et al. (2014). The Messinian Salinity Crisis: New Seismic Evidence in the West-Sardinian Margin and Eastern Sardo-Provençal basin (West Mediterranean Sea). *Mar. Geology.* 351, 76–90. doi:10.1016/j.margeo.2014.03.019

Hübscher, C., Tahchi, E., Klaucke, I., Maillard, A., and Sahling, H. (2009). Salt Tectonics and Mud Volcanism in the Latakia and Cyprus Basins, Eastern Mediterranean. *Tectonophysics* 470, 173–182. doi:10.1016/j.tecto.2008.08.019

Italiano, F., Romano, D., Caruso, C., Longo, M., Corbo, A., and Lazzaro, G. (2019). Magmatic Signature in Submarine Hydrothermal Fluids Vented Offshore Ventotene and Zannone Islands (Pontine Archipelago, Central Italy). *Geofluids* 2019, 1–15. doi:10.1155/2019/8759609

Iyer, K., Rüpke, L., and Galerne, C. Y. (2013). Modeling Fluid Flow in Sedimentary Basins with Sill Intrusions: Implications for Hydrothermal Venting and Climate Change. *Geochem. Geophys. Geosyst.* 14, 5244–5262. doi:10.1002/2013GC005012

Lawrence, G. W. M., and Cartwright, J. A. (2010). The Stratigraphic and Geographic Distribution of Giant Craters and Remobilised Sediment mounds on the Mid Norway Margin, and Their Relation to Long Term Fluid Flow. *Mar. Pet. Geology.* 27 (4), 733–747. doi:10.1016/j.marpetgeo.2009.10.012

Loreto, M. F., Düşünür-Doğan, D., Üner, S., İşcan-Alp, Y., Ocakoğlu, N., Cocchi, L., et al. (2019). Fault-controlled Deep Hydrothermal Flow in a Back-Arc

Tectonic Setting, SE Tyrrhenian Sea. *Sci. Rep.* 9, 17724. doi:10.1038/s41598-019-53696-z

Lupton, J., De Ronde, C., Sprovieri, M., Baker, E. T., Bruno, P. P., Italiano, F., et al. (2011). Active Hydrothermal Discharge on the Submarine Aeolian Arc. *J. Geophys. Res.* 116, 1–22. doi:10.1029/2010JB007738

Madof, A. S. (2018). Gas Hydrates in Coarse-Grained Reservoirs Interpreted from Velocity Pull up: Mississippi Fan, Gulf of Mexico. *Geology* 46 (6), 559–562. doi:10.1130/G40031.1

Magee, C., Duffy, O. B., Purnell, K., Bell, R. E., Jackson, C. A. L., and Reeve, M. T. (2016). Fault-controlled Fluid Flow Inferred from Hydrothermal Vents Imaged in 3D Seismic Reflection Data, Offshore NW Australia. *Basin Res.* 28, 299–318. doi:10.1111/bre.12111

Malinverno, A. (2012). Evolution of the Tyrrhenian Sea-Calabrian Arc System: The Past and the Present. *Rend. Online Soc. Geol. Ital.* 21, 11–15.

Marani, M., and Gamberi, F. (2004). "Distribution and Nature of Submarine Volcanic Landforms in the Tyrrhenian Sea: the Arc vs the Back-Arc," in *From Seafloor to Deep Mantle: Architecture of the Tyrrhenian Backarc basin. APAT, Memorie Descrittive Della Carta Geologica d'Italia*. Editors M. P. Marani, F. Gamberi, and E. Bonatti, 64, 109–126.

McGinnis, D. F., Greinert, J., Artemov, Y., Beaubien, S. E., and Wüest, A. (2006). Fate of Rising Methane Bubbles in Stratified Waters: How Much Methane Reaches the Atmosphere? *J. Geophys. Res.* 111, 1–15. doi:10.1029/2005JC003183

Milia, A., Turco, E., Pierantoni, P. P., and Schettino, A. (2009). Four-dimensional Tectono-Stratigraphic Evolution of the Southeastern Peri-Tyrrhenian Basins (Margin of Calabria, Italy). *Tectonophysics* 476, 41–56. doi:10.1016/j.tecto.2009.02.030

Minelli, A., Tassetti, A. N., Hutton, B., Pezzuti Cozzolino, G. N., Jarvis, T., and Fabi, G. (2021). Semi-automated Data Processing and Semi-supervised Machine Learning for the Detection and Classification of Water-Column Fish Schools and Gas Seeps with a Multibeam Echosounder. *Sensors* 21 (9), 2999. doi:10.3390/s21092999

Müller, S., Reinhardt, L., Franke, D., Gaedicke, C., and Winsemann, J. (2018). Shallow Gas Accumulations in the German North Sea. *Mar. Pet. Geology.* 91, 139–151. doi:10.1016/j.marpetgeo.2017.12.016

Naudts, L., Greinert, J., Artemov, Y., Beaubien, S. E., Borowski, C., and Batist, M. D. (2008). Anomalous Sea-Floor Backscatter Patterns in Methane Venting Areas, Dnepr paleo-delta, NW Black Sea. *Mar. Geology.* 251, 253–267. doi:10.1016/j.margeo.2008.03.002

Omosanya, K. O., Eruteya, O. E., Siregar, E. S. A., Zieba, K. J., Johansen, S. E., Alves, T. M., et al. (2018). Three-dimensional (3-D) Seismic Imaging of Conduits and Radial Faults Associated with Hydrothermal Vent Complexes (Vøring Basin, Offshore Norway). *Mar. Geology.* 399, 115–134. doi:10.1016/j.margeo.2018.02.007

Passaro, S., Tamburrino, S., Vallefuoco, M., Tassi, F., Vaselli, O., Giannini, L., et al. (2016). Seafloor Doming Driven by Degassing Processes Unveils Sprouting Volcanism in Coastal Areas. *Sci. Rep.* 6. doi:10.1038/srep22448

Pepe, F., Sulli, A., Bertotti, G., and Cella, F. (2010). Architecture and Neogene to Recent Evolution of the Western Calabrian continental Margin: An Upper Plate Perspective to the Ionian Subduction System, central Mediterranean. *Tectonics* 29. doi:10.1029/2009TC002599

Plaza-Faverola, A., Bünz, S., Johnson, J. E., Chand, S., Knies, J., Mienert, J., et al. (2015). Role of Tectonic Stress in Seepage Evolution along the Gas Hydrate-Charged Vestnesa Ridge, Fram Strait. *Geophys. Res. Lett.* 42, 733–742. doi:10.1002/2014GL062474

Procesi, M., Ciotoli, G., Mazzini, A., and Etiope, G. (2019). Sediment-hosted Geothermal Systems: Review and First Global Mapping. *Earth-Science Rev.* 192, 529–544. doi:10.1016/j.earscirev.2019.03.020

Riedel, M., Scherwath, M., Römer, M., Veloso, M., Heesemann, M., and Spence, G. D. (2018). Distributed Natural Gas Venting Offshore along the Cascadia Margin. *Nat. Commun.* 9. doi:10.1038/s41467-018-05736-x

Roelofse, C., Alves, T. M., and Omosanya, K. d. O. (2021). Reutilisation of Hydrothermal Vent Complexes for Focused Fluid Flow on continental Margins (Modgunn Arch, Norwegian Sea). *Basin Res.* 33, 1111–1134. doi:10.1111/bre.12507

Rollet, N., McGiveron, S., Hashimoto, T., Hackney, R., Petkovic, P., Higgins, K., et al. (2012). Seafloor Features and Fluid Migration in the Capel and Faust Basins, Offshore Eastern Australia. *Mar. Pet. Geology.* 35, 269–291. doi:10.1016/j.marpetgeo.2012.03.011

Römer, M., Blumenberg, M., Heeschen, K., Schloemer, S., Müller, H., Müller, S., et al. (2021). Seafloor Methane Seepage Related to Salt Diapirism in the Northwestern Part of the German North Sea. *Front. Earth Sci.* 9. doi:10.3389/feart.2021.556329

Römer, M., Sahling, H., Pape, T., Bohrmann, G., and Spieß, V. (2012). Quantification of Gas Bubble Emissions from Submarine Hydrocarbon Seeps at the Makran continental Margin (Offshore Pakistan). *J. Geophys. Res.* 117, a–n. doi:10.1029/2011JC007424

Rossi, P. L., Bocchi, G., and Lucchini, F. (1980). A Manganese deposit from the South Tyrrhenian Region. *Oceanol. Acta* 3 (1), 107–114.

Rovere, M., Mercorella, A., Frapiccini, E., Funari, V., Spagnoli, F., Pellegrini, C., et al. (2020). Geochemical and Geophysical Monitoring of Hydrocarbon Seepage in the Adriatic Sea. *Sensors (Basel)* 20 (5). doi:10.3390/s20051504

Rovere, M., Gamberi, F., Mercorella, A., Rashed, H., Gallerani, A., Leidi, E., et al. (2014). Venting and Seepage Systems Associated with Mud Volcanoes and Mud Diapirs in the Southern Tyrrhenian Sea. *Mar. Geology.* 347, 153–171. doi:10.1016/j.margeo.2013.11.013

Rovere, M., Rashed, H., Pecchioni, E., Mercorella, A., Ceregato, A., Leidi, E., et al. (2015). Habitat Mapping of Cold Seeps Associated with Authigenic Mineralization (Paola Ridge, Southern Tyrrhenian Sea): Combining Seafloor Backscatter with Biogeochemistry Signals. *Ijg* 134, 23–31. doi:10.3301/IJG.2014.15

Schneider von Deimling, J., Rehder, G., Greinert, J., McGinnnis, D. F., Boetius, A., Linke, P., et al. (2011). Quantification of Seep-Related Methane Gas Emissions at Tommeliten, North Sea. *Continental Shelf Res.* 31, 867–878. doi:10.1016/j.csr.2011.02.012

Serié, C., Huuse, M., and Schødt, N. H. (2012). Gas Hydrate Pingoes: Deep Seafloor Evidence of Focused Fluid Flow on continental Margins. *Geology* 40, 207–210. doi:10.1130/G32690.1

Simoneit, B. R. T., Kawka, O. E., and Brault, M. (1988). Origin of Gases and Condensates in the Guaymas Basin Hydrothermal System (Gulf of California). *Chem. Geology.* 71, 169–182. doi:10.1016/0009-2541(88)90113-1

Svensen, H., Planke, S., Malthe-Sørenssen, A., Jamtveit, B., Myklebust, R., Rasmussen Eidem, T., et al. (2004). Release of Methane from a Volcanic basin as a Mechanism for Initial Eocene Global Warming. *Nature* 429, 542–545. doi:10.1038/nature0257510.1038/nature02566

Svensen, H., Jamtveit, B., Planke, S., and Chevallier, L. (2006). Structure and Evolution of Hydrothermal Vent Complexes in the Karoo Basin, South Africa. *J. Geol. Soc.* 163, 671–682. doi:10.1144/1144-764905-037

Svensen, H., Planke, S., Jamtveit, B. r., and Pedersen, T. (2003). Seep Carbonate Formation Controlled by Hydrothermal Vent Complexes: a Case Study from the Vøring Basin, the Norwegian Sea. *Geo-Marine Lett.* 23, 351–358. doi:10.1007/s00367-003-0141-2

Sydnes, M., Fjeldskaar, W., Grunnaleite, I., Fjeldskaar Løtveit, I., and Mjelde, R. (2019). Transient Thermal Effects in Sedimentary Basins with Normal Faults and Magmatic Sill Intrusions-A Sensitivity Study. *Geosciences* 9, 160. doi:10.3390/geosciences9040160

Würtz, M., and Rovere, M. (2015). *Atlas of the Mediterranean Seamounts and Seamount-like Structures*. IUCN, Malaga, 275 p. ISBN: 978-2-8317-1750-0. doi:10.2305/IUCN.CH.2015.07.en

Waage, M., Portnov, A., Serov, P., Bünz, S., Waghorn, K. A., Vadakkepuliyambatta, S., et al. (2019). Geological Controls on Fluid Flow and Gas Hydrate Pingo Development on the Barents Sea Margin. *Geochem. Geophys. Geosyst.* 20, 630–650. doi:10.1029/2018GC007930

Conflict of Interest: The authors declare that the research was conducted in the absence of any commercial or financial relationships that could be construed as a potential conflict of interest.

Publisher's Note: All claims expressed in this article are solely those of the authors and do not necessarily represent those of their affiliated organizations, or those of the publisher, the editors and the reviewers. Any product that may be evaluated in this article, or claim that may be made by its manufacturer, is not guaranteed or endorsed by the publisher.

frontiers in Earth Science

ORIGINAL RESEARCH
published: 15 March 2022
doi: 10.3389/feart.2022.833661

Fate of Methane Released From a Destroyed Oil Platform in the Gulf of Mexico

*Mauricio Silva[1], Camilo Roa[2], Nizar Bel Haj Ali[3], Carrie O'Reilly[1], Tarek Abichou[4] and Ian R. MacDonald[1]**

[1]Dept Earth Ocean and Atmospheric Science, Florida State University, Tallahassee, FL, United States, [2]Marine Science Deptartment, Florida International University, Miami, FL, United States, [3]LASMAP, Ecole Polytech Tunisie, University of Carthage, Tunis, Tunisia, [4]School of Engineering, Florida State University, Tallahassee, FL, United States

In 2004, destruction of a Gulf of Mexico oil platform by Hurricane Ivan initiated a discharge of oil and gas from a water depth of 135 m, where its bundle of well conductors was broken below the seafloor near the toppled wreckage. Discharge continued largely unabated until 2019, when findings partly reported herein prompted installation of a containment device that could trap oil before it entered the water column. In 2018, prior to containment, oil and gas bubbles formed plumes that rose to the surface, which were quantified by acoustic survey, visual inspection, and discrete collections in the water column. Continuous air sampling with a cavity ring-down spectrometer (CRDS) over the release site detected atmospheric methane concentrations as high as 11.7, ~6 times greater than an ambient baseline of 1.95 ppmv. An inverse plume model, calibrated to tracer-gas release, estimated emission into the atmosphere of 9 g/s. In 2021, the containment system allowed gas to escape into the water at 120 m depth after passing through a separator that diverted oil into storage tanks. The CRDS detected transient peaks of methane as high as 15.9 ppmv ppm while oil was being recovered to a ship from underwater storage tanks. Atmospheric methane concentrations were elevated 1–2 ppmv over baseline when the ship was stationary within the surfacing plumes of gas after oil was removed from the flow. Oil rising to the surface was a greater source of methane to the atmosphere than associated gas bubbles.

Keywords: marine methane flux, atmospheric methane concentration, oil spill, gas seep, gas plume, methane bubble, oily bubble

OPEN ACCESS

Edited by:
Miriam Römer, University of Bremen, Germany

Reviewed by:
Jonas Gros, Helmholtz Association of German Research Centres (HZ), Germany
Laura Lapham, University of Maryland Center for Environmental Science (UMCES), United States

****Correspondence:***
Ian R. MacDonald
imacdonald@fsu.edu

Specialty section:
This article was submitted to Marine Geoscience, a section of the journal Frontiers in Earth Science

Received: *11 December 2021*
Accepted: *14 February 2022*
Published: *15 March 2022*

Citation:
Silva M, Roa C, Ali NBH, O'Reilly C, Abichou T and MacDonald IR (2022) Fate of Methane Released From a Destroyed Oil Platform in the Gulf of Mexico. Front. Earth Sci. 10:833661. doi: 10.3389/feart.2022.833661

INTRODUCTION

Methane seepage on outer continental margins supports microbial consortia and symbioses that are the basis of chemosynthetic food webs. Seeps can be identified visually by the presence of pockmarks (Marcon et al., 2014; Mason et al., 2019), authigenic carbonates (Feng et al., 2010), gas hydrate outcroppings—when within the hydrate stability zone—(MacDonald et al., 2003), lush biological communities (Roy et al., 2007), or bubble plumes (Fu et al., 2021). Seeps can be detected acoustically because bubbles are strong reflectors in scanning or swath-mapping sonar (Römer et al., 2012). So, many active seeps have been discovered during geophysical surveys (Skarke et al., 2014). In the Gulf of Mexico and other oil-generating provinces, seeping hydrocarbons often include oil that rises along with the gas and reaches the ocean surface, where it forms oil slicks that can be detected by remote

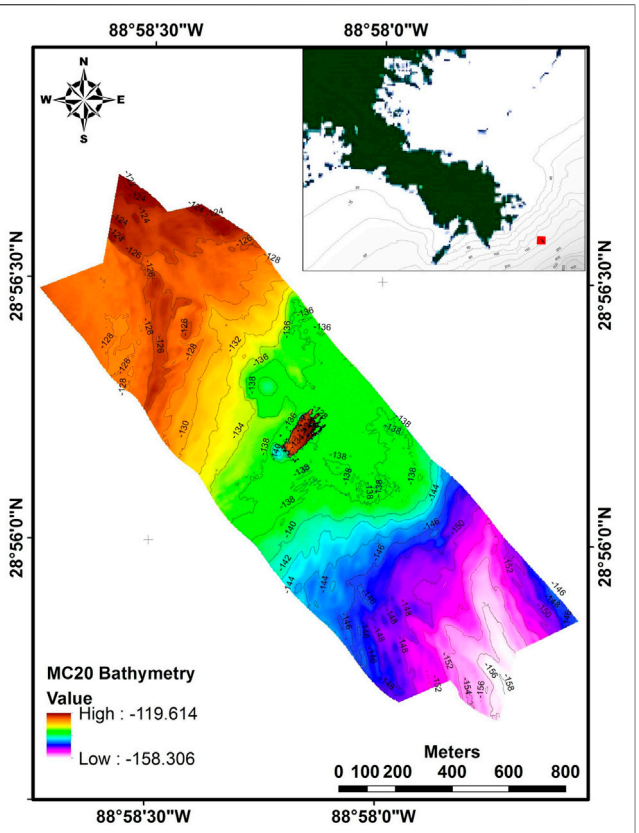

FIGURE 1 | Study area is the site of the sunken Taylor Energy platform in the northern Gulf of Mexico in the MC20 lease block (red square) approximately 18 km southeast of the Mississippi River Delta, original Fig. 2.1 (Mason et al., 2019).

sensing techniques, especially synthetic aperture radar (SAR) (Garcia-Pineda et al., 2010). However, geophysical surveys of the Gulf and elsewhere have also detected many bubble plumes or flares that were not associated with oil slicks and did not extend to the surface (Mitchell et al., 2018) because, presumably, methane bubbles from "dry" or oil-free seeps dissolve within the water column before reaching the surface (Rehder et al., 2002; Rehder et al., 2009).

The fate of marine methane releases is important because, in the U.S. waters alone, Skarke et al. (2014) have identified over 500 gas seeps. Satellite SAR images have identified over 900 persistent oil seeps in the Gulf (MacDonald et al., 2015) and elsewhere (Jatiault et al., 2017), and many of these have been confirmed by submersible sampling (Roberts and Boland, 2010). Moreover, seep occurrences might be increasing in number and magnitude due to ongoing changes in ocean conditions such as continental rebound or climate-related warming and the potential instability of gas hydrates (Westbrook et al., 2009; Altuna et al., 2021). Accidental releases of oil and gas due to marine energy production and pipeline pumping are also a concern (Eckle et al., 2012). A basic question concerns the effect of methane seeps from natural sources or methane leaks from production facilities: Does methane primarily dissolve in seawater, where it will be oxidized to CO_2 and its dissociation products (Dickens et al., 1995), or does it also reach the atmosphere where it could contribute to greenhouse forcing (McGinnis et al., 2006; Böttner et al., 2020)? Such impacts might increase in future if ocean warming destabilizes marine gas hydrates or aging energy infrastructure. In this study, we have been able to conduct a natural experiment by measuring the properties of a prolific anthropogenic discharge of methane from 135 m when abundant oil was first present, then largely removed.

STUDY AREA AND PREVIOUS REPORTING

Hurricane Ivan struck the Gulf of Mexico in September 2004, passed to the east of the Taylor Energy oil production platform in the MC20 lease block, and made landfall on 16 September with category 4 strength. This passage generated individual waves estimated to be more than 40 m high in the eye wall (Wang et al., 2005), which probably hit the platform as breaking waves when they contacted the surrounding water depths of 135 m. Remarkably, Ivan then blew across the SE United States into the Atlantic Ocean, curved to the south, then back across Florida, reentered the Gulf, and made its final landfall on 23 September in Louisiana to the west of the platform, which was located in the MC20 lease block at 28°56.3′N and 89°58.2′W, approximately 18 km from the SE tip of the Mississippi River Delta (**Figure 1**). Discharge of storm surging back into the Gulf triggered a massive mudslide (Nodine et al., 2007) that impacted energy infrastructure across a broad front. Notably, it completed destruction of the MC20 platform, toppling its pilings off their base and pushing it 200 m to the southeast, where its wreckage remained tethered to the connectors that had previously supplied oil and gas to the platform from as many as 28 producing wells.

All personnel had been evacuated prior to the storm, but subsea cutoff valves, which should have staunched flow up the conductors, either had not been engaged or failed to function properly; as early as 28 September 2004, satellite images showed oil slicks over the wreck site not previously reported. Acoustic surveys in the early months of 2005 detected columnar targets rising from the wreckage. How should such targets be described? Note that authors quantifying acoustic targets in the water column caused by gas bubbles escaping from natural seeps have used the term "flare" to describe these features (Römer et al., 2019), whereas the term "plume" has been used to designate a broad variety of water column features that includes methane bubbles (Sauter et al., 2006), hydrothermal fluids (Elderfield and Schultz, 1996), or hydrocarbons released by industrial accidents such as the Deepwater Horizon oil spill (Socolofsky et al., 2015). Previous publications have used "plume" to describe multiphase columns in MC20 (Mason et al., 2019; Bryant et al., 2020), and that usage will continue herein.

Response efforts in the years following the storm included dredging, wreckage removal, and attempts to plug as many as nine of the platform's wells. What remained on the site were 8, 145 m platform pilings, the jacket, and their foundation, the template, through which the well conductors formerly passed. Eventually, surveys would confirm the presence of an erosion

crater at the northern end of the jacket, from which plumes were consistently emitted (Bryant et al., 2020; O'Reilly, 2020). Although controversial technical and legal issues have attended response operations (Court of Appeals for the Federal Circuit, 2020), oil and gas have been flowing up those conductors and into the Gulf to the present day and the site remains classified as an active oil spill under supervision of the United States Coast Guard (United States Coast Guard, 2019).

The results reported herein were derived from data collected during an expedition on the R/V Brooks McCall in September 2018 and a follow-up sampling expedition on the M/V Brandon Bordelon in November 2021 and January 2022. Sampling in 2018 utilized the ROV Comanche operated by SeaTrepid. Sampling activities addressed bubble plumes escaping from pockmarks near the northernmost end of the jacket and an additional minor plume detected near the template (**Figure 1**). More extensive results from the 2018 expedition, including a historical review, a detailed description of methodologies, and findings concerning oil discharges, can be found in a published action report by Mason et al. (2019). This article focuses on analyses of the gaseous component of the plumes as observed before and after the installation of a containment system that captured and removed oil from the discharge. Many additional details concerning materials, methods, and findings from the 2018 expedition can be found in the report of Mason et al. (2019), and individual chapters of the report will be cited to direct readers to this information.

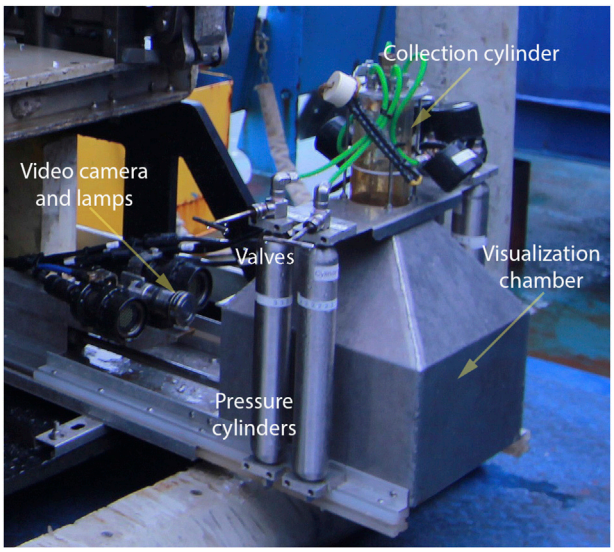

FIGURE 2 | Bubblometer on the deck: the bubblometer extended from the front of the ROV where bubbles can flow through the open bottom and funnel into the collection cylinder: Camera and lamps can record the inside of the chamber when the device is extended; bubbles accumulate inside the collection cylinder until valves are opened, original Fig. 4.1 (Mason et al., 2019).

MATERIALS AND METHODS

Acoustic Mapping

During the 2018 expedition, acoustic surveys were conducted from the research vessel and the ROV. Ship-based echosounders were installed on an overboard pole that was oriented vertically during survey operations. Sensors included an HiPAP Model 350 Ultra-Short Baseline transducer (USBL) for tracking the ROV and beacons, a 300 kHz Teledyne RDI Workhorse Acoustic Doppler Current Profiler (ADCP), a 500 kHz Kongsberg Mesotech M3 MBES, and three frequencies of Simrad EK80 SBES transducers operating at 70, 120, and 200 kHz. A Teledyne DMS-25 was installed to account for ship motion. Acoustic mapping surveys were conducted daily to account for changing currents and consequent orientation of hydrocarbon plume in the water column (**Supplementary Figure S1A**). Initial passes were interpreted to establish the main axis of the plume, and subsequent passes were run parallel to that axis. Mapping of the plumes was conducted with the ROV with the use of Simard EK80 and Kongberg M3 sonars to localize and delineate separate components of the hydrocarbon plume and their sources on the seabed. Details of the calibration and data processing procedures can be found in the work of Taylor and Boswell (2019).

Water Sample Collection and Analysis

Water samples analyzed for methane concentration were collected in Niskin bottles and, to a lesser extent, using methods described in *Collection and Imaging of Gas Bubbles*. During the 2018 samplings, the bottles were deployed on a rosette and triggered at preset depths. The rosette casts were deployed over the site of the erosion crater while monitoring the acoustic signature of the hydrocarbon plume and attempting to maintain the rosette within the plume. Rosette casts were lowered to a maximum depth of 120 m to avoid entanglement with the platform jacket and midwater gear suspended above the jacket. Additional water samples were obtained from the bubblometer pressure chambers (described below). These samples were sealed at depth and were collected when oil bubbles were observed passing through the device.

During the 2021 samplings, the Niskin bottles were deployed from an ROV and triggered by its manipulator arm. The containment system, which was installed in May 2019, encloses the plume sources under a dome suspended approximately 3 m above the bottom. The contained hydrocarbon plumes are channeled into a patented separator system (Couch, 2010), through which oil is passively diverted into underwater storage tanks, while gas bubbles are continually released into the water at a depth of 123 m. These tanks are periodically emptied in a pump-off procedure that transfers the oil to storage tanks on the M/V Brandon Bordelon. Observations in 2021 and 2022 were cruises of opportunity accommodated by these operations. For the ROV sampling, the bubble plume was readily detected in the ROV scanning sonar, allowing the vehicle to maneuver to where bubbles were visible for water collections. Samples were generally collected in replicate pairs. Water samples were stored in gas-tight vials at 4 C. Methane concentrations were determined with the use of a GC coupled to a flame ionization detector, Shimadzu 8a packed carbosphere column, 140 C oven,

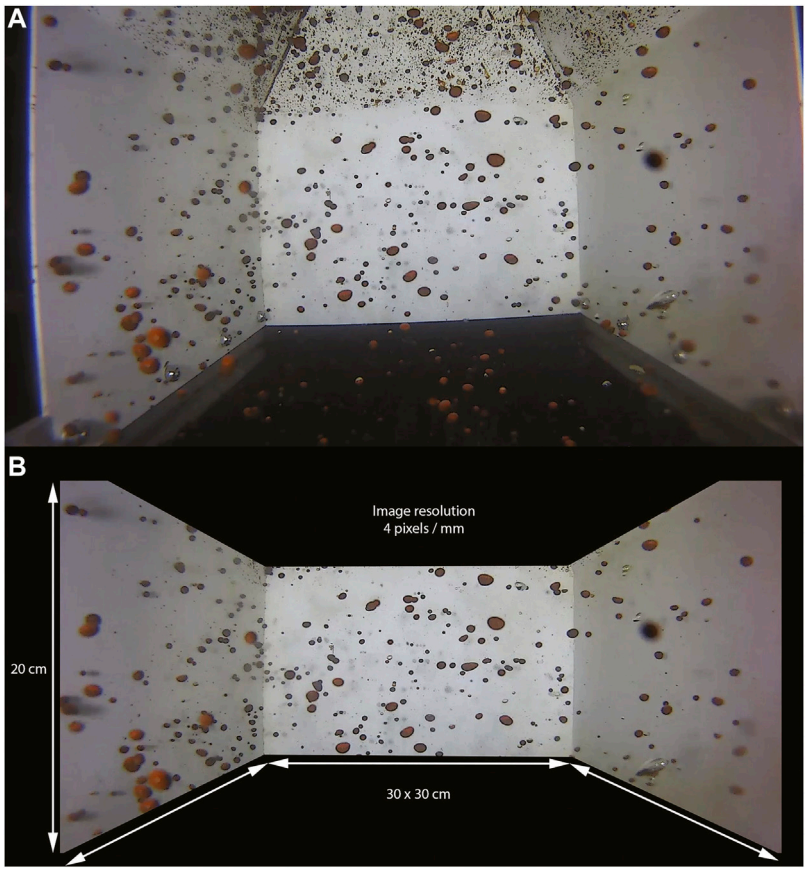

FIGURE 3 | Example of the still images recorded with the bubblometer digital video camera: **(A upper)** unprocessed frame grab; **(B lower)** the same image after cropping to remove non-quantified portions of the image and rotating to correct camera placement, original Fig. 4.2 (Mason et al., 2019).

and detector at 180 C. Standards were obtained from Restek with accuracy ±5% and precision ±1%.

Collection and Imaging of Gas Bubbles

A custom device called the "bubblometer" was fabricated to collect oil and gas samples in the water column and record digital image samples of the bubble plume for quantification (**Figure 2**). Its major component was an inverted funnel mounted atop a 30 × 30 cm-wide, 20 cm-high, three-sided visualization chamber, which was open at its bottom and at the side facing the ROV. The funnel was fed into a 300 ml acrylic collection tube that could accumulate water plus oil and gas. Four pressure cylinders, evacuated and sealed at the surface, were plumbed into the collection cylinder and could be filled individually by hydrostatic pressure when their respective valves are opened. Closing these valves then sealed the samples and prevented methane from degassing during ascent. A digital video camera (Deepsea Power and Light model HD Multi Seacam™) with two high-intensity lamps (Deepsea Power and Light Sealite™ 2,300 lumen) was mounted 30 cm from the rear opening of the visualization chamber. The entire device including camera and lamps was fixed to a frame with a hydraulic actuator. This arrangement allowed it to be extended from the front of the ROV so that the bubbles could flow through the bottom of the chamber for imaging or sample collection, or retracted to block the flow. Buoyant oil and gas would pass through the visualization chamber and be funneled into the collection tube. The camera and lamps on the bubblometer allowed observers to monitor bubbles passing through the chamber, while the separate video feed from the ROV allowed them to watch oil and gas displacing seawater at the top of the collection tube and determine when to open a valve and collect a sample.

Output from the bubblometer camera was monitored from the ship while the ROV navigated toward the MC20 hydrocarbon plumes. The ROV approached the bubble plumes with its sonar system until bubbles were observed in the camera, and then, thrusters were secured and drifted until a plume had been traversed and bubbles were no longer visible. A digital video was recorded when bubbles were observed passing through the chamber. Sample frames were subsequently captured at 5 s intervals from the recorded video. The camera was mounted at a fixed distance from the chamber, so images had a constant scale, but were cropped to a constant size of 1971 × 1,173 pixels, which showed only the interior of the chamber (**Figure 3**). In total, 665 individual image samples were collected from the video records during two

lowerings of the ROV on 5 and 6 September 2018, respectively.

Post-containment estimates of bubble size for gas released from the separator were obtained from the video of bubbles passing in front of a panel with scale markings. This material was collected from the MV Brandon Bordelon ROV in January 2022. Frame captures were taken at intervals when visibility permitted, and bubbles were measured in comparison to the scale markings using Image-J.

Gas Analysis

Samples of gas captured in the water column by using the bubblometer and collected into pressure vessels at depth were transferred on the deck to evacuate foil gas bags with a valve containing a septum to allow subsampling. Triplicate, 10 µl aliquots of each gas bag sample were injected via a gas-tight syringe onto a HS-GC/FID (HP 5890) configured with a porous layer open tubular (PLOT) column to separate and quantitate the C_1–C_5 light hydrocarbon gases. Multiple injections of each gas bag sample were introduced into the GC/IRMS configured with a PLOT column to separate the C_1–C_5 hydrocarbon gases and determine their carbon isotopic ratios. A reference carbon dioxide standard (−37.5‰ versus PDB) was used to linearize the detector. An external standard containing all of the C_1–C_5 analytes of interest with known carbon isotopic ratios was used to verify the PDB accuracy +/1 1‰ of the GC/IRMS (Gaskins et al., 2019).

Image Processing for Bubble Quantification

The front of the ROV acted as a baffle that only allowed bubbles to enter the bubblometer chamber, where the camera system recorded images at constant scale and illumination. However, objects in its images appeared larger or smaller depending on their distance from the camera within the chamber. Calibration in a laboratory setting showed that the camera resolved 8 pixels/mm at the front of the chamber closest to the camera, 4 pixels/mm in the center, and 2 pixels/mm at the rear of the chamber, with no discernable distortion due to vertical position at a given distance. The single camera could not reliably determine the distance between it and an object within the chamber. It was assumed that bubble distributions within the chamber were uniformly random and a constant scale of 4 pixels/mm was used to estimate the size of bubbles, which unavoidably meant that there was a two-fold uncertainty in any estimate of bubble diameter and an ~eight-fold uncertainty in an estimate for the volume of a spherical bubble, while most bubbles were somewhat elliptical in shape, with dimensions that tended to vary as the bubbles moved within the chamber. For these reasons, bubble sizes were estimated for confirmation of general impressions gained by comparing bubbles to adjacent objects of known size and to provide parameters for calibration of the acoustic surveying (MacDonald et al., 2019), but are not used as quantification of bubble volumes in this paper.

A neural network process called Object Detection was chosen for the detection and classification of the bubbles in the image samples and implemented with use of a Faster Region Convolutional Neural Network (Faster R-CNN) variant. The MATLAB© Computer Vision toolbox was used for performance of Faster R-CNN classification. Both the training set and test set are taken from the ground truth set. The training set uses 70% randomly assigned images, while the remaining 30% goes to the test set. The training process completed automatically by MATLAB generated a detector that can be used on any image, or a set of images, and it identifies, classifies, and measures their targets. **Figure 4** shows examples of images processed by the algorithm. The detector was tested on the remaining 30% of the images. It shows an overall accuracy of 60%, which increases to 62% for oil bubbles (**Table 1**). Most of the error is attributable to false positives due to either overlapping detections or detections that were not considered in the training set.

Two classes were selected for the targets: gas bubbles with a minor fraction of oil and oil bubbles assumed to be predominantly oil. A total of 68 cropped and prepared images were chosen, and bubbles were manually classified and stored as the ground truth set. Bubbles resolved with less than 8 pixels (nominally 2 mm) of radius were excluded to reduce process noise. Half bubbles, partially occluded bubbles, or bubbles too close to the black boundary were also left out of the training set for similar reasons.

Atmospheric Monitoring

The atmospheric concentration of methane was continuously measured with the use of a cavity ring-down spectrometer (CRDS) Picarro® G2203 Analyzer for CH_4/C_2H_2 that drew air samples (4 Hz) from an intake tube located on the starboard side of the ship, 3 m above the water surface and below the level of the exhaust stacks of the vessel. The instrument was calibrated to gas standard following a three-point procedure (Piccaro, 2011). The length of the intake line introduced a 60 s lag between intake and measurement. Data were recorded during the entire time the vessels R/V Brooks McCall or M/V Brandon Bordelon were on station. Ship tracks for surveys during the 2018 and 2021 campaigns are shown in **Supplementary Figure S1**. Sample readings were georeferenced in real time using a GPS antenna connected to the computer of the CRDS. Identical instrumentation and collection procedures were used on the 2018 and 2021 expeditions.

Tracer Experiment

During the final day of operations in the 2018 expedition, a tracer release experiment was conducted in order to test whether methane concentrations in the air in the study area could be linked to the persistent hydrocarbon plume that reached the ocean surface near the toppled MC20 oil platform and also to establish the path and dispersion of methane gas in the area. Because the CRDS-Picarro 2,203 has the capability of detecting acetylene gas with a precision in the parts per million range, the tracer experiment also utilized this gas as a reference compound. The acetylene tracer release technique has been widely used in the quantification of fugitive methane in landfills (Mønster et al., 2014; Mønster et al., 2015). To adapt this technique for the open ocean, a floating raft was constructed which held a small acetylene tank. The acetylene tank was connected to a mass flow regulator to produce a constant release of tracer gas into the atmosphere (15 L/min). In addition, a meteorological station installed on the

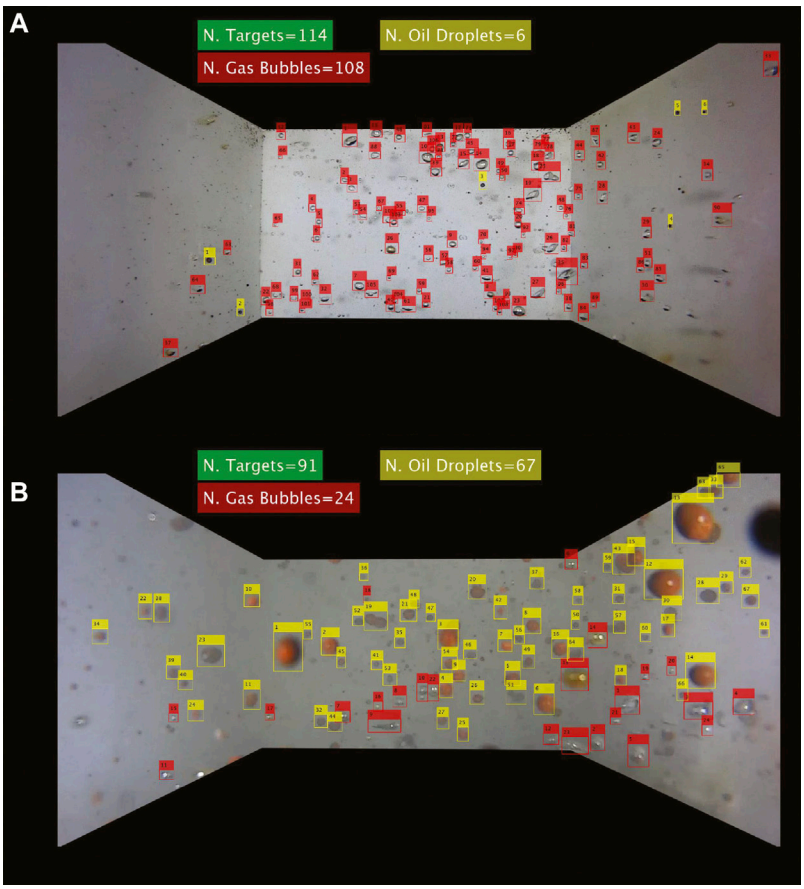

FIGURE 4 | Classified bubblometer images: samples of detector results with predominantly gas targets **(A upper)** and predominantly oil targets **(B lower)**, original Fig. 4.3 (Mason et al., 2019).

TABLE 1 | Average recognition and area accuracy achieved by the R-CNN bubble recognition algorithm.

Target class	Image set	Average accuracy (%)	Area error (%)
Gas bubbles	Training	63	22
	Test	53	11
	All images	62	18
Oil bubbles	Training	67	63
	Test	74	47
	All images	64	58
All targets	Training	67	24
	Test	58	24
	All images	64	24

raft collected records of the ambient wind speed and direction, temperature, and humidity in the area during the controlled acetylene release event. The raft was moored, as close as was possible, to the area where the MC20 hydrocarbon plume reached the ocean surface. Once the raft was successfully deployed, the vessel drifted downwind to increase the chances of detecting both atmospheric methane concentrations and the known volume of tracer gas. In practice, the scope of the raft anchor line allowed it to drift away from the bubble surfacing area.

Inverse Plume Modeling

Inverse plume modeling combined with atmospheric methane concentrations is used to estimate methane emission rate from the hydrocarbon plume into the atmosphere. The employed approach originally presented in landfill applications (Kormi et al., 2017; Kormi et al., 2018; Ali et al., 2020) tackles the problem of determining a contaminant source emission rate for a given set of measurements. The Gaussian plume model is coupled with an optimization-based identification method, to estimate fugitive methane emissions. Methane concentration is used to infer emissions though dispersion modeling and optimization. This is achieved through tracing dispersed methane back to potential emission sources. In the subsequent sections, we briefly summarize this optimization-based approach (Silva et al., 2019) and refer the reader to the work of Kormi et al. (2017) and Kormi et al. (2018) for a more thoroughly detailed presentation of the method.

Input parameters of the methane emission estimation method include methane concentration measurements and locations along with meteorological conditions, the most important being wind speed and direction and

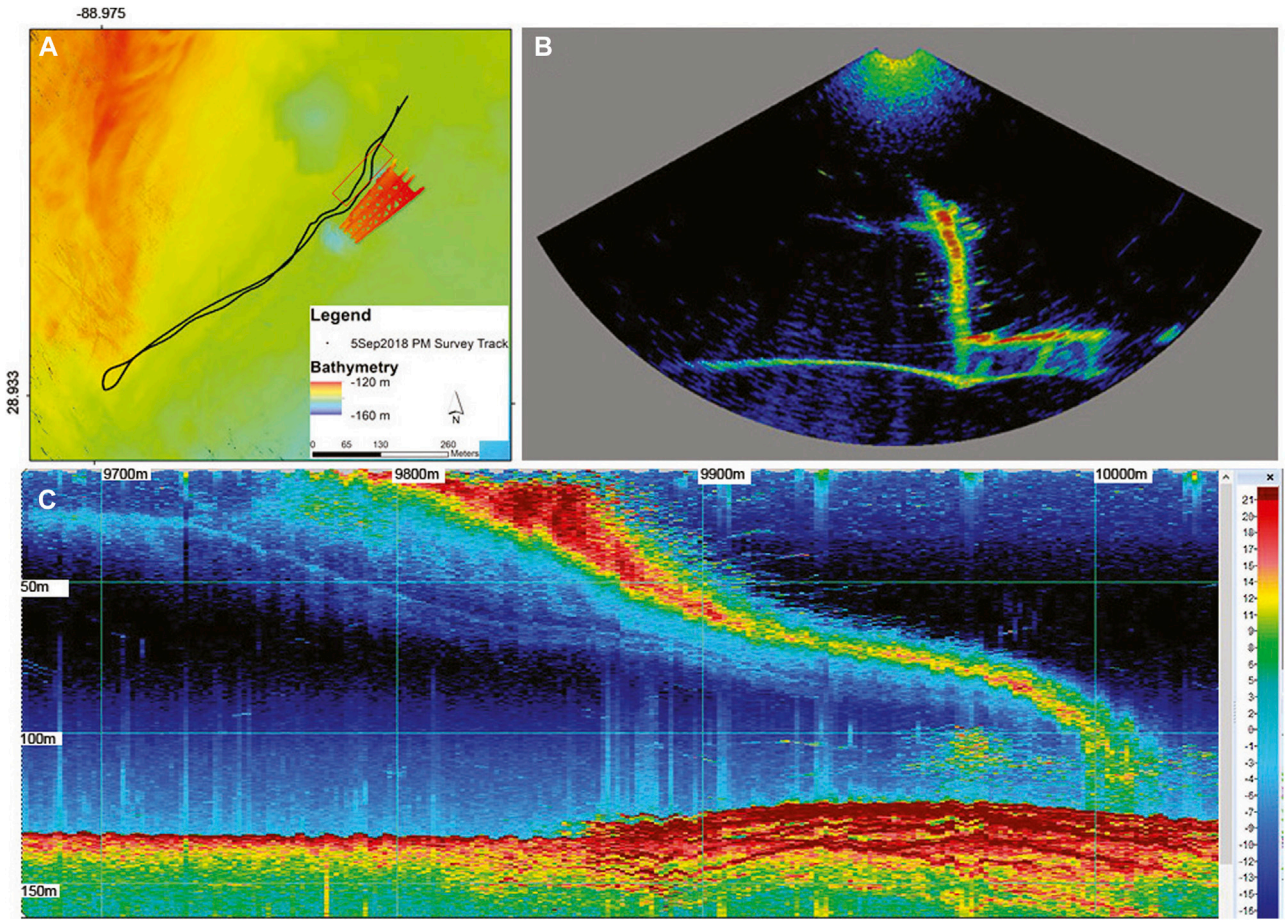

FIGURE 5 | Map and sample echograms from the survey conducted on the evening of 5 September. **(A upper left)** Map of the echosounder survey; bathymetry is represented by the colored ramp, and the red box represents the approximate area shown in the maximum intensity echogram. **(B upper right)** A single ping from the multibeam swath. **(C lower)** Multibeam echogram shown as maximum intensity across the beam swath and compressed along the track to show the trajectory and extent relative to the jacket. Two plume components are visible in the lower echogram, original Fig. 3.9 (Mason et al., 2019).

temperature. An implemented code is used to generate multiple configurations of source positions and emission rates. Each sample configuration is evaluated through calculating the corresponding methane concentrations at each measurement point. This is carried out through the backward application of an atmospheric dispersion model. As such, source identification can be treated as an inverse optimization task where the objective is to obtain the configuration of sources (locations and emission rates) that best fits the measured concentrations. The performance of a source configuration is further evaluated through the difference between measured and predicted methane concentrations. To predict methane concentrations at locations where effective measurements are performed, an atmospheric dispersion model is needed. In the proposed method, modeling of methane dispersion is carried out using Gaussian dispersion **Eq. 1**. This equation models the dispersion of a non-reactive gaseous pollutant (here, methane) from an elevated point source. **Eq. 1** predicts the steady-state concentration (C) in $\mu g/m^3$ at a point (*x, y, z*) located downwind from the source.

$$C(x,y,z) = \frac{Q}{2\pi u \sigma_y \sigma_x} e^{\frac{-y^2}{2\sigma_y^2}} \left(e^{\frac{(z+H)^2}{2\sigma_z^2}} + e^{\frac{(z-H)^2}{2\sigma_z^2}} \right) \quad (1)$$

In **Eq. 1** "Q" is the emission rate (μg/s), "σy" and "σz" (m) are the horizontal and vertical spread parameters that are functions of wind distance "*x*," respectively, and atmospheric stability is a measure of the resistance of the atmosphere to vertical air motion. Continuing, "*u*" is the average wind speed at stack height (m/s), "*y*" is the crosswind distance from the source to the receptor (m), "*z*" is the vertical distance above the ground (m), and "*H*" is the effective stack height (physical stack height plus plume rise) expressed in m.

The Gaussian dispersion equation uses a relatively simple calculation requiring only two dispersion parameters (σy and σz) to identify the variation of gas concentrations away from the diffusion source. These dispersion coefficients, σy and σz, are functions of wind speed, cloud cover, and surface heating by the Sun. Generally, the evaluation of the diffusion coefficients is based

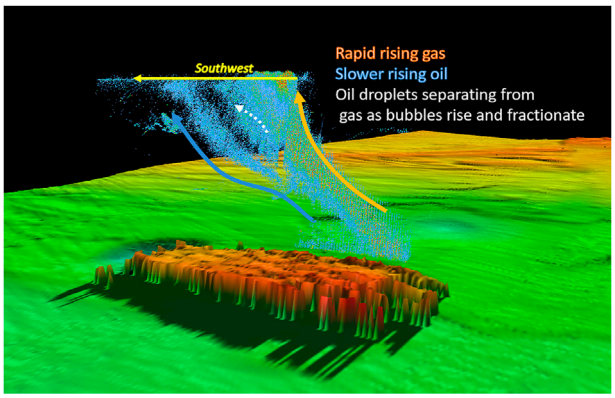

FIGURE 6 | Three-dimensional model of the oil and gas plume on 2 September 2018: Relative backscatter intensity from the M3 multibeam is scaled as blue–orange: low–high. Arrows define the components of the plume. See text for explanation, original Fig. 3.16 (Mason et al., 2019).

on atmospheric stability class. In the employed method, Pasquill–Gifford stability classes are used, and dispersion coefficients are calculated using the Briggs model (Briggs, 1965).

The optimization task is tackled using genetic algorithm routines in MATLAB. As a stochastic search method, including genetic algorithm optimization can efficiently explore complex and large solution space without getting trapped in low-quality minima. Although there is no guarantee of reaching a global optimum, near-optimal solutions are usually obtained.

RESULTS

Surface Echosounder Surveys

A total of eight surface echosounder surveys were conducted between 1 and 7 September 2018. At least, one survey was conducted each day, except for 4 September, due to evacuation of the MC20 site during severe weather associated with Tropical Storm Gordon (composite displays of all survey results can be seen in Chapter 3 of the work of Mason et al. (2019)). Survey tracklines varied in number and orientation, depending on the orientation and extent of the hydrocarbon plume and the daily operating plan coordinated among research investigators (**Supplementary Figure S1A**). Along-track and cross-track observations of the plume in the SBES and MBES revealed two or more sub-plumes emanating from a seabed position within an erosional pit at the northwest corner of the platform jacket. Visually differentiating the components of the plume in the acoustic echograms depended on the trajectory of the plume in the water column and the orientation of the survey trackelines. The components of the plume showed differential rise rates consistent with faster rising gas bubbles separated from slower-rising oil bubbles. On some occasions, relatively low noise on the 200 kHz channel permitted detection of components of the plume with backscatter intensity relatively higher than backscatter intensity in the 120 kHz for portions of the plume, consistent with the expected backscatter intensity patterns of liquid-filled spheres of oil, i.e., oil bubbles. Similarly, the high-frequency 500 kHz M3 multibeam surveys provided further evidence of separate components of the plume consistent with separate oil and gas components in the plume.

Figure 5 shows the components of the echogram and multibeam survey results for operations on the evening of 5 September 2018, close in time to visual plume observations reported in *Gas Bubbles in the Water Column*. For this survey, the vessel tracked along current, starting north of the jacket and continuing along for approximately 1,000 m to the southwest (**Figure 5A**). A single ping from the multibeam swath shows the jacket and a cross section of the plume (**Figure 5B**). It is noticed how the plume appears truncated where the beam bisects it in midwater. The trackline composite shows the entire length of the plume originating near the base of the jacket and deflecting approximately 300 m SW before reaching the surface (**Figure 5C**).

Figure 6 shows the 3D interpreted components of the plume observed on 2 September 2018, when currents deflected the plume to the southwest. High-backscatter components appeared to diverge upwards from relatively lower-backscatter components, which were rising more slowly, consistent with lower buoyancy of oil bubbles compared with gas bubbles. A possible second divergence occurred within the high backscatter plume as it approaches the surface, suggesting the ongoing fractionation of gas and oil components occurring closer to the surface. Drone surveillance of the ship parked within the plumes as they surfaced showed the separation of gas-dominated and oil-dominated components of the plume along the length of the vessel. An additional, much fainter, plume target was observed on 2 September 2018 about 200 m NW of the erosion crater over the location of the platform's original foundation and well template (**Supplementary Figure S1C**).

ROV Sonar Surveys

The ROV collected clear images of the plume components and as they vented within a ~10 m-wide and ~2 m-deep erosion pit at the base of the platform jacket (**Figure 7**). Closer examination with the M3 sonar revealed four or five subcomponents of the plume: a pair of smaller plumes to the southwest of the erosional pit and two separate larger plumes to the north. A fifth feature was less defined between the pair of smaller plumes and the southernmost of the two larger plumes. The characteristics of the backscatter intensity suggested the smaller pair was composed of oil, whereas the ones with higher backscatter intensity were composed of gas.

Gas Bubbles in the Water Column

A total of 5,881 gas bubbles and 6,258 oil bubbles were counted and measured based on image samples collected by using the bubblometer. Combining the depth of the vehicle as image collections were made with its navigation track meant that each image sample, and the number of bubbles detected in that sample, could be mapped in three dimensions (**Figure 8**). Bubble counts and densities were used to fit a cross section that

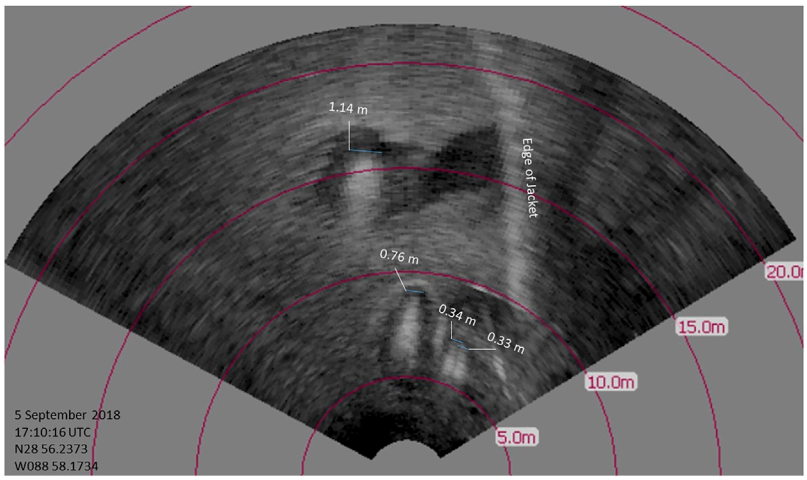

FIGURE 7 | Imaging sonar perspective of erosion crater and plume sources from the ROV: MC20 jacket in the background and multiple plumes observed in the foreground, original Fig. 3.21 (Mason et al., 2019).

segments the high-bubble-density core of the plume, shown as the red, blue, and yellow polygons in **Figures 8B–D**. The volume of this "core" plume region is the height of each depth region multiplied by the core cross section. The results showed that bubble abundance was variable among image samples, while the apparent density of bubbles observed was different within different depth ranges; that is, image samples within the erosion crater (>135 m), between the seafloor and the upper extent of the platform (135–125 m) and in the water column above the jacket (<125 m), tended to show different bubble abundances (**Table 2**). The number of bubbles per sample could be extrapolated to estimate the abundance of bubbles per m^3 according to the volume of the bubblometer's imaging chamber (0.018 m^3).

Bubble size and size frequency distributions were estimated for the observations prior to and after installation of the containment system. The pre-containment mean bubble diameter was 8.1 mm (n = 5,881: median 7.2 mm, stdev 3.16) for bubbles observed at water depths from >135 to 120 m; the post-containment mean bubble diameter was 7.4 mm (n = 585: median 6.7 mm, stdev 3.13) for bubbles observed at 120 m. Size frequency distributions were similar for the two datasets (**Supplementary Figure S2**). There were small differences. The 2018 distribution had several folds more of the 2.5 mm bubbles, and peaked at 7.5 mm, while the 2022 distribution peaked at 5 mm. This type of differences may not always be negligible in terms of bubble dissolution (see the work of McGinnis et al. (2006), for example).

The pre-containment collections were slightly skewed toward bubbles of large diameter (>20 mm) compared with post-containment observations. Bubble measurement procedures for the post-containment observations were based on ROV video under marginal water clarity. Both sets of measurements were approximate due to scaling uncertainty.

Bubble gas analysis

Analysis of the gas samples collected in midwater with the use of the pressure chamber showed that the gas bubbles comprised predominantly methane with a mixture of higher hydrocarbons consistent with thermogenic gases typical of the Gulf of Mexico (**Table 3**). Additional details regarding hydrocarbon analysis from MC20 can be found in the work of Gaskins et al. (2019).

4.5 Water Column Methane Concentrations

The concentration of methane in all water samples, including the 2018 and 2021 Niskin samples and the 2018 bubblometer water samples, spans in five orders of magnitude (**Figure 9**), from an expected background level of 0.003 μM CH_4, for seawater equilibrated with ambient air, to extreme values of >60 μM CH_4 measured in water samples from the bubblometer pressure cylinders and associated most closely with the copious flux of oil. Generally, the 2018 Niskin samples, the collection of which was targeted using the acoustic signal of the plume rather than visual observation of bubbles in the water column, showed methane levels that were slightly elevated versus expected background, consistent with the influence of the plume. The 2021 Niskin samples were collected using the ROV video feed to verify the presence of bubbles. The reader should recall that these bubbles had passed through a passive separator that removed oil and allowed gas to pass through unimpeded. Reference samples, collected >30 m from the bubble release point, with no bubbles visible, showed background concentrations of methane. The highest methane concentrations in the 2021 collections (~1 μM CH_4) were observed in samples collected among copious visible bubbles at depths of 123 m directly above the release point and 82 m amid copious visible bubbles. Overall, Niskin samples from the bubble plume taken at >30 m depth in 2021 (n = 20: mean = 0.550 μM CH_4, stdev = 0.680) were significantly greater ($p < 0.005$) than the comparable samples from 2018 (n = 34: mean = 0.014 μM CH_4, stdev = 0.0157). Extreme methane concentrations in the

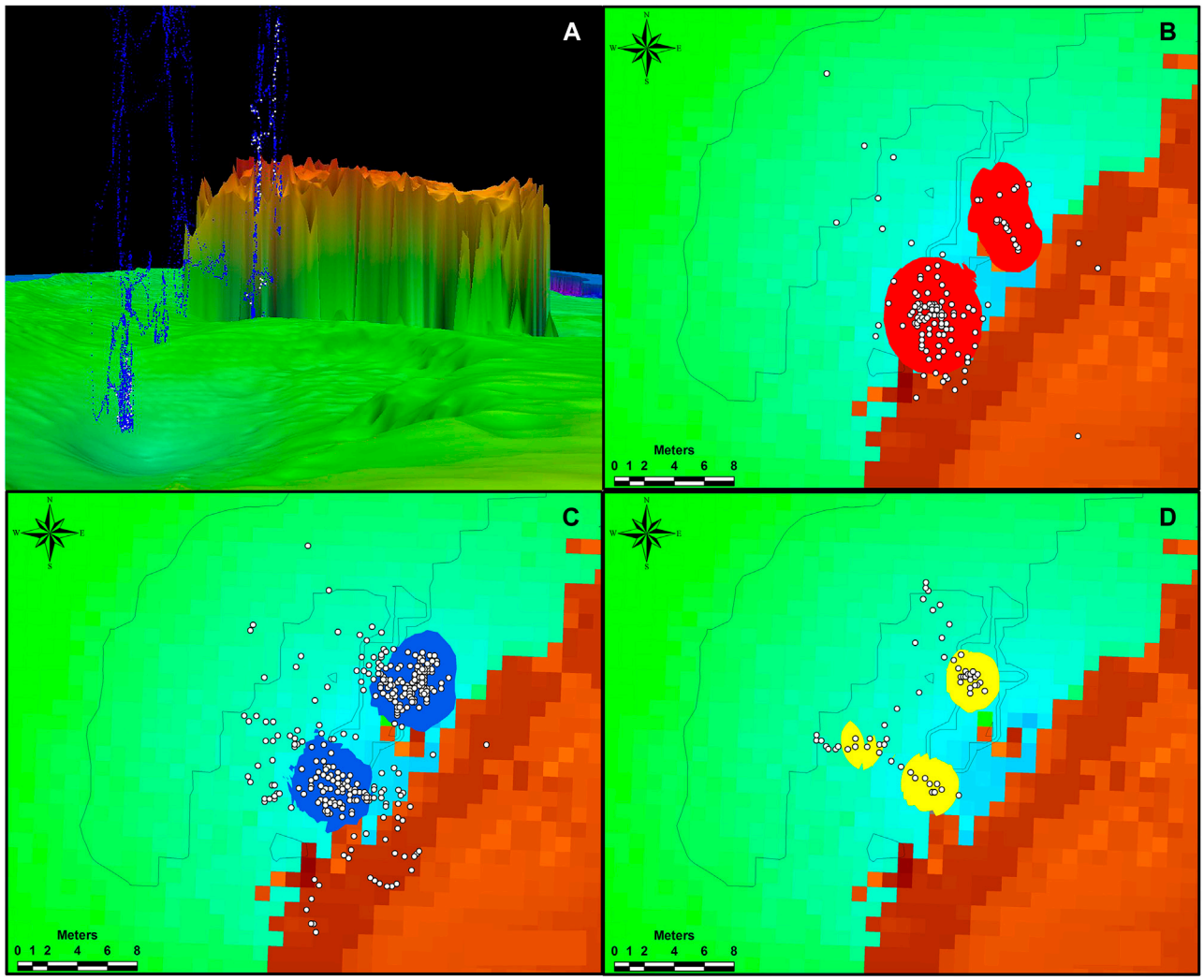

FIGURE 8 | Locations of image samples from the plume: **(A upper left)** vertical plot, blue points show the ROV locations during sampling and white points show where video image samples were taken; outline of the well jacket is approximately 10 m above the seabed (green); **(B upper right)** samples from the plume in the crater with the outline of the kernel polygon for this interval; **(C lower left)** samples from the plume in the benthic layer with the outline of the kernel polygon for this interval; and **(D lower right)** samples from the plume in midwater with the outline of the kernel polygon. Brown color represents the location of the collapsed well jacket, original Fig. 4.11 (Mason et al., 2019).

TABLE 2 | Summary of gas bubble abundances observed in image samples from the bubblometer in three depth ranges of hydrocarbon plume, as counted by the R-CNN algorithm.

Depth range (m)	<125	135–125	>135
Image samples	17	237	57
Total gas bubbles observed	74	5,310	409
Mean abundance, bubbles per sample	4.4	22.4	7.2
Stdev., bubbles per sample	4.15	27.97	12.93
Est., bubbles per m^3	242	1,245	399
Est. volume, main plume volume m^3	382	540	122

*Plume volumes were estimated from mapped bubble abundance (**Figure 8**).*

bubblometer water collections from 2018 reflect collection into a pressure cylinder that includes a head volume of gas and liquid oil.

Atmospheric Methane Measurements

The cavity ring-down spectrometer (CRDS) was in near-continuous operation recording at 4 Hz the atmospheric concentrations of methane (ppmv) at 3 m above the ocean surface in the vicinity of the Taylor platform site in MC20 for 1–7 September 2018, except for about 36 h when the ship had to vacate during the passage of Tropical Storm Gordon. The CRDS also operated continuously during 13–17 November 2021, except for a 1 h restart of the instrument during 15 November, also at 3 m above the ocean surface. These measurements are summarized in **Table 4**. Note that the CRDS recorded a slightly elevated average methane concentration in 2021 compared to 2018. The 2021 summary data are presented with and without the interval when oil was being pumped into transfer tanks on the ship deck. The major difference between the two

TABLE 3 | Results of gas analysis for samples collected from the mid-water column (approximately 125 m) into pressure vessels on the bubblometer.

	Methane (C_1)	Ethane (C_2) (%)	Propane (C_3) (%)	i-Butane (C_4) (%)	n-Butane (C_4) (%)	i-Pentane (C_5) (%)	n-Pentane (C_5) (%)	C_1/(C_2+C_3) (%)	$\delta^{13}C$ methane
Plume sample 1	92.70	3.45	2.40	0.51	0.58	0.20	0.12	15.9	–59.1‰
Plume sample 2	94.90	2.48	1.69	0.36	0.39	0.12	0.06	22.8	–59.7‰
Plume sample 3	94.80	2.51	1.75	0.38	0.40	0.12	0.07	22.2	–59.0‰

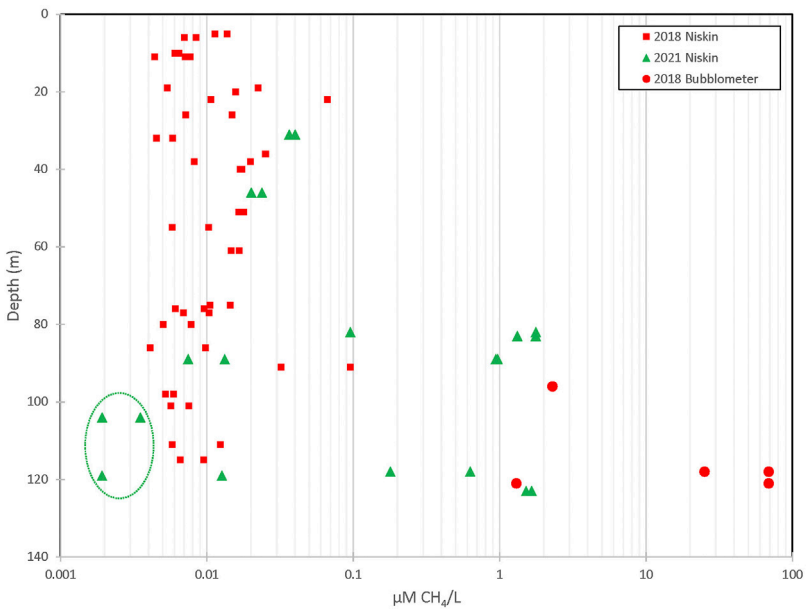

FIGURE 9 | Methane concentrations in the water column: samples from 2018 (red squares) were collected with Niskin bottles deployed within the oil and gas plume profile and with the pressurized cylinders sealed at depth by using the bubblometer (red circles). Samples from 2021 (green triangles) were collected by Niskin bottles deployed from an ROV in the oil-free gas plume with bubble presence verified by a real-time video; background reference samples were collected at a location ~35 m from the bubbles source (dashed circle).

TABLE 4 | Summary statistics for atmospheric methane concentrations (ppmv) recorded from the cavity ring-down spectrometer in September 2018 and during the 2021 cruise of opportunity.

Data source	Count	Mean	Minimum	Maximum	Stdev
2018	15.6×10^5	1.93	1.77	11.74	0.270
2021, all data	9.19×10^5	2.10	1.90	15.93	0.241
2021, excluding pump-off	8.24×10^5	2.09	1.90	5.13	0.186

Results for 2021 consider all data and separately the period when oil was pumped into storage tanks on the ship.

CRDS surveys was the broad distribution of peak methane concentrations in 2018. **Figure 10** shows the comparative plots of mean atmospheric methane concentrations observed over the MC20 site; **Figure 10A** shows the results for 2018 and **Figure 10B**, for 2021—excluding the period when oil was being pumped up to the ship. Note that, during 2018, acoustic surveys and other operations meant that the ship's track covered a much broader area at the MC20 site, while in 2021, broader area surveys were more curtailed and the ship was mostly positioned directly over the platform wreckage (**Supplementary Figure S1**).

Results were strongly dependent on the circumstances of hydrocarbon release at the seafloor and operations of the vessels. During 2018, gas and oil rose unimpeded to the surface, with water column currents largely slack or moderate (<0.3 m/s). In April 2019, authorities installed the containment system that diverted oil from the hydrocarbon plume into storage

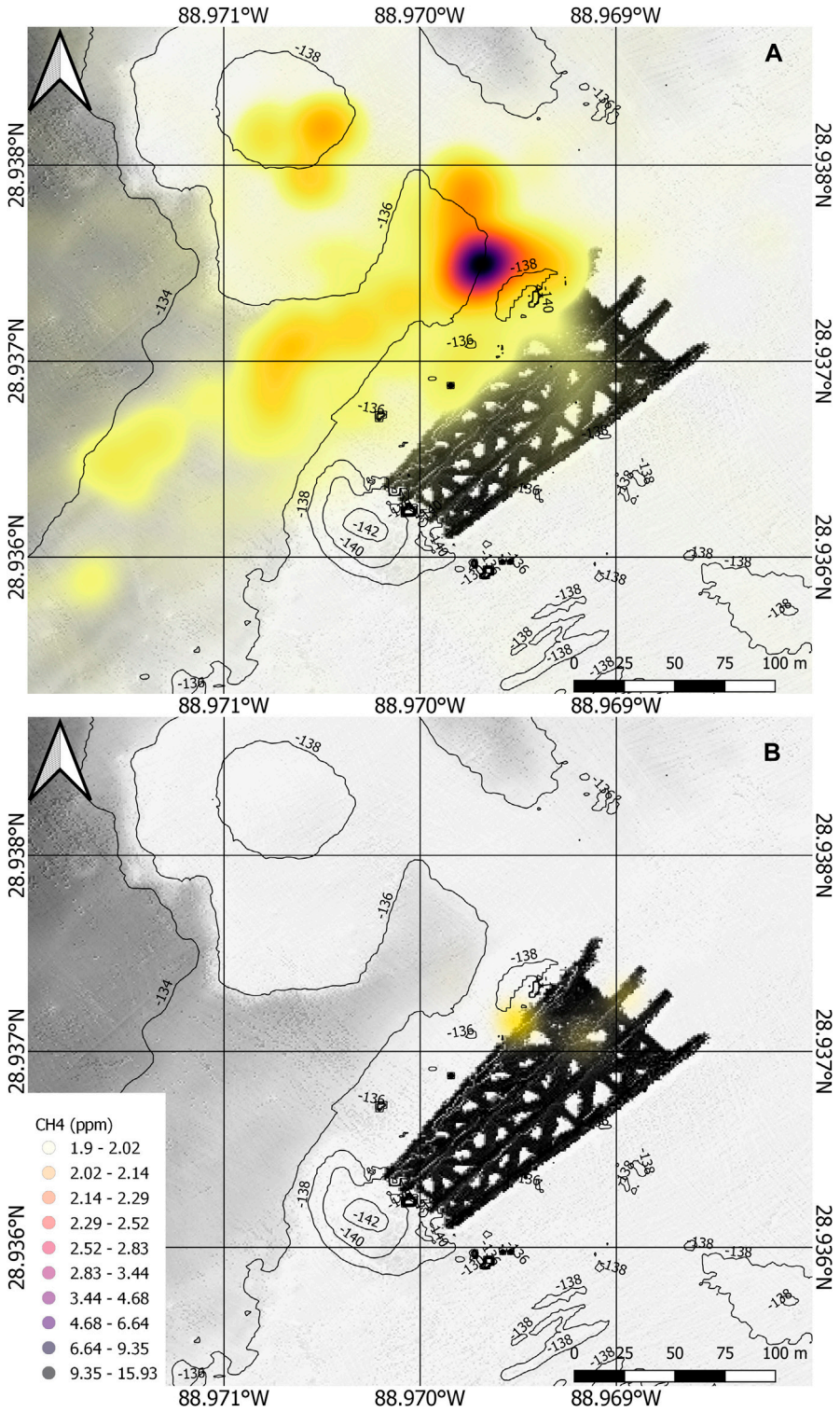

FIGURE 10 | Heat maps of methane concentrations: CRDS readings recorded 9 m above sea surface over the MC 20 site. **(A upper)** 2018, before oil containment; **(B lower)** 2021, after oil containment.

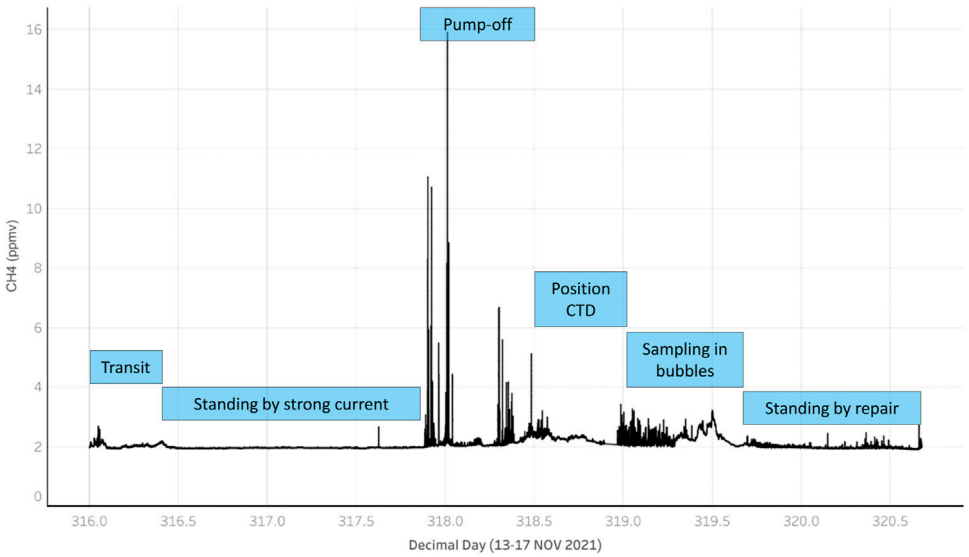

FIGURE 11 | Annotated timeline of CRDS measurements during the 2021 cruise of opportunity: major methane peaks confined to periods when oil was pumped into storage tanks or released due to operations under the containment dome. Minor methane peaks observed with the ship stationary over the bubble stream.

tanks. Oil recovery rates from these storage tanks subsequently showed that oil being released into the water column and rising to the surface would have exceeded 4.5 m^3/d during 2018 (O'Reilly, 2020). Oil was continuously observed over the site during 2018 and produced the large surface oil slicks typical of this spill (Daneshgar Asl et al., 2015). During 2021, in contrast, there was little visible oil that rose to the surface. However, large amounts of oil were pumped up from the underwater storage tanks to the ship and into transport tanks that vented to the air. The pump-off period lasted 12 h and was followed by an exercise to moor a CTD so that it was suspended over the erosion crater and under the containment. **Figure 11** shows the annotated timelines of CRDS observations over the MC20 sites during 2018 and 2021.

Tracer Experiment and Plume Modeling

During the acetylene tracer experiment conducted in 2018 and the routine CRDS measurements, background acetylene concentrations fluctuated between 0 and 0.9 parts per billion (ppb). During the tracer experiment, when acetylene was being released from the raft tethered over the wreck site at a controlled rate of 15 L/min (0.29 g/s at STP), three major spikes on the CRDS for acetylene were detected with values that exceeded 200 ppb of acetylene in the air. The highest concentration of the acetylene tracer gas was detected only a few meters away from the raft deployment in the "bubbling zone" (1,024.2 ppb), and after that, two more spikes on the tracer gas were detected downwind (11.16 knots, ESE) at approximately 310 and 430 m away from the deployment site, respectively. Because the vessel R/V Brooks McCall was drifting downwind during the tracer study raft deployment, there were at least three opportunities where the tracer spikes almost perfectly matched the relatively high measurements of methane in the air, further confirming that the source of additional methane in the air was sourced from the "bubbling zone" where the hydrocarbon plume was actively reaching the ocean surface (**Supplementary Figure S3**).

Tracer gas (acetylene) air concentration measurements were also employed to calibrate/validate the inverse plume measurements method that is proposed to estimate methane emission rate estimates. Acetylene measurements are used as an input for the method in order to test its ability to predict the actual emission rate of the tracer gas (15 L/min). Wind direction and speed, along with a set 4,175 data points (acetylene concentrations and measurement locations), were used as inputs for the identification method. The average acetylene emission rate predicted by the method was equal to 0.26 g/s which approximately corresponded to the actual emission rate of 15 L/min (0.29 g/s at STP). The results obtained with the tracer (acetylene) gas release, in a controlled manner, show that the inverse plume modeling method can be used to estimate methane emission rates under marine conditions.

The inverse plume modeling combined with atmospheric methane concentrations was used to estimate transfer from the hydrocarbon plume into the atmosphere. These estimates provide an average methane emission rate equal to 9 g/s with a standard deviation of 1.1. This corresponds to a discharge equivalent to 0.8 t CH_4/d. However, it is important to note that this estimation method is prone to variability in wind direction and speed.

DISCUSSION OF RESULTS

The fate of hydrocarbon gas released from the seabed is an important research question because seeps are common in the coastal ocean and methane is a potent greenhouse gas. Moreover, recent history shows that oil and gas spills originating from the seafloor can be a significant environmental hazard. Natural gas

seeps can be challenging to study because they are often cryptic and ephemeral. These results of this study offer insights into this process and the means for investigating it; however, circumstances of the release we studied constrain these insights in significant ways. The release rate of methane and higher hydrocarbon gases in MC20 was one component of long-running oil spill that discharged in excess of 4.5 m^3/d (https://couvillionmc20response.com/). This spill, although presently mitigated by the containment system, will continue until the wells can be permanently plugged with cement through difficult and costly engineering. The platform and its wells were aged at the time (2004) when a hurricane and mudslide destroyed the structure and initiated the spill. This aged condition is shared by hundreds of other production platforms and a vast network of pipelines along the northern margin of the Gulf of Mexico in an era when intense hurricanes are expected to become more prevalent (Knutson et al., 2020) and potential for slope instability under storm conditions is increasingly recognized (Fan et al., 2020). It is to be hoped that this accidental experiment will not be repeated.

Findings made during the 2018 research expedition led to installation of the containment system that mitigated the release of oil. However, it is concerning that nearly 15 years elapsed between the onset of the spill and collection of data that definitively demonstrated the magnitude of the problem. Acoustic surveys in 2018 did reveal the source and water column characteristics of the hydrocarbon plume in MC20, in particular, how currents influenced the path of the plume and the separation of oil and gas components (**Figures 5**, **6**). However, although previous acoustic survey had also detected persistent hydrocarbon plumes emanating from the platform wreckage, the volume of oil they contained and the geochemical source of gas in the plume were disputed (O'Reilly, 2020). The dispositive observations that led to containment were a direct visual confirmation of copious oil in the plume and collection of gas for chemical analysis. The gas was shown to be a reservoir-sourced mixture of thermogenic hydrocarbons, rather than biogenic methane possibly sourced from microbial degradation of organic material (**Table 3**). The method used to collect gas mid-water and store it under pressure requires straightforward engineering that could be adapted for greater water depths.

The visualization chamber of the bubblometer provided replicated samples for determining the density of gas bubbles, with the application of a machine-learning algorithm that counted individual targets. Integrating these results with the 3D location of the ROV showed that the density of bubbles in the plume was affected by where in the water column it was sampled (**Table 2**). In the two erosion craters, the ROV sonar survey showed that bubbles were released from several individual vents (**Figure 7**). Similar venting has been reported from natural seeps (De Beukelaer et al., 2003; Johansen et al., 2014; Sahling et al., 2016; Johansen et al., 2020; Meurer et al., 2021). Under such circumstances, bubble density would be locally variable. Above the crater, but in the lee of the platform wreckage, the individual bubble streams from the vents merged into larger plumes that nonetheless reflected the discrete origins from the two craters. The density of bubbles was the greatest between the seafloor and the top of the platform wreckage, possibly because of turbulence caused by the structure. Bubble density decreased abruptly above the level of the wreckage, where moderate currents and mixing in the water column dispersed the plume (**Figure 8** and **Table 2**). The origin, dispersion, and separation of oil and gas components of the plume detected by visual means were consistent with its acoustic signatures (**Figures 5**, **6**).

Bubble size is an important consideration in the rise speed of bubbles, the rate of mass transfer from the ascending bubbles into seawater, and potential for gas transfer to atmosphere. Installation of the containment system diverts the gas bubbles through a separator before they are released to the water column (Couch, 2010), while the pre-containment releases were through seafloor sediment. Average bubble diameter was 9% smaller for the

Water samples collected by Niskin bottles and from the bubblometer pressure chambers showed a five order of magnitude range of methane concentrations (**Figure 9**). Water column methane concentrations in the bubble plumes were elevated above seawater ambient (for 100–120 m depth) in 2018 and more elevated in the visually targeted 2021 collections. Previous results suggest that methane, being undersaturated in seawater, should rapidly be exchanged for nitrogen and oxygen as methane bubbles rise in the water column (McGinnis et al., 2006; Rehder et al., 2009). The best available measurements of bubble size (**Supplementary Figure S2**) are comparable to "larger" bubble diameters (8.5 mm) modelled by McGinnis et al. (2006) for pure methane rising from 90 m (McGinnis et al., 2006, **Figure 11**). Those results predicted >95% of original methane mass due to dissolution over this transit. Average methane concentrations in 2021 were significantly greater ($p < 0.005$) by nearly two orders of magnitude compared with Niskin samples from 2018 (**Figure 9**). Bubblometer samples were collected and returned to the surface at near *in situ* pressure in the collection cylinders and then decanted into sample vials with minimum degassing; they reflected the greater saturation of methane in seawater at ~100 m depth. It was not possible to replicate exactly the collections and observations made in 2018 prior to installation of the containment system with observations of gas released from the separator apparatus, but measurements indicate generally higher concentrations when oil was separated from the gas. Previous studies at oil seeps (Leifer and MacDonald, 2003) have speculated that oil coatings in bubbles could retard this process. This being the case, one would expect water in a bubble plume to have lower concentration of methane if the bubbles were oil coated, as was the case in 2018, than they would if the bubbles were effectively oil free. Therefore, the differences in water column methane concentrations between the 2018 (oily) and 2021 (unoiled) Niskin samples are consistent with reduced gas exchanged in oil-coated bubbles. However, one should consider the fact that the 2021 samples were visually targeted and the 2018 samples were not included while evaluating this result.

The most pronounced difference between observations in 2018 and 2021 was the detection of atmospheric methane concentrations (**Figure 10**). When methane above background levels was detected in both years, detection took the form of

transient peaks that rose to maxima over a matter of seconds and then declined (**Figure 11** and **Supplementary Figure S3**). During the 2018 expedition, peaks that were as much as five-fold greater than background (~10 ppmv) were detected with high frequency, particularly when the vessel was loitering over the plume source. During the 2021 cruise of opportunity, major methane peaks were only detected when oil was being pumped into the transfer tanks on the deck or reaching the ocean surface due to operations under the containment dome (**Figure 11**). However, moderate methane detections (~3.5 ppmv) continued while the ship was parked directly over the bubble stream for collection of the Niskin samples, so transfer of methane to the reservoir was substantially reduced. What caused this change?

The gas content of oil is of concern for safe management of the product on offshore platforms, particularly for volatile oils, but is of lesser operational interest for the so-called black oil, which supports gas to oil ratios of <300:1. Daily production from the Taylor platform prior to its destruction comprised 190 m^3 oil and 1.7×108 m^3 gas (Bryant et al., 2020), but oil production was well past peak levels and likely comprised black oil. General material-balance equations indicate that black oil should retain a GOR of ~15:1 after transit to the surface, but the GOR would decline toward zero as the oil degassed over time (McCain, 1991). This would explain the methane peaks observed while oil stored in the containment system was venting from storage tanks on the ship during 2021. These results indicate that methane transfer to the atmosphere was most pronounced when oil was a major component of the hydrocarbon plume that reached the surface, but it also occurred at a reduced level when oil was removed from the plume. Detection of major methane peaks during the 2021 oil pump-off period suggests that the oil itself may be as or more important a vector for transferring methane to the atmosphere compared with oil-coated bubbles. Although this was a vigorous plume of methane, its footprint on the surface was small. Detection of methane from marine seeps may be highly dependent on positioning the detector directly over the surfacing bubbles.

The tracer experiment during the 2018 cruise demonstrates that eddy-diffusion methods used to estimate methane fluxes can be applied in marine settings under favorable circumstances. We assume that the bubble-surfacing location was reasonably constant during the ~2.5 h experiment; however, the raft that deployed the tracer release did move on its anchor line with shifting wind direction. The most useful measurements occurred when the methane source, tracer source, and detector were aligned (**Supplementary Figure S2**). The experiment could readily be replicated for submarine sources at depths of ~100 m and would be improved by positioning the raft with tracer release more directly in the bubble-surfacing location.

Methane emissions from oceanic sources are challenging to measure directly, and it is informative to compare these results, made under relatively controlled conditions at moderate depth, with observations from methane seeps and leaks across a range of water depths in the Gulf of Mexico. A methane and oil seep at the Chapopote asphalt volcano in 3,400 m produced multiple acoustic bubble flares and 30 μM/L methane concentrations at depth; the flares and methane concentrations dissipated before reaching the surface, while associate oil formed persistent slicks (Römer et al., 2019). Researchers who used a submersible to visually track bubbles rising from the 540 m seep at Bush Hill measured near-surface methane concentrations up to 1,000 time saturation with atmospheric concentration (Solomon et al., 2009); however, oil contamination of the submersible may have affected results (personal observation). Hu et al. (2012), who collected pumped water samples from the surface interface, failed to confirm this result at Bush Hill and a second ~1,000 m seep. Meurer et al. (2021), sampling with MET sensors deployed on gliders over Bush Hill, measured methane concentrations of up to 0.4 μM/L, well below the observations of Solomon et al. (2009). Notably, results from the work of Yvon-Lewis et al. (2011), using techniques to similar to those used by Hu et al. (2012) and Ryerson et al. (2011), using airborne measurements, suggested that oil reaching the surface (~3,000 m^3/d) from the Deepwater Horizon oil spill, which leaked from 4,500 m depth, was a negligible source of methane to air.

While the aforementioned studies measured concentrations to infer source magnitude, other studies have attempted to integrate emission or dissolution processes across seep areas to estimate fluxes. At GC600, a 1,100 m seep in the Gulf of Mexico marked by prolific oil slicks (Garcia-Pineda et al., 2009), Johansen et al. (2020) integrated sub-bottom profiles with mapping and surveillance of bubble venting and other seep features to estimate a flux of ~4×10^6 mol/y from a seep area of ~0.5 km^2. However, this budget was for methane released to the water and did not quantify the gas and oil reaching the surface over the site. In a study from the Comea seep in the Timor Sea at water depth (84 m), Brunskill et al. (2011), captured seep bubbles from the water column to measure directly their methane content. They found concentrations of ~0.7 μM/L in the water associated with "bubble streams," findings quite similar to present results. Integrating across a carbonate hard ground that was the source of the bubbles, they estimated a flux to the atmosphere of 0.13–1.3 t CH_4/d from a seep area of 0.7 km^2. In terrestrial landfills, where the measurement challenges for estimating methane flux are quite different from those at marine seeps and leaks, results are quite dependent on soil cover over landfill material (O'Brien, 2014). Investigating areas with fine clay cover, the author reported a flux of 2.1 t CH_4/d from a landfill area of 0.37 km^2.

Converting these estimates to commonly used flux units yields 0.19–1.9 and 5.7 g CH_4/m^2/d for the Comea seep and a well-covered landfill, respectively. The discharge we report for the 2018 observations was 0.8 t CH_4/d. At MC20, gas was emitted from a seafloor erosion crater ~10 m in diameter. This source produced a flux to the atmosphere from ocean surface of ~10,000 g CH_4/m^2/d. Why is there such a huge discrepancy? A natural marine seep and a municipal landfill are actually not that dissimilar. Both generate methane from buried organic material in a dispersed bioreactor. The stable isotope ratios for the methane components of the gas samples were also consistent with a mixed thermogenic and biogenic source and with an origin within the reservoirs produced by the oil platform prior to its destruction. Emissions at MC20 are well leaks that funnel thermogenic gas and oil from multiple reservoirs (Stout and

Litman, in press), primarily through pipes that are largely intact reaching to a single point on the seabed. However, the MC20 site also includes a secondary, much smaller bubble source from the well template (**Supplementary Figure S1C**), which was possibly detected as an anomaly in the atmosphere methane concentrations recorded by the CRDS (**Figure 10A**). Brunskill et al. (2011) found measurable atmospheric methane associated with plugged and abandoned wells in the North Sea and suggested that "drilling induced fractures" around well boreholes are persistent seep conduits. They conclude that plugged and abandoned wells might be a source of methane to the water column, but not significant for greenhouse processes. Similar investigations of the northern Gulf of Mexico energy infrastructure across the continental shelf are indicated. A greater concern, however, is the vulnerability of the aging array of wells and pipelines to slope instability and hurricane impacts (Nodine et al., 2007). This is particularly true in view of how difficult it has been to stop the leaking wells at MC20. In balance, the literature indicates that bubbles emitted from deep (>500 m) marine sources principally contribute methane to the ocean, not the air, whereas this study and similar investigations (Brunskill et al., 2011; Böttner et al., 2020) show that methane can reach the atmosphere from sources ~100 m deep. Oil emitted by seeps or leaks is an additional source that should be considered in light of the abundant oil seeps in the Gulf of Mexico (MacDonald et al., 2015), the Congo Basin (Jatiault et al., 2017), and elsewhere.

DATA AVAILABILITY STATEMENT

The raw data supporting the conclusions of this article will be made available by the authors, without undue reservation.

AUTHOR CONTRIBUTIONS

MS and CO provided 2018 data collection at sea, geospatial modeling, and contributions to text. CO measured bubble sizes in 2022. CR provided custom R-CNN bubble counting algorithm and contributions to text. NA and TA provided inverse plume modeling and contributions to text. IM provided 2018 and 2021 data collection at sea and wrote the paper.

FUNDING

The 2018 survey was jointly funded by the U.S. Department of the Interior, Bureau of Safety and Environmental Enforcement, and the U.S. Department of Commerce, National Oceanic and Atmospheric Administration, through Interagency Agreement E18PG00016 and TDI-Brooks International. The 2021 data collection was made possible by the support to IM from the Environmental Enforcement Section, Environment and Natural Resources Division, United States Department of Justice. Additional support to MS and CO was extended from ExxonMobil Upstream Research Co., Gulf of Mexico Seeps Study.

ACKNOWLEDGMENTS

The authors gratefully acknowledge the 2018 expedition team and crew of R/V Brooks McCall and, especially, A. Mason and C. Taylor from the NOAA for their essential contributions to the 2018 expedition and the acoustic survey results presented in this paper. B. Bernard and M. Gaskins of TDI-Brooks International provided logistic support and hydrocarbon gas analysis. J. Chanton provided analysis and insights regarding methane concentrations in water samples. W. Meurer and L. Zhao of ExxonMobil provided insights regarding gas: oil transport processes and application of the McCain (1991) model. IM thanks D. Hoffman and the Couvillion engineering team for generous assistance during the 2021 and 2022 operations on M/V Brandon Bordelon.

SUPPLEMENTARY MATERIAL

The Supplementary Material for this article can be found online at: https://www.frontiersin.org/articles/10.3389/feart.2022.833661/full#supplementary-material

REFERENCES

Bel Hadj Ali, N., Abichou, T., and Green, R. (2020). Comparing Estimates of Fugitive Landfill Methane Emissions Using Inverse Plume Modeling Obtained with Surface Emission Monitoring (SEM), Drone Emission Monitoring (DEM), and Downwind Plume Emission Monitoring (DWPEM). *J. Air Waste Manag. Assoc.* 70 (4), 410–424. doi:10.1080/10962247.2020.1728423

Böttner, C., Haeckel, M., Schmidt, M., Berndt, C., Vielstädte, L., and Kutsch, J. A. (2020). Greenhouse Gas Emissions from marine Decommissioned Hydrocarbon wells: Leakage Detection, Monitoring and Mitigation Strategies. *Int. J. Greenhouse Gas Control.* 100. doi:10.1016/j.ijggc.2020.103119

Brunskill, G. J., Burns, K. A., and Zagorskis, I. (2011). Natural Flux of Greenhouse Methane from the Timor Sea to the Atmosphere. *J. Geophys. Research-Biogeosciences 116*. doi:10.1029/2010jg001444

Bryant, W. L., Camilli, R., Fisher, G. B., Overton, E. B., Reddy, C. M., Reible, D., et al. (2020). Harnessing a Decade of Data to Inform Future Decisions: Insights into the Ongoing Hydrocarbon Release at Taylor Energy's Mississippi Canyon Block 20 (MC20) Site. *Mar. Pollut. Bull.* 155. doi:10.1016/j.marpolbul.2020.111056

Couch, W. (2010). System and Method for Underwater Oil and Gas Separator. *United States patent Appl. US 20100038324A1*.

Court of Appeals for the Federal Circuit (2020). "Taylor Energy Company LLC V. United States, 19-1983 (Fed. Cir. *2020)*". (

Daneshgar Asl, S., Amos, J. F., Woods, P., Garcia-Pineda, O., and MacDonald, I. R. (2015). Chronic, Anthropogenic Hydrocarbon Discharges in the Gulf of Mexico. *Deep Sea Res. Part Topical Stud. Oceanography* 129, 187–195. doi:10.1016/j.dsr2.2014.12.006

De Beukelaer, S. M., MacDonald, I. R., Guinnasso, N. L., and Murray, J. A. (2003). Distinct Side-Scan Sonar, RADARSAT SAR, and Acoustic Profiler Signatures of Gas and Oil Seeps on the Gulf of Mexico Slope. *Geo-Marine Lett.* 23 (3-4), 177–186. doi:10.1007/s00367-003-0139-9

Dickens, G. R., Oneil, J. R., Rea, D. K., and Owen, R. M. (1995). Dissociation of Oceanic Methane Hydrate as a Cause of the Carbon-Isotope Excursion at the

End of the Paleocene. *Paleoceanography* 10 (6), 965–971. doi:10.1029/95pa02087

Eckle, P., Burgherr, P., and Michax, E. (2012). Risk of Large Oil Spills: A Statistical Analysis in the Aftermath of Deepwater Horizon. *Environ. Sci. Tech.* 46 (23), 13002–13008. doi:10.1021/es3029523

El bani Altuna, N., Rasmussen, T. L., Ezat, M. M., Vadakkepuliyambatta, S., Groeneveld, J., and Greaves, M. (2021). Deglacial Bottom Water Warming Intensified Arctic Methane Seepage in the NW Barents Sea. *Commun. Earth Environ.* 2 (1), 9. doi:10.1038/s43247-021-00264-x

Elderfield, H., and Schultz, A. (1996). Mid-ocean ridge Hydrothermal Fluxes and the Chemical Composition of the Ocean. *Annu. Rev. Earth Planet. Sci.* 24, 191–224. doi:10.1146/annurev.earth.24.1.191

Fan, W. Y., McGuire, J. J., and Shearer, P. M. (2020). Abundant Spontaneous and Dynamically Triggered Submarine Landslides in the Gulf of Mexico. *Geophysical Research Letters* 47(12). doi:10.1029/2020gl087213

Feng, D., Chen, D., Peckmann, J., and Bohrmann, G. (2010). Authigenic Carbonates from Methane Seeps of the Northern Congo Fan: Microbial Formation Mechanism. *Mar. Pet. Geology.* 27 (4), 748–756. doi:10.1016/j.marpetgeo.2009.08.006

Fu, X., Waite, W. F., and Ruppel, C. D. (2021). Hydrate Formation on Marine Seep Bubbles and the Implications for Water Column Methane Dissolution. *J. Geophys. Res. Oceans* 126 (9), e2021JC017363. doi:10.1029/2021JC017363

Garcia-Pineda, O., MacDonald, I., Zimmer, B., Shedd, B., and Roberts, H. (2010). Remote-sensing Evaluation of Geophysical Anomaly Sites in the Outer continental Slope, Northern Gulf of Mexico. *Deep-Sea Res. Part II-Topical Stud. Oceanography* 57 (21-23), 1859–1869. doi:10.1016/j.dsr2.2010.05.005

Garcia-Pineda, O., Zimmer, B., Howard, M., Pichel, W., Li, X., and MacDonald, I. R. (2009). Using SAR Images to Delineate Ocean Oil Slicks with a Texture Classifying Neural Network Algorithm (TCNNA). *Can. J. Remote Sensing* 35 (5), 411–421. doi:10.5589/m09-035

Gaskins, M., Bernard, B., and Brooks, J. M. (2019). "Chapter 6: Chemical Analysis of Gas Samples Collected from the MC20 Leak in the Northern Gulf of Mexico," in *An Integrated Assessment of Oil and Gas Release into the Marine Environment at the Former Taylor Energy MC20 Site(* (USA: NOAA National Ocean Service, National Centers for Coastal Ocean Science), 71–78.

Hu, L., Yvon-Lewis, S. A., Kessler, J. D., and MacDonald, I. R. (2012). Methane Fluxes to the Atmosphere from deepwater Hydrocarbon Seeps in the Northern Gulf of Mexico. *J. Geophys. Research-Oceans 117*. doi:10.1029/2011jc007208

Jatiault, R., Dhont, D., Loncke, L., and Dubucq, D. (2017). Monitoring of Natural Oil Seepage in the Lower Congo Basin Using SAR Observations. *Remote Sensing Environ.* 191, 258–272. doi:10.1016/j.rse.2017.01.031

Johansen, C., Macelloni, L., Natter, M., Silva, M., Woosley, M., Woolsey, A., et al. (2020). Hydrocarbon Migration Pathway and Methane Budget for a Gulf of Mexico Natural Seep Site: Green Canyon 600. *Earth Planet. Sci. Lett.* 545. doi:10.1016/j.epsl.2020.116411

Johansen, C., Todd, A. C., Dewar, W., Shedd, W., and MacDonald, I. R. (2014).Quantifying the Volume and Frequency of Bubble Release from Hydrocarbon Seeps in the Gulf of Mexico: GC600 (Poster Presentation)", in: Gulf of Mexico Oil Spill & Ecosystem Science Conference).

Knutson, T., Camargo, S. J., Chan, J. C. L., Emanuel, K., Ho, C. H., Kossin, J., et al. (2020). Tropical Cyclones and Climate Change Assessment: Part II: Projected Response to Anthropogenic Warming. *Bull. Am. Meteorol. Soc.* 101 (3), E303–E322. doi:10.1175/bams-d-18-0194.1

Kormi, T., Ali, N. B. H., Abichou, T., and Green, R. (2017). Estimation of Landfill Methane Emissions Using Stochastic Search Methods. *Atmos. Pollut. Res.* 8 (4), 597–605. doi:10.1016/j.apr.2016.12.020

Kormi, T., Mhadhebi, S., Ali, N. B. H., Abichou, T., and Green, R. (2018). Estimation of Fugitive Landfill Methane Emissions Using Surface Emission Monitoring and Genetic Algorithms Optimization. *Waste Manag.* 72, 313–328. doi:10.1016/j.wasman.2016.11.024

Leifer, I., and MacDonald, I. (2003). Dynamics of the Gas Flux from Shallow Gas Hydrate Deposits: Interaction between Oily Hydrate Bubbles and the Oceanic Environment. *Earth Planet. Sci. Lett.* 210 (3-4), 411–424. doi:10.1016/s0012-821x(03)00173-0

MacDonald, I. R., Garcia-Pineda, O., Beet, A., Daneshgar Asl, S., Feng, L., Graettinger, G., et al. (2015). Natural and Unnatural Oil Slicks in the Gulf of Mexico. *J. Geophys. Res. Oceans* 120 (12), 8364–8380. doi:10.1002/2015jc011062

MacDonald, I. R., O'Reilly, C., Roa, C., and Silva, M. (2019). "Chapter 4: Quantitative Imaging of Oil and Gas Bubbles Discharged at MC20," in," in *An Integrated Assessment of Oil and Gas Release into the Marine Environment at the Former Taylor Energy MC20 Site*, 43–58.

MacDonald, I. R., Sager, W. W., and Peccini, M. B. (2003). Association of Gas Hydrate and Chemosynthetic Fauna in Mounded Bathymetry at Mid-slope Hydrocarbon Seeps: Northern Gulf of Mexico. *Mar. Geology.* 198, 133–158. doi:10.1016/s0025-3227(03)00098-7

Marcon, Y., Sahling, H., Allais, A. G., Bohrmann, G., and Olu, K. (2014). Distribution and Temporal Variation of Mega-Fauna at the Regab Pockmark (Northern Congo Fan), Based on a Comparison of Videomosaics and Geographic Information Systems Analyses. *Mar. Ecology-an Evol. Perspective* 35 (1), 77–95. doi:10.1111/maec.12056

Mason, A. L., Taylor, J. C., and MacDonald, I. R. (2019). *An Integrated Assessment of Oil and Gas Release into the Marine Environment at the Former Taylor Energy MC20 Site*.: NOAA National Ocean Service, National Centers for Coastal Ocean Science.

McCain, J. D., Jr (1991). Reservoir-Fluid Property Correlations-State of the Art. *SPE Res. Eng.* 6 (2), 266–272. doi:10.2118/18571-PA

McGinnis, D. F., Greinert, J., Artemov, Y., Beaubien, S. E., and Wuest, A. (2006). Fate of Rising Methane Bubbles in Stratified Waters: How Much Methane Reaches the Atmosphere? *Journal of Geophysical Research-Oceans* doi:10.1029/2005jc003183

Meurer, W. P., Blum, J., and Shipman, G. (2021). Volumetric Mapping of Methane Concentrations at the Bush Hill Hydrocarbon Seep, Gulf of Mexico. *Front. Earth Sci.* 9. doi:10.3389/feart.2021.604930

Mitchell, G. A., Orange, D. L., Gharib, J. J., and Kennedy, P. (2018). Improved Detection and Mapping of deepwater Hydrocarbon Seeps: Optimizing Multibeam Echosounder Seafloor Backscatter Acquisition and Processing Techniques. *Mar. Geophys. Res.* 39 (1-2), 323–347. doi:10.1007/s11001-018-9345-8

Nodine, M. C., Jeong, Y. C., Wright, S. G., and Gilbert, R. B. (2007). Mudslides during Hurricane Ivan and an Assessment of the Potential for Future Mudslides in the Gulf of Mexico. *Minerals Manag. Serv. Offshore Tech. Res. Cent* 552, 177.

O'Brien, J. (2014). "Practical Methods for Measuring Landfill Methane Emissions", in: Solid Waste Association of North America. (Retrieved 24 Jan 2022: MSW Management).

O'Reilly, C. (2020). *The Taylor Energy Oil Spill: Implications for Marine Oil Spill Science and Policy. Master of Science*. Florida State University.

Piccaro (2011). Picarro G2301-M Analyzer User's Guide Rev. C 2/11/11. https://www.picarro.com/support/library/documents/g2301_analyzer_datasheet.

Rehder, G., Brewer, P. W., Peltzer, E. T., and Friederich, G. (2002). Enhanced Lifetime of Methane Bubble Streams within the Deep Ocean. *Geophysical Research Letters* 29(15). doi:10.1029/2001gl013966

Rehder, G., Leifer, I., Brewer, P. G., Friederich, G., and Peltzer, E. T. (2009). Controls on Methane Bubble Dissolution inside and outside the Hydrate Stability Field from Open Ocean Field Experiments and Numerical Modeling. *Mar. Chem.* 114 (1-2), 19–30. doi:10.1016/j.marchem.2009.03.004

Roberts, H., and Boland, G. (2010). Gulf of Mexico Cold Seeps: Preface. *Deep Sea Res. Part Topical Stud. Oceanography* 57 (21-23), 1835–1837. doi:10.1016/j.dsr2.2010.05.001

Römer, M., Hsu, C.-W., Loher, M., MacDonald, I. R., dos Santos Ferreira, C., Pape, T., et al. (2019). Amount and Fate of Gas and Oil Discharged at 3400 M Water Depth from a Natural Seep Site in the Southern Gulf of Mexico. *Front. Mar. Sci. 6*. doi:10.3389/fmars.2019.00700

Römer, M., Sahling, H., Pape, T., Bohrmann, G., and Spiess, V. (2012). Quantification of Gas Bubble Emissions from Submarine Hydrocarbon Seeps at the Makran continental Margin (Offshore Pakistan). *J. Geophys. Research-Oceans* 117, 19. doi:10.1029/2011jc007424

Roy, K. O. L., Caprais, J. C., Fifis, A., Fabri, M. C., Galeron, J., Budzinsky, H., et al. (2007). Cold-seep Assemblages on a Giant Pockmark off West Africa: Spatial Patterns and Environmental Control. *Mar. Ecology-an Evol. Perspective* 28 (1), 115–130. doi:10.1111/j.1439-0485.2006.00145.x

Ryerson, T. B., Aikin, K. C., Angevine, W. M., Atlas, E. L., Blake, D. R., Brock, C. A., et al. (2011). Atmospheric Emissions from the Deepwater Horizon Spill Constrain Air-Water Partitioning, Hydrocarbon Fate, and Leak Rate. *Geophys. Res. Lett.*, 38. doi:10.1029/2011gl046726

Sahling, H., Borowski, C., Escobar-Briones, E., Gaytan-Caballero, A., Hsu, C. W., Loher, M., et al. (2016). Massive Asphalt Deposits, Oil Seepage, and Gas Venting

Support Abundant Chemosynthetic Communities at the Campeche Knolls, Southern Gulf of Mexico. *Biogeosciences* 13 (15), 4491–4512. doi:10.5194/bg-13-4491-2016

Sauter, E. J., Muyakshin, S. I., Charlou, J. L., Schluter, M., Boetius, A., Jerosch, K., et al. (2006). Methane Discharge from a Deep-Sea Submarine Mud Volcano into the Upper Water Column by Gas Hydrate-Coated Methane Bubbles. *Earth Planet. Sci. Lett.* 243 (3-4), 354–365. doi:10.1016/j.epsl.2006.01.041

Silva, M., Bel Hadj Ali, N., Abichou, T., and MacDonald, I. R. (2019). "Chapter 5. Atmospheric Methane (CH4) Concentrations at the MC20 Site in the Northern Gulf of Mexico," in *An Integrated Assessment of Oil and Gas Release into the Marine Environment at the Former Taylor Energy MC20 Site*, 59–70.

Skarke, A., Ruppel, C., Kodis, M., Brothers, D., and Lobecker, E. (2014). Widespread Methane Leakage from the Sea Floor on the Northern US Atlantic Margin. *Nat. Geosci.* 7 (9), 657–661. doi:10.1038/ngeo2232

Socolofsky, S. A., Adams, E. E., Boufadel, M. C., Aman, Z. M., Johansen, et al. (2015). Intercomparison of Oil Spill Prediction Models for Accidental Blowout Scenarios with and without Subsea Chemical Dispersant Injection. *Mar. Pollut. Bull.* 96 (1–2), 110–126. doi:10.1016/j.marpolbul.2015.05.039

Solomon, E. A., Kastner, M., MacDonald, I. R., and Leifer, I. (2009). Considerable Methane Fluxes to the Atmosphere from Hydrocarbon Seeps in the Gulf of Mexico. *Nat. Geosci.* 2 (8), 561–565. doi:10.1038/ngeo574

Stout, S. A., and Litman, E. R. (in press). Quantification of Synthetic-Based Drilling Mud Olefins in Crude Oil and Oiled Sediment by Liquid Column Silver Nitrate and Gas Chromatography. *Environ. Forensics*.

Taylor, J. C., and Boswell, K. (2019). "Chapter 3. Surface and ROV Acoustic Mapping of the MC20 Oil and Gas Leak in the Northern Gulf of Mexico," in *inAn Integrated Assessment of Oil and Gas Release into the Marine Environment at the Former Taylor Energy MC20 Site*, 19–42.

United States Coast Guard (2019). Oil Pollution Act Liability Limits in 2019. https://www.uscg.mil/Portals/0/NPFC/docs/PDFs/Reports/2020-02-25-Oil-Pollution-Act-Liability-Limits-in-2019.pdf.

Wang, D. W., Mitchell, D. A., Teague, W. J., Jarosz, E., and Hulbert, M. S. (2005). Extreme Waves under Hurricane Ivan. *Science* 309 (5736), 896. doi:10.1126/science.1112509

Westbrook, G. K., Thatcher, K. E., Rohling, E. J., Piotrowski, A. M., Pälike, H., Osborne, A. H., et al. (2009). Escape of Methane Gas from the Seabed along the West Spitsbergen continental Margin. *Geophys. Res. Lett.* 36 (15), L15608. doi:10.1029/2009gl039191

Yvon-Lewis, S. A., Hu, L., and Kessler, J. (2011). Methane Flux to the Atmosphere from the Deepwater Horizon Oil Disaster. *Geophys. Res. Lett* 38. doi:10.1029/2010gl045928

Conflict of Interest: The authors declare that the research was conducted in the absence of any commercial or financial relationships that could be construed as a potential conflict of interest.

The handling Editor declared a past co-authorship with one of the authors IM.

Publisher's Note: All claims expressed in this article are solely those of the authors and do not necessarily represent those of their affiliated organizations, or those of the publisher, the editors, and the reviewers. Any product that may be evaluated in this article, or claim that may be made by its manufacturer, is not guaranteed or endorsed by the publisher.

frontiers in Earth Science

ORIGINAL RESEARCH
published: 17 March 2022
doi: 10.3389/feart.2022.864809

Variability of Marine Methane Bubble Emissions on the Clayoquot Slope, Offshore Vancouver Island, Between 2017 and 2021

Yann Marcon[1], Miriam Römer[1], Martin Scherwath[2], Michael Riedel[3], Knut Ola Dølven[4] and Martin Heesemann[2]*

[1]MARUM Center for Marine Environmental Research and Department of Geosciences, University of Bremen, Bremen, Germany, [2]Ocean Networks Canada, University of Victoria, Victoria, BC, Canada, [3]GEOMAR Helmholtz Centre for Ocean Research, Kiel, Germany, [4]Centre for Arctic Gas Hydrate, Environment and Climate, UiT The Arctic University of Norway, Tromsø, Norway

Seabed methane gas emissions occur worldwide at cold seeps located along most continental margins. Fluxes of methane gas released from the seabed in the form of bubbles can be extremely variable even over short time intervals. Some factors controlling the variability are still poorly understood. Here, we report on the results of continuous long-term sonar monitoring of bubble emissions at a depth of 1,260 m on the Clayoquot Slope, northern Cascadia margin. With a total monitoring duration of 4 years and a sampling period of 1 h, this is by far the longest high temporal resolution monitoring of seabed methane gas release ever conducted. Our results provide evidence that the diurnal and semi-diurnal tides influence the timing of the onset and cessation of bubble emissions. However, gas emissions within the monitoring area are active more than 84% of the time, indicating that tides alone are not sufficient to make venting pause. We hypothesize that the gas fluxes are transient but generally sufficiently high to maintain ebullition independently of the tidally-induced bottom pressure variations. Results also show that the tides do not seem to modulate the vigor of active gas emissions.

Keywords: methane, gas emissions, seep, bubble plume, cascadia margin, multibeam, cabled observatory, long-term monitoring

OPEN ACCESS

Edited by:
Katrien Van Landeghem, Bangor University, United Kingdom

Reviewed by:
Alan Judd, RETIRED, United Kingdom
Jianghui Li, University of Southampton, United Kingdom

****Correspondence:***
Yann Marcon
ymarcon@marum.de

Specialty section:
This article was submitted to Marine Geoscience, a section of the journal Frontiers in Earth Science

Received: *28 January 2022*
Accepted: *04 March 2022*
Published: *17 March 2022*

Citation:
Marcon Y, Römer M, Scherwath M, Riedel M, Dølven KO and Heesemann M (2022) Variability of Marine Methane Bubble Emissions on the Clayoquot Slope, Offshore Vancouver Island, Between 2017 and 2021. Front. Earth Sci. 10:864809. doi: 10.3389/feart.2022.864809

INTRODUCTION

Natural marine gas emissions have been reported at numerous regions along ocean continental margins across the globe (Fleischer et al., 2001; Mazurenko and Soloviev, 2003; Phrampus et al., 2020), representing areas where hydrocarbons from the sediments enter the hydrosphere. A better understanding of gas bubble fluxes – consisting mainly of methane – is important to determine the global inventory of carbon in marine sediments (Klauda and Sandler, 2005; Wallmann et al., 2012; Ruppel and Kessler, 2017) and to discern processes related to ocean chemistry and biology (Wallmann et al., 2006). An increasing number of studies focus on the quantification of gas released from the seafloor to the hydrosphere and to the atmosphere. These studies often use short-term observations acquired during research expeditions, which are limited in documenting spatial and temporal variability. In fact, various studies (e.g. Tryon et al., 1999; Boles et al., 2001; Varadharajan and Hemond, 2012; Kannberg et al., 2013) have shown the highly transient nature of gas emissions in a wide range of time scales. Repeated measurements during research expeditions

are limited in detecting changes over time, as the speed and dynamic range of observed changes remain unknown. Continuous long-term observations of seep systems are needed to better understand these dynamic environments (Suess et al., 2001; Heeschen et al., 2003). To date, the most advanced and effective way to continuously monitor the seafloor is through permanent seafloor observatories that provide high power and data bandwidth to the deep sea, allowing for the operation of various experiments in addition to optimizing recording parameters in reaction to seafloor events (Barnes et al., 2011). Ocean Networks Canada has been operating cabled observatories since 2006 and has been providing continuous data from the northern Cascadia continental margin since 2009. Using real-time data from NEPTUNE observatory's widely distributed sensor networks (Barnes et al., 2011), the scientific community is able to investigate the dynamic changes of seep environments along this margin (Scherwath et al., 2019).

The northern Cascadia continental margin offshore Vancouver Island lies along the subduction zone of the Juan de Fuca Plate. The sediments deposited on the incoming oceanic crust are accreted and progressively folded and faulted, forming elongated anticlinal ridges up to 700 m in height (Davis and Hyndman, 1989). The occurrence of seafloor seepage and mud volcanism is typical at accretionary margins, as the degradation of organic matter often leads to high amounts of light hydrocarbons in the sediments within the prism, and fluid flux, driven by buoyancy, may be facilitated by tectonic forces during the accretion process (Kopf, 2002; Zühlsdorff and Spieß, 2004; Judd and Hovland, 2007; Suess, 2010). The Cascadia accretionary prism, however, is seismically locked (Hyndman and Wang, 1993; Obana et al., 2015; McGuire et al., 2018) and almost no seafloor motion is observed (Stone et al., 2018). There are several known areas of seepage along the Cascadia continental margin (Riedel et al., 2018; Scherwath et al., 2019) including the seep area at Clayoquot Slope, investigated in this study. Several studies focused on quantification and variability of fluid fluxes released along this margin (e.g. Heeschen et al., 2003; Kannberg et al., 2013; Hautala et al., 2014; Johnson et al., 2015; Philip et al., 2016; Römer et al., 2016; Riedel et al., 2018; Marcon et al., 2021). However, most of these studies are based on small-scale or short-term observations. Long-term variations of fluid fluxes over seasonal timespans or over decades are still widely unknown.

The Clayoquot Slope is part of the accretionary prism off Vancouver Island, BC, and located at a mid-slope basin in about 1,260 m water depth, and approximately 20 km landward of the deformation front. It hosts several gas emission sites characterized by various concentrations of gas in the sediments. In this work, we study a zone called Gastown Alley, a SW-NE elongated seep zone defined by several aligned flares (Römer et al., 2016). Gastown Alley extends for about 400–500 m from the Bullseye Vent area (a seafloor depression with shallow gas accumulations and hydrate occurrences surrounded by thin carbonate crusts) towards the Bubbly Gulch vents (a slope failure with strong gas ebullition from exposed sedimentary layers) (Riedel et al., 2006a, 2006b; Lapham et al., 2013; Paull et al., 2015). Gas and/or hydrate accumulations at Gastown Alley are located deeper than at Bullseye Vent and occur about 20 mbsf (Riedel et al., 2006a, 2006b; Willoughby et al., 2008; Römer et al., 2016). However, gas venting was detected at Gastown Alley but not at Bullseye Vent, where carbonate and/or hydrate capping of the sediments likely prevents ebullition at the seabed. Methane hydrates are occurring at the Bullseye Vent depression close to the seafloor down to at least 40 mbsf (Riedel et al., 2006a) but were not encountered in the shallow sub-seafloor outside of the depression. The presence of gas hydrates below Gastown Alley has not been confirmed. Gastown Alley lies well within the gas hydrate stability zone and gas hydrates should be expected to be stable. However, the sulfate-methane interface (SMI), above which gas hydrates cannot form (Paull et al., 2005; Bhatnagar et al., 2011; Riedel and Collett, 2017), is located about six to eight mbsf at Gastown Alley (Solem et al., 2002; Riedel et al., 2006b). At Bubbly Gulch, hydrates were encountered within 30 cm of the seafloor right at the seepage zone but were absent in the sediments around it (Paull et al., 2015).

A year-long acoustic monitoring of gas ebullition in an area located close to Bubbly Gulch (**Figure 1**) between July 2012 and July 2013 showed that decreasing bottom pressures during falling tides facilitated the gas migration in the sediments and the onset of gas ebullition at the seabed (Römer et al., 2016). Three gas ebullition phases, each lasting several months, were observed: phases 1 and 3 were characterized by transient gas release, whereas phase two was characterized by intense ongoing gas release. These three phases were postulated to be caused by variable gas supply rates in the subsurface. The study also found no link between the gas emissions variability (both short-term variations and activity phases) and the seismicity, the wave height variations or the seasonal oceanographic variability.

Using long-term acoustic monitoring we expand on previous work and now offer a 4 years long timeseries of data to address important questions on the variability of gas venting. In particular, we look into the role of tides on the timing and intensity of gas emissions, investigate if there are seasonal variations in bubble release over the 4 years of observations, or if other drivers can also be identified that explain the observed variability.

MATERIALS AND METHODS

Sonar Monitoring

Active bubble emissions were monitored with a 360° rotating multibeam echosounder located on the seabed and operated through the Ocean Networks Canada's NEPTUNE deep-sea cabled observatory (Link to multibeam rotary sonar: https://www.oceannetworks.ca/observatories/infrastructure/devices-sensors/33). The echosounder (Imagenex 837B Delta-T, 260 kHz) swath was oriented vertically as described by Römer et al. (2016) and had a detection range of 100 m, allowing it to monitor a circular area of at least 31,000 m^2 (**Figure 1**). For each sample within the acoustic beam, the sonar records the amplitude of the backscattered pressure wave (analog signal) as a quantized 8-bit integer value referred to as 'magnitude' (digital signal). The sonar

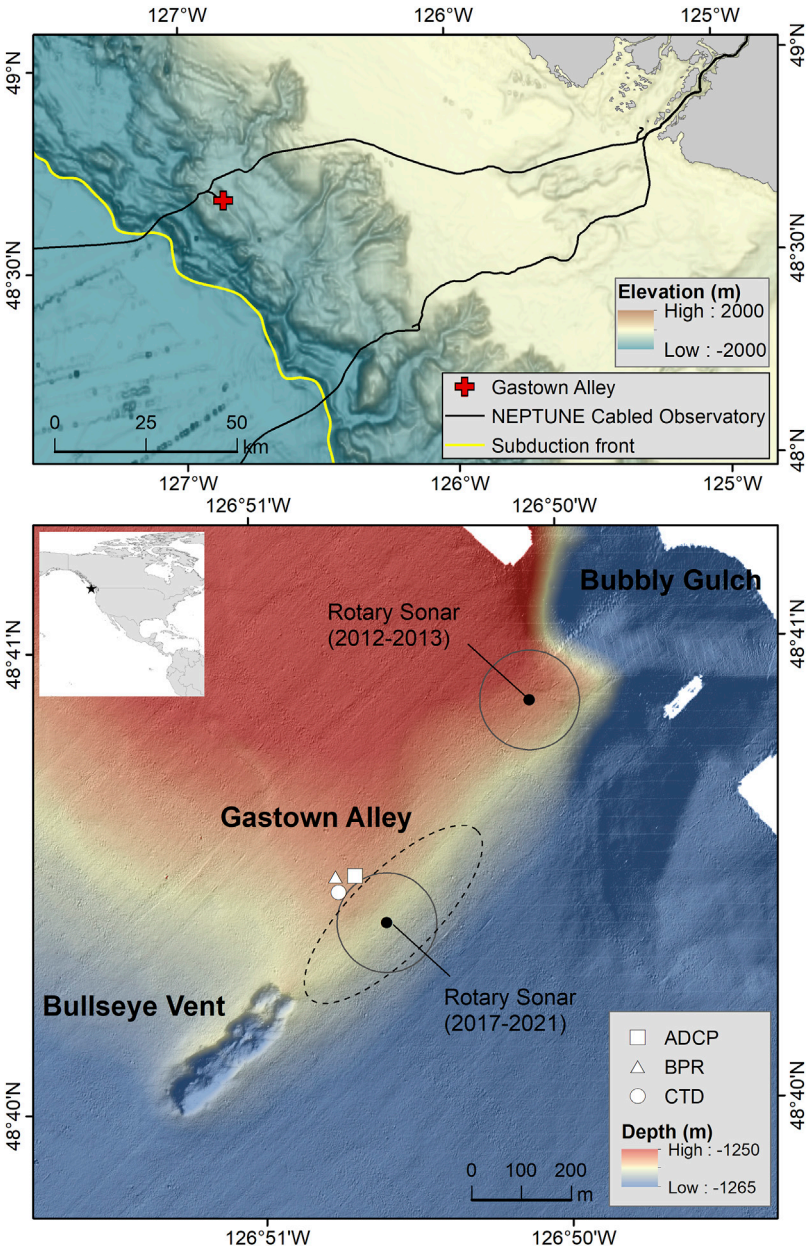

FIGURE 1 | Top: location map showing Gastown Alley in relation to Vancouver Island and the subduction front. Bathymetry data from GEBCO Compilation Group (2021). Bottom: overview map showing the location of the cabled instruments used in this work and the main seep areas in the vicinity of Gastown Alley. The rotary sonar used by Römer et al. (2016) for the 2012-2013 monitoring is also shown. The grey circles have a radius of 100 m and delineate the monitoring areas of the sonars. Bathymetry data from AUV D. Allan B. (MBARI).

magnitude data also include a time-varying gain correction aimed at accounting for distance-related transmission losses (geometrical spreading of sound energy and sound attenuation in water). We analyzed hourly 360° scans of the water column acquired from 22 June 2017 to 30 May 2021, totaling 33,650 scans over nearly 4 years. Acoustic flares (anomalies caused by the presence of streams of bubbles rising through the water column) were detected from the raw sonar data using the MCubed-Viewer program (Marcon et al., 2019). For each scan, the processed data outputs include the number, location and mean backscatter magnitude of flares detected by the program. In this work we assume that the flare mean magnitude reflects the bubble flux, that is, that a low/high magnitude represents a reduced/elevated bubble flux, respectively. However, the relation between magnitude and bubble flux is not linear. Hence, it is not possible to quantify gas fluxes with this system, as this would require to calibrate the sonar and measure the sizes and rise speeds of the bubbles within the plumes.

For each consecutive scan the status of the venting activity was classified in one of four categories: start (scan *k-1* is inactive, scan *k* is active), active (scan *k-1* is active, scan *k* is active), stop (scan *k-1* is active, scan *k* is inactive), inactive (scan *k-1* is inactive, scan *k* is inactive). Non-consecutive scans, that is, the first scan following each data gap (when one or more scans were missing between two scans), were classified as either "active" or "inactive" to prevent introducing bias if the status of the venting activity were to change during the data gap. Furthermore, visual inspection of the sonar scans showed that the automated flare detection is not infallible and failed to detect small flares in certain instances ("false non-detections"). Hence, inactive times shorter than 2 h were ignored for the analyses to exclude erroneous start and stop events that otherwise would have been caused by the false non-detections.

Bottom Pressure

Bottom pressure was measured by a bottom pressure recorder (BPR) located about 140 m northwest of the sonar instrument (**Figure 1**) and operated by the ONC's NEPTUNE observatory (Link to BPR instrument: https://www.oceannetworks.ca/observatories/infrastructure/device-listing/22503). The BPR recorded the bottom pressure at a 1 Hz frequency over the entire monitoring period of the multibeam rotary sonar. A spectrogram was computed from the 1 Hz BPR data to identify intervals of strong short-period frequency components caused by increased wave heights during seasonal winter storms (Davis and Heesemann, 2015; Römer et al., 2016). To identify longer-period forcing, we used a 10 min moving average to exclude the high-frequency noise from the data. For ease of reading, the pressure data are presented in decibars (dbar) as one dbar is approximately equivalent to 1 m of water column.

Bottom Currents

The bottom current velocity data used in this work were recorded from 14 June 2017 to 30 June 2018 and from 16 September 2020 to 31 May 2021 by an upward-looking acoustic Doppler current profiler (RDI Workhorse Long Ranger ADCP 75 kHz) located approximately 110 m northwest of the sonar (Link to ADCP instrument: https://www.oceannetworks.ca/observatories/infrastructure/device-listing/12108). The data for the northward, eastward and upward current velocities were down-sampled into 5 min bins and aggregated by their mean. Bottom current directions were computed from the eastward and northward current velocities.

Bottom Temperature

Bottom temperature was measured by a CTD probe located about 115 m northwest of the sonar instrument (**Figure 1**) and operated by the ONC's NEPTUNE observatory (Link to CTD instrument: https://www.oceannetworks.ca/observatories/infrastructure/device-listing/23029). The CTD recorded the bottom temperature at a 1 Hz frequency over the entire monitoring period of the multibeam rotary sonar. The 10 min moving average data were used.

Spectral Analyses

The dominant periodicities making up the sonar data timeseries were identified by computing discrete Fourier spectra of the timeseries. Before applying the discrete Fourier transform (DFT) to the time-domain data, the DC component (average backscatter value over the full timeseries) was removed, the data gaps were padded with zeros, and a Hamming window was applied to the data. Due to the hourly sampling period (Ts = 1 h) of the sonar, periodic variations of the gas ebullition with periods shorter than 2 h (Nyquist frequency) cannot be identified. The results of the spectral analyses are presented in the form of spectrograms (**Figure 2**), which show the frequency spectrum of the timeseries as it varies with time, and power spectral density plots (**Figure 3** and **Figure 4**), which show the distribution of the timeseries power across frequency. For readability, the frequency axes are labeled in cycles per day (cpd).

RESULTS

Flares were detected in 28,430 out of 33,650 scans, that is, at least 84% of the monitoring period (22 June 2017 to 30 May 2021). Times of inactivity of gas emissions (hereafter referred to as "inactive times") were non-uniformly distributed throughout the monitoring period. Some months contained numerous inactive times – up to 43 stop-and-start events in March and June 2018, accounting for almost 50% of inactivity – whereas other months had no inactive time at all (**Figure 2**; **Table 1**).

Frequency analyses of the mean backscatter of detected flares show that the timeseries contains diurnal and semi-diurnal constituents corresponding to those of the local mixed tide regime (**Figure 2**), suggesting a tidal influence on the gas emissions. The local mixed tide is defined by two tidal cycles of unequal amplitude per day, which result from the sum of both diurnal and semi-diurnal constituents. The power of the tidal frequencies in the sonar data varies throughout the timeseries and appears to be strongest during periods when the venting stops and starts intermittently (**Figure 2**). Frequency analyses of selected timeseries segments, one with discontinuous venting (June 2018) and two with continuous venting (August 2017 and April 2020), showed that the semi-diurnal and diurnal tidal harmonic constituents were clearly present in the June 2018 timeseries but weak or even absent in the August 2017 and April 2020 timeseries (**Figure 3**). This implies that tidal cycles control the alternation of active/inactive times but to a lesser degree the variation in intensity of the gas release during active venting phases. This is confirmed by the power spectral density of the binary timeseries of active and inactive times (0: inactive, 1: active), which also reveals distinct peaks at the dominant tidal frequencies (**Figure 4**). This result clearly demonstrates that tides influence the timing of the venting activity in the monitoring area. However, fluctuations of backscatter magnitude during active venting phases correlate neither with the bottom pressure data [Pearson correlation coefficient r = -0.01, p-value = 0.1, n = 28,402, and 95% confidence interval (-0.02, 0.00)] nor with the rate of bottom pressure change [Pearson correlation coefficient r = 0.01, p-value = 0.04, n = 28,402, and 95% confidence interval

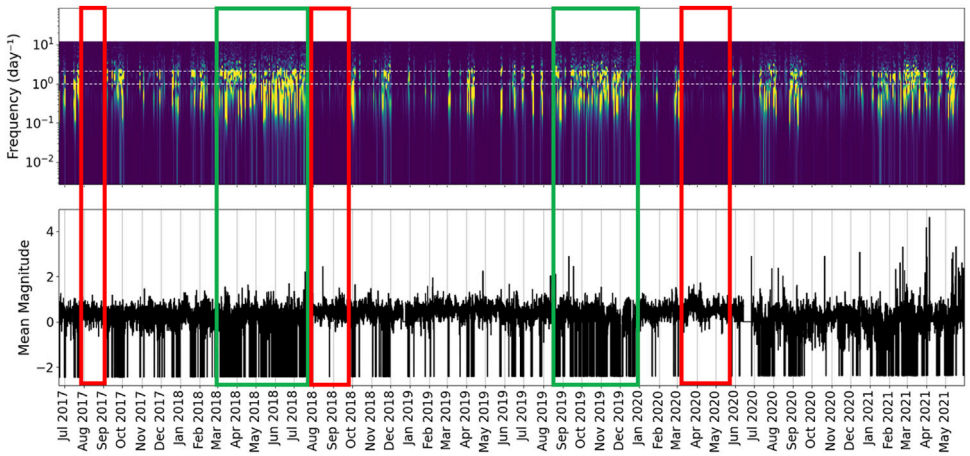

FIGURE 2 | Top: spectrogram showing the dominant frequencies (bright colors) present in the sonar magnitude data over time. The two horizontal dashed lines show the locations of the diurnal (lower line) and semi-diurnal (upper line) tidal frequencies. Bottom: timeseries of the sonar magnitude data (without DC component). Magnitude data are dimensionless. The diurnal and semi-diurnal tidal frequencies are the dominant frequency constituents of the sonar data indicating a tidal influence on the gas emissions. However, the tidal frequencies are not continuously detectable in the sonar data indicating that the strength of the tidal influence varies over time. Intervals when venting is frequently interrupted coincide with intervals of strong tidal influence (green boxes). By contrast, tidal influence is low at times when venting is continuously active and rarely stops (red boxes).

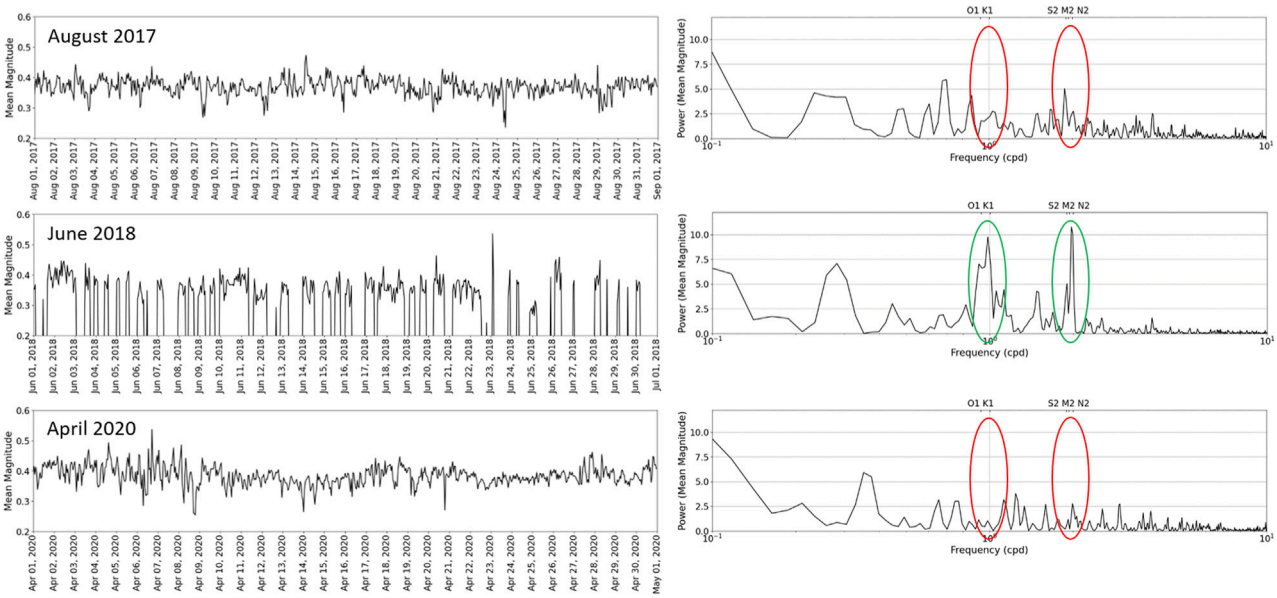

FIGURE 3 | Left: timeseries of mean backscatter for 2 months of continuous venting (August 2017 and April 2020) and 1 month of discontinuous venting (June 2018). Magnitude data are dimensionless. Right: Corresponding power spectral density plots. For readability, the diurnal (O1 and K1) and semi-diurnal (M2, N2, and S2) harmonic constituents of the local tides are reported at the top of each plot. The diurnal and semi-diurnal tidal frequencies are clearly present in the sonar data when venting is discontinuous (green ellipses) but either absent or hardly detectable when venting is continuous (red ellipses).

(0.00, 0.02)], another indication that the vigor of active gas emissions may not be influenced by bottom pressure variations.

The bottom pressure is largely controlled by the mixed local tide and averaged around 1,284.16 dbar (median = 1,284.21 dbar) during the monitoring period (**Supplementary Figure S1**). Each venting activity phase (start, stop, active, inactive) was observed at all tidal phases and was not uniquely restricted to any particular tidal phase (**Table 2**). Venting start times were observed predominantly during falling tides (64.7%) (**Figure 5A**) and at pressures higher than the mean pressure (61.7%) (**Figure 5B**). By contrast, venting stop times were almost equally distributed around the mean pressure but significantly more common

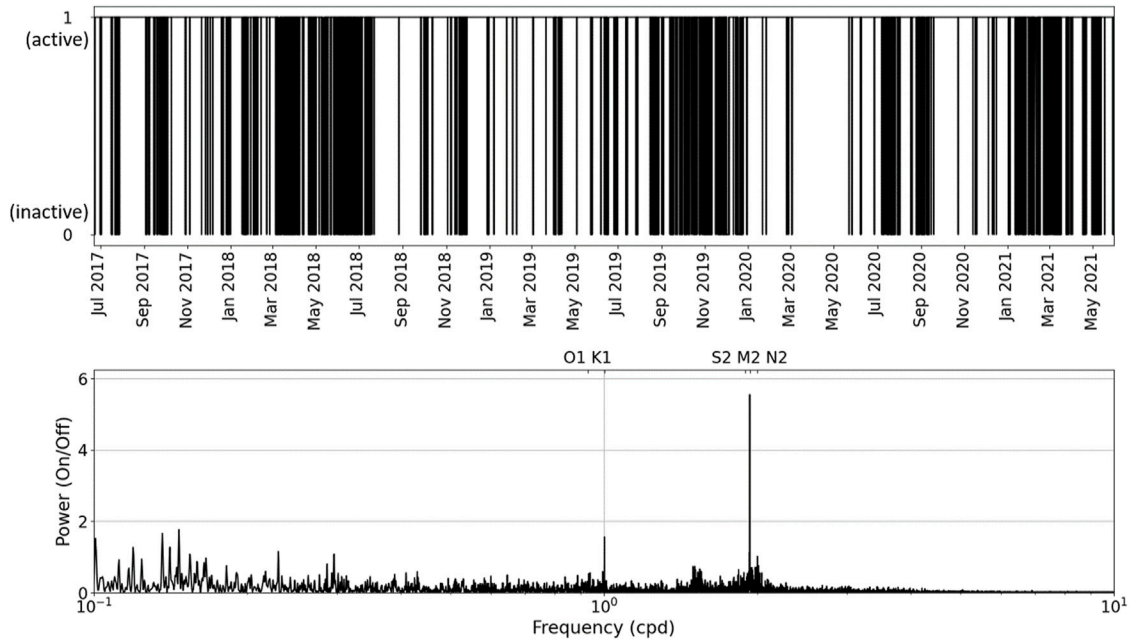

FIGURE 4 | Top: binary timeseries plot indicating the status of the venting activity (1: active, 0: inactive). The (near) vertical black lines indicate a change of state (active to inactive or inactive to active). Note the nearly continuous horizontal black line next to the one tick value, which indicates that the venting was active over most (>84%) of the monitoring period. Bottom: power spectral density plot of the binary timeseries. For readability, the diurnal (O1 and K1) and semi-diurnal (M2, N2, and S2) harmonic constituents of the local tide are reported at the top of the plot. The tidal frequencies are strongly present in the data demonstrating that tidal cycles have an influence on the timing of the gas emissions.

(72.6% vs. 27.4%) during rising tides compared to falling tides. Active venting times appeared to be independent from both absolute bottom pressure and sign of pressure change, whereas inactive venting was slightly more common at pressures above average (61.8%) and during rising tides (55.8%). The amplitude of the falling tides (ebb amplitude: min = 0.24 m, max = 4.17 m, mean = 2.03 m, standard deviation = 0.84 m) and of the rising tides (flow amplitude: min = 0.62 m, max = 3.47 m, mean = 2.03 m, standard deviation = 0.58 m) did not appear to influence the activation and cessation of gas emissions (**Figure 5C**).

The distributions of bottom current velocities in the lowest ADCP depth-bin, corresponding to water depths from 1,234 m to 1,242 m, are similar during active and inactive times, and during ebb and flow tides (**Figure 6**). This suggests that bottom current velocities do not affect the venting activity.

Bottom current directions in the lowest ADCP bin show a different distribution pattern depending on whether gas emissions are active or inactive (**Figure 7**, **Figure 8** and **Supplementary Figure S2**). The bottom current directions during active times are strongly correlated to the bottom current directions of ebb tides [Pearson correlation coefficient $r = 0.96$, p-value $= 2.4 \times 10^{-20}$, $n = 36$, and 95% confidence interval (0.92, 0.98)] and the bottom current directions during inactive times are correlated to the bottom current directions of flow tides [Pearson correlation coefficient $r = 0.91$, p-value $= 1.4 \times 10^{-14}$, $n = 36$, and 95% confidence interval (0.83, 0.95)]. By contrast, the current directions during active times are less correlated to the bottom current directions of flow tides [Pearson correlation coefficient $r = 0.69$, p-value $= 3.1 \times 10^{-6}$, $n = 36$, and 95% confidence interval (0.47, 0.83)] and the current directions during inactive times show no correlation to the current directions during ebb tides [Pearson correlation coefficient $r = 0.22$, p-value $= 0.2$, $n = 36$, and 95% confidence interval (−0.12, 0.51)]. Furthermore, the distribution of current directions during inactive times shows a higher proportion of westward (flowing towards west) bottom currents than the distribution of current directions during flow tides (**Figure 7**): almost 66% of inactive gas emissions co-occurred with bottom current flow directions ranging from 210° to 320° relative to North. By contrast, dominantly westward bottom currents within the same range of directions occurred during only half (51%) of the flow tidal phases. In other words, the venting activity pauses preferentially when bottom current flow towards southwest and west, not only during flow tides but also during ebb tides. This suggests that there is a connection, with or without causality, between the current direction and the cessation of venting.

Bottom water temperatures between June 2017 and May 2021 (**Figure 9**) ranged from 2.64 to 3.15°C (mean: 2.90°C, standard deviation: 0.067°C). A clear semi-diurnal periodicity shows that the intraday temperature variations are related to the tidally controlled bottom currents (**Figure 8** and **Supplementary Figure S2**). Amplitudes of daily variations ranged from 0.03 to 0.31°C (mean: 0.14°C, standard deviation: 0.039°C). Longer multiday temperature variations are also present (**Figure 9**, **Supplementary Figure S1**,

TABLE 1 | Percentages of activity and inactivity of gas emissions and numbers of gas emission activations (start) and cessations (stop) for each month from 22 June 2017 until 30 May 2021. The monthly percentages of missing hourly sonar scans (data gaps) are also given. The high percentages of data gaps in June 2017 and June 2020 are due to the fact that the monitoring period started on 22 June 2017 and that maintenance work was conducted on the sonar in June 2020. The activity/inactivity percentages ignore data gaps.

Year-month	Active (%)	Inactive (%)	Start/Stop (counts)	Data gaps (%)
2017-06	86.6	13.4	3/4	70.0
2017-07	82.8	17.2	16/15	7.1
2017-08	100.0	0.0	0/0	0.0
2017-09	80.5	19.5	23/23	0.3
2017-10	93.8	6.2	8/7	0.0
2017-11	96.4	3.6	5/5	0.0
2017-12	90.3	9.7	14/14	0.0
2018-01	91.0	9.0	12/12	0.1
2018-02	89.3	10.7	12/12	0.1
2018-03	54.4	45.6	42/43	0.0
2018-04	67.7	32.3	30/29	0.1
2018-05	75.3	24.7	24/23	0.0
2018-06	50.7	49.3	41/42	0.8
2018-07	76.2	23.8	22/22	0.4
2018-08	99.5	0.5	1/1	0.0
2018-09	97.6	2.4	4/4	0.0
2018-10	92.3	7.7	8/8	0.0
2018-11	85.6	14.4	23/23	0.0
2018-12	97.3	2.7	5/4	14.2
2019-01	99.1	0.9	2/2	0.0
2019-02	98.8	1.2	2/2	0.0
2019-03	98.1	1.9	4/4	0.0
2019-04	91.9	8.1	10/10	0.0
2019-05	96.0	4.0	6/6	0.0
2019-06	86.0	14.0	13/13	0.1
2019-07	93.1	6.9	9/9	0.0
2019-08	85.5	14.5	19/18	3.8
2019-09	84.4	15.6	23/23	1.3
2019-10	80.8	19.2	29/30	0.7
2019-11	61.5	38.5	36/36	0.1
2019-12	60.7	39.3	19/18	3.2
2020-01	98.9	1.1	2/2	0.8
2020-02	97.7	2.3	3/3	1.3
2020-03	98.5	1.5	2/2	0.0
2020-04	100.0	0.0	0/0	0.0
2020-05	97.7	2.3	3/3	0.7
2020-06	97.6	2.4	3/3	42.9
2020-07	75.4	24.6	28/28	2.7
2020-08	89.1	10.9	14/14	0.0
2020-09	83.9	16.1	19/19	5.7
2020-10	99.6	0.4	1/1	1.5
2020-11	98.5	1.5	3/3	0.0
2020-12	98.2	1.8	4/4	5.2
2021-01	83.8	16.2	25/24	0.1
2021-02	77.4	22.6	23/25	5.4
2021-03	76.4	23.6	34/32	2.0
2021-04	87.5	12.5	11/11	21.0
2021-05	79.8	20.2	21/22	3.5

TABLE 2 | Counts of bubble emission activity phases during ebb tides (decreasing bottom pressures) and during low tides (when pressure is lower than the mean pressure recorded during the monitoring period). In each column, the percentages are the ratios of the counts (number of observations during ebb tide or during low tide) to n (total number of observations in each activity phase). They are not supposed to add up to 100%, as decreasing tides and low tides are neither exclusive tidal phases, nor do they represent all tidal phases. Percentage values that point to a pressure influence are emboldened.

	Start	Active	Stop	Inactive
n	658	28,614	657	3,667
Decreasing pressure (ebb tides)	426 (**64.7%**)	14,390 (50.3%)	180 (**27.4%**)	1,619 (**44.2%**)
Below mean pressure (<1,284.16 dbar)	252 (**38.3%**)	14,179 (49.6%)	355 (54%)	1,401 (**38.2%**)

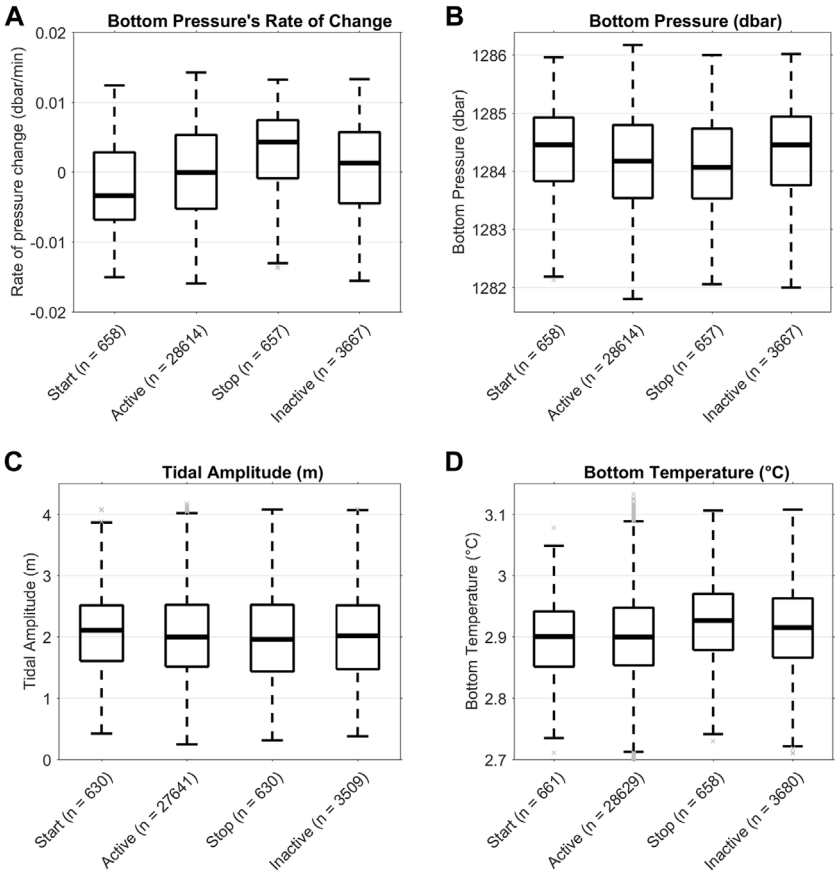

FIGURE 5 | Boxplots showing the distribution of venting states in relation to **(A)** the rate of bottom pressure change, which represents the rate of tidal rise/fall **(B)** the bottom pressure, **(C)** tidal amplitude, and **(D)** the bottom temperature. Inactive times and venting onsets are slightly more common at higher pressures than at lower pressures. The boxes represent the interquartile range (IQR), that is, the distance between the 25th percentile (q_1) and the 75th percentile (q_3). The solid line in the box is the median. The whiskers (dashed lines) show the full range of the dataset excluding any outlier. The grey crosses show the outliers. Points are shown as outliers if they are smaller than q_1 – 1.5 IQR or larger than q_3 + 1.5 IQR.

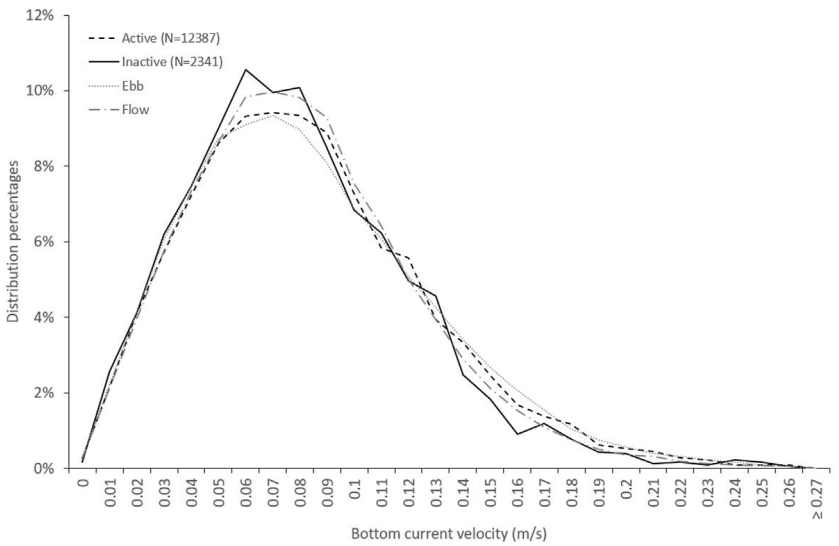

FIGURE 6 | Distribution of bottom current speeds at water depths from 1,234 m to 1,242 m during active and inactive gas emissions and during ebb and flow tides.

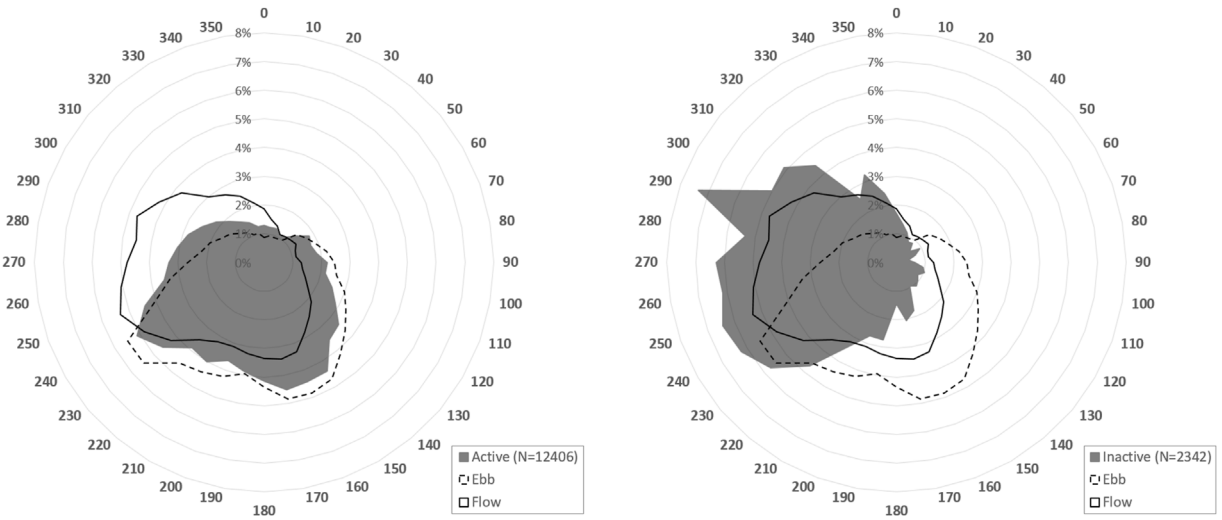

FIGURE 7 | Rose diagrams showing the distribution of bottom current flow directions at water depths from 1,234 m to 1,242 m during active (left diagram) and inactive (right diagram) gas emissions, and during ebb and flow tides (both diagrams). Current directions during active venting largely reflect current directions during ebb tides. Times when gas emissions were inactive are strongly linked with predominantly westward (flowing towards west) currents.

Supplementary Figure S2), which could not be related to the tidal cycles and are likely linked to longer-term changes of the bottom water masses possibly caused by seasonal variations or variability in the regional deep-ocean circulation. Fluctuations of backscatter magnitude during active venting phases do not correlate with the temperature variations of bottom waters [Pearson correlation coefficient $r = 0.07$, p-value $= 3.5 \times 10^{-34}$, n = 28,418, and 95% confidence interval (0.06, 0.08)], an indication that the vigor of active gas emissions may not be influenced by temperature variations. Venting stop times and inactive times were associated with bottom temperatures 0.01 and 0.03°C above average (**Figure 5D**). Median temperatures were 2.90°C during start times and active times, 2.92°C during stop times and 2.91°C during inactive times. However, high temperatures were not consistently associated with inactive times indicating that temperature alone is unlikely to be responsible for pausing gas emissions.

Storms occurred every year mainly between November and April (**Figure 10**). The data indicate that the November-to-April months do not show a pattern of co-occurrence either with periods of elevated/reduced venting or with intervals of continuous/discontinuous venting.

The number of detected flares varied during the monitoring period and ranged from 0 to 8 with a median value of 2 (**Figure 11**). The outlets of the bubble release on the seabed cannot be located precisely with this sonar but the spatial distribution of their estimated positions reveal two main areas of recurrent seepage around the sonar (**Figure 12**). The southern cluster is active most often, but it is widespread and likely coalesces several smaller clusters that could not be resolved due to the uncertainties in the flare basepoint estimations. The northeastern cluster is smaller and less continuously active than the southern cluster.

DISCUSSION

Venting within our monitoring area is active more than 84% of the time but affected by recurrent interruptions related to local tides. It is evident that the onset and the cessation of bubble emissions are largely controlled by the diurnal and semi-diurnal frequencies of the local mixed tidal regime. While vent activation is more common during falling tides, cessation is observed predominantly during rising tides. This result corroborates previous results from similar monitoring efforts in deep sea settings near Bubbly Gulch in 2012–2013 and at Southern Hydrate Ridge in 2018, where bubble emission activation was found to peak during falling tides (Römer et al., 2016; Marcon et al., 2021).

Interestingly, the no-venting phases are not regularly distributed through the monitoring period and there are numerous week- and months-long intervals of continuous venting during which no venting interruptions were recorded. It is unclear why the bubble release is at times continuously active and does not stop and start with the tidal cycles. For instance, our results showed that the distribution of active and inactive times is unaffected by the amplitude of the pressure variations related to the spring and neap tidal cycles. Furthermore, seismic tremors or seasonal storms were not found to be related to the activity of gas emissions on the Clayoquot Slope (Lapham et al., 2013; Römer et al., 2016) and at Southern Hydrate Ridge (Marcon et al., 2021). The accretionary prism of the Cascadia Subduction Zone is fully locked (Hyndman and Wang, 1993; Obana et al., 2015), especially in our study area (McGuire et al., 2018), and local shaking levels are practically nonexistent (Scherwath et al., 2011; Stone et al., 2018). Hence, seismicity is unlikely to be responsible for the frequent alternation of transient and continuous ebullition phases that we observed. In this study, we also did not observe any clear

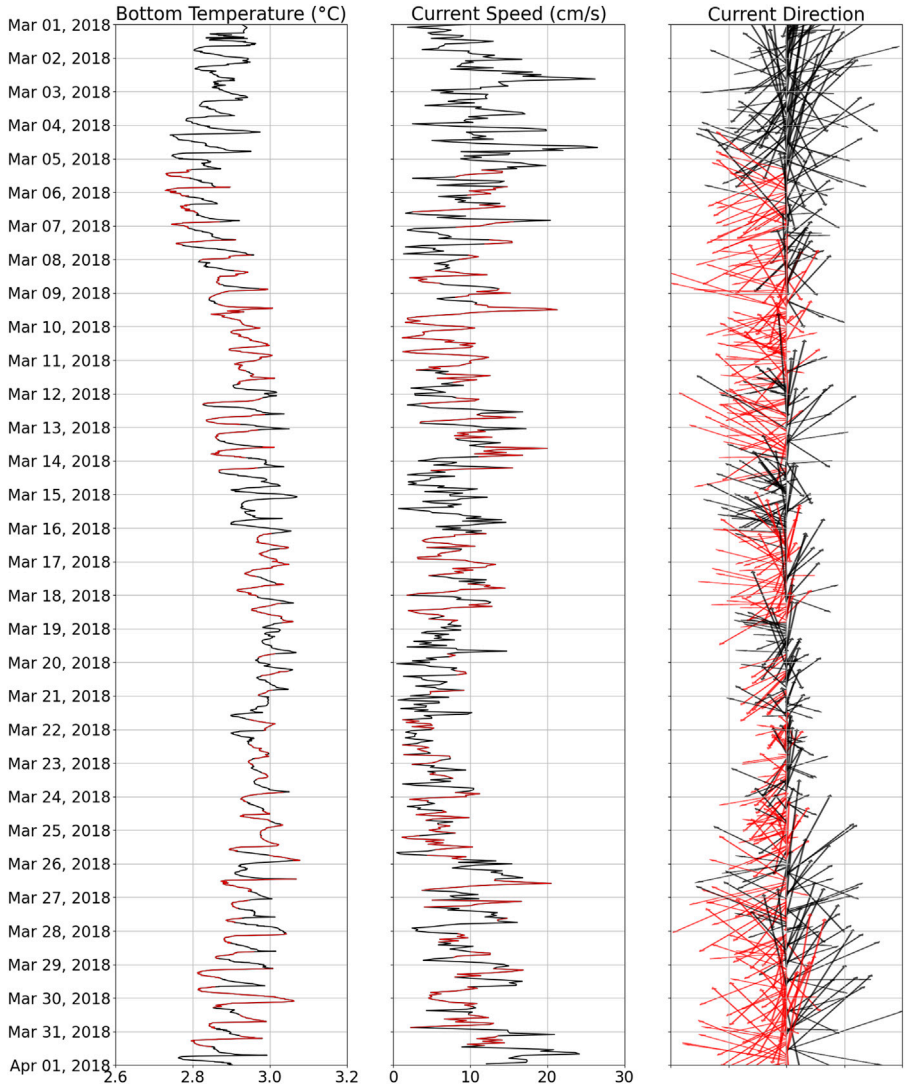

FIGURE 8 | Temperature, current velocities and current directions of bottom waters in March 2018. On the current direction plot, the North is up and the length of the arrows reflects the current velocity. The red colors indicate times with no gas emissions. Periods of inactivity are more frequent when the bottom currents have a westward trend. The plots for the entire ADCP monitoring period are provided in the **Supplementary Figure S2**.

link between the continuity or intermittence of the gas emissions and the seasonal winter storms (**Figure 10**). Accumulations of gas and possibly hydrates are known to occur at Gastown Alley at about 20 mbsf (Römer et al., 2016). One hypothesis is that the fluid supply at depth is transient and not always sufficiently high to ensure continuous bubble release at the sediment surface independently to the bottom pressure variations. Such a mechanism was postulated by Römer et al. (2016) to explain the observed activity phases of the gas ebullition. Unfortunately, we cannot test this hypothesis with our current results, as information about subsurface fluid supply over time is not available. Although the timeseries may show small decreases in venting intensity prior to some intervals of intermittent venting, this is not consistent throughout the timeseries (**Figure 2**). Another possibility could be that the bubble release in the Gastown Alley area is in fact continuous but so spatially variable that it does not always occur within the range of the sonar. This is a reasonable assumption given that the Gastown Alley is an elongated seep area about 400–500 m long (Römer et al., 2016), large parts of which lie outside of the monitoring area of the rotary sonar (**Figure 1**). Continuous but spatially variable venting was observed at the Southern Hydrate Ridge summit using an overview sonar that monitored the whole active area of the summit (Marcon et al., 2019). There, single vents were found to pause frequently but rarely, if ever, all simultaneously (Marcon et al., 2021). Similarly, the number of active flares within our monitoring area varies considerably over time (**Figure 11**) and is non-zero more than 84% of the time. Hence, it is likely that the venting over the entire active area of Gastown Alley rarely pauses completely. At Southern Hydrate Ridge, hydrate formation in the

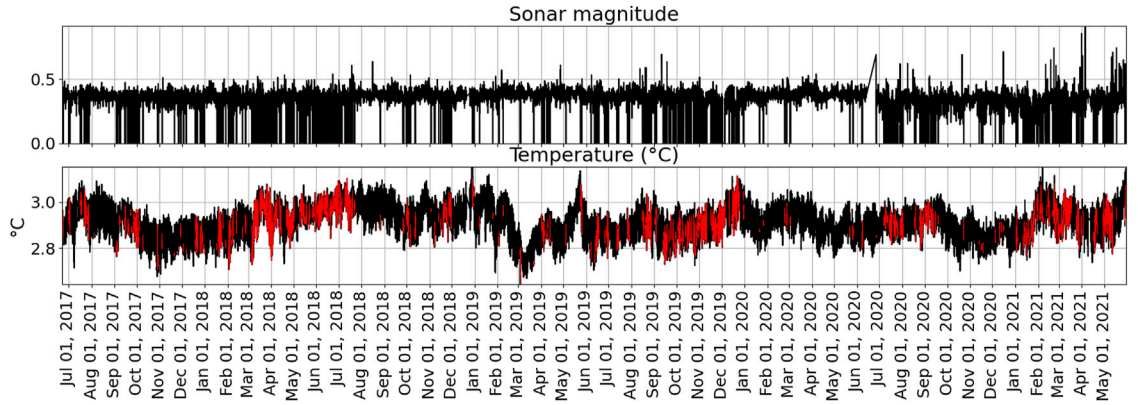

FIGURE 9 | Sonar magnitude and bottom temperature. The red color indicates times of vent inactivity. Magnitude data are dimensionless.

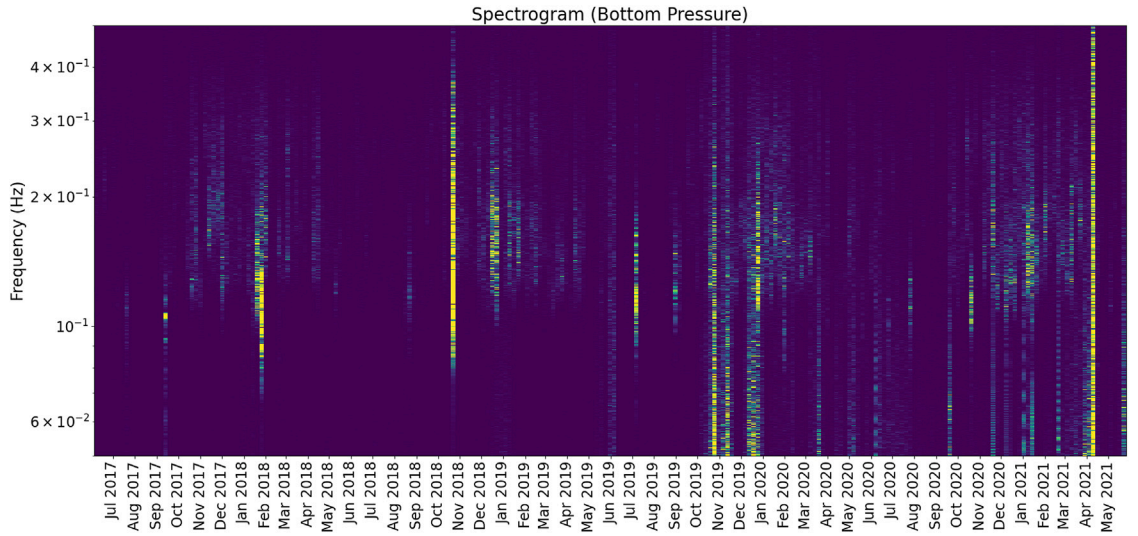

FIGURE 10 | Spectrogram of the 1 Hz bottom pressure data. Storm events are characterized by higher wave heights, which translates into stronger frequency constituents with periods below 20 s (bright colors). The vertical axis is logarithmic and ranges from 0.05 Hz (bottom, T = 20 s) up to the Nyquist frequency of 0.5 Hz (top, T = 2 s).

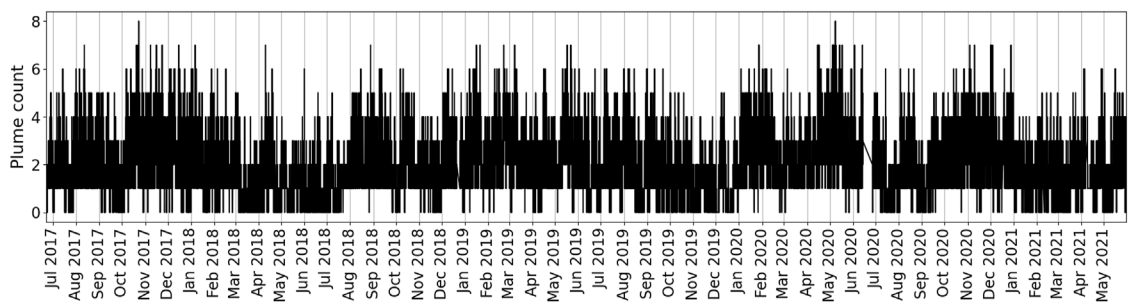

FIGURE 11 | Number of detected flares throughout the monitoring period (between 22 June 2017 and 30 May 2021).

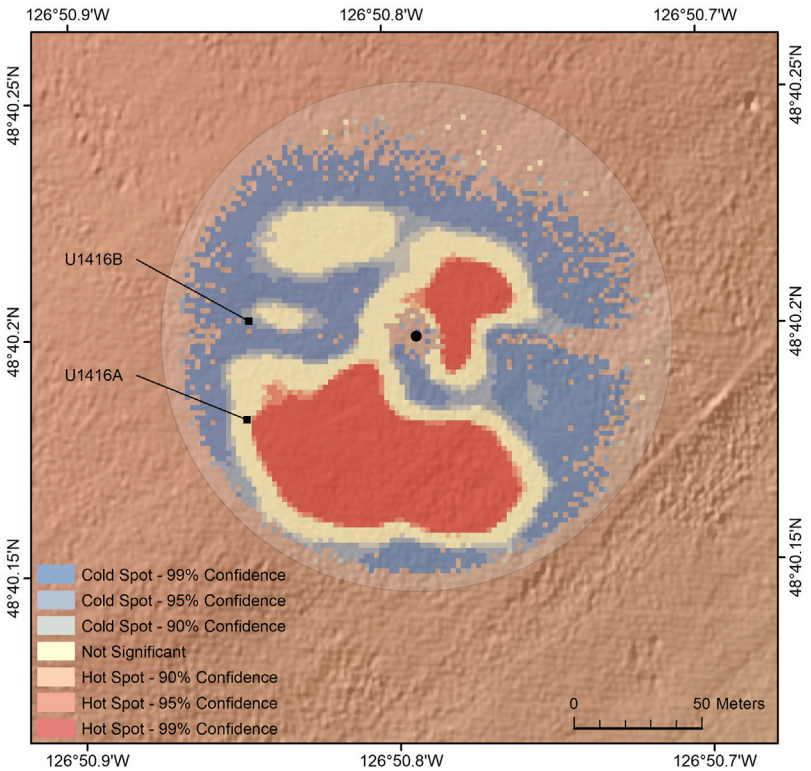

FIGURE 12 | Hotspot analysis of the flare basepoints showing the areas where the gas emissions are the most likely to be observed. The flare locations are not uniformly distributed and reveal at least two distinct areas where gas ebullition occurs. The central black dot represents the sonar location; the circle has a radius of 100 m and delineates the sonar monitoring area. The grey shaded area within the monitoring area represents zero-likelihood of gas source. The black squares are the locations of the IODP boreholes.

shallow subsurface is considered to be responsible for the short-term spatial and temporal variability of the bubble release (Marcon et al., 2021). Although Gastown Alley lies deep within the gas hydrate stability zone, the presence or absence of gas hydrates in the shallow sediments at Gastown Alley was never confirmed. However, the sulfate-methane interface (SMI) at Gastown Alley is located about 6–8 mbsf (Solem et al., 2002; Riedel et al., 2006b), and gas hydrates can only occur below the SMI and possibly much deeper, where methane exists above solubility (Paull et al., 2005; Bhatnagar et al., 2011; Riedel and Collett, 2017). Riedel and Collett (2017) compared data from 58 drill sites from ten different geological regions, including in the northern Cascadia Margin, and found that in the absence of advection, the top of the gas hydrate occurrence zone was always deeper than 30 mbsf. Potentially, hydrate formation in the pore and fracture spaces below this depth could block pathways for gas migration and cause individual gas emissions to temporarily pause.

The current understanding is that low bottom pressures associated with falling tides facilitate the activation of bubble emissions by reducing the total stress on the sediments (Tryon et al., 1999, 2002; Boles et al., 2001; Leifer and Boles, 2005; Liu and Flemings, 2009; Scandella et al., 2011). However, the vent activation times at Gastown Alley are more common at higher than average bottom pressures. Hence, it seems to be the pressure decrease rather than the absolute pressure that helps trigger ebullition. Because of fracture resistance, a pressure drop can cause a temporary dynamic disequilibrium between the pore pressure within gas-rich sediments and the hydrostatic pressure, favoring the advection of gas (Leifer and Boles, 2005; Sultan et al., 2020). Römer et al. (2016) found that bubble emission activation is more common at low pressures close to the low tide turning point. This difference with our results indicates that activation of gas emissions at Gastown Alley is sensitive to smaller pressure decreases than in the 2012-2013 study area. This is interesting since the study area from Römer et al. (2016) is located only 530 m from our monitoring area in the direction of Bubbly Gulch.

It is likely that gas fluxes are higher at Gastown Alley than in the 2012-2013 study area. This is supported by the findings from sub-bottom profiles, which show that the sedimentary layers below Gastown Alley contain large gas accumulations at about 20 mbsf (Römer et al., 2016). By contrast, gas occurrence in the sediments below the study area of the 2012-2013 monitoring is more diffuse and likely related to lower and more transient upward fluxes. Furthermore, flux estimations derived from acoustic flares detected with a calibrated vessel-mounted splitbeam echosounder indicated that instantaneous fluxes at Gastown Alley (min = 0.1 L/min, mean = 4.4 L/min, max = 17.9 L/min) were generally stronger than near the 2012-2013 study area (min = 0.3 L/min, mean = 2.7 L/min, max = 4.7 L/min)

(Riedel et al., 2018). Although acoustic quantification of gas emissions is subject to large uncertainties, the flux estimations from Gastown Alley were the largest methane emission fluxes calculated along the Cascadia Margin (Riedel et al., 2018).

Inactive times at Gastown Alley are also strongly associated with westward bottom currents. This association is partly explained by the fact that these are the most represented current directions during rising tides (**Figure 7**), when inactive times are more common. However, westward bottom currents are in higher proportion during inactive times than they are during flow tides, which raises the question if and how bottom current directions could also play a role in the activation or cessation of gas emissions. Seabed morphology can generate high form drag at the sediment surface (Nash and Moum, 2001) leading to pressure and velocity fluctuations within the sediment pore system (Higashino et al., 2009). Furthermore, bottom currents are known to facilitate ebullition onsets in shallow lakes by causing shear stress at the sediment surface (Joyce and Jewell, 2003). Our results do not show any indication that the activity of gas emissions is influenced by current velocities. However, given the particular mid-slope location of Gastown Alley we cannot exclude that certain current directions might cause increased or reduced form drag that would affect the pore pressure and, thus, the release of gas. Another possibility is that current-induced temperature variations might affect the methane solubility. For instance, a temperature decrease could be expected to pause ebullition by increasing the solubility of methane in the bottom water (Riedel et al., 2021). Our results do not support this possibility since positive and negative temperature variations did not consistently coincide with activation and cessation of venting (**Supplementary Figure S1**). Also, we observed that inactive times were not more frequent at lower temperatures, which seems to rule out that temperature-driven solubility variations cause the onset or cessation of gas emissions. At Gastown Alley, a temperature decrease of 0.14°C (mean amplitude of daily variations) would result in a methane solubility increase of 2×10^{-4} mol of methane per kilogram of seawater (Duan and Mao, 2006; Kossel et al., 2013). This corresponds to 3.6 µl of methane (at the seabed conditions of pressure and temperature). Assuming that the volume of pore water that is affected by the temperature increase is 1 m^3 (a large overestimation used for the sake of simplification), the volume of extra dissolved methane would reach 3.6 ml, which corresponds to about 15 bubbles of a typical bubble-size distribution (Römer et al., 2016). Hence, we consider it unlikely that the daily temperature variations alone would cause the gas ebullition to pause. Furthermore, pore water in the shallow sediments above the SMI is unlikely to be close to saturation.

The flare source distribution showed at least two main clusters within the monitoring area, possibly reflecting distinct pathways for gas migration within the sediments (**Figure 1**, **Figure 12**). The AUV-based bathymetry (**Figure 1** and Paull et al., 2015) does not reveal any obvious local topographical features around those vents that might be associated with the bubble release, as is known from other seep areas both in the immediate vicinity of Gastown Alley and farther along the Cascadia margin. The Bullseye Vent area located 250 m SW of the sonar location is characterized by large 5–6 m deep depressions surrounded by thin carbonate crusts, whereas Bubbly Gulch (650 m NE of the sonar location) coincides with a slope failure and hosts hydrate mounds (Paull et al., 2015). Hydrate Ridge is associated with topographic highs, hydrate mounds and depressions shaped by focused methane venting (Suess et al., 2001; Tréhu et al., 2004; Bangs et al., 2011; Philip et al., 2016; Marcon et al., 2021). By contrast, the seabed within the sonar monitoring area at Gastown Alley is gently sloping towards the southeast (**Figure 1**) and it is covered with soft sediments from which bubble release occurs (Link to seabed footage: https://data.oceannetworks.ca/SeaTube?resourceTypeId=1000&resourceId=1001&diveId=410&time=2014-05-24T07:20:10.000Z). White microbial mats occur within the monitoring area but not where the bubble outlets were observed. The bubble release does not visibly alter the local shape of the seabed around the outlets. This might be due to the low-permeability fine silty and clayey sediments (Riedel et al., 2006a) and the absence of gas hydrates in the shallow sediments, which may favor a more direct transfer of gas through fractures. Alternatively, this seepage area may have formed as a result of the sealing of Bullseye Vent with carbonates or hydrates (Riedel et al., 2002, 2006b; Römer et al., 2016) and may represent a shift of the gas migration from Bullseye Vent towards the northeast. This would be consistent with previous work, which showed that new fractures had formed at Bullseye Vent between 2000 and 2005 (Riedel, 2007), and that the presence of extensive microbial mats and the absence of carbonate crusts at the sediment surface in the area northeast of Bullseye Vent indicate venting in this area may be more recent (Furlong, 2013). With time, the venting activity might also shape the seabed at Gastown Alley. However, more data about the sub-seabed plumbing network at Gastown Alley are needed to investigate these hypotheses further.

CONCLUSION

The 4 years monitoring of gas emissions at Gastown Alley showed clearly that tides influence the timing of gas emissions start and stop times. However, it could not confirm that the vigor of active gas emissions is modulated by tides. Furthermore, the occurrence of month-long intervals of uninterrupted venting within the monitoring area suggests that tidally-induced bottom pressure variations alone were not sufficient to pause the venting. We cannot exclude that external factors (e.g. bottom currents, temperature, transient gas supply) might influence the onset and cessation of bubble plumes, but it is likely that the venting at Gastown Alley during the 4 years monitoring period has been sufficiently intense to remain mostly active independently of the tidal cycles, but not always occurring within range of the sonar.

DATA AVAILABILITY STATEMENT

The original contributions presented in the study are included in the article/**Supplementary Material** and can be downloaded through Ocean Networks Canada's data portal (https://data.oceannetworks.ca). Further inquiries can be directed to the corresponding author.

AUTHOR CONTRIBUTIONS

YM,MRö designed the study. All authors contributed to the interpretation and discussion. YM processed the data and wrote the manuscript with the help of all authors. MRö, MS, MRi, KD, and MH commented on the manuscript.

FUNDING

This work is supported by the German Federal Ministry of Education and Research (BMBF) under the grant number 03F0854A. Ocean Networks Canada is an initiative of the University of Victoria and has primarily been funded by the Canadian Foundation for Innovation, Transport Canada, Fisheries and Oceans Canada, and the Canadian Province of British Columbia.

ACKNOWLEDGMENTS

We greatly appreciate the support by Charles K. Paull and Dave Caress for sharing bathymetric data of AUV D. Allan B. (owned by MBARI) with us.

SUPPLEMENTARY MATERIAL

The Supplementary Material for this article can be found online at: https://www.frontiersin.org/articles/10.3389/feart.2022.864809/full#supplementary-material

REFERENCES

Bangs, N. L. B., Hornbach, M. J., and Berndt, C. (2011). The Mechanics of Intermittent Methane Venting at South Hydrate Ridge Inferred from 4D Seismic Surveying. *Earth Planet. Sci. Lett.* 310, 105–112. doi:10.1016/j.epsl.2011.06.022

Barnes, C. R., Best, M. M. R., Pautet, L., and Pirenne, B. (2011). Understanding Earth– Ocean Processes Using Real-Time Data from NEPTUNE, Canada's Widely Distributed Sensor Networks, Northeast Pacific. *Geosci. Can.* 38. Available at: https://journals.lib.unb.ca/index.php/GC/article/view/18588 (Accessed April 10, 2019).

Bhatnagar, G., Chatterjee, S., Chapman, W. G., Dugan, B., Dickens, G. R., and Hirasaki, G. J. (2011). Analytical Theory Relating the Depth of the Sulfate-Methane Transition to Gas Hydrate Distribution and Saturation. *Geochem. Geophys. Geosyst.* 12, a–n. doi:10.1029/2010GC003397

Boles, J. R., Clark, J. F., Leifer, I., and Washburn, L. (2001). Temporal Variation in Natural Methane Seep Rate Due to Tides, Coal Oil Point Area, California. *J. Geophys. Res.* 106, 27077–27086. doi:10.1029/2000JC000774

Davis, E. E., and Heesemann, M. (2015). Resonant Seismic and Microseismic Ground Motion of the Cascadia Subduction Zone Accretionary Prism and Implications for Seismic Velocity. *J. Geophys. Res. Solid Earth* 120, 993–1004. doi:10.1002/2014JB011644

Davis, E. E., and Hyndman, R. D. (1989). Accretion and Recent Deformation of Sediments along the Northern Cascadia Subduction Zone. *GSA Bull.* 101, 1465–1480. doi:10.1130/0016-7606(1989)101<1465:aardos>2.3.co;2

Duan, Z., and Mao, S. (2006). A Thermodynamic Model for Calculating Methane Solubility, Density and Gas Phase Composition of Methane-Bearing Aqueous Fluids from 273 to 523K and from 1 to 2000bar. *Geochim. Cosmochim. Acta* 70, 3369–3386. doi:10.1016/j.gca.2006.03.018

Fleischer, P., Orsi, T., Richardson, M., and Anderson, A. (2001). Distribution of Free Gas in marine Sediments: a Global Overview. *Geo-Marine Lett.* 21, 103–122. doi:10.1007/s003670100072

Furlong, J. (2013). Characteristic Morphology, Backscatter, and Sub-seafloor Structures of Cold-Vents on the Northern Cascadia Margin from High-Resolution Autonomous Underwater Vehicle Data. Available at: https://dspace.library.uvic.ca/handle/1828/4648 (Accessed January 24, 2022).

GEBCO Compilation Group (2021). *GEBCO 2021 Grid*. doi:10.5285/c6612cbe-50b3-0cff-e053-6c86abc09f8f

Hautala, S. L., Solomon, E. A., Johnson, H. P., Harris, R. N., and Miller, U. K. (2014). Dissociation of Cascadia Margin Gas Hydrates in Response to Contemporary Ocean Warming. *Geophys. Res. Lett.* 41, 8486–8494. doi:10.1002/2014GL061606

Heeschen, K. U., Tréhu, A. M., Collier, R. W., Suess, E., and Rehder, G. (2003). Distribution and Height of Methane Bubble Plumes on the Cascadia Margin Characterized by Acoustic Imaging. *Geophys. Res. Lett.* 30, 1643. doi:10.1029/2003GL016974

Higashino, M., Clark, J. J., and Stefan, H. G. (2009). Pore Water Flow Due to Near-Bed Turbulence and Associated Solute Transfer in a Stream or lake Sediment Bed. *Water Resour. Res.* 45. doi:10.1029/2008WR007374

Hyndman, R. D., and Wang, K. (1993). Thermal Constraints on the Zone of Major Thrust Earthquake Failure: The Cascadia Subduction Zone. *J. Geophys. Res.* 98, 2039–2060. doi:10.1029/92JB02279

Johnson, H. P., Miller, U. K., Salmi, M. S., and Solomon, E. A. (2015). Analysis of Bubble Plume Distributions to Evaluate Methane Hydrate Decomposition on the continental Slope. *Geochem. Geophys. Geosyst.* 16, 3825–3839. doi:10.1002/2015GC005955

Joyce, J., and Jewell, P. W. (2003). Physical Controls on Methane Ebullition from Reservoirs and Lakes. *Environ. Eng. Geosci.* 9, 167–178. doi:10.2113/9.2.167

Judd, A. G., and Hovland, M. (2007). *Seabed Fluid Flow: The Impact of Geology, Biology and the marine Environment*. Cambridge: Cambridge University Press.

Kannberg, P. K., Tréhu, A. M., Pierce, S. D., Paull, C. K., and Caress, D. W. (2013). Temporal Variation of Methane Flares in the Ocean above Hydrate Ridge, Oregon. *Earth Planet. Sci. Lett.* 368, 33–42. doi:10.1016/j.epsl.2013.02.030

Klauda, J. B., and Sandler, S. I. (2005). Global Distribution of Methane Hydrate in Ocean Sediment. *Energy Fuels* 19, 459–470. doi:10.1021/ef049798o

Kopf, A. J. (2002). Significance of Mud Volcanism. *Rev. Geophys.* 40, 2–1. doi:10.1029/2000RG000093

Kossel, E., Bigalke, N., Piñero, E., and Haeckel, M. (2013). The SUGAR Toolbox. *PANGAEA*, doi:10.1594/PANGAEA.816333

Lapham, L., Wilson, R., Riedel, M., Paull, C. K., and Holmes, M. E. (2013). Temporal Variability Ofin Situmethane Concentrations in Gas Hydrate-Bearing Sediments Near Bullseye Vent, Northern Cascadia Margin. *Geochem. Geophys. Geosyst.* 14, 2445–2459. doi:10.1002/ggge.20167

Leifer, I., and Boles, J. (2005). Turbine Tent Measurements of marine Hydrocarbon Seeps on Subhourly Timescales. *J. Geophys. Res.* 110, C01006. doi:10.1029/2003JC002207

Liu, X., and Flemings, P. (2009). Dynamic Response of Oceanic Hydrates to Sea Level Drop. *Geophys. Res. Lett.* 36, L17308. doi:10.1029/2009GL039821

Marcon, Y., Kopiske, E., Leymann, T., Spiesecke, U., Vittori, V., Wahl, T. v., et al. (2019). "A Rotary Sonar for Long-Term Acoustic Monitoring of Deep-Sea Gas Emissions," in Proceedings of the IEEE/MTS OCEANS 2019 conference, Marseille, France, 17-20 June 2019, 1–8. doi:10.1109/OCEANSE.2019.8867218

Marcon, Y., Kelley, D., Thornton, B., Manalang, D., and Bohrmann, G. (2021). Variability of Natural Methane Bubble Release at Southern Hydrate Ridge. *Geochem. Geophys. Geosyst.* 22, e2021GC009894. doi:10.1029/2021GC009894

Mazurenko, L. L., and Soloviev, V. A. (2003). Worldwide Distribution of Deep-Water Fluid Venting and Potential Occurrences of Gas Hydrate Accumulations. *Geo-Marine Lett.* 23, 162–176. doi:10.1007/s00367-003-0146-x

McGuire, J. J., Collins, J. A., Davis, E., Becker, K., and Heesemann, M. (2018). A Lack of Dynamic Triggering of Slow Slip and Tremor Indicates that the Shallow Cascadia Megathrust Offshore Vancouver Island Is Likely Locked. *Geophys. Res. Lett.* 45, 11,095–11,103. doi:10.1029/2018GL079519

Nash, J. D., and Moum, J. N. (2001). Internal Hydraulic Flows on the continental Shelf: High Drag States over a Small Bank. *J. Geophys. Res.* 106, 4593–4611. doi:10.1029/1999JC000183

Obana, K., Scherwath, M., Yamamoto, Y., Kodaira, S., Wang, K., Spence, G., et al. (2015). Earthquake Activity in Northern Cascadia Subduction Zone off Vancouver Island Revealed by Ocean-Bottom Seismograph Observations. *Bull. Seismol. Soc. Am.* 105, 489–495. doi:10.1785/0120140095

Paull, C. K., Ussler, W., Lorenson, T., Winters, W., and Dougherty, J. (2005). Geochemical Constraints on the Distribution of Gas Hydrates in the Gulf of Mexico. *Geo-mar. Lett.* 25, 273–280. doi:10.1007/s00367-005-0001-3

Paull, C. K., Caress, D. W., Thomas, H., Lundsten, E., Anderson, K., Gwiazda, R., et al. (2015). Seafloor Geomorphic Manifestations of Gas Venting and Shallow Subbottom Gas Hydrate Occurrences. *Geosphere* 11, 491–513. doi:10.1130/GES01012.1

Philip, B. T., Denny, A. R., Solomon, E. A., and Kelley, D. S. (2016). Time-series Measurements of Bubble Plume Variability and Water Column Methane Distribution above Southern Hydrate Ridge, Oregon. *Geochem. Geophys. Geosyst.* 17, 1182–1196. doi:10.1002/2016GC006250

Phrampus, B. J., Lee, T. R., and Wood, W. T. (2020). A Global Probabilistic Prediction of Cold Seeps and Associated SEAfloor FLuid Expulsion Anomalies (SEAFLEAs). *Geochem. Geophys. Geosyst.* 21, e2019GC008747. doi:10.1029/2019GC008747

Riedel, M., and Collett, T. S. (2017). Observed Correlation between the Depth to Base and Top of Gas Hydrate Occurrence from Review of Global Drilling Data. *Geochem. Geophys. Geosyst.* 18, 2543–2561. doi:10.1002/2017GC006805

Riedel, M., Spence, G. D., Chapman, N. R., and Hyndman, R. D. (2002). Seismic Investigations of a Vent Field Associated with Gas Hydrates, Offshore Vancouver Island. *J. Geophys. Res.* 107, EPM 5-1–EPM 5-16. doi:10.1029/2001JB000269

Riedel, M., Collett, T. S., and Malone, M.; the Expedition 311 Scientists (2006a). "Site U1328," in Proceedings of the IODP Expedition 311 (Integrated Ocean Drilling Program). 28 August–28 October 2005.doi:10.2204/iodp.proc.311.2006

Riedel, M., Novosel, I., Spence, G. D., Hyndman, R. D., Chapman, R. N., Solem, R. C., et al. (2006b). Geophysical and Geochemical Signatures Associated with Gas Hydrate-Related Venting in the Northern Cascadia Margin. *Geol. Soc. Am. Bull.* 118, 23–38. doi:10.1130/B25720.1

Riedel, M., Scherwath, M., Römer, M., Veloso, M., Heesemann, M., and Spence, G. D. (2018). Distributed Natural Gas Venting Offshore along the Cascadia Margin. *Nat. Commun.* 9, 3264. doi:10.1038/s41467-018-05736-x

Riedel, M., Hähnel, L., Bialas, J., Bachmann, A. K., Gaide, S., Wintersteller, P., et al. (2021). Controls on Gas Emission Distribution on the Continental Slope of the Western Black Sea. *Front. Earth Sci.* 8. doi:10.3389/feart.2020.601254

Riedel, M. (2007). 4D Seismic Time-Lapse Monitoring of an Active Cold Vent, Northern Cascadia Margin. *Mar. Geophys. Res.* 28, 355–371. doi:10.1007/s11001-007-9037-2

Römer, M., Riedel, M., Scherwath, M., Heesemann, M., and Spence, G. D. (2016). Tidally Controlled Gas Bubble Emissions: A Comprehensive Study Using Long-Term Monitoring Data from the NEPTUNE Cabled Observatory Offshore Vancouver Island. *Geochem. Geophys. Geosyst.* 17, 3797–3814. doi:10.1002/2016GC006528

Ruppel, C. D., and Kessler, J. D. (2017). The Interaction of Climate Change and Methane Hydrates. *Rev. Geophys.* 55, 126–168. doi:10.1002/2016RG000534

Scandella, B. P., Varadharajan, C., Hemond, H. F., Ruppel, C., and Juanes, R. (2011). A Conduit Dilation Model of Methane Venting from lake Sediments. *Geophys. Res. Lett.* 38, L06408. doi:10.1029/2011GL046768

Scherwath, M., Spence, G., Obana, K., Kodaira, S., Wang, K., Riedel, M., et al. (2011). Seafloor Seismometers Monitor Northern Cascadia Earthquakes. *Eos Trans. AGU* 92, 421–422. doi:10.1029/2011EO470001

Scherwath, M., Thomsen, L., Riedel, M., Römer, M., Chatzievangelou, D., Schwendner, J., et al. (2019). Ocean Observatories as a Tool to Advance Gas Hydrate Research. *Earth Space Sci.* 6, 2644–2652. doi:10.1029/2019EA000762

Solem, R. C., Spence, G. D., Vukajlovich, D., Hyndman, R. D., Riedel, M., Novosel, I., et al. (2002). "Methane Advection and Gas Hydrate Formation within an Active Vent Field Offshore Vancouver Island," in Proceedings of the 4th international conference on gas hydrate. Yokohama, 19-23 May 2002, 84–89.

Stone, I., Vidale, J. E., Han, S., and Roland, E. (2018). Catalog of Offshore Seismicity in Cascadia: Insights into the Regional Distribution of Microseismicity and its Relation to Subduction Processes. *J. Geophys. Res. Solid Earth* 123, 641–652. doi:10.1002/2017JB014966

Suess, E., Torres, M., Bohrmann, G., Collier, R., Rickert, D., Goldfinger, C., et al. (2001). "Sea Floor Methane Hydrates at Hydrate Ridge, Cascadia Margin," in *Natural Gas Hydrates: Occurrence, Distribution, and Detection*. *Geophysical Monograph Series* (Washington, D.C: American Geophysical Union), Volume 124, 87–98. doi:10.1029/GM124p0087

Suess, E. (2010). "Marine Cold Seeps," in *Handbook of Hydrocarbon and Lipid Microbiology* (Springer Berlin Heidelberg), 185–203. doi:10.1007/978-3-540-77587-4_12

Sultan, N., Plaza-Faverola, A., Vadakkepuliyambatta, S., Buenz, S., and Knies, J. (2020). Impact of Tides and Sea-Level on Deep-Sea Arctic Methane Emissions. *Nat. Commun.* 11, 5087. doi:10.1038/s41467-020-18899-3

Tréhu, A. M., Flemings, P. B., Bangs, N. L., Chevallier, J., Gràcia, E., Johnson, J. E., et al. (2004). Feeding Methane Vents and Gas Hydrate Deposits at South Hydrate Ridge. *Geophys. Res. Lett.* 31, L23310. doi:10.1029/2004GL021286

Tryon, M. D., Brown, K. M., Torres, M. E., Tréhu, A. M., McManus, J., and Collier, R. W. (1999). Measurements of Transience and Downward Fluid Flow Near Episodic Methane Gas Vents, Hydrate Ridge, Cascadia. *Geol* 27, 1075–1078. doi:10.1130/0091-7613(1999)027<1075:motadf>2.3.co;2

Tryon, M. D., Brown, K. M., and Torres, M. E. (2002). Fluid and Chemical Flux in and Out of Sediments Hosting Methane Hydrate Deposits on Hydrate Ridge, OR, II: Hydrological Processes. *Earth Planet. Sci. Lett.* 201, 541–557. doi:10.1016/S0012-821X(02)00732-X

Varadharajan, C., and Hemond, H. F. (2012). Time-series Analysis of High-Resolution Ebullition Fluxes from a Stratified, Freshwater lake. *J. Geophys. Res.* 117, G02004. doi:10.1029/2011JG001866

Wallmann, K., Aloisi, G., Haeckel, M., Obzhirov, A., Pavlova, G., and Tishchenko, P. (2006). Kinetics of Organic Matter Degradation, Microbial Methane Generation, and Gas Hydrate Formation in Anoxic marine Sediments. *Geochim. Cosmochim. Acta* 70, 3905–3927. doi:10.1016/j.gca.2006.06.003

Wallmann, K., Pinero, E., Burwicz, E., Haeckel, M., Hensen, C., Dale, A., et al. (2012). The Global Inventory of Methane Hydrate in Marine Sediments: A Theoretical Approach. *Energies* 5, 2449–2498. doi:10.3390/en5072449

Willoughby, E., Mir, R., Scholl, C., and Edwards, R. N. (2008). "Neptune-Canada Based Geophysical Imaging of Gas Hydrate in the Bullseye Vent," in Proceedings of the 6th International Conference on Gas Hydrates (Vancouver, Canada: University of British Columbia). doi:10.14288/1.0040987

Zühlsdorff, L., and Spieß, V. (2004). Three-dimensional Seismic Characterization of a Venting Site Reveals Compelling Indications of Natural Hydraulic Fracturing. *Geol* 32, 101–104. doi:10.1130/G19993.1

Conflict of Interest: The authors declare that the research was conducted in the absence of any commercial or financial relationships that could be construed as a potential conflict of interest.

Publisher's Note: All claims expressed in this article are solely those of the authors and do not necessarily represent those of their affiliated organizations, or those of the publisher, the editors and the reviewers. Any product that may be evaluated in this article, or claim that may be made by its manufacturer, is not guaranteed or endorsed by the publisher.

frontiers in Earth Science

ORIGINAL RESEARCH
published: 17 March 2022
doi: 10.3389/feart.2022.833918

Mechanism of Faster CH_4 Bubble Growth Under Surface Waves in Muddy Aquatic Sediments: Effects of Wave Amplitude, Period, and Water Depth

*Abhishek Painuly and Regina Katsman**

Dr. Moses Strauss Department of Marine Geosciences, Leon H. Charney School of Marine Science, University of Haifa, Haifa, Israel

Methane (CH_4) transport from organic-rich fine-grained (muddy) shallow aquatic sediments to water column is mediated dominantly by discrete bubbles, which is an important natural source of greenhouse CH_4. The lifespan of these bubbles within the sediment comprises two successive stages: growth from nucleation up to a mature size and then buoyant ascent toward the sediment–water interface. Bubbles often experience an oscillating overburden load due to the passage of winds and/or storm-induced short period surface waves or long-period tides, which can potentially affect both stages of the bubble's lifespan. However, little is known about the wave effects over bubble growth phase. In the present work, this subject is investigated using a numerical single-bubble mechanical/solute transport model, which quantifies the effects of different parameters (amplitude and period) of the wave loading and of the water depth, over the bubble growth pattern in sediments and its specific characteristics. It was found that bubbles induce early sediment fracturing in the presence of waves, attributed to the low overburden load appearing at wave troughs. Bubbles at shallow depth rapidly grow at wave troughs by inducing multiple intense fracturing events. However, this ability decreases with an increasing water depth because of a slower solute influx. In the presence of waves, bubbles mature in shorter time, whose contrast to the no wave case is controlled by the ratio of wave amplitude to equilibrium water depth. Due to the higher frequency of occurrence of wave troughs for shorter-period waves, bubble growth is accelerated compared with the case of longer-period waves. Overall, our modeling suggests that the fastest bubble growth can be predicted for higher amplitude, short-period waves traveling in shallow water. We further infer that accelerated bubble growth, along with subsequent wave-induced ascent can sufficiently shorten the bubble's total lifespan in sediment, which explains the observed episodic *in situ* ebullitions correlated with wind- or storm-induced waves.

Keywords: methane bubbles, gassy sediment, muddy sediment, bubble growth, sediment fracturing, fracture mechanics, modeling

OPEN ACCESS

Edited by:
Michel Michaelovitch Mahiques, University of São Paulo, Brazil

Reviewed by:
Bernhard Wehrli, ETH Zürich, Switzerland
Victor Mikhailovich Stepanenko, Lomonosov Moscow State University, Russia

****Correspondence:***
Regina Katsman
rkatsman@univ.haifa.ac.il

Specialty section:
This article was submitted to Marine Geoscience, a section of the journal Frontiers in Earth Science

Received: *12 December 2021*
Accepted: *21 January 2022*
Published: *17 March 2022*

Citation:
Painuly A and Katsman R (2022) Mechanism of Faster CH_4 Bubble Growth Under Surface Waves in Muddy Aquatic Sediments: Effects of Wave Amplitude, Period, and Water Depth. Front. Earth Sci. 10:833918. doi: 10.3389/feart.2022.833918

INTRODUCTION

Formation of methane (CH_4) bubbles in shallow aquatic sediments is a widespread phenomenon (Bastviken et al., 2011), which is usually associated with synthesis of CH_4 during microbial remineralization of organic matter. Fine-grained cohesive (muddy) aquatic sediments develop discrete diffusion-fed bubbles (markedly larger than pore scale; Wheeler, 1988; Anderson et al., 1998), which elastically deform the sediment matrix and grow by fracturing (Abegg and Anderson, 1997; Johnson et al., 2002; Van Kesteren and van Kessel, 2002; Best et al., 2004; Boudreau et al., 2005; Reed et al., 2005; Jain and Juanes, 2009; Boudreau, 2012; Katsman et al., 2013). They rise in the sediment toward the water column due to buoyancy forces (Wheeler, 1990; Van Kesteren and van Kessel, 2002; Boudreau et al., 2005; Algar et al., 2011a; Algar et al., 2011b; Boudreau, 2012; Sirhan et al., 2019). Within aquatic environments, their entire life cycle is a matter of a great concern, due to the significant contribution of shallow aquatic sites to the global atmospheric CH_4 budget (USEPA, 2010; Saunois et al., 2016), and the bubbles ability to alter effective properties of gassy sediments—compressibility (Nageswaran, 1983; Sills and Wheeler, 1992) and undrained shear strength (Sills et al., 1991; Sills and Wheeler, 1992), which may induce slope failure in aquatic environments (Esrig and Kirby, 1977; Hovland et al., 2002; Bünz et al., 2005; Best et al., 2006).

The life cycle of a bubble within the sediment includes two subsequent stages: 1) bubble growth from its nucleation to mature size and configuration (with a closed tail, just prior to its ascent) (Abegg and Anderson, 1997; Johnson et al., 2002; Van Kesteren and van Kessel, 2002; Best et al., 2004; Reed et al., 2005; Barry et al., 2010; Katsman et al., 2013); and 2) subsequent rise of mature bubble from its place of nucleation toward the sediment - water interface (Wheeler, 1990; Van Kessel and Van Kesteren, 2002; Van Kesteren and van Kessel, 2002; Haeckel et al., 2004; Shin and Santamarina, 2010; Algar et al., 2011a; Algar et al., 2011b; Boudreau, 2012; Sirhan et al., 2019). Both of these stages within the sediment layers are governed by a complex interplay between geochemical properties of the ambient pore fluids (Martens and Klump, 1980; Abegg and Anderson, 1997) and the mechanical properties (fracture toughness, Young's modulus, and Poisson's ratio) of the sediment (Johnson et al., 2002; Algar and Boudreau, 2010; Boudreau, 2012; Katsman, 2015).

In addition, aquatic sediments often experience fluctuating loads, produced, for instance, by surface waves due to winds or storms, by swells or tides, and seasonal water level changes. Bubbles react to the mechanical energy of the varying hydrostatic load by rectifying their sizes and adjusting inner pressure, in accordance with the fluctuating overburden load. This is coupled with the process of CH_4 diffusion to a growing bubble from within the ambient sediments, responsible for bubble growth (Algar and Boudreau, 2009). Field studies often discern a correlation between episodic ebullition from aquatic sediments with variations in hydrostatic pressure (Martens and Klump, 1980; Miller and Oremland, 1988; Chanton et al., 1989; Mattson and Likens, 1990; Keller and Stallard, 1994; Scandella et al., 2011; Chen and Slater, 2016; Scandella et al., 2016; Chen et al., 2017), which was also recently confirmed by lab observations (Scandella et al., 2017) and numerical studies (Algar et al., 2011b; Katsman, 2019).

However, despite its importance, little is known about the effects of varying wave loading over the bubble growth phase, i.e., from its nucleation to mature configuration at the start of its ascent. A strong coupling between the net solute transport from the ambient sediment to the growing bubble with fluctuating size, along with difficulties in precise measuring and assessing bubble growth rates due to mud opacity, make it extremely complicated to explore this process *in situ* and to define its controls in aquatic sediments. Only a few studies based on numerical modeling quantified bubble growth under periodic wave loadings in muddy aquatic sediments (e.g., Boudreau et al., 2001; Algar and Boudreau, 2009; Algar et al., 2011b). These studies focused on bubble growth under a semidiurnal tidal loading (wave periods of 12 h) and its effect on processes of rectified diffusion and solute transport (due to pressure oscillations) to the growing bubble. The rectified diffusion was suggested to become important as $(\Delta P/P)^2 \rightarrow 1$, where ΔP is magnitude of wave induced load fluctuation, and P is the overburden load of the water column. The magnitude of $(\Delta P/P)^2$ is on the order of 0.0001–0.001 in the usual wind-induced waves (Boudreau et al., 2001) and can be up to ~0.05 in tides (Algar and Boudreau, 2009; Algar et al., 2011b). Due to a substantially lower magnitude of $(\Delta P/P)^2$ and the low frequency of oscillations of tides during the entire bubble growth period (about a week, Algar et al., 2011b), waves' contribution to bubble volume growth was suggested to be marginal (Boudreau et al., 2001; Algar and Boudreau, 2009; Algar et al., 2011b). However, due to the high surface area-to-volume ratio (an indicator of bubble's sensitivity to ambient solute field) of the thin sub-vertical bubbles growing in muds by fracturing, tidal actions could roughly contribute seven times more to bubble volume growth, compared with spherical bubbles of the equivalent volume (Algar and Boudreau, 2009). Nevertheless, an overall consistent quantification of the wave loading effect on bubble growth dynamics is missing. Specifically, it is unclear how the wave characteristics (wave period and amplitude) and water depths affect a bubble's growth in aquatic muds, and which factors would dominate.

In the present study, an underlying general quantitative mechanistic pattern and specific features of bubble growth in aquatic sediments, prior to bubble's ascent, under the action of surface wave loadings, are explored. Bubble growth is simulated under distinct wave characteristics (wave amplitude and period) at various ambient water depths. Results indicate that under the wave action, the bubbles grow faster compared with the no wave case, especially at shallow water depths and under higher amplitude and shorter wave periods. This is attributed to an early appearance of sediment fracturing, and in some cases to intense and frequent fracturing events that appear at the wave trough. Our findings associate this mechanism of accelerated bubble growth with episodic ebullitions at various aquatic sites to be correlated with wind or storm-induced surface waves, which is important in the context of a long-persisting uncertainty related to net CH_4 fluxes from shallow aquatic sediments.

MATERIALS AND METHODS

To analyze the effects of wave-induced periodic loadings on CH_4 bubble growth within muddy sediment, we used a coupled mechanical/solute transport numerical model, previously developed in Katsman et al. (2013) and Katsman (2015). This single-bubble model is applicable to fine-grained cohesive (muddy) sediments, where a bubble grows by a crack propagation within the framework of linear elastic fracture mechanics (LEFM) (e.g., Johnson et al., 2002; Boudreau et al., 2005; Best et al., 2006; Barry et al., 2010; Boudreau, 2012). The model simulates the coupled process of diffusion-driven bubble expansion due to a concentration gradient of dissolved CH_4 at the bubble surface, and the sediment's elastic-fracture mechanical response (Broek, 1982; Lawn, 1993; Gross and Seelig, 2017) to bubble growth. The modeling setup (**Figure 1A**) includes a small penny-shaped bubble seed with dimensions larger than a pore scale, embedded at the symmetry plane of a 3D sediment cell. The bubble's (crack's) spatial opening implicitly depends upon the inner bubble pressure, which continuously mounts due to an uninterrupted solute supply from the ambient sediment. This causes the bubble to grow elastically and gain stress intensity factor (Mode I SIF, K_I, a measure of the stress state at the crack front characterized by deformations normal to the crack surfaces; Broek, 1982; Lawn, 1993; Gross and Seelig, 2017). As such, K_I at each point of the crack front, F (**Figure 1A**), is evaluated employing a one-point methodology, using displacements at point P prescribed on the crack surface in the vicinity of point F (Citarella and Cricrì, 2010; Katsman et al., 2013):

$$K_I = \frac{E}{4(1-\nu^2)}\sqrt{\frac{\pi}{2d}}2w_n^P, \tag{1}$$

where ν is the Poisson's ratio, E is the Young's modulus, d is the distance between the points (**Figure 1A**), and w_n^P is a normal displacement of the crack surface at point P. As per the principles of LEFM, when the maximum value of SIF, K_I, over the front exceeds the sediment's Mode I fracture toughness, K_{IC} (a material parameter quantifying the sediment's crack resisting ability; Lawn, 1993; Gross and Seelig, 2017), the bubble (crack) initiates discrete differential fracturing along the front. Notably, the SIF along bubble front is always maximum at bubble's head (point B, **Figure 1A**; denoted here by K_{head}), since gravity-dependent compressive stress component in the ambient sediment produces a maximum opening there (Katsman et al., 2013; Katsman, 2015). Therefore, maximum crack increment always occurs at the buoyant bubble head (point B, **Figure 1A**) and decreases toward its tail (point A, **Figure 1A**) (Katsman et al., 2013). With an increase in the bubble's vertical height, the differences between local compressive stresses within the sediment at its head and tail increase (due to their dependence on gravity; Katsman, 2015); ultimately resulting in closure of the bubble's tail (i.e., zero openings), as an indicator of its mature configuration prior to its ascent. The model equations and input parameters used in simulations are listed in **Supplementary Tables S1** and **S2**, described in detail in Katsman et al. (2013) and Katsman (2015).

Under the action of surface waves, the effective water column height (H_{eff}) pulsates around its mean level (H_{eq}), approximated here as:

$$H_{eff} = H_{eq} + A\sin\left(\frac{2\pi t}{T}\right) \tag{2}$$

where A is the amplitude, T is the period of pulsation of the surface wave, and t is the time. A corresponding effective overburden load, σ_z^0, is described here as the sum of pulsating hydrostatic pressure of the water column (σ_H), and the permanent lithostatic pressure of the overlying sediment layer (σ_L), i.e., $\sigma_z^0 = \sigma_H + \sigma_L$. Here, $\sigma_L = \rho_s g H_s$, and $\sigma_H = \rho_w g H_{eff}$ (ρ_s, ρ_w are bulk sediment and water densities, g is gravity acceleration, and H_s is the thickness of the sediment layer overlying the modeled computation domain, **Figure 1A**).

For clarity of further analysis, the periodic oscillations in the effective overburden load (σ_z^0) produced by propagation of surface waves, can be differentiated in two subsequent loading phases: 1) "*unloading" phase 1*, described as the continuous fall of the overburden load, σ_z^0 (σ_z^{max} to σ_z^{min}), in response to a declining water level; and 2) *"loading" phase 2*, attributed to a continuous rise of the overburden load (σ_z^{min} to σ_z^{max}). A schematic illustration of the fluctuations in σ_z^0, induced by a surface wave having an amplitude of 0.22 m (A) and a time period of 3 s (T) over sediment submerged under 18 m of water (H_{eq}), is presented in **Figure 1B**.

Simulations are initiated with a small penny-shaped bubble having a radius of 4 mm (**Figure 1A**) and continue until the bubble attains mature size and configuration with closed tail (Katsman et al., 2013). This time period is specified as "Bubble maturity time" designated by t_m. Numerical simulations are performed at distinct ambient water column heights (H_{eq}, presented in subsection *Effect of the water depth on bubble growth*), and with distinct surface wave characteristics (A, T, presented in subsections *Role of ratio of wave amplitude to water depth over bubble growth* and *Role of wave periods over bubble growth*). Input conditions related to these characteristics used in simulations are summarized in **Table 1**. The model was designed within the COMSOL Multiphysics simulation environment, v.5.5.

RESULTS

Pattern of Bubble Growth Under the Wave Loading

First, we explore the general pattern and specific features of bubble growth under the wave action. In parallel and for comparison, bubble growth is simulated in the absence and presence of wave loadings, with conditions summarized in **Table 1** (runs 1, 2, respectively). Corresponding results of evolution of Mode I stress intensity factor at the bubble head, K_{head} (SIF at point B in **Figure 1A**), are demonstrated in **Figure 2**. In the absence of waves (run 1, green line), following the elastic expansion of the initial bubble cavity, K_{head} rises linearly (t = 0–10.95 s; see left inset of **Figure 2**), until K_{head} reaches the

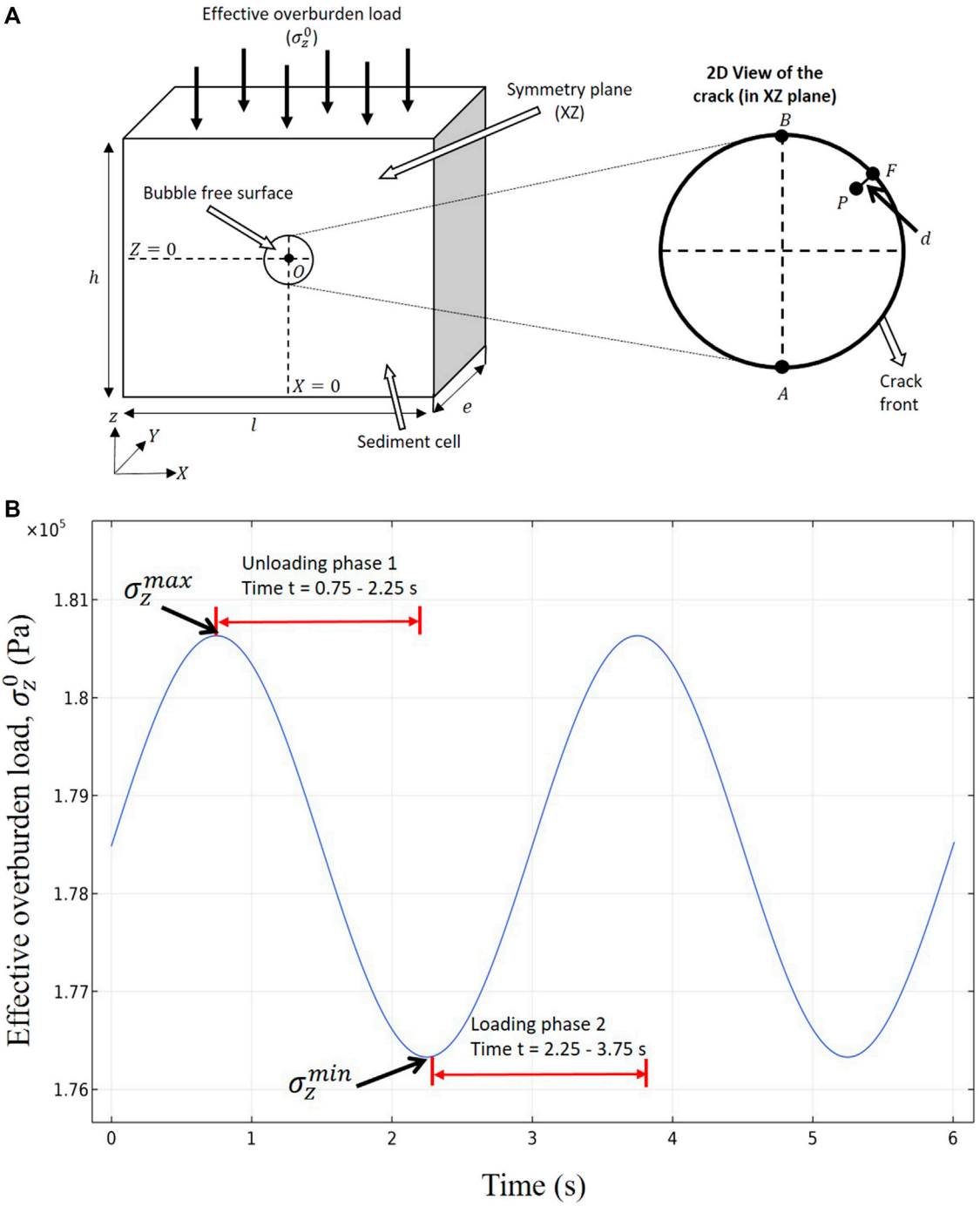

FIGURE 1 | Schematic illustration of modeling setup: **(A)** Computational domain consists of a 3D sediment box cut by a symmetry plane (XZ), with an embedded penny-shaped bubble seed (centered at origin, O). (X, Y, Z) depicts the global coordinate system. Top boundary of sediment is subjected to an effective overburden load, σ_z^0. Inset plot presents 2D in-plane view of penny-shaped (Mode I) crack surface and its front. Points A and B denote a bubble's tail and head, correspondingly. Point P on bubble surface (at fixed distance *d* from crack front) is specified to estimate the Stress Intensity Factor at the adjacent point F of the evolving bubble front. **(B)** Temporal evolution of effective overburden load (σ_z^0) over sediment submerged under 18-m water depth under surface waves of amplitude 0.22 m having a period of 3 s. In unloading phase 1 (t = 0.75–2.25 s, 3.75–5.25 s, etc.), the overburden load continuously decreases from its maximum (σ_z^{max}) to minimum (σ_z^{min}) value, and in loading phase 2 (t = 0–0.75 s, 2.25–3.75 s, and 5.25–6 s, etc.), the overburden load continuously rises from minimum (σ_z^{min}) to maximum (σ_z^{max}) value.

TABLE 1 | Input conditions used in simulations: to illustrate 1) a general pattern of bubble growth without and with (runs 1, 2) waves; 2) an effect of water depth (runs 3, 4) over the bubble growth; 3) an effect of wave amplitude-to-water depth ratio (runs 5, 6); and 4) an effect of wave periods (runs 7–10).

Run no	Mean water column height, H_{eq} (m)	Wave amplitude, A (m)	Wave period, T (s)	Wave amplitude-to-water column height ratio ($\bar{r} = A/H_{eq}$)	Bubble maturity time, t_m(s)	$\bar{t}^a$	Related figure
1	2	0	0	NA	391	NA	2, 3
2	2	0.22	3	0.11	353	9.71%	2, 3
3	18	0	0	NA	8,245	NA	4
4	18	0.22	3	0.012	7,976	3.2%	4
5	10	0	0	NA	2,897	NA	5
6	10	1.1	3	0.11	2,555	11.8%	5
7	2	0.22	10	0.11	357	8.6%	6
8	2	0.22	20	0.11	372	4.8%	6
9	2	0.22	30	0.11	377	3.5%	6
10	2	0.22	50	0.11	382	2.3%	6

[a]*Note: A contrast in time taken by bubbles to mature with and without wave loadings is measured (in percentage) as* $\bar{t} = 100 \cdot |t_m\,(no\ wave) - t_m\,(with\ wave)|/t_m\,(no\ wave)$.

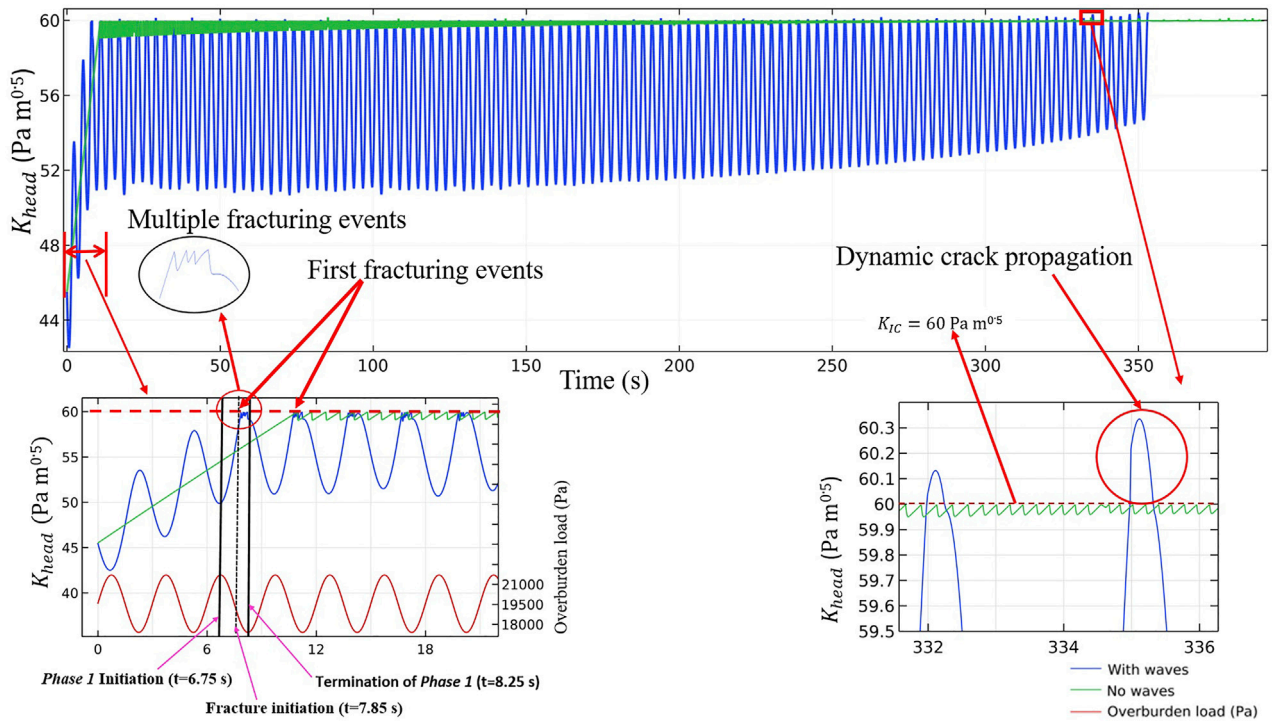

FIGURE 2 | The evolution of stress intensity factor at bubble head, K_{head}, for bubble growing in the presence (run 2, blue curve) and absence (run 1, green curve) of waves. Insets show the zoomed section of K_{head} profiles for t = 0–22 s (left inset) and t = 332 s–336 s (right inset). Left inset also depicts the corresponding oscillating overburden load, σ_z^0 (red curve, connected to the right axis). Under wave loadings, bubbles induce early fracturing (see first fracturing events marked in the left inset). K_{head} exhibits also periods of intense fracturing events (e.g., for t = 7.85 s–8.25 s, 10.75 s–11.25 s, etc.) at wave troughs and stages of temporarily ceased fracturing (e.g., for t = 8.25 s–10.75 s, 11.25 s–13.7 s, etc.). Stable saw tooth fracturing under the waves is produced at t = 0–~300 s; however, at later stages, bubble grows by temporarily inducing a dynamic fracturing (~t >300 s), where K_{head} exceeds K_{IC}. However, in contrast, under no wave conditions (run 1), K_{head} profile exhibits a continuous stable fracturing only (see left inset).

sediment's fracture toughness, K_{IC} (60 Pa m$^{1/2}$). At this time fracturing initiates, which in-turn results in a sharp drop in K_{head} (at t = 10.95 s; see left inset of **Figure 2**). With the continuous solute supply from the ambient sediment, this yields a repeated pattern of elastic expansion and sediment fracturing, thus, generating a saw-tooth-like K_{head} profile (**Figure 2**; observed also in other studies such as in Johnson et al., 2002; Algar and Boudreau, 2009; Boudreau, 2012; Katsman et al., 2013).

In contrast, in the presence of waves, the stress intensity factor at the bubble head (K_{head}) (**Figure 2**, blue line, run 2) oscillates around the corresponding values of K_{head} attained by the bubble at the elastic expansion stage under no-wave

conditions (left inset of **Figure 2**). Under the wave actions, there are two specific fracturing features that make this different from the fracturing pattern in the absence of wave loadings:

1. Early fracture initiation due to decline in σ_z^0 in the unloading stage (phase 1, **Figure 1B**).
2. Intense multiple fracturing events in the unloading stage (phase 1) near the wave trough.

Early fracturing appearance due to a σ_z^0 decline in the unloading stage (phase 1): Due to the wave action, fluctuations of $\sim\pm 4\ \mathrm{Pa\ m^{1/2}}$ in K_{head} are observed compared with corresponding values of K_{head} in the no wave case (**Figure 2**). Essentially, K_{head} is reversely synchronized to the oscillating effective overburden load, σ_z^0, in the presence of waves (red line in the left inset of **Figure 2**). Therefore, waves aid in achieving the fracturing condition ($K_{head} \geq K_{IC}$) a bit earlier, in comparison with a bubble grown in the absence of waves, due to the declining σ_z^0 in the unloading stage (phase 1 in **Figure 1B**, see a detailed explanation on this issue in **Supplementary Text S1**). Specifically, due to wave loading, the first fracturing event is observed at t = 7.85 s (see black dashed line in the left inset of **Figure 2**), in contrast to t = 10.95 s in the absence of waves (left inset in **Figure 2**).

Intense multiple fracturing events in the unloading stage (phase 1) near wave trough: Under the action of wave loadings, the K_{head} profile exhibits sequences of temporarily ceased fracturing events, with termination of the unloading phase 1 near wave troughs (e.g., between t = 8.25–10.75 s and 11.25–13.7 s, etc.; **Figure 2**), in contrast to the no wave case where fracturing continuously persists after its start (green profile, **Figure 2**). The fracturing temporally halts at the beginning of loading phase 2 (**Figure 1B**) because of the reduction in the bubble openings and, hence, in K_{head} (see **Eq. 1** and **Supplementary Text S1**), despite the continuous solute supply to the bubble. As waves decrease the overburden load near their troughs (red solid line, i.e., $\sigma_z^0 \rightarrow \sigma_z^{min}$), fracturing events re-appear (for example, between t = 7.85–8.25 s and 10.75–11.25 s, etc.; see left inset of **Figure 2**). Therefore, when the wave approaches its trough (i.e., $\sigma_z^0 \rightarrow \sigma_z^{min}$, red solid line), and fracturing re-initiates again, the bubble rapidly increases in size by more frequent and intense fracturing events compared with the no wave case. This rapid crack propagation at the wave troughs is due to the continuous piling-up of solute at the preceding wave loading stage. In simulation, this crack growth is manifested by two fracturing mechanisms (see two inset plots of **Figure 2**): 1) occurrence of multiple fracturing events in a stable fracturing regime (i.e., when K_{head} remains below K_{IC}, for time ~0–300 s, left inset); 2) bubble growth by dynamic fracture propagation (i.e., when despite the fracturing events, K_{head} temporarily rises higher than K_{IC}, at wave troughs, at a more advanced stage, ~t >300 s, applicable for a large bubble, right inset). Both stable and dynamic fracturing scenarios cease with initiation of loading phase 2, bringing K_{head} below K_{IC}.

As a result of the appearance of these early and multiple fracturing features, the bubble in run 2 earlier attains a larger surface area (e.g., between t = 7.85 and 10.95 s, **Figure 2**) and thus, grows with a higher total diffusive flux over its surface as compared with the bubble growing under no waves in run 1 (**Figure 3**). Therefore, bubbles growing under the wave action are able to mature in less time (t_m = 353 s) compared with bubbles growing under no waves (t_m = 391 s), **Table 1**.

Effect of the Water Depth on Bubble Growth

To explicitly demonstrate the effect of water depth on bubble maturity time, t_m, and fracturing pattern, we simulate bubble growth in sediment under a water depth of 18 m (without and with waves, runs 3 and 4, respectively, **Table 1**) and compare the results with those from run 2 simulated with the same wave amplitude and period. It can be seen from **Figure 4**, where evolution of K_{head} for runs 3, and 4 are shown, that bubbles do induce early fracturing (first fracturing at t = 80.75 s in the presence of waves and at t = 92.17 s in the absence of waves), but no multiple fracturing is observed. This is attributed to low diffusive flux of orders of 10^{-13} to $1.9 \cdot 10^{-12}$ kg/s for bubbles at water depth 18 m (run 3, 4) in contrast to $3.04 \cdot 10^{-13}$ to $4.02 \cdot 10^{-12}$ kg/s at 2 m water depth in run 2, over the entire bubble growth period, as explained below.

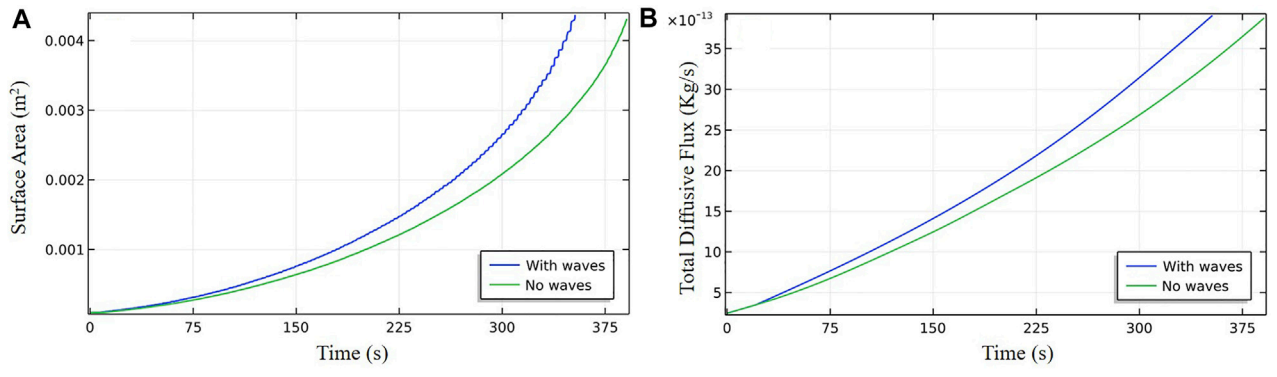

FIGURE 3 | Temporal growth of surface area [panel **(A)**] and total diffusive flux [panel **(B)**] for bubbles growing in sediment under a 2 m water depth, in the presence (run 2, blue curve) and absence (run 1, green curve) of waves. Attributed to early and multiple fracturing, bubbles growing in the presence of waves gain surface area and total diffusive flux comparatively faster, thus, maturing in less time (t_m = 353 s, 391 s in the presence and the absence of waves, respectively).

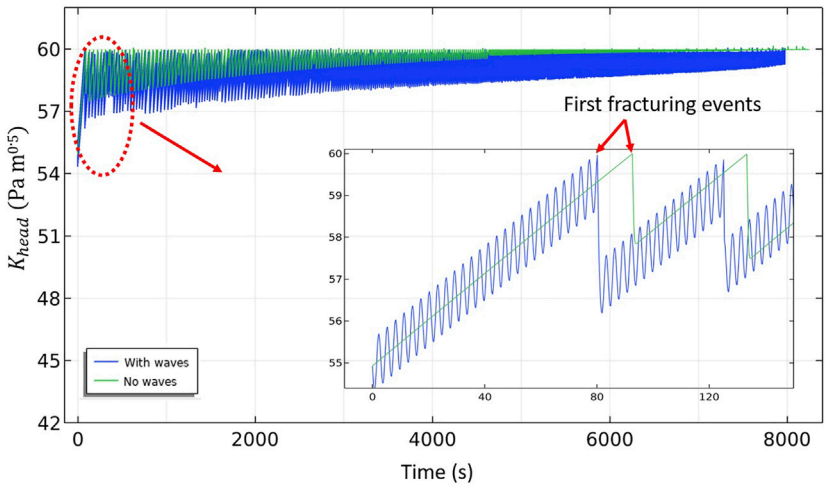

FIGURE 4 | Evolution of K_{head} for bubbles from run 3 and run 4, presented to quantify an effect of water column height. Inset plot presents a zoomed section of K_{head} profile for time interval t = 0–140 s. In the presence of waves (run 4, blue curve), K_{head} fluctuates around the corresponding mean value from the no-wave case (run 3, green curve) and induces first fracturing at 80.07 s in contrast to first fracturing at t = 92.17 s in the absence of waves. Attributed to higher overburden load (of 18 m water column), and hence, lower total solute flux, a bubble is not able to induce multiple fracturing at wave troughs (see text for detailed explanations).

Bubbles in deeper water (i.e., under the higher overburden load, σ_z^0) grow with higher inner pressure, P_b (Eq. 15 in Katsman, 2015). This, in turn, increases the solute concentration at the bubble surface (**Supplementary Equation S6** in **Supplementary Material**) and, thus, reduces the temporal total diffusive flux to the growing bubble (**Supplementary Equation S3** in **Supplementary Material**). Therefore, the CH_4 flux supplied to the growing bubble, and thus, the gaseous CH_4 accumulated in the bubble per wave period, naturally decreases with an increase in the water depth. Consequently, after a first fracturing event, the amount of solute required to induce the next fracturing event may accumulate over a substantially large number of wave periods (e.g., see inset of **Figure 4** between t = 80 and 125 s; attributed to a slower bubble influx). Hence, deeper water decreases the potential to induce multiple fracturing events near the wave trough (as is observed in the shallow depth of run 2, **Figure 2**).

Therefore, in sediments submerged under shallow water depths (as modeled in run 2), bubbles incur early fracturing as well as induce multiple fracturing events (as described in **Figure 2**) near the wave troughs, sometimes supplemented by a dynamic fracturing regime at a later stage of the bubble growth, which expedites bubble growth (**Figure 2**). Therefore, a bubble under 2 m of water was able to mature in nearly ~9.71% ($\bar{t}$) less time compared with a bubble in the absence of waves (run 1, 2; **Table 1**). Additionally, simulation in shallower water at a depth of 0.5 m (not shown here) under the same wave conditions as in runs 2, 4, indicated a ~30% decrease in bubble maturity time (see **Supplementary Table S3** in **Supplementary Material**). However, a bubble's ability to induce multiple fracturing under a wave trough distinctively decreases with increasing water column height, as indicated above. Thus, the bubble in run 4 with 18 m water column height could only grow nearly ~3.2% ($\bar{t}$) faster compared with the bubble in the absence of waves, run 3 (the maturity time, t_m, is 7,976 and 8,245 s, correspondingly). This indicates that the effectiveness of wave loadings to expedite bubble growth decreases with increasing water column height (for constant A, T).

Role of Ratio of Wave Amplitude to Water Depth Over Bubble Growth

To further explore the role of the ratio of wave amplitude to water depth ($\bar{r} = A/H_{eq}$), over the bubble maturity time, t_m, we analyze results of bubble growth from runs 5, 6 (**Table 1**) and compare their maturity times with those from run 2. Ambient water column height and wave characteristics in runs 5, 6 were chosen in a way to preserve a constant ratio, $\bar{r}$ = 0.11, as in run 2.

The magnitude of fluctuations in K_{head} in runs 2 and 6 is approximately the same, i.e., ~ ±4 Pa m$^{1/2}$ (left inset of **Figure 2** and inset of **Figure 5**), and is attributed to the same values of the ratio, $\bar{r}$. Therefore, in run 6, at each wave trough, K_{head} is effectively enhanced by ~4 Pa m$^{1/2}$, compared with the mean value of K_{head} in the no wave case (runs 6 and 5, respectively; **Figure 5**). This enables bubbles to induce early fracturing at t = 74.25 s in the presence of waves (run 6), compared with t = 115.2 s under no wave conditions (run 5). By incurring early fracturing events due to wave loadings, a bubble under a 10 m water column is able to attain maturity in 2,555 s (run 6), while in the absence of waves the bubble takes 2,897 s to mature (run 5). Despite distinct overburden loads, the contrast in bubble maturity time in runs 2 and 6 is quite similar (at water depths of 2, and 10 m, bubble maturity time is reduced by nearly 9.71% and 11.8% ($\bar{t}$), respectively, under the same $\bar{r}$).

Furthermore, following **Eq. 2**, the rate of change in scaled hydrostatic overburden load ($\sigma_H^s = \sigma_{eff}/\sigma_{eq}$, where $\sigma_{eff} = \rho_w g H_{eff}$ and $\sigma_{eq} = \rho_w g H_{eq}$) induced by waves is given as:

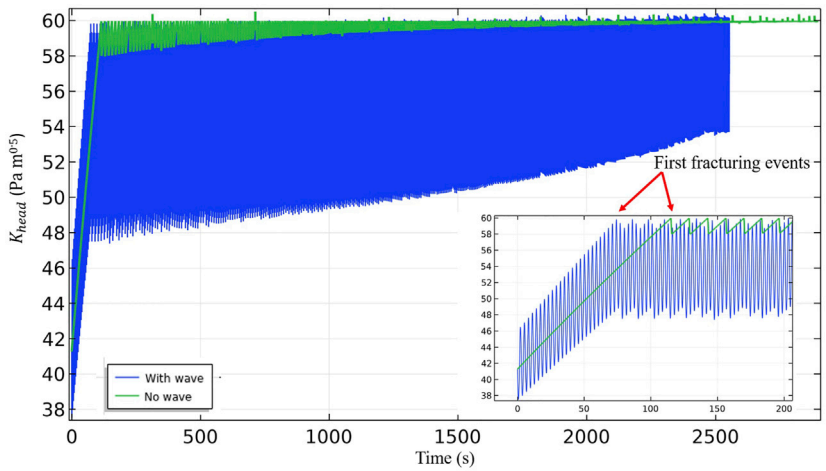

FIGURE 5 | Evolution of K_{head} for bubbles from runs 5 (without wave loading, green curve), 6 (with wave loading, blue curve) focused on wave amplitude to water depth ratio verification. Zoomed section of K_{head} profile for time interval t = 0–200 s is presented in inset. Under action of waves of amplitude 1.1 m, K_{head} fluctuates about ±4 Pa m$^{1/2}$ around corresponding mean values of K_{head} in the absence of wave loadings. At each wave trough, a bubble's K_{head} is effectively enhanced by ~4 Pa m$^{1/2}$, enabling the bubble to attain first fracturing event earlier, at t = 74.25 s in the presence of wave, while at t = 115.2 s in the absence of waves.

$$\frac{\partial(\sigma_H^s)}{\partial t} = \bar{r} \cdot \cos\left(\frac{2\pi t}{T}\right) \cdot \frac{2\pi}{T} \tag{3}$$

where H_{eff}, H_{eq} are the effective and the equilibrium water column heights (as given by **Eq. 2**), respectively. The horizontal load at the bubble surface (σ_y) is related to vertical overburden load (σ_{eff}) by the relation $\sigma_y = \frac{\nu}{1-\nu} \cdot \sigma_{eff}$, where ν is Poisson's ratio (under the uniaxial (vertical) strain boundary condition, as prescribed in the present model, Katsman et al., 2013; Katsman 2015). For same time period values, T, **Eq. 3** suggests that the rate of change in σ_H^s and, thus, in σ_y, explicitly depends upon the ratio of wave amplitude to water depth, $\bar{r}$. As a result, this generates oscillations of equivalent magnitude in bubble openings (w_n, **Supplementary Equation S10**) and, hence, in K_{head}, in bubbles growing in environments with similar ratios, $\bar{r}$.

Notably, as attributed to increased water depths, the total solute flux to bubble in run 6 (of orders of ~$20 \cdot 10^{-13}$ kg/s at mature configuration) is smaller compared with that in run 2 (of orders of ~$40 \cdot 10^{-13}$ kg/s at the corresponding mature configuration; **Figure 3B**), and hence, their maturity time t_m is different (2,555 s and 353 s, respectively). Therefore, a similarity, in contrast to relative times taken by bubbles to mature with and without wave loadings, $\bar{t}$, should be attributed to $\bar{r}$. However, in run 2, bubble growth is enhanced due to the appearance of multiple fracturing (**Figure 2**) affected by an efficient solute influx. In contrast, in run 6, the growth is swift compared with the corresponding bubble in run 5, due to longer duration of early fracturing affected by a high $\bar{r}$ value, while the bubble in run 5, under no waves, still experiences an elastic expansion stage caused by the slow solute influx. Finally, to achieve the same values of ratio $\bar{r}$ in deep waters, high-amplitude waves would be a prerequisite to significantly expedite the bubble growth.

Role of Wave Periods Over Bubble Growth

In order to understand the effect of wave periods (T) over bubble growth, we simulate bubble growth under fixed water column height (H_{eq} = 2 m) and with constant wave amplitudes (A = 0.22 m) (as in run 2), but with different wave periods, T (runs 7 to 10, **Table 1**). A comparison between bubble maturity times (t_m) for runs 2 (T = 3 s), 7 (T = 10 s), 8 (T = 20 s), 9 (T = 30 s), and 10 (T = 50 s) with that in the no wave case (run 1) is presented in **Figure 6**.

Simulations reveal that smaller period waves expedite bubble growth (**Figure 6**): for instance, a bubble matures in 353 s when T = 3 s (run 2), compared with 382 s when T = 50 s (run 10). For smaller wave periods, the bubble is exposed to wave trough loadings (i.e., low overburden load) more frequently, over the entire period of its growth. Thus, bubble growth via early and/or multiple fracturing events occurs more frequently in the presence of short period waves. This facilitates bubbles attaining mature size in less time, as seen in **Figure 6**.

DISCUSSION

Our calculations assert that surface waves developed in the water column with the passage of winds or storms, reduce the duration of the growth phase of bubbles, and thus allow early upward buoyant bubble rise. For instance, the water depth and surface wave characteristics simulated in runs 1 and 2 (**Table 1**) may be associated with the usual ambient conditions in the shallow littoral zone of Lake Constance, Europe, in the presence of synoptic scale winds from the southwest-west and northeast (Appt et al., 2004; Hofmann et al., 2008). The data in runs 3 and 4 agree with ambient conditions at the 18 m isobaths of Lake Kinneret, Israel, in the presence of Mediterranean summer sea breezes (Serruya, 1975; Zohary et al., 2014). There is a reduction of ~9% and 3% in the time duration of the bubble growth period

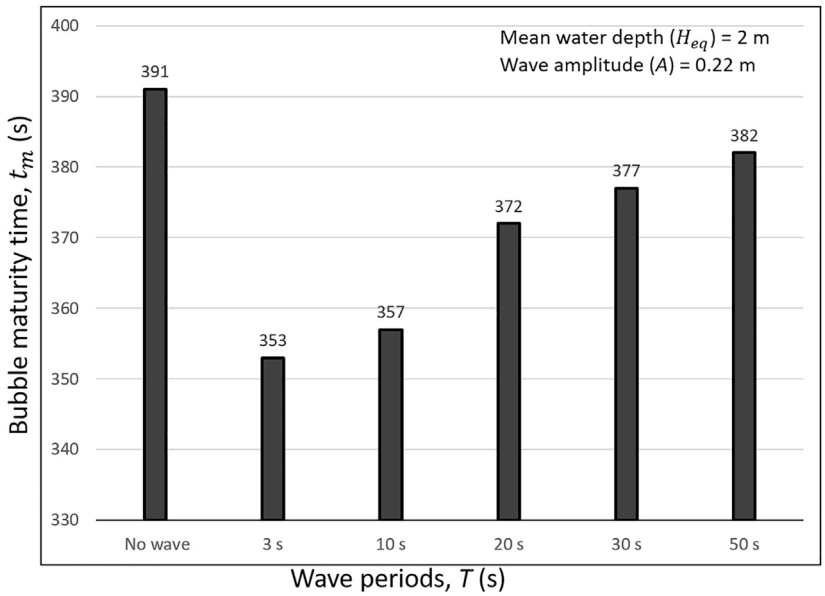

FIGURE 6 | Maturity time, t_m, of bubbles growing under a 2 m-deep water under wave amplitude (A = 0.22 m), with different wave periods, T = 3, 10, 20, 30, 50 s, and under no waves. Under shorter period waves, a bubble matures in comparatively less time (see text for detailed explanations).

at the respective sites in the presence of the surface waves under the modeled conditions.

In shallow water sites (e.g., under water depth 2 m, run 2), at the stage when bubbles gain sufficiently large heights, they are able to grow by inducing a dynamic fracturing style at each wave trough (right inset of **Figure 2**). This agrees with the principles of LEFM (Broek, 1982; Lawn, 1993; Gross and Seelig, 2017; Sirhan et al., 2019), which assert that a crack grows dynamically (runs unrestrictedly) when mechanical energy dissipated per unit crack increment exceeds the energy required to create new crack surfaces (Lawn, 1993). In our simulation (run 2), the dynamic crack propagation appeared when the crack's vertical height and total size grew beyond a critical limit (see Sirhan et al., 2019, for details). Such bubbles can unrestrictedly proceed from a dynamic growth stage to a dynamic ascent toward the sediment–water interface and can potentially escape from the sediment (Sirhan et al., 2019), if the wave action halts. Quantifying these processes provides a valuable insight into understanding the observed correlation between winds and enhanced gas effluxes at various sites with microbially mediated CH_4 (Miller and Oremland, 1988; Mattson and Likens, 1990; Keller and Stallard, 1994). For example, at Lake Gatun (Panama) average winds of 4–7 $m\,s^{-1}$ appear to enhance gas fluxes up to ~500 $ml\,m^{-2}\,h^{-1}$. This is about ~20 $ml\,m^{-2}\,h^{-1}$ under no wind conditions (in 1.4–4.5 m water depth), ~98% of which occurred by bubbling (Keller and Stallard, 1994). A gas flux of ~500 $ml\,m^{-2}\,h^{-1}$ indicates liberation of nearly 24×10^3 mature bubbles per square meter of the lake surface per hour (assuming a volume of one mature bubble as $21 \times 10^{-9}\,m^3$, following the current model) and nearly 960 bubbles in the absence of winds (neglecting CH_4 bubble volume loss in the oxidizing zone, which is negligible for rapidly rising bubbles in shallow waters, Katsman, 2019). The high contrast in the amount of the escaping bubbles indicates that they rapidly grow in size, gain maturity in the presence of waves, and are effectively able to escape the sediments. Also, the continuous persistence of intensive bubbling up to 4–6 h (Keller and Stallard, 1994) is indirect evidence of the accelerated permanent bubbles growth that ultimately reach their maturity sizes under the waves. This is especially important for cases when bubble "no-growth" condition (Algar and Boudreau, 2010) occurs within the sediment under no waves, wherein the wave action may induce a persistent bubble growth.

Moreover, intense ebullition in the presence of surface waves can be attributed to a dynamic ascent of mature bubbles, which are pulled out from their stationary positions at a gas horizon and propagate unrestrictedly toward the sediment–water interface (Katsman, 2019). In shallow water depths where wave height is comparable with the water column height (as in run S2, **Supplementary Table S3**), acceleration in bubble growth (prior to its ascent) is significant (~30% contrast in the maturity times) and can also significantly decrease the bubble lifespan. However, in other cases simulated in this study, it is smaller (~2%–12% contrast in the maturity times, **Table 1**) and contributes to the enhanced ebullition fluxes via the mechanisms discussed above.

Our results indicate that waves with large periods (for example, tides) would have a very marginal effect over the bubble maturity time (as indicated in **Figure 6**, runs 7–10), as was also suggested previously by Boudreau et al. (2001), Algar and Boudreau (2009), and Algar et al. (2011b). However, a correlation of gas emissions with falling tides observed at a cold seep offshore Vancouver Island, British Columbia, Canada, was attributed to a decreasing pressure on the sub-

bottom fluid system (Römer et al., 2016). According to our study, this should shorten the bubble growth period due to the enhanced solute transport (run 2 compared with run 4). Decreased CH_4 solubility under the decreasing tidal load can fairly enhance the bubble exsolution (Römer et al., 2016; Blouin et al., 2019).

Moreover, a long period of tidal loading could affect migration of mature bubbles toward the sediment–water interface. For example, Chanton et al. (1989) found at White Oak River estuary, North Carolina, that bubbles release from sediment were closely coupled with daily tidal activities. The rate of bubble liberation rate to the water column was found to increase significantly, when the water column declined from its highest to its lowest water level (at an ambient water depth of ~70 cm, wave amplitude ~20 cm; $\bar{r}$ ~0.285). Rising bubbles enhanced the gas flux from ~0.05 ml min^{-1} m^{-2} at a high tide to ~3 ml min^{-1} m^{-2} at a low tide (a release of respectively 12 and 144 bubbles min^{-1} m^{-2} at high and low tide, respectively; assuming a volume of one mature bubble as 21×10^{-9} m^3, following the current model). Such an enhanced ebullition can be attributed to release of bubbles from shallow gas horizons due to a decrease in overburden load at low tides (as suggested by Katsman, 2019).

Bubble growth in muds is linked to the available dissolved CH_4 concentration in the ambient sediment, which is site specific, depending on local CH_4 production rate (Martens and Klump, 1980; Abegg and Anderson, 1997; Liu et al., 2020), and also to the diffusion process, supplying solute to the bubble (see **Supplementary Equation S3**). This process is controlled by: 1) the concentration gradient of CH_4 at the bubble surface and the ambient dissolved CH_4 concentration in the pore waters; and 2) the tortuosity-corrected CH_4 diffusion coefficient in the bulk sediment. Under deeper waters, bubbles in mud grow by developing higher inner pressures, P_b (see Eq.15 in Katsman, 2015) and, hence, gain higher CH_4 concentrations at their surfaces (**Supplementary Equations S4 and S6**). This depletes the concentration gradient between the bubble surface and ambient sediment, slowing the overall growth rate of the bubble (as noticed in run 3 compared with runs 1 and 5, **Table 1**).

Ambient dissolved CH_4 concentrations in pore waters of shallow sediments is a result of a long term CH_4 production. Zero CH_4 local production rate (**Supplementary Equation S2**) is used in our simulations to avoid a permanent increase in concentrations within our small computational domain where no CH_4 consumption is prescribed. Identical CH_4 concentration boundary conditions are prescribed in all the simulations to allow a consistent comparison, associated with supersaturation under all the modeled overburden loads. In the natural settings, such quasi-steady state CH_4 concentrations (Adler et al., 2011) as those simulated in this study are produced by spatially separated CH_4 production and consumption zones under a small temporal variability in their rates that interchange the solute by diffusion (Martens and Berner, 1977). Modeling these more complex settings in a larger computational domain seem unnecessary for the bubble growth problem studied here in contrast to the bubble migration.

Additionally, the local production rates that rely on a variety of geochemical and environmental factors predefine the ambient CH_4 pore water concentrations and differ significantly between the environments (Zamanpour et al., 2020). Persistent fracture-driven bubble growth is also dependent on muddy sediment mechanical properties, suggesting that weaker sediments along with larger CH_4 production may significantly expedite bubble growth and induce its ebullition (Zamanpour et al., 2020). Wave action studied in this paper also contributes to this process.

Mud constitutes a mixture of clay- and silt-sized (<63 μm; NEN, 1989; Winterwerp and van Kesteren, 2004) particles. The hygroscopic properties of flat, small clay particles with large surface areas reduce the effective porosity and, thus, mobility of water content through the sediment's pore structure (Mitchell and Soga, 2005; Sevee, 2010). Therefore, the effective porosity of clayey muds can be much smaller than that of sandy sediment (see Sirhan et al., 2019 and references therein). It can be smaller than 20% of the effective porosity specified in the current paper (**Supplementary Table S2**). This will hamper the supply of dissolved CH_4 and will yield a slower diffusive flux to the growing bubble and, hence, slower bubble growth in muds (e.g., a week-long scale of a bubble's growth was suggested by Algar et al., 2011b). In this case, even the tides (with shorter periods than the bubble growth time scale) may expedite the bubble growth, by a more frequent exposure to the tide/wave trough loadings, according to our study.

Muddy *in situ* sediments can maintain partially annealed rise paths (Martens, 1976; Martens and Klump, 1980) formed by the upward migration of older bubbles, leading to the partial breakage of cohesive interparticle bonds (Algar et al., 2011b; Boudreau, 2012). After the initial bubbles leave the sediment, subsequent bubbles with smaller volumes may rise through these tracts, correlated with a temporal reduction in fracture toughness (Algar et al., 2011b) or tensile strength (Scandella et al., 2017) of these conduits or channels. Subsequent bubbles can have mean volumes as low as 1/200 compared with the initially rising bubble in intact sediment (Algar et al., 2011b). In the presence of wave loadings, not only the subsequent bubbles could grow faster, but the vertical conduits or channels through which they rise are also forced to dilate periodically (Scandella et al., 2011), in response to fluctuations in the effective overburden load; paving the way for their "easy" liberation into the water column (e.g., Martens and Klump, 1980; Scandella et al., 2011; Algar et al., 2011b; Scandella et al., 2017). This facilitates a "dynamic" bubble escape from the shallow gas horizon within the sediment under shorter-period waves of higher amplitude traveling in shallow water (Katsman, 2019), and explains the rise of multiple bubbles observed in the field in the presence of wind- or storm-induced surface waves (Martens, 1976; Martens and Klump, 1980; Mattson and Likens, 1990).

Natural lakes occasionally have regions with irregular bathymetry with significant depth changes, for instance, Lake Kinneret in Israel, with a maximum depth of ~40 m (Zohary et al., 2014). This enforces spatially distinct hydrostatic conditions over the lake (when the ratio, $\bar{r} = A/H_{eq}$, varies substantially due to the variability in H_{eq}). The present study suggests that in water bodies where organic matter is distributed mainly in littoral zones by river inflow (e.g., Lake Kariba in Zambia and Zimbabwe; Coche, 1974; DelSontro et al., 2011), wave loadings should contribute substantially to bubble growth (DelSontro et al., 2011) and, hence, enhance ebullition fluxes from those regions. Conversely, in aquatic sites where organic matter is concentrated in

profundal deeper zones, the slow bubble growth at CH_4-generating sites attributed to higher hydrostatic loading, could ultimately lead to the occurrence of stationary bubbles (or their slow growth over the large time scale) forming sub-surface gas horizons despite the wave action. For instance, major bubble formation is reported to occur in Kinneret sediments under the deeper waters, thus, resulting in higher gas content in the deepest zone of the lake (water depth >15 m; Uzhansky et al., 2020; Liu et al., 2020). This is attributed to refocusing of autochthonous organic matter generated during seasonal phytoplankton blooms (Zohary et al., 2014) by a complex hydrodynamic regime and lake stratification in these deep zones (Ostrovsky and Tęgowski, 2010).

There is a persistent uncertainty associated with atmospheric CH_4 contributed from shallow aquatic sediments (Kirschke et al., 2013). This is largely due to the heterogeneous spatiotemporal nature of bubble growth and migration in aquatic sediments. The current work is intended to better characterize the bubble growth in sediments subjected to periodic wave actions, which allows an evaluation of their connections to bubble emissions to the water column.

CONCLUSION

We demonstrate that periodic wave loading accelerates growth of bubbles incubated within cohesive fine-grained aquatic sediments. We analyze the specific mechanisms by means of which bubble growth is altered, compared with the calm water/no wave case. The following conclusions can be drawn:

1. Under shallow water depth, bubbles induce early as well as induce multiple fracturing under the troughs of waves passing overhead. At a later stage bubble growth can be supplemented by a dynamic fracturing regime that may contribute to initiation of unrestricted upward migration of bubbles in sediment. However, under deeper water, bubbles induce only early fracturing and no multiple fracturing from passage of wave troughs. Therefore, as the water depth increases, the effectivity of wave loadings to expedite bubble growth decreases.
2. Similar values of the wave amplitude to water depth ratio ($\bar{r} = A/H_{eq}$) induce similar rates of change in the scaled hydrostatic overburden load over sediments. Thus, the relative contrast in bubble maturity time in the presence and absence of waves, for aquatic sediments with similar $\bar{r}$, is similar.
3. With an increase in wave periods, the frequency of wave trough unloading (when early fracturing and/or multiple fracturing events occur) decreases over the entire time of bubble growth. Therefore, the time of bubble maturity increases with the increase in wave period.
4. Overall, our modeling suggests that the fastest bubble growth can be predicted when higher-amplitude short-period waves travel in shallow water (i.e., high $\bar{r}$ ratio and short wave period).

DATA AVAILABILITY STATEMENT

The original contributions presented in the study are included in the article/**Supplementary Material**, Further inquiries can be directed to the corresponding author.

AUTHOR CONTRIBUTIONS

Conceptualization, AP and RK; numerical computations, AP; result validation, RK; formal analysis, AP and RK; original draft preparation, AP; review and editing, funding acquisition and resources, RK. All authors have read and agreed to the published version of the manuscript.

FUNDING

This project was supported by the Israel Science Foundation, Grant No. 1441-14, by United States-Israel Binational Science Foundation, Grant No. 2018150, and by the Institutional Postdoctoral Fellowships from the University of Haifa, Israel.

ACKNOWLEDGMENTS

We would like to thank the Editor and two Reviewers for their contributions in enhancing this paper. Improvement of the text by Dr. John K. Hall is greatly appreciated.

SUPPLEMENTARY MATERIAL

The Supplementary Material for this article can be found online at: https://www.frontiersin.org/articles/10.3389/feart.2022.833918/full#supplementary-material

REFERENCES

Abegg, F., and Anderson, A. L. (1997). The Acoustic Turbid Layer in Muddy Sediments of Eckernföerde Bay, Western Baltic: Methane Concentration, Saturation and Bubble Characteristics. *Mar. Geology.* 137 (1-2), 137–147. doi:10.1016/S0025-3227(96)00084-9

Adler, M., Eckert, W., and Sivan, O. (2011). Quantifying Rates of Methanogenesis and Methanotrophy in Lake Kinneret Sediments (Israel) Using Pore-Water Profiles. *Limnol. Oceanogr.* 56 (4), 1525–1535. doi:10.4319/lo.2011.56.4.1525

Algar, C. K., Boudreau, B. P., and Barry, M. A. (2011a). Initial Rise of Bubbles in Cohesive Sediments by a Process of Viscoelastic Fracture. *J. Geophys. Res.* 116, B04207. doi:10.1029/2010JB008133

Algar, C. K., Boudreau, B. P., and Barry, M. A. (2011b). Release of Multiple Bubbles from Cohesive Sediments. *Geophys. Res. Lett.* 38, L08606. doi:10.1029/2011GL046870

Algar, C. K., and Boudreau, B. P. (2010). Stability of Bubbles in a Linear Elastic Medium: Implications for Bubble Growth in marine Sediments. *J. Geophys. Res.* 115, F03012. doi:10.1029/2009JF001312

Algar, C. K., and Boudreau, B. P. (2009). Transient Growth of an Isolated Bubble in Muddy, fine-grained Sediments. *Geochimica et Cosmochimica Acta* 73 (9), 2581–2591. doi:10.1016/j.gca.2009.02.008

Anderson, A. L., Abegg, F., Hawkins, J. A., Duncan, M. E., and Lyons, A. P. (1998). Bubble Populations and Acoustic Interaction with the Gassy Floor of Eckernförde Bay. *Continental Shelf Res.* 18 (14-15), 1807–1838. doi:10.1016/S0278-4343(98)00059-4

Appt, J., Imberger, J., and Kobus, H. (2004). Basin-scale Motion in Stratified Upper Lake Constance. *Limnol. Oceanogr.* 49 (4), 919–933. doi:10.4319/lo.2004.49.4.0919

Barry, M. A., Boudreau, B. P., Johnson, B. D., and Reed, A. H. (2010). First-order Description of the Mechanical Fracture Behavior of fine-grained Surficial marine Sediments during Gas Bubble Growth. *J. Geophys. Res.* 115, F04029. doi:10.1029/2010JF001833

Bastviken, D., Tranvik, L. J., Downing, J. A., Crill, P. M., and Enrich-Prast, A. (2011). Freshwater Methane Emissions Offset the continental Carbon Sink. *Science* 331 (6013), 50. doi:10.1126/science.1196808

Best, A. I., Richardson, M. D., Boudreau, B. P., Judd, A. G., Leifer, I., Lyons, A. P., et al. (2006). Shallow Seabed Methane Gas Could Pose Coastal hazard. *Eos Trans. AGU* 87 (22), 213–217. doi:10.1029/2006EO220001

Best, A. I., Tuffin, M. D. J., Dix, J. K., and Bull, J. M. (2004). Tidal Height and Frequency Dependence of Acoustic Velocity and Attenuation in Shallow Gassy marine Sediments. *J. Geophys. Res.* 109, B08101. doi:10.1029/2003JB002748

Blouin, A., Sultan, N., Callot, J.-P., and Imbert, P. (2019). Sediment Damage Caused by Gas Exsolution: A Key Mechanism for Mud Volcano Formation. *Eng. Geology.* 263, 105313. doi:10.1016/j.enggeo.2019.105313

Boudreau, B. P., Algar, C., Johnson, B. D., Croudace, I., Reed, A., Furukawa, Y., et al. (2005). Bubble Growth and Rise in Soft Sediments. *Geol* 33 (6), 517–520. doi:10.1130/G21259.1

Boudreau, B. P., Gardiner, B. S., and Johnson, B. D. (2001). Rate of Growth of Isolated Bubbles in Sediments with a Diagenetic Source of Methane. *Limnol. Oceanogr.* 46 (3), 616–622. doi:10.4319/lo.2001.46.3.0616

Boudreau, B. P. (2012). The Physics of Bubbles in Surficial, Soft, Cohesive Sediments. *Mar. Pet. Geology.* 38 (1), 1–18. doi:10.1016/j.marpetgeo.2012.07.002

Broek, D. (1982). *Elementary Engineering Fracture Mechanics*. 3rd ed. Boston, Mass: Kluwer Academic Publishers.

Bunz, S., Mienert, J., Bryn, P., and Berg, K. (2005). Fluid Flow Impact on Slope Failure from 3D Seismic Data: a Case Study in the Storegga Slide. *Basin Res.* 17 (1), 109–122. doi:10.1111/j.1365-2117.2005.00256.x

Chanton, J. P., Martens, C. S., and Kelley, C. A. (1989). Gas Transport from Methane-Saturated, Tidal Freshwater and Wetland Sediments. *Limnol. Oceanogr.* 34 (5), 807–819. doi:10.4319/lo.1989.34.5.0807

Chen, X., Schäfer, K. V. R., and Slater, L. (2017). Methane Emission through Ebullition from an Estuarine Mudflat: 2. Field Observations and Modeling of Occurrence Probability. *Water Resour. Res.* 53 (8), 6439–6453. doi:10.1002/2016WR019720

Chen, X., and Slater, L. (2016). Methane Emission through Ebullition from an Estuarine Mudflat: 1. A Conceptual Model to Explain Tidal Forcing Based on Effective Stress Changes. *Water Resour. Res.* 52 (6), 4469–4485. doi:10.1002/2015WR018058

Citarella, R., and Cricrì, G. (2010). Comparison of DBEM and FEM Crack Path Predictions in a Notched Shaft under Torsion. *Eng. Fracture Mech.* 77 (11), 1730–1749. doi:10.1016/j.engfracmech.2010.03.012

Coche, A. G. (1974). "Limnological Study of a Tropical Reservoir," in *Lake Kariba: A Man-Made Tropical Ecosystem in Central Africa*. Editors E. K. Balon and A. G. Coche (The Hague, Netherlands: Dr. W. Junk Publishers).

DelSontro, T., Kunz, M. J., Kempter, T., Wüest, A., Wehrli, B., and Senn, D. B. (2011). Spatial Heterogeneity of Methane Ebullition in a Large Tropical Reservoir. *Environ. Sci. Technol.* 45 (23), 9866–9873. doi:10.1021/es2005545

Esrig, M. I., and Kirby, R. C. (1977). Implications of Gas Content for Predicting the Stability of Submarine Slopes. *Mar. Geotechnology* 2 (1-4), 81–100. doi:10.1080/10641197709379771

Gross, D., and Seelig, T. (2017). *Fracture Mechanics: With an Introduction to Micromechanics*. 3rd ed. Berlin: Springer.

Haeckel, M., Suess, E., Wallmann, K., and Rickert, D. (2004). Rising Methane Gas Bubbles Form Massive Hydrate Layers at the Seafloor. *Geochimica et Cosmochimica Acta* 68, 4335–4345. doi:10.1016/j.gca.2004.01.018

Hofmann, H., Lorke, A., and Peeters, F. (2008). The Relative Importance of Wind and Ship Waves in the Littoral Zone of a Large lake. *Limnol. Oceanogr.* 53 (1), 368–380. doi:10.4319/lo.2008.53.1.0368

Hovland, M., Gardner, J. V., and Judd, A. G. (2002). The Significance of Pockmarks to Understanding Fluid Flow Processes and Geohazards. *Geofluids* 2 (2), 127–136. doi:10.1046/j.1468-8123.2002.00028.x

Jain, A. K., and Juanes, R. (2009). Preferential Mode of Gas Invasion in Sediments: Grain-Scale Mechanistic Model of Coupled Multiphase Fluid Flow and Sediment Mechanics. *J. Geophys. Res.* 114, B08101. doi:10.1029/2008JB006002

Johnson, B. D., Boudreau, B. P., Gardiner, B. S., and Maass, R. (2002). Mechanical Response of Sediments to Bubble Growth. *Mar. Geology.* 187 (3-4), 347–363. doi:10.1016/S0025-3227(02)00383-3

Katsman, R. (2015). Correlation of Shape and Size of Methane Bubbles in fine-grained Muddy Aquatic Sediments with Sediment Fracture Toughness. *J. Struct. Geology.* 70, 56–64. doi:10.1016/j.jsg.2014.11.002

Katsman, R. (2019). Methane Bubble Escape from Gas Horizon in Muddy Aquatic Sediment under Periodic Wave Loading. *Geophys. Res. Lett.* 46 (12), 6507–6515. doi:10.1029/2019GL083100

Katsman, R., Ostrovsky, I., and Makovsky, Y. (2013). Methane Bubble Growth in fine-grained Muddy Aquatic Sediment: Insight from Modeling. *Earth Planet. Sci. Lett.* 377-378, 336–346. doi:10.1016/j.epsl.2013.07.011

Keller, M., and Stallard, R. F. (1994). Methane Emission by Bubbling from Gatun Lake, Panama. *J. Geophys. Res.* 99 (D4), 8307–8319. doi:10.1029/92JD02170

Kirschke, S., Bousquet, P., Ciais, P., Saunois, M., Canadell, J. G., Dlugokencky, E. J., et al. (2013). Three Decades of Global Methane Sources and Sinks. *Nat. Geosci* 6, 813–823. doi:10.1038/ngeo1955

Lawn, B. R. (1993). *Fracture of Brittle Solids*. 2nd ed. New York: Cambridge University Press.

Liu, L., Sotiri, K., Dück, Y., Hilgert, S., Ostrovsky, I., Uzhansky, E., et al. (2020). The Control of Sediment Gas Accumulation on Spatial Distribution of Ebullition in Lake Kinneret. *Geo-mar Lett.* 40 (4), 453–466. doi:10.1007/s00367-019-00612-z

Martens, C. S., and Berner, R. A. (1977). Interstitial Water Chemistry of Anoxic Long Island Sound Sediments. 1. Dissolved Gases1. *Limnol. Oceanogr.* 22 (1), 10–25. doi:10.4319/lo.1977.22.1.0010

Martens, C. S. (1976). Control of Methane Sediment-Water Bubble Transport by Macroinfaunal Irrigation in Cape Lookout Bight, North Carolina. *Science* 192 (4243), 998–1000. doi:10.1126/science.192.4243.998

Martens, C. S., and Val Klump, J. (1980). Biogeochemical Cycling in an Organic-Rich Coastal marine basin-I. Methane Sediment-Water Exchange Processes. *Geochimica et Cosmochimica Acta* 44 (3), 471–490. doi:10.1016/0016-7037(80)90045-9

Mattson, M. D., and Likens, G. E. (1990). Air Pressure and Methane Fluxes. *Nature* 347 (6295), 718–719. doi:10.1038/347718b0

Miller, L. G., and Oremland, R. S. (1988). Methane Efflux from the Pelagic Regions of Four Lakes. *Glob. Biogeochem. Cycles* 2 (3), 269–277. doi:10.1029/GB002i003p00269

Mitchell, J. K., and Soga, K. (2005). *Fundamentals of Soil Behavior*. 3rd ed. Hoboken, New Jersey: John Wiley & Sons.

Nageswaran, S. (1983). *Effect of Gas Bubbles on the Seabed Behaviour*. Oxford, England: Oxford University. PhD thesis.

NEN (1989). *Geotechniek - Classificatie Van Onverharde Grondmonsters, NEN 5104*. Delft: Nederlands Normalisatie-instituut.

Ostrovsky, I., and Tęgowski, J. (2010). Hydroacoustic Analysis of Spatial and Temporal Variability of Bottom Sediment Characteristics in Lake Kinneret in Relation to Water Level Fluctuation. *Geo-mar Lett.* 30 (3), 261–269. doi:10.1007/s00367-009-0180-4

Reed, A. H., Boudreau, B. P., Algar, C., and Furukawa, Y. (2005). "Morphology of Gas Bubbles in Mud: A Microcomputed Tomographic Evaluation," in Proceedings of The International Conference "Underwater Acoustic Measurements: Technologies & Results", Heraklion, Crete, Greece, 28th June -1st July 2005. https://apps.dtic.mil/sti/citations/ADA454883.

Römer, M., Riedel, M., Scherwath, M., Heesemann, M., and Spence, G. D. (2016). Tidally Controlled Gas Bubble Emissions: A Comprehensive Study Using Long-Term Monitoring Data from the NEPTUNE Cabled Observatory Offshore Vancouver Island. *Geochem. Geophys. Geosyst.* 17 (9), 3797–3814. doi:10.1002/2016GC006528

Saunois, M., Bousquet, P., Poulter, B., Peregon, A., Ciais, P., Canadell, J. G., et al. (2016). The Global Methane Budget 2000–2012. *Earth Syst. Sci. Data* 8 (2), 697–751. doi:10.5194/essd-8-697-2016

Scandella, B. P., Delwiche, K., Hemond, H. F., and Juanes, R. (2017). Persistence of Bubble Outlets in Soft, Methane-generating Sediments. *J. Geophys. Res. Biogeosci.* 122 (6), 1298–1320. doi:10.1002/2016JG003717

Scandella, B. P., Pillsbury, L., Weber, T., Ruppel, C., Hemond, H. F., and Juanes, R. (2016). Ephemerality of Discrete Methane Vents in lake Sediments. *Geophys. Res. Lett.* 43 (9), 4374–4381. doi:10.1002/2016GL068668

Scandella, B. P., Varadharajan, C., Hemond, H. F., Ruppel, C., and Juanes, R. (2011). A Conduit Dilation Model of Methane Venting from lake Sediments. *Geophys. Res. Lett.* 38 (6), L06408. doi:10.1029/2011GL046768

Serruya, S. (1975). Wind, Water Temperature and Motions in Lake Kinneret: General Pattern. *SIL Proc* 19 (1), 73–87. doi:10.1080/03680770.1974.11896041

Sevee, J. E. (2010). Effective Porosity Measurement of a marine clay. *J. Environ. Eng.* 136 (7), 674–681. doi:10.1061/(ASCE)EE.1943-7870.0000205

Shin, H., and Santamarina, J. C. (2010). Fluid-driven Fractures in Uncemented Sediments: Underlying Particle-Level Processes. *Earth Planet. Sci. Lett.* 299 (1-2), 180–189. doi:10.1016/j.epsl.2010.08.033

Sills, G. C., and Wheeler, S. J. (1992). The Significance of Gas for Offshore Operations. *Continental Shelf Res.* 12 (10), 1239–1250. doi:10.1016/0278-4343(92)90083-V

Sills, G. C., Wheeler, S. J., Thomas, S. D., and Gardner, T. N. (1991). Behaviour of Offshore Soils Containing Gas Bubbles. *Géotechnique* 41 (2), 227–241. doi:10.1680/geot.1991.41.2.227

Sirhan, S. T., Katsman, R., and Lazar, M. (2019). Methane Bubble Ascent within fine-grained Cohesive Aquatic Sediments: Dynamics and Controlling Factors. *Environ. Sci. Technol.* 53 (11), 6320–6329. doi:10.1021/acs.est.8b06848

T. Zohary, A. Sukenik, T. Berman, and A. Nishri (Editors) (2014). *Lake Kinneret: Ecology and Management* (New York, Heidelberg, Dordrecht and London: Springer), 6.

USEPA (2010). *Methane and Nitrous Oxide Emissions from Natural Sources*. Washington DC: US Environmental Protection Agency. EPA 430-R-10–001.

Uzhansky, E., Katsnelson, B., Lunkov, A., and Ostrovsky, I. (2020). Spatial and Temporal Variability of Free Gas Content in Shallow Sediments: Lake Kinneret as a Case Study. *Geo-mar Lett.* 40 (4), 491–505. doi:10.1007/s00367-019-00629-4

Van Kessel, T., and Van Kesteren, W. G. M. (2002). Gas Production and Transport in Artificial Sludge Depots. *Waste Manag.* 22 (1), 19–28. doi:10.1016/S0956-053X(01)00021-6

Van Kesteren, W., and van Kessel, T. (2002). "Gas Bubble Nucleation and Growth in Cohesive Sediments," in *Finite Sediment Dynamics in the marine Environment*. Proceedings in Marine Science. Editors J. C. Winterwerp and C. Kranenburg (Amsterdam: Elsevier), 5 329–341. doi:10.1016/s1568-2692(02)80025-0

Wheeler, S. J. (1988). A Conceptual Model for Soils Containing Large Gas Bubbles. *Géotechnique* 38 (3), 389–397. doi:10.1680/geot.1988.38.3.389

Wheeler, S. J. (1990). Movement of Large Gas Bubbles in Unsaturated fine-grained Sediments. *Mar. Geotechnology* 9 (2), 113–129. doi:10.1080/10641199009388234

Winterwerp, J. C., and van Kesteren, W. G. M. (2004). *Introduction to the Physics of Cohesive Sediment Dynamics in the marine Environment*, 6. Amsterdam, Netherlands: Elsevier.

Zamanpour, M. K., Kaliappan, R. S., and Rockne, K. J. (2020). Gas Ebullition from Petroleum Hydrocarbons in Aquatic Sediments: A Review. *J. Environ. Manage.* 271, 110997. doi:10.1016/j.jenvman.2020.110997

Conflict of Interest: The authors declare that the research was conducted in the absence of any commercial or financial relationships that could be construed as a potential conflict of interest.

Publisher's Note: All claims expressed in this article are solely those of the authors and do not necessarily represent those of their affiliated organizations, or those of the publisher, the editors, and the reviewers. Any product that may be evaluated in this article, or claim that may be made by its manufacturer, is not guaranteed nor endorsed by the publisher.

frontiers | Frontiers in Environmental Science

ORIGINAL RESEARCH
published: 19 April 2022
doi: 10.3389/fenvs.2022.876540

Acoustic Mapping of Gas Stored in Sediments of Shallow Aquatic Systems Linked to Methane Production and Ebullition Patterns

Lediane Marcon[1,2], Klajdi Sotiri[3], Tobias Bleninger[1,4], Andreas Lorke[2], Michael Männich[4] and Stephan Hilgert[3]*

[1]Post-graduate Program on Water Resources and Environmental Engineering (PPGERHA), Federal University of Paraná, Curitiba, Brazil, [2]Institute for Environmental Sciences, University of Koblenz-Landau, Landau, Germany, [3]Institute for Water and River Basin Management, Department of Aquatic Environmental Engineering, Karlsruhe Institute of Technology, Karlsruhe, Germany, [4]Department of Environmental Engineering, Federal University of Paraná, Curitiba, Brazil

OPEN ACCESS

Edited by:
Shohei Minato, Delft University of Technology, Netherlands

Reviewed by:
Michael Anderson, University of California, Riverside, United States
Boris Katsnelson, University of Haifa, Israel

***Correspondence:**
Lediane Marcon
ledi.marcon@gmail.com

Specialty section:
This article was submitted to Environmental Informatics and Remote Sensing, a section of the journal Frontiers in Environmental Science

Received: *15 February 2022*
Accepted: *04 April 2022*
Published: *19 April 2022*

Citation:
Marcon L, Sotiri K, Bleninger T, Lorke A, Männich M and Hilgert S (2022) Acoustic Mapping of Gas Stored in Sediments of Shallow Aquatic Systems Linked to Methane Production and Ebullition Patterns. Front. Environ. Sci. 10:876540. doi: 10.3389/fenvs.2022.876540

Bubble-mediated transport is the predominant pathway of methane emissions from inland waters, which are a globally significant sources of the potent greenhouse gas to the atmosphere. High uncertainties exist in emission estimates due to high spatial and temporal variability. Acoustic methods have been applied for the spatial mapping of ebullition rates by quantification of rising gas bubbles in the water column. However, the high temporal variability of ebullition fluxes can influence estimates of mean emission rates if they are based on reduced surveys. On the other hand, echo sounding has been successfully applied to detect free gas stored in the sediment, which provide insights into the spatial variability of methane production and release. In this study, a subtropical, midsize, mesotrophic drinking water reservoir in Brazil was investigated to address the spatial and temporal variability of free gas stored in the sediment matrix. High spatial resolution maps of gas content in the sediment were estimated from echo-sounding surveys. The gas content was analyzed in relation to water depth, sediment deposition, and organic matter content (OMC) available from previous studies, to investigate its spatial variability. The analysis was further supported by measurements of potential methane production rates, porewater methane concentration, and ebullition flux. The largest gas content (above average) was found at locations with high sediment deposition, and its magnitude depended on the water depth. At shallow water depth (<10 m), high methane production rates support gas-rich sediment, and ebullition is observed to occur rather continuously. At larger water depth (>12 m), the gas stored in the sediment is released episodically during short events. An artificial neural network model was successfully trained to predict the gas content in the sediment as a function of water depth, OMC, and sediment thickness (R^2 = 0.89). Largest discrepancies were observed in the regions with steep slopes and for low areal gas content (<4 L m^{-2}). Although further improvements are proposed, we demonstrate the potential of echo-sounding for gas detection in the sediment, which combined with sediment and water body characteristics provides insights into the processes that regulate methane emissions from inland waters.

Keywords: methane ebullition, reservoirs, spatial variability, temporal variability, emission prediction, artificial neural network, echo-sound

1 INTRODUCTION

Methane (CH_4) is a potent atmospheric greenhouse gas, whose concentration has increased nearly three-fold since pre-industrial times, primarily due to anthropogenic activity (IPCC, 2013; Saunois et al., 2020). Although CH_4 emissions represent only 3% of the anthropogenic carbon dioxide emissions in units of carbon mass flux, the increase in atmospheric CH_4 concentrations contribute ~23% (~0.62 W m^{-2}) to the additional radiative forcing during the last century (Etminan et al., 2016). Recent estimates suggest that emissions from inland waters contribute nearly half of the total current CH_4 emissions from natural and anthropogenic sources (Rosentreter et al., 2021). These emissions represent the largest uncertainty in current CH_4 budgets (Saunois et al., 2020). Although freshwater CH_4 emissions are considered as natural sources, they are expected to increase in response to climate warming and to anthropogenic activities including cultural eutrophication and modifications of aquatic ecosystems (Pekel et al., 2016; DelSontro et al., 2018; Beaulieu et al., 2019; Peacock et al., 2021). Manmade reservoirs have been estimated to contribute 2–8% to freshwater CH_4 emissions (Deemer et al., 2016).

The estimation of methane emissions from inland waters is sensitive to the upscaling method and on accounting for spatial variability and temporal dynamics occurring within and among different systems (Schmiedeskamp et al., 2021). In lakes and reservoirs, methane is mainly produced in the bottom sediment by methanogenic archaea and bacteria during the process of anoxic organic matter degradation (Valentine et al., 2004; Bastviken, 2009). The buildup of methane in the sediment matrix can lead to the formation of gas voids if the dissolved gas pressure exceeds the ambient hydrostatic pressure. Gas voids have complex shapes (Boudreau et al., 2005; Liu et al., 2018), growth dynamics, and mobility (Scandella et al., 2011; Katsman et al., 2013).

In shallow waters, bubble mediated transport is the most efficient way of transferring methane to the atmosphere, bypassing methane oxidation in the oxic water column (McGinnis et al., 2006). Its temporal variability is a result of changes in local net methane production and accumulation in the sediment, and the episodic occurrence of triggers for bubble release (Varadharajan and Hemond 2012; Maecket al., 2014; Jansen et al., 2019). Whereas, spatial variability of ebullition in lakes and reservoirs results from variations of methane production rates in the sediment, which depend on sediment temperature (Wilkinson et al., 2015), sediment thickness (Maeck et al., 2013) and organic matter content (Grasset et al., 2018). Shallow areas with high deposition rates of organic matter, such as river inflow regions, have been identified as ebullition hot spots (Beaulieu et al., 2016; Linkhorst et al., 2021).

Only few existing studies related ebullition rates to measured distributions of gas voids in the sediment of inland waters. First, because of the lack of a robust and accurate method for assessing the distribution of gas voids in the sediment. Second, there are still uncertainties around methods based on the extraction of sediment cores (Dück et al., 2019b) and the large temporal variability of ebullition adds additional uncertainties to the flux estimation. Uzhansky et al. (2020) applied an inverse geoacoustic technique to derive the sound speed in the sediment for estimating sediment gas content. Katsnelson et al. (2017) applied a similar inverse geoacoustic technique for the estimation of gas content in the sediment and to investigate its spatial variability in lake Kinneret, Liu et al. (2019) correlated CH_4 pore water concentrations to acoustically derived parameters for that lake.

Nevertheless, acoustic remote sensing has been widely used in aquatic systems for obtaining information on sediment properties, such as wet bulk density and organic matter content (Sotiri et al., 2019b), grain size distribution (Tegowski, 2005), sound velocity in gassy sediments (Lunkov and Katsnelson, 2020), and total organic carbon (Neto et al., 2016). Echo sounders have also been used to quantify the ebullition flux through the detection of rising bubbles in the water column (Ostrovsky and Tegowski, 2010). Wilkens and Richardson (1998) pointed out that the acoustic propagation of soundwaves in gassy sediment depends on how sediment particles and gas voids are distributed and suggested the application of acoustic methods for obtaining bubble size distribution in the sediment. Katsnelson et al. (2017) found that the distribution of gas content in the sediment derived from an inverse geoacoustic technique agreed with sediment organic content and methane ebullition. In another study, Anderson and Martinez (2015) proposed the maximum backscatter strength at a frequency of 201 kHz to obtain gas volume distribution in the sediment per unit area, which was applied to two lakes and a reservoir in the United States.

In this study, we aim to analyze the spatial and temporal variability of gas content in the sediment of a freshwater reservoir and to investigate its relation to sediment properties and methane ebullition. Acoustic parameters derived from echo-sounding surveys are used to obtain estimates of sediment-gas-contents with the method proposed by Anderson and Martinez (2015). We then combine the estimated gas content distribution with available data on sediment properties, potential of methane production, and continuous ebullition measurements to 1) map and analyze the spatial distribution of gas content in the sediment; 2) to test different models for the prediction of gas content in the sediment from bulk properties; and 3) to investigate temporal variations of gas content in the sediment.

2 MATERIAL AND METHODS

In our analysis, we combine the results from intensive field measurements and monitoring campaigns that were conducted at Passaúna Reservoir between 2016 and 2019 and have partially

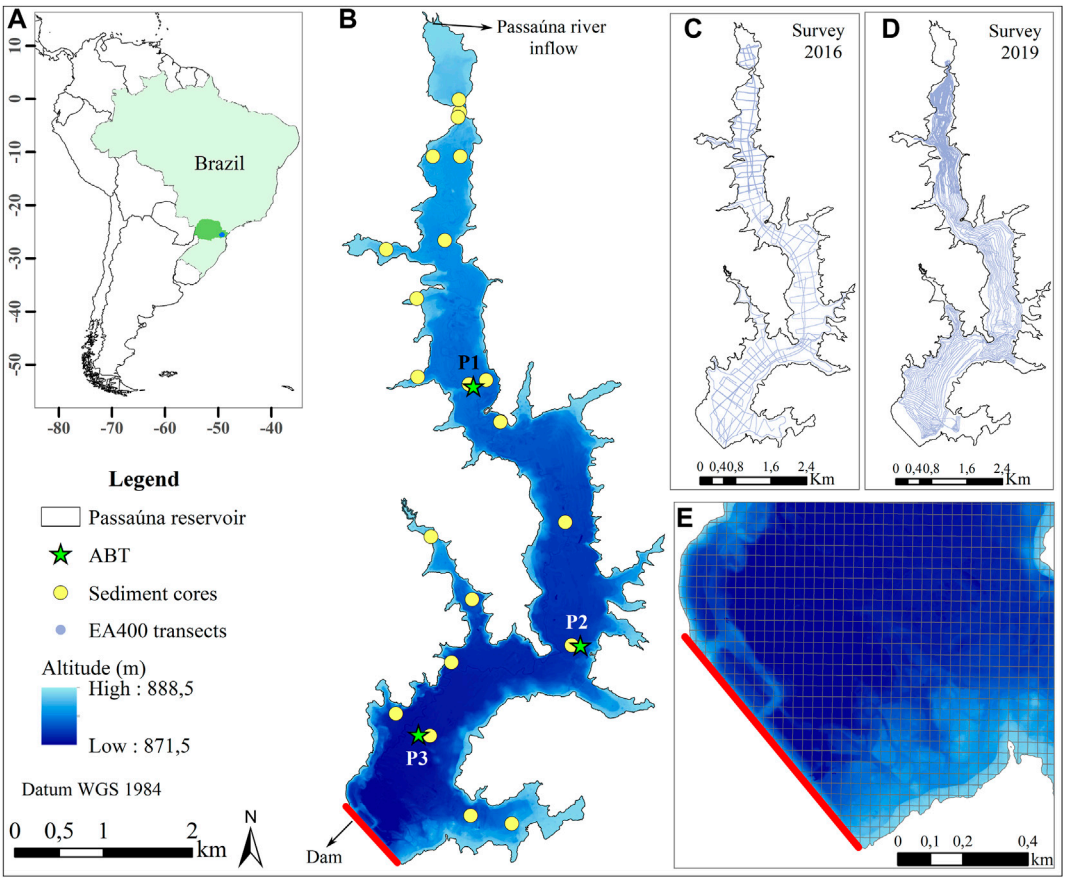

FIGURE 1 | (A) Location of the study site Passaúna Reservoir in South America; **(B)** Bathymetric map of Passaúna Reservoir and measurement locations (see legend); **(C)** echo-sounding transects during the survey in 2016; **(D)** echo-sounding transects during the 2019 survey; **(E)** Zoom to the dam area with overlaid analysis grid.

been analyzed in former studies, but with different objectives. Re-analysis of echo-sounding surveys from Sotiri et al. (2019b) and Sotiri et al. (2021) are used to derive maps of gas content in the sediment. These results are related to new data on methane porewater concentration and ebullition flux, and to existing data on sediment thickness distribution estimated by Sotiri et al. (2021), loss on ignition (LOI 550°C) mapping from Sotiri (2020), and potential methane production rates reported by Hilgert et al. (2019a).

2.1 Study Site

Passaúna Reservoir is located at the Passaúna River in the southern part of Brazil, near to the city of Curitiba (25.53°S and 49.39°W, **Figure 1**). The reservoir was constructed in 1989 for drinking water supply. Passaúna is a polymictic and mesotrophic reservoir (Xavier et al., 2017), with an average depth of 8.3 m. It is elongated in the North-South direction with approximately 10 km length and 0.6 km width. Its main inflow is the Passaúna river with an average annual discharge of 2 $m^3 s^{-1}$ (Carneiro et al., 2016).

According to the updated Köppen climate classification, the region is characterized by temperate oceanic climate (Cfb), with monthly mean temperatures below 22°C for all months and no significant precipitation difference between seasons (Beck et al., 2018). The mean annual precipitation in the region ranges between 1,400 and 1,600 mm. During measurements covering a full annual cycle conducted in 2018–2019, the reservoir water temperature ranged from 16 to 28°C, with August being the coldest month with an averaged bottom temperature of 16.5°C (Ishikawa et al., 2021). Meteorological data for this study was provided by the company SANEPAR which manages the reservoir. Weather data is logged at a station installed near to the dam.

2.2 Ebullition Flux and Pore Water Methane Concentration Measurements

Ebullition flux and pore water methane concentration were measured at three sampling sites distributed along the reservoir (**Figure 1B**). The site P1 is located most closely to the main river inflow (Passaúna River) at a water depth of 8 m. The site P2 was placed in the central region of the reservoir, near to the water intake facility, where the water depth is 12.5 m. Site P3, was placed in the deepest region of the reservoir,

approximately 810 m upstream of the dam, at a water depth of 14 m.

The ebullition measurements analyzed in the present study are a continuation of the measurements that started in 2017 and were described by Marcon et al. (2019). The ebullition flux was monitored continuously by automated bubble traps (ABT, Senect GmbH, Germany) from January to March 2019. The ABT were attached to a surface buoy and deployed at a depth of approximately 4–5 m above the sediment surface. The device consists of a 1 m diameter funnel, which collects rising gas bubbles, and a differential pressure sensor to monitor the gas volume that accumulated during fixed time intervals (30 s). The device also measured water temperature and pressure, which were used to convert the collected gas volume to standard pressure and temperature (1,013.25 mbar and 20°C). In addition, bubbles were collected from the sediment near to the ABT's location to estimate the methane fraction within the bubbles. The captured gas was transferred to vials with saturated salt solution until its analysis in the laboratory with an Ultraportable Greenhouse Gas Analyzer (UGGA, Los Gatos Research Inc.).

Dissolved methane concentration in the sediment pore water was measured with a dialysis pore water sampler (DPS) as described by Hilgert (2014) and Hölzlwimmer (2013). The DPS is a perforated aluminum frame of 70 cm height divided into 15 chambers of 4 cm width each. A cellulose membrane bag of 50 ml filled with ultra-pure water was added to each chamber. On 02 February 2019 three DPS's were deployed by divers in the bottom sediment at each ABT location (P1, P2, and P3) and positioned vertically such that seven chambers were inside the sediment and eight chambers in the overlaying water column. The devices were deployed for 5 days, to allow the ultra-pure water of the bags to equilibrate with the ambient water or pore water. Directly after recovery, a sample of 5 ml was extracted from each bag with a plastic syringe, a headspace of 5 ml was created in the syringe and after rigorous shaking, the headspace gas was transferred to vials containing saturated salt solution, previously sealed with a rubber stopper and crimp-capped. The vials were stored upside-down until analysis in the laboratory, where the methane concentration was measured with an Ultraportable Greenhouse Gas Analyzer (UGGA, Los Gatos Research Inc.) in a closed loop arrangement, as described by Wilkinson et al. (2018); Wilkinson et al. (2019b). The corresponding methane concentration in the water sample (C_{CH4} in mol L^{-1}) was calculated as proposed by Bossard et al. (1981) as:

$$C_{CH4} = \left(\frac{V_{Hs}}{V_W} \frac{\left(X_{eq} - X_{back}\right)}{RT} + X_{eq} K_H \right) \times P_{atm},$$

where V_{Hs} is the headspace volume in L, V_W is the water sample volume in L, X_{eq} and X_{back} are the methane mole fractions measured with the gas analyzer after equilibration and in the initial headspace in ppm respectively. K_H is the temperature dependent Henry gas solubility coefficient, which was calculated according to Goldenfum (2010) in mol L^{-1} atm^{-1}, T is temperature in K, R is the gas constant ($R = 0.08205$ L atm mol^{-1} K^{-1}), and P_{atm} is the atmospheric pressure in atm.

2.3 Data Re-Analyses

The following sections describe the re-analysis and additional processing of data from acoustic surveys conducted in Passaúna Reservoir during former studies.

2.3.1 Potential Methane Production

The potential methane production (PMP) in sediment samples collected at the ABT deployment locations (P1, P2, and P3, **Figure 1**) was analyzed in Hilgert et al. (2019b). The potential production rates were obtained for samples from different sediment layers, that were anaerobically incubated under laboratory conditions as described by Wilkinson et al. (2015). The potential methane production was calculated for *in-situ* sediment temperature by the relationship proposed by Wilkinson et al. (2019a)

$$PMP_T = PMP_{20}\, 10^{\theta(T-20)},$$

where PMP_T (in $mgCH_4$ L^{-1} d^{-1}) is the potential methane production rate at *in-situ* temperature T (in °C), and PMP_{20} is the rate measured during laboratorial incubations at 20°C. We used a value of the temperature coefficient θ of 0.045, as suggested by Wilkinson et al. (2019a) for incubated freshwater sediments.

The PMP was integrated over the top 10 cm sediment layer by multiplication of the averaged PMP_T with layer thickness to provide a potential areal flux (in $mgCH_4$ m^{-2} d^{-1}) at the sediment water interface (Wilkinson et al., 2019a).

2.3.2 Acoustic Parameters and Mapping of Gas Content in the Sediment

The analysis of gas content in the sediment conducted in the present study is based on echo-sounding surveys with a dual frequency (38 and 200 kHz) echo-sounder EA400 (Kongsberg Inc. 2006). The surveys have been analyzed for different aspects before (Sotiri et al., 2019a; 2019b, 2021). For the measurements, the echo-sounder was fixed 0.45 m below the water surface to an aluminum vessel, and zig-zag transects were measured along and across the reservoir (**Figure 1** panels (C) and (D)). The surveys were conducted from 26 February to 07 March 2016, and from 04 February to 07 February 2019 and covered approximate distances of 75 km in 2016 and 219 km in 2019. The echo-sounder was operated with an output power of 100 W, and pulse lengths of 0.512 and 0.128 ms for the 38 and 200 kHz channels, respectively, resulting in vertical resolutions of 0.096 and 0.024 m for the two frequencies. For an average water depth of 8.3 m, the footprint area of the acoustic beams were 5.0 m^2 (38 kHz with opening angles of 13° for the longitudinal and 21° for the transversal direction) and 0.8 m^2 (200 kHz with longitudinal and transversal opening angle of 7°). The measurement positions during the surveys were recorded using a Leica 1200 DGPS (Differential Global Positioning System) system. Vertical temperature profiles for sound speed correction were measured with a CTD–Conductivity-Temperature-Depth (CastAway®-CTD) probe.

For this study, the conversion and processing of the acoustic data was done using the Sonar5-Pro software (Lindem Data Acquisition, Oslo, Norway). Two main acoustic parameters of the first bottom echo from the 200 kHz measurements exported from the software were considered: attack and maximum backscatter strength. The values are defined for each ping

TABLE 1 | Summary of the study site characteristics and echo-sounder details of the study by Anderson and Martinez (2015) for which an empirical relationship between maximum backscatter strength and sediment gas content was established, and the corresponding information for Passaúna Reservoir.

	Anderson and Martinez (2015)			This Study
Name	**Elsinore**	**Hodges**	**Skinner**	**Passaúna**
Type	lake	reservoir	lake	reservoir
Mean depth (m)	7.5	7.5	11.2	8.3
Maximum depth (m)	11	35	24	17
Trophic state	eutrophic	eutrophic	[a]	mesotrophic
Echo-sounder		BioSonics DTX-200		Kongsberg EA 400
Frequency (kHz)		201		200
Pulse length (ms)		0.4		0.13
Ping rate (Pings per second)		5		10 (average)

[a]*Trophic state of lake Skinner was not reported by the authors, nevertheless, the lake is described to have better water quality as Elsinore and Hodges, as it is used for water supply purposes.*

(sound pulse). The envelope of the backscatter profile across the sediment-water interface is generally characterized by an increase of the backscatter strength at the sediment surface, reaching a peak amplitude (maximum backscatter), and followed by a decay with increasing depth (Sternlicht and de Moustier, 2003) (see **Supplementary Figure S1**). Attack is defined as the vertically integrated backscatter strength values occurring over a duration of one pulse length from the bottom detection point (Hilgert et al., 2016) and was used to estimate the organic content in the sediment (see below). The maximum backscatter (named as bottom peak in Sonar5-Pro), is the maximum value (dB) of the backscatter that occurred starting from the detected bottom downward and searched by the software until three transmitted pulse lengths (Balk et al., 2011).

Anderson and Martinez (2015) analyzed the acoustic parameters from three productive lakes in Southern California (United States). The authors established a relationship between maximum backscatter (measurements at 201 kHz frequency) and gas volume in the sediment (corrected to the local hydrostatic pressure) per unit area:

$$gc = e^{\left(0.327 \times S_{y\,max} + 3.48\right)},$$

where gc is gas content per unit area in L m^{-2} and $S_{y\,max}$ is the maximum backscatter strength in dB. The maximum backscatter was found to explain 93% of the variance in estimated gas content (R^2 = 0.93) (Anderson and Martinez, 2015). We adopted the proposed equation to estimate the gas content per unit area, hereinafter also referred to as gas content, in the sediment of Passaúna Reservoir, which is justified by the similar conditions in respect to water depths, trophic state, bottom sediments, and acoustic measurements in comparison to the study of Anderson and Martinez (2015) (**Table 1**). Although the pulse lengths differed between the studies, the maximum backscatter values are expected to be unaffected, and thus the application of Anderson and Martinez (2015) relationship is expected to be a valid estimate for addressing the spatial variability of sediment gas content in Passaúna Reservoir during both echo-sounding surveys (2016 and 2019). The gas content estimated for the higher-resolution survey conducted in 2019 was then analyzed in relation to organic matter content in the sediment (LOI at 550°C), sediment magnitude distribution, and bathymetry.

2.3.3 Organic Matter, Sediment Thickness, and Bathymetry

Information on the reservoir bathymetry, organic matter content in sediments, and sediment thickness distribution were taken from Sotiri et al. (2021). The reservoir bathymetry was measured with a multibeam echo sounder (WASSP F3Xi) measuring with a frequency of 160 kHz. The bathymetric map was then used in this study to derive the bottom slope.

Sediment distribution and magnitude in the reservoir was measured by Sotiri et al. (2021) with a dynamic free-fall penetrometer. The mapping of the organic matter content was derived from a former study conducted by Sotiri (2020) at Passaúna Reservoir, which was based on measurements of loss on ignition at 550°C (LOI 550°C) for more than 20 sediment cores with echo-sounding measurements at each core location. The empirical relationship proposed by Sotiri (2020) had a R^2 of 0.66, in which LOI is calculated from a polynomial equation as a function of the acoustic parameter Attack (Att),

$$LOI\ 550°\mathrm{C} = -44.6 + (-10.4\,\mathrm{Att}) + \left(-0.6\mathrm{Att}^2\right) + \left(-0.01\mathrm{Att}^3\right),$$

where Att is derived from the echo-sounder EA400 measurements at 200 kHz frequency.

The LOI is widely applied as a proxy for quantifying organic matter content in the sediment, nevertheless for clay rich sediments LOI is reported to overestimate the organic matter content, as during the burning at 550°C the loss of clay structural water and breakdown of carbonates have a share on the weight loss in addition to the organic matter (Frangipane et al., 2008). Therefore, although LOI is adopted as a proxy for organic matter distribution, its absolute values might differ from organic matter measured by other methods. However, for sediment samples from two reservoirs in a neighboring watershed, Hilgert (2014) found strong significant correlation (Pearson correlation 0.76) between LOI and organic carbon, which showed the potential to consider LOI for representing organic matter distribution as the organic carbon was not directly measured at Passaúna reservoir.

2.4 Statistical Models for Predicting the Sediment Gas Content

We developed statistical and data driven models to predict the spatial distribution of the estimated sediment gas content from maps of water depth, sediment thickness, and organic matter content (LOI 550°C) as predictor variables. The input variables and the prediction of gas content were analyzed within a spatial grid created for the reservoir based on the acoustic survey conducted in 2019. The analysis grid was created using the Geographical Information System (GIS) software ArcGIS (v. 10.2.2) with the geoprocessing tool *Fishnet*, in which we divided the surface area of Passaúna reservoir in 8,454 rectangular grid cells with dimensions of 33 m by 33 m (**Figure 1E**). Additional information about the grid selection is provided in the supplementary material (**Supplementary Figure S2**). The size of the grid cells was chosen to be sufficiently small to resolve the spatial heterogeneities of the measured parameters occurring in the sediment (longitudinal and transversal variations), and large enough to analyze all parameters in terms of spatial averages, that integrate small-scale (unresolved) structures. Mean values of all parameters (water depth, bottom slope, sediment thickness, organic content through LOI 550°C, and gas content) were calculated for all grid cells for which survey data are available.

To reduce the uncertainty of parameters derived from acoustic measurements, we excluded grid cells with an average bottom slope larger than 10° from all subsequent analysis. This is justified by the fact that the acoustic backscatter strength of sediment surfaces and sediment layers depends on the grazing angle of the soundwave (angle between incident wave and the tangent to the surface). For incidence angles of the soundwave near to the normal direction in relation to the sediment surface, scattering (attack values) dominate the backscattering, in contrast for inclined conditions (i.e., grazing angles in the range 30–60°) the volume scattering dominates (Fonseca et al., 2002). Sternlicht and de Moustier (2003) showed that the effect of slopes is lengthening the echo, resulting in prolongated rising and decaying parts of the echograms, leading to a reduction of the maximum backscatter independent from the sediment composition.

Steep slopes in Passaúna Reservoir occurred mainly near the banks or along the old Thalweg of the Passaúna River as described by Sotiri et al. (2021). The slope threshold resulted in removal of 1,034 grid cells, thus 4,651 grid cells were classified as valid cells (with data of all parameters measured and in agreement with the slope criterion).

The potential CH_4 production (PMP), dissolved CH_4 concentration in pore water, and ebullition were not extrapolated to the entire reservoir, as they were measured at only three locations. Nevertheless, the measurements are used to support our discussion on the spatial distribution and dynamics of the estimated sediment gas content.

Three multiple linear regression models were tested for gas content prediction in which the water depth, sediment thickness, and LOI 550°C were the predictors. The first model (MLR I) was a simple multiple linear regression, for the second model (MLR II) the predicted value (gas content) was log transformed, and for the third statistical model a stepwise multiple regression (SMR) with untransformed values was performed. The main difference of the stepwise multiple regression to the two other models is that predictors are included sequentially in the model and accepted if a *p-value* criterion is met for a significance level of 5%. Furthermore, interactions of the input variables are tested in this model as predictors.

The data driven model is a supervised artificial neural network (ANN). The ANN architecture had three layers, one input layer with three neurons, one hidden layer with 10 neurons, and one output layer with one neuron (**Figure 2**). The input variables were water depth, sediment thickness, and LOI 550°C. For improving the performance of the ANN, the input variables were normalized to range from 0 to 1. The Hidden layer is a processing layer where the transfer function was a hyperbolic tangent sigmoid function, in which the values transferred to the output layer will vary between − 1 to 1. The output layer is the gas content per unit area in $L\ m^{-2}$.

We used the Levenberg—Marquardt backpropagation for training of the ANN. During the training step, the algorithm randomly divided the data into three parts. 70% of the data points are used for the actual training of the neural network, 15% are used for the validation of the ANN during the training calculations to avoid overfitting, and the remaining 15% are not included for the training and are used for testing the trained model.

The model's result for gas content prediction were evaluated considering the coefficient of determination (R^2) between observed and predicted gas content and through the relative error. The relative error, which was expressed in percentage, was calculated for each grid cell as

$$Error_{relative} = \left(\frac{\left|y_{predicted} - y_{observed}\right|}{y_{observed}}\right) \times 100$$

where $y_{predicted}$ and $y_{observed}$ are the predicted and estimated gas content, respectively.

Lastly, the gas content in the sediment derived from the hydro acoustic surveys performed in 2016 and in 2019 was compared to analyze the temporal changes in different regions of the reservoir and to check the application of the prediction model from 2019 against the measurements of 2016. The temporal change in gas content between 2016 and 2019 was tested for each valid grid cell using a non-parametric hypothesis test (Wilcoxon rank sum test), considering only cells that contained 30 or more pings (sound pulses), which resulted in 1,321 cells for the comparison.

3 RESULTS

3.1 PMP, Porewater CH_4, and Ebullition Gas Flux

The highest values of potential methane production for all three sampling locations were found in the top 10 cm sediment layer. The maximum PMP values ranged from 3.4 $mgCH_4\ L^{-1}\ d^{-1}$ at P3 to 5.9 $mgCH_4\ L^{-1}\ d^{-1}$ at P2. From the near-surface layer, PMP

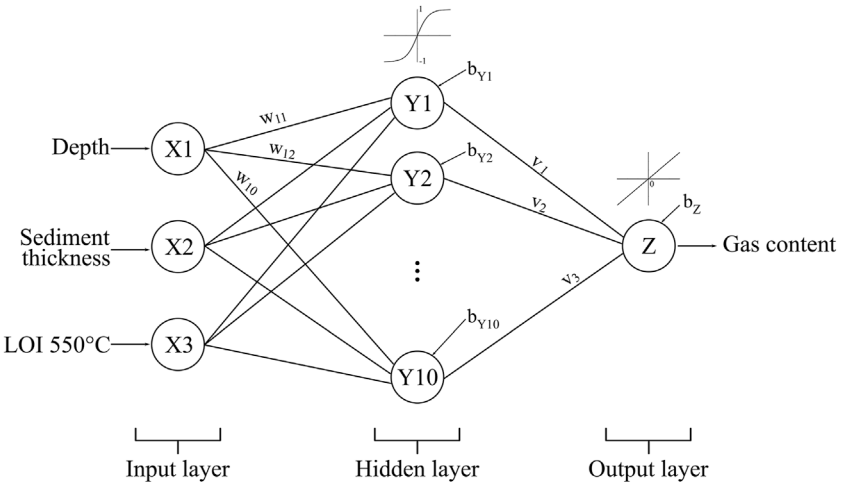

FIGURE 2 | Architecture of the artificial neural network implemented in this study for the prediction of gas content in sediment. X1, X2, and X3 are the neurons in the input layer, Y1 to Y10 are the neurons in the hidden, Z is the neuron at the output layer. w denotes the weight of each neuron connection from the input to the hidden layer, v are the weights of hidden layer connections to the output layer, and b are the bias for each neuron in the hidden and output layers.

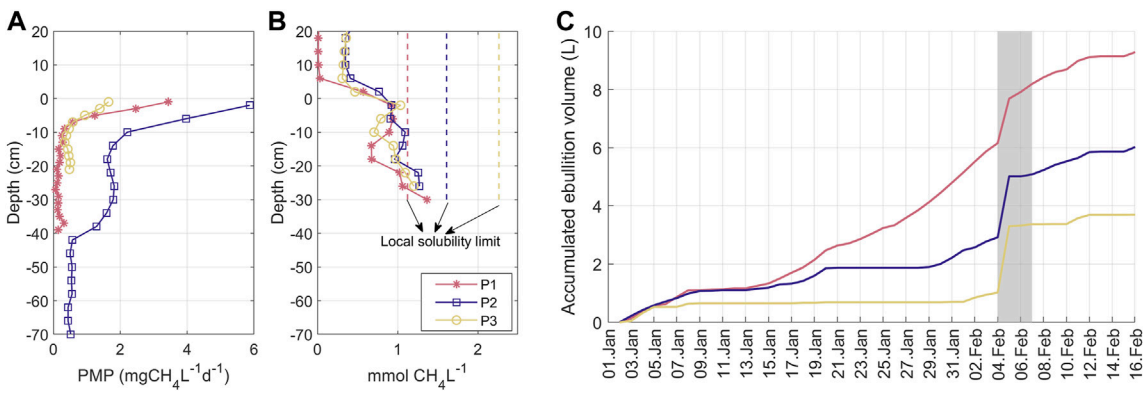

FIGURE 3 | (A) Depth profiles of potential methane production (PMP) in the sediment [data from Hilgert et al. (2019b)] **(B)** dissolved methane concentration in the pore water and overlaying water at the sediment-water interface measured in 2019. The origin of the depth-axis is at the water-sediment interface. The dashed lines show the respective CH_4 solubility limit for each location, calculated as a function of temperature, salinity, and hydrostatic pressure according to Dale et al. (2008). **(C)** Time series of accumulated gas volume recorded by the automated bubble traps (ABTs) from 1 January to 15 February 2019. The grey shaded area marks the days when the echo-sounding survey was conducted in 2019. All three panels show measurements at the three sampling locations in Passaúna Reservoir (P1, P2 and P3, see **Figure 1**).

decayed approximately exponentially with increasing depth in the sediment (**Figure 3A**). The integrated temperature corrected PMP for the top 10 cm resulted in a potential methane flux at the water-sediment interface of 306.4, 450.2, and 91.1 $mgCH_4$ m^{-2} d^{-1} at locations P1, P2, and P3 respectively.

Dissolved methane concentration was lowest in the overlying water with a strong increase in concentration towards the water-sediment interface (**Figure 3B**). In the sediment, the dissolved methane concentration continued to increase with increasing depth with comparable vertical gradients at all three locations. The maximum porewater methane concentrations were measured in the deepest DPS chamber at 25–30 cm sediment depth (1.4 mmol L^{-1} at location P1, 1.3 mmol L^{-1} at P2, and 1.2 mmol L^{-1} at P3).

Gas ebullition flux was continuously measured during 45 days, starting prior to the acoustic survey conducted in 2019. The largest amount of gas was collected by the bubble trap at location P1 (9.3 L), followed by locations P2 (6.0 L), and P3 (3.7 L) (**Figure 3C**). For the 45 measurement days, the recorded volume represents a methane ebullition flux of 118.1, 77.5, and 48.1 $mgCH_4$ m^{-2} d^{-1} at the locations P1, P2, and P3 respectively (with CH_4 fraction in bubbles collected from the three locations of 68.9 ± 6.8%).

At locations P2 and P3 (near to the water intake and in the dam region) the dynamics of gas accumulation is characterized by

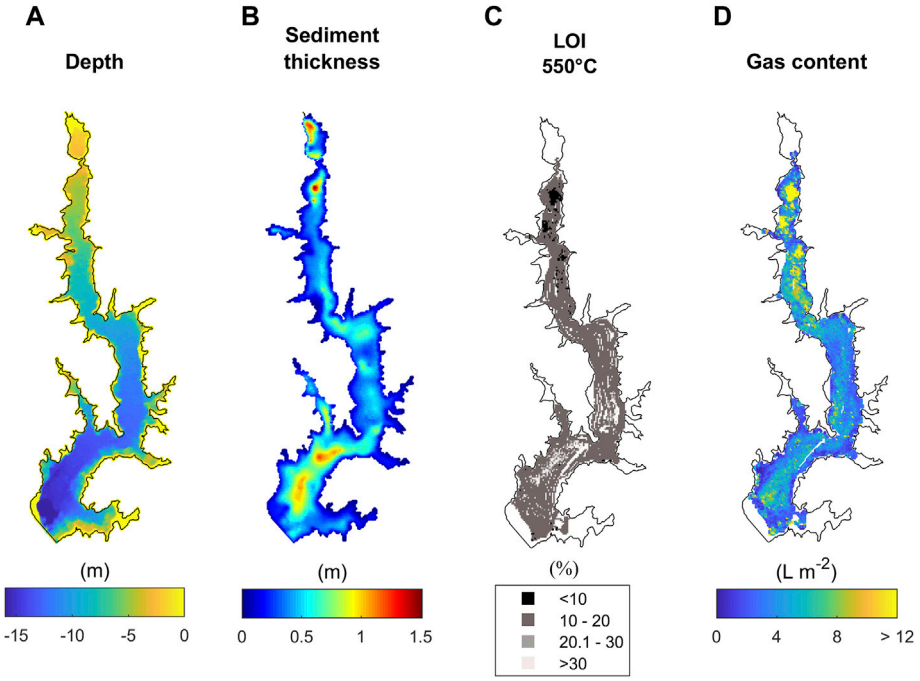

FIGURE 4 | (A) Passaúna Reservoir water depth and **(B)** sediment thickness distribution from Sotiri et al. (2021). **(C)** LOI 550°C extrapolated to the entire reservoir as a function of the acoustic parameter Attack with the relation proposed by Sotiri (2020). **(D)** Distribution of estimated gas content in the sediment estimated from the equation proposed by Anderson and Martinez (2015). All data are averaged for individual cells of the analysis grid. Blank areas in **(C)** and **(D)** indicate missing data and grid cells with high bottom slope (>10°).

stepwise increases, in which periods of several days without ebullition are interrupted by ebullition events. At P1 in contrast, more continuous ebullition events occurred throughout the measurement period, as it can be observed by the prolonged rise of the accumulated gas volume curve (**Figure 3C**). At all locations, pronounced ebullition was observed on February 5th during the period when the echo-sounding surveys were conducted. This ebullition event was associated with a weather change; from February 04th to February 07th, there was a reduction of the air temperature by approximately 10°C in comparison to the previous days (**Supplementary Figure S3**). Atmospheric pressure strongly decreased starting from February 05th. During the surveys, the water level in the reservoir decreased by 2 cm (from February 05th to February 07th) and the mean wind velocity was 1.6 ± 0.4 m s^{-1} (average ± standard deviation).

3.2 Acoustic Mapping of the Reservoir Sediment

According to Sotiri et al. (2021), the reservoir bottom is overlaid by an unconsolidated fine-grained low-density material layer. The analysis of the sediment cores showed that the bottom sediment is dominated by silt-clay grain sizes and an average loss on ignition (LOI) of 17 ± 8.5%. The averaged LOI in the sediment estimated from the acoustic parameter attack (**Figure 4C**) was 14.7 ± 4.9% for the whole reservoir, in which 3.9% of the valid grid cells had LOI of less than 10% and a minimum value of 1.8%.

The sediment magnitude estimated by Sotiri et al. (2021) varied from 0 to a maximum of 1.8 m, with highest sediment accumulation in the upstream region near to the river inflow and in the region near to the dam (see **Figure 4B**), where the water depth varies from 10 to 15 m. Average sediment thickness in the analysis grid ranged from 0 to 1.5 m, with a mean value of 0.5 ± 0.2 m.

The overall mean value of the maximum acoustic backscatter in the analyzed grid cells was −6.6 ± 2.0 dB. According to the empirical relationship proposed by Anderson and Martinez (2015), this corresponds to a mean sediment gas content for the whole reservoir of 4.6 ± 3.2 L m^{-2}. The largest values of sediment gas content were estimated for the upstream region of the reservoir, whilst the smallest values were found near the banks and in the deepest region of the reservoir in front of the dam (**Figure 4D**). Elevated (above average) gas content was also estimated for the central part of the deeper region near the dam. At the locations where the automated bubble traps were deployed, the averaged gas content in the sediment was 6.2 ± 2.1 L m^{-2}, 4.1 ± 1.6 L m^{-2}, and 5.6 ± 2.0 L m^{-2}, for the P1 to P3 respectively (**Table 2**).

3.3 Models for the Prediction of Gas Content in the Sediment

The variables water depth, which ranged from 1.4–15.35 m (8.9 ± 3.3 m), sediment thickness with values in the range of 0.03–1.5 m (0.5 ± 0.2 m), and LOI 550°C varying from 1.8–53.5% (14.7 ± 4.9%) were tested as predictor variables for the gas content in the

TABLE 2 | Parameters at the three monitoring sites P1, P2, and P3. Loss on ignition (LOI) from sediment cores were provided by Sotiri (2020); the PMP was integrated for the top 10 cm sediment layer; methane ebullition was calculated with the measured methane fraction in the gas bubbles of 68.9%; and the estimated gas content in the sediment was acoustically derived and averaged for the areas surrounding the location of each bubble trap deployment.

Site	Water depth (m)	LOI 550°C (%)	PMP Integrated ($mgCH_4\ m^{-2}\ d^{-1}$)	Methane ebullition ($mgCH_4\ m^{-2}\ d^{-1}$)	Ebullition total volume (L)	Estimated gas content in sediment ($L\ m^{-2}$)
P1	8.0	15	306.4	118.1	9.3	6.2
P2	12.5	22	450.2	77.5	6.0	4.1
P3	14.0	16	91.1	48.1	3.7	5.6

TABLE 3 | Summary of the three statistical models (MLR I, MLR II, and SMR) and the data driven model (ANN) tested for the prediction of sediment gas content (***y***) from the variables $\boldsymbol{X}1$ = water depth, $\boldsymbol{X}2$ = sediment thickness, and $\boldsymbol{X}3$ = LOI at 550°C. For the trained ANN $\boldsymbol{y\_in_k}$ denotes the input value for neuron $\boldsymbol{Y_k}$, $\boldsymbol{b_{Y_k}}$ is the bias of neuron $\boldsymbol{Y_k}$ of the hidden layer, and $\boldsymbol{x_i}$ is the value of the predictor $\boldsymbol{i}$. $\boldsymbol{y\_out_k}$ is the value calculated by the transfer function and $\boldsymbol{b_z}$ is the bias of the output neuron. $\boldsymbol{w_{ij}}$, and $\boldsymbol{v_i}$ are the weights of the neurons connecting the input to the hidden layer and the hidden layer to the output neuron, respectively.

Model	Prediction Model for gas Content	R^2	Relative Error (%)
Multiple linear regression I (MLR I)	$y = 7.35 + (-0.30 \times X1) + (5.41 \times X2) + (-0.19 \times X3)$	0.24	73.0
Multiple linear regression II (MLR II)	$\ln(y) = 1.63 + (-0.05 \times X1) + (1.06 \times X2) + (-0.03 \times X3)$	0.16	58.7
Stepwise multiple regression (SMR)	$y = 27.604 + (-2.39 \times X1) + (6.51 \times X2) + (-1.60 \times X3) + (0.26 \times X1 \times X2) + (0.15 \times X1 \times X3) + (-0.43 \times X2 \times X3)$	0.54	61.2
Artificial Neural Network (ANN)	i. $y\_in_k = b_{Y_k} + \sum_i x_i w_{ij}$ ii. $y\_out_k = \frac{2}{(1+e^{-2*y\_in_k})} - 1$ iii. $z_{in} = b_z + \sum_i y\_out_i v_i$ iv. $y = z_{in}$	0.89	42.5

sediment, which varied from 0.1 to 40.4 L m^{-2} (4.6 ± 3.2 L m^{-2}). In an exploratory analysis of the variables, a Spearman rank correlation test was applied to check statistical correlation among the parameters (see **Supplementary Figure S4**). Considering the individual correlations between gas content and the predictor variables, the strongest correlation was found between gas content and LOI (Spearman correlation $r_s = -0.58$ and $p = 0$), whereas weaker, yet significant, correlations were found between gas content and water depth ($r_s = -0.12$, $p < 0.05$) and gas content and sediment thickness ($r_s = -0.18$ $p < 0.05$).

Multiple linear regression (model MLR I) resulted in a coefficient of determination (R^2) of estimated gas content of 0.24 ($p < 0.05$for the *F-test* on the model). As the distribution of gas content in the sediment deviates from a normal distribution (**Supplementary Figure S4**), a multiple linear regression with log transformed gas content (MLR II) was tested, resulting in a R^2 of 0.16 ($p < 0.05$for the *F-test* on the model). The stepwise multiple regression (SMR) resulted in a R^2 of 0.54 ($p = 0$ for the *F-test* on the model). The full model equations are presented in **Table 3**. The trained artificial neural network (ANN) reproduced 89% of the gas content variance (R^2 = 0.89 for all data points). Comparable coefficients of determination were obtained for the test data set which was not included during the training of the ANN ($R^2 = 0.91$, **Supplementary Figure S5**).

The largest relative errors (>80%) for all models occurred near the banks at deepest region near to the dam (**Figure 5** panels (B), (C), and (D)). The averaged relative error for the 4,651 grid cells was 42.5, 61.2, and 72.96% for the ANN, SMR, and MLR I model, respectively. In addition, the linear regressions applied to the predicted and estimated gas content indicate a systematic underestimation of all three models compared to observations (**Figure 5A**). The frequency distributions of the relative error showed that for all models the most frequent relative errors obtained were smaller than 25% (see **Supplementary Figure S6** panels (A) and (B)). On the other hand, the largest relative errors values (above 500%) occurred for the grid cells with gas content per unit area of less than 4 L m^{-2}.

3.4 Temporal Variability of Gas Distribution in the Sediment

The gas content in the sediment was also calculated with the hydro acoustic data recorded during the 2016 survey. In both surveys (March 2016 and February 2019), the water column was thermally stratified, with a warmer top layer of ~26°C and colder bottom water with the lowest temperature of ~21°C at location P3 (**Supplementary Figure S7** panels (A) to (C)). Small variations of the reservoir water level were recorded during the hydro acoustic surveys of both years (3 cm in 2016 and 2 cm in 2019). However, for the 2016 survey the water level was ~1 m higher than the water level recorded during the survey of 2019.

In both years, the estimated gas content in the sediment of the reservoir was similar with mean values of 4.4 ± 3.1 L m^{-2} in 2016

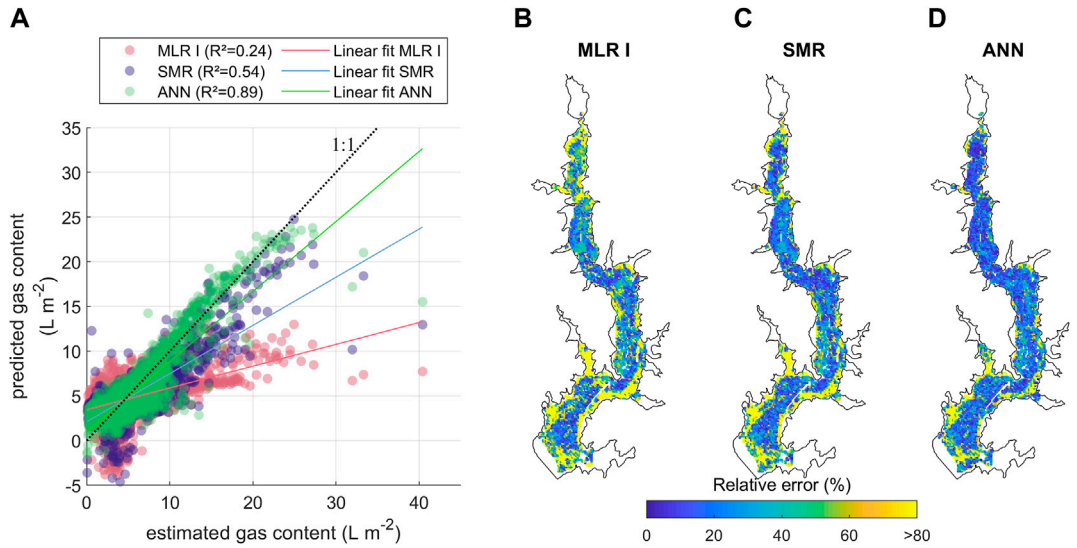

FIGURE 5 | (A) Scatter plot of predicted vs. estimated gas content and gas content for the survey in 2019 using three different empirical models (model MLR I are pink dots, SMR are the purple dots, and ANN are the green dots). Colored solid lines show linear regressions for each model with the following regression equations: MLR I $\boldsymbol{y} = 3.46 + 0.24\boldsymbol{x}$ (pink line); SMR $\boldsymbol{y} = 2.11 + 0.54\boldsymbol{x}$ (blue line), and ANN $\boldsymbol{y} = 1.02 + 0.78\boldsymbol{x}$ (green line). The dotted black line shows a 1:1 ($\boldsymbol{y} = \boldsymbol{x}$) relationship. **(B)** Spatial distribution of the relative error between predicted and estimated gas content from the multiple linear regression I (MLR I) in which 21.6% of the grid cells had errors larger than 80%. **(C)** Relative error of the predicted gas content from the stepwise multiple regression (SMR) in which 17.7% of the grid cells had errors larger than 80%. **(D)** relative error of the gas content predicted by the artificial neural network (ANN) in which 10.7% of the grid cells had error larger than 80%.

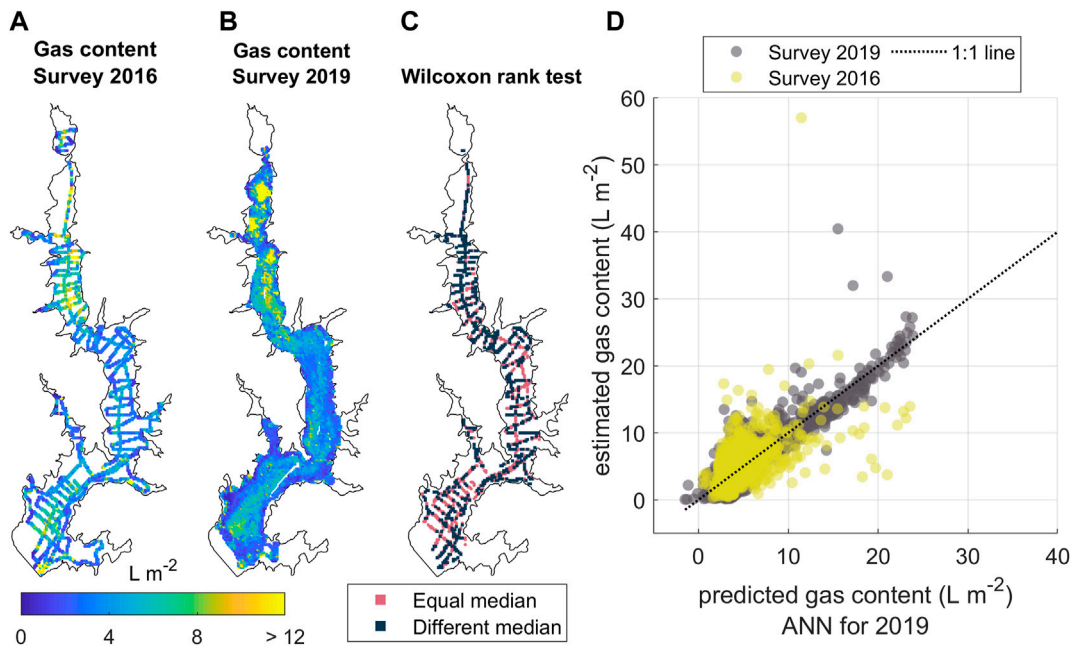

FIGURE 6 | (A) Areal gas content in the sediment for the 2016 acoustic survey. **(B)** Gas content in the sediment for the 2019 survey. **(C)** Results of the Wilcoxon rank test comparing the median gas content from both years, in which pink dots mark grid cells for which the null hypothesis of data from both years having the same distribution and equal median is accepted, and the dark blue dots mark the grid cells where the null hypothesis was rejected. **(D)** Scatter plot of observed vs. predicted gas content by the artificial neural network model with data from 2016 (yellow dots) and 2019 (grey dots). The dotted black line shows a 1:1 relationship.

and 4.6 ± 3.2 L m^{-2} in 2019. Nevertheless, the range of the spatial variation of the gas content was slightly different with larger values in 2016 (2016: 0.1–57.0 L m^{-2}; 2019: 0.1–40.4 L m^{-2}). In both years, the largest gas content was estimated for sediments in the upstream part of the reservoir. Nevertheless, the coarser spatial resolution of the echo-sounding transects conducted in

2016 (partial loss of data) did not allow for capturing the spatial structure of the gas content hotspots in this region (**Figure 6A**).

As the spatial coverage of the acoustic transects during the 2016 survey was coarser than in the 2019 measurements, only 1,321 grid cells could be considered for comparing the gas content between both years. A non-parametric hypothesis test was performed for each grid cell to verify the occurrence of a significant difference in the median gas content between both years (**Figure 6**). 48% of the cells had no significant difference in the median gas content and 52% were found to have different median gas content. Significant differences between both years occurred mainly at the shallower upstream part of the reservoir (near monitoring location P1), where the gas content was lower in 2019 compared to 2016 (**Supplementary Figure S8**). Higher gas content was detected in the reservoir stretch between the monitoring locations P1 and P3.

Lastly, we compared the predicted gas content from the artificial neural network model, which was based on 2019 data, with estimated gas content in 2016 and 2019. The gas content in the sediment in 2016 agreed with the predicted and estimated gas content of 2019, as shown in **Figure 6D** ($R^2 = 0.45$ for a linear fit with no intercept between predicted gas content from the ANN model and estimated gas content in 2016, $p = 0$ for the estimated coefficient). As previously mentioned, the upstream areas of potential high gas content in the sediment were not resolved in the 2016 survey. Nevertheless, grid cells with higher gas content in 2016 were observed in the vicinity of that region.

4 DISCUSSION

4.1 Spatial-Temporal Mapping of Sediment Gas Content

A high spatial resolution sediment gas content mapping was obtained as a function of the acoustic parameter maximum backscatter using the empirical relationship proposed by (Anderson and Martinez, 2015). The average maximum backscatter in Passaúna Reservoir (−6.6 ± 2.0 dB) is in the range of the values obtained by Anderson and Martinez (2015) for the eutrophic reservoir Hodges. The gas content ranged between 0.1 and 40.4 L m^{-2}, which for a 10 cm sediment layer represents a volumetric gas content of 0.1–40.4% (vol). The addition of gas voids to the sediment matrix results in a decrease in the sediment wet bulk density leading to instability of the sediment matrix and release of gas bubbles (Van Kessel and Van Kesteren, 2002; Liu et al., 2018). Van Kessel and Van Kesteren (2002) found that for muddy sediments, gas fraction in the range of 25–37% results in instabilities in the sediment matrix. For Passaúna reservoir less then 1% of the cells had gas content larger than 25% (**Supplementary Figure S9**). Moreover, considering the sediment wet bulk density mapped by Sotiri et al. (2019b), the regions with lower wet bulk density had relatively less gas content.

For lake Kinneret the upper limit of gas fraction in the sediment from acoustic measurements were 0.2% (Katsnelson et al., 2017) and 3.8% (Uzhansky et al., 2020). Nevertheless, for laboratory conditions Liu et al. (2016) found a maximum gas content in incubated clay sediment of 46.8% with a depth-average of 18.8% for this fine sediment. Thus, the few highest fractions of gas content found (<1% cells) at Passaúna are in the same range as the values reported by Liu et al. (2016), whereas the averaged values of gas content are one order the values found in Lake Kinneret (Uzhansky et al., 2020).

Transversal and longitudinal variation of gas content in the sediment were observed along the reservoir. Longitudinally, the largest amount of free gas in the sediment was detected in the upstream part of the reservoir, closest to the main inflow (**Figure 4D**), in a region with the largest sediment thickness and low water depth. We found that the gas content in the sediment tended to be higher in regions of preferred sedimentation (i.e. large sediment thickness), nevertheless with gas content magnitude being additionally affected by the water depth. For instance, at the deepest region of the reservoir where elevated sediment deposition was also mapped, the gas content was lower (up to 10 L m^{-2}) compared to the shallow upstream region (up to 30 L m^{-2}, **Supplementary Figure S10C**).

The occurrence of temporal change in gas content in the sediment was verified by analyzing two available echo-sounding surveys conducted 3 years apart from each other. The two surveys were done during summer at comparable water temperature and thermal stratification, and with small water level variation during both surveys, see **Supplementary Figure S7**. The mean sediment gas content was similar during both surveys (4.4 ± 3.1 L m^{-2} in 2016 and 4.6 ± 3.2 L m^{-2} in 2019). The range of its spatial variability, however, differed and the maximum gas content in 2016 (56.9 L m^{-2}) was almost 50% higher than the maximum value in 2019 (40.4 L m^{-2}). We found that 52% of the analyzed sediment area had statistically different gas content between both surveys and lower gas content in 2019 was mainly estimated for the shallower upstream region (around location P1) (see **Supplementary Figure S8**). The lower gas content can be related to the 1 m higher water level in 2016. Higher water level would represent additional hydrostatic pressure at the water-sediment interface, and thus increases the burden for bubble formation. A strong linear decrease of sediment gas content with increasing water level has been observed in Lake Kinneret, where acoustic surveys were conducted across several years (Uzhansky et al., 2020). In addition to water depth, the proximity to the main inflow Passaúna river makes this region more affected by floods events which can alter the bottom sediment conditions.

Although small-scale variability of gas content in the sediment is not resolved in this study, either due to the echo response which is resulting from a bottom area (0.8 m^2 at 8.3 m depth) and from the averaging with the grid cell; measurements with closer distributed hydro acoustic transects were important for detecting spatial patterns in the gas content. For instance, in the 2016 survey, which covered a distance 3 times shorter than the survey performed in 2019, the areas of high gas content located at the upstream region of the reservoir were not captured due to missing data points.

4.2 Methane Production, Concentration, and Ebullition

The results from the incubated sediment cores showed that the top sediment layer has the largest potential for methane

production (PMP). The finding that the top 10 cm sediment layer is most productive is in agreement with Isidorova et al. (2019), who considered sediment within the range of sediment age (<6–12 years) as still active for methane production. In Passaúna, the first 10 cm of sediment have an age of 5 years, based on the findings of Sotiri et al. (2021), who estimated a sedimentation rate of 1.9 cm yr^{-1}.

The integrated PMP over the 10 cm depth resulted in a potential methane flux at the sediment water interface of 306, 450, and 91 $mgCH_4\ m^{-2}\ d^{-1}$ at the locations P1, P2, and P3 respectively at an average sediment temperature. The PMP of Passaúna sediment is within the range found in sediments from impoundments in Germany (Wilkinson et al., 2015) and the potential fluxes at the water-sediment interface are higher than the values reported for tropical lakes in Uganda (15.4–144 $mgCH_4\ m^{-2}\ d^{-1}$) (Morana et al., 2020). The largest integrated PMP value at location P2 coincided with the highest organic matter content (indicated by LOI 550°C) from sediment cores (LOI 550°C 15% at P1, 22% at P2, and 16% at P3), which is in agreement with other studies that reported enhanced methane production for sediments with higher organic matter content (West et al., 2012; Grasset et al., 2021).

The averaged methane ebullition fluxes were 2.6, 5.8, and 1.9 times smaller than the corresponding potential flux at the water-sediment interface estimated from the integrated PMP at the three locations (see **Table 2**). The lower emission rates compared to sediment CH_4 production differ from observations by Wilkinson et al. (2015), in which the measured ebullition flux was comparable to the potential methane flux from PMP of shallow (<4 m) impoundments. We attribute this difference to the higher water depths of Passaúna Reservoir (average of 8.3 m), which can favour the diffusive flux of methane from the sediment (Langenegger et al., 2019). The transported methane can accumulate in the overlaying water where it is susceptible to oxidation or release to the atmosphere during mixing events (Vachon et al., 2019). In fact, from the dissolved methane concentrations in the water overlaying the sediment, the shallowest upstream location, which is more likely to have mixing due to its lower water depth, had methane concentrations that were one order of magnitude smaller than at the other two sites (0.02, 0.36, and 0.33 $mmolCH_4\ L^{-1}$ for locations P1, P2, and P3).

Furthermore, although location P1 had a lower integrated PMP than location P2, the methane ebullition flux was 1.5 times higher, which we attribute in addition to the enhanced diffusion of CH_4 to the water, to the larger water depth and thus, to the total pressure at the water-sediment interface. As the solubility limit of methane in the porewater increases with higher hydrostatic pressure (**Figure 3B**), larger dissolved gas concentrations are required for gas bubble formation (Bazhin, 2003; Langenegger et al., 2019). As shown in **Figure 1**, the methane concentration measured in sediment porewater at locations P2 and P3 were lower than the methane saturation limit considering the local water depth at these two sites. On the other hand, at the shallower location P1, the methane concentration in the sediment porewater was above the saturation limit for the deeper sediment layers. Lastly, an important aspect to consider, is that the PMP was obtained for laboratory conditions which may differ from the dynamic environmental conditions in the reservoir.

Ebullition is widely characterized in the literature as being highly variable in space and in time (Wik et al., 2013; Maeck et al., 2014). For Passaúna Reservoir, it was previously observed that ebullition events at the three monitoring locations where synchronized on a daily basis in which the ebullition events were triggered by large-scale forcing, such as drops in the atmospheric pressure (Marcon et al., 2019). For the 45-days time-series analyzed in the present study, a larger release of gas from the sediment was observed for February 4th to February 7th, which we could associate with the beginning of a period of decreasing atmospheric pressure (**Supplementary Figure S3**). We suggest that the drop in atmospheric pressure during the echo-sounding survey in 2019 potentially triggered gas release from the bottom sediment. Nevertheless, considering the elevated potential methane production of the bottom sediments, we assumed that the spatial patterns of gas in the sediment estimated from the echo-sounding was valid, as the ebullition trigger, in this case the atmospheric pressure drop, acted over the whole reservoir area.

Heterogeneities in gas distribution in the sediment are caused by different mutually influencing factors. Methane production in the sediment is driven by organic matter supply (Grasset et al., 2021) and its degradability (Sobek et al., 2012; West et al., 2012; Praetzel et al., 2019), as well as by temperature (Aben et al., 2017; Wilkinson et al., 2019a) and the presence of alternate electron acceptors (Bastviken, 2009). Nevertheless, not all the produced methane escapes the sediment as ebullition, as also observed at Passaúna. The methane accumulation in the sediment is affected by CH_4 oxidation (Bastviken, 2009; Martinez-Cruz et al., 2018) and its transport out of sediment by diffusive fluxes (Langenegger et al., 2019). Once the methane concentration in porewater reaches saturation gas voids are formed. The distribution and persistence of gas voids is further dependent on sediment properties such as grain size (Boudreau et al., 2005; Algar and Boudreau, 2009) and the sediment capacity to hold the free gas (Van Kessel and Van Kesteren, 2002; Liu et al., 2016). The ebullition flux (i.e., release of free gas from the sediment matrix as gas bubbles), is then a result of triggers facilitating gas release provided that there is free gas accumulated in the sediment. Drops in hydrostatic (Scandella et al., 2011; Maeck et al., 2014) and atmospheric pressure (Casper et al., 2000; Natchimuthu et al., 2016) and bottom currents (Joyce and Jewell, 2003) have been reported as ebullition triggers.

The hotspot of gas content acoustically detected at the upstream region of Passaúna Reservoir indicates a higher potential for methane ebullition, which is confirmed by the highest ebullition flux recorded at the location P1. This is in accordance with numerous other studies, reporting high CH_4 fluxes in regions near to the main inflow river with high sedimentation rates (DelSontro et al., 2011; Grinham et al., 2018; Hilgert et al., 2019a; Linkhorst et al., 2021). Whereas in the deeper locations of the reservoir (monitoring sites P2 and P3), higher methane partial pressure is required for bubble formation, **Figure 3B**, which combined with the deposition of finer sediment

particles may increase sediment cohesivity and capacity to hold the produced gas in the sediment, and thus, would explain the observed dynamics of cumulative ebullition fluxes (**Figure 3C**) at locations P2 and P3 with longer periods (days) of no ebullition.

4.3 Prediction of Gas Content in the Sediment

The capability of predicting gas content in the sediment is a useful tool for estimating methane ebullition from inland water. Large parts of the spatial variations in the estimated sediment gas content in Passaúna Reservoir could be explained by variations in more readily accessible characteristics of the reservoir and its sediment, including water depth, sediment thickness, and organic matter content of the sediment. The latter was estimated from the attack phase of the bottom echo.

Considering the relationships between gas content and individual parameters, the gas content was positively correlated with sediment thickness (r_s = 0.2 p = $3.4\,10^{-36}$) which may serve as a proxy for the deposition rate of fresh sediment (**Supplementary Figure S4**). Water depth was negatively correlated with gas content (r_s = − 0.1 p = $4.7\,10^{-17}$), and accounts for hydrostatic pressure, as well as an indirect measure of sediment temperature (colder at largest depths), dissolved oxygen concentration in the hypolimnion (formation of bottom anoxic layer is favored during periods of stratification). Surprisingly, LOI was negatively correlated to gas content (r_s = − 0.6 p = 0). However, the correlation varied with water depth (**Supplementary Figure S10**) and the negative correlation was mainly caused by data from the upstream region of the reservoir, where large sediment thickness with high gas content occurred together with lowest LOI values (<10%) were found. Gas content and LOI were acoustically derived. Although they are calculated from different parameters (maximum backscatter and attack), there is a strong dependency between maximum backscatter and attack (Spearman correlation r_s = 0.9 p = 0). On the other hand the acoustic derived LOI values agreed with the measurements from sediment samples (Sotiri, 2020). In addition, in this study the available data set didn't allow to verify the relationship of LOI and organic matter content for the sediment characteristics of Passaúna Reservoir.

As discussed above, the gas content in the sediment depends on a combination of different parameters, thus the combination of available information was tested as predictors of gas content. The multiple regression (MR) models resulted in a lower agreement between predicted and estimated gas content in comparison to the artificial neural network (ANN) model (R^2 < 0.55 for MR and R^2 = 0.89 for the ANN). The ANN model has the capability of accounting for nonlinearities among the variables and to handle high-dimensional multi-scale systems, thus identifying hidden patterns in the data set (Fausett, 1994). In the present application, this was observed in the contrasting magnitude of gas content for comparable sediment thickness regions with differing water depths.

The largest relative errors between the predicted and estimated sediment gas content were found for low gas content (<4 L m^{-2}), at the deepest region of the reservoir near to the dam, and towards the reservoir banks. Steep slopes are known to affect acoustic backscatter measurements of bottom sediments (Sternlicht and de Moustier, 2003). This supports the application of a slope threshold in our spatial analyses. On the other hand, no evident dependence of the relative error on the average slope of the respective grid cell was observed for slopes smaller than the threshold (**Supplementary Figure S6C**). In addition, compact sediments are reported to have higher maximum backscatter comparable to the acoustic response of gassy sediments (Hilgert et al., 2016; Sotiri et al., 2019a).

We contrasted the predicted gas content from the trained artificial neural network for 2019 with the estimated gas content derived from the 2016 and 2019 hydroacoustic surveys and found good agreement between both years (**Figure 6D**). In this way, we denote that even though small spatial scale heterogeneities occur, which were averaged within grid cells, the main underlaying spatial variability of gas content was maintained between the years and that the trained artificial neural network (ANN) model for gas content prediction is valid for both years. The prediction of the ANN model can be complemented and tested further with a stricter slope criterion and with the inclusion of additional relevant parameters. For instance, the origin of the organic matter (West et al., 2012), sediment exposure to dissolved oxygen concentrations (Yvon-Durocher et al., 2014), and potential of methane production in the sediment (Wilkinson et al., 2015) were reported to be relevant to methane ebullition. However, mapping of such parameters for the whole reservoir would require the combination of the *in-situ* measurements complemented with modelling or upscaling techniques.

4.4 Further Considerations and Limitations

In this study, we derived gas content in the sediment from acoustic measurements and investigate its spatial-temporal variability in a subtropical reservoir. The analysis was supported by comparing gas content estimates with spatial maps of sediment thickness, loss on ignition, and bathymetry and considering the three locations with estimated potential methane production, dissolved methane concentration in the pore water, and continuously measured ebullition flux.

The potential of using the echo-sounding approach for detecting gas content in the sediment and the need for further investigations of its spatial distribution and relation to methane fluxes was highlighted in previous studies (Anderson and Martinez, 2015; Katsnelson et al., 2017; Uzhansky et al., 2020) and corroborated in this study. One remaining challenge is the lack of direct measurements of sediment gas content under *in-situ* conditions that can serve for testing and calibration of acoustic approaches. Anderson and Martinez (2015) collected gas that was released from the sediment upon mechanical disturbance, which can be difficult when applied from a boat at larger water depth where an accurate definition of the disturbed area that contributes to the collected volume of gas is not possible. More recent studies analyzed sediment cores frozen under *in-situ* conditions [freezed cores (Dück et al., 2019a)], which are analyzed in an X-ray CT scanner to quantify the amount of free gas (Dück et al., 2019b; Liu et al., 2019). However, freezing of the sediment cores is also reported to cause mechanical disturbances in the sediment core

and result in additional bubble formation (Dück et al., 2019b). Sampling of pressurized sediment cores (e.g., Wilkens and Richardson (1998)) certainly allow for most accurate estimates of column-integrated gas content in the laboratory, yet they require the support of divers for sediment sampling and are also affected by bubbles that escape during corer penetration.

The understanding of spatial variability and temporal dynamics of methane fluxes from inland waters can be improved by knowing the process that affect the production, transport, oxidation, and emission of CH_4, which include storage of free gas in the sediment. High resolution acoustic surveys can provide estimates of sediment gas content and its spatial and temporal dynamics. Nevertheless, additional sampling locations for echo-sounding and ebullition monitoring would be required to explore relationships between gas storage and ebullition. A main advantage of acoustic gas content measurements as a proxy for ebullition flux is the high potential areal coverage of echo-sounding in comparison to the limited area sampled by bubble traps (funnel diameter of 1 m) and the possibility to measure transects covering the entire reservoir. As an additional aspect, it remains to be investigated if the uncertainties of flux measurements that are associated with temporal variability of ebullition can be reduced by accessing the gas stored in the sediment.

5 CONCLUSION

In this study, we used data from echo-sounding surveys with high spatial resolution to analyze the distribution of free gas in the sediments of a freshwater reservoir and discussed the observed spatial heterogeneity. The gas content mapping for the entire reservoir provided improved understanding of the environmental factors that regulate methane production and emission in reservoirs and other inland waters. We demonstrate a shift of the drivers of spatial variability in ebullition fluxes from proximity to the main inflow in the upstream part, to water depth and its associated effects (in deeper water occurs colder temperature at the bottom, water stratification, and higher total pressure at the water-sediment interface) in the downstream part of the reservoir. In the shallower upstream part, where the observed ebullition fluxes were the highest, the sediment gas content was highest, and the ebullition gas flux was rather continuous. In the deeper downstream sections of the reservoir, the sediment gas storage became more relevant in controlling the intermittent ebullition dynamics. The spatial variations of the estimated sediment gas content could be well predicted by sediment thickness, water depth, and sediment organic matter content (here inferred from loss on ignition) with an artificial neural network model. The largest discrepancies between estimated and predicted gas content were found for low gas content ($<4\ L\ m^{-2}$). Finally, the comparison of gas content estimates derived from acoustic surveys conducted in two different years suggested that the main pattern of the spatial variability of gas content was similar, while the total amount of gas stored in the sediment was higher during the year with higher water level. Improved sampling techniques for undisturbed measurements of gas content in aquatic sediments are required to validate and to further improve acoustic sampling techniques.

DATA AVAILABILITY STATEMENT

The original data set generated for this study is provided in the article. The re-analysis of existing data sets were from published studies which were cited in the article. Requests to access these datasets should be directed to ledi.marcon@gmail.com.

AUTHOR CONTRIBUTIONS

LM, KS, TB, AL and SH contributed to the conception of the manuscript. LM, KS, TB, MM and SH conducted field work for data Acquisition. LM, KS and SH performed data processing. LM performed the statistical analysis, models implementation and wrote the first draft of the manuscript. LM, KS, TB, AL, MM and SH contributed to the manuscript revision and editing. TB, AL, MM and SH contributed to funding acquisition.

FUNDING

The following financial support are acknowledged: Grant 02WGR1431A, in the framework of the research project MuDak-WRM (https://www.mudak-wrm.kit.edu) for data acquisition; Bleninger acknowledges the productivity stipend from the National Council for Scientific and Technological Development–CNPq, grant no. 312211/2020-1 call 09/2020; and Lorke was financially supported by the German Research Foundation (DFG, grant no. LO 1150/16-1).

ACKNOWLEDGMENTS

The authors kindly thank the German Federal Ministry of Education and Research (BMBF) for the financial support for the field measurements within Grant 02WGR1431A, in the framework of the research project MuDak-WRM (https://www.mudak-wrm.kit.edu). We cordially thank SANEPAR (Water and waste management company of Paraná) for allowing the study to be conducted at Passaúna Reservoir and for providing data. Special thanks goes to the team of PPGERHA (Post-graduate Program on Water Resources and Environmental Engineering) at the Universidade Federal do Parana and to the Environmental Physics Group at the University Koblenz-Landau for support during field and laboratorial measurements. LM thanks the Brazilian agency CAPES (Coordination for the Improvement of Higher Education Personnel) for providing a Ph.D. scholarship.

SUPPLEMENTARY MATERIAL

The Supplementary Material for this article can be found online at: https://www.frontiersin.org/articles/10.3389/fenvs.2022.876540/full#supplementary-material

REFERENCES

Aben, R. C. H., Barros, N., Van Donk, E., Frenken, T., Hilt, S., Kazanjian, G., et al. (2017). Cross continental Increase in Methane Ebullition under Climate Change. *Nat. Commun.* 8, 1–8. doi:10.1038/s41467-017-01535-y

Algar, C. K., and Boudreau, B. P. (2009). Transient Growth of an Isolated Bubble in Muddy, fine-grained Sediments. *Geochimica et Cosmochimica Acta* 73, 2581–2591. doi:10.1016/j.gca.2009.02.008

Anderson, M. A., and Martinez, D. (2015). Methane Gas in lake Bottom Sediments Quantified Using Acoustic Backscatter Strength. *J. Soils Sediments* 15, 1246–1255. doi:10.1007/s11368-015-1099-1

Balk, H., Lindem, T., and Carnero, N. S. (2011). *Sonar4 and Sonar5 Pro post Processing Systems Operator Manual.*

Bastviken, D. (2009). "Methane," in *Encyclopedia of Inland Waters* (Oxford: Elsevier), 783–805. doi:10.1016/b978-012370626-3.00117-4

Bazhin, N. M. (2003). Theoretical Consideration of Methane Emission from Sediments. *Chemosphere* 50, 191–200. doi:10.1016/S0045-6535(02)00479-4

Beaulieu, J. J., DelSontro, T., and Downing, J. A. (2019). Eutrophication Will Increase Methane Emissions from Lakes and Impoundments during the 21st century. *Nat. Commun.* 10, 3–7. doi:10.1038/s41467-019-09100-5

Beaulieu, J. J., McManus, M. G., and Nietch, C. T. (2016). Estimates of Reservoir Methane Emissions Based on a Spatially Balanced Probabilistic-survey. *Limnol. Oceanogr.* 61, S27–S40. doi:10.1002/lno.10284

Beck, H. E., Zimmermann, N. E., McVicar, T. R., Vergopolan, N., Berg, A., and Wood, E. F. (2018). Present and Future Köppen-Geiger Climate Classification Maps at 1-km Resolution. *Sci. Data* 5, 1–12. doi:10.1038/sdata.2018.214

Bossard, P., Joller, T., and Szabó, E. (1981). Die quantitative Erfassung von Methan im Seewasser. *Schweiz. Z. Hydrologie* 43, 200–211. doi:10.1007/bf02502482

Boudreau, B. P., Algar, C., Johnson, B. D., Croudace, I., Reed, A., Furukawa, Y., et al. (2005). Bubble Growth and Rise in Soft Sediments. *Geol* 33, 517–520. doi:10.1130/G21259.1

Carneiro, C., Kelderman, P., and Irvine, K. (2016). Assessment of Phosphorus Sediment-Water Exchange through Water and Mass Budget in Passaúna Reservoir (Paraná State, Brazil). *Environ. Earth Sci.* 75, 564. doi:10.1007/s12665-016-5349-3

Casper, P., Maberly, S. C., Hall, G. H., and Finlay, B. J. (2000). Fluxes of Methane and Carbon Dioxide from a Small Productive lake to the Atmosphere. *Biogeochemistry* 49, 1–19. doi:10.1023/A:1006269900174

Dale, A. W., Aguilera, D. R., Regnier, P., Fossing, H., Knab, N. J., and Jørgensen, B. B. (2008). Seasonal Dynamics of the Depth and Rate of Anaerobic Oxidation of Methane in Aarhus Bay (Denmark) Sediments. *J. Mar. Res.* 66, 127–155. doi:10.1357/002224008784815775

Deemer, B. R., Harrison, J. A., Li, S., Beaulieu, J. J., Delsontro, T., Barros, N., et al. (2016). Greenhouse Gas Emissions from Reservoir Water Surfaces: A New Global Synthesis. *Bioscience* 66, 949–964. doi:10.1093/biosci/biw117

DelSontro, T., Beaulieu, J. J., and Downing, J. A. (2018). Greenhouse Gas Emissions from Lakes and Impoundments: Upscaling in the Face of Global Change. *Limnol. Oceanogr. Lett.* 3, 64–75. doi:10.1002/lol2.10073

DelSontro, T., Kunz, M. J., Kempter, T., Wüest, A., Wehrli, B., and Senn, D. B. (2011). Spatial Heterogeneity of Methane Ebullition in a Large Tropical Reservoir. *Environ. Sci. Technol.* 45, 9866–9873. doi:10.1021/es2005545

Dück, Y., Liu, L., Lorke, A., Ostrovsky, I., Katsman, R., and Jokiel, C. (2019a). A Novel Freeze Corer for Characterization of Methane Bubbles and Assessment of Coring Disturbances. *Limnol. Oceanogr. Methods* 17, 305–319. doi:10.1002/lom3.10315

Dück, Y., Lorke, A., Jokiel, C., and Gierse, J. (2019b). Laboratory and Field Investigations on Freeze and Gravity Core Sampling and Assessment of Coring Disturbances with Implications on Gas Bubble Characterization. *Limnol. Oceanogr. Methods* 17, 585–606. doi:10.1002/lom3.10335

Etminan, M., Myhre, G., Highwood, E. J., and Shine, K. P. (2016). Radiative Forcing of Carbon Dioxide, Methane, and Nitrous Oxide: A Significant Revision of the Methane Radiative Forcing. *Geophys. Res. Lett.* 43 (12), 12614–12623. doi:10.1002/2016GL071930

Fausett, L. (1994). *Fundamentals of Neural Networks: Architctures, Algorithms, and Applications*. Prentice-Hall, 461.

Fonseca, L., Mayer, L., Orange, D., and Driscoll, N. (2002). The High-Frequency Backscattering Angular Response of Gassy Sediments: Model/data Comparison from the Eel River Margin, California. *The J. Acoust. Soc. America* 111, 2621–2631. doi:10.1121/1.1471911

Frangipane, G., Pistolato, M., Molinaroli, E., Guerzoni, S., and Tagliapietra, D. (2009). Comparison of Loss on Ignition and thermal Analysis Stepwise Methods for Determination of Sedimentary Organic Matter. *Aquat. Conserv: Mar. Freshw. Ecosyst.* 19, 24–33. doi:10.1002/aqc.970

Goldenfum, J. A. (2010). in *GHG Measurement Guidelines for Freshwater Reservoirs. The Internati Onal Hydropower Associati on (IHA).* Editor J. A. Goldenfum (London.

Grasset, C., Mendonça, R., Villamor Saucedo, G., Bastviken, D., Roland, F., and Sobek, S. (2018). Large but Variable Methane Production in Anoxic Freshwater Sediment upon Addition of Allochthonous and Autochthonous Organic Matter. *Limnol. Oceanogr.* 63, 1488–1501. doi:10.1002/lno.10786

Grasset, C., Moras, S., Isidorova, A., Couture, R. M., Linkhorst, A., and Sobek, S. (2021). An Empirical Model to Predict Methane Production in Inland Water Sediment from Particular Organic Matter Supply and Reactivity. *Limnol. Oceanogr.* 66, 3643–3655. doi:10.1002/lno.11905

Grinham, A., Dunbabin, M., and Albert, S. (2018). Importance of Sediment Organic Matter to Methane Ebullition in a Sub-tropical Freshwater Reservoir. *Sci. Total Environ.* 621, 1199–1207. doi:10.1016/j.scitotenv.2017.10.108

Hilgert, S. (2014). Analysis of Spatial and Temporal Heterogeneities of Methane Emissions of Reservoirs by Correlating Hhydro-Acoustic with Sediment Parameters. Availbleat: https://hdl.handle.net/1884/58429

Hilgert, S., Scapulatempo Fernandes, C. V., and Fuchs, S. (2019a). Redistribution of Methane Emission Hot Spots under Drawdown Conditions. *Sci. Total Environ.* 646, 958–971. doi:10.1016/j.scitotenv.2018.07.338

Hilgert, S., Sotiri, K., Marcon, L., Liu, L. I. U., Bleninger, T., Mannich, M., et al. (2019b). "Resolving Spatial Heterogeneities of Methane Ebullition Flux from a Brazilian Reservoir by Combining Hydro-Acoustic Measurements with Methane Production Potential," in 38 IAHR World Congress Water - connecting the world (Panamá). doi:10.3850/38wc092019-0866

Hilgert, S., Wagner, A., Kiemle, L., and Fuchs, S. (2016). Investigation of echo Sounding Parameters for the Characterisation of Bottom Sediments in a Sub-tropical Reservoir. *Adv. Ocean Limnol* 7, 93–105. doi:10.4081/aiol.2016.5623

Hölzlwimmer, S. (2013). *Analysis of the Relationship between Sediment Composition and Methane Concentration in Sediments of Subtropical Reservoirs Using Sediment Peepers*.

Ishikawa, M., Bleninger, T., and Lorke, A. (2021). Hydrodynamics and Mixing Mechanisms in a Subtropical Reservoir. *Inland Waters* 11, 286–301. doi:10.1080/20442041.2021.1932391

Isidorova, A., Grasset, C., Mendonça, R., and Sobek, S. (2019). Methane Formation in Tropical Reservoirs Predicted from Sediment Age and Nitrogen. *Sci. Rep.* 9, 1–9. doi:10.1038/s41598-019-47346-7

Jansen, J., Thornton, B. F., Cortes, A., Snöälv, J., Wik, M., MacIntyre, S., et al. (2019). Drivers of Diffusive lake CH₄ Emissions on Daily to Multi-Year Time Scales. *Biogeosciences Discuss.*, 1–37. doi:10.5194/bg-2019-322

Joyce, J., and Jewell, P. W. (2003). Physical Controls on Methane Ebullition from Reservoirs and Lakes. *Environ. Eng. Geosci.* 9, 167–178. doi:10.2113/9.2.167

Katsman, R., Ostrovsky, I., and Makovsky, Y. (2013). Methane Bubble Growth in fine-grained Muddy Aquatic Sediment: Insight from Modeling. *Earth Planet. Sci. Lett.* 377-378, 336–346. doi:10.1016/j.epsl.2013.07.011

Katsnelson, B., Katsman, R., Lunkov, A., and Ostrovsky, I. (2017). Acoustical Methodology for Determination of Gas Content in Aquatic Sediments, with Application to Lake Kinneret, Israel, as a Case Study. *Limnol. Oceanogr. Methods* 15, 531–541. doi:10.1002/lom3.10178

Langenegger, T., Vachon, D., Donis, D., and McGinnis, D. F. (2019). What the Bubble Knows: lake Methane Dynamics Revealed by Sediment Gas Bubble Composition. *Limnol. Oceanogr.* 64, 1526–1544. doi:10.1002/lno.11133

Linkhorst, A., Paranaíba, J. R., Mendonça, R., Rudberg, D., DelSontro, T., Barros, N., et al. (2021). Spatially Resolved Measurements in Tropical Reservoirs Reveal Elevated Methane Ebullition at River Inflows and at High Productivity. *Glob. Biogeochem. Cycles* 35, 1–16. doi:10.1029/2020GB006717

Liu, L., De Kock, T., Wilkinson, J., Cnudde, V., Xiao, S., Buchmann, C., et al. (2018). Methane Bubble Growth and Migration in Aquatic Sediments Observed by X-ray μCT. *Environ. Sci. Technol.* 52, 2007–2015. doi:10.1021/acs.est.7b06061

Liu, L., Sotiri, K., Dück, Y., Hilgert, S., Ostrovsky, I., Uzhansky, E., et al. (2019). The Control of Sediment Gas Accumulation on Spatial Distribution of Ebullition in Lake Kinneret. *Geo-mar Lett.* 40, 453–466. doi:10.1007/s00367-019-00612-z

Liu, L., Wilkinson, J., Koca, K., Buchmann, C., and Lorke, A. (2016). The Role of Sediment Structure in Gas Bubble Storage and Release. *J. Geophys. Res. Biogeosci.* 121, 1992–2005. doi:10.1002/2016JG003456

Lunkov, A. A., and Katsnelson, B. G. (2020). Using Discrete Low-Frequency Components of Shipping Noise for Gassy Sediment Characterization in Shallow Water. *J. Acoust. Soc. America* 147, EL428–EL433. doi:10.1121/10.0001277

Maeck, A., DelSontro, T., McGinnis, D. F., Fischer, H., Flury, S., Schmidt, M., et al. (2013). Sediment Trapping by Dams Creates Methane Emission Hot Spots. *Environ. Sci. Technol.* 47, 8130–8137. doi:10.1021/es4003907

Maeck, A., Hofmann, H., and Lorke, A. (2014). Pumping Methane Out of Aquatic Sediments - Ebullition Forcing Mechanisms in an Impounded River. *Biogeosciences* 11, 2925–2938. doi:10.5194/bg-11-2925-2014

Marcon, L., Bleninger, T., Männich, M., and Hilgert, S. (2019). High-frequency Measurements of Gas Ebullition in a Brazilian Subtropical Reservoir-Identification of Relevant Triggers and Seasonal Patterns. *Environ. Monit. Assess.* 191, 357. doi:10.1007/s10661-019-7498-9

Martinez-Cruz, K., Sepulveda-Jauregui, A., Casper, P., Anthony, K. W., Smemo, K. A., and Thalasso, F. (2018). Ubiquitous and Significant Anaerobic Oxidation of Methane in Freshwater lake Sediments. *Water Res.* 144, 332–340. doi:10.1016/j.watres.2018.07.053

McGinnis, D. F., Greinert, J., Artemov, Y., Beaubien, S. E., and Wüest, A. (2006). Fate of Rising Methane Bubbles in Stratified Waters: How Much Methane Reaches the Atmosphere? *J. Geophys. Res.* 111, 1–15. doi:10.1029/2005JC003183

Morana, C., Bouillon, S., Nolla-Ardèvol, V., Roland, F. A. E., Okello, W., Descy, J.-P., et al. (2020). Methane Paradox in Tropical Lakes? Sedimentary Fluxes rather Than Pelagic Production in Oxic Conditions Sustain Methanotrophy and Emissions to the Atmosphere. *Biogeosciences* 17, 5209–5221. doi:10.5194/bg-17-5209-2020

Natchimuthu, S., Sundgren, I., Gålfalk, M., Klemedtsson, L., Crill, P., Danielsson, Å., et al. (2016). Spatio-temporal Variability of lake CH4 Fluxes and its Influence on Annual Whole lake Emission Estimates. *Limnol. Oceanogr.* 61, S13–S26. doi:10.1002/lno.10222

Neto, A. A., Mota, B. B., Belem, A. L., Albuquerque, A. L., and Capilla, R. (2016). Seismic Peak Amplitude as a Predictor of TOC Content in Shallow marine Sediments. *Geo-mar Lett.* 36, 395–403. doi:10.1007/s00367-016-0449-3

Ostrovsky, I., and Tęgowski, J. (2010). Hydroacoustic Analysis of Spatial and Temporal Variability of Bottom Sediment Characteristics in Lake Kinneret in Relation to Water Level Fluctuation. *Geo-mar Lett.* 30, 261–269. doi:10.1007/s00367-009-0180-4

Peacock, M., Audet, J., Bastviken, D., Futter, M. N., Gauci, V., Grinham, A., et al. (2021). Global Importance of Methane Emissions from Drainage Ditches and Canals. *Environ. Res. Lett.* 16, 044010. doi:10.1088/1748-9326/abeb36

Pekel, J.-F., Cottam, A., Gorelick, N., and Belward, A. S. (2016). High-resolution Mapping of Global Surface Water and its Long-Term Changes. *Nature* 540, 418–422. doi:10.1038/nature20584

Praetzel, L. S. E., Plenter, N., Schilling, S., Schmiedeskamp, M., Broll, G., and Knorr, K.-H. (2019). Organic Matter and Sediment Properties Determine in-lake Variability of Sediment CO₂ and CH₄ Production and Emissions of a Small and Shallow lake. *Biogeosciences Discuss.*, 1–39. doi:10.5194/bg-2019-284

Rosentreter, J. A., Borges, A. V., Deemer, B. R., Holgerson, M. A., Liu, S., Song, C., et al. (2021). Half of Global Methane Emissions Come from Highly Variable Aquatic Ecosystem Sources. *Nat. Geosci.* 14, 225–230. doi:10.1038/s41561-021-00715-2

Saunois, M., Stavert, A. R., Poulter, B., Bousquet, P., Canadell, J. G., Jackson, R. B., et al. (2020). The Global Methane Budget 2000–2017. *Earth Syst. Sci. Data* 12, 1561–1623. doi:10.5194/essd-12-1561-2020

Scandella, B. P., Varadharajan, C., Hemond, H. F., Ruppel, C., and Juanes, R. (2011). A Conduit Dilation Model of Methane Venting from lake Sediments. *Geophys. Res. Lett.* 38, a–n. doi:10.1029/2011GL046768

Schmiedeskamp, M., Praetzel, L. S. E., Bastviken, D., and Knorr, K. H. (2021). Whole-lake Methane Emissions from Two Temperate Shallow Lakes with Fluctuating Water Levels: Relevance of Spatiotemporal Patterns. *Limnol. Oceanogr.* 66, 2455–2469. doi:10.1002/lno.11764

Sobek, S., Delsontro, T., Wongfun, N., and Wehrli, B. (2012). Extreme Organic Carbon Burial Fuels Intense Methane Bubbling in a Temperate Reservoir. *Geophys. Res. Lett.* 39, a–n. doi:10.1029/2011GL050144

Sotiri, K., Hilgert, S., and Fuchs, S. (2019a). Derivation of a Hydro-Acoustic Sediment Classification Methodology from an Extensive Dataset of Sixreservoirs. *Water Connect. World* 38, 51–60. doi:10.3850/38wc092019-0549

Sotiri, K., Hilgert, S., and Fuchs, S. (2019b). Sediment Classification in a Brazilian Reservoir: Pros and Cons of Parametric Low Frequencies. *Adv. Ocean Limnol* 10. doi:10.4081/aiol.2019.7953

Sotiri, K., Hilgert, S., Mannich, M., Bleninger, T., and Fuchs, S. (2021). Implementation of Comparative Detection Approaches for the Accurate Assessment of Sediment Thickness and Sediment Volume in the Passaúna Reservoir. *J. Environ. Manage.* 287, 112298. doi:10.1016/j.jenvman.2021.112298

Sotiri, K. (2020). *Integrated Sediment Yield and Stock Assessment for the Passaúna Reservoir, Brazil*.doi:10.5445/IR/1000127716

Sternlicht, D. D., and de Moustier, C. P. (2003). Time-dependent Seafloor Acoustic Backscatter (10-100 kHz). *J. Acoust. Soc. Am.* 114, 2709. doi:10.1121/1.1608018

Tęgowski, J. (2005). Acoustical Classification of the Bottom Sediments in the Southern Baltic Sea. *Quat. Int.* 130, 153–161. doi:10.1016/j.quaint.2004.04.038

IPCC (2013). in *Contribution of Working Group I to the Fifth Assessment Report of the Intergovernmental Panel on Climate Change*. T. F. Stocker, D. Qin, G. K. Plattner, M. M. B. Tignor, S. K. Allen, J. Boschung, et al. (Cambridge, United Kingdom and New York: Cambridge University Press). doi:10.1017/CBO9781107415324.Summary

Uzhansky, E., Katsnelson, B., Lunkov, A., and Ostrovsky, I. (2020). Spatial and Temporal Variability of Free Gas Content in Shallow Sediments: Lake Kinneret as a Case Study. *Geo-mar Lett.* 40, 491–505. doi:10.1007/s00367-019-00629-4

Vachon, D., Langenegger, T., Donis, D., and McGinnis, D. F. (2019). Influence of Water Column Stratification and Mixing Patterns on the Fate of Methane Produced in Deep Sediments of a Small Eutrophic lake. *Limnol. Oceanogr.* 64, 2114–2128. doi:10.1002/lno.11172

Valentine, D. L., Chidthaisong, A., Rice, A., Reeburgh, W. S., and Tyler, S. C. (2004). Carbon and Hydrogen Isotope Fractionation by Moderately Thermophilic Methanogens 1 1Associate Editor: N. E. Ostrom. *Geochimica et Cosmochimica Acta* 68, 1571–1590. doi:10.1016/j.gca.2003.10.012

Van Kessel, T., and Van Kesteren, W. G. M. (2002). Gas Production and Transport in Artificial Sludge Depots. *Waste Management* 22, 19–28. doi:10.1016/S0956-053X(01)00021-6

Varadharajan, C., and Hemond, H. F. (2012). Time-series Analysis of High-Resolution Ebullition Fluxes from a Stratified, Freshwater lake. *J. Geophys. Res. Biogeosciences* 117. doi:10.1029/2011jg001866

West, W. E., Coloso, J. J., and Jones, S. E. (2012). Effects of Algal and Terrestrial Carbon on Methane Production Rates and Methanogen Community Structure in a Temperate lake Sediment. *Freshw. Biol.* 57, 949–955. doi:10.1111/j.1365-2427.2012.02755.x

Wik, M., Crill, P. M., Varner, R. K., and Bastviken, D. (2013). Multiyear Measurements of Ebullitive Methane Flux from Three Subarctic Lakes. *J. Geophys. Res. Biogeosci.* 118, 1307–1321. doi:10.1002/jgrg.20103

Wilkens, R. H., and Richardson, M. D. (1998). The Influence of Gas Bubbles on Sediment Acoustic Properties: *In Situ*, Laboratory, and Theoretical Results from Eckernförde Bay, Baltic Sea. *Continental Shelf Res.* 18, 1859–1892. doi:10.1016/S0278-4343(98)00061-2

Wilkinson, J., Bodmer, P., and Lorke, A. (2019a). Methane Dynamics and thermal Response in Impoundments of the Rhine River, Germany. *Sci. Total Environ.* 659, 1045–1057. doi:10.1016/j.scitotenv.2018.12.424

Wilkinson, J., Bors, C., Burgis, F., Lorke, A., and Bodmer, P. (2019b). Correction: Measuring CO2 and CH4 with a Portable Gas Analyzer: Closed-Loop Operation, Optimization and Assessment. *PLoS One* 14, e0206080. doi:10.1371/journal.pone.0206080

Wilkinson, J., Bors, C., Burgis, F., Lorke, A., and Bodmer, P. (2018). Measuring CO2 and CH4 with a Portable Gas Analyzer: Closed-Loop Operation, Optimization and Assessment. *PLoS One* 13, e0193973–16. doi:10.1371/journal.pone.0193973

Wilkinson, J., Maeck, A., Alshboul, Z., and Lorke, A. (2015). Continuous Seasonal River Ebullition Measurements Linked to Sediment Methane Formation. *Environ. Sci. Technol.* 49, 13121–13129. doi:10.1021/acs.est.5b01525

Xavier, C. da. F., Dias, L. N., and Brunkow, R. F. (2017). *Qualidade das águas dos reservatórios do estado do Paraná*. Curitiba.

Yvon-Durocher, G., Allen, A. P., Bastviken, D., Conrad, R., Gudasz, C., St-Pierre, A., et al. (2014). Methane Fluxes Show Consistent Temperature Dependence across Microbial to Ecosystem Scales. *Nature* 507, 488–491. doi:10.1038/nature13164

Conflict of Interest: The authors declare that the research was conducted in the absence of any commercial or financial relationships that could be construed as a potential conflict of interest.

Publisher's Note: All claims expressed in this article are solely those of the authors and do not necessarily represent those of their affiliated organizations, or those of the publisher, the editors and the reviewers. Any product that may be evaluated in this article, or claim that may be made by its manufacturer, is not guaranteed or endorsed by the publisher.

frontiers | Frontiers in Earth Science

ORIGINAL RESEARCH
published: 27 April 2022
doi: 10.3389/feart.2022.852853

Barkley Canyon Gas Hydrates: A Synthesis Based on Two Decades of Seafloor Observation and Remote Sensing

M. Riedel[1], M. Scherwath[2], M. Römer[3], C. K. Paull[4], E. M. Lundsten[4], D. Caress[4], P. G. Brewer[4], J. W. Pohlman[5], L. L. Lapham[6], N. R. Chapman[7], M. J. Whiticar[7], G. D. Spence[7], R. J. Enkin[8] and K. Douglas[8]*

[1]GEOMAR Helmholtz Centre for Ocean Research Kiel, Kiel, Germany, [2]Ocean Networks Canada, University of Victoria, Victoria, BC, Canada, [3]MARUM - Center for Environmental Sciences and Department of Geosciences at the University of Bremen, Bremen, Germany, [4]Monterey Bay Aquarium Research Institute, Moss Landing, CA, United States, [5]U.S. Geological Survey, Woods Hole Coastal and Marine Science Center, Woods Hole, MA, United States, [6]University of Maryland Center for Environmental Science, Chesapeake Biological Laboratory, Solomons, MD, United States, [7]School of Earth and Ocean Sciences, University of Victoria, Victoria, BC, Canada, [8]Geological Survey of Canada, Pacific, Victoria, BC, Canada

OPEN ACCESS

Edited by:
Davide Oppo, University of Louisiana at Lafayette, United States

Reviewed by:
Dong Feng, Shanghai Ocean University, China
Peter Feldens, Leibniz Institute for Baltic Sea Research (LG), Germany

***Correspondence:**
M. Riedel
mriedel@geomar.de

Specialty section:
This article was submitted to Marine Geoscience, a section of the journal Frontiers in Earth Science

Received: *11 January 2022*
Accepted: *24 February 2022*
Published: *27 April 2022*

Citation:
Riedel M, Scherwath M, Römer M, Paull CK, Lundsten EM, Caress D, Brewer PG, Pohlman JW, Lapham LL, Chapman NR, Whiticar MJ, Spence GD, Enkin RJ and Douglas K (2022) Barkley Canyon Gas Hydrates: A Synthesis Based on Two Decades of Seafloor Observation and Remote Sensing. Front. Earth Sci. 10:852853. doi: 10.3389/feart.2022.852853

Barkley Canyon is one of the few known sites worldwide with the occurrence of thermogenic gas seepage and formation of structure-II and structure-H gas hydrate mounds on the seafloor. This site is the location of continuous seafloor monitoring as part of the Ocean Networks Canada (ONC) cabled observatory off the west coast off Vancouver Island, British Columbia, Canada. We combine repeat remotely operated vehicle (ROV) seafloor video observations, mapping with an autonomous underwater vehicle (AUV), ship-, ROV-, and AUV-based identification of gas flares, as well as seismic and Chirp data to investigate the distribution of fluid migration pathways. Geologically, the site with the prominent gas hydrate mounds and associated fluid seepage is covering an area of ~0.15 km^2 and is situated on a remnant of a rotated fault block that had slipped off the steep flanks of the north-east facing canyon wall. The gas hydrate mounds, nearly constant in dimension over the entire observation period, are associated with gas and oil seepage and surrounded by debris of chemosynthetic communities and authigenic carbonate. The formation of gas hydrate at and near the seafloor requires additional accommodation space created by forming blisters at the seafloor that displace the regular sediments. An additional zone located centrally on the rotated fault block with more diffuse seepage (~0.02 km^2 in extent) has been identified with no visible mounds, but with bacterial mats, small carbonate concretions, and clam beds. Gas venting is seen acoustically in the water column up to a depth of ~300 m. However, acoustic water-column imaging during coring and ROV dives showed rising gas bubbles to much shallower depth, even <50 m, likely a result of degassing of rising oil droplets, which themselves cannot be seen acoustically. Combining all observations, the location of the gas hydrate mounds is controlled by a combination of fault-focused fluid migration from a deeper reservoir and fluid seepage along more permeable strata within the rotated slope block. Fluids must be provided continuously to allow the sustained presence of the gas hydrate mounds at the seafloor.

Keywords: gas hydrate, fluid seepage, Barkley Canyon hydrates, AUV (autonomous underwater vehicle), ROV (remote operated vehicle)

INTRODUCTION AND GEOLOGICAL BACKGROUND

Gas hydrates (clathrates) are solid substances composed of an assemblage of rigid cages of water molecules that enclose molecules of natural gas (Sloan and Koh, 2008). Due to their dependency on high pressure and low temperature regimes for stability, natural occurrences of gas hydrates are limited to continental slopes (>~ 500 m, e.g., McIver, 1981; Klauda and Sandler, 2005) or polar terrestrial regions in association with permafrost (e.g., Ruppel, 2007, 2015). Depending on the type of gas molecule trapped, natural gas hydrates occur in three types of structures: structure-I (s-I) is associated with mostly methane as the guest molecule, structure-II (s-II) and structure-H (s-H) occur if larger molecules (ethane, propane, etc.) are incorporated into the water cages (Sloan and Koh, 2008). Estimates of the amount of carbon sequestered by natural gas hydrate globally range over four orders of magnitude from as low as ~0.2×10^{15} m^3 (100 Gt carbon; Soloviev, 2002) to as high as ~$3{,}000 \times 10^{15}$ m^3 (1.6×10^6 Gt carbon, Trofimuk et al., 1973). A complete historic evolution of all global estimates from the early 1970s until 2010 was summarized by Boswell and Collett (2011) who also highlighted the current scientific advances made in assessing the technically recoverable fraction of methane from hydrates as an energy resource. The global recoverable volumes of methane from hydrate were estimated to be in the order of ~3×10^{13} m^3, or an equivalent 1.5×10^3 Gt of carbon (Boswell and Collett, 2011). Additional estimates of the total amount of methane found in gas hydrates was provided in a review by Ruppel and Kessler (2017).

Because methane bound by gas hydrate is a potent greenhouse gas with a warming potential 25 times greater than CO_2 over a 100-years time span, transferring a portion of gas hydrate methane to the atmosphere has the potential to enhance global warming (e.g., Kennett et al., 2003; Buffett and Archer, 2004; Archer et al., 2009). However, presently there is no evidence for a significant atmospheric contribution from gas hydrate (Ruppel and Kessler, 2017).

Most naturally occurring marine gas hydrate accumulations are formed from gas generated during the microbially-mediated biodegradation of sediment organic matter and petroleum at temperatures typically below 80°C and depths less than 2 km from the seafloor (e.g., Kvenvolden and McMenamin, 1980; Kvenvolden, 1988; Milkov, 2005; Ruppel and Kessler, 2017). Only a few sites are known worldwide, where gas hydrates contain significant amounts of thermogenic hydrocarbons formed during the breakdown of organic matter at higher temperature (typically above 150°C) and greater depth (>5 km below the seafloor). Examples of settings with thermogenic gas hydrate are within the Gulf of Mexico (e.g., Brooks et al., 1984; Sassen and MacDonald, 1994, 1999, 2001; MacDonald et al., 2003), the Gumusut-Kakap province off Borneo (e.g., Paganoni et al., 2016), near the Eel Canyon of Northern California (e.g., Gwiazda et al., 2016) and Barkley Canyon (e.g., Pohlman et al., 2005), which is the focus of this study. There are also suggestions of potential combinations of microbial and thermogenic contributions to gas hydrate accumulations, such as off the Falkland Islands (Foschi et al., 2019), off New Zealand (Kroeger et al., 2015), or at the Umitaka Spur, Japan Sea (Lu et al., 2008; Freire et al., 2011). Microbial and thermogenic gases are typically distinguished by the carbon ($^{13}C/^{12}C$) and hydrogen (D/H) stable isotope ratios of methane and the molecular and isotopic composition of associated gases. Microbial gases are predominantly methane that is enriched with ^{12}C and H, while thermogenic gases consist of methane enriched with ^{13}C isotope as well higher hydrocarbons (C_2-C_5) formed during the thermal breakdown of organic matter (Bernard et al., 1976; Whiticar et al., 1986; Whiticar, 1999). However, these generalizations are viewed as guidelines. Recent reviews and studies have shown the boundaries for gas classification overlap (e.g., Milkov and Etopie, 2018; Whiticar 2021), making interpretation of gas sources more complex.

Remote detection of natural gas hydrates in sediments along continental margins is often suggested based on the identification of a bottom-simulating reflector (BSR) in seismic reflection data (e.g., Shipley et al., 1979; Hyndman and Spence, 1992; Holbrook, 2001). The BSR in general marks the base of the gas hydrate stability zone and free gas occurrences underneath. This results in a reflection polarity opposite to the seafloor from the velocity inversion at this interface (e.g., Haacke et al., 2007; Spence et al., 2010). At some gas hydrate occurrences with a thermogenic gas contribution, a second (deeper) BSR at the base of the structure-II gas hydrates has been observed (e.g., Laird and Morley, 2011; Paganoni et al., 2016; Qian et al., 2018). Other incidences of multiple BSRs have been attributed to paleo climate conditions linked to glacial-interglacial variations in sea level and sea bottom temperature (e.g., Bangs et al., 2005; Auguy et al., 2017; Zander et al., 2017), or possibly channel migration and/or erosion (e.g., Hornbach et al., 2003; Zhang et al., 2020), or uplift from tectonic forces (e.g., Foucher et al., 2002; Pecher et al., 2014).

Natural gas hydrates were first suggested to occur within the accretionary prism sediments of the northern Cascadia margin based on BSRs seen in regional multichannel seismic (MCS) reflection data (Spence et al., 1991; Hyndman and Davis, 1992; Hyndman and Spence, 1992). This early discovery was followed up by numerous additional conventional and high-frequency deep-towed seismic (Chapman et al., 2002), heat-flow, and electromagnetic investigations to describe the regional distribution of gas hydrates along the margin (see summaries and references in Spence et al., 2000; Hyndman et al., 2001; Riedel et al., 2022). In addition, scientific drilling, coring, and logging was conducted during Ocean Drilling Program (ODP) Leg 146 (Westbrook et al., 1994) and Integrated Ocean Drilling Program Expedition 311 (Riedel et al., 2006a, 2010b; Pohlman et al., 2009) describing the gas hydrate system across the prism. A more recent focus of gas hydrate-related scientific studies off northern Cascadia is on cold vent systems and gas venting (e.g., Riedel et al., 2006b; Lapham et al., 2013; Pohlman et al., 2013; Wilson et al., 2015; Römer et al., 2016; Riedel et al., 2018; Scherwath et al., 2019).

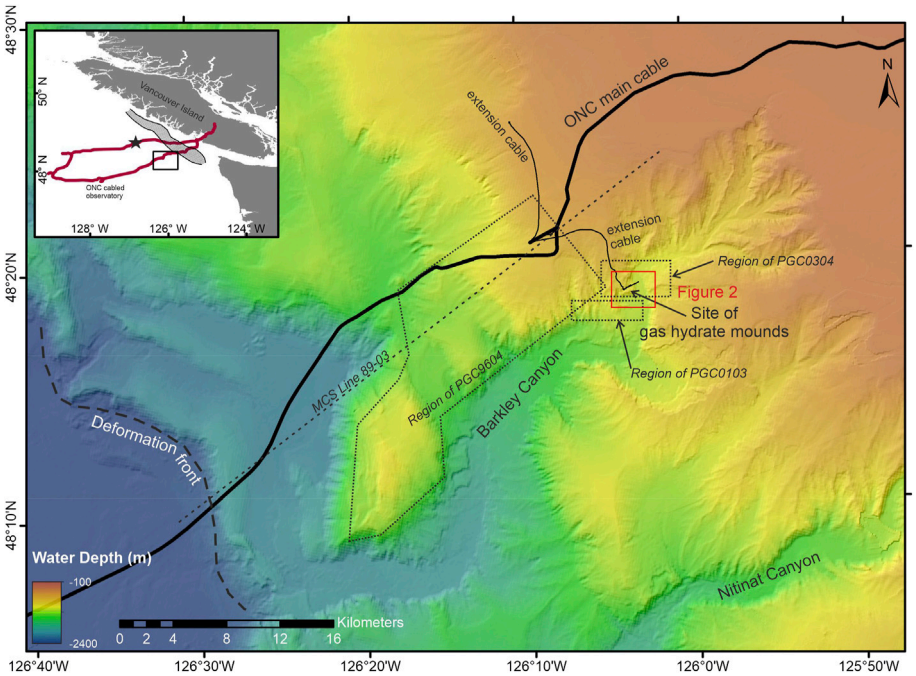

FIGURE 1 | Location of the study site with gas hydrate mounds at the Ocean Networks Canada cabled observatory. Location of two survey with densely spaced 2D seismic lines (PGC9604, PGC0103, PGC0304) are shown as dotted polygons. The location of regional seismic line 89–03 is shown by a dashed line. The site of the gas hydrate mounds is highlighted in **Figure 2**. Inset shows the location of the study region off Vancouver Island, British Columbia, Canada, with the ONC cable (red line) and the approximate extent of the Tofino Basin as hashed-region. Other vent locations used for comparison are at the Clayoquot slope node of the ONC cable, indicted by the black star.

Cold seep systems are observed worldwide along active and passive continental margins (e.g., Suess, 2014 and references therein). These systems are inherently heterogenous and exhibit a high degree of variability (in space and time) of the abundance and types of chemo-synthetic communities and venting-associated seafloor morphologies (e.g., Paull et al., 2015 and references therein).

One of the most intensely studied seep-sites along the northern Cascadia margin is located within Barkley Canyon (**Figure 1**), where massive seafloor outcrops of gas hydrate are located in water depths of ~860 m. The site itself was found when an estimated 1.5 ton of solid gas hydrate was dredged off the seafloor by a fishing trawler in November 2000 (Spence et al., 2001a). Shortly after this discovery, dives with the ROV ROPOS (Remotely Operated Platform for Ocean Science) confirmed the occurrence of large mounds of solid gas hydrate on the seafloor (Chapman et al., 2004). Work on samples recovered from these early dives revealed that the site is unique, in that it is a location with thermogenic gas hydrate occurrences (Pohlman et al., 2005), the only known site to date off northern Cascadia. Furthermore, pore-water analyses from sediment push cores recovered near the mounds indicated very high fluid flux and shallow depths of the sulfate-methane interface (Lapham et al., 2010; Pohlman et al., 2011). Detailed geochemical analyses on hydrate samples collected, further recognized that the mounds contain not only s-II, but also s-H gas hydrate (Lu et al., 2007).

The monitoring of these mounds within this gas hydrate rich environment became a focus for the Ocean Networks Canada (ONC) cabled underwater observatory (Barnes et al., 2011) studies. The first reconnaissance ROV survey by ONC was conducted in 2006 with the ROV ROPOS (Dive R0996) as part of the initial route-survey. Since then, numerous additional dives with different ROVs have been conducted by ONC and the Monterey Bay Aquarium Research Institute (MBARI), out of which we used 57 dives to investigate the seafloor environment (**Supplementary Table S1**). In addition, three expeditions using the ROVs Tiburon and Doc Ricketts from MBARI were conducted in 2006, 2009, and 2011. The gas hydrate mounds and seepage system became the target of several monitoring experiments operated by ONC, including the use of a remotely operated crawler, called Wally (Thomsen et al., 2012). A dedicated survey to map the seafloor around the gas hydrate mounds was conducted in 2009 (**Figure 2**) with an autonomous underwater vehicle (AUV). The multibeam data revealed details of the seafloor morphology with a horizontal resolution of ~1 m (e.g., Paull et al., 2015).

Following discovery of the mounds, a seismic survey as part of the *Ventflux2* expedition was carried out to map the region around the mounds with single-channel seismic methods (Spence et al., 2001b), followed by a second attempt in 2003 during the *BofFiNS* expedition (Willoughby and Fyke, 2003). Here, we show results from these expeditions for the first time

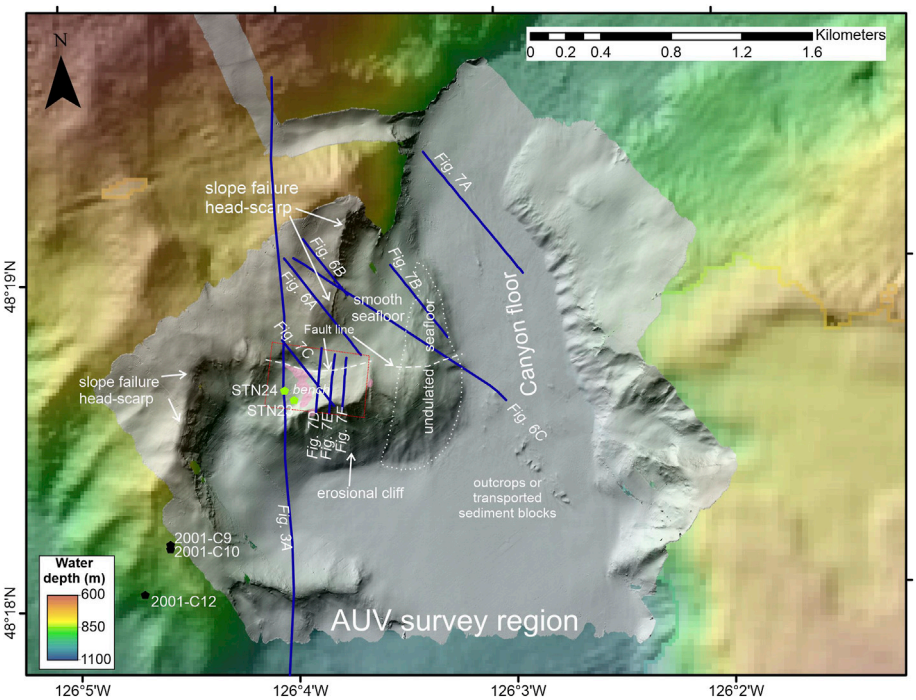

FIGURE 2 | Area mapped with AUV multibeam at 150 m line spacing shown with grey shading. AUV line spacing was reduced to 25 m to cover a small area with more closely spaced Chirp lines (rectangular region outlined with a red dotted line). Locations of gas hydrate mounds are highlighted with pink-shaded transparent polygons on top of the bathymetric bench. Location of seismic and AUV Chirp data shown in subsequent figures are indicated by blue lines. Core locations from the expedition in 2001 (*Ventflux2*) are shown as black solid symbols, ~ 1 km to the SW of the mound-region. Cores from the 2008 expedition (STN 23 & 24) taken near the gas hydrate mounds are shown by green solid symbols.

and integrate these data with regional seismic data acquired during previous seismic surveys.

Our goal is to fill a large knowledge gap, despite all efforts and monitoring campaigns, and answer the following questions:

- What is the mechanism for the development of gas hydrate mounds on the northern wall of Barkley Canyon?
- Is the presence of thermogenic hydrocarbon seeps at the seafloor indicative of a s-II gas hydrate system at greater depth?
- What are the migration pathways for fluids supporting the gas hydrate mounds exposed on the seafloor?

To address these questions, we first combine ROV dives with repeated seafloor video observations and the AUV bathymetry data to establish an inventory of characteristic fluid seepage features, such as occurrences of gas hydrate mounds, bacterial mats, clams, carbonate crusts, as well as oil- and gas discharge sites. These data are then combined with AUV sub bottom profiler images of the sedimentary structures in the shallow sub-surface to investigate fluid migration pathways, and finally integrated into the larger tectonic setting of Barkley Canyon and regional occurrences of BSRs from seismic imaging. This study integrates data from many different expeditions, encompassing different disciplines and techniques, and combines data of different vintage. This study provides a synthesis of our understanding of the Barkley Canyon gas hydrate occurrence to date and – despite all efforts made – addresses remaining knowledge gaps and suggests new long-term monitoring targets not yet undertaken.

METHODS

This study combines various remote-sensing techniques and ROV-based video imaging capabilities over the time span from the initial discovery of Barkley Canyon gas hydrates in November 2000 (Spence et al., 2001a) and initial ROV dives, followed by seismic imaging attempts in 2001 and 2003, until the last maintenance cruise operated by ONC in the summer of 2021. Additional regional seismic reflection data from the northern Cascadia margin are incorporated. A list of all scientific expeditions, ROV dives, and associated investigations used are given in the **Supplementary Table S1**.

Seismic Data and Bottom-Simulating Reflectors

A grid of single channel seismic (SCS) reflection lines were acquired during expeditions in 2001 (Spence et al., 2001b) and 2003 (Willoughby and Fyke, 2003). Data acquisition during the 2001 expedition used a single 40 in^3 sleeve gun as source

(dominant frequency 100 Hz) at a shot-spacing of 12.5 m. Data were recorded with a 25 m long single-channel streamer at a sampling rate of 0.5 ms. A pre-amplifier bandpass filter of 30–2,100 Hz was used during acquisition. This allowed a detailed imaging of seafloor topography as well as BSRs and associated sediment structures. Data from 2003 (acquired with same sized airgun and single-channel streamer) suffer from a low signal-to-noise ratio and imaging artefacts from strong topography-related diffractions due to a wide shot-spacing (~30 m), and pre-amplifier bandpass filter settings restricting the frequency band to 50–200 Hz prior to digital recording. However, the 2003 data were able to detect BSRs.

To compare the 2001 and 2003 SCS data acquired from inside the canyon with the regional structures and associated BSRs north of Barkley canyon, we have chosen two data sets from previous surveys. Deep-penetrating multichannel seismic (MCS) line 89–03 (maximum 3,700 m offset) was selected from the archived seismic survey conducted in 1989 with a 125 L volume airgun array, providing a low-frequency (8–60 Hz) image of the structural setting down to ~2 s two-way time. For details on acquisition and processing, see e.g., Hyndman and Spence (1992) and Hyndman (1995). A set of parallel high-resolution seismic lines (8–240 Hz) was acquired in 1996 (spacing ~400 m) using a 24-channel solid-state streamer (max. 290 m offset) on the northern bathymetric bench above Barkley Canyon with a single 120 in^3 Bolt airgun (cruise PGC9604). Details on the acquisition parameters are provided in Mi (1998) and Ganguly et al. (2000). Because original processed lines were lost, these data were recovered from archives and re-processed for our study. Survey geometry was linked back to the original archived survey navigation in 1996. Processing involved geometry definition, predictive deconvolution for bubble-suppression, normal-move-out correction and stacking, and frequency-wavenumber time-migration. Post-migration predictive deconvolution and band-pass filtering (12–280 Hz) were added to further suppress the prominent airgun bubble from the data.

The seismic data were mainly used to identify the BSR and to estimate regional heat-flow patterns from its depth variation. This technique has been widely used on the northern Cascadia margin (e.g., Ganguly et al., 2000; He et al., 2007; Riedel et al., 2010a) and elsewhere (e.g., Yamano et al., 1982; Grevemeyer and Villinger, 2001; Kinoshita et al., 2001; Villinger et al., 2010; Phrampus et al., 2017). In our case, we assume a hydrostatic pressure regime down to the depth of the BSR and convert depth to pressure (in kPa) using a constant seawater density of 1,028 kg m^{-3}. Depth of the BSR (D_{BSR}) defined as meters below seafloor (m bsf) is derived using an average velocity for the sediments between seafloor and BSR of 1,600 m/s, in general agreement with previous velocity studies and drilling at this margin (e.g., Riedel et al., 2010b).

The s-I gas hydrate phase-boundary curve is defined after Sloan and Koh (2008) for a seawater salinity of 3.4 wt% and a pure methane system. For simplicity of the calculations, temperature at the BSR (T_{BSR}) is given as function of the hydrostatic pressure at the BSR (P_{BSR}) in values of MPa using this function:

$$T_{BSR} = -4.77713016 \times 10^{-7} \times P_{BSR}{}^{6} + 5.22043912 \times 10^{-5} \times P_{BSR}{}^{5} - 2.32953642 \times 10^{-3} \times P_{BSR}{}^{4} + 5.51150830 \times 10^{-2} \times P_{BSR}{}^{3} - 0.757440615 \times P_{BSR}{}^{2} + 6.50932289 \times P_{BSR} - 13.967,$$

which is defined as optimal polynomial fit to the theoretical gas hydrate phase curve (for a pressure-range of 3.3–29.1 MPa, and a temperature range from 1–21°C). We also adopt a depth-dependent seafloor temperature (T_{seaf} in °C) following the empirical equation as used in Riedel et al. (2018), which was derived from oceanographic data sets available online through the World Ocean Circulation Experiment (WOCE) atlas (http://woceatlas.ucsd.edu/):

$$T_{seaf} = 0.00000076 \times D^2 - 0.00364 \times D + 6.205$$

where seafloor depth (D) is given in meters (m). The geothermal gradient is then calculated from the difference in BSR- and seafloor temperatures, divided by the BSR depth (D_{BSR}) defined as meters below seafloor (m bsf). Heat flow is then given after multiplying this gradient with a depth-dependent thermal conductivity (*tc*) (following Davis et al., 1990):

$$tc = 1.07 + 5.86 \times 10^{-4} \times D_{BSR} - \left(3.24 \times 10^{-7} \times D^2{}_{BSR}\right)$$

Conversion of observed seismic two-way travel time to depth below seafloor includes uncertainties from each required input parameter described above. We estimated the combined total uncertainty to ±10 m by converting travel-time to depth using extreme values for velocity, thermal conductivity, and sea floor temperatures.

High Resolution Bathymetry and AUV Operations

The study region around the gas hydrate mounds was investigated with an AUV survey in 2009 (e.g., Paull et al., 2015). During this survey, MBARI's AUV "D Allan B" acquired multibeam bathymetry (Reson 200 kHz multi-beam sonar), side-scan sonar (Edgetech 110 and 410 kHz), and Chirp data (2–12 kHz) along multiple track lines. The AUV was flown at a height of ~50 m above seafloor and 150 m line spacing to nominally achieve 100% multibeam coverage. Line spacing was reduced to 25 m in a small area (region outlined with a red dotted line in **Figure 2**) to provide more Chirp coverage on the mounds. Multibeam data were processed with the software MB-System (Caress et al., 2017) and corrected for sound velocity to generate a grid of seafloor topography at a 1 m lateral resolution. A final navigation adjustment was made to account for AUV navigational uncertainty (a base shift relative to prominent topography) revealing positioning accuracy of <10 m. The AUV Chirp data are recorded initially relative to the height of the AUV flying above seafloor. The recorded fly-depth information of the AUV was then used to shift the data to true travel-time below sea surface. All Chirp data are presented in envelope (instantaneous amplitude) mode.

Water-Column Imaging

Acoustic detection of gas emissions in the water-column from ship-based multibeam or single-beam echosounder data (EK60) was made using the QPS Fledermaus Midwater tool. An initial set of known gas flares (recorded in publicly available data sets) was taken from previous analyses (Riedel et al., 2018). The AUV water-column backscatter information was visualized inside the software CARIS® to detect gas flares following the approach described in Römer et al. (2014). The location of gas emission sites from AUV data can be located within a few meters. The ship-mounted single-beam was used to estimate gas flare locations but since the sounder foot-print radius is ~160 m in 800 m water depth, gas flare locations can span laterally over ~320 m. For the purpose of this study we incorporated additional EK60 echosounder data (12 and 18 kHz) from the expedition conducted in 2008 (Haacke et al., 2022) from periods while the vessel was kept stationary during coring. As individual bubble streams can be tracked while rising in the water column, a more detailed analysis of bubble-rise rate behaviour and depth-limitation of degassing was possible. Similar EK60 echosounder data were recorded during dives with the ROV Doc Ricketts, but only photos of the echosounder image are available for analysis.

ROV Video Operations

Numerous ROV dives were conducted as part of the ongoing ONC monitoring efforts at Barkley Canyon and during surveys to the site by MBARI (2006, 2009, 2011). Most of the ONC-managed dives are dedicated to operations at instrument platforms and do not allow additional exploration. We have selected from the dives conducted a sub-set of surveys that incorporated regional surveying (e.g., ROPOS Dive 996 from 2006) or visual bottom transects between individual experiments. A list of these dives is given in the **Supplementary Table S1** including a map of dive-track and acoustic imaging lines across the region (**Supplementary Figure S1**). These transect lines were conducted with the ROV <2 m above seafloor, recording video with a visual footprint of only 2–3 m width. In some cases, the ROV video was recorded with parallel laser-beams providing a quantitative horizontal scale. When no laser beams were recorded, the size of objects was estimated from observations made during previous dives, or by using other representative objects like known fish species.

The ONC database includes dive logs with entries of the various observations made (all times are given in UTC). These logs were scanned for key words to get the coordinates for observations related to fluid seepage and seafloor morphology ("hydrate", "gas", "bubble", "oil", "carbonate", "clam", "bacterial mat", "mound", "crest", "rock", "coral", and "ridge"). An issue with this approach is that the recorded observations may not be entered into the log at the exact time when the ROV was passing the object noted or refer to objects not in the direct (frontal) view of the camera, but are within the general vicinity of the ROV. Thus, video recordings were inspected to verify the positions of all entries in the dive logs. Where available, the ROV camera heading information at the time of observation was used, or estimated from consecutive navigation points during a portion of a transect before and after a dive-log entry was made, assuming the camera position was not changed. The ROV may be several meters off from the actual object reported in the dive log and thus observations can scatter even when the same object is repeatedly noted in consecutive dives. Yet, as ROV positioning is limited by ultra-short baseline (USBL) systems, the uncertainties in the locations reported by visual inspections are usually not better than ±8–10 m (equivalent to ~1% of the water depth).

Oil Sample Collection and Gas Analyses

During two dives with the ROV Doc Ricketts in 2011, we collected oil from sediments at a gas hydrate mound in the central portion of the study area. While the ROV sat stationary on the seafloor, the upper few centimetres of sediment in front of the ROV was stirred with a metal rod to release oil using one of the robotic arms. Rising oil bubbles were collected with a funnel attached to the second robotic arm, and stored in a pressurized canister. Images taken during sampling (Dive DR273 and DR279) are shown in **Supplementary Figures S2, S3**. After the ROV was recovered, 4 sub-samples were created from the two pressurized canisters and shipped to the lab at the School of Earth and Ocean Sciences (University of Victoria) for gas composition determinations. The stable carbon and hydrogen isotope ratio measurements of the light hydrocarbons (methane–butane) were made by Continuous Flow–Isotope Ratio Mass Spectrometry (CF-IRMS, e.g., Whiticar and Hovland, 1995, **Supplementary Table S2**). All isotope data are reported here in the conventional delta notation in permil relative to the international Vienna Pee Dee Belemnite (VPDB) standard for $\delta^{13}C$ (precision ±0.2‰) and the Vienna Standard Mean Ocean Water (VSMOW) for $\delta^{2}H$ (precision ±2‰). The hydrocarbon gas composition was determined using the mass 44 peak by CF-IRMS.

Sediment Physical Property Measurements and Pore Water Sampling

Two piston cores were taken during expedition PGC0807 within the region of known gas hydrate mounds and above previously recognized gas vents (**Figure 2**). Three piston cores were taken ~1.5 km west of the gas hydrate mounds during expedition PGC0103 (**Figure 2**). Cores were cut on deck into whole-round core sections. Cores were then split into two halves, with one half dedicated to geochemical sub-sampling, and the second half was used for core-photography and physical property measurements. Two Munsell Soil Colour Charts (5Y and Gley) were included in each photograph frame to allow for adjustments to any changes in light conditions. Magnetic susceptibility was measured using a Bartington MS2E high resolution susceptibility probe with a measurement spacing of 1 cm. Electrical resistivity was measured on all cores from both expeditions with a small Wenner probe. Calibration of the probe was made against sea water (Standard Mean Ocean Water with salinity of 35 ppm).

Temperature was monitored constantly throughout the procedures. Measurement spacing depended on core quality and was adjusted to avoid zones with cracks and voids. Using a simplified Archie's relationship (Archie, 1942), the resistivity data were converted to porosity. We assumed the empirical parameters a and m to be 1 and 2, respectively, as no independent porosity data are available for this location. The three piston cores taken during expedition PGC0103 in 2001 (*Ventflux2*) were treated in the same manner, but only electrical resistivity was measured on Cores C10 and C12. Digital photographs were taken, but uncalibrated without Munsell Colour Charts.

From the piston cores, samples were taken for porewater sulfate analyses. Whole round core sections (5–10 cm in length) were taken, cleaned, and squeezed onboard. A complete description of the pore-squeezing procedure and sample treatment is given in Haacke et al. (2022). During 2004, several push cores (up to 22 cm in length) were taken with the ROV ROPOS from the sediment close to gas hydrate mounds from which porewaters were extracted with Rhizons (Seeber-Elverfeldt et al., 2005). Sulfate concentrations were measured on the pore water by ion chromatograph according to standard published methods (Lapham et al., 2008) and are reported in units of mmol l^{-1} (mM).

Gas Hydrate Phase Boundary

The gas hydrate phase boundary in seawater was calculated using the software CSMHyd (Sloan and Koh, 2008) for different hydrocarbon mixtures encountered at the Cascadia margin. A pure methane system and one system resembling the gas mixture extracted from gas hydrate at the seafloor (Pohlman et al., 2005) was incorporated in our study. Measurements of the seawater properties (conductivity and temperature) were required for calculating the theoretical phase boundary of gas hydrate in the water column. We obtained vertical profiles of seawater properties at the gas hydrate mounds of Barkley canyon through ROV dives using the conductivity, temperature-depth (CTD) sensor attached to the ROV Doc Ricketts. For comparison, we also use CTD data obtained during a sampling expedition in 2010 at Bullseye Vent (Riedel et al., 2014).

RESULTS

Seismic Constraints and BSR-Based Heat-Flow

Seismic imaging within the steep canyon, especially near the location of the gas hydrate mounds, was difficult (**Figure 3**). The strong, continuous reflection mimicking seafloor topography and of opposite polarity relative to the seafloor reflection seen at ~0.19 s two-wave time below seafloor roughly 1 km south from the site of gas hydrate mounds exemplifies the BSR in this area (**Figures 3A,B**). Similar reflections from the same survey were seen over an area of ~2.5 km^2. No equivalent BSR can be identified on the steeper flanks of the canyon wall despite prominent and well-imaged sediment layering along the lines.

More wide-spread BSRs are seen on the northern flank of the canyon wall, starting approximately 3 km west of the gas hydrate mound region. We selected Line 18 from the 1996 survey as an example for the BSR nature in this setting (**Figure 3C**). Again, a polarity-reversed reflection can be traced for much of the profile at similar sub-seafloor depths near 0.19 s two-way time (twt) at just over 1,000 m water depths. However, as the upper sediments are nearly seafloor parallel themselves, the BSR is possibly masked at many places. For comparison, one profile from the low-frequency MCS survey in 1989 was selected providing a regional representative view of the stratigraphy and BSR (**Figure 3D**) further west and north of the canyon region. None of the seismic lines investigated along the Barkley Canyon region and along the entire northern Cascadia margin show evidence of a deeper second BSR. This is in contrast to the southern Cascadia margin, where a second BSR exists under Southern Hydrate Ridge, attributed to shifts in temperature and pressure regimes after the last glacial period and not migration of thermogenic gas (Bangs et al., 2005).

Using the BSR as a proxy for temperature, heat-flow values were estimated (**Figure 4**). The results show the expected range in heat-flow values along the margin in accordance with accretionary prism deformation and subduction (Davis et al., 1990; Hyndman et al., 1993). A strong overprint of the heat flow values is clearly associated with the topography, with focusing in synclines (yielding higher heat flow) and defocusing at anticlines or exposed ridges (yielding reduced heat flow) as already previously noted by Ganguly et al. (2000). For the examples chosen in **Figures 3A,B**, the heat flow is ~75 mW m^{-2} at an approximate distance of 30 km from the deformation front.

The seismic profiles from around the Barkley Canyon region show that the sedimentary section can be roughly divided into two units: 1) an upper veneer of sedimentary layers being nearly parallel to the seafloor and 2) an underlying unit of sediment layers showing strong folding. Both units additionally show signs of faulting with some of the faults penetrating the entire depth range imaged, while others are occurring in the lower unit only. The seismic records for line 89–03 (**Figure 3D**) and line 18 from the 1996 survey (**Figure 3C**) best illustrate this separation. The canyon itself has eroded deep into the sedimentary systems, roughly to a depth of 1.4 s twt, equivalent to ~600 m below seafloor depth (relative to the seafloor depth at the north-western bench of the slope projected to a similar margin-parallel location). This depth is marked on **Figures 3C,D** and clearly illustrates that the erosion has reached depth intervals within the lower folded and faulted sedimentary unit, thus exposing these presumably much older sediments.

Detailed AUV Bathymetry and Chirp Data

The region of the gas hydrate mounds is located at an average water depth of 860 m. The region was surveyed in 2009 with an AUV covering a total area of ~8 km^2 (**Figure 2**). The floor of Barkley Canyon is clearly seen as an ~0.5 km wide nearly flat seafloor S-shaped meandering band through which a line of outcrops or blocks of transported material sticks up through the otherwise gentle seafloor morphology. North-west of the

canyon floor the seafloor can be divided into several smaller sub-regions, based on their distinctive morphology. Immediately north-west at the edge of the canyon floor, seafloor rises gently in a region with an undulating seafloor morphology (compare to **Figure 2**, **5**). Upslope from the undulated topography, the seafloor becomes smoother, up to a cliff or failure head-scarp. This region is truncated by an apparent fault-line from a seafloor bench that itself shows a sharp erosional cliff with down-slope slumping into the deeper located canyon floor. The surface of the bench is marked with a rough seafloor morphology hosting the gas hydrate mounds. This distinctive bench is ~650 m long (measured along the erosional cliff) and up to 250 m wide.

The AUV bathymetric data were used to prepare a 3D perspective view using ArcScene® (**Figure 5**). The perspective view of bathymetry illustrates the region of the gas hydrate mounds is situated on a tilted bathymetric bench resembling the body of a rotated fault block. The northern boundary of the block is marked by the sinusoidal fault-line, resembling the look of a strike-slip fault. The bench or fault-block reveals a general dip towards the northern canyon wall but increasing steepness to the east.

The canyon wall above the fault line is characterized by numerous head-scarps (**Figure 5**) associated with blocky, rotational failure (**Figure 6**). The AUV data show older sediments covered with sediments sloughed off from upslope and that the blocks have progressively moved downslope, as sediment layering is warped (**Figures 6A,B**). Thus, the unstable flank of the canyon appears to gradually fail. These fault-blocks resemble the form of the bathymetric bench on which the gas hydrate mounds are situated. The only existing airgun seismic line (**Figure 6C**) shows similar such fault blocks, but on a larger-scale. Additionally, the data reveal a basal reflection of the flank sediment mass which appears to be buttressed against a sediment block of weakly reflective, but dominantly flat lying strata.

Selected examples of the AUV Chirp data highlight details of the various subregions of the canyon's flank and the bench hosting the gas hydrate mounds (**Figure 7**). The meandering canyon floor is characterized by thick uniform sediment fill in the central portion of the canyon and a wedge-shaped stack of layers developed along the west flank of the meandering path (**Figure 7A**). A similar change in this depositional character is seen on the south-facing side of the canyon. The lower flank of the canyon's side is characterized by an undulating morphology (**Figures 2**, **7B**). On the bench the undulating surface morphology changes to a smooth seafloor. The boundary between the two sub-regimes of seafloor morphology marks the location where the sediment fill no longer covers the seafloor (at distance 680 m along the profile shown in **Figure 7B**) and underlying sediment/rock is exposed. Chirp data across the bench (**Figures 7C–F**) show an abrupt change in character across the fault near the gas hydrate mounds. The surface of the bench to the south of the fault is tilted towards the north, and show northward dipping strata which apparently truncate along the fault (**Figures 7C,D,F**). Sediments north of the fault line are flat-lying and penetration of the Chirp data is three times as deep. The AUV lines across the patch hosting the prominent gas hydrate mounds reveal a unique character. The seafloor is warped upwards forming blisters, elevated by ~5 m above surrounding seafloor, especially along the fault line. Acoustically, these blisters are opaque, similar to observations made by Sager et al. (2003) who identified similar pop-up features at methane vents associated with gas hydrate mounds in the Gulf of Mexico.

Detailed Location of Fluid Seepage Features

We reviewed video-data from 57 individual ROV dives and identified fluid-seepage related features on the seafloor. Investigating repeatedly visited sites, we utilize similarities in shape and size of the gas hydrate mounds, as well as specific markers left behind during several dives to estimate the coordinates of the seepage features (**Figures 8–11**). All video-log entries are plotted on top of the AUV bathymetric map at 1 m grid resolution to assign seafloor morphological structures to physical features on the seafloor (**Figures 8**, **10**). An overview of all events identified including ROV dive tracks utilized is given in **Supplementary Figure S1**. Examples of fluid seepage features are shown in **Figures 9**, **11**.

The gas hydrate mounds are certainly the most distinctive feature of the seafloor around this site and a sub-set of mounds along the sinusoidal fault-line are the target of repeat monitoring efforts using the crawler Wally (Thomsen et al., 2012). Individual mounds are largely sediment covered, but patches of solid hydrate are exposed (**Figure 9A**). Some of the gas hydrate mounds are also associated with gas and oil seepage. The height of these mounds was estimated to be between 1–3 m above surrounding seafloor (**Figures 9B,C**). The mounds host living chemosynthetic communities (*Beggiatoa* bacterial mats, *Vesicomyid* clams, *Solemya reidi* clam) and are also surrounded by debris of clam shells and authigenic carbonate (**Figure 9B**). Some of this debris appears to be transported downslope on the western portion of the bench and at the steep south-facing erosional cliff (**Figure 8**). The observations of gas hydrate mounds repeatedly seen over 15 years and the dense clustering of bacterial mats, clams, carbonates, and associated gas and oil venting (i.e., fluid seepage indicators) outline two regions of focused fluid seepage.

The main focused seepage region which includes most of the mounds is about 0.025 km^2 in areal extent and is located in the south-western region of the rotated fault-block (grey-shaded patches shown in **Figure 8**). In this main focused fluid flow region, all but one of the gas hydrate mounds are situated south of the prominent fault line. The gas hydrate mounds nearest to this fault line are the site of the repeat observations with the crawler Wally (Thomsen et al., 2012). A small trough is situated on the hanging wall of the fault line and one gas hydrate mound is seen ~50 m to the NW of that trough (**Figure 8**). This site is also associated with gas flares and oil-bubble leakage. Further south of the fault line, several additional mounds are observed, with the southern-most cluster being visited repeatedly and

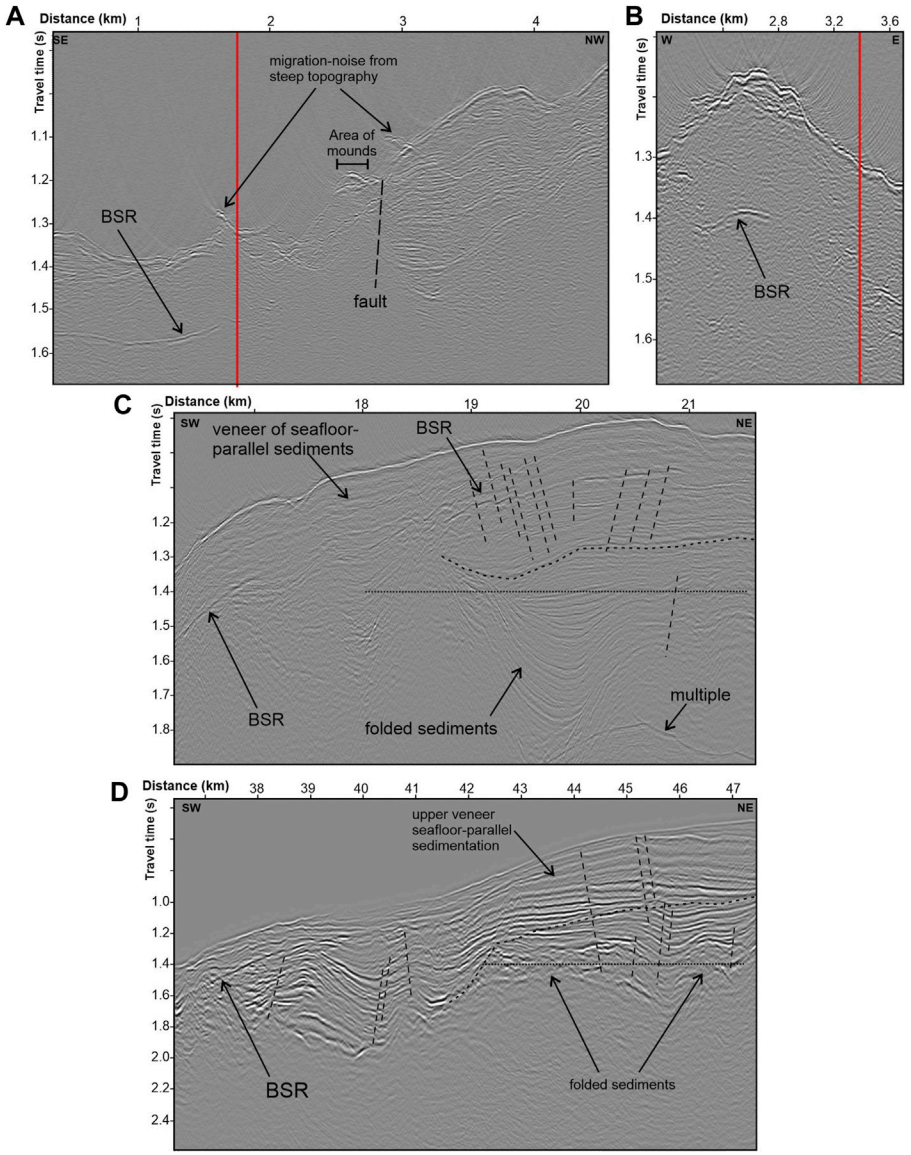

FIGURE 3 | (A) Seismic record (expedition PGC0103) showing a BSR, ~1 km south of the gas hydrate mounds. The BSR is seen up to line-kilometre 1.5, but is absent in the remainder of the profile. A prominent fault separates visible layering along the canyon wall to the NW from acoustically weakly reflective sediments to the SE. **(B)** A neighbouring line (crossing point is marked by red line) shows a small portion of a BSR underneath the topographic high. Data are migrated but steep seafloor topography results in migration-noise. **(C)** Seismic record (expedition PGC9604) along the northern flank of the canyon ~5 km to the NW of the gas hydrate mounds. A BSR is only weakly developed. An unconformity separates the upper veneer of seafloor-parallel sediments from a deeper unit of older, folded sediments. The depth to which the canyon has eroded at its present floor is marked by the horizontal dotted line. **(D)** Portion of multichannel seismic line 89–03 showing a BSR along the western section up to line-kilometre 39. The section between line-kilometre 42 and 47 projects to the location of the gas hydrate mounds. The erosion depth of the canyon in indicated by a horizontal dotted line. An unconformity marks the boundary between the upper younger and mostly seafloor-parallel sediments and underlying older and folded sediments. Both units are also cut by numerous faults (dashed lines).

having been the focus of a long-term study using a pore-fluid array (Wilson et al., 2015). Thus, the gas hydrate mounds in this focused fluid flow region spread over ~250 m in a nearly N-S orientation. Although not always imaged from the same camera standpoint and with different camera systems of the various ROVs (with changing colour calibration), individual gas hydrate mounds repeatedly visited over the 15 years of data availability appear to be only slightly changing in dimension (width and height) and overall character (i.e., abundance of chemosynthetic communities and bacterial mats).

A second focused fluid flow region is seen at the eastern edge of the rotated block (**Figure 10**) covering a small region of 0.005 km^2 (approximately 40 m E-W by 220 m N-S). Here, three gas hydrate mounds are also associated with oil seepage, gas emissions, bacterial mats, and living clams. Downslope of this region, bacterial mats and clam colonies were identified during

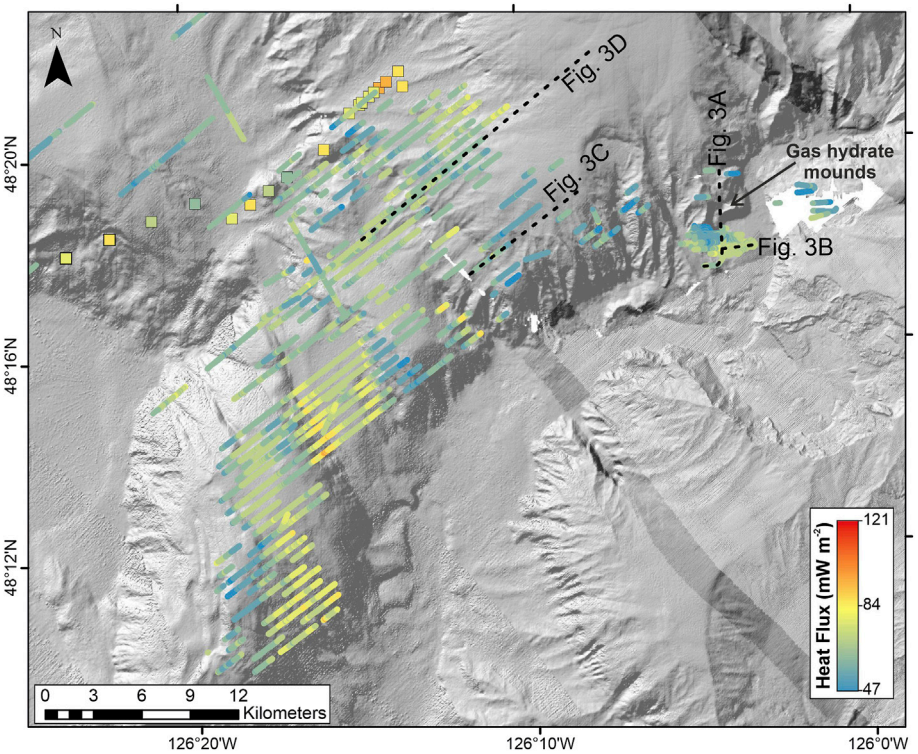

FIGURE 4 | Map of heat flow values derived from BSR depths. Heat flow values derived with a heat-probe (Davis et al., 1990) are shown as large squares. On average, heat flow is ~75 mW m^{-2} at the location in the Barkley Canyon, ~1 km south of the gas hydrate mounds (**Figures 3A,B**), and very similar to the region upslope above the canyon, as shown in **Figures 3C,D**.

one dive (DR059) occurring in an elongated depression over several meters. Examples of the seepage features in this second region are given in **Figure 11**.

At some of the gas hydrate mounds, the hydrate was seen to occur with a yellow colour (**Figures 9A,B**), indicative of the co-existence of thermogenic hydrocarbons as reported by Pohlman et al. (2005). Lu et al. (2007) reported the occurrence of s-II and s-H gas hydrate from these sites. The upper 1.3 m of sediments of piston core STN23, recovered outside the main focused fluid seepage region and ~125 m west of the nearest oil-leakage site, were described to contain oily fluids with a kerosene smell (Haacke et al., 2022). Oil-samples were taken at two locations at the same mound during ROV dive DR273 and 279 (**Supplementary Figures S2, S3**).

Areas of sparse and isolated occurrences of bacterial mats, clams, and carbonate chunks are taken to identify "diffuse venting" and characteristically associated with a seafloor morphology that is showing some minor undulations (<1 m in height, but unrelated to the presence of gas hydrate), compared to regions of entirely smooth seafloor barren of any observations indicating seepage. The diffuse venting area on the central portion of the bench covers an area of ~0.13 km^2.

Gas flares were known to be present in the study region from previous ship-mounted single-beam EK60 echosounding efforts (Haacke et al., 2022; compiled in; Riedel et al., 2018). Seven flare locations (one cluster with three individual flares inside a 25 m radius) were noted across the region of the gas hydrate mounds, and two flares are located further east, outside of the focused fluid seepage zone (**Figures 8**, **10**). The AUV data identified 35 flare locations, of which five match the ship-mounted EK60 locations within 50 m, acknowledging the navigation uncertainties of all data respectively. ROV-video observations of gas flares match four of the AUV-based flare sites (within 20 m) and the cluster of three ship-based flares. There was only one gas flare identified in the AUV data at the western edge of the region defined as diffuse seepage. Several gas flares were seen in the AUV-data west of the gas hydrate mounds, where otherwise only debris of dead clam shells and carbonate rocks were seen. In this region, the two piston cores from expedition PGC0807 were taken.

Throughout the regions of focussed fluid flow, and especially along the erosion cliff (**Figures 11A,B**), the seafloor is also covered with rock debris (see distribution in **Figures 8**, **10**). More abundant rock debris is found at the eastern portion of the study zone, over the region marked as "undulating seafloor" in **Figures 2**, **5**. A detailed look into that region that is mostly devoid of fluid seepage features is given in **Supplementary Figures S4 and S5**.

Geochemistry of Oil Samples

A comprehensive analysis of the gas evolved from gas hydrate samples and a vent gas taken at the gas hydrate mounds is given

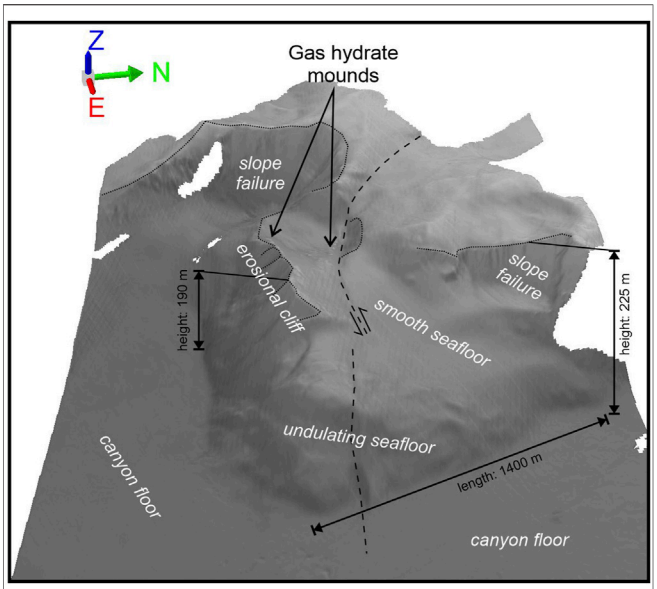

FIGURE 5 | Perspective view of the AUV shaded bathymetry relief showing the location of the gas hydrate mounds situated on a bench, resembling the shape of a rotated fault block. Approximate height of geographic features is indicated. The prominent sinusoidal fault line is shown as dashed line. Head scarps of slope failures along the canyon wall and the erosion cliff at the fault block are indicated by dotted black lines. Two regions of distinct seafloor morphology (smooth vs. undulating) are indicated.

by Pohlman et al. (2005). Here, we add results from additional analyses of the oil associated gas, i.e., extracted from oil-samples collected in 2011. The fundamental finding by Pohlman et al. (2005) of a predominantly thermogenic source for the hydrate and vent gases, based on molecular and stable isotope composition is supported by these new data. However, there are differences in the composition of the hydrate and vent gas vs. the oil associated gases. The oil associated gases in this study generally have a greater relative abundance of the C_{2+} hydrocarbons (21–72 vol%), i.e., ethane (C_2) propane (C_3) and iso-, n-butanes (i-C_4, n-C_4), compared to methane (CH_4) (**Figure 12A**). The hydrate gas varies from 14–30 vol% C_{2+}, whereas the vent gas is a methane-rich, dry gas with a C_{2+} of 2.7 vol% (Pohlman et al., 2005). Although the gas composition can be strongly influenced by mechanisms related to the place and method of sampling, e.g., effects of diffusion, advection, sorption, solubility etc., the abundance of higher hydrocarbon gases is a strong indication of the presence of thermogenic hydrocarbons in the system. The dominant contribution of thermogenic gas is supported by the diagnostic Bernard parameter ($C_1/[C_2+C_3]$, Bernard et al., 1976) that ranges from 1.4 to 44.2 (**Figure 12A**). For comparison, a dominantly microbial gas has a Bernard parameter from 10^2 to ca. 10^5 (Whiticar, 2020).

In combination with the molecular composition, the interpretation of the hydrocarbon gas type can be further aided by their stable C- and H-isotope signatures. The $\delta^{13}C$ values for C_{2+} hydrocarbons are essentially identical in all samples (**Figure 12B**, closed symbols), and diagnostic for thermogenic gases with $\delta^{13}C_2H_6$, ranging from −24.8 to −26.6‰, $\delta^{13}C_3H_8$ from −21.9 to −24.0‰, $\delta^{13}iC_4H_{10}$ from −24.3 to −25.9‰ and $\delta^{13}nC_4H_{10}$ from −21.3 to −23.7‰. In contrast, the $\delta^{13}CH_4$ shows great variability from −42.1 to −58.1‰, with the oil associated gases more ^{12}C-enriched (−50.5 to −58.1‰) than the hydrate and vent gases (−42.1 to −43.4‰). Assuming that the C_{2+} hydrocarbons present are typical of thermogenic origin and neglecting the ubiquitous, low-level background and diagenetic gases in sediments (e.g., Hunt et al., 1980), then the trajectory of the $\delta^{13}C_{2+}$ values in the Chung et al. (1988) isotope plot (**Figure 12B**) can be used to predict the co-genetic methane $\delta^{13}CH_4$. The intercept of dashed line for the theoretical thermogenic gas in Barkley Sound, shown in **Figure 12B**, indicates that the expected $\delta^{13}CH_4$ would be roughly −32 ± ~2‰. This is calculated using a probable humic, Type III kerogen source with an approximate 5–7‰ offset (based on Berner and Faber, 1996) from the measured $\delta^{13}C_2H_6$ of −24.8 to −26.6‰. This estimated range in $\delta^{13}CH_4$ of −30 to −34‰ assumes a source rock kerogen maturity of around 0.5% vitrinite reflectance equivalent and a $\delta^{13}C_{kerogen}$ of −23‰, although the estimate is not strongly dependent on these parameters. The actual measured range in $\delta^{13}CH_4$ of −42.1 to −58.1‰ indicates the admixture (dotted lines in **Figure 12B**) to the thermogenic gas of more ^{12}C-enriched methane that is most probably microbial gas. The amount of microbial methane added differs for the different sample types, with the oil associated gas in this study containing the greatest amount.

The hydrogen isotope ratios of the C_{2+} hydrocarbons shown in **Figure 12B** (open symbols) have a relatively tight range in values, similar to $\delta^{13}C_{2+}$, with δ^2H-C_2H_6, from −115 to −138‰, δ^2H-C_3H_8 from −83 to −99‰, δ^2H-iC_4H_{10} from −88 to −92‰ and δ^2H-nC_4H_{10} from −89 to −95‰. This further implies a common thermogenic source for all these gases. Consistent with $\delta^{13}CH_4$, the δ^2H-CH_4 indicates the admixture of microbial methane to all the gases. Also consistent with $\delta^{13}CH_4$, is that the oil associated gases in this study are more ^2H depleted than the hydrate or vent gases, due to a greater contribution of microbial gas commingled with the thermogenic gas.

The carbon and deuterium (CD) diagram of $\delta^{13}CH_4$ vs. δ^2H-CH_4 (**Figure 12C**, Whiticar, 2021) demonstrates the progressive addition of microbial methane to the thermogenic gas. In addition, the data trend in the CD diagram (dashed line) indicates that 1) the thermogenic methane endmember of the mixture is likely derived from a humic, Type III kerogen source, rather than marine or lacustrine Type I or II kerogen, and 2) the microbial endmember is likely methanogenesis by the hydrogenotrophic pathway (Whiticar, 2020), typical of anoxic marine sediments, rather than a more freshwater, land-based acetoclastic methanogenic pathway. The $\delta^{13}CH_4$ vs. δ^2H-CH_4 isotope trend line in **Figure 12C** could alternatively be explained by bacterial methane oxidation that would result in the observed methane ^{13}C and ^2H enrichments. However, this interpretation is unreasonable and inconsistent with the abundance of higher hydrocarbons present.

The carbon isotope difference plot modified from Jenden et al. (1993) (**Figure 12D**) characterizes natural gases using the relative

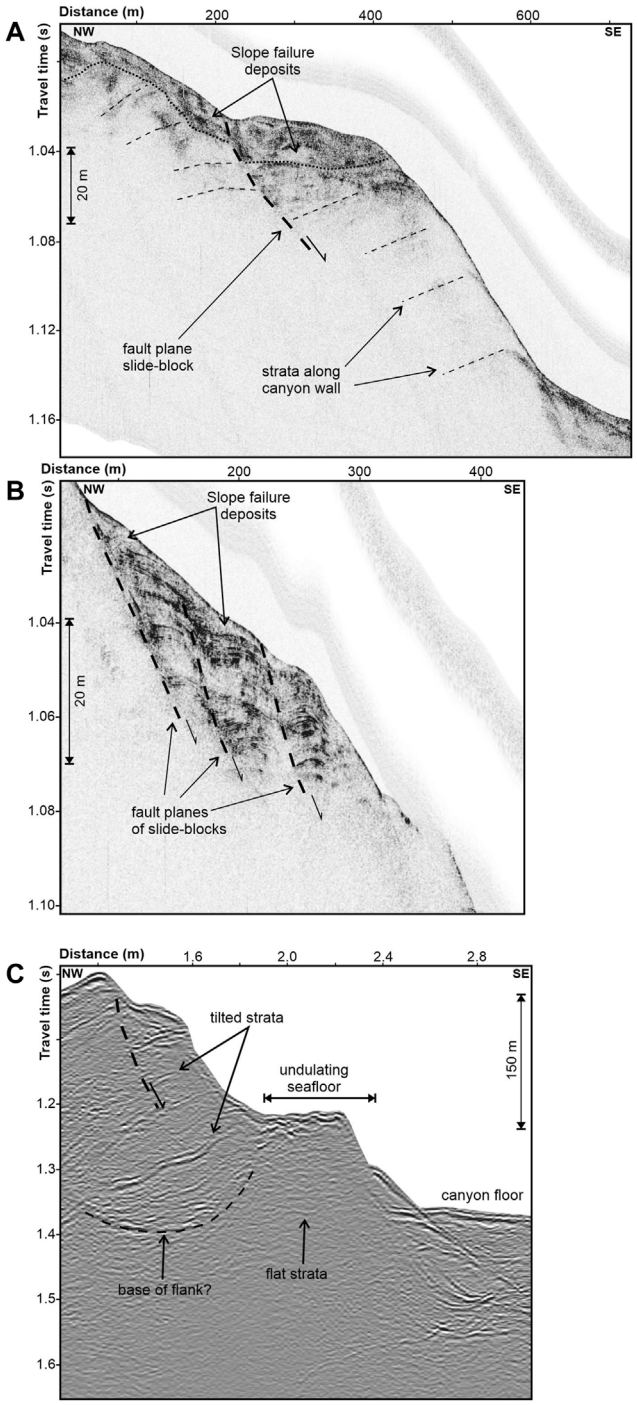

FIGURE 6 | Examples of rotational block failures along the north-western canyon wall. Location of lines are shown in **Figure 2**. **(A)** AUV Chirp data showing a veneer of chaotically deposited slope failure debris above layered strata. One prominent fault is seen along which a slope-block slides downward and is being gradually tilted. **(B)** Chirp data of a section of canyon wall with rotational slide blocks that have not fully failed yet. Sediment layering is gradually deformed across the fault lines. **(C)** The only available airgun section from expedition PGC0103 along the canyon wall shows the entire flank of the canyon wall as larger slide block failure complex, with tilted strata.

(*Continued*)

FIGURE 6 | The complex appears buttressed against a section of sediment that shows the undulating seafloor morphology (compare to **Figure 2**). Some weak layering is predominantly flat (seafloor parallel), likely a portion of much older sediment exposed by the canyon erosion process.

carbon isotopic difference between $\delta^{13}CH_4$, $\delta^{13}C_2H_6$, and $\delta^{13}C_3H_8$, rather than relying on their absolute isotope values. Although the plot is calibrated to Type II kerogens, **Figure 12D** affirms the thermogenic-microbial mix and/or in the case of the hydrate and vent gases, the presence of low maturity thermogenic gas. The amount of microbial methane admixed with the thermogenic methane can be estimated using a simple isotope mass balance of $m_{total} \times \delta_{total} = m_{thermo} \times \delta_{thermo} + m_{microb} \times \delta_{microb}$ and taking the δ_{thermo} to be −32‰ and the δ_{microb} to be −65‰ (typical of marine microbial methane, Whiticar, 2020). The added microbial methane ranges from ~18 to 19% for the hydrate gas, 17% for the vent gas and 31 to 44% for the oil associated samples. It is interesting to note that the driest gas (greatest methane vol%) is the vent gas, and the oil associated gas has the largest component of microbial methane. Compound partitioning in the different sample types likely influences the molecular composition, whereas the isotope fractionation due to migration or alteration effects, such as microbial oxidation, are not significant.

In summary, the gas compositions indicate a low maturity, humic (Type III kerogen) thermogenic gas mixed with a surficial marine microbial methane which agrees with a similar analysis performed on hydrate and vent gas from Barkley Canyon by Pohlman et al. (2005). The amount of microbial methane admixed varies according to sample type. This thermogenic gas interpretation is corroborated by the maturation model of Bustin (1995) and Petroleum System Model (PSM) by Schümann et al. (2008) of the Tertiary sediments in the Tofino Basin. Based on the seismic reflection line 85–01 and using calibration with the anticipated heat flow histories (average 70–80 mW/m^2) and the three exploration wells, Prometheus H-68, Pluto I-87 and Zeus D-14, the PSM demonstrated that hydrocarbon generation (predominantly gas prone) from the Type III kerogens is possible.

Water-Column Acoustic Observations

Acoustic water column imaging is commonly used to detect gas venting from the seafloor while the ship is in transit or during multibeam mapping surveys. Here, we show EK60 acoustic data from a single beam echosounder (18 kHz) collected while the ship was nearly stationary, thus allowing more accurate detection of individual gas outlets and definition of gas bubble rise rates (**Figure 13**). The EK60 data indicate relatively constant rise rates of 18–20 cm/s for both locations investigated. Trails of gas bubbles can be followed as they rise to a water depth of ~300 m, where a highly reflective zone of zooplankton obscures the bubble-associated reflections. In the zone shallower than 200 m, mixed acoustic returns from individual fish are distinctly seen as either flat or up- and downward bending acoustic trails. Most gas plumes do not emerge above the plankton layer. However, one example (**Figure 13A**) taken above the Wally crawler region has strong acoustic returns of nearly linear streaks of

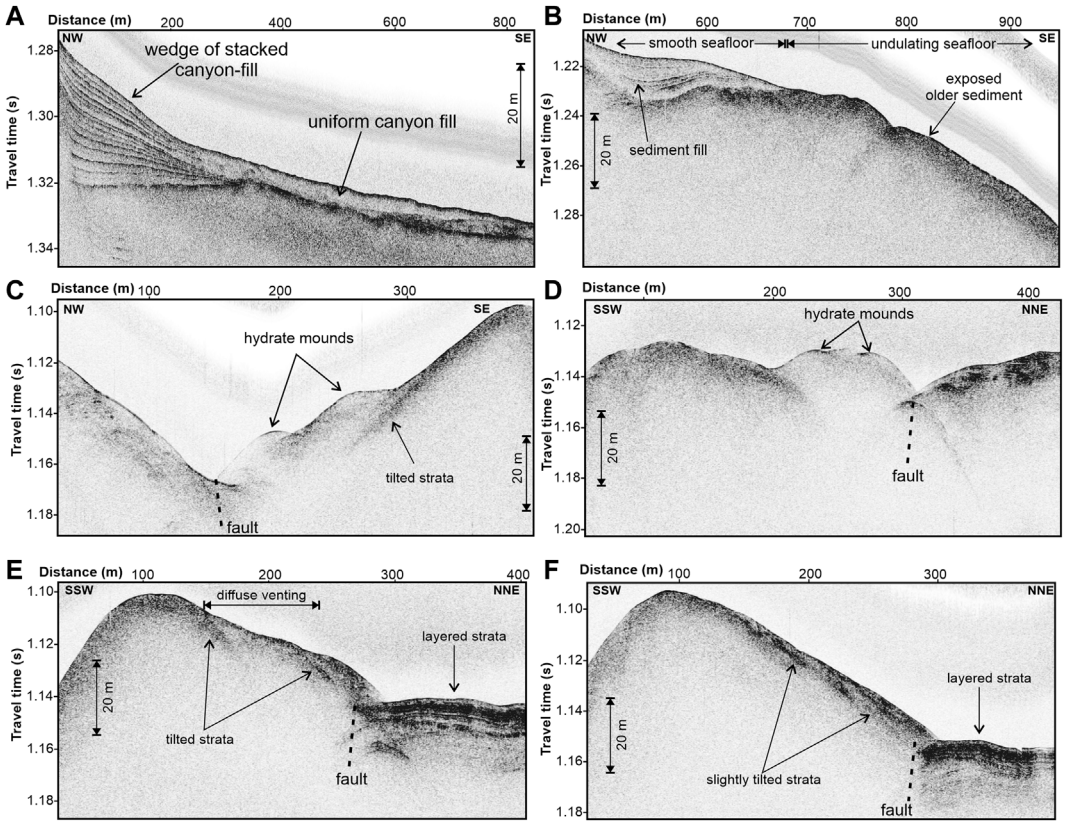

FIGURE 7 | Examples of AUV Chirp data showing important acoustic characteristic of the sub-surface structures around the general region of Barkley Canyon gas hydrate mounds (location see **Figure 2**). **(A)** Profile through the central portion of the meandering canyon floor shows a wedge of layers on the lee-side of the meander and thick, acoustically turbid canyon fill. **(B)** Profile showing the sub-surface regime across the change in seafloor pattern from undulating to smooth morphology. **(C)** and **(D)** Profiles illustrate the acoustically turbid character of the gas hydrate mounds or blisters, that are warped up by ~5 m higher than the surrounding seafloor. **(E)** Section of a line across the region with diffuse seepage and tilted strata, sharply truncated at the fault line to the NNE-section with layered sediments. **(F)** Profile showing slightly tilted strata and prominent truncation at the fault line. This line is located at the eastern edge outside of the diffuse seepage zone.

rising gas bubbles (rise rate ~18 cm/s) even in water depths shallower than 300 m. At this location, abundant oil seepage was reported during ROV dives and the acoustic trails in the EK60 data extend to 50 m below sea surface, the shallowest that the EK60 system covers. Two piston cores were taken slightly west of the main zone of gas hydrate mounds and where gas flares were acoustically detected. The EK60 record of the time during coring at STN23 is depicted in **Figure 13B**. The data show the rising gas bubbles and the same acoustic band of zooplankton. Additionally, a strong return of the down- and up-going corer-device is clearly seen in the record. Upon ascent of the core, additional strong acoustic trails appear above ~250 m water depth emanating from the corer-assembly, unconnected to trails starting at the seafloor. During dives with the ROV Doc Ricketts in 2011, the ship's 12 kHz echosounder data was running. After completion of operations on the seafloor of dive DR273, the EK60 echogram showed unusual gas-bubble trails emanating from the echogram of the ROV upon ascent at water depth of ~250 m (**Figure 13C**). The ROV sampling had not obtained any hydrate, but the ROV was covered in oily residue, especially, after the effort to collect oil-samples. The oil started to degas at shallow water depth, giving rise to the acoustic imaging of gas trails, similar to observations made during the ascent of the piston core at station STN23. We obtained photographs of the computer-screen but no gain-adjustments or post-processing were possible as the data was not recorded digitally.

Sediment Physical Property Measurements and Pore-Water Sampling

To date, only two piston cores from the region close to the gas hydrate mounds are available (Haacke et al., 2022) and neither contained observable gas hydrate (**Figure 8**). Core STN23 was 2.26 m long but was noted to contain oily fluids above 1.1 m bsf. The upper 1.1 m bsf are green to green-grey soft sediment, containing open cracks and fractures, shell fragments, and carbonate concretions (**Supplementary Figure S6**). Below that depth, the core was devoid of oil and contained a dense, light grey glaciomarine clay unit with some ice-rafted granodiorite debris and fine sand, but

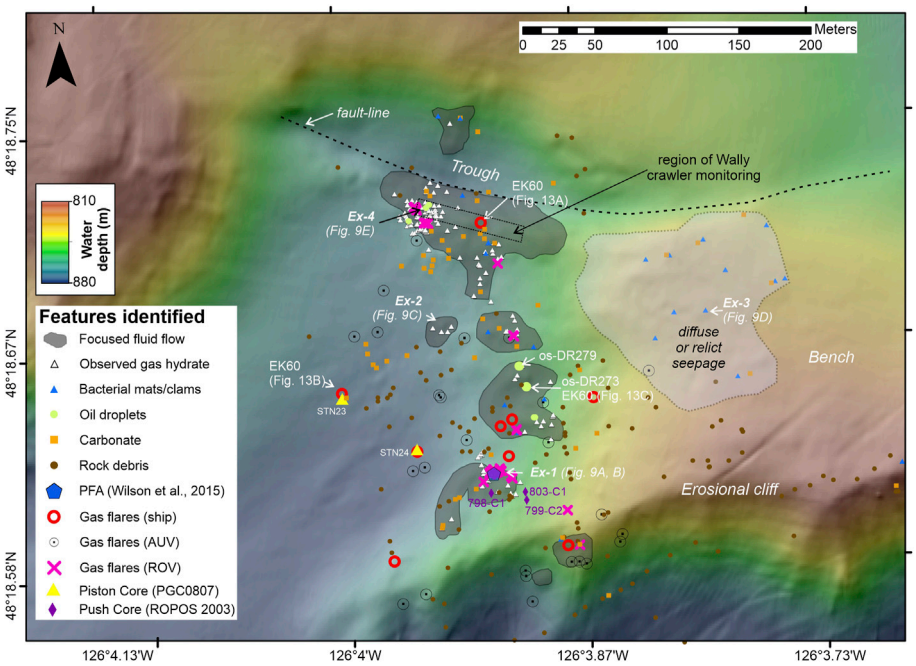

FIGURE 8 | Detailed map of AUV-bathymetry with location of sightings of fluid-seepage related features. Examples (Ex-1 to Ex-4) of video images are given in **Figure 9**. The pore-fluid array (PFA) site (Wilson et al., 2015) is at the southern-most mound-complex (Ex-1). We interpreted sites of focused fluid flow (Ex-1, -2, and -4) based on repeated video sightings and characteristic seafloor morphology, marked as dark-shaded regions. In contrast, a zone of diffuse (or relict) seepage on the eastern side of the bench was identified based on fewer seepage-related features (Ex-3), an absence of gas hydrate mounds, and a gentle seafloor morphology. Location of the two oil-samples (*os*) collected in 2011 and analysed for our study are marked with large green circles, as well as locations for EK60 data from ship-mounted data, and acquired during the ascent of the ROV after dive DR273.

no fractures. Only 38 cm of sediment were recovered at STN24. The sediments of STN24 were described as medium olive grey pebbly sand to silty clay (**Supplementary Figure S6**). This core ended in carbonate crusts. For both cores, magnetic susceptibility and electrical resistivity (**Supplementary Figure S7**) were measured immediately onboard revealing details of the sediment composition. An intriguing similarity is a sharp decrease in susceptibility values within the upper 10 cm. The susceptibility record for the glaciomarine clay seen at STN23 is overall much more variable than that seen within the upper section, which may be a result from transported material, such as ice-rafted debris. Electrical resistivity varies slightly between 0.4 and 0.8 Ωm throughout the two cores and shows a general higher average value within the glaciomarine sediments below 1.1 m bsf. Using Archie's relationship (Archie, 1942) we converted the resistivity data to porosity. The porosity values obtained are only a rough estimate as no independent porosity data are available. However, they differentiate well the two different lithologies found. Porosity within the upper sediments is between 0.6 and 0.7, and is reduced to ~0.5 within the glaciomarine sediments. Some potential outliers were noted in the data (marked in **Supplementary Figure S7**) from the occurrence of minor core disturbance (cracks and voids).

During a previous expedition in 2001 (*Ventflux2*, Spence et al., 2001b) coring was conducted approximately 1.5 km further SW of the prominent gas hydrate mounds. Three cores were taken (C9, C10 and C12) that contrast the results from the region of the gas hydrate mounds. Sediments were described as dominantly homogenous greenish-grey clay with some lamination containing silty clay or thin sandy intervals (Spence et al., 2001b). Electrical resistivity and converted porosity on cores C10 and C12 are nearly constant throughout the entire cored interval reflecting the homogenous sediment type (**Supplementary Figure S8**).

Pore water sulfate concentration profiles are a proxy for methane flux/advection rates (Borowski et al., 1996). Sulfate profiles from piston and push cores demonstrate high methane flux/advection rates at the gas hydrate mounds (**Supplementary Figure S9**). The depth to no sulfate is <20 cm directly at the gas hydrate mounds (push cores 798-C1, 799-C2, and 803-C1, with linear sulfate gradients of 1.95, 2.11, and 1.58 mmol cm^{-1}, respectively). With increasing distance from the mounds, the depth to no sulfate increases gradually. At Core STN24 (~50 m from the mound where push cores were taken), the depth of no sulfate is projected to ~50 cm (although the sulfate profile is not linear). At core STN23, ~100 m away from the same mound, this depth is at ~1 m with a linear sulfate gradient of 0.27 mmol cm^{-1}. The two cores taken more than 1 km away from the mounds (2001-C9, -C12, linear sulfate gradients of 0.036 and 0.033 mmol cm^{-1}, respectively) reflect low flux

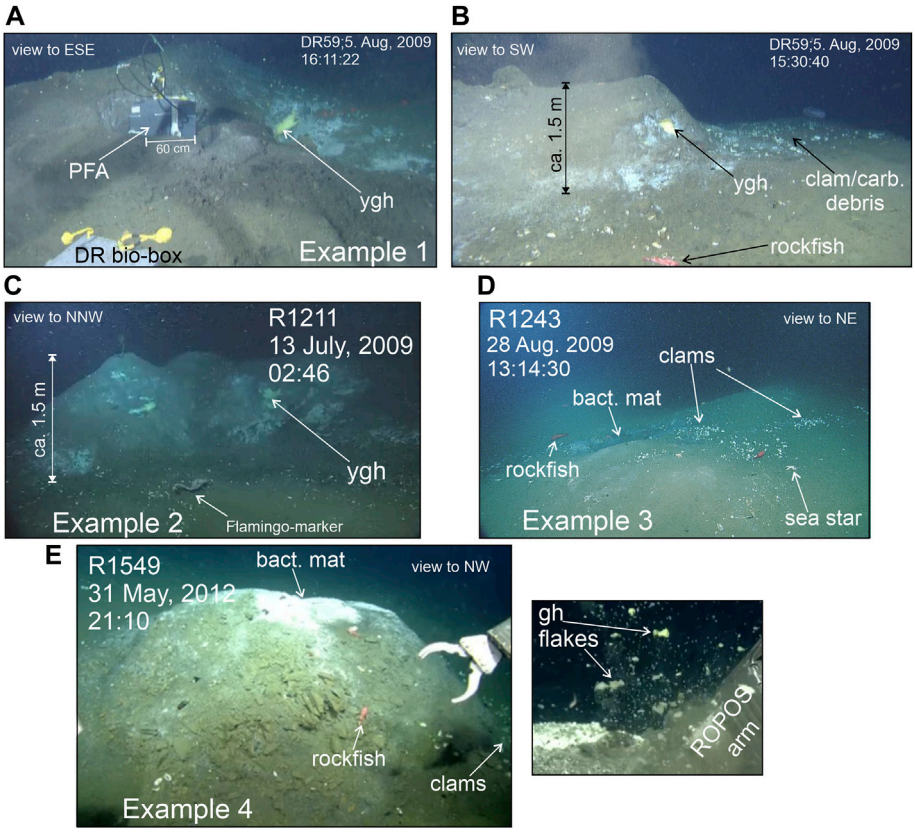

FIGURE 9 | Examples of focused seepage-features identified from repeat video observations. **(A)** Example 1 is a location of the southern-most mound-complex where a pore-fluid array (PFA) was deployed (Wilson et al., 2015). Yellow gas hydrate (*ygh*) outcrops are seen at this site and abundant oil- and gas venting was observed. **(B)** The mound complex is roughly 1.5 m elevated above surrounding seafloor. All around the mound, debris of clams and carbonates are found. The seafloor is covered with various patches of grey/black or white-coloured bacterial mats. **(C)** Example 2 is located in the central region of all mounds identified. The gas hydrate mounds (with yellow-coloured gas hydrate) form an elongated topographically distinct ridge of ca. 1.5 m height. **(D)** Example 3 is within the region of diffuse seepage with a gentle topography (<1 m height of smaller mounds), occurrence of some clams (mostly dead) and carbonate debris within patches of grey/black or white-coloured bacterial mats. **(E)** Example 4 is at the western zone of Wally-operations. Footage shows a ~0.5 m tall outcrop covered with grey/white coloured bacterial mats. Upon probing with the robotic arm of ROPOS, oil droplets and flakes of white and yellow-coloured gas hydrate (some with remains of bacterial mats attached) floated upwards. Size of the largest flakes were estimated to be ca. 5 cm in diameter.

rates with the depth of no sulfate being >8 m, which has been observed previously along the northern Cascadia margin away from other known vent sites (Solem et al., 2002; Riedel et al., 2006b; Pohlman et al., 2013). Using the approach by Borowski et al. (1996) to convert the linear sulfate gradients into sulfate flux rates, we used an average porosity of 0.6 based on our electrical resistivity data and simplified Archie conversion, and a sulfate diffusion coefficient of $5.8 \times 10^{-6}\,cm^2\,s^{-1}$ (Li and Gregory, 1974). The region of the gas hydrate mound experiences an average sulfate flux rate of $\sim 75 \times 10^{-3}\,mM\,cm^{-2}\,yr^{-1}$ whereas the background sulfate flux rate far away from the mounds is $1.4 \times 10^{-3}\,mM\,cm^{-2}\,yr^{-1}$, which is smaller by a factor of ~50 than the mound region flux. Assuming a stoichiometric balance between the downward flux in sulfate and the upward flux of methane (with a diffusion coefficient of $0.9 \times 10^{-5}\,cm^2\,s^{-1}$ at 5°C and ~9 MPa pressure for the average water depth where our cores were taken; Kossel et al., 2013), the sulfate flux rates translate to average methane gradients of $1.1\,mmol\,m^{-1}$ as the background value, compared to $\sim 58\,mmol\,m^{-1}$ near the mounds.

DISCUSSION

Origin of Thermogenic Fluid Seepage

The occurrence of the gas hydrate mounds and associated leakage of thermogenic hydrocarbons at Barkley Canyon is rather unique. No location with similar gas composition has been identified to date along the northern Cascadia margin, despite the wide spatial extent of the oil-bearing Tofino Basin (e.g., Johns et al., 2006; Hayward and Calvert, 2007; Johns et al., 2012), the presumed source region for the thermogenic hydrocarbons leaking at Barkley Canyon (Pohlman et al., 2005). Compositional and carbon isotope ratio data from gases extracted from oil samples collected in 2011 (**Figure 12**) further strengthen this link. Additionally, analyses of authigenic carbonate rocks recovered at the gas hydrate mounds show evidence of a deep-

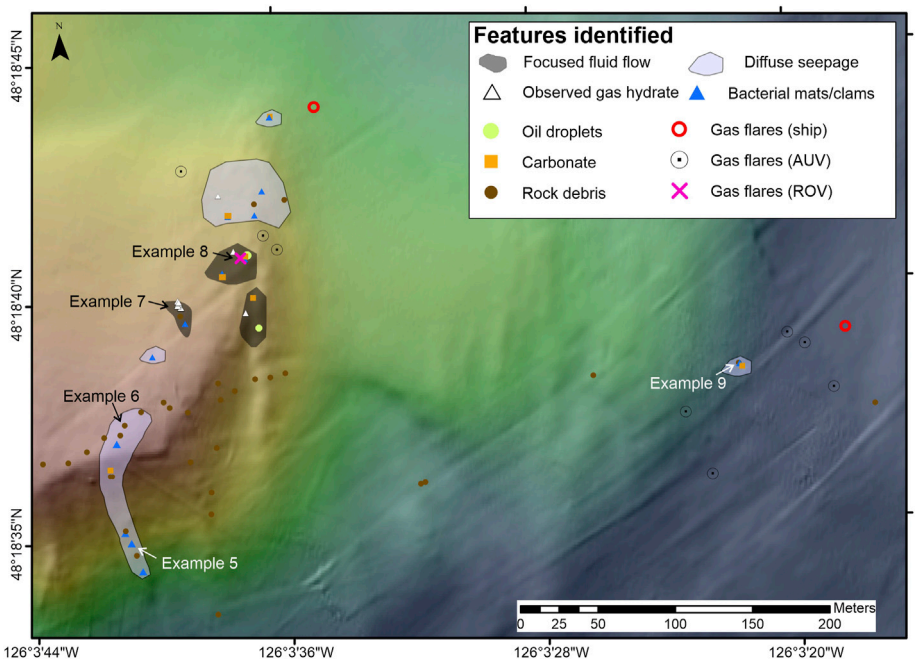

FIGURE 10 | Detailed map of AUV-bathymetry along the eastern edge of the bench with location of seepage-related features (similar in nomenclature as in **Figure 8**). Examples of seepage-related features and unique rock-debris are shown in **Figure 11**. A zone of focused fluid seepage is defined based on occurrence of exposed gas hydrate, gas and oil bubbling, and a morphology of pronounced mounds above surrounding seafloor (dark shaded region). Diffuse seepage (purple shaded region) is suggested based on the observation of only few bacterial mats and clams and only minor topographic variations.

rooted fluid source (Joseph et al., 2012, 2013). Although the geochemical composition of the gases, hydrates, and carbonate samples suggest a connection to the Tofino Basin (the only basin deep and old enough for thermal conditions appropriate for hydrocarbon generation off northern Cascadia (Schümann et al., 2008)), the tectonic setting of the margin and deformation of the basin (e.g., Hayward and Calvert, 2007; Yelisetti and Spence, 2021) makes a simple lateral migration pathway difficult. It is, however, possible, that during early hydrocarbon generation, a portion of that oil and gas did migrate in a westerly direction and may have gotten trapped in sub-basins that are presently disconnected from the source region. As the seismic data demonstrate, Barkley Canyon has eroded into the unit of older folded and faulted sediments (**Figure 3**). Drilling on the Cascadia shelf was completed in the past at several well locations (Shouldice, 1971), but correlation of ages to seismically imaged strata proved highly complex (Naranyan et al., 2005; Hayward and Calvert, 2007). However, it is conceivable that sediments identified as likely reservoir rocks (traps) by Schümann et al. (2008) are occurring within the depth range of Barkley Canyon's erosional cut. Faulting as seen on the seismic data of these units thus may provide pathways for oil and gas migration to the seafloor from these formerly trapped reservoirs.

An additional, previously unrecognized, feature of the area of the gas hydrate mounds is the emplacement of the seepage nearly exclusively on a rotational fault block. Two deeper penetrating seismic profiles provide useful images of the canyon wall structures, and corroborate that rotational block failure is a common style of canyon flank collapse (**Figures 3A**, **6C**). A large sinusoidal fault line on the northern flank of the canyon wall is identified on the AUV bathymetric data (**Figures 5**, **8**) and Chirp profiles (**Figure 7**) that marks the north-western limit of seepage features and the fault block (**Figure 8**). Thus, the sinusoidal fault is inferred to be a pathway for hydrocarbon migration.

BSR and s-II Gas Hydrate

Seismic imaging of the mound-region proved highly difficult due to the complex nature of steep canyon topography. Where clear images of a BSR were obtained, they were at a sub-seafloor depth of around 150 m (0.19 s twt, average sediment P-wave velocity of 1,600 m/s), about 1 km south of the fault-block that hosts the gas hydrate mounds (**Figure 3**). BSRs are wide-spread in all other seismic data sets acquired across the north-western canyon-wall (esp. those data from 1996) and further upslope of the canyon itself, which suggests a similar thermal regime with an expected BSR depth in accordance with the s-I methane hydrate phase boundary. The available gas composition provided in Pohlman et al. (2005) enables the theoretical phase boundary for such hydrocarbon mix to be calculated and compared to the s-I methane hydrate system in seawater (**Figure 14**). As expected, the thermogenic hydrate phase boundary is shifted to higher temperatures for equivalent pressure values. If we assume a thermal gradient representative for the distance of the mounds relative to the deformation front (~30 km), we would expect a

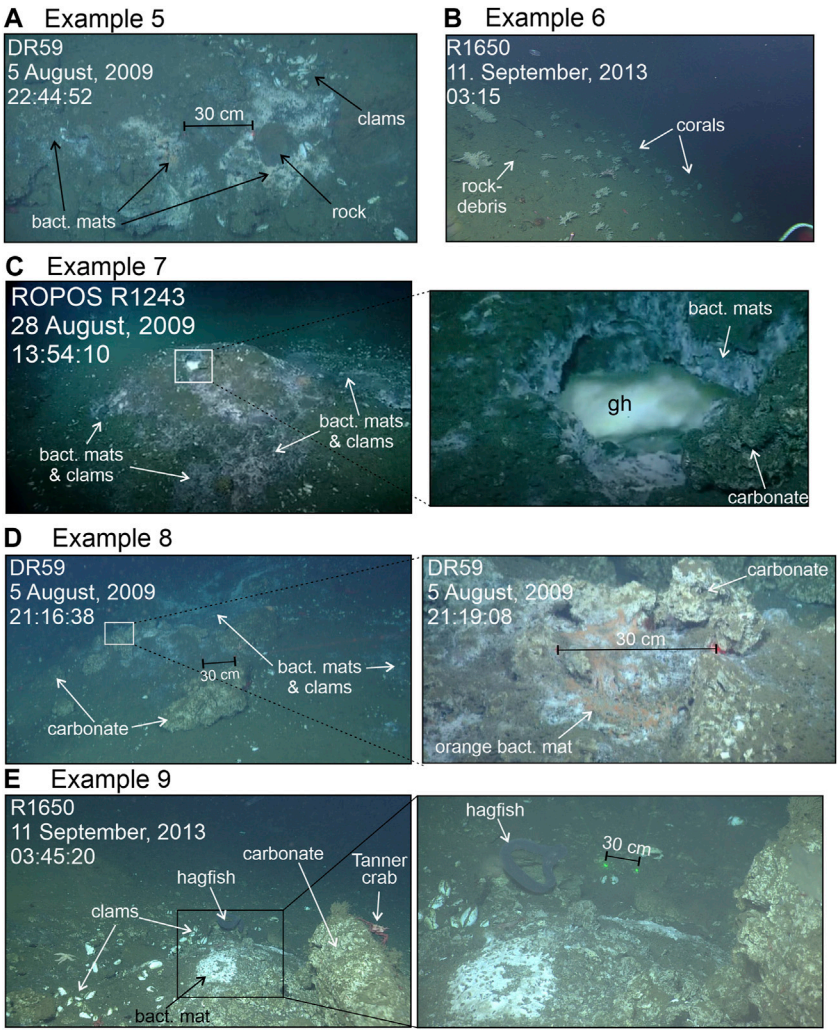

FIGURE 11 | Examples of seepage-features at the eastern edge of the bench. **(A)** At the cliff edge and downslope, few clams and bacterial mats are observed. **(B)** Abundant rock debris associated with cold-water corals are seen at the cliff edge and downslope towards the canyon floor. **(C)** Example of white gas hydrate (gh) outcropping on a small mound surrounded by bacterial mats and clams. **(D)** Larger carbonate concretions, bacterial mats, and clams. Here, also orange-coloured bacterial mats are found. **(E)** A small seep site with bacterial mats, clams and carbonate near the foot of the region marked as "undulating seafloor morphology" (**Figures 2**, **5**).

heat value of 70–80 mW/m^2 in accordance with the fluid-expulsion model and overall subduction-related thermal structure of the accretionary prism (e.g., Hyndman and Davis, 1992; Riedel et al., 2010b). Assuming a linear geothermal gradient, the predicted depth of the s-I related BSR is ~140 m bsf and nearly twice as deep for the theoretical gas hydrate phase boundary containing thermogenic gases (at ~280 m bsf). Acknowledging the uncertainties in all the calculations required to convert BSR depth on seismic data to depth (foremost unknown velocity), the BSRs identified anywhere along our data are most consistent with s-I methane hydrate, i.e., the regional BSR is not formed primarily from the thermogenic gas. No second BSR is seen anywhere along the margin, which leads to the conclusion that thermogenic gases at depth are occurring (if at all) at such low concentrations, that no pervasive s-II hydrate regime is developed (as seen at the seafloor), giving rise to either a significantly deeper primary BSR or a second impedance contrast, as for example seen off Borneo (Paganoni et al., 2016).

Localized Lateral Fluid Migration

The elongated, sinusoidal fault-line is interpreted as a major fluid pathway, but this does not fully explain the wide distribution over 250 m N-S of the gas hydrate mounds and also the more diffuse seepage features observed (**Figures 8–11**). The Chirp data show that sediment layers within the upper ~10 m bsf of the rotated fault block are themselves tilted towards the fault-line (**Figures 7D–F**). We therefore propose that the fluids initially migrating from depth upwards along the sinusoidal fault-line are then laterally distributed along more permeable sediment layers. The geometry of the tilted layers and the overall surface of the fault block promotes fluid drainage,

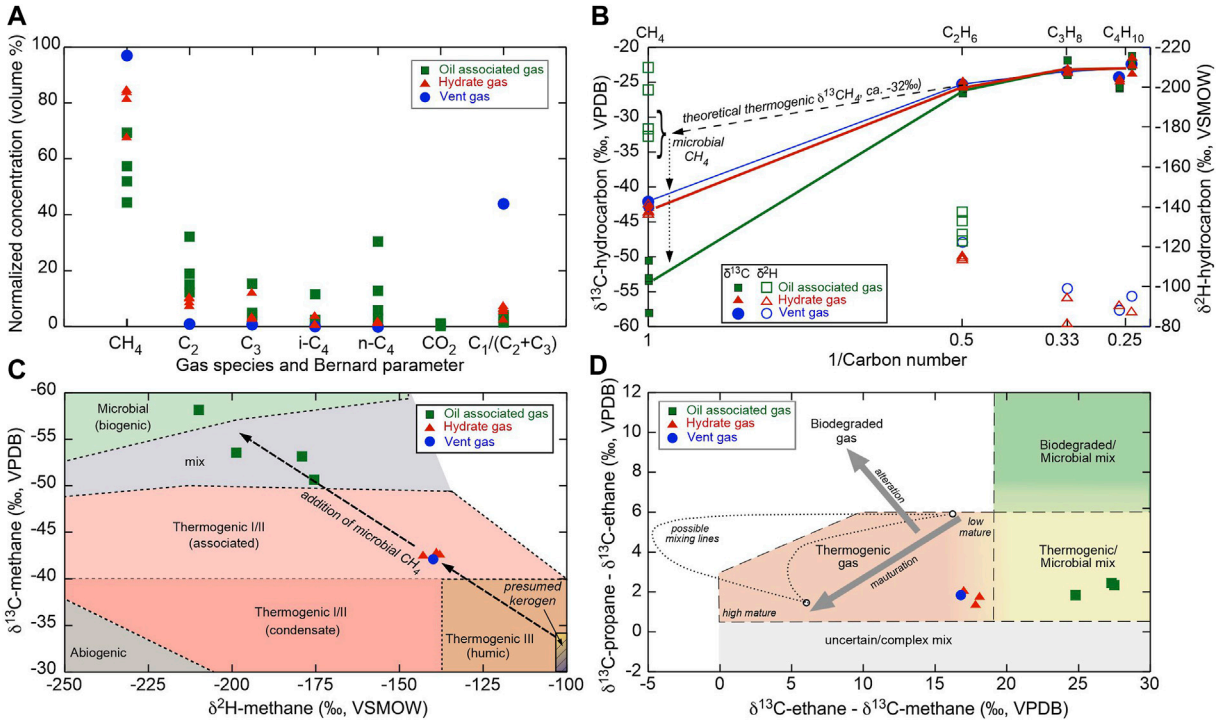

FIGURE 12 | (A) Normalized concentrations (vol%) and Bernard parameter ($C_1/[C_2+C_3]$) of hydrocarbon and CO_2 gases in samples from hydrate (red triangles) and vent (blue dot) gas samples reported by Pohlman et al. (2005) and oil samples taken during MBARI expedition in 2011 (green squares). **(B)** Chung isotope gas plot (Chung et al., 1988) of $\delta^{13}C$ and δ^2H for C_1-C_4 hydrocarbons. The expected $\delta^{13}CH_4$ from a humic, Type III kerogen source is indicated along with the shift due to the addition of microbial methane. **(C)** expanded CD diagram ($\delta^{13}CH_4$ vs. δ^2H-CH_4 from Whiticar, 2021) illustrating the mixture of recent, microbial methane with migrated thermogenic methane. The expected thermogenic $\delta^{13}CH_4$ vs. δ^2H-CH_4 endmember is shown **(D)** Carbon isotope difference plot (modified from Jenden et al., 1993) reinforces that interpretation of a lower maturity, thermogenic gas mixed with a microbial gas.

which is buoyancy-driven. The formation of gas hydrate requires additional accommodation space and blisters are formed on the seafloor, displacing surrounding sediment (**Figures 7C,D**). Although coring was successful only at one location to greater depths, the one core recovered (STN23) indicates that the occurrence of oil-stained sediment is primarily a surface phenomenon rather than pervasively infusing the strata that comprise the fault block throughout the entire depth ranges recovered. The lower glaciomarine clay was barren of any hydrocarbon and showed no signs of fractures or fluid-pathways.

Distribution of Fluid Seepage Features

We have managed to review nearly 60 individual ROV dive-videos capturing fluid-seepage related features on the seafloor (**Figures 8–11**, **Supplementary Figures S4, S5**) allowing an interpretation of the longevity of fluid seepage and possible lateral variations therein.

Gas Hydrate Mounds

The gas hydrate mounds are the most distinctive feature of the seafloor suggesting active and sustained fluid advection from depth. Yet, gas hydrate is inherently unstable in direct contact with seawater as ocean water is devoid of any methane, thus the question of how stable these gas hydrate mounds are arises. Long-term geochemical fluid-sampling with a pore-fluid array directly at the southern-most gas hydrate mound (location see **Figure 8**) reported by Wilson et al. (2015) showed slower dissolution rates for the sediment-covered gas hydrate than what was expected from laboratory measurements. Observations made on recovered hydrate samples from the gas hydrate mounds showed dissolution rates within 20% of the predicted theoretical values and a retreat-rate of 1 m/year for the exposed hydrate surfaces was estimated (Hester et al., 2009). Pore fluid analyses reported by Lapham et al. (2010) reveal that pore-fluids in sediments near the gas hydrate mounds are greatly under-saturated in methane with respect to expected values for equilibrium with the gas hydrate so that the mounds should be dissolving. The fact that the mounds have been seen in nearly identical dimensions throughout the 15 years of repeated video-observations supports the conclusion by Lapham et al. (2010) that some diffusion-retarding process protects the mounds and enhances their stability. But more so, fluids rich in hydrocarbons are likely constantly replenished from depth to maintain the gas hydrate mounds, which is supported by the high methane flux rates found by our new analyses. The determined sulfate flux rates at the gas hydrate mound (**Supplementary Figure S9**) where the pore-fluid array was located indicate an average downward sulfate flux rate of 75 mM cm^{-2} yr^{-1}, equivalent to an average methane gradient of 58 mM m^{-1}, which is about 50 times the average background fluxes distal to the seepage area.

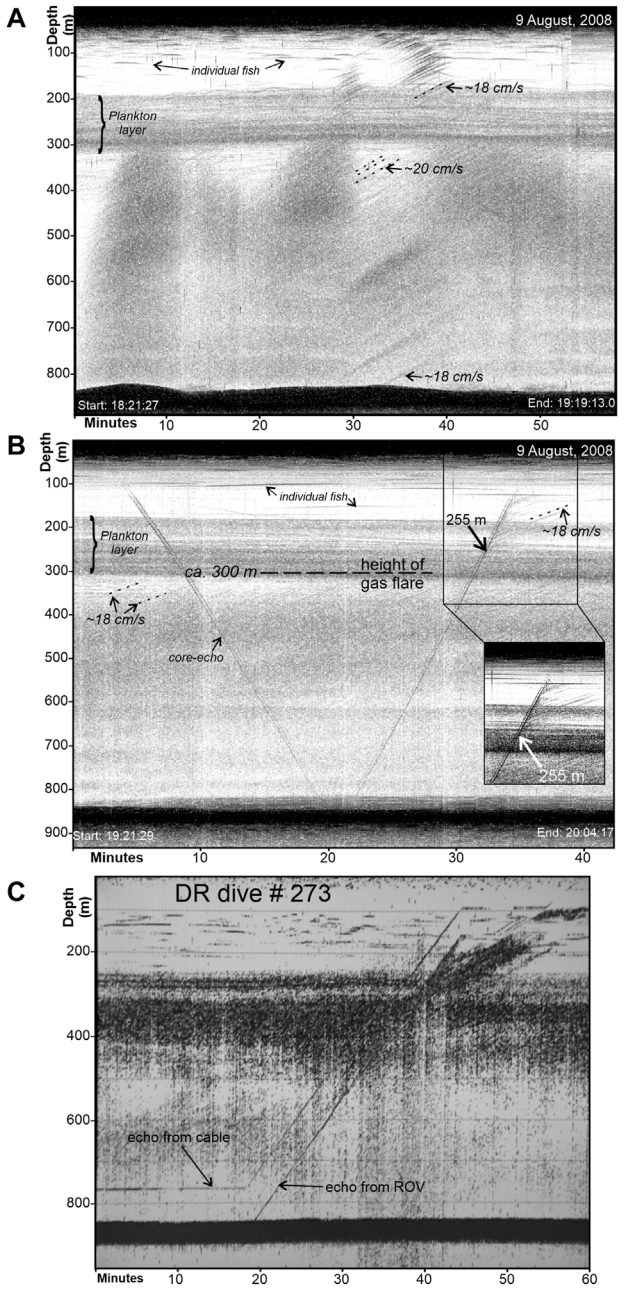

FIGURE 13 | Examples of EK60 echograms: **(A)** from expedition PGC0807 at location above gas hydrate mounds near the fault line, **(B)** at piston core taken at STN23, and **(C)** photograph of echogram onboard R/V Western Flyer, taken during ascent of ROV Doc Ricketts (for locations see **Figure 8**). On all examples, gas rising from the seafloor can be clearly seen up to a depth of ~300 m. Additional gas bubble trails unconnected to the seafloor are seen starting at ~ 250 m up to depths as shallow as ~ 50 m (limit of sounder-resolution). Bubble rise-rates are consistently around 18–20 cm/s.

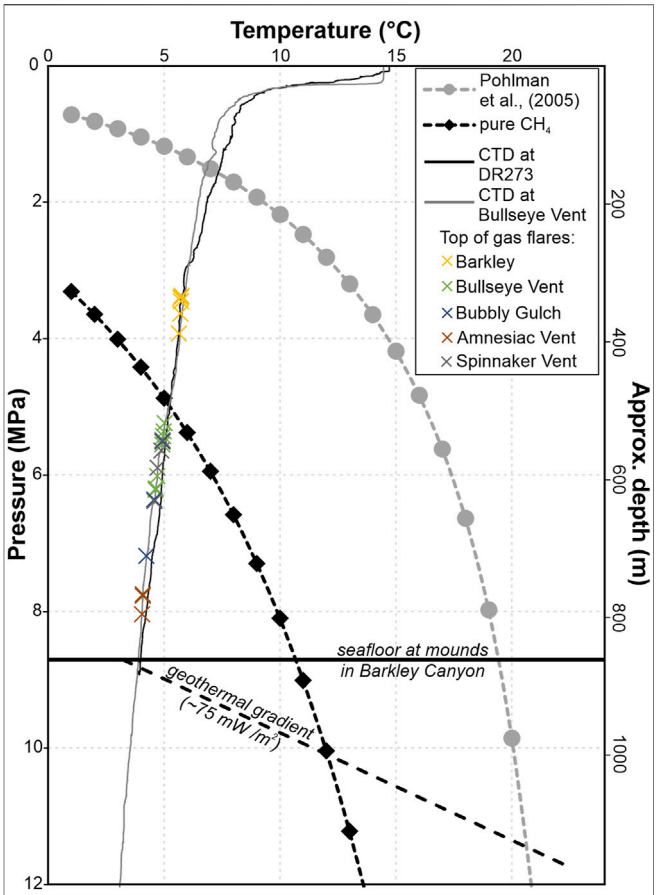

FIGURE 14 | Gas hydrate phase boundaries for two hydrocarbon mixtures in seawater calculated with the CSMHYD-software (Sloan and Koh, 2008). A simple linear geothermal gradient representative of the expected average regional thermal regime intersects the s-I phase boundary at ~ 140 m bsf and the thermogenic phase boundary at ~ 280 m bsf. Data from a CTD at Bullseye Vent (~50 km NW of Barkley Canyon) and from ROV dive DR273 at Barkley Canyon are shown together with the temperature/pressure points for the maximum height of gas plumes at vent locations seen in northern Cascadia (see inset of **Figure 1**) reported by Scherwath et al. (2019). Approximate depth was defined using a seawater density of 1,030 kg/m^3.

Gas Flares and Oil-Seepage

Acoustic detection of gas flares was made initially by ship-mounted single-beam echosounders, but provided a broad footprint and thus large uncertainty in actual vent location of ~150 m. The use of the AUV's side-scan sonar provided us with an opportunity to better mark the gas-flare positions, in addition to the video-based definition from the ROV dives. In many cases, the gas flare positions from all these sources agree within a radius of ~20 m. The AUV side-scan sonar data showed 35 flare sites in total across the study area (**Figures 8**, **10**), out of which five are associated with locations defined by ship single-beam data. Four of the AUV flare sites match with ROV video observations, but not all ROV gas observations were matched by either AUV or ship-based data. The mismatch between observations is that venting is known to be episodic or discontinuous (e.g., Römer et al., 2016). Yet, the AUV-defined gas flares west of the prominent gas hydrate mounds, in a region otherwise completely devoid of any features suggesting active fluid seepage, are enigmatic. A possible explanation is a mismatch in observational coverage between the narrow ROV bottom video footage of a few meters and the wider AUV water-column

imaging (up to 100 m width to both sides of the AUV). Active fluid seepage sites may be small and have simply not been found yet in this region.

Following the gas flares acoustically to shallower water depths using the ship-mounted echosounder data allows us to further investigate the fate of these gases in the water column (**Figure 13**). Gas flares above the gas hydrate mounds at Barkley Canyon are seen up to a water depth of ~300 m. Using CTD data measured during a ROV descent we are able to plot these depths into the theoretical gas hydrate phase diagrams (**Figure 14**). Those gas flares plot all above the s-I methane hydrate phase boundary. This is in contrast to other gas flares previously detected at other vents (e.g., Römer et al., 2016; Riedel et al., 2018; Scherwath et al., 2019) that all are occurring below the s-I phase boundary (here using CTD data measured directly above Bullseye Vent (~50 km NW of Barkley Canyon) during a water sampling campaign in 2010). Gas escaping at the seafloor is always immediately coated by a thin shell of gas hydrate, which helps stabilize the ascent of the gas bubble (Topham, 1984; Rehder et al., 2002). Acoustic detection of gas flares is thus often limited to the depths of the hydrate stability in seawater, as the gas is quickly dissolved into the ocean upon the loss of the hydrate coating and thus becomes acoustically invisible. Thus, gas escaping at the gas hydrate mounds must be coated with a mix of s-I and s-II gas hydrate. With this in mind, the occurrence of gas trails in echosounder data in water depths between 250 and 50 m at two sites above gas hydrate mounds at Barkley Canyon is unusual (**Figures 13A,B**). We interpret this as acoustic returns from gas that escapes from rising oil-covered bubbles. Degassing of oil was probably the cause of free gas release upon the ascent of the ROV Doc Ricketts in 2011 after oil samples were collected at the seafloor (**Figure 13C**). Since oil droplets rising in the water column cannot easily be distinguished from gas bubbles, these observations of unusually shallow gas bubble trails in water column acoustic data may be a way to remotely detect oil-seepage at the seafloor.

Occurrence of Rock Debris

The overall canyon wall is prone to repeated slope failures and many head-scarps are identified on the AUV bathymetry (**Figures 2**, **5**). Sediment sloughed off the canyon wall is deposited in small catchment mini-basins or transported further downward into the canyon floor and subsequently transported further downslope. These mini-basins are regions identified with a smooth seafloor morphology barren of any seepage features. This is contrasted by regions of rougher morphology (undulating seafloor, see **Figures 2**, **5**, **7B**) that also are riddled by rock-debris (**Supplementary Figures S2, S3**). The abundant occurrence of these rocks in the region identified as undulating seafloor suggests either transport of these rocks downslope by small debris flows or as outcrop/remnant of older sedimentary units where finer sediments are scoured by seafloor currents. However, similar rocks are seen across the entire region of gas hydrate mounds and at the steep cliffs and south-facing wall of the rotational fault block. These rocks here are possibly drop stones (from ice bergs or ice rafts floating out from the shelf at the end of the last ice age) or deposited during former downslope failure processes, as this sub-region is presently isolated from new sediment input due to the elevated topography and fault-line-related development of a mini-basin (**Figure 8**). However, abundant gas seepage, microbial activity and macro-fauna bioerosion results in constant re-working of the upper sediment cover and its removal by currents, thus keeping these rocks exposed.

SUMMARY AND CONCLUSION

Overall, the Barkley Canyon area is unique along the northern Cascadia margin because of the occurrence of numerous seafloor gas hydrate mounds linked to thermogenic fluids resulting in the formation of s-II and s-H gas hydrate within a relatively small (0.02 km^2) area. The origin of these thermogenic fluids is explained by lateral fluid-migration in the Eocene during early hydrocarbon generation from the Tofino Basin (~60 km landwards of the study site), trapping in sub-basins further to the west, and subsequent erosion by Barkley Canyon. Despite the occurrence of thermogenic hydrocarbons and complex gas hydrate structures at the seafloor, the seismic data suggest no presence of significant amounts of such clathrate structures at greater depth, as no second BSR was identified anywhere in the region. The suggested source-region for thermogenic hydrocarbons in the Tofino Basin is perhaps much broader than just a small zone near Barkley Canyon, as the Tofino Basin extends up to 100 km northward along the coast. If significant amounts of thermogenic hydrocarbons exist at greater depth that could promote s-II gas hydrate formation, a second BSR would be expected. The seismic data coverage inside the canyon and above the gas hydrate mounds is sparse but the few examples seen suggest a BSR depth in equilibrium to s-I methane hydrate representing the regional heat-flow regime of around 70–80 mW m^{-2}. Identical ranges in heat flow and associated BSR depths are seen north of the canyon. There are two possible reasons for the apparent lack of a 2nd BSR: either the thermogenic hydrocarbons are tightly focused to only a few migration pathways preventing regional spreading, or concentrations at greater depths are too small to allow formation of abundant s-II hydrates to form a permeability barrier for free gas that then gives rise to an impedance contrast imageable with seismic methods.

Due to the migration of thermogenic fluids and abundant oil seepage from the seafloor, another unique characteristic of this study site is the occurrence of gas flares reaching to near sea surface, which has not been observed elsewhere along the Cascadia margin. Usually, gas flares in water depths >800 m are acoustically observed to near the upper limit of the s-I gas hydrate stability zone. Gas flares above the gas hydrate mound region instead reach to an upper limit of ~300 m, shallower than s-I hydrate, suggesting gas bubbles coated with more complex clathrate structures. Additionally, gas is acoustically seen from 250 m to < ~50 m suggesting that oil-coated bubbles start to degas upon reaching such shallow water depths. This may promote hydrocarbon release into the atmosphere which otherwise is rather limited due to the uptake of gas into the water column

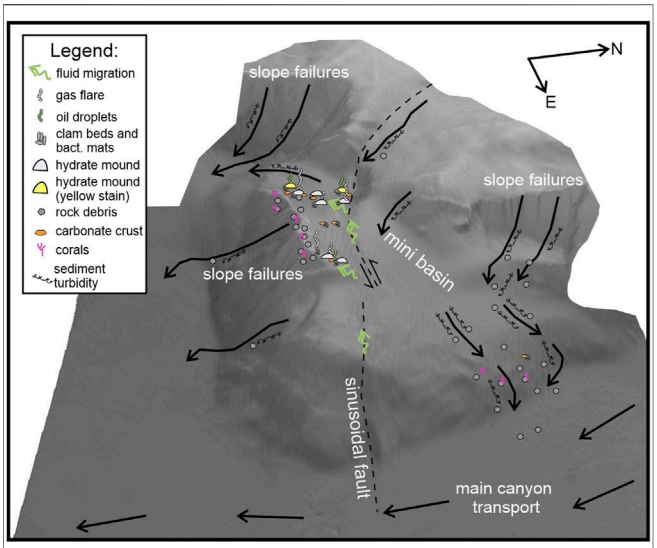

FIGURE 15 | Diagram of processes allowing gas hydrate emplacement at the Barkley Canyon site. The canyon has eroded deep into the sedimentary section of the accretionary prism, exposing sediment/rocks that had accumulated thermogenic fluids in the past. The fluids seep upwards along faults and the edges of the rotated block that had slipped down the canyon wall. Additional buoyancy-driven fluid seepage occurs along sedimentary strata. Gas hydrate mounds form on the seafloor and excess fluids are expelled into the ocean. Over time, the edges of the block are eroded and sediment and debris are transported downslope into the main canyon channel or are left behind on the seafloor. Slope failures along the upper canyon wall are caught in smaller mini basins or are bypassed downslope.

by chemical (solution, oxidation) and biological (metabolism) processes. The Barkley Canyon site would benefit from repeat remote radar satellite observations for natural oil-slicks, similar to sites in the Gulf of Mexico (e.g., MacDonald et al., 1996), to better understand temporal variability and amount of hydrocarbon migration.

Seafloor topography from the AUV mapping and repeat ROV video surveys suggest a zone of focused fluid flow including oil seepage and gas hydrate occurrence in two sub-regions of the rotated fault block. The largest of these sub-regions is approximately 200 m by 200 m in extent at the western end of the block (with the site of the seafloor crawler Wally) and hosts at least 20 individual mounds (or mound-complexes). The gas hydrate mounds host unique chemosynthetic communities with bacterial mats, clam colonies, and other macro-fauna within a tightly limited habitat-zone in a perimeter of only few meters around the individual mounds. A second focused fluid flow sub-region that is much smaller in spatial extent (~40 m (E-W) by ~220 m (N-S)) is located at the eastern edge of the fault block and hosts three visually confirmed gas hydrate mounds. In between these two sub-regions, a zone of diffuse venting with only few distinctive chemosynthetic organisms and minor carbonate crusts was recognized. Here, seafloor topography is much more subtle and no gas hydrate mounds have been seen.

From our analysis of AUV bathymetry data and Chirp imaging, we conclude emplacement of the Barkley Canyon site is uniquely associated with a rotated fault block, promoting focused fluid seepage. The surface of the fault-block is in itself tilted towards the north-eastern canyon wall of Barkley Canyon. The dense clustering of gas hydrate mounds is the result of focused fluid seepage predominantly at the edges of the rotated fault block. Fluid migration is further facilitated away from the main feeding-fault along more permeable sedimentary layers as suggested by the AUV Chirp data. The existing cores only recovered oil-stained sediments within a thin 1.3 m bsf upper veneer. The underlying dense glaciomarine clay unit was barren of any indications of oil, fractures, or other possible seepage pathways. Thus, the oil was possibly not migrating from below through (semi-) vertical pathways, but rather appears lithology controlled, suggesting a more pronounced lateral transport. This is corroborated by the AUV's Chirp data that showed tilted sediment strata within the upper 10 m bsf of the marked bathymetric bench that hosts the gas hydrate mounds. A conceptual diagram (**Figure 15**) depicts the occurrence of the bathymetric bench and associated fluid seepage and gas hydrate mounds as a result of fault-focused fluid migration from some deeper reservoir and then lateral diversion through permeable strata across the bench. This could be verified with new piston coring and some carefully designed seismic imaging, best with deep-towed systems, to improve imaging inside the steep canyon topography.

DATA AVAILABILITY STATEMENT

Video and image data used from ROV dives are available at Ocean Networks Canada online database https://data.oceannetworks.ca/DataSearch.

AUTHOR CONTRIBUTIONS

MRi wrote the initial manuscript and performed all analyses of the seismic and acoustic data used, esp. the repeat-video investigation. CP and PB were chief scientists of MBARI ROV exepditions in 2009 and 2011. GS and NC were chief scientists of several expeditions providing seismic, piston core, and ROV data. EL and DC provided AUV bathymetry, backscatter and Chirp data and conducted together with MRö all work for data integration. KD and MS provided all ROV video data and other ONC monitoring information. MW, JP, and LL provided all geochemical data and interpretation. RE provided the sediment core physical property data. All authors contributed to manuscript revision, read, and approved the submitted version.

FUNDING

The David and Lucile Packard Foundation provided support for the MBARI operations used in this study. Any use of trade, firm, or product names is for descriptive purposes only and does not imply endorsement by the U.S. Government.

ACKNOWLEDGMENTS

The authors would like to express their sincere gratitude towards the many individual people who were involved in the various expeditions, ROV-dives, data acquisition, and processing of data, including all ship's crews and technical support staff. The ROPOS ROV data as well all other ONC data are accessible though Ocean Networks Canada's data portal data. oceannetworks.ca. MRi is grateful for the support provided from ONC's data stewardship team, as well as its data analytics and quality team and the science team through ONC's Enhanced Support Program. Ocean Networks Canada is an initiative of the University of Victoria and has primarily been funded by the Canadian Foundation for Innovation, Transport Canada, Fisheries and Oceans Canada, and the Canadian Province of British Columbia. This is UMCES contribution # 6119.

SUPPLEMENTARY MATERIAL

The Supplementary Material for this article can be found online at: https://www.frontiersin.org/articles/10.3389/feart.2022.852853/full#supplementary-material

REFERENCES

Archer, D., Buffett, B., and Brovkin, V. (2009). Ocean Methane Hydrates as a Slow Tipping point in the Global Carbon Cycle. *Proc. Natl. Acad. Sci.* 106 (49), 20596–20601. doi:10.1073/pnas.0800885105

Archie, G. E. (1942). The Electrical Resistivity Log as an Aid in Determining Some Reservoir Characteristics. *Trans. AIME* 146, 54–62. doi:10.2118/942054-G

Auguy, C., Calvès, G., Calderon, Y., and Brusset, S. (2017). Seismic Evidence of Gas Hydrates, Multiple BSRs and Fluid Flow Offshore Tumbes Basin, Peru. *Mar. Geophys. Res.* 38, 409–423. doi:10.1007/s11001-017-9319-2

Bangs, N. L. B., Musgrave, R. J., and Tréhu, A. M. (2005). Upward Shifts in the Southern Hydrate Ridge Gas Hydrate Stability Zone Following Postglacial Warming, Offshore Oregon. *J. Geophys. Res.* 110, B03102. doi:10.1029/2004JB003293

Barnes, C. R., Best, M., Johnson, F. R., Pautet, L., and Pirenne, B. (2011). Understanding Earth - Ocean Processes Using Real-Time Data from NEPTUNE Canada's Widely Distributed Sensor Networks, Northeast Pacific. *Geosci. Can.* 38 (1), 21–30. Available at: https://journals.lib.unb.ca/index.php/gc/article/view/18588/20203 ([last accessed February 21, 2022).

Bernard, B. B., Brooks, J. M., and Sackett, W. M. (1976). Natural Gas Seepage in the Gulf of Mexico. *Earth Planet. Sci. Lett.* 31, 48–54. doi:10.1016/0012-821X(76)90095-9

Berner, U., and Faber, E. (1996). Empirical Carbon Isotope/maturity Relationships for Gases from Algal Kerogens and Terrigenous Organic Matter, Based on Dry, Open-System Pyrolysis. *Org. Geochem.* 24 (10-11), 947–955. doi:10.1016/S0146-6380(96)00090-3

Borowski, W. S., Paull, C. K., and Ussler, W., III (1996). Marine Pore-Water Sulfate Profiles Indicate *In Situ* Methane Flux from Underlying Gas Hydrate. *Geol* 24, 6552–6658. doi:10.1130/0091-7613(1996)024<0655:MPWSPI>2.3.CO

Boswell, R., and Collett, T. S. (2011). Current Perspectives on Gas Hydrate Resources. *Energy Environ. Sci.* 4, 1206–1215. doi:10.1039/C0EE00203H

Brooks, J. M., Kennicutt, M. C., II, Fay, R. R., McDonald, T. J., and Sassen, R. (1984). Thermogenic Gas Hydrates in the Gulf of Mexico. *Science* 225 (4660), 409–411. doi:10.1126/science.225.4660.409

Buffett, B., and Archer, D. (2004). Global Inventory of Methane Clathrate: Sensitivity to Changes in the Deep Ocean. *Earth Planet. Sci. Lett.* 227, 185–199. doi:10.1016/j.epsl.2004.09.005

Bustin, R. M. (1995). Organic Maturation and Petroleum Source Rock Potential of Tofino Basin, Southwestern British Columbia. *Bull. Can. Pet. Geology.* 43 (2), 177–186. doi:10.35767/gscpgbull.43.2.177

Caress, D. W., Chayes, D. N., and dos Santos Ferreira, C. (2017). MB-system: Mapping the Seafloor. Available at: https://www.mbari.org/products/research-software/mb-system/(last accessed October 14, 2021).

Chapman, N. R., Gettrust, J. F., Walia, R., Hannay, D., Spence, G. D., Wood, W. T. R. D., et al. (2002). High-resolution, Deep-towed, Multichannel Seismic Survey of Deep-sea Gas Hydrates off Western Canada. *Geophysics* 67, 1038–1047. doi:10.1190/1.1500364

Chapman, R., Pohlman, J., Coffin, R., Chanton, J., and Lapham, L. (2004). Thermogenic Gas Hydrates in the Northern Cascadia Margin. *Eos Trans. AGU* 85 (38), 361. doi:10.1029/2004EO380001

Chung, H. M., Gormly, J. R., and Squires, R. M. (1988). Origin of Gaseous Hydrocarbons in Subsurface Environments: Theoretical Considerations of Carbon Isotope Distribution. *Chem. Geology.* 71 (1-3), 97–104. doi:10.1016/0009-2541(88)90108-8

Davis, E. E., Hyndman, R. D., and Villinger, H. (1990). Rates of Fluid Expulsion across the Northern Cascadia Accretionary Prism: Constraints from New Heat Row and Multichannel Seismic Reflection Data. *J. Geophys. Res.* 95 (B6), 8869–8889. doi:10.1029/JB095iB06p08869

Foschi, M., Paganoni, M., Cartwright, J. A., and Idiz, E. (2019). Microbial vs Thermogenic Gas Hydrates in the South Falkland Basin: BSR Distribution and Fluid Origin. *Mar. Pet. Geology.* 102, 695–703. doi:10.1016/j.marpetgeo.2019.01.023

Foucher, J. P., Nouzé, H., and Henry, P. (2002). Observation and Tentative Interpretation of a Double BSR on the Nankai Slope. *Mar. Geol.* 187 (1), 161–175. doi:10.1016/S0025-3227(02)00264-5

Freire, A. F. M., Matsumoto, R., and Santos, L. A. (2011). Structural-stratigraphic Control on the Umitaka Spur Gas Hydrates of Joetsu Basin in the Eastern Margin of Japan Sea. *Mar. Pet. Geology.* 28 (10), 1967–1978. doi:10.1016/j.marpetgeo.2010.10.004

Ganguly, N., Spence, G. D., Chapman, N. R., and Hyndman, R. D. (2000). Heat Flow Variations from Bottom-Simulating Reflectors on the Cascadia Margin. *Mar. Geol.* 164 (1–2), 53–68. doi:10.1016/S0025-3227(99)00126-7

Grevemeyer, I., and Villinger, H. (2001). Gas Hydrate Stability and the Assessment of Heat Flow through continental Margins. *Geophys. J. Int.* 145, 647–660. doi:10.1046/j.0956-540x.2001.01404.x

Gwiazda, R., Paull, C. K., Caress, D. W., Lorenson, T., Brewer, P. G., Peltzer, E. T., et al. (2016). "Eel Canyon Slump Scar and Associated Fluid Venting," in *Submarine Mass Movements and Their Consequences, 7th International Symposium*. Editors G. Lamarche, J. Mountjoy, S. Bull, T. Hubble, S. Krastel, A. Micallef, et al. (Springer), 411–418. doi:10.1007/978-3-319-20979-1_41

Haacke, R., Hamilton, T. S., Enkin, R. J., Esteban, L., and Pohlman, J. W. (2022). *2008007PGC Cruise Report: study of marine gas hydrates at the frontal ridge and mid-slope areas of the Vancouver Island accretionary wedge; Geological Survey of Canada, Open File 8874*, 172. doi:10.4095/329697

Haacke, R. R., Westbrook, G. K., and Hyndman, R. D. (2007). Gas Hydrate, Fluid Flow and Free Gas: Formation of the Bottom-Simulating Reflector. *Earth Planet. Sci. Lett.* 261 (3), 407–420. doi:10.1016/j.epsl.2007.07.008

Hayward, N., and Calvert, A. J. (2007). Seismic Reflection and Tomographic Velocity Model Constraints on the Evolution of the Tofino Forearc basin, British Columbia. *Geophys. J. Int.* 168 (2), 634–646. doi:10.1111/j.1365-246X.2006.03209.x

He, T., Spence, G. D., Riedel, M., Hyndman, R. D., and Chapman, N. R. (2007). Fluid Flow and Origin of a Carbonate mound Offshore Vancouver Island: Seismic and Heat Flow Constraints. *Mar. Geology.* 239, 83–98. doi:10.1016/j.margeo.2007.01.002

Hester, K. C., Peltzer, E. T., Walz, P. M., Dunk, R. M., Sloan, E. D., and Brewer, P. G. (2009). A Natural Hydrate Dissolution experiment on Complex Multi-Component Hydrates on the Sea Floor. *Geochimica et Cosmochimica Acta* 73, 6747–6756. doi:10.1016/j.gca.2009.08.007

Holbrook, W. S. (2001). "Seismic Studies of the Blake Ridge: Implications for Hydrate Distribution, Methane Expulsion, and Free Gas Dynamics," in *Natural*

Gas Hydrates: Occurrence, Distribution, and Detection. Editors C. K. Paull and W. P. Dillon (Washington, DC: AGU Geophysical Monograph), 124, 235–256. doi:10.1029/GM124p0235

Hornbach, M. J., Holbrook, W. S., Gorman, A. R., Hackwith, K. L., Lizarralde, D., and Pecher, I. (2003). Direct Seismic Detection of Methane Hydrate on the Blake Ridge. *Geophysics* 68, 92–100. doi:10.1190/1.1543196

Hunt, J. M., Huc, A. Y., and Whelan, J. K. (1980). Generation of Light Hydrocarbons in Sedimentary Rocks. *Nature* 288, 688–690. doi:10.1038/288688a0

Hyndman, R. D., and Davis, E. E. (1992). A Mechanism for the Formation of Methane Hydrate and Seafloor Bottom-Simulating Reflectors by Vertical Fluid Expulsion. *J. Geophys. Res.* 97 (B5), 7025–7041. doi:10.1029/91jb03061

Hyndman, R. D., and Spence, G. D. (1992). A Seismic Study of Methane Hydrate marine Bottom Simulating Reflectors. *J. Geophys. Res.* 97 (B5), 6683–6698. doi:10.1029/92JB00234

Hyndman, R. D., Spence, G. D., Chapman, R., Riedel, M., and Edwards, R. N. (2001). "Geophysical Studies of marine Gas Hydrate in Northern Cascadia," in *Natural Gas Hydrates: Occurrence, Distribution, and Detection*.. Editors C. K. Paull and W. P. Dillon, 124, 273–295.Geophys. Monogr

Hyndman, R. D. (1995). The Lithoprobe Corridor across the Vancouver Island continental Margin: the Structural and Tectonic Consequences of Subduction. *Can. J. Earth Sci.* 32, 1777–1802. doi:10.1139/e95-138

Hyndman, R. D., Wang, K., Yuan, T., and Spence, G. D. (1993). Tectonic Sediment Thickening, Fluid Expulsion, and the thermal Regime of Subduction Zone Accretionary Prisms: the Cascadia Margin off Vancouver Island. *J. Geophys. Res.* 98 (B12), 21865. doi:10.1029/93JB02391

Jenden, P. D., Drazan, D. J., and Kaplan, I. R. (1993). Mixing of Thermogenic Natural Gases in Northern Appalachian Basin. *Bulletin* 77 (6), 980–998. doi:10.1306/BDFF8DBC-1718-11D7-8645000102C1865D

Johns, M. J., Barnes, C. R., and Narayan, Y. R. (2006). Cenozoic Ichthyolith Biostratigraphy: Tofino Basin, British Columbia. *Can. J. Earth Sci.* 43, 177–204. doi:10.1139/E05-102

Johns, M. J., Trotter, J. A., Barnes, C. R., and Narayan, Y. R. (2012). Biostratigraphic, Strontium Isotopic, and Geologic Constraints on the Landward Movement and Fragmentation of Terranes within the Tofino Basin, British Columbia. *Can. J. Earth Sci.* 49, 819–856. doi:10.1139/e2012-032

Joseph, C., Campbell, K. A., Torres, M. E., Martin, R. A., Pohlman, J. W., Riedel, M., et al. (2013). Methane-derived Authigenic Carbonates from Modern and Paleoseeps on the Cascadia Margin: Mechanisms of Formation and Diagenetic Signals. *Palaeogeogr. Palaeoclimatol. Palaeoecol.* 390, 52–67. doi:10.1016/j.palaeo.2013.01.012

Joseph, C., Torres, M. E., Martin, R. A., Haley, B. A., Pohlman, J. W., Riedel, M., et al. (2012). Using the 87Sr/86Sr of Modern and Paleoseep Carbonates from Northern Cascadia to Link Modern Fluid Flow to the Past. *Chem. Geology.* 334, 122–130. doi:10.1016/j.chemgeo.2012.10.020

Kennett, J. P., Cannariato, K. G., Hendy, I. L., and Behl, R. J. (2003). *Methane Hydrates in Quaternary Climate Change: The Clathrate Gun Hypothesis*. Washington, D. C: AGU, 216.

Kinoshita, M., Moore, G. F., and Kido, Y. N. (2011). Heat Flow Estimated from BSR and IODP Borehole Data: Implication of Recent Uplift and Erosion of the Imbricate Thrust Zone in the Nankai Trough off Kumano. *Geochem. Geophys. Geosyst.* 12, a–n. doi:10.1029/2011GC003609

Klauda, J. B., and Sandler, S. I. (2005). Global Distribution of Methane Hydrate in Ocean Sediment. *Energy Fuels* 19 (2), 459–470. doi:10.1021/ef049798o

Kossel, E., Bigalke, N., Piñero, E., and Haeckel, M. (2013). The SUGAR Toolbox - A Library of Numerical Algorithms and Data for Modelling of Gas Hydrate Systems and marine Environments. *GEOMAR Rep. (N. Ser.)* 8, 160. doi:10.3289/geomar_rep_ns_8_2013

Kroeger, K. F., Plaza-Faverola, A., Barnes, P. M., and Pecher, I. A. (2015). Thermal Evolution of the New Zealand Hikurangi Subduction Margin: Impact on Natural Gas Generation and Methane Hydrate Formation - A Model Study. *Mar. Pet. Geology.* 63, 97–114. doi:10.1016/j.marpetgeo.2015.01.020

Kvenvolden, K. A., and McMenamin, M. A. (1980). *Hydrates of Natural Gas: A Review of Their Geological Occurrences*. Arlington, VA: U.S. Geol. Survey Circ. No. 825. Available at: https://pubs.usgs.gov/circ/1980/0825/report.pdf (Accessed October 26, 2021).

Kvenvolden, K. A. (1988). Methane Hydrate - A Major Reservoir of Carbon in the Shallow Geosphere? *Chem. Geol.* 71 (1), 41–51. doi:10.1016/0009-2541(88)90104-0

Laird, A. P., and Morley, C. K. (2011). Development of Gas Hydrates in a Deep-Water Anticline Based on Attribute Analysis from Three-Dimensional Seismic Data. *Geosphere* 7 (1), 240–259. doi:10.1130/GES00598.1

Lapham, L. L., Chanton, J. P., Chapman, R., and Martens, C. S. (2010). Methane Under-saturated Fluids in Deep-Sea Sediments: Implications for Gas Hydrate Stability and Rates of Dissolution. *Earth Planet. Sci. Lett.* 298, 275–285. doi:10.1016/j.epsl.2010.07.016

Lapham, L. L., Chanton, J. P., Martens, C. S., Sleeper, K., and Woolsey, J. R. (2008). Microbial Activity in Surficial Sediments Overlying Acoustic Wipeout Zones at a Gulf of Mexico Cold Seep. *Geochem. Geophys. Geosyst.* 9, a–n. doi:10.1029/2008GC001944

Lapham, L., Wilson, R., Riedel, M., Paull, C. K., and Holmes, M. E. (2013). Temporal Variability of in situ Methane Concentrations in Gas Hydrate-Bearing Sediments Near Bullseye Vent, Northern Cascadia Margin. *Geochem. Geophys. Geosyst.* 14 (7), 2445–2459. doi:10.1002/ggge.20167

Li, Y., and Gregory, S. (1974). Diffusion of Ions in Sea Water and in Deep-Sea Sediments. *Geochimica et Cosmochimica Acta* 38, 703–714. doi:10.1016/0016-7037(74)90145-8

Lu, H., Moudrakovski, I., Matsumoto, R., Dutrisac, R., and Ripmeester, J. (2008). The Characteristics of Gas Hydrates Recovered from Shallow Sediments at Umitaka spur, Eastern Margin of the Sea of Japan. AGU, Fall Meeting 2008, OS33A-1315, available online at: https://ui.adsabs.harvard.edu/abs/2008AGUFMOS33A1315L/abstract (last accessed October 27, 2021).

Lu, H., Seo, Y.-t., Lee, J.-w., Moudrakovski, I., Ripmeester, J. A., Chapman, N. R., et al. (2007). Complex Gas Hydrate from the Cascadia Margin. *Nature* 445, 303–306. doi:10.1038/nature05463

MacDonald, I. R., Reilly, J. F., Jr., Best, S. E., Venkataramaiah, R., Sassen, R., Amos, J., et al. (1996). "A Remote-Sensing Inventory of Active Oil Seeps and Chemosynthetic Communities in the Northern Gulf of Mexico," in *Hydrocarbon Migration and its Near-Surface Expression, AAPG Mem* (Tulsa, Okla: Am. Assoc. of Pet. Geol.), 66, 27

MacDonald, I. R., Sager, W. W., and Peccini, M. B. (2003). Gas Hydrate and Chemosynthetic Biota in Mounded Bathymetry at Mid-slope Hydrocarbon Seeps: Northern Gulf of Mexico. *Mar. Geology.* 198 (1-2), 133–158. doi:10.1016/s0025-3227(03)00098-7

McIver, R. D. (1981). "Gas Hydrates," in *Long-Term Energy Resources*. Editors R. F. Meyer and J. C. Olson (Boston, MA: Pitman), 713–726.

Mi, Y. (1998). *Seafloor Sediment Coring and Multichannel Seismic Studies of Gas Hydrate*. Victoria, BC, Canada: offshore Vancouver Island, MSc thesis, School of Earth and Ocean Sciences, University of Victoria.

Milkov, A. V., and Etiope, G. (2018). Revised Genetic Diagrams for Natural Gases Based on a Global Dataset of >20,000 Samples. *Org. Geochem.* 125, 109–120. doi:10.1016/j.orggeochem.2018.09.002

Milkov, A. V. (2005). Molecular and Stable Isotope Compositions of Natural Gas Hydrates: A Revised Global Dataset and Basic Interpretations in the Context of Geological Settings. *Org. Geochem.* 36, 681–702. doi:10.1016/j.orggeochem.2005.01.010

Naranyan, Y. R., Barnes, C. R., and Johns, M. J. (2005). Taxonomy and Biostratigraphy of Cenozoic Foraminifers from Shell Canada wells, Tofino Basin, Offshore Vancouver Island, British Columbia. *Micropaleontology* 51 (2), 101–167. doi:10.1661/0026-2803(2005)051

Paganoni, M., Cartwright, J. A., Foschi, M., Shipp, R. C., and Van Rensbergen, P. (2016). Structure II Gas Hydrates Found below the Bottom-Simulating Reflector. *Geophys. Res. Lett.* 43, 5696–5706. doi:10.1002/2016GL069452

Paull, C. K., Caress, D. W., Thomas, H., Lundsten, E., Anderson, K., Gwiazda, R., et al. (2015). Seafloor Geomorphic Manifestations of Gas Venting and Shallow Subbottom Gas Hydrate Occurrences. *Geosphere* 11, 491–513. doi:10.1130/GES01012.1

Pecher, I., Crutchley, G., Mountjoy, J., Gorman, A., Fraser, D., Kroeger, K., et al. (2014). Double BSRs on the Hikurangi Margin, New Zealand - Possible Implications for Gas Hydrate Stability and Composition. in" Proc. of the 8th Intl. Conf. on Gas Hydrates (ICGH8-2014), 28th July–1st Aug. abstract available online at:last accesss https://meetingorganizer.copernicus.org/EGU2018/EGU2018-10236.pdf (last accessed October 27, 2021).

Phrampus, B. J., Harris, R. N., and Tréhu, A. M. (2017). Heat Flow Bounds over the Cascadia Margin Derived from Bottom Simulating Reflectors and Implications for thermal Models of Subduction. *Geochem. Geophys. Geosyst.* 18, 3309–3326. doi:10.1002/2017GC00707710.1002/2017gc007077

Pohlman, J. W., Bauer, J. E., Waite, W. F., Osburn, C. L., and Chapman, N. R. (2011). Methane Hydrate-Bearing Seeps as a Source of Aged Dissolved Organic Carbon to the Oceans. *Nat. Geosci* 4, 37–41. doi:10.1038/ngeo1016

Pohlman, J. W., Canuel, E. A., Chapman, N. R., Spence, G. D., Whiticar, M. J., and Coffin, R. B. (2005). The Origin of Thermogenic Gas Hydrates on the Northern Cascadia Margin as Inferred from Isotopic (13C/12C and D/H) and Molecular Composition of Hydrate and Vent Gas. *Org. Geochem.* 36 (5), 703–716. doi:10.1016/j.orggeochem.2005.01.011

Pohlman, J. W., Kaneko, M., Heuer, V. B., Coffin, R. B., and Whiticar, M. (2009). Methane Sources and Production in the Northern Cascadia Margin Gas Hydrate System. *Earth Planet. Sci. Lett.* 287 (3-4), 504–512. doi:10.1016/j.epsl.2009.08.037

Pohlman, J. W., Riedel, M., Bauer, J. E., Canuel, E. A., Paull, C. K., Lapham, L., et al. (2013). Anaerobic Methane Oxidation in Low-Organic Content Methane Seep Sediments. *Geochimica et Cosmochimica Acta* 108, 184–201. doi:10.1016/j.gca.2013.01.022

Qian, J., Wang, X., Collett, T. S., Guo, Y., Kang, D., and Jin, J. (2018). Downhole Log Evidence for the Coexistence of Structure II Gas Hydrate and Free Gas below the Bottom Simulating Reflector in the South China Sea. *Mar. Pet. Geology.* 98, 662–674. doi:10.1016/j.marpetgeo.2018.09.024

Rehder, G., Brewer, P. W., Peltzer, E. T., and Friederich, G. (2002). Enhanced Lifetime of Methane Bubble Streams within the Deep Ocean. *Geophys. Res. Lett.* 29, 21–1. doi:10.1029/2001GL013966

Riedel, M., Collet, T., Scherwath, M., Pohlman, J., Hyndman, R. D., and Spence, G. D. (2022). "World Atlas of Submarine Gas Hydrates in Continental Margins," in *World Atlas of Submarine Gas Hydrates in Continental Margins*. Editors J. Mienert and C. Berndt, doi:10.1007/978-3-030-81186-0

Riedel, M., Collett, T. S., and Malone, M. (2010b). "Expedition 311 Synthesis: Scientific Findings," in *The Expedition 311 Scientists, Proc. IODP*. Editors M. Riedel, T. S. Collett, and M. J. Malone (Washington, DC: Integrated Ocean Drilling Program Management International, Inc.), 311. doi:10.2204/iodp.proc.311.213.201010.2204/iodp.proc.311.213.2010

Riedel, M., Collett, T. S., and Malone, M. J.the Expedition 311 Scientists (2006a). *Proc. IODP, 311*. Washington, DC: Integrated Ocean Drilling Program Management International, Inc.. doi:10.2204/iodp.proc.311.2006

Riedel, M., Côté, M. M., Neelands, P. J., Obana, K., Wania, R., Price, A., et al. (2014). Report on Cruise 2010007PGC, C.C.G. Vessel John P. Tully, 30 June - 10 July 2010, SeaJade-I Seafloor Earthquake Array - Japan Canada Cascadia Experiment, Ocean Bottom Seismometer Recovery, Methane Gas-Plume Acoustic Imaging, and CTD-Water Sampling Program. *Geol. Surv. Can. Open File* 7557, 295545. doi:10.4095/295545

Riedel, M., Novosel, I., Spence, G. D., Hyndman, R. D., Chapman, R. N., Solem, R. C., et al. (2006b). Geophysical and Geochemical Signatures Associated with Gas Hydrate-Related Venting in the Northern Cascadia Margin. *Geol. Soc. America Bull.* 118 (1), 23–38. doi:10.1130/B25720.1

Riedel, M., Scherwath, M., Römer, M., Veloso, M., Heesemann, M., and Spence, G. D. (2018). Distributed Natural Gas Venting Offshore along the Cascadia Margin. *Nat. Commun.* 9, 3264. doi:10.1038/s41467-018-05736-x

Riedel, M., Tréhu, A. M., and Spence, G. D. (2010a). Characterizing the thermal Regime of Cold Vents at the Northern Cascadia Margin from Bottom-Simulating Reflector Distributions, Heat-Probe Measurements and Borehole Temperature Data. *Mar. Geophys. Res.* 31, 1–16. doi:10.1007/s11001-010-9080-2

Römer, M., Riedel, M., Scherwath, M., Heesemann, M., and Spence, G. D. (2016). Tidally Controlled Gas Bubble Emissions: A Comprehensive Study Using Long-Term Monitoring Data from the NEPTUNE Cabled Observatory Offshore Vancouver Island. *Geochem. Geophys. Geosyst.* 17, 3797–3814. doi:10.1002/2016GC006528

Römer, M., Sahling, H., Pape, T., dos Santos Ferreira, C., Wenzhöfer, F., Boetius, A., et al. (2014). Methane Fluxes and Carbonate Deposits at a Cold Seep Area of the Central Nile Deep Sea Fan, Eastern Mediterranean Sea. *Mar. Geology.* 347, 27–42. doi:10.1016/j.margeo.2013.10.011

Ruppel, C. D., and Kessler, J. D. (2017). The Interaction of Climate Change and Methane Hydrates. *Rev. Geophys.* 55 (1), 126–168. doi:10.1002/2016RG000534

Ruppel, C. (2015). Permafrost-associated Gas Hydrate: Is it Really Approximately 1% of the Global System? *J. Chem. Eng. Data* 60 (2), 429–436. doi:10.1021/je500770m

Ruppel, C. (2007). Tapping Methane Hydrates for Unconventional Natural Gas. *Elements* 3 (3), 193–199. doi:10.2113/gselements.3.3.193

Sager, W. W., MacDonald, I. R., and Hou, R. (2003). Geophysical Signatures of Mud mounds at Hydrocarbon Seeps on the Louisiana continental Slope, Northern Gulf of Mexico. *Mar. Geol.* 198, 5. doi:10.1016/S0025-3227(03)00097-5

Sassen, R., Joye, S., Sweet, S. T., DeFreitas, D. A., Milkov, A. V., and MacDonald, I. R. (1999). Thermogenic Gas Hydrates and Hydrocarbon Gases in Complex Chemosynthetic Communities, Gulf of Mexico continental Slope. *Org. Geochem.* 30, 485–497. doi:10.1016/S0146-6380(99)00050-9

Sassen, R., and MacDonald, I. R. (1994). Evidence of Structure H Hydrate, Gulf of Mexico continental Slope. *Org. Geochem.* 22 (6), 1029–1032. doi:10.1016/0146-6380(94)90036-1

Sassen, R., Sweet, S. T., Milkov, A. V., DeFreitas, D. A., and Kennicutt, II, M. C. (2001). Thermogenic Vent Gas and Gas Hydrate in the Gulf of Mexico Slope: Is Gas Hydrate Decomposition Significant? *Geol*, 2, 1072–1110. doi:10.1130/0091-7613(2001)029<0107:TVGAGH>2

Scherwath, M., Thomsen, L., Riedel, M., Römer, M., Chatzievangelou, D., Schwendner, J., et al. (2019). Ocean Observatories as a Tool to advance Gas Hydrate Research. *Earth Space Sci.* 6, 2644–2652. doi:10.1029/2019EA000762

Schümann, T. K., Whiticar, M. J., and Rohr, K. M. M. (2008). *Petroleum Resource Potential of the Tofino Basin*. Victoria, BC, Canada: University of Victoria and the Ministry of Energy, Mines and Petroleum Resources MEMPR, 60.

Seeberg-Elverfeldt, J., Schlüter, M., Feseker, T., and Kölling, M. (2005). Rhizon Sampling of Porewaters Near the Sediment-Water Interface of Aquatic Systems. *Limnol. Oceanogr. Methods* 3 (8), 361–371. doi:10.4319/lom.2005.3.361

Shipley, T. H., Houston, M. H., Buffler, R. T., Shaub, F. J., McMillen, K. J., Ladd, J. W., et al. (1979). Seismic Reflection Evidence for Widespread Occurrence of Possible Gas Hydrate Horizons on continental Slopes and Rises. *AAPG Bull.* 63, 2204–2213. doi:10.1306/2f91890a-16ce-11d7-8645000102c1865d

Shouldice, D. H. (1971). Geology of the Western Canadian continental Shelf. *Bull. Can. Soc. Petrol. Geol.* 19, 405

Sloan, E. D., and Koh, C. (2008). *Clathrate Hydrates of Natural Gases*. 3rd ed.. Boca Raton, Fla, USA: CRC Press.

Solem, R. C., Spence, G. D., Vukajlovich, D., Hyndman, R. D., Riedel, M., Novosel, I., et al. (2002). Methane Advection and Gas Hydrate Formation within an Active Vent Field Offshore Vancouver Island. *Fourth Int. Conf. Gas Hydrates*.

Soloviev, V. (2002). Global Estimation of Gas Content in Submarine Gas Hydrate Accumulations. *Russ. Geol. Geophys.* 43, 609

Spence, G. D., Chapman, N. R., Hyndman, R. D., and Cleary, C. (2001a). Fishing Trawler Nets Massive "catch" of Methane Hydrates. *Eos Trans. AGU* 82 (50), 621. doi:10.1029/01eo00358

Spence, G. D., Coffin, R., and Hoehne, J. (2001b). VENTFLUX 2: Single Channel Seismics, Piston Coring and CTD Casts Associated with Gas Hydrates Offshore Vancouver Island, Report of Cruise PGC01-003 C.C.G. Vessel John P. Tully 23 July – 12 August 2001, available online at: https://apps.dtic.mil/sti/pdfs/ADA411571.pdf (last accessed October 13, 2021).

Spence, G. D., Haacke, R. R., and Hyndman, R. D. (2010). "4. Seismic Indicators of Natural Gas Hydrate and Underlying Free Gas," in *Geophysical Characterization of Gas Hydrates*. Editors M. Riedel, E. C. Willoughby, and S. Chopra (Houston, TX, USA: Society of Exploration Geophysicists), 39–71. Chapter 4. doi:10.1190/1.9781560802197.ch4

Spence, G. D., Hyndman, R. D., Chapman, N. R., Riedel, M., Edwards, N., and Yuan, J. (2000). "Cascadia Margin, Northeast Pacific Ocean: Hydrate Distribution from Geophysical Observations," in *Natural Gas Hydrate*. Editor M. D. Max (Dordrecht, The Netherlands: Kluwer Academic Publishers), 183–198.

Spence, G. D., Hyndman, R. D., Langton, S., Davis, E. E., and Yorath, C. J. (1991). Analysis and Interpretation of Seismic Data from the Western Canada continental Margin, Part 2: Multichannel Reflection Data across the Vanocuver Island Margin, marine Multichannel Seismic Reflection Survey across the Northern Cascadia Accretionary Prism. *Geol. Surv. Can. Open File* 2391, 132398. doi:10.4095/132398

Suess, E. (2014). Marine Cold Seeps and Their Manifestations: Geological Control, Biogeochemical Criteria and Environmental Conditions. *Int. J. Earth Sci. (Geol Rundsch)* 103, 1889–1916. doi:10.1007/s00531-014-1010-0

Thomsen, L., Barnes, C., Best, M., Chapman, R., Pirenne, B., Thomson, R., et al. (2012). Ocean Circulation Promotes Methane Release from Gas Hydrate Outcrops at the NEPTUNE Canada Barkley Canyon Node. *Geophys. Res. Lett.* 39, a–n. doi:10.1029/2012GL052462

Topham, D. R. (1984). The Formation of Gas Hydrates on Bubbles of Hydrocarbon Gases Rising in Seawater. *Chem. Eng. Sci.* 39 (5), 821–828. doi:10.1016/0009-2509(84)85051-4

Trofimuk, A., Cherskiy, N., and Tsarev, V. (1973). Accumulations of Natural Gases in Zones of Hydrate Formation in the Hydrosphere. *Doklady Akademii Nauk SSSR* 212, 931

Villinger, H. W., Tréhu, A. M., and Grevemeyer, I. (2010). "18. Seafloor Marine Heat Flux Measurements and Estimation of Heat Flux from Seismic Observations of Bottom Simulating Reflectors," in *Geophysical Characterization of Gas Hydrates, Society of Exploration Geophysicists*. Editors M. Riedel, C. E. Willoughby, and S. Chopra (Houston, TX, USA: Society of Exploration Geophysicists), 279–300. doi:10.1190/1.9781560802197.ch18

Westbrook, G. K., Carson, B., and Musgrave, R. J. (1994). *Proceedings of the Ocean Drilling Program, 146 Part 1 Initial Reports*, 146. College Station, TX: Ocean Drilling Program. doi:10.2973/odp.proc.ir.146-1.1994Pt. 1

Whiticar, M. J. (1999). Carbon and Hydrogen Isotope Systematics of Bacterial Formation and Oxidation of Methane. *Chem. Geology.* 161, 291–314. doi:10.1016/S0009-2541(99)00092-3

Whiticar, M. J. (2021). "Carbon Isotopes in Petroleum Science," in *Encyclopedia of Petroleum Geoscience. Encyclopedia of Earth Sciences Series*. Editor R. Sorkhabi (Springer), 1–19. Cham. doi:10.1007/978-3-319-02330-4_310-1

Whiticar, M. J., Faber, E., and Schoell, M. (1986). Biogenic Methane Formation in marine and Freshwater Environments: CO2 Reduction vs. Acetate Fermentation-Isotope Evidence. *Geochimica et Cosmochimica Acta* 50, 693–709. doi:10.1016/0016-7037(86)90346-7

Whiticar, M. J., and Hovland, M. (1995). "Data Report: Molecular and Stable Isotope Analyses of Sorbed and Free Hydrocarbon Gases of Leg 146, Cascadia and Oregon Margins," in *Proceedings-Ocean Drilling Program Scientific Results*. Editors B. Carson, G. K. Westbrook, R. J. Musgrave, and E. Suess (College Station, TX: National Science Foundation), 439–450. doi:10.2973/odp.proc.sr.146-1.212.1995

Whiticar, M. J. (2020). "The Biogeochemical Methane Cycle," in *Hydrocarbons, Oils and Lipids: Diversity, Origin, Chemistry and Fate. Handbook of Hydrocarbon and Lipid Microbiology*. Editor H. Wilkes (Cham: Springer), 669–746. doi:10.1007/978-3-319-90569-3_5

Willoughby, E., and Fyke, J. (2003). *BofFiNS 2003: Gas Hydrate Investigation at Bullseye and Fish-Boat and Survey of the Intersection of the Nootka Fault with the continental Margin Using Single-Channel Seismic Streamer Cruise PGC03-004: 3 August- 29 August, 2003 C.C.G.S. John P. Tully, CEOR*. Victoria, BC, Canada: School of Earth and Ocean Sciences, University of Victoria, 57

Wilson, R. M., Lapham, L. L., Riedel, M., Holmes, M. E., and Chanton, J. P. (2015). Observing Methane Hydrate Dissolution Rates under Sediment Cover. *Mar. Chem.* 172, 12–22. doi:10.1016/j.marchem.2015.03.004

Yamano, M., Uyeda, S., Aoki, Y., and Shipley, T. H. (1982). Estimates of Heat Flow Derived from Gas Hydrates. *Geol* 10, 339–343. doi:10.1130/0091-7613(1982)10<339:eohfdf>2.0.co;2

Yelisetti, S., and Spence, G. D. (2021). Seismic Velocity Structure beneath the Tofino Forearc Basin Using Full Waveform Inversion. *Energies* 14 (11), 3099–3124. doi:10.3390/en14113099

Zander, T., Haeckel, M., Berndt, C., Chi, W.-C., Klaucke, I., Bialas, J., et al. (2017). On the Origin of Multiple BSRs in the Danube Deep-Sea Fan, Black Sea. *Earth Planet. Sci. Lett.* 462, 15–25. doi:10.1016/j.epsl.2017.01.006

Zhang, W., Liang, J., Wan, Z., Su, P., Huang, W., Wang, L., et al. (2020). Dynamic Accumulation of Gas Hydrates Associated with the Channel-Levee System in the Shenhu Area, Northern South China Sea. *Mar. Pet. Geology.* 117, 104354. doi:10.1016/j.marpetgeo.2020.104354

Conflict of Interest: The authors declare that the research was conducted in the absence of any commercial or financial relationships that could be construed as a potential conflict of interest.

Publisher's Note: All claims expressed in this article are solely those of the authors and do not necessarily represent those of their affiliated organizations, or those of the publisher, the editors and the reviewers. Any product that may be evaluated in this article, or claim that may be made by its manufacturer, is not guaranteed or endorsed by the publisher.

frontiers | Frontiers in Earth Science

ORIGINAL RESEARCH
published: 09 May 2022
doi: 10.3389/feart.2022.835685

Microbial Methane Generation and Implications for Stability of Shallow Sediments on the Upper Slope, U.S. Atlantic Margin

Olin R. Carty[1,2]* *and Hugh Daigle*[1,2]

[1]Hildebrand Department of Petroleum and Geosystems Engineering, The University of Texas at Austin, Austin, TX, United States, [2]Center for Subsurface Energy and the Environment, The University of Texas at Austin, Austin, TX, United States

Dissociation of methane hydrates in shallow marine sediments due to increasing global temperatures can lead to the venting of methane gas or seafloor destabilization. Along the U.S. Atlantic margin there is a well-documented history of slope failure and numerous gas seeps have been recorded. However, it is not fully understood whether the observed gas seepages can lead to slope failure as seafloor data is often sparse. We used machine learning algorithms to predict total organic carbon (TOC) and porosity at the seafloor on the U.S. Atlantic margin. Within this region, an area of high TOC predictions (1.5—2.2% dry weight) occurred along the continental slope from (35.4°N, 75.0°W) to (39.0°N, 72.0°W), aligning with documented gas seeps in the region. Elsewhere, predicted values of TOC were near or below 1% dry weight. In the area of high TOC, we modeled hydrate and gas formation over a 120,000 years glacial cycle. Along the feather edge, average hydrate saturations at the base of the hydrate stability zone (BHZ) were between 0.2% and 0.7% with some models predicting hydrate saturation above 3% and average peak gas saturations ranged from 4% to 6.5%. At these locations we modeled the pore pressure response of sediments at the BHZ to hydrate dissociation due to an increase in temperature. We focused on purely drained and undrained loading environments and used a non-linear Hoek-Brown failure envelope to assess whether failure criteria were met. In a drained loading environment, where excess pore pressure is instantly dissipated, we found that the change in effective stress due to hydrate dissociation is small and no failure is expected to occur. In an undrained loading environment, where excess pore pressure does not dissipate, the change in effective stress due to hydrate dissociation is larger and shear failure is expected to occur even at low hydrate saturations (0.2%—1%) forming final gas saturations below 0.1%. Therefore, we conclude that the dissociation of hydrates along the feather edge can lead to the conditions necessary for sediment failure.

Keywords: methane hydrate, hydrate dissociation, machine learning, k-nearest neighbor, slope failure

OPEN ACCESS

Edited by:
Andreas Lorke,
University of Koblenz and Landau, Germany

Reviewed by:
Daniela Fontana,
University of Modena and Reggio Emilia, Italy
Christian Stranne,
Stockholm University, Sweden

***Correspondence:**
Olin R. Carty
ocarty@utexas.edu

Specialty section:
This article was submitted to Marine Geoscience, a section of the journal Frontiers in Earth Science

Received: *14 December 2021*
Accepted: *20 April 2022*
Published: *09 May 2022*

Citation:
Carty OR and Daigle H (2022) Microbial Methane Generation and Implications for Stability of Shallow Sediments on the Upper Slope, U.S. Atlantic Margin. Front. Earth Sci. 10:835685. doi: 10.3389/feart.2022.835685

1 INTRODUCTION

Methane hydrates are solid, crystalline structures composed of methane and water. Hydrates are stable in an environment with low temperature, high pressure, and where sufficient methane is present (Kvenvolden and Claypool, 1988). Hydrates are stable beneath the seafloor when the bottom water temperature approaches 0°C and the water depth is greater than 300 m (Kvenvolden and Lorenson, 2001). The depth range at which methane hydrates are stable is known as the gas hydrate stability zone (GHSZ). The GHSZ continues below the seafloor to the base of the hydrate stability zone (BHZ) where the hydrate phase envelope intersects the geotherm. The depth of the BHZ can be found up to 2000 m below the seafloor but is typically found at much shallower depths (Kvenvolden, 1993).

An increase in local temperature or decrease in local pressure can cause destabilization and the subsequent dissociation of hydrates (Phrampus and Hornbach, 2012; Ruppel and Kessler, 2017). Methane gas released due to hydrate dissociation can migrate up to the seafloor and into the water column. In the water column, it can oxidize into CO_2 causing ocean acidification, or it may continue through the water column and into the atmosphere as a greenhouse gas (Biastoch et al., 2011). Increasing temperatures and the subsequent dissociation of hydrate is especially a concern at the BHZ where the *in-situ* pressure and temperature conditions intersect the hydrate phase envelope and even minor changes in temperature can cause hydrate dissociation. There is evidence that within the last 100 years, increases in global ocean temperatures have led to hydrate instability and the shifting of the hydrate stability zone along the Beaufort shelf and off the Svalbard coast (Ferré et al., 2012; Sarkar et al., 2012; Phrampus et al., 2014). In shallower water (around 500 m) where the BHZ is at or near the seafloor, also known as the feather edge, the increase in seafloor temperature is problematic (Ruppel, 2011). As water depth increases, this becomes less of an issue as the GHSZ thickens. In shallow marine sediments within 132 m of the seafloor, the presence of gas can lead to tensile fracturing in the sediments, and gas in these shallower sediments can occupy a much larger volume than hydrate under the same conditions (Daigle et al., 2020).

We are interested in the geomechanical properties of the seafloor sediment when methane gas is formed due to hydrate dissociation from increasing temperatures. We focus specifically on the feather edge where the hydrate stability zone is the thinnest. To begin, we model TOC along the U.S. Atlantic margin. At a few locations where estimated seafloor TOC is high, we use a 1D sediment burial and methanogenesis model to simulate hydrate and gas formation over a 120,000 years glacial cycle. At locations along the feather edge, we assume a 1°C increase in temperature at the BHZ and model the geomechanical response of the system as hydrate dissociates to methane gas and water. We are interested in determining if the conditions for sediment failure due to an increase in temperature can exist under the right circumstances. Thus, at each location we calculate a Hoek-Brown failure envelope to determine if failure occurs due to dissociation.

2 BACKGROUND

Ocean Drilling Program (ODP) boreholes give an insight into locations where methane gas and methane hydrate occur along the U.S. Atlantic margin. Along the upper continental slope, offshore of New Jersey, ODP boreholes report subsurface microbial methane, indicating methanogenesis in the area (Shipboard Scientific Party, 1994a; Shipboard Scientific Party, 1994b; Shipboard Scientific Party, 1994c; Shipboard Scientific Party, 1994d; Shipboard Scientific Party, 1994e; Shipboard Scientific Party, 1998a). South of this region, offshore of North Carolina and South Carolina, seismic profiles from the ODP show a strong bottom-simulating reflector (BSR) at some locations, inferring the presence of hydrate in the area (Shipboard Scientific Party, 1996b; Shipboard Scientific Party, 1996c; Holbrook et al., 1996; Dickens et al., 1997).

In sediment near the seafloor, gas-driven tensile failure can occur due to a combination of low stresses and weak sediments. Fine grained sediments with a higher clay fraction are more prone to failure as gas within these sediments has a higher capillary pressure. Therefore, less gas is required to be present to cause failure (Daigle et al., 2020). One mechanism for gas generation is the dissociation of methane hydrates although gas generated directly from microbial methanogenesis can also lead to tensile failure.

The release of methane gas from the seafloor can be seen in water column acoustic anomalies which correspond to gas plumes (Judd, 2003; Skarke et al., 2014). In global surveys summarizing free gas distribution in marine sediments, Fleischer et al. (2001) and Judd (2003) both note occurrences of free gas along the U.S. Atlantic margin. The release of gas is evident in the development of pockmarks on the seafloor which form due to the accumulation of gas beneath a seal, and the subsequent release of gas when the seal fails (Cathles et al., 2010; Brothers et al., 2014; Sultan et al., 2014). Along the U.S. Atlantic margin, pockmarks just shallow of the feather edge were reported by Brothers et al. (2014). In addition, asymmetric depressions corresponding to elongated gas blowouts were reported by Hill et al. (2004) along the U.S. Atlantic margin.

Investigations by Skarke et al. (2014) found instances of methane gas leakage from the seafloor along the U.S. Atlantic margin at a higher concentration than previously thought. Skarke et al. (2014) identified 570 gas plumes on the northern U.S. Atlantic margin, with 440 of these seeps (77%) lying between the shelf break (~180 m below sea level) and 600 m below sea level. The location of these plumes would lie just updip of the feather edge of the GHSZ. The seeps in this area were further explored by Prouty et al. (2016) who suggest that seepage may have begun as early as 15 kya in the Baltimore Canyon seep field, and between one to three kya at the deeper Norfolk seep field (**Figure 1**). Gas seeps in this region have $\delta^{13}C$ values between −73.5‰ and −109‰ and methane:ethane ratios between 385 and 926 indicating that the gas is microbial in origin (Pohlman et al., 2017).

3 MATERIALS AND METHODS

The Global Predictive Seabed Model (GPSM) was used to model and create maps of total organic carbon (TOC) and porosity at the seafloor. In areas with high predicted values of TOC, we used

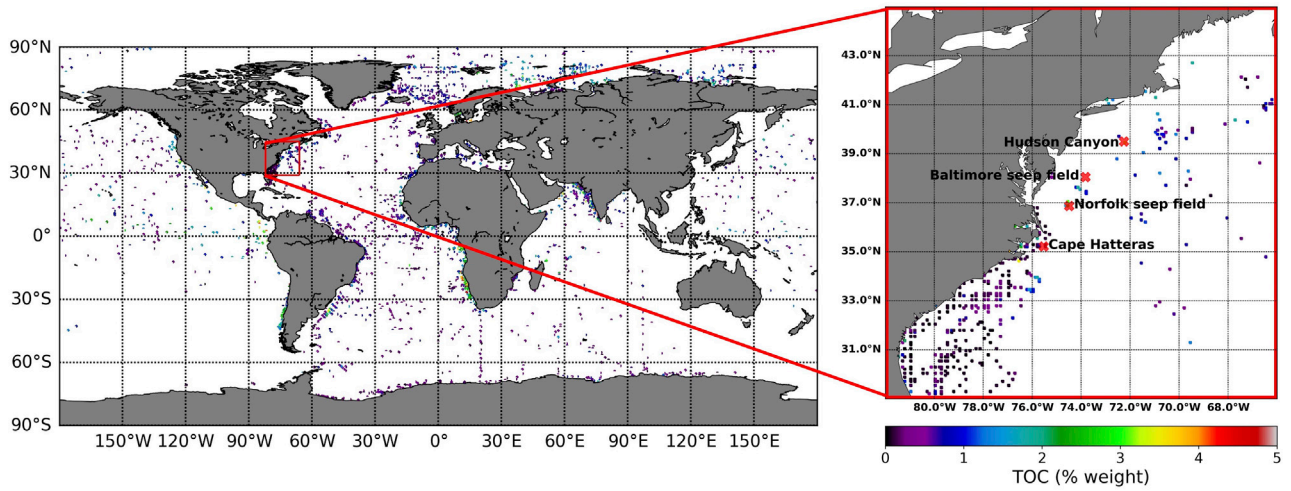

FIGURE 1 | Known measurements of total organic carbon (TOC) globally and within the area 29°N–45°N and 82°W–66°W. In the zoomed in region, the locations of Hudson Canyon, Baltimore seep field, Norfolk seep field, and Cape Hatteras are also indicated.

Dakota and PFLOTRAN to model the generation of methane gas and hydrate due to methanogenesis and the burial of the seafloor sediment. In locations where the BHZ was close to the seafloor, we modeled the geomechanical response of sediment to gas generated by hydrate dissociation to better understand whether shear failure or tensile failure would occur. We specifically focused on hydrate dissociation caused by an increase in temperature at the BHZ. The hydrate formed through the PFLOTRAN model and subsequently dissociated in the geomechanical model was assumed to be structure I methane hydrate.

3.1 The Global Predictive Seabed Model

GPSM is a geospatial machine learning model developed by the Naval Research Laboratory and can be used to predict TOC, porosity, sediment composition, and other properties of seafloor sediments in areas where no measurements have been sampled or recorded (Martin et al., 2015). GPSM offers a variety of machine learning methods to create geospatial models including k-nearest neighbor regression, support vector regression, and random forest regression. In these geospatial machine learning models, predictions do not assume spatial autocorrelation. Instead, the characteristics or parameters of locations are compared rather than the geographic proximity of two points.

3.1.1 Modeling Seafloor Total Organic Carbon

To model seafloor TOC, we followed the methodology of Lee et al. (2019) and used a k-nearest neighbor (kNN) approach. For our model, a value of k = 5 was chosen. When predicting TOC values on the seafloor at unknown locations, GPSM compares various observed attributes of the unknown location with the same observed attributes at locations with known TOC values. These observed attributes are known as predictors and are found in global grids known as predictor grids. In our model 1749 predictor grids were used including data from multiple global surveys such as seamount censuses, global river fluxes of carbon and sediments to the ocean, and decadal trends in oxygen concentration in subsurface waters, among others (Phrampus et al., 2020). Therefore, our model differs slightly from that of Lee et al. (2019) as we are using both new and additional predictor grids.

In our model, 5,595 individual locations with known TOC values were sampled (Seiter et al., 2004). These are from the upper 5 cm of sediment and so are roughly Pleistocene in age. Of these, we excluded values of TOC over 5% to mitigate outliers in the predictions. We then averaged values for each 5 × 5 arc-minute grid cell to obtain a uniformly spaced grid. Of the 5,595 locations with known TOC, 126 points had measurements greater than 5% TOC (2.2% of the data) and were excluded. After creating a uniformly spaced grid, 4,879 useable observations remained (**Figure 1**).

We used tenfold validation to validate our model. In tenfold validation, the data is first randomly split into 10 equal sized groups. One group is excluded as a test set and the remaining 90% of the data is used to form a training set. A model (in this case kNN) is created using the training set of data and then tested on the remaining 10% of the data where the predicted value from the model can be compared to the actual value of the test set. This process is done 10 times. Plotting the observed versus predicted data values gives us the validation graph in **Figure 2**. The validation of this data shows an R^2 value of 0.6151, lying below the ideal 1:1 fit at high observed TOC values. Other k values between 3 and 20 were tested to optimize for the highest R^2 value. We chose k = 5 for our model as it was among the top performing models and is consistent the work done by Lee et al. (2019).

After forming a model using tenfold cross validation, we checked the predictor grids for collinearity. Grids with a correlation coefficient over 0.99 were removed, leaving 1,622 of the 1,749 predictor grids. In addition, an error grid was used to remove predictor grids with high error. Since this grid is made of random, uniform noise, it should have no influence on the data being modelled. The predictors grids can be ordered by individual error and any predictor grids with a higher

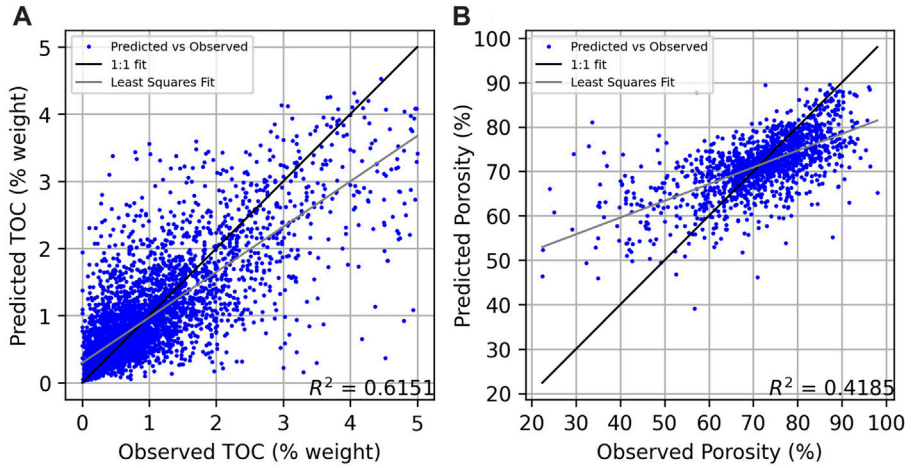

FIGURE 2 | Validation plot of **(A)** observed TOC values versus predicted TOC values for the k-nearest neighbor model (k = 5) and **(B)** observed porosity values versus predicted porosity values for the random forest model using 100 trees and a minimum samples per leaf of 3. The 1:1 fit line shows where observed values match the predicted values. The least squares regression fit of the model is depicted by the gray line.

error than the noise grid is ignored and not used in the model. This left us with 1,618 predictor grids which were used for the prediction. TOC predictions were made on the 5 × 5 arc-minute grid within the area 29°N–45°N and 82°W–66°W (**Figure 1**).

3.1.2 Modeling Seafloor Porosity

We also used GPSM to model seafloor porosity in our region of interest. The same 1,749 predictor grids used to predict seafloor TOC were used in our seafloor porosity model. In this model, 2027 individual locations with known seafloor porosity values were sampled (Martin et al., 2015). Of these, values of porosity over 90% and below 20% were excluded and the remaining values were averaged for each 5 × 5 arc-minute grid leaving us with 1,440 useable observations. Both a kNN approach and a random forest regression (RFR) approach were modeled. The RFR methodology followed a similar workflow to the work done by Graw et al. (2021) and is similar to the work done to predict seafloor TOC. As we previously did, we used a tenfold cross validation method to determine model variation. A similar validation plot to TOC was calculated for both the kNN and RFR methods using tenfold validation for seafloor porosity. A maximum R^2 value for the RFR method was calculate using 100 trees and a minimum samples per leaf of 3 (**Figure 2**). Although this R^2 value (0.4185) was less than the R^2 value for the kNN test (0.4562), we chose to use the RFR model due to lower standard deviations of the porosity predictions at our points of interest.

3.2 Dakota and PFLOTRAN

Dakota and PFLOTRAN were used to model the burial of seafloor sediments and the resulting generation of methane hydrate and methane gas in an approach similar to Eymold et al. (2021). Both Dakota and PFLOTRAN are open-source software developed by Sandia National Laboratories. Dakota was developed to provide optimization tools for simulations and we used it to sample PFLOTRAN input parameters, creating a distribution of model results (Adams et al., 2021).

PFLOTRAN is a parallel subsurface flow code which solves a system of nonlinear partial differential equations describing flow and transport in porous medium (Hammond et al., 2014). Following the work of Eymold et al. (2021) and Nole et al. (2017), we used PFLOTRAN to simulate hydrate and gas formation from microbial gas during sediment burial. Eymold et al. (2021) and Nole et al. (2017) use a primary variable switch method to solve for mass and energy conservation with phase change (hydrate versus gas phase). The governing equations are set up as a finite volume difference discretization, and variables are then solved for in a fully implicit manner using a nonlinear Newton-Raphson iteration. The methane generation rate was calculated following Malinverno (2010):

$$q(z) = k_\alpha \lambda \alpha \exp\left[-\frac{\lambda}{\omega}(z - z_{\mathrm{SMT}})\right] \quad (1)$$

where $q(z)$ is methane generation rate with depth in kg/m^3/s, k_α = 2,241 kg/m^3 is the conversion factor of TOC to methane, λ is the methanogenesis rate (s^{-1}), ω is the sedimentation rate (m/s), and z is the sediment depth (m). The depth of the sulfate-methane transition (z_{SMT}) was set at 15 m below seafloor (mbsf) based on work done by Malinverno (2010) and Egger et al. (2018). The metabolizable organic carbon remaining at the SMT (α) was set at 75% (Bhatnagar et al., 2007).

Initial conditions and boundary conditions for the simulation were also set up following the methodology of Eymold et al. (2021) and Nole et al. (2017). The initial conditions were set using Dirichlet temperature values, Dirichlet mole fraction values, and hydrostatic pressure at the seafloor. Temperature was set throughout the sediment column at a fixed temperature gradient from the seafloor. In addition, the mole fraction for methane in the aqueous phase was set to 0.001 along the entire profile. At the U.S Atlantic margin, there is documentation of gas in sediments as old as the Oligocene as well as deeper Mesozoic accumulations of thermogenic gas (Shipboard Scientific Party, 1994a; Shipboard

TABLE 1 | Input parameters for Dakota and PFLOTRAN.

Parameter	Status	Value	Units
Seafloor TOC	Modeled with GPSM (max 5%)	Variable	%
Seafloor porosity (ϕ_0)	Modeled with GPSM (0.2–0.9)	Variable	—
Porosity	$\phi_0 e^{(-depth/1251)}$ Kominz et al. (2011)	Variable	—
Sedimentation Rate	From Restreppo et al. (2020)	Variable	m/s
Heat Flux	48 ± 2 Fuchs et al. (2021)	Variable	mW/m^2
Methanogenesis Rate	Fixed	5×10^{-14}	s^{-1}
Geothermal Gradient	Variable, based on porosity/heat flux	Variable	°C/m
Pressure Change Limit	Max change per time step	1×10^5	Pa
Temperature Change Limit	Max change per time step	1	°C
Gravity	Fixed	−9.8	m/s^2
Labile Portion of TOC	Set to 75% TOC	Variable	%
Conversion Factor of Methane	Fixed	2,241	kg/m^3
Diffusion Coefficient of Methane	Fixed	1×10^{-9}	m^2/s
Gas Viscosity	Methane	1.1×10^{-5}	Pa-s
Tortuosity	Fixed	1.4	—
Rock Density	Fixed	2,700	kg/m^3
Thermal Conductivity (dry)	Fixed	1	W/m/°C
Thermal Conductivity (wet)	Fixed	1	W/m/°C
Heat Capacity	Fixed	830	J/kg°C
Permeability	Fixed	1×10^{-15}	m^2
SMT Depth	Fixed	15	mbsf
Van Genuchten Pressure	Fixed	5.8×10^{-4}	Pa^{-1}
Van Genuchten Pore Size Factor	Fixed	0.189	—
Liquid Residual Saturation	Fixed	0.1	—
Max Capillary Pressure	Fixed	1×10^8	Pa
Gas Residual Saturation	Fixed	0.15	-
Initial Liquid Pressure	Initial Condition	Variable	Pa
Initial Mole Fraction	Initial Condition	1×10^{-3}	—
Initial Temperature	Initial Condition	Variable	°C
Initial Hydrostatic Liquid Pressure	Initial Condition	Variable	Pa
Initial Dirichlet Hydrate Saturation	Initial Condition	1×10^{-8}	—
Initial Dirichlet Temperature	Initial Condition	Variable	°C
Neumann Liquid Flux	Bottom Boundary Condition	0	m/yr
Neumann Gas Flux	Bottom Boundary Condition	0	m/yr
Neumann Energy Flux	Bottom Boundary Condition	Q	W/m^2
Hydrostatic Liquid Pressure	Top Boundary Condition	Variable	Pa
Dirichlet Mole Fraction	Top Boundary Condition	1×10^{-3}	—
Dirichlet Temperature	Top Boundary Condition	Variable	°C

Scientific Party, 1994b; Shipboard Scientific Party, 1994c; Shipboard Scientific Party, 1994d; Shipboard Scientific Party, 1994e; Party, 1998a; Shipboard Scientific Party, 1998a; Party, 1998b). However, since we were most interested in gas and hydrate close to the seafloor and the role of seafloor TOC in generating it, we chose to ignore the hydrate and gas that may already exist in the areas we model. At the bottom of the depth profile, Neumann boundary conditions were set such that the liquid and gas flux at the base of the profile were both 0, and heat flux at the boundary was equal to the heat flux sampled by Dakota. Since we were interested in the hydrate saturation near the feather edge, a maximum depth of 1,000 mbsf was used for our model. This ensured that the bottom boundary conditions (constant flux) did not directly influence hydrate and gas predictions at the feather edge.

3.3 Dakota and PFLOTRAN Inputs

We used PFLOTRAN to simulate methanogenesis and hydrate formation in a 1D model over time. A period of 120,000 years was chosen, representing the length of a glacial-interglacial cycle. Although this length of time was chosen to represent the glacial-interglacial cycle length, our goal was not to simulate the actual conditions over the last 120,000 years since many of the exact parameters and conditions are unknown to us. Even at the locations we are modeling, there are few constraints on the distribution and amount of gas and hydrate in the system. Therefore, we chose to model a variety of outcomes using Dakota to sample different initial seafloor conditions (TOC, porosity, sedimentation rate, and heat flux) while leaving other conditions such as seafloor temperature and pressure constant over time. This allowed us to get a general sense of how much gas and hydrate could form over a set amount of time which we then used as a basis to predict what might happen if the ocean warms. To set up this probabilistic model, Dakota was used to provide a distribution of results by sampling the PFLOTRAN input parameters TOC, sedimentation rate, heat flux, and porosity (**Table 1**). Specifically, Dakota used Latin hypercube sampling to provide a distribution of input variables that were modeled with PFLOTRAN. **Table 1** summarizes the input variables used in the PFLOTRAN/Dakota model, with many values chosen following the work of Eymold et al. (2021).

TABLE 2 | Locations picked for PFLOTRAN/Dakota simulation.

#	Location	Depth (m)	
	Along Shelf Strike		
1	(36.6966, −74.6463)	508	Feather edge
2	(37.2228, −74.4960)	510	Feather edge
3	(37.7490, −74.1523)	497	Feather edge
4	(38.1570, −73.6906)	487	Feather edge
	Along Shelf Dip		
5	(37.5865, −74.26)	434	
6	(37.5805, −74.2494)	651	Feather edge
7	(37.3822, −73.8646)	1901	
8	(37.2049, −73.5260)	2,595	
9	(36.9652, −73.1084)	3,061	

Dakota sampled TOC, sedimentation rate, heat flux, and seafloor porosity using a normal distribution. As previously discussed, TOC predictions and standard deviations were modeled using GPSM predictor grids from Phrampus et al. (2020) and observed data points from Seiter et al. (2004) (**Figure 1**). To avoid values of zero, a lower bound of TOC was set to 0.01%. An upper bound of TOC was set at 5%, like the GPSM model, to avoid unrealistically high values. Similarly, seafloor porosity was modeled using GPSM predictor grids from Phrampus et al. (2020) and observed data points from Martin et al. (2015). The lower and upper bounds on seafloor porosity were set to 20% and 90% respectively. At depth, porosity was calculated using the trend for marine silty clays presented by Kominz et al. (2011):

$$\phi(z) = \phi_0 e^{-\frac{z}{1251}} \tag{2}$$

where ϕ is porosity. Here we assumed the regression of porosity followed the trend presented by Kominz et al. (2011), changing ϕ_0 to the value predicted at a given location in our region of interest. Sedimentation rates and standard deviations were determined from Restreppo et al. (2020) who modeled global oceanic sediment accumulation rates using GPSM at a 5 × 5 arc-minute resolution. Bounds on sedimentation rates were set to a minimum of 1×10^{-14} m/s (3.16×10^{-5} cm/yr) and to a maximum of 1 m/s. For the studied area, heat flux was sampled from Fuchs et al. (2021), and was set to 48 ± 2 mW/m^2. A methanogenesis rate of $\lambda = 5 \times 10^{-14}$ s^{-1} was chosen based on estimates of $\lambda = 1 \times 10^{-14}$ s^{-1} from Bhatnagar et al. (2007) and $\lambda = 1 \times 10^{-13}$ s^{-1} from Malinverno (2010). This value for methanogenesis rate also lies between the constraints of $1 \times 10^{-15} \leq \lambda \leq 1 \times 10^{-13}$ s^{-1} used by Eymold et al. (2021).

We focused our investigation on the area bounded by 36.6°N–38°N and 74.5°W–73.1°W. This area shows some of the higher TOC estimates in the modeled region. **Table 2** summarizes the locations where PFLOTRAN and Dakota were used to model hydrate and gas generation. We picked four points along the strike of the continental shelf, located near the feather edge, and five locations along the shelf dip.

At each location, the depth of the seafloor was determined with the Global Multi-Resolution Topography (GMRT) Synthesis (Ryan et al., 2009). The GMRT Synthesis provides high resolution bathymetry data for almost 10% of the global ocean. Individual locations can be queried through the GMRT PointServer Web Service to retrieve accurate water depths at specific latitude and longitude locations.

Seafloor temperatures were calculated at a given depth through a polynomial regression. Data from Boyer et al. (2018) provided 47 temperature profiles from conductivity-temperature-depth (CTD) casts within the 36.6°N–38°N and 74.5°W–73.1°W study area. Since the area of focus was the GHSZ feather edge, near the continental slope, a visual inspection of profile location was used to choose temperature profiles near the continental slope. This left 10 temperature profiles, and a 6th order polynomial regression was used to create a model of water temperature for depths shallower than 1,000 m:

$$T(z) = 5.450\text{x}10^{-16}z^6 - 1.641\text{x}10^{-12}z^5 + 1.763\text{x}10^{-9}z^4 - 7.746\text{x}10^{-7}z^3 + 1.075\text{x}10^{-4}z^2 - 8.606\text{x}10^{-3}z + 12.504. \tag{3}$$

As done with the initial conditions and boundary conditions, the other parameters in the PFLOTRAN model were chosen following the work of Eymold et al. (2021). Many of the values chosen are comparable to values measured at ODP wells in the region. For example, the thermal conductivity parameters for wet and dry sediment of 1 W/m/°C lie between the values found at ODP well site 1,073, ranging between 0.89 and 1.5 W/m/°C (Shipboard Scientific Party, 1998a). ODP wells (sites 902, 903, and 1,073) in this region have permeability measurements in the range of $10^{-17} - 10^{-16}$ m^2 (Blum et al., 1996; Dugan et al., 2003). However, we chose to use the permeability value of 10^{-15} m^2 as done by Eymold et al. (2021) which can account for siltier beds that may occur in the region.

3.4 Geomechanics Model

Following the PFLOTRAN/Dakota simulation of sediment burial and methanogenesis two geomechanical models were used to simulate hydrate dissociation at the BHZ due to an increase in temperature. Our goal was to determine if the conditions needed for sediment failure can exist under the right circumstances, particularly for expected amounts of gas generated microbially, rather than determining the exact conditions needed for sediment failure.

As hydrate dissociates, gas pressure of the system increases causing a reduction in effective stress of the sediment. This can lead to elastic volumetric deformation of the sediment. Although some volumetric expansion will occur due to the increase in gas pressure, shallow marine sediments can still fracture and this fracturing behavior is well described by linear elastic fracture mechanics (Boudreau, 2012; Johnson et al., 2012). Since we are focused near the seafloor, at the feather edge, effective stresses will be small and we are unlikely to build up enough gas pressure to lead to large strains. Therefore, we chose to ignore the volumetric expansion of the sediment. Mechanics for plastic volumetric deformation due to hydrate dissociation have been discussed by Lee et al. (2010) and Waite et al. (2009). In sediments with hydrate saturations of 50–100% Lee et al. (2010) found a decrease in sediment porosity due to hydrate dissociation. However, Waite

et al. (2009) discuss that S_h = 25% seems to be a threshold above which pore-filling hydrate becomes load-bearing hydrate. At low saturations, the pore-filling hydrate does not change the shear stiffness of the sediment (Waite et al., 2009). Therefore, in our model we will ignore plastic deformation and possible dilation during dissociation.

We focused specifically on the five hydrate bearing locations at the feather edge and modeled the drained and undrained responses that these sediments exhibit during loading. In the drained loading environment, water is allowed to flow out of the sediment during hydrate dissociation and the pore water pressure remains constant. Since the amount of gas formed during dissociation is small, we do not exceed the mobility threshold of gas (Daigle et al., 2020). Therefore, the gas formed will not dissipate through porous flow and will stay in the pore space. In an undrained loading environment, neither water nor gas are allowed to flow and the pore water pressure increases. In both the drained and undrained loading models, the initial pore space of the system was assumed to contain only hydrate and water. The hydrate dissociation reaction was assumed to go to completion (**Eq. 4**), leading to a final pore space containing only methane gas and water. In addition, no response to dissociation was modeled until the hydrate had fully dissociated to methane gas and water. In this way the final state of the system we model only includes gas and water in the pore space.

$$CH_4 \cdot 5.75H_2O \rightarrow CH_4 + 5.75H_2O \tag{4}$$

In modeling the dissociation reaction only at start and at completion, we ignore changes in pressure within the system that can cause hydrate to reform as local pressure and temperature conditions change during deformation. In addition, we ignore the rate of temperature change and fluid flow as we allow the increase in temperature and final state of the pore space to exist without any additional phase equilibrium calculations.

3.4.1 Drained Model

In the drained loading end member response to hydrate dissociation, water pressure before and after dissociation is constant. Capillary pressure was found using the van Genuchten parameterization:

$$u_c = P_o\left(\left[\frac{S_w - S_{wirr}}{1 - S_{wirr}}\right]^{-1/m} - 1\right)^{1-m} \tag{5}$$

where u_c is the capillary pressure, S_w is the wetting phase (water) saturation, S_{wirr} is the irreducible wetting phase saturation, P_o is the capillary entry pressure, and m is a shape defining parameter (van Genuchten, 1980). The van Genuchten parameters were constrained using mercury intrusion capillary pressure (MICP) measurements performed on marine sediments from locations around the world (Daigle et al., 2020). The following correlations were determined for P_o and m:

$$m = (0.601 \pm 0.0297)e^{(0.640\pm0.0972)f_c} \tag{6}$$

$$P_o = (0.101 \pm 0.0284)e^{(6.019\pm0.541)\left(1-\phi+S_{wirr}\right)f_c} \tag{7}$$

where f_c is the clay fraction (mass fraction of particles with equivalent diameter < 3.8 microns) and the reported errors are ±1 standard deviation (**Figure 3**). Clay fraction was set to 50% (f_c = 0.5) to represent a typical marine silty clay and porosity was calculated with depth as described above. To determine S_{wirr}, we used the correlation reported by Daigle et al. (2015):

$$S_{wirr} = (0.326 \pm 0.0220)f_c^{0.219\pm0.103} + (0.0262 \pm 0.00915)\big/\phi. \tag{8}$$

Using the parameters in **Eqs 6–8** and f_c = 0.5, **Figure 3** shows the van Genuchten capillary drainage curve for porosities of 0.5, 0.6, and 0.7.

The Peng and Robinson (1976) equation of state was used to calculate the pressure of methane gas based on temperature and the molar volume of the methane gas. We assumed values for methane critical temperature (T_c = 190.56 K), methane critical pressure (P_c = 45.99 bar), and methane acentric factor (ω = 0.011) based on Poling et al. (2001).

The relationship between gas pressure (u_g) and water pressure (u_w) is given by:

$$u_g = u_w + u_c. \tag{9}$$

Using **Eqs 2,5–9** and inputs of water depth, sediment depth, hydrate saturation, original temperature, and final temperature, we solved for capillary pressure using Newton-Raphson optimization. From the capillary pressure solution and the above equations, we were able to calculate final values for water pressure, gas pressure, methane molar volume, gas saturation, water saturation, and capillary pressure.

3.4.2 Undrained Model

In the undrained loading end member response to hydrate dissociation, methane and water mass are both conserved during the dissociation reaction. Thus, $mol_{CH_4,i} = mol_{CH_4,f}$ and $mol_{H_2O,i} = mol_{H_2O,f}$. To model undrained loading, we used a process similar to the drained loading model. In addition to **Eqs 2,5–9**, final water saturation ($S_{w,f}$) had to be considered as well as water density before and after hydrate dissociation. Water density was determined at a given temperature using the seawater equation of state of Safarov (2003):

$$u_w = A\rho_w^2 + B\rho_w^8 + C\rho_w^{12} \tag{10}$$

where u_w has units MPa and ρ_w is in g/cm^3. The coefficients A, B, C are polynomial functions of temperature (Safarov, 2003; Safarov et al., 2009).

In both the drained and undrained loading responses to hydrate dissociation, porosity was assumed constant. Thus, we were able to use the relation between hydrate and gas saturation from Daigle et al. (2020):

$$S_h = S_g\frac{V_{m,h}}{V_{m,g}} \tag{11}$$

where the molar volume of gas is represented by $V_{m,g}$. We are assuming a structure I hydrate, so the molar volume of hydrate, represented by $V_{m,h}$, is a constant value: $V_{m,h}$ = 132 cm^3/mol. In a similar process to the drained loading method, final water

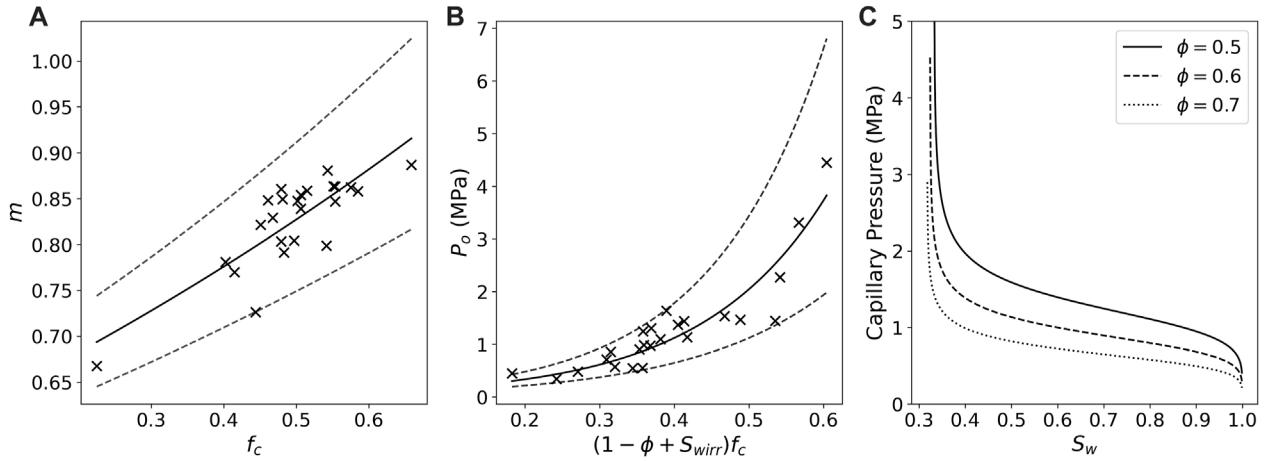

FIGURE 3 | Best fit lines for van Genuchten parameters **(A)** m (**Eq. 6**) and **(B)** P_o (**Eq. 7**). Error bars of ±1 standard deviation are represented by gray dashed lines. Black X's represent MICP measurements performed on marine sediments. **(C)** Water saturation graphed against capillary pressure for porosity ϕ =0.5 (solid line), ϕ =0.6 (dashed line), and ϕ =0.7 (dotted line).

pressure was calculated using Newton-Raphson optimization. We then calculated other values using **Eqs 2**,**5**–**11**.

3.4.3 Calculating Stresses

To calculate *in situ* stresses before hydrate dissociation, a simple calculation for hydrostatic water pressure was used:

$$u_w = (z_{water} + z_{sed})\rho_w g \tag{12}$$

where z_{water} is water depth in meters, z_{sed} is depth below seafloor in meters, ρ_w = 1,024 kg/m^3, g = 9.81 m/s^2, and u_w is in Pa. Overburden stress (σ_v) was determined by:

$$\sigma_v = z_{water}\rho_w g + g\int_0^{z_{sed}} \rho_b \tag{13}$$

where σ_v is in Pa. Bulk density (ρ_b) was determined at a given depth using the calculated porosity curve:

$$\rho_b = \phi(z_{sed})\rho_w + \left(1-\phi(z_{sed})\right)\rho_g \tag{14}$$

with a grain density ρ_g = 2,700 kg/m^3.

Effective stress (σ') prior to hydrate dissociation can be simply calculated as:

$$\sigma' = \sigma - u_w. \tag{15}$$

Following the methods of Daigle et al. (2020), we assumed that the maximum principal stress is vertical ($\sigma_1 = \sigma_v$) and the sediments are vertically transversely isotropic ($\sigma_2 = \sigma_3 = \sigma_h$). The relation of σ_h' and σ_v' can be expressed as:

$$\sigma_h' = \frac{\nu}{1-\nu}\sigma_v' \tag{16}$$

or

$$\sigma_h = \frac{\nu}{1-\nu}(\sigma_v - u_w) + u_w \tag{17}$$

where ν is Poisson's ratio and subscripts v and h represent vertical and horizontal stresses respectively. To calculate Poisson's ratio with depth, a sixth-order polynomial was fit to marine sediment data up to 650 m deep from Hamilton (1979).

$$\nu(z) = 2.467\text{x}10^{-18}z^6 - 8.363\text{x}10^{-15}z^5 + 1.108\text{x}10^{-11}z^4 - 7.234\text{x}10^{-9}z^3 + 2.390\text{x}10^{-6}z^2 - 4.234\text{x}10^{-4}z + 0.487. \tag{18}$$

After dissociation, the pore space is a two-phase system of methane gas and water. To calculate effective stress, we followed the methods of Bishop (1959) and Nuth and Laloui (2008):

$$\sigma' = \sigma - \pi \tag{19}$$

$$\pi = S_w u_w + S_g u_g \tag{20}$$

where the equivalent pore pressure, π, is a weighted average of the water pressure and gas pressure in the system. **Eqs 19**,**20** also hold for the pre-dissociation case with no gas pressure as u_g = 0 and thus $\pi = u_w$. With this, the change in effective stress at the BHZ due to hydrate dissociation was calculated.

3.4.4 Failure Model

A nonlinear Hoek-Brown failure envelope was constructed at each location with two goals in mind: 1. to determine if any failure occurred due to hydrate dissociation, and 2. which type of failure occurred (tensile or shear failure). This followed the work of Hoek and Brown (1997) and the methodology of Daigle et al. (2020). We assumed that the sediments were initially intact with no faults, fractures, or joints, so the tensile strength, T, was calculated by:

$$T = \frac{c_u}{2}\left(m_i - \sqrt{m_i^2 + 4}\right) \tag{21}$$

where c_u is the unconfined compressive strength and m_i is the Hoek-Brown constant. We set m_i = 4 as reported by Hoek and Brown (1997) for claystones. This also follows the work done by

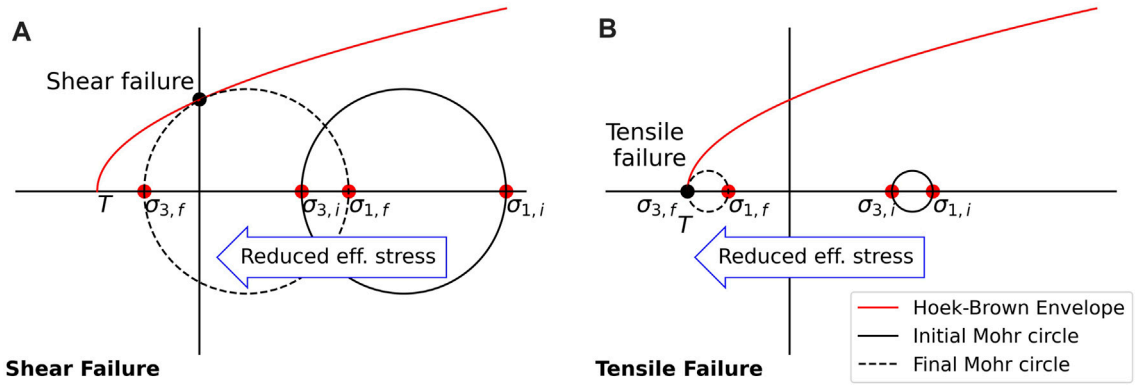

FIGURE 4 | Example movement of Mohr circle due to hydrate dissociation. Initial stresses are denoted with the subscript *i*. Final stresses are denoted with the subscript *f*. In **(A)**, shear failure occurs when the Mohr circle intersects the Hoek-Brown envelope at $|\sigma_3'| < |T|$. In **(B)**, tensile failure occurs when the Mohr circle intersects the Hoek-Brown envelope at $|\sigma_3'| = |T|$.

Daigle et al. (2020) who note that $m_i = 4 \pm 2$ is consistent with results from multiple triaxial shear experiments performed on marine muds and mudstones.

To calculate c_u, we used the correlation derived for muds and mudrocks by Ingram and Urai (1999):

$$\log_{10} c_u = -6.36 + 2.45 \log_{10}(0.86 V_p - 1172) \tag{22}$$

where c_u is in MPa and V_p is the compressional wave velocity in m/s. At each depth we calculated V_p using the equation derived from Hamilton (1979) for marine sediments:

$$V_p(z) = 0.257z^3 - 0.741z^2 + 1.304z + 1.511. \tag{23}$$

Finally, the Hoek-Brown failure envelope was calculated from Hoek and Brown (1997):

$$\tau = A c_u \left(\frac{\sigma_n' - T}{c_u} \right)^B, \tag{24}$$

where τ is the shear stress of the sample, σ_n' is the effective normal stress of the sample, and A and B are Hoek-Brown fitting parameters. Values of $A = 1.02$ and $B = 0.858$ were calculated by fitting failure envelopes to the results of triaxial tests performed on marine clays from the Gulf of Mexico and the Bay of Bengal (Silva et al., 2000; Moses et al., 2003; Dugan and Germaine, 2009).

The Hoek-Brown failure envelope was calculated based on the initial sediment properties prior to dissociation. Once dissociation occurred, both σ_v' and σ_h' were recalculated using **Equation 19**. Failure occurs if any points of the new Mohr circle lie to the left of the Hoek-Brown failure envelope. Since we assumed that the dissociation reaction went to completion, it was possible that the new effective stresses ($\sigma_{v,f}'$ and $\sigma_{h,f}'$) both lie past the Hoek-Brown failure envelope. In reality, failure would initiate as soon as the Mohr circle began to cross the Hoek-Brown envelope: tensile failure occurring if the Mohr circle crossed the failure envelope at $\sigma_3' = T$ (where $\sigma_3' = \sigma_h'$) and shear failure occurring if the Mohr circle crossed the failure envelope when $|\sigma_3'| < |T|$ (**Figure 4**).

4 RESULTS

4.1 GPSM

The weight percent of TOC at the seafloor predicted with GPSM is shown in **Figure 5** as well as the standard deviation and mean inexperience of these predictions. The highest TOC values were predicted along the line from (35.4°N, 75.0°W) to (39.0°N, 72.0°W). Comparing this region in the prediction map to the standard deviation map, known seafloor TOC values are sparse in this area and TOC standard deviations are higher than the rest of the predicted grid. The locations chosen along the shelf strike can be found in this area. The mean inexperience is calculated as the average distance in parameter space from the predicted location to its five nearest neighbors. Compared to the standard deviation map, a relatively low mean experience can be seen along the line from (35.4°N, 75.0°W) to (39.0°N, 72.0°W). Thus, although there is a high variance of predictions, there are other locations globally that are parametrically close to locations along this shelf strike line. A summary of the predicted weight percent of TOC for the nine modeled locations can be found in **Table 3**.

4.2 Dakota and PFLOTRAN

The range of input values sampled by Dakota and used in the PFLOTRAN burial process to generate gas and hydrate are summarized in **Table 3**.

Average TOC predictions were around 2% dry weight at the shallower locations near the feather edge (sites 1–6). At deeper locations (sites 7–9), TOC predictions were closer to 1% dry weight. Seafloor porosity was around 65% at shallow locations and predictions increased to 73% for deeper location. Average sedimentation rates were just over 0.007 cm/yr with standard deviations around 0.1 cm/yr (Restreppo et al., 2020). As discussed in the Methods section, to avoid negative sedimentation rates, a lower bound for sedimentation rate was set at 3.16×10^{-5} cm/yr and any values sampled smaller than this value were set to 3.16×10^{-5} cm/yr. These sedimentation rates are lower than the sedimentation rates on the U.S. Atlantic margin found to the north and south, but the studied location could simply be in an

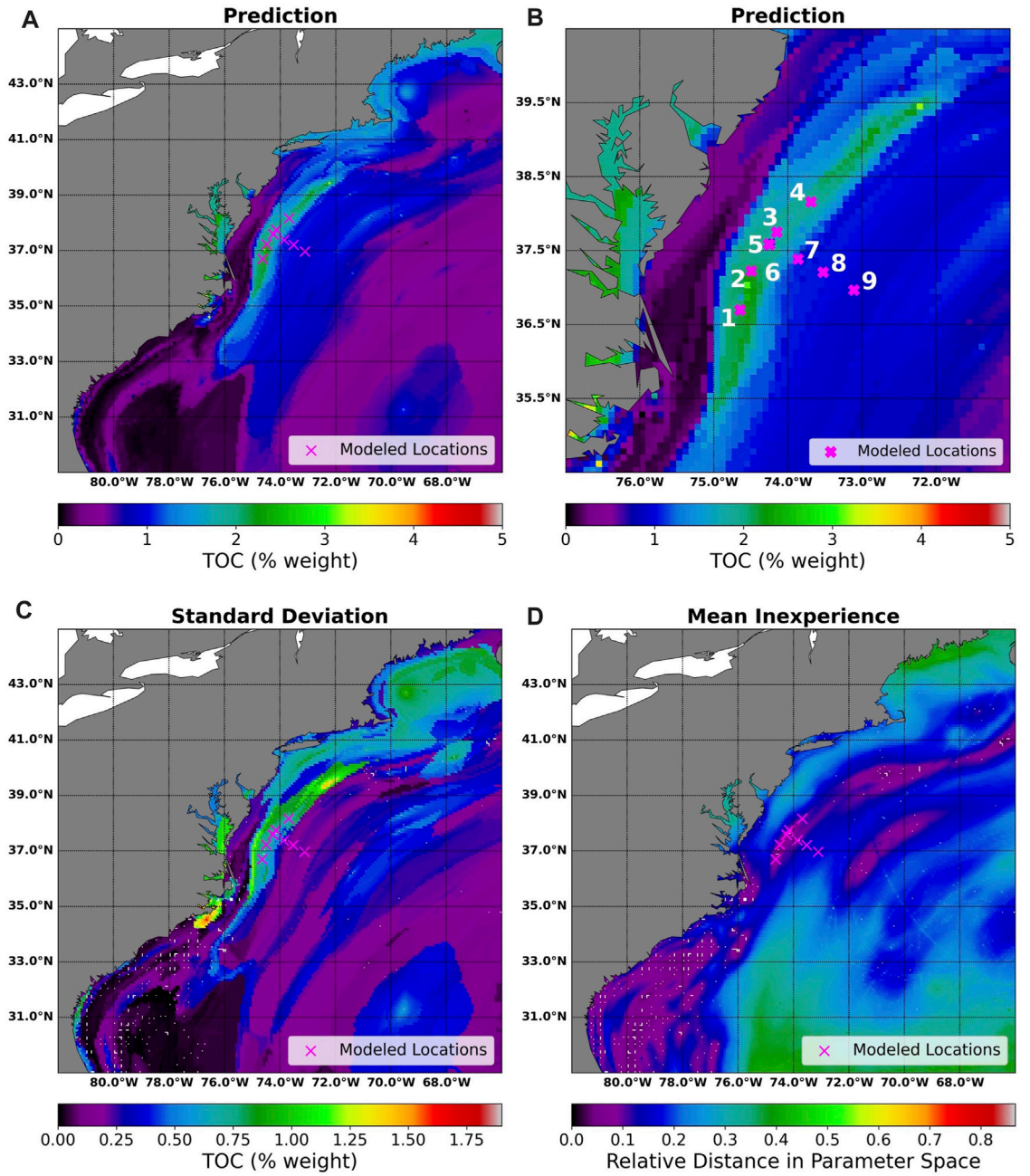

FIGURE 5 | Output maps from GPSM over the area 29°N–45°N and 82°W–66°W. Plot **(A)** depicts the predicted weight percent of total organic carbon (TOC) on the seafloor. Plot **(B)** is the same mapped zoomed in around the area of interest with the locations modeled with PFLOTRAN/Dakota numbered. Between (35.4°N, 75.0°W) and (39.0°N, 72.0°W) an area of increased seafloor TOC was predicted. The locations along the shelf strike can be found in this area. Plots **(C,D)** show the standard deviation and mean inexperience of predictions over the region. Locations with known TOC values are marked by white dots on the standard deviation and mean inexperience maps. The nine locations where gas and hydrate formation was modeled are marked with a magenta ×.

area of low sediment influx. Measurements to the north along the U.S. Atlantic margin (offshore of New Jersey) range from 0.011 cm/yr to 0.058 cm/yr (Shipboard Scientific Party, 1994a; Shipboard Scientific Party, 1994b; Shipboard Scientific Party, 1994c; Shipboard Scientific Party, 1994d; Shipboard Scientific Party, 1994e; Shipboard Scientific Party, 1998a) while locations to the south (offshore North Carolina) are closer to 0.02 cm/yr (Shipboard Scientific Party, 1994b; Shipboard Scientific Party, 1994c; Shipboard Scientific Party, 1996a; Shipboard Scientific Party, 1998b). Location nine had a much lower predicted sedimentation rate than the other eight locations, corresponding to its further distance from the shelf edge and seacoast, as well as its overall depth. Heat flux for all simulations were between 42.3 and 52.2 mW/m^2.

TABLE 3 | Value ranges used in PLFOTRAN/Dakota model (gas locations[g] and feather edge locations[f]). For all locations, heat flux ranged from 42.3–52.2 mW/m^2.

#	Location	z_{water} (m)	T_{sf} (°C)	TOC Range (% dry weight)	ϕ_0 Range	Sed. Range (cm/yr)
	Along Shelf Strike					
1[f]	(36.6966, −74.6463)	508	5.573	0.627–3.781	0.430–0.883	0.00047–0.218
2[f]	(37.2228, −74.4960)	510	5.552	0.509–4.081	0.415–0.881	0.00072–0.353
3[f]	(37.749, −74.1523)	497	5.694	0.179–3.500	0.387–0.869	0.00047–0.218
4[f]	(38.157, −73.6906)	487	5.814	0.446–3.496	0.409–0.871	0.00073–0.356
	Along Shelf Dip					
5[g]	(37.5865, −74.26)	434	6.611	0.280–3.700	0.386–0.866	0.00047–0.217
6[f]	(37.5805, −74.2494)	651	4.980	0.391–3.385	0.420–0.881	0.00072–0.353
7	(37.3822, −73.8646)	1901	3.100	0.281–1.969	0.538–0.884	0.00090–0.442
8	(37.2049, −73.5260)	2,595	2.900	0.654–1.471	0.536–0.890	0.00095–0.469
9	(36.9652, −73.1084)	3,061	2.700	0.460–1.410	0.546–0.886	0.00059–0.287

At each location, we ran 50 simulations using PFLOTRAN, and sampled the seafloor TOC, seafloor porosity, sedimentation rate, and heat flux inputs with Dakota. For an individual location, the resulting output profiles of gas, hydrate, and temperature were plotted against depth, and a base of hydrate stability was calculated. **Figure 6** shows the hydrate saturation profiles and the gas saturation profiles with depth for the nine study locations.

Figure 7 shows an example temperature profile with depth for site 1, and includes the hydrate phase envelope calculated from Kamath (1984):

$$P = \exp\left[38.980 - \frac{8533.80}{T}\right] \tag{25}$$

where hydrostatic pressure, P (kPa), can be calculated at a given sediment depth using **Eq. 12**, allowing us to calculate temperature, T (K). The phase envelope was included to illustrate the difference in the BHZ between simulations. Due to the diversity of sampled heat flux values, the geothermal gradient for each simulation is different, leading to a range of depths where the phase envelope is crossed and thus a range of BHZ depths.

Table 4 summarizes the hydrate profiles shown in **Figure 6**. Some simulations failed to run or ran into oscillatory errors, thus producing no hydrate or gas predictions. The number of runs that produced hydrate and gas profiles (successful runs) is noted at each location. In addition, the number of runs where hydrate formed is summarized. At each site, the average BHZ was calculated as the depth where the hydrate phase envelope from Kamath (1984) intersected the average temperature profile at the location. In addition, we noted the maximum depth at which hydrate formed (Max hyd. depth) at each location. This depth represents the extent of the zone of actual hydrate occurrence where the concentration of methane exceeds the solubility of methane in seawater in addition to the pressure and temperature conditions of the hydrate stability zone (Xu and Ruppel, 1999). At sites 1-4 and site 6, the average extent of the zone of hydrate occurrence is very similar the calculated BHZ. Looking at the profiles for these five locations, hydrate concentrations are often at a maximum at this depth before they drop to zero and methane gas is witnessed instead. The minimum and maximum extent of the zone of hydrate occurrence are also noted, illustrating the varying extent of the BHZ between models as shown in **Figure 7**.

At sites 7-9, fewer simulations result in the growth of hydrate. As was done for sites 1-4 and 6, the average depth of the BHZ was calculated for these sites. Interestingly, at these deeper locations, the average extent of the zone of hydrate occurrence was much shallower than the depth of the BHZ. At site 7, the average BHZ is 516.5 mbsf, although graphically it can be seen that a majority of the hydrate profiles do not reach this depth (**Figure 6**). Even fewer simulations form hydrate at sites 8 and 9, and none of the simulations produce hydrate near the depth of the BHZ (601.4 mbsf and 647.7 mbsf respectively) at these locations. In profile 5, no hydrate forms. This location is upslope of the feather edge and outside of the hydrate stability zone.

A distribution of total hydrate mass for each profile is shown in **Figure 8**. Site 6 has the largest distribution of total hydrate formed, however site 7 has the largest amounts of hydrate formed in a run. The larger values of hydrate mass in sites 7-9 can be attributed to the thickness of the hydrate stability zone at these locations. Near the feather edge (sites 1–4) many runs do not generate hydrate, and those that do have very thin hydrate layers due to the shallow BHZ. This leads to much lower predictions of total hydrate formed in this area.

The gas saturation profiles shown in **Figure 6** are summarized in **Table 5**. Gas generation occurs within the modeled 1,000 m sediment column in eight of the simulations. The only simulation in which no gas was generated during the 50 runs was at the deepest location, site 9. When calculating the maximum gas saturation and the depth of the maximum gas saturation in **Table 5**, only maximum saturations shallower than 1,000 m were considered. Therefore, site eight does not have a maximum gas saturation value or depth. The maximum gas saturation for site seven occurs in only one run and may be an outlier. Comparing the remaining six locations, site 5 has the largest average maximum gas saturation. As discussed, this site is upslope of the feather edge and outside of the hydrate stability zone.

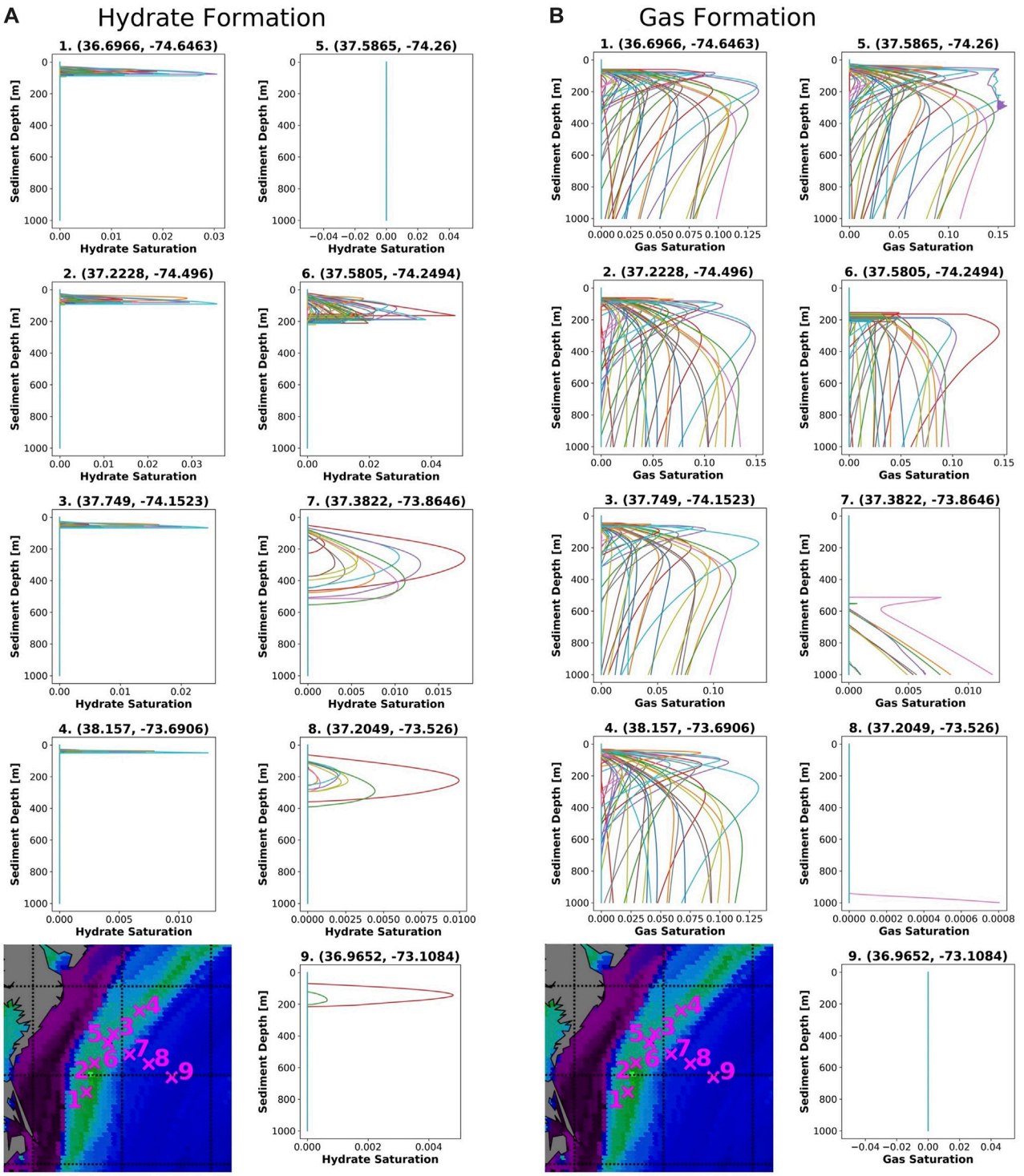

FIGURE 6 | Figure **(A)** shows simulation outputs of hydrate saturation with depth at each modeled location. Figure **(B)** shows simulation outputs of gas saturation with depth at each modeled location.

4.3 Dissociation and Failure Criteria

At the five locations along the feather edge (sites 1–4, 6) we modeled hydrate dissociation at the BHZ due to a temperature increase of 1°C, ignoring any changes in pressure over time due to the rise and fall of sea level were ignored. At each location, we calculated a final gas saturation due to dissociation, along with the resulting final water pressure, final gas pressure, and capillary pressure (**Table 6**). A value for π (**Eq. 20**) was also calculated at

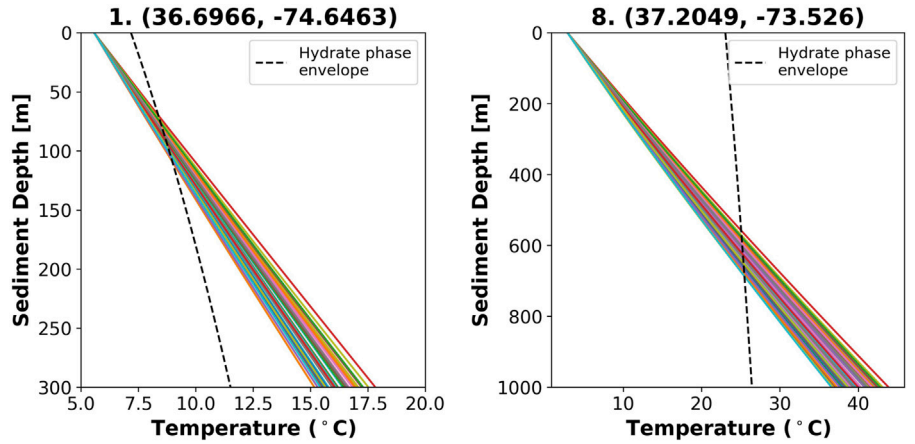

FIGURE 7 | Temperature with depth at Site 1 (36.6966, −74.6463) and Site 8 (37.2049, −73.5260). Hydrates are stable where the temperature profile is to the left of the hydrate phase envelope (black dashed line). Around 80 mbsf sediment depth at Site 1 (water depth 508 m), temperature profiles begin to cross the hydrate phase envelope, so hydrate is no longer stable. At the deeper Site 8 (water depth 2,595 m), temperature profiles begin to cross the hydrate phase envelope around 550 mbsf. Note the different depth scales between the two temperature profiles. This was done to better visualize the intersection of the phase envelope at Site 1.

TABLE 4 | Summary of hydrate profiles modeled with PFLOTRAN and Dakota (gas locations[g] and feather edge locations[f]).

#	Total Runs	Success Runs	Hydrate Runs	BHZ avg m)	Max hyd depth AVG (m)	Max hyd depth MIN (m)	Max hyd depth MAX (m)	Hydrate saturation BHZ	Temp. At at BHZ (°C)
	Along Shelf Strike								
1[f]	50	48	38	76.9	76.1	59.5	93.5	0.0070	8.48
2[f]	50	47	40	78.3	78.1	60.5	96.5	0.0071	8.53
3[f]	50	46	24	61.7	56.9	44.5	67.5	0.0063	8.05
4[f]	50	43	15	48.2	41.3	32.5	50.5	0.0022	7.65
	Along Shelf Dip								
5[g]	50	46	0	n/a	n/a	n/a	n/a	n/a	n/a
6[f]	50	46	37	179.3	182.1	108.5	220.5	0.0104	11.77
7	50	50	12	516.5	409.1	145.5	551.5	0.0011	22.32
8	50	50	9	601.4	285.3	152.5	390.5	0	25.20
9	50	50	2	647.7	208.5	202.5	214.5	0	26.76

each location. Comparing the drained and undrained models, both predict a decrease from the initial saturation of hydrate to the final saturation of gas. This is because a constant density (and thus molar volume) was chosen for hydrate whereas the methane gas that forms is compressible. Although the BHZ at these locations is relatively near the seafloor, there is still enough pressure from the 50–100 m of sediment and 500 m of water to compress any gas that forms. In the drained model, hydrate saturation decreases to the final gas saturation by a factor of about four ($\frac{1}{4}S_h \approx S_g$). In the undrained model, the decrease in hydrate saturation to gas saturation is over twice as large ($\frac{1}{10}S_h \approx S_g$). In the undrained environment water pressure is not held constant during dissociation and instead the total moles of water before and after dissociation is constant, leading to a larger decrease in hydrate to gas saturation. The impact of drainage can also be seen when comparing the water pressures calculated before ($u_{w,i}$) and after ($u_{w,f}$) dissociation for both models. By definition, the drained model has a constant water pressure during hydrate dissociation. This leads to final gas pressures ($u_{g,f}$) that are similar to the water pressure. On the other hand, when hydrate dissociates in the undrained model, water pressure nearly doubles at every location. Capillary pressure (u_c) in the undrained model is similar to capillary pressure in the drained model, however the large increase in water pressure leads to a higher final gas pressure and higher π value (**Eq. 20**).

At each location, the total horizontal and vertical stresses and the effective horizontal and vertical stresses were calculated before and after hydrate dissociation (**Table 6**). Total stresses were relatively consistent among the five locations as they all lie along the shelf strike. During dissociation, the effective stress on

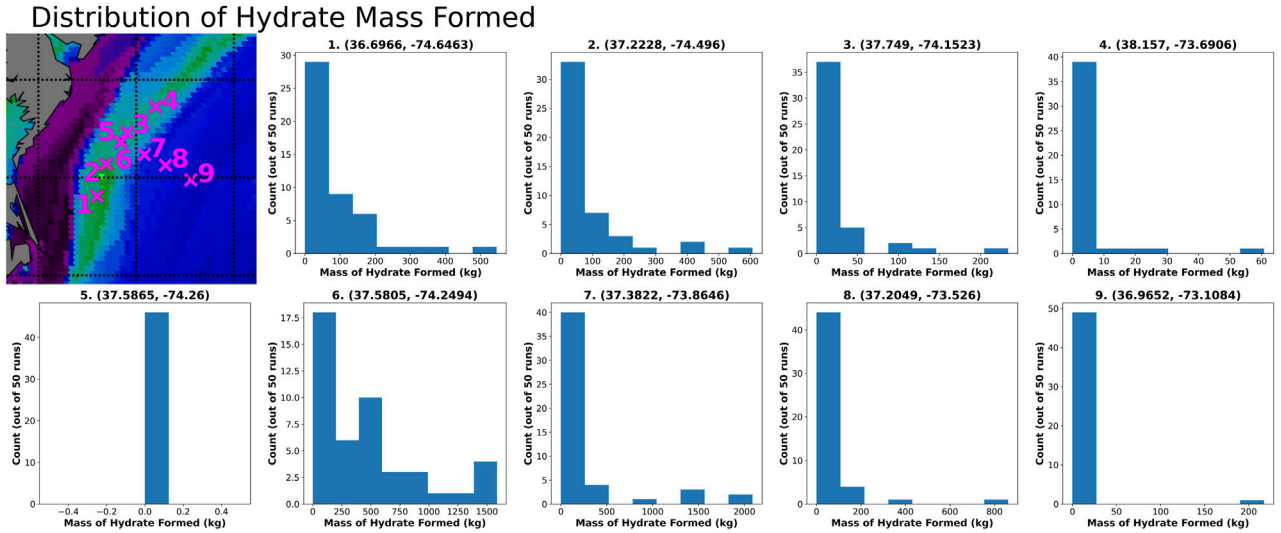

FIGURE 8 | Distribution of the mass of hydrate formed at each location.

TABLE 5 | Summary of gas profiles modeled with PFLOTRAN and Dakota (gas locations[g] and feather edge locations[f]).

#	Total Runs	Success Runs	Gas Runs	Max. Gas Saturation	Depth Max Gas Sat. (m)
	Along Shelf Strike				
1[f]	50	48	43	0.0536	218.92
2[f]	50	47	43	0.0625	304.93
3[f]	50	46	36	0.0522	213.61
4[f]	50	43	39	0.0534	309.27
	Along Shelf Dip				
5[g]	50	46	42	0.0645	214.64
6[f]	50	46	30	0.0463	395.83
7	50	50	9	0.0064	994.50
8	50	50	1	n/a	n/a
9	50	50	0	n/a	n/a

TABLE 6 | Geomechanical Model: Pressures and stresses due to hydrate dissociation along the shelf edge. An increase in temperature by 1 °C was used to initiate dissociation for both the drained and undrained models.

Site #	z_{water} (m)	BHZ (m)	T_i (°C)	S_h (%)	$S_{g,f}$ (%)	$u_{w,i}$ (MPa)	$u_{w,f}$ (MPa)	$u_{g,f}$ (MPa)	σ_v (MPa)	σ_h (MPa)	Failure
Drained											
1	508	76.87	8.48	0.70	0.17	5.88	5.88	6.31	6.31	6.27	None
2	510	78.33	8.53	0.71	0.17	5.91	5.91	6.36	6.37	6.32	None
3	497	61.70	8.05	0.63	0.16	5.61	5.61	6.09	6.00	5.97	None
4	487	48.18	7.65	0.22	0.06	5.38	5.38	5.75	5.67	5.64	None
6	651	179.28	11.77	1.04	0.17	8.34	8.34	8.86	9.45	9.31	None
Undrained											
1	508	76.87	8.48	0.70	0.06	5.88	16.32	16.21	6.31	6.27	Shear
2	510	78.33	8.53	0.71	0.06	5.91	16.52	16.33	6.37	6.32	Shear
3	497	61.70	8.05	0.63	0.05	5.61	15.02	15.47	6.00	5.97	Shear
4	487	48.18	7.65	0.22	0.03	5.38	10.85	11.09	5.67	5.64	Shear
6	651	179.28	11.77	1.04	0.07	8.34	20.73	20.26	9.45	9.31	Shear

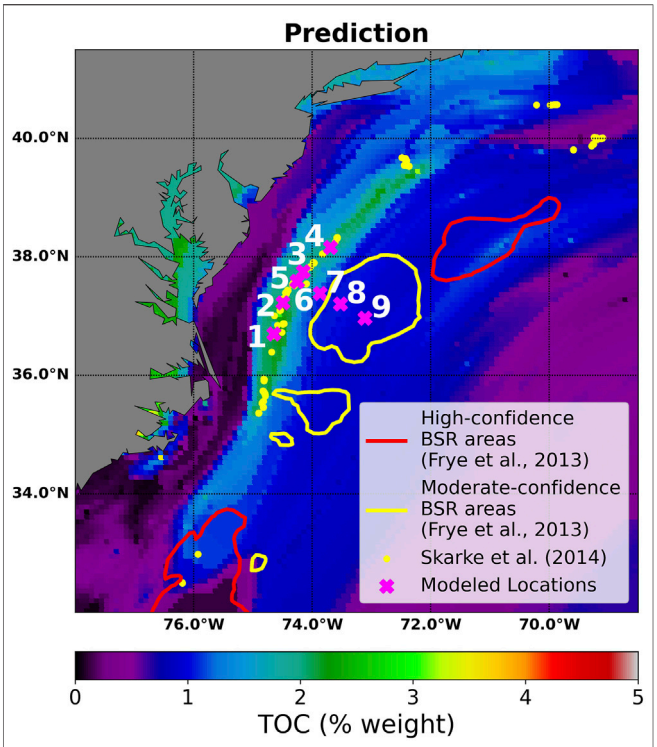

FIGURE 9 | Output maps from GPSM over the area 32°N–41.5°N and 78°W–68.5°W. Methane seeps (yellow dots) identified by Skarke et al. (2014) are also plotted and support the increased TOC prediction between (35.4°N, 75.0°W) and (39.0°N, 72.0°W). Locations where we modeled hydrate and gas formation are marked with a magenta × and numbered. Red and yellow outlines are areas where the U.S. Bureau of Ocean Energy Management (BOEM) identified BSRs in seismic data (Frye et al., 2013).

the sediment decreases ($\sigma'_{v,f} < \sigma'_{v,i}$ and $\sigma'_{h,f} < \sigma'_{h,i}$). In the drained environment, no failure was modeled at any location as the representative Mohr circle never crosses the Hoek-Brown failure envelope during the hydrate dissociation. In the undrained system, the effective vertical and horizontal stresses decrease to the point where the representative Mohr circle intersects with the Hoek-Brown failure envelope. At each location this occurred when $|\sigma'_3| < |T|$ so we expect shear failure.

5 DISCUSSION

5.1 GPSM

Our predictive map of seafloor TOC from GPSM was comparable to the work done by Lee et al. (2019) and Eymold et al. (2021). The global map of seafloor TOC produced by Lee et al. (2019) also predicted an area of increased TOC off the east coast of the United States in the same region [(35.4°N, 75.0°W) to (39.0°N, 72.0°W)] predicted in our model. The map of seafloor TOC predicted by Eymold et al. (2021) covers about a quarter of the area of our prediction. In this prediction, trends of TOC are similar to the trends we predict as Eymold et al. (2021) also predicts an increase in TOC at the southern end of the (35.4°N, 75.0°W) to (39.0°N, 72.0°W) region. It is unsurprising that the areas with increased TOC predictions are similar between this work and the work done by Lee et al. (2019) and Eymold et al. (2021). Although the data sets used between the three predictions differed slightly, the general methodology was consistent across the models.

To ensure the accuracy of our seafloor TOC model, it is additionally important to compare the results to field data in the area. Investigations by Skarke et al. (2014) have found multiple instances of methane gas leakage from the seafloor along the U.S. Atlantic margin in the form of gas plumes (**Figure 9**). The sites of these methane seeps correspond with areas predicted by our GPSM model to have higher values of seafloor TOC, specifically in the region between (35.4°N, 75.0°W) and (39.0°N, 72.0°W). The seeps identified by Skarke et al. (2014) are mostly found just updip of the feather edge. At these locations, seepage is most likely due to small tensile failures that occur when microbial gas is generated close to the seafloor (Daigle et al., 2020). However, at the feather edge where we modeled hydrate and gas formation with PFLOTRAN/Dakota, if hydrate dissociates it will instead cause shear failure.

Around the U.S. Atlantic margin, the U.S. Bureau of Ocean Energy Management (BOEM) identified six unique regions with BSRs of moderate and high confidence (Frye et al., 2013). Some of these regions with identified BSRs overlay the region where we predicted high TOC values and modeled hydrate and gas formation. Our model forms hydrate and gas through methanogenesis and therefore suggests that the BSRs identified by Frye et al. (2013) may have a similar local microbial origin and that the concentration of gas and hydrate in the pore space may be small.

5.2 Hydrate and Gas Formation

When using PFLOTRAN, a 120,000 years time period corresponding to the length of a glacial-interglacial cycle was chosen to simulate methanogenesis and hydrate formation. This gave us a good idea of hydrate profiles along the feather edge of hydrate stability, and we demonstrated that conditions exist in which failure will occur due to dissociation. If we instead wanted to model the actual burial history and hydrate formation in this area, we would need to include changes in temperature, pressure, and sedimentation rate over time. However, even though gas seeps (Skarke et al., 2014) and regions with BSRs of moderate to high confidence (Frye et al., 2013) have been identified in the area we are modeling (**Figure 9**), there are still few constraints on the distribution and amount of gas and hydrate in the area. Therefore, we chose to model a variety of outcomes using Dakota to sample different initial seafloor conditions.

Once the hydrate/gas profile has been put in place we assumed an increase in temperature on a time scale much shorter than 120,000 years. One cause of this temperature change could be a weakened Atlantic Meridional Overturning Circulation (AMOC) which could lead to increased surface and seafloor temperatures in our area of interest (Liu et al., 2020; Garcia-Soto et al., 2021). The movement of the feather edge due to changes in seafloor temperature has also been shown on a shorter timescale by Phrampus and Hornbach (2012) just south of the region we modeled. Changes in sea level can also alter the GHSZ as pressure changes as the seafloor. Not only can changes in sea level shift the feather edge, but lower past sea levels can create an area within the

current GHSZ where hydrate was unable to accumulate over time (Stranne et al., 2016).

In the area of study, varying sedimentation rates over the Pleistocene are noted by McHugh and Olson (2002). Since our model relies on sedimentation to transport organic matter, it would seem that given identical TOC measurements, the sedimentation rate would increase the amount of methane hydrate and gas formed in the simulation. This is discussed by Eymold et al. (2021) who concur that as the sedimentation rate approaches zero, hydrate growth is unexpected. Eymold et al. (2021) also note that increasing sedimentation rate in their experience can eventually lead to reduced hydrate growth as the organic carbon is buried so quickly it cannot go through the methanogenesis process. In reality, changing sedimentation rates over time will affect the concentration of TOC on the ocean floor. In the area we model, organic matter on the seafloor is mainly marine-driven with only a little mixing of terrestrial material (Shipboard Scientific Party, 1994a; Shipboard Scientific Party, 1994b; Shipboard Scientific Party, 1994c; Shipboard Scientific Party, 1994d; Shipboard Scientific Party, 1994e). Higher sedimentation rates in the area would lead to a larger flux of terrestrial organic to the seafloor, however there would also be more sediment deposited relative to the standard background flux of marine organic carbon. Therefore, a variable sedimentation rate over time would have to consider the changing seafloor TOC concentrations and may still result in predictions similar to models where seafloor TOC and sedimentation rates are held constant.

Sampling methanogenesis rate in the PFLOTRAN/Dakota model also changes the outcomes of the simulations. Since we do not know the exact methanogenesis rate in the area or the probability distribution of the methanogenesis rate, we chose a constant value within the range modeled by Eymold et al. (2021) and also between the values of λ estimated by Bhatnagar et al. (2007) and Malinverno (2010). The effect of changing methanogenesis rate in the model is discussed by Eymold et al. (2021) who found that higher methanogenesis rates led to a deeper BHZ but a lower maximum hydrate saturation. We have included additional hydrate and gas profiles in the supplementary materials where we sampled methanogenesis rate in addition to the other previously sampled parameters.

5.3 Sediment Failure Model

In all five locations along the feather edge (sites 1–4, 6) shear failure occurred in the undrained model while no shear failure occurred in the drained model. At these sites, the largest average saturation of hydrate at the BHZ was predicted to be 1% (site 6). At the other four sites, the average predicted hydrate saturation at the BHZ was at or below 0.7%. At these locations gas saturation after dissociation was no more than 0.2%. In the undrained environment, gas saturations formed from dissociation were below 0.1%. Even with these relatively low saturations of gas formed from dissociation, hydrate dissociation under undrained conditions led to shear failure. This differs from the conclusion of Daigle et al. (2020) who suggest that tensile fracturing is generally favored in the shallowest sediments near the feather edge. The BHZ modeled in this paper with PFLOTRAN is at depths between 40 and 80 m (along with site 6 at 182 m). Thus, the sediments modeled may still be too deep below the seafloor to experience gas-driven tensile fracturing.

In the undrained model, shear failure occurs due to increased pore pressure and gas pressure in the sediment. As pore pressure increases, the effective stress decreases to the point where the sediment enters a failure regime. As depicted in **Figure 4**, this can be visualized as the Mohr circle shifting to the left until it intersects with the Hoek-Brown failure envelope. Due to the depths of our modeled BHZ, the representative Mohr circle intersected with Hoek-Brown failure envelope at $|\sigma_3'| < |T|$. Closer to the seafloor the stresses are nearly isotropic, and the representative Mohr circle could be small enough that a decrease in effective stress leads to tensile failure when $|\sigma_3'| = |T|$. Stranne et al. (2017) note that fractures will not occur near the feather edge in sediments with permeabilities larger than $10^{-15}\,m^2$. Although we use a permeability value of $10^{-15}\,m^2$ in our burial model to account for siltier beds, multiple ODP wells (sites 902, 903, and 1,073) in the region describe permeabilities between 10^{-17} and $10^{-16}\,m^2$ (Blum et al., 1996; Dugan et al., 2003), so shear failure still may occur due to hydrate dissociation.

The low saturation of gas formed from hydrate dissociation needed for the dissociation to cause shear failure has interesting implications on slope stability for the region. Looking at the area of high TOC values predicted with GPSM that overlap with the methane seepage locations highlighted by Skarke et al. (2014), there is a 250 km region along the continental slope where high TOC values are expected (and where methane seeps have already been found). Even with low hydrate concentrations between 0.2% and 1%, if this hydrate dissociates in an undrained environment, shear failure could ensue. In reality, the drainage environment will be somewhere between the drained and undrained endmembers. Therefore, it will eventually be important to have a mixed-drainage model to determine the possibility of failure due to hydrate dissociation in a region. In addition, it will be important to look at hydrate dissociation as a step by step process where local pressure change during dissociation can cause hydrate to reform. When considering this, the rate at which temperature changes and the rate of fluid flow are important in correctly modeling the grain space.

For slope failure or submarine landslides to occur in an area, there needs to be some sort of triggering mechanism such as an earthquake, changing sea level, or high internal pore pressure causing the downslope component of stress to become larger than the resisting stress (Hampton et al., 1996). The dissociation of methane hydrate has also been found to lead to shear failure in seafloor sediments resulting in seafloor slumping and submarine landslides (Kvenvolden, 1993; Hampton et al., 1996; Hornbach et al., 2007; Elger et al., 2018). The timing of slope failure due to hydrate dissociation has been investigated by Lee (2009), Maslin et al. (2004), and Nixon and Grozic (2007), who have shown possible connections globally between hydrate dissociation and submarine landslides. The mechanism by which hydrate dissociation leads to slope instability has been discussed as well. In both fine grained and coarse grained sediments, fluid migration towards the seafloor can occur along active thrust faults

leading to a build up of gas pressure, resulting in lower effective stresses and sediment instability (Conti et al., 2008; Argentino et al., 2019). In areas without thrust faults to act as a conduit for gas migration, Kvenvolden (1993) suggests that the dissociation of hydrates can create an "enhanced fluidized layer" beneath the GHSZ, leading to the slope failure. Elger et al. (2018) suggest that the overpressure of gas at the BHZ creates a gas pipe to shallower sediments, and it is in these shallower coarse-grained sediments where gas builds up, leading to shear failure.

A factor of safety calculation, containing the seafloor slope variable, compares resisting to shearing forces in a sediment and can be used to determine if slope failure is likely to occur at a submarine location (Løseth, 1999; ten Brink et al., 2009). Along the U.S. Atlantic continental slope most submarine landslides originate from areas with a seafloor slope angle between 2 and 4°(Booth et al., 1993). In the area of our study, the gradient of the continental slope is mostly between 4 and 8 with some areas reaching 8–12°(Twichell et al., 2009) thus slope failure may be a concern under the undrained conditions that we modeled.

6 CONCLUSION

We used a geospatial machine learning model to create a global map of TOC on the seafloor. Focusing specifically on the U.S. Atlantic margin, the region with high TOC predictions between (35.4°N, 75.0°W) and (39.0°N, 72.0°W) was consistent with methane gas seeps located by Skarke et al. (2014). We then modeled hydrate and gas formation over a 120,000 years time period at nine locations in this area: five hydrate bearing locations along the feather edge, one gas location updip of the feather edge, and three hydrate bearing locations downdip of the feather edge. For each of these locations, hydrate and gas formation were modeled by sampling seafloor TOC, seafloor porosity, sedimentation rate, and heat flux.

At the feather edge, we modeled hydrate dissociation at the BHZ due to an increase in temperature while ignoring the change in pressure due to the rise and fall of sea level. In a purely drained environment, no failure is expected to occur due to hydrate dissociation. However, in an undrained environment, the criterion for shear failure is quickly met during hydrate dissociation. Even as gas saturations due to hydrate dissociation stayed below 0.1% (hydrate saturations: 0.2%—1%) shear failure was predicted to occur. This suggests that the hydrate that forms over one glacial cycle can cause submarine slope failure upon dissociation.

DATA AVAILABILITY STATEMENT

The raw data supporting the conclusion of this article will be made available by the authors, without undue reservation.

AUTHOR CONTRIBUTIONS

OC performed the numerical modeling and wrote the manuscript. HD supervised the project and edited the manuscript. Both authors read and approved the final manuscript.

FUNDING

This work was supported by the University of Texas at Austin, and the Laboratory Directed Research and Development program at Sandia National Laboratories. Sandia National Laboratories is a multimission laboratory managed and operated by National Technology and Engineering Solutions of Sandia, LLC., a wholly owned subsidiary of Honeywell International, Inc., for the U.S. Department of Energy's National Nuclear Security Administration under contract DE-NA-0003525.

ACKNOWLEDGMENTS

The authors thank Ali Shirani Lapari and Mitchel Broten for preliminary machine learning work. Constructive comments from CS, DF, and Editor AL helped strengthen this paper.

SUPPLEMENTARY MATERIAL

The Supplementary Material for this article can be found online at: https://www.frontiersin.org/articles/10.3389/feart.2022.835685/full#supplementary-material

REFERENCES

Adams, B. M., Bohnhoff, W. J., Dalbey, K. R., Ebeida, M. S., Eddy, J. P., Eldred, M. S., et al. (2021). enDakota, A Multilevel Parallel Object-Oriented Framework for Design Optimization, Parameter Estimation, Uncertainty Quantification, and Sensitivity Analysis: Version 6.14. *User's Man.* 354. doi:10.2172/1784843

Argentino, C., Conti, S., Crutchley, G. J., Fioroni, C., Fontana, D., and Johnson, J. E. (2019). Methane-derived Authigenic Carbonates on Accretionary Ridges: Miocene Case Studies in the Northern Apennines (Italy) Compared with Modern Submarine Counterparts. *Mar. Petroleum Geol.* 102, 860–872. doi:10.1016/j.marpetgeo.2019.01.026

Bhatnagar, G., Chapman, W. G., Dickens, G. R., Dugan, B., and Hirasaki, G. J. (2007). Generalization of Gas Hydrate Distribution and Saturation in Marine Sediments by Scaling of Thermodynamic and Transport Processes. *Am. J. Sci.* 307, 861–900. doi:10.2475/06.2007.01

Biastoch, A., Treude, T., Rüpke, L. H., Riebesell, U., Roth, C., Burwicz, E. B., et al. (2011). enRising Arctic Ocean Temperatures Cause Gas Hydrate Destabilization and Ocean Acidification. *Geophys. Res. Lett.* 38. doi:10.1029/2011gl047222

Bishop, A. W. (1959). The Principle of Effective Stress. *Tek. Ukebl.* 39, 859–863.

Blum, P., Xu, J., and Donthireddy, S. (1996). enGeotechnical Properties of Pleistocene Sediments from the New Jersey Upper Continental Slopeof Proceedings of the Ocean Drilling Program. *Sci. Results Ocean. Drill. Program.* 150. doi:10.2973/odp.proc.sr.150.1996

Booth, J. S., O'Leary, D. W., Popenoe, P., and Danforth, W. W. (19932002). "US Atlantic Continental Slope Landslides: Their Distribution, General Attributes, and Implications," in *Submarine Landslides: Selected Studies in the US Exclusive Economic Zone* (U.S. Geol. Surv. Bull.), 14–22.

Boudreau, B. P. (2012). The Physics of Bubbles in Surficial, Soft, Cohesive Sediments. *Mar. Petroleum Geol.* 38, 1–18. doi:10.1016/j.marpetgeo.2012.07.002

Boyer, T. P., Baranova, O. K., Coleman, C., Garcia, H. E., Grodsky, A., Locarnini, R. A., et al. (2018). *enWorld Ocean Database*, 2018, 207.

Brothers, D. S., Ruppel, C., Kluesner, J. W., ten Brink, U. S., Chaytor, J. D., and Hill, J. C. (2014). enSeabed Fluid Expulsion along the Upper Slope and Outer Shelf of the U.S. Atlantic Continental Margin. *Geophys. Res. Lett.* 41, 96–101. doi:10.1002/2013GL058048

Cathles, L. M., Su, Z., and Chen, D. (2010). enThe Physics of Gas Chimney and Pockmark Formation, with Implications for Assessment of Seafloor Hazards and Gas Sequestration. *Mar. Petroleum Geol.* 27, 82–91. doi:10.1016/j.marpetgeo.2009.09.010

Conti, S., Fontana, D., and Lucente, C. (2008). enAuthigenic Seep-Carbonates Cementing Coarse-Grained Deposits in a Fan-Delta Depositional System (Middle Miocene, Marnoso-Arenacea Formation, Central Italy). *Sedimentology* 55, 471–486. doi:10.1111/j.1365-3091.2007.00910.x

Daigle, H., Cook, A., Fang, Y., Bihani, A., Song, W., and Flemings, P. B. (2020). enGas-Driven Tensile Fracturing in Shallow Marine Sediments. *J. Geophys. Res. Solid Earth* 125. doi:10.1029/2020JB020835

Daigle, H., Ghanbarian, B., Henry, P., and Conin, M. (2015). enUniversal Scaling of the Formation Factor in Clays: Example from the Nankai Trough. *J. Geophys. Res. Solid Earth* 120, 7361–7375. doi:10.1002/2015JB012262

Dickens, G. R., Paull, C. K., and Wallace, P. (1997). enDirect Measurement of *In Situ* Methane Quantities in a Large Gas-Hydrate Reservoir. *Nature* 385, 426–428. doi:10.1038/385426a0

Dugan, B., and Germaine, J. T. (2009). Data Report: Strength Characteristics of Sediments from IODP Expedition 308, Sites U1322 and U1324. *Proc. Integr. Ocean Drill. Program* 308, 1–13. doi:10.2204/iodp.proc.308.210.2009

Dugan, B., Olgaard, D. L., Flemings, P. B., and Gooch, M. (2003). enData Report: Bulk Physical Properties of Sediments from ODP Site 1073, Vol. 174A of Proceedings of the Ocean Drilling Program. *Sci. Results Ocean. Drill. Program.* doi:10.2973/odp.proc.sr.174A.2003

Egger, M., Riedinger, N., Mogollón, J. M., and Jørgensen, B. B. (2018). enGlobal Diffusive Fluxes of Methane in Marine Sediments. *Nat. Geosci.* 11, 421–425. doi:10.1038/s41561-018-0122-8

Elger, J., Berndt, C., Rüpke, L., Krastel, S., Gross, F., and Geissler, W. H. (2018). enSubmarine Slope Failures Due to Pipe Structure Formation. *Nat. Commun.* 9, 715. doi:10.1038/s41467-018-03176-1

Eymold, W. K., Frederick, J. M., Nole, M., Phrampus, B. J., and Wood, W. T. (2021). enPrediction of Gas Hydrate Formation at Blake Ridge Using Machine Learning and Probabilistic Reservoir Simulation. *Geochem. Geophys. Geosystems* 22. doi:10.1029/2020GC009574

Ferré, B., Mienert, J., and Feseker, T. (2012). enOcean Temperature Variability for the Past 60 Years on the Norwegian-Svalbard Margin Influences Gas Hydrate Stability on Human Time Scales. *J. Geophys. Res. Oceans* 117. doi:10.1029/2012JC008300._eprint

Fleischer, P., Orsi, T. H., Richardson, M. D., and Anderson, A. L. (2001). enDistribution of Free Gas in Marine Sediments: a Global Overview. *Geo-Marine Lett.* 21, 103–122. doi:10.1007/s003670100072

Frye, M., Shedd, W., and Schuenemeyer, J. (2013). *Gas Hydrate Resource Assessment: Atlantic Outer Continental Shelf*. Washington, D.C: U.S. Bureau of Ocean Energy Management. Technical Report RED 2013-01.

Fuchs, S., Norden, B., and Commission, I. H. F. (2021). *enThe Global Heat Flow Database: Release 2021 GFZ Data Services*.

Garcia-Soto, C., Cheng, L., Caesar, L., Schmidtko, S., Jewett, E. B., Cheripka, A., et al. (2021). An Overview of Ocean Climate Change Indicators: Sea Surface Temperature, Ocean Heat Content, Ocean pH, Dissolved Oxygen Concentration, Arctic Sea Ice Extent, Thickness and Volume, Sea Level and Strength of the AMOC (Atlantic Meridional Overturning Circulation). *Front. Mar. Sci.* 8. doi:10.3389/fmars.2021.642372

Graw, J. H., Wood, W. T., and Phrampus, B. J. (2021). enPredicting Global Marine Sediment Density Using the Random Forest Regressor Machine Learning Algorithm. *J. Geophys. Res. Solid Earth* 126, e2020JB020135. doi:10.1029/2020JB020135

Hamilton, E. L. (1979). enV_p/V_s and Poisson's Ratios in Marine Sediments and Rocks. *J. Acoust. Soc. Am.* 66, 1093–1101. doi:10.1121/1.383344

Hammond, G. E., Lichtner, P. C., and Mills, R. T. (2014). enEvaluating the Performance of Parallel Subsurface Simulators: An Illustrative Example with PFLOTRAN. *Water Resour. Res.* 50, 208–228. doi:10.1002/2012WR013483

Hampton, M. A., Lee, H. J., and Locat, J. (1996). enSubmarine Landslides. *Rev. Geophys.* 34, 33–59. doi:10.1029/95rg03287

Hill, J. C., Driscoll, N. W., Weissel, J. K., and Goff, J. A. (2004). enLarge-Scale Elongated Gas Blowouts along the U.S. Atlantic Margin. *J. Geophys. Res. Solid Earth* 109. doi:10.1029/2004JB002969

Hoek, E., and Brown, E. T. (1997). enPractical Estimates of Rock Mass Strength. *Int. J. Rock Mech. Min. Sci.* 34, 1165–1186. doi:10.1016/S1365-1609(97)80069-X

Holbrook, W. S., Hoskins, H., Wood, W. T., Stephen, R. A., and Lizarralde, D. (1996). Leg 164 Science Party enMethane Hydrate and Free Gas on the Blake Ridge from Vertical Seismic Profiling. *Science* 273, 1840–1843. doi:10.1126/science.273.5283.1840

Hornbach, M. J., Lavier, L. L., and Ruppel, C. D. (2007). enTriggering Mechanism and Tsunamogenic Potential of the Cape Fear Slide Complex, U.S. Atlantic Margin. *Geochem. Geophys. Geosystems* 8. doi:10.1029/2007GC001722

Ingram, G. M., and Urai, J. L. (1999). enTop-Seal Leakage through Faults and Fractures: the Role of Mudrock Properties. *Geol. Soc. Lond. Spec. Publ.* 158, 125–135. doi:10.1144/GSL.SP.1999.158.01.10

Johnson, B. D., Barry, M. A., Boudreau, B. P., Jumars, P. A., and Dorgan, K. M. (2012). enIn Situ Tensile Fracture Toughness of Surficial Cohesive Marine Sediments. *Geo-Marine Lett.* 32, 39–48. doi:10.1007/s00367-011-0243-1

Judd, A. G. (2003). enThe Global Importance and Context of Methane Escape from the Seabed. *Geo-Marine Lett.* 23, 147–154. doi:10.1007/s00367-003-0136-z

Kamath, V. A. (1984). *EnglishStudy of Heat Transfer Characteristics during Dissociation of Gas Hydrates in Porous Media*. United States – Pennsylvania: Ph.D., University of Pittsburgh.

Kominz, M. A., Patterson, K., and Odette, D. (2011). Lithology Dependence of Porosity in Slope and Deep Marine Sediments. *J. Sediment. Res.* 81, 730–742. doi:10.2110/jsr.2011.60

Kvenvolden, K. A., and Claypool, G. E. (1988). "Gas Hydrates in Oceanic Sediment," in *Tech. Rep.U.S. Geological Survey* (Publication Title: Open-File Report), 88–216. ISSN: 2331-1258. doi:10.3133/ofr88216

Kvenvolden, K. A. (1993). enGas Hydrates—Geological Perspective and Global Change. *Rev. Geophys.* 31, 173–187. doi:10.1029/93RG00268

Kvenvolden, K. A., and Lorenson, T. D. (2001). "enThe Global Occurrence of Natural Gas Hydrate," in *Natural Gas Hydrates: Occurrence, Distribution, and Detection* (American Geophysical Union AGU), 3–18.

Lee, H. J. (2009). enTiming of Occurrence of Large Submarine Landslides on the Atlantic Ocean Margin. *Mar. Geol.* 264, 53–64. doi:10.1016/j.margeo.2008.09.009

Lee, J. Y., Santamarina, J. C., and Ruppel, C. (2010). enVolume Change Associated with Formation and Dissociation of Hydrate in Sediment. *Geochem. Geophys. Geosystems* 11. doi:10.1029/2009GC002667

Lee, T. R., Wood, W. T., and Phrampus, B. J. (2019). enA Machine Learning (kNN) Approach to Predicting Global Seafloor Total Organic Carbon. *Glob. Biogeochem. Cycles* 33, 37–46. doi:10.1029/2018GB005992

Liu, W., Fedorov, A. V., Xie, S.-P., and Hu, S. (2020). enClimate Impacts of a Weakened Atlantic Meridional Overturning Circulation in a Warming Climate. *Sci. Adv.* 6, eaaz4876. doi:10.1126/sciadv.aaz4876

Løseth, T. M. (1999). *Submarine Massflow Sedimentation: Computer Modelling and Basin-Fill Stratigraphy*, 82. Springer.

Malinverno, A. (2010). enMarine Gas Hydrates in Thin Sand Layers that Soak up Microbial Methane. *Earth Planet. Sci. Lett.* 292, 399–408. doi:10.1016/j.epsl.2010.02.008

Martin, K. M., Wood, W. T., and Becker, J. J. (2015). enA Global Prediction of Seafloor Sediment Porosity Using Machine Learning. *Geophys. Res. Lett.* 42 (10640–10), 646. doi:10.1002/2015GL065279

Maslin, M., Owen, M., Day, S., and Long, D. (2004). enLinking Continental-Slope Failures and Climate Change: Testing the Clathrate Gun Hypothesis. *Geology* 32, 53. doi:10.1130/G20114.1

McHugh, C. M. G., and Olson, H. C. (2002). enPleistocene Chronology of Continental Margin Sedimentation: New Insights into Traditional Models, New Jersey. *Mar. Geol.* 186, 389–411. doi:10.1016/S0025-3227(02)00198-6

Moses, G. G., Rao, S. N., and Rao, P. N. (2003). enUndrained Strength Behaviour of a Cemented Marine Clay under Monotonic and Cyclic Loading. *Ocean. Eng.* 30, 1765–1789. doi:10.1016/S0029-8018(03)00018-0

Nixon, M. F., and Grozic, J. L. (2007). Submarine Slope Failure Due to Gas Hydrate Dissociation: a Preliminary Quantification. *Can. Geotechnical J.* 44, 314–325. NRC Research Press. doi:10.1139/t06-121

Nole, M., Daigle, H., Cook, A. E., Hillman, J. I. T., and Malinverno, A. (2017). enLinking Basin-Scale and Pore-Scale Gas Hydrate Distribution Patterns in Diffusion-Dominated Marine Hydrate Systems. *Geochem. Geophys. Geosystems* 18, 653–675. doi:10.1002/2016GC006662

Nuth, M., and Laloui, L. (2008). enEffective Stress Concept in Unsaturated Soils: Clarification and Validation of a Unified Framework. *Int. J. Numer. Anal. Methods Geomechanics* 32, 771–801. doi:10.1002/nag.645

Party, S. S. (1998a). *Site 1071. Proceedings of the Ocean Drilling Program*, 37–97. Initial Reports 174A.

Party, S. S. (1998b). *Site 1072. Proceedings of the Ocean Drilling Program*, 99–152. *Initial Reports* 174A.

Peng, D.-Y., and Robinson, D. B. (1976). enA New Two-Constant Equation of State. *Industrial Eng. Chem. Fundam.* 15, 59–64. doi:10.1021/i160057a011

Phrampus, B. J., and Hornbach, M. J. (2012). enRecent Changes to the Gulf Stream Causing Widespread Gas Hydrate Destabilization. *Nature* 490, 527–530. doi:10.1038/nature11528

Phrampus, B. J., Hornbach, M. J., Ruppel, C. D., and Hart, P. E. (2014). enWidespread Gas Hydrate Instability on the Upper U.S. Beaufort Margin. *J. Geophys. Res. Solid Earth* 119, 8594–8609. doi:10.1002/2014JB011290

Phrampus, B. J., Lee, T. R., and Wood, W. T. (2020). *Predictor Grids for "A Global Probabilistic Prediction of Cold Seeps and Associated Seafloor Fluid Expulsion Anomalies (SEAFLEAs)"*. Dataset. doi:10.5281/zenodo.3459805

Pohlman, J., Ruppel, C. D., Wang, D. T., Ono, S., Kluesner, J., Xu, X., et al. (2017). Natural Gas Sources from Methane Seeps on the Northern U.S. Atlantic Margin 2017, OS11B–1133. Conference Name: AGU Fall Meeting Abstracts ADS Bibcode: 2017AGUFMOS11B1133P

Poling, B. E., Prausnitz, J. M., and O'Connell, J. P. (2001). *enThe Properties of Gases and Liquids*. 5th edn. New York: McGraw-Hill.

Prouty, N. G., Sahy, D., Ruppel, C. D., Roark, E. B., Condon, D., Brooke, S., et al. (2016). enInsights into Methane Dynamics from Analysis of Authigenic Carbonates and Chemosynthetic Mussels at Newly-Discovered Atlantic Margin Seeps. *Earth Planet. Sci. Lett.* 449, 332–344. doi:10.1016/j.epsl.2016.05.023

Restreppo, G. A., Wood, W. T., and Phrampus, B. J. (2020). enOceanic Sediment Accumulation Rates Predicted via Machine Learning Algorithm: towards Sediment Characterization on a Global Scale. *Geo-Marine Lett.* 40, 755–763. doi:10.1007/s00367-020-00669-1

Ruppel, C. D., and Kessler, J. D. (2017). enThe Interaction of Climate Change and Methane Hydrates. *Rev. Geophys.* 55, 126–168. doi:10.1002/2016RG000534

Ruppel, C. D. (2011). Methane Hydrates and Contemporary Climate Change. *Nat. Eduction Knowl.* 2, 13.

Ryan, W. B. F., Carbotte, S. M., Coplan, J. O., O'Hara, S., Melkonian, A., Arko, R., et al. (2009). enGlobal Multi-Resolution Topography Synthesis. *Geochem. Geophys. Geosystems* 10, 9. doi:10.1029/2008GC002332

Safarov, J., Millero, F., Feistel, R., Heintz, A., and Hassel, E. (2009). enThermodynamic Properties of Standard Seawater: Extensions to High Temperatures and Pressures. *Ocean Sci.* 5, 235–246. doi:10.5194/os-5-235-2009

Safarov, J. T. (2003). enThe Investigation of the (P, ρ, T) and (P_s, ρ_s, T_s) Properties of \{(1–x)CH_3OH+xLiBr\} for the Application in Absorption Refrigeration Machines and Heat Pumps. *J. Chem. Thermodyn.* 35, 1929–1937. doi:10.1016/j.jct.2003.08.015

Sarkar, S., Berndt, C., Minshull, T. A., Westbrook, G. K., Klaeschen, D., Masson, D. G., et al. (2012). enSeismic Evidence for Shallow Gas-Escape Features Associated with a Retreating Gas Hydrate Zone Offshore West Svalbard. *J. Geophys. Res. Solid Earth* 117. _eprint:. doi:10.1029/2011JB009126

Seiter, K., Hensen, C., Schröter, J., and Zabel, M. (2004). enOrganic Carbon Content in Surface Sediments—Defining Regional Provinces. *Deep Sea Res. Part I Oceanogr. Res. Pap.* 51, 2001–2026. doi:10.1016/j.dsr.2004.06.014

Shipboard Scientific Party (1998b). *enSites 1054 and 1055. Proceedings of the Ocean Drilling Program: Initial Reports*, 172, 33–76.

Shipboard Scientific Party (1998a). *Site 1073. Proceedings of the Ocean Drilling Program*, 174A, 153–191. *Initial Reports*.

Shipboard Scientific Party (1994a). *Site 902. Proceedings of the Ocean Drilling Program: Initial Reports*, 150, 63–127.

Shipboard Scientific Party (1994b). *Site 903. Proceedings of the Ocean Drilling Program*, 150, 129–205. *Initial Reports*.

Shipboard Scientific Party (1994c). *Site 904. Proceedings of the Ocean Drilling Program*, 150, 129–205. *Initial Reports*.

Shipboard Scientific Party (1994d). *Site 905. Proceedings of the Ocean Drilling Program: Initial Reports*, 150, 255–308.

Shipboard Scientific Party (1994e). *Site 906. Proceedings of the Ocean Drilling Program: Initial Reports*, 150, 309–357.

Shipboard Scientific Party (1996a). *Site 994. Proceedings of the Ocean Drilling Program: Initial Reports*, 164, 99–174.

Shipboard Scientific Party (1996b). *Site 995. Proceedings of the Ocean Drilling Program: Initial Reports*, 164, 175–240.

Shipboard Scientific Party (1996c). *Site 997. Proceedings of the Ocean Drilling Program: Initial Reports*, 164, 277–334.

Silva, A., Baxter, C., Bryant, W., Bradshaw, A., and LaRosa, P. (2000). "enStress-Strain Behavior and Stress State of Gulf of Mexico Clays in Relation to Slope Processes," in *Offshore Technology Conference (OnePetro)*. doi:10.4043/12091-MS

Skarke, A., Ruppel, C., Kodis, M., Brothers, D., and Lobecker, E. (2014). enWidespread Methane Leakage from the Sea Floor on the Northern US Atlantic Margin. *Nat. Geosci.* 7, 657–661. doi:10.1038/ngeo2232

Stranne, C., O'Regan, M., Dickens, G. R., Crill, P., Miller, C., Preto, P., et al. (2016). enDynamic Simulations of Potential Methane Release from East Siberian Continental Slope Sediments. *Geochem. Geophys. Geosystems* 17, 872–886. doi:10.1002/2015GC006119

Stranne, C., O'Regan, M., and Jakobsson, M. (2017). enModeling Fracture Propagation and Seafloor Gas Release during Seafloor Warming-Induced Hydrate Dissociation. *Geophys. Res. Lett.* 44, 8510–8519. doi:10.1002/2017GL074349

Sultan, N., Bohrmann, G., Ruffine, L., Pape, T., Riboulot, V., Colliat, J.-L., et al. (2014). enPockmark Formation and Evolution in Deep Water Nigeria: Rapid Hydrate Growth versus Slow Hydrate Dissolution. *J. Geophys. Res. Solid Earth* 119, 2679–2694. doi:10.1002/2013JB010546

ten Brink, U. S., Lee, H. J., Geist, E. L., and Twichell, D. (2009). enAssessment of Tsunami Hazard to the U.S. East Coast Using Relationships between Submarine Landslides and Earthquakes. *Mar. Geol.* 264, 65–73. doi:10.1016/j.margeo.2008.05.011

Twichell, D. C., Chaytor, J. D., ten Brink, U. S., and Buczkowski, B. (2009). enMorphology of Late Quaternary Submarine Landslides along the U.S. Atlantic Continental Margin. *Mar. Geol.* 264, 4–15. doi:10.1016/j.margeo.2009.01.009

van Genuchten, M. T. (1980). enA Closed-form Equation for Predicting the Hydraulic Conductivity of Unsaturated Soils. *Soil Sci. Soc. Am. J.* 44, 892–898. doi:10.2136/sssaj1980.03615995004400050002x

Waite, W. F., Santamarina, J. C., Cortes, D. D., Dugan, B., Espinoza, D. N., Germaine, J., et al. (2009). enPhysical Properties of Hydrate-Bearing Sediments. *Rev. Geophys.* 47. doi:10.1029/2008RG000279

Xu, W., and Ruppel, C. (1999). enPredicting the Occurrence, Distribution, and Evolution of Methane Gas Hydrate in Porous Marine Sediments. *J. Geophys. Res. Solid Earth* 104, 5081–5095. doi:10.1029/1998JB900092

Conflict of Interest: The authors declare that the research was conducted in the absence of any commercial or financial relationships that could be construed as a potential conflict of interest.

Publisher's Note: All claims expressed in this article are solely those of the authors and do not necessarily represent those of their affiliated organizations, or those of the publisher, the editors and the reviewers. Any product that may be evaluated in this article, or claim that may be made by its manufacturer, is not guaranteed or endorsed by the publisher.

frontiers | Frontiers in Earth Science

ORIGINAL RESEARCH
published: 31 May 2022
doi: 10.3389/feart.2022.856496

Hydrocarbon Gases in Seafloor Sediments of the Edge Shelf Zone of the East Siberian Sea and Adjacent Part of the Arctic Ocean

Andrey Yatsuk[1]*, *Alexander Gresov*[1] and *Glen Tritch Snyder*[2,3]

[1]Laboratory Gas Geochemistry, V.I. Il'ichev Pacific Oceanological Institute Far Eastern Branch Russian Academy of Sciences, Vladivostok, Russia, [2]Atmosphere and Ocean Research Institute, University of Tokyo, Kashiwa Campus, Kashiwa, Japan, [3]Gas Hydrate Research Laboratory, Meiji University, Ikuta Campus, Chiyoda, Japan

The continental margins of the East Siberian Sea and Arctic Ocean are among the Earth's most inaccessible marine environments for hydrocarbon research due to the almost year-round presence of ice cover. Despite this, limited preliminary assessments which have been carried out to date have all yielded some indication of high oil and gas production potential in these regions. This article presents the results of gas-geochemical studies of seafloor sediments of the East Siberian Sea, obtained in three expeditions onboard the R/V "Akademik Lavrentiev" in 2008 (LV45), 2016 (LV77), and 2020 (LV90). The composition of sorbed hydrocarbon gases in seafloor sediments was analyzed. In addition, the stable isotopic composition of carbon was determined for CH_4, C_2H_6, and CO_2 in gases, which were desorbed from marine sediments. The sediments were also analyzed for organic matter content. Despite the absence of observable gas seepage directly into the water column, at some stations, increased concentrations of methane and hydrocarbon gases were encountered, indicating the widespread predominance of thermogenically derived gases. We present a hydrocarbon classification system which delineates eight identifiable sources of regional gas occurrences (coal gas, igneous rocks, solid bitumen, condensate-gas, gas-condensate, oil gas, gas oil, and oil gases). A stable isotopic analysis of carbon in CH_4, C_2H_6, and CO_2 indicates varying degrees of mixing between a shallow, early-kerogen gas source and a deeper mantle carbon source in some areas of the study.

Keywords: methane, hydrocarbons, carbon isotopes, genesis, East Siberian Arctic shelf

OPEN ACCESS

Edited by:
Regina Katsman, University of Haifa, Israel

Reviewed by:
Andrey Maslov, Geological Institute (RAS), Russia
Kate Waghorn, UiT The Arctic University of Norway, Norway
Anirban Chakraborty, Idaho State University, United States

***Correspondence:**
Andrey Yatsuk
yatsuk@poi.dvo.ru

Specialty section:
This article was submitted to Marine Geoscience, a section of the journal Frontiers in Earth Science

Received: *17 January 2022*
Accepted: *20 April 2022*
Published: *31 May 2022*

Citation:
Yatsuk A, Gresov A and Snyder GT (2022) Hydrocarbon Gases in Seafloor Sediments of the Edge Shelf Zone of the East Siberian Sea and Adjacent Part of the Arctic Ocean. Front. Earth Sci. 10:856496. doi: 10.3389/feart.2022.856496

1 INTRODUCTION

The marginal-shelf zone of the East Siberian Sea (ESS), continental slope, and Podvodnikov basin of the Arctic Ocean (AO) have only in recent decades garnered close attention by scientists from around the world. This is related not only to improved access in the region but also to a growing body of geological evidence, indicating the presence of oil and gas fields of production potential (Sherwood, 1998; Kim et al., 2007; Khain et al., 2009; Bird and Houseknecht, 2011; Kim et al., 2016; Kazanin et al., 2017a; Kazanin et al., 2017c; Houseknecht et al., 2019) and a general interest in the consequences of global warming related to hydrocarbon release from polar regions (Shakhova et al., 2010).

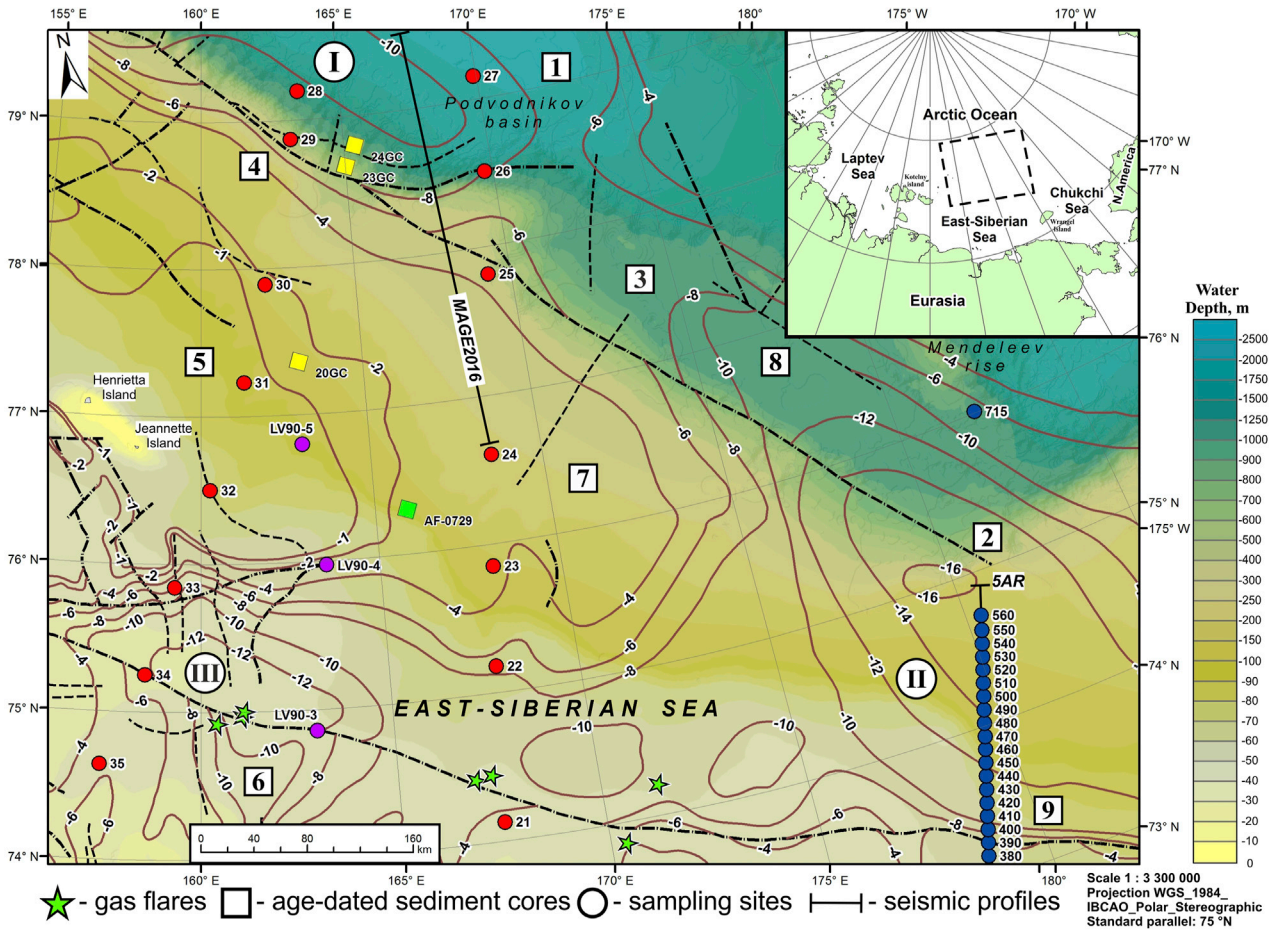

FIGURE 1 | Structural tectonic map of the research area with isolines showing sedimentary cover thickness in kilometer (After Geological Map, 2015 and Geological Map of Russian Federation and Adjacent Waters, 2016) and bathymetry from IBCAO version 3.0 (Jakobsson et al., 2012). Sedimentary basins are as follows I) Cis-East Siberian, II) North Chukchi, and III) Novosibirsk. Geological structures are as follows: 1) Vilkitsky Depression West, 2) North Chukchi Depression, 3) Kucherov uplift, 4) Lomonosov–Mendeleyev flexure–faults zone, 5) De Long uplift, 6) Novosibirsk Depression, 7) North structural terrace, 8) Vilkitsky Depression East, and 9) Kolyuchinsky graben-rift. Position of observed gas flares (green stars) is from Thornton et al. (2020). The location of age-dated sediment cores (square) is from O'Regan et al. (2017), yellow square; and Geological Map (2015), green square. Gas geochemical sampling sites (circle) were sampled in 2008 (LV45), blue circle; 2017 (LV77), red circle, and 2020 (LV90), violet circle. Seismic profiles: 5AR from Sakulina et al. (2011) and MAGE 2016 from Kazanin et al. (2017a).

Gas geochemistry is among the main methods used for prospecting hydrocarbon deposits (Horvitz, 1985; Hunt et al., 2002; Abrams, 2005; Gresov, 2011; Abrams, 2017). Such geochemical analyses of hydrocarbon gases (HCGs) that have migrated to the surface can provide useful information on subsurface hydrocarbon systems, especially in poorly explored "frontier" areas which lack information on petroleum systems which would otherwise be gleaned from deep drilling (Weniger et al., 2019). The main methodological approaches in the field of isotope gas geochemistry are well-documented by (Bernard et al., 1976; Schoell, 1983; Whiticar et al., 1986; Schoell, 1988; Whiticar, 1996; Galimov, 2006; Faber et al., 2015; Milkov and Etiope, 2018). The study of concentration and distribution of HCGs in gas-saturated sediments is, therefore, of key importance in understanding the conditions which have given rise to the formation of active gas seep systems. Arctic seeps are actively being studied in various regions of the AO; however, there are limited data regarding gas genesis. Several previous investigations have been conducted in the western region of the AO (Westbrook et al., 2009; Portnov et al., 2013; Mau et al., 2017; Pohlman et al., 2017; Pape et al., 2020) and in the Laptev Sea (Sapart et al., 2017; Baranov et al., 2020; Steinbach et al., 2021). Gas seeps have also recently been discovered in the East Siberian Sea (Thornton et al., 2020) (**Figure 1**).

Hydrocarbon gases in seafloor sediments are primarily the result of two types of genesis: microbial (syngenetic) and thermogenic (epigenetic coupled with migration). Microbial HCGs, predominantly CH_4, form within seafloor sediments as a result of microbial degradation of organic matter, where methane is the primary gas produced at relatively low temperature (Claypool and Kaplan, 1974; Whiticar et al., 1986; Stolper et al., 2014). Thermogenic HCGs, on the other hand, tend to have a much higher concentrations of C_1–C_5 gases and form in deep sediments and rocks through the thermal cracking of

organic matter (Claypool and Kvenvolden, 1983; Stolper et al., 2014). Oils generated through thermal cracking can also undergo microbial degradation, resulting in secondary hydrocarbon gases (Head et al., 2003; Etiope et al., 2009; Milkov, 2011). In addition, CH_4 can be of abiogenic origin and is produced in different geologic environments under a wide range of temperature and pressure during magmatic, volcanic, and high-temperature hydrothermal processes (Giggenbach, 1997; Etiope and Sherwood, 2013; Wen et al., 2016); however, in these cases methane is often not the primary gas present; CO_2 is much more abundant.

Previous investigations have indicated several different isotopic features of HCGs in various areas of the Arctic Ocean (Knies et al., 2004; Cramer and Franke, 2005; Matveeva et al., 2015; Serov et al., 2015; Blumenberg et al., 2016; Lorenson et al., 2016; Graves et al., 2017; Sapart et al., 2017; Sevastyanov et al., 2019; Weniger et al., 2019; Kim et al., 2020).

Isotopic and gas-geochemical features of HCGs of seafloor sediments of the East Siberian Sea shelf has been discussed in a number of studies over the past decade (Shakirov et al., 2013; Gresov et al., 2016; Gresov et al., 2017; Gresov A. I. and Yatsuk A. V., 2020; Gresov A. I. and Yatsuk A. V., 2020; Gresov and Yatsuk, 2021). As a result of these works, the gas saturation and isotope-geochemical characteristics of HCGs in the bottom sediments of the southeastern sector of the ESS (Ayon, Longa, and Pegtymel sedimentary basins) have been studied. Potentially promising oil-bearing areas of the shelf have been identified and a comparative assessment of continental and subaqueous sources of hydrocarbons has been carried out.

In general, despite the significant amount of preliminary research which has been carried out in the East Arctic region, the degree to which detailed gas-geochemical data have been applied to ascertain the regional distribution of hydrocarbons and other gases in the bottom sediments of the ESS and the AO remains extremely limited.

The aim of this work is to study the chemical and isotopic composition of hydrocarbon gases (HCGs) in the seafloor sediments and determine gas-geochemical parameters and potential gas sources of the research area. By carrying out such work, we hope to determine the prospects of oil and gas potential across the region, filling in some of the gaps in our current knowledge of hydrocarbon distribution in the area.

2 STUDY AREA AND GEOLOGICAL SETTING

The study area is located in the central part of the outer shelf of the ESS and the adjacent deep-water sector of the AO. This sector is covered almost year-round with ice and only occasionally in recent years have the waters been navigable for marine research.

The outer shelf of the study area is represented by the transition of a subhorizontal plain to an inclined plain which replaces it, with the overall bathymetry complicated by the island uplifts of Jeannette and Henrietta (**Figure 1**). De Long's Ledge and a series of underwater valleys, mostly parallel to each other, also cross-cut the otherwise uniform bottom topography (Geological Map, 2015). The marginal-shelf zone of the ESS comprises the outer shelf and edge of the shelf and is bounded by isobaths of −100 and −200 m. At depths greater than 300 m, the slope steepens appreciably, with the maximum slope occurring between 500 and 700 m water depth. In Podvodnikov Basin (PB), where sea depths exceed 2500 m, the terrace and foot of the basin are traced to depths of 1200–2000 m and 2100–2400 m, respectively (Kazanin et al., 2017a).

Late Pleistocene and Holocene sediments of the study area are represented by clayey silt and silty clay, respectively. The total thickness of Quaternary sediments does not exceed 200 m (Geological Map, 2015; Kazanin et al., 2017a). Most of the bottom sediments of the outer shelf are reduced gray, dark gray, or black clayey silt sediments. Oxidized light brown, brown, and greenish silty clay sediments are characteristic of the continental slope, PB, and the deep-water part of the AO, respectively. The upper 0.1–0.6 meters of seafloor sediments are characterized by the Holocene age, and the deeper intervals are characterized by the Late Pleistocene age (Geological Map, 2015; O'Regan et al., 2017). Based on the small number of stations with age dating of sediments (**Figure 1**), presumably all the deep intervals of core samples from bottom stations studied by us are characterized by sediments of the Late Pleistocene age.

The tectonic structure of the study area is represented by three large sedimentary basins: Cis-East Siberian, North Chukchi (marginal-shelf basins), and Novosibirsk (intrashelf basin). Sedimentary basins are separated by the North structural terrace and by the De Long and Kucherov uplifts (**Figure 1**). An important structural and tectonic element that unites the Cis-East Siberian and North Chukchi basin is the Lomonosov–Mendeleev flexure-fault zone. In the Novosibirsk Basin, a similar element is the fault zone of the same name, complicated by its feathering thrusts (Geological Map, 2015; Kazanin et al., 2017a; Kazanin et al., 2017b). The geological structure of the region is characterized by a block structure of the earth's crust and is limited by steeply dipping faults. The amplitude of displacement along faults reaches 2 km. Rifting is the leading process in the formation of most geological structures in the study area (Geological Map, 2015).

Information about the geological structure of the study area is based on published material from seismic surveys by Sevmorgeo, VNIIOkeangeologia, and MAGE (Sakulina et al., 2011; Verba, 2016; Kazanin et al., 2017a; Kazanin et al., 2017b; Kazanin et al., 2017c; Poselov et al., 2017) and seismic exploration and drilling of deep wells in the American sector of the Chukchi Sea (Sherwood, 1998; Bird and Houseknecht, 2011; Lorenson et al., 2011; Houseknecht et al., 2019). Because there is no drilling on the ESS shelf, an important source of information is also geological mapping of the nearest island territories (Franke and Hinz, 2012; Geological Map, 2015; Kus et al., 2015; Borukaev, 2017).

Geologically, in the study area, the Pre-Paleozoic formations are distinguished, represented by the basic layer of the lower crust and the diorite layer of the upper crust (**Figure 2A**). The depth of the mantle in the eastern part of the region is 29–30 km and that of basic and diorite layers is 17–20 and 13–17 km, respectively. The Archean–Proterozoic granite metamorphic layer of the upper crust along the 5AP profile was recorded up to station

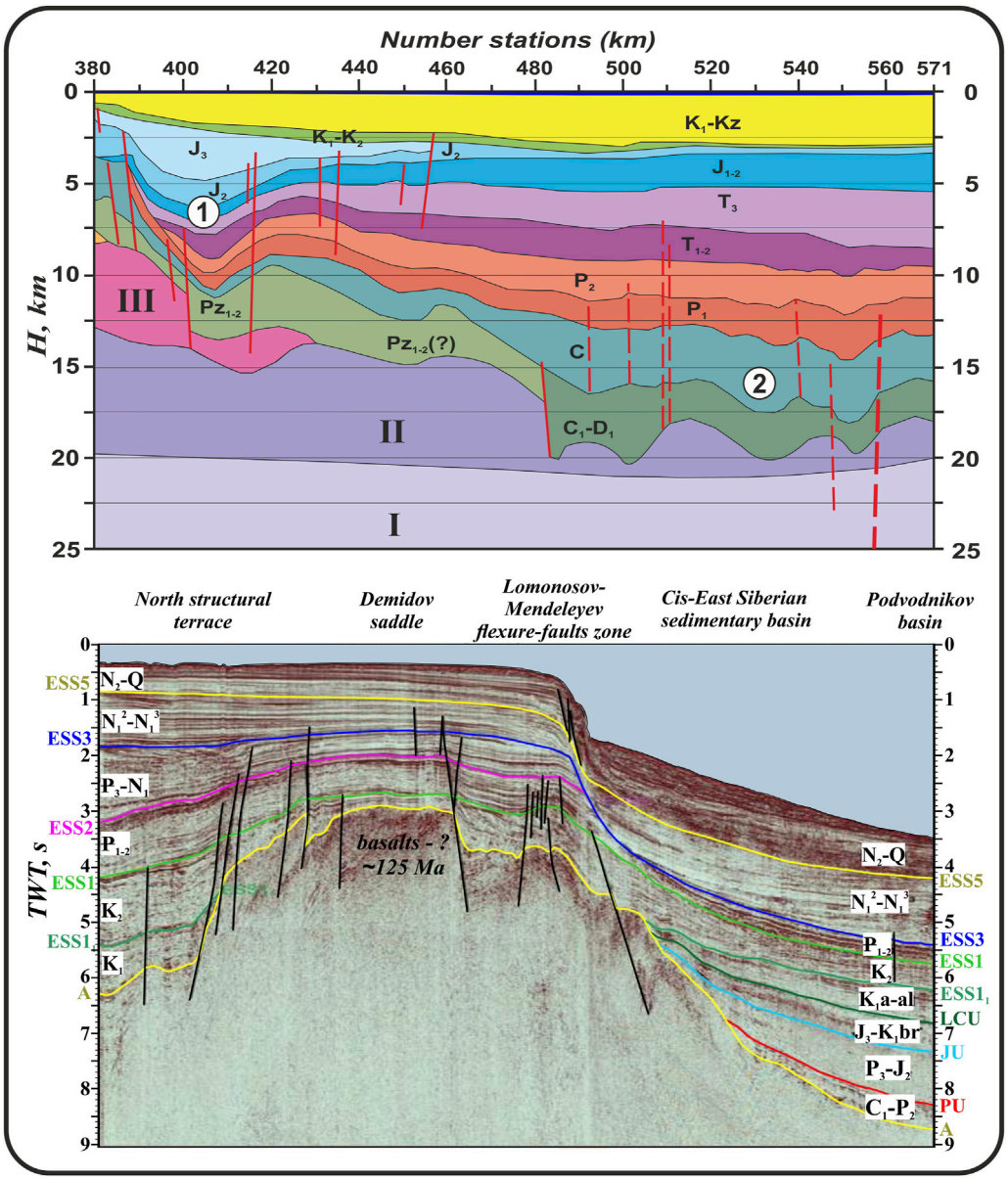

FIGURE 2 | Geoseismic profiles of the East Siberian Sea: **(A)** 5AR—after Sakulina et al. (2011). Geostructures are as follows: 1) Kolyuchinsky graben-rift and 2) North Chukchi Depression. Pre-Paleozoic formations are **(I)** basite layer of the lower crust, II) diorite layer of the upper crust, and III) Archean–Upper Proterozoic granite-metamorphic layer of the upper crust. Red lines—known faults (solid) and assumed (discontinuous). **(B)** MAGE2016—after Kazanin et al. (2017a). Colored lines—reflectors of geoseismic rock associations and black lines—faults.

440 (**Figure 2A**) (Sakulina et al., 2011; Kazanin et al., 2017c). In the western part of the study area, Archean–Proterozoic rocks are closest to the surface on the De Long uplift and in the area of Henrietta and Jeannette Islands (Franke and Hinz, 2012; Geological Map, 2015; Nikishin et al., 2021).

In the overlying Paleozoic, Mesozoic, and Cenozoic formations, by analogy with the American part of the Chukchi Sea (CS) and Northern Alaska, five structural and stratigraphic seismic complexes are distinguished (**Figure 2B**), separated by the surfaces of regional unconformities EU, PU, JU, BU ($ESS1_1$), mCU (ESS1), ESS2, RU (ESS3), and MU (ESS5): Lower Elsmir (Devonian–Lower Permian), Upper Elsmir (Upper Permian–Triassic–Lower Jurassic), Rift (Upper Jurassic–Barremian), Lower Brook and Upper Bermian (Aptian–Upper Bermian) complex, and others. These complexes are identified in the American sector of CS by using the well-drilling data (Sherwood, 1998; Bird and Houseknecht, 2011; Houseknecht et al., 2019) and can be traced to the west in the Russian sector of the CS and ESS, which suggests that the development and structure of these study areas are similar (Kazanin et al., 2017a; Kazanin et al., 2017b; Poselov et al., 2017; Nikishin et al., 2021). The similarity of the

TABLE 1 | General information about the research area.

Station	Latitude (N)	Longitude (E)	Cruise	Water depth (m)	Total core length (cm)	Sample interval, (Cmbsf)	TC (%)	Remark
380	73,1641	178,6098	LV45	55	80	70–80	0.92	KGR
390	73,2495	178,6985	LV45	56	60	50–60	0.88	KGR
400	73,3355	178,7924	LV45	56	90	80–90	0.78	KGR
410	73,4204	178,8797	LV45	56	90	80–90	0.85	KGR
420	73,5060	178,9751	LV45	58	110	100–110	0.87	KGR
430	73,5916	179,0676	LV45	60	70	60–70	0.81	KGR
440	73,6772	179,1632	LV45	63	70	60–70	0.79	NC
450	73,7628	179,2591	LV45	66	190	180–190	0.78	NC
460	73,8486	179,3553	LV45	67	125	115–125	0.71	NC
470	73,9338	179,4520	LV45	70	110	100–110	0.75	NC
480	74,0194	179,5495	LV45	72	70	60–70	0.76	NC
490	74,1046	179,6498	LV45	85	220	210–220	0.96	NC
500	74,1898	179,7515	LV45	99	225	215–225	0.89	NC
510	74,2752	179,8546	LV45	112	90	80–90	0.67	NC
520	74,3607	179,9579	LV45	127	140	130–140	0.82	NC
530	74,4449	−179,9351	LV45	143	145	135–145	0.76	NC
540	74,5299	−179,8321	LV45	160	80	70–80	0.72	NC
550	74,6144	−179,7236	LV45	182	120	110–120	0.57	NC
560	74,7105	−179,6069	LV45	201	140	130–140	0.57	NC
715	76,0114	−177,8036	LV45	1052	200	190–200	0.56	MR
21	74,1270	167,5080	LV77	43	110	100–110	0.64	N
22	75,1790	167,8190	LV77	65	164	150–164	0.68	N
23	75,8510	168,1140	LV77	140	120	95–110	0.70	NST
24	76,6000	168,5140	LV77	248	120	100–115	0.40	NST
25	77,8150	169,2770	LV77	296	250	225–245	0.40	CES
26	78,5090	169,7190	LV77	1494	412	390–410	0.50	CES
27	79,1610	169,8890	LV77	2565	410	380–400	0.16	CES
28	79,1970	163,4800	LV77	1365	410	400–410	0.20	CES
29	78,8710	163,1390	LV77	370	320	300–320	0.60	CES
30	77,8910	162,0680	LV77	132	45	35–45	0.80	DLU
31	77,2280	161,3100	LV77	90	118	90–110	0.60	DLU
32	76,5020	160,2560	LV77	67	165	140–160	0.70	DLU
33	75,8440	159,2620	LV77	46	220	205–220	0.97	N
34	75,2510	158,5010	LV77	36	110	95–110	1.17	N
35	74,6400	157,3950	LV77	43	260	245–260	0.82	N
LV90-3	74,8593	163,0044	LV90	45	173	163–173	0.80	N
LV90-4	75,9765	163,5042	LV90	57	137	117–127	0.70	N
LV90-5	76,7996	162,9975	LV90	104	320	290–310	0.70	DLU

Sedimentary basins and geostructures: KGR, Kolyuchinsky graben-rift; NC, North Chukchi sedimentary basin; MR, Mendeleev rise, N—Novosibirsk sedimentary basin, NST, North structural terrace; CES, Cis-East Siberian sedimentary basin; DLU, De Long uplift. Cmbsf: cm below seafloor.

geological structure and the proven commercial oil and gas reservoir of the American sector of CS and Northern Alaska allow a favorable assessment of the hydrocarbon potential of the ESS.

3 MATERIALS AND METHODS

The data for research ESS and AO were collected during three expeditions onboard the R/V Akademik M.A. Lavrentiev (**Figure 1**). Cruise LV45 was carried out in August/September 2008 along the meridional geological and geophysical profile 5AR (Sakulina et al., 2011; Shakirov et al., 2013; Verba, 2016; Gresov et al., 2017). The sample profile of the cruise LV45 (step of the stations is 10 km each) coincides with a multichannel seismic line 5AR ("Sevmorgeo"). Cruises LV77 (September 2016) and LV90 (September 2020) were carried out within the framework of the Russian–Chinese Arctic program "Arctic Silk Way". On these cruises, the stations were operated along sparse profiles, depending on the actual ice conditions.

3.1 Sampling

Seafloor sediments were collected using gravity corers of different length, ranging from 3 m to 8.35 m. Each core contained precut plastic liners (from 2.5 to 6 m in length). After arriving on the vessel deck, the gravity corers were disassembled, and the liners were immediately moved to the ship's laboratory for sediment sampling. In total, coring was completed for 38 stations (**Figure 1**) at depths from 36 to 2565 m (**Table 1**). The total core length recovered from each gravity core ranged from 45 to 412 cm.

TABLE 2 | Average values of gas composition (ppm, 10^{-4} vol%), C_1/C_{2+} ratio, and carbon stable isotope ratios of sorbed gases in sediments from study area.

Station	CH_4	C_2H_4	C_2H_6	C_3H_6	C_3H_8	ΣC_4H_{10}	ΣC_5H_{12}	ΣC_2–C_5	C_1/C_{2+}	$\delta^{13}C$ CH_4	$\delta^{13}C$ C_2H_6	$\delta^{13}C$ CO_2
380	4.80	0.16	0.05	0.06	0.03	0.05		0.35	60.0			
390	9.70	0.21	0.04	0.07	0.04	0.17	0.06	0.58	130.4			
400	9.10	0.30	0.06	0.17	0.05	0.25	0.23	1.06	82.7			
410	7.72	0.21	0.10	0.07	0.05	0.24	0.06	0.73	51.2	−53.2	−26.0	−22.8
420	8.60	0.40	0.07	0.15	0.06	0.28	0.03	0.99	67.7			
430	25.40	0.40	0.24	0.21	0.12	0.40	0.30	1.67	70.6	−58.3		−24.3
440	12.00	0.30	0.06	0.13	0.04	0.35	0.15	1.03	126.3	−48.2		
450	64.79	0.30	0.10	0.20	0.04	0.07	0.06	0.77	462.8	−59.3		
460	31.00	0.50	0.24	0.23	0.05	0.50	0.32	1.84	106.9	−46.2		−20.8
470	24.20	0.40	0.44	0.21	0.08	0.51	0.01	1.65	47.0	−46.9		−22.0
480	8.20	0.20	0.15	0.13	0.03	0.39	0.33	1.23	45.6	−42.0		−21.8
490	74.27	0.05	0.07		0.32	0.07	0.12	0.63	189.4	−58.9		−23.4
500	46.32	0.11	0.09	0.02	0.01	0.06	0.13	0.42	453.2	−58.0		−22.4
510	3.96	0.12	0.02	0.04	0.01	0.07	0.06	0.33	115.6	−50.4		−23.0
520	11.10	0.20	0.04	0.10	0.02	0.22	0.20	0.78	185.0	−51.0		−23.2
530	4.26	0.12	0.04	0.87	0.001	0.001		1.03	104.8	−41.0		−20.0
540	2.90	0.01	0.01	0.01	0.02	0.09	0.02	0.16	96.8	−50.3	−21.0	−23.0
550	4.32	1.31	0.33	0.31	0.18	0.47	0.11	2.72	8.5	−40.5	−20.0	−19.0
560	29.98	0.33	0.16	0.13	0.02	0.29		0.94	158.2	−42.4		−20.7
715	6.10	0.08	0.02	0.03	0.02	0.12		0.27	152.5	−49.1		−20.4
21	100.19	1.30	1.59		1.33	0.62	0.10	4.93	34.3	−54.4		−22.0
22	97.53	3.02	0.20		1.43	0.58	0.05	5.28	60.0	−53.2	−26.4	−22.8
23	71.10	1.20	2.00		1.15	0.91	0.10	5.36	22.6	−51.0	−25.1	−20.4
24	121.34	4.69	4.95		5.10	4.15	0.48	19.38	12.1	−43.8	−21.0	−20.8
25	6.02	0.80	1.99		1.53	1.19	0.04	5.56	1.7	−36.7	−17.2	−20.4
26	11.27	2.84	0.44		1.01	1.09	0.10	5.48	7.8	−36.2	−16.8	−20.8
27	9.49	0.10	1.94		0.43	0.15		2.62	4.0	−43.7	−21.2	−20.2
28	27.53	3.02	5.90		4.13	1.60	0.04	14.69	2.7	−37.0	−19.4	−19.0
29	8.04	1.00	1.18		0.68	0.72	0.09	3.67	4.3	−36.0	−18.0	−18.0
30	9.99	0.40	1.80		0.91	0.82	0.08	4.01	3.7	−37.2	−18.2	−18.4
31	24.95	1.10	2.40		1.10	1.19	0.01	5.81	7.1	−39.9	−21.4	−19.7
32	56.92	3.00	8.30		4.16	3.42	0.07	18.95	4.6	−48.4	−21.7	−21.0
33	36.25	6.38	3.24		3.60	2.75	0.08	16.06	5.3	−40.2	−19.6	−19.6
34	82.28	0.53	6.39		3.48	2.90	0.14	13.44	8.3	−45.7	−19.8	−20.7
35	74.17	3.90	4.90		3.78	3.28	0.24	16.09	8.6	−39.8	−21.8	−19.9
LV90-3	20.79	0.36	0.11	0.19	0.06	0.09		0.80	123.3			
LV90-4	31.04	0.37	0.33	0.11	0.08	0.52		1.41	75.7			
LV90-5	14.27	0.35	0.18	0.02	0.05	0.46		1.06	62.0			

Gas extraction from sediments was carried out by thermal vacuum degassing (TVD). Sediment samples (70–80 ml) were taken with 20-ml plastic syringes in 116-ml glass clear vials and immediately closed by sealed rubber caps with a closing valve. The lowest part of each core was used for sampling (**Table 1**). A total of 88 vials with sediments were selected (replicated two to three samples for each core). Sorbed gases were extracted using compact degassing systems of laboratory gas geochemistry POI, connected to each collecting vials. The maximum heating temperature was 60 °C. The working vacuum in the system was 0.9 atm. Degassing of each sample included three stages: free gas extraction at room temperature, thermal degassing (heating in water bath), and thermal vacuum degassing. The duration of gas extraction, depending on the type of sediment, was from 30 to 60 min. The work was carried out according to the current regulatory instructions (IGD'Skochinsky, 1977; VNIIGRIugol', 1988), adapted to the features of marine sediments. The extracted gas sample was transferred into 68-ml sealed glass vials. In total, 198 gas samples were received after extraction. Duplicate samples were averaged for each station and thus formed the final selection of 38 samples (**Table 2**). Gas analysis was carried out immediately in ship laboratories (cruises LV45, LV90) or after completion of work (LV77); in this case, the samples were stored at 4 °C until GC analysis.

3.2 Analytical Methods

Gas analysis was performed by gas chromatography on a "CRISTALLUX 4000M" gas chromatograph ("Meta-Chrome", Yoshkar-Ola, Russia). The sample was injected into the chromatograph using a sealed syringe. The minimum sample injection volume is 4 ml. The chromatograph module has three detectors: two thermal conductivity (TCD) and one flame ionization (FID) detectors. FID allows one to study the quantitative content of hydrocarbon composition (C_1–C_6) with a sensitivity of 10^{-6}%. Inorganic gases, such as nitrogen, oxygen, carbon dioxide, and methane, with a concentration of more than 1%, were analyzed on a TCD, the sensitivity of which is 0.01%. A gas chromatograph has two packed columns: HayeSep R column,

2.5 m length, 2.5 mm i.d, 80/100, "Meta-Chrome"; NaA column, 3 m length, 3 mm i.d, 60/80. The temperature program was 50°C, 3 min hold, heating at 10°C/min to 190°C, 14 min hold at 190°C, and 3 min hold. The temperature for detectors was 195°C and that for the evaporator was 160°C. Carrier gas was ultrapure helium 6.0. The carrier gas flow rate was 20 ml/min, for hydrogen 30 ml/min, and for air 250 ml/min. Total analysis time was 20 min. Calibration gas mixtures of HCGs were manufactured by Air Liquide (Scott™), PGS Service, and VNIIM (concentration ranged from 1 ppm to 1%). The relative error of measurements does not exceed 5%. For laboratory gas geochemistry, POI FEB RAS was certified for measurements by Rosstandart (Russia).

Determination of carbon isotope composition δ^{13}C-CH_4, C_2H_6, and CO_2 was carried out in the laboratory of stable isotopes of the Far East Geological Institute (FEGI) and the Center for Isotope Research of the Russian Geological Research Institute (VSEGEI). The following equipment was used to perform the analyses: a high-vacuum setup for preparing samples for isotopic analysis and a mass spectrometer for the analysis of stable isotopes, Finnigan MAT 253 or Deltaplus XL using a double inlet system for measuring $^{13}C/^{12}C$ isotope ratios. Sample preparation for isotopic analysis was carried out using the method described by Velivetskaya et al., (2015). The measurement results for δ^{13}C are given relative to the international VPDB standard and are expressed in ppm (‰):

$$\delta = \left(Rsample/Rstandard - 1\right) \bullet 1000‰, \quad [1]$$

where R is the carbon isotope ratio $^{13}C/^{12}C$. Reproducibility of δ^{13}C results in repeated analyses is ±0.2‰. In total, the stable carbon isotope ratios of methane were measured in 31 samples, ethane in 17 samples, and carbon dioxide in 29 samples (**Table 2**).

Total carbon (TC) contents of the lowest part of sediments were determined on subsamples collected in intervals for sorbed gas analysis. A total of 38 samples were analyzed by IR detection on a TOC-VCPN analyzer (Shimadzu, Japan). The measurement relative error did not exceed 1.5%. Measurements were carried out at the accredited Analytical Center (laboratory of analytical chemistry) of FEGI FEB RAS.

Cartographic data were produced in the ESRI® ArcGIS 10.2 software package. Distribution diagrams were compiled using Grapher 12.0. Statistical data were processed in the STATISTICA 10 program.

3.3 Hydrocarbon Characterization

A complex of quantitative geochemical indicators was used to determine the genesis of HCGs: molecular mass of the hydrocarbon fraction, weight concentrations of particular hydrocarbons, their ratios, and data on the carbon isotope composition of δ^{13}C-CH_4, C_2H_6, and CO_2.

The molecular mass of the hydrocarbon fraction (MM_{HC}) is the average weighted sum of the hydrocarbon component (Velev, 1974; Velev, 1981; Gresov, 2011). MM_{HC} was based on the sum of the molecular weights of each hydrocarbon gas (C_1—C_5, g/mol). The next important parameter closely related to MM_{HC} is weight concentrations of hydrocarbons normalized in relation to MM_{HC} in parts per thousand (Velev, 1974; Velev, 1981; Gresov, 2011). These parameters are used for gas geochemical classification of gas sources.

A change in the composition of HCGs during their long existence in reservoirs, under changing thermobaric and geochemical conditions, is accompanied by a change in methane homolog content. With an increase in temperature, redistribution of methane homologs occurs—the conversion of propane to ethane and butane and propane and butane to ethane and pentane. To assess the degree of conversion of methane homologs, we used the ratio of the concentration product of ethane and butane to the propane content. The parameter is called the coefficient of the transformation hydrocarbon fraction (Gresov, 2011) in the form of

$$Ktr = (C2 \bullet C4)/C3, \quad [2]$$

where C2, C3, and C4 are the weighted concentrations of ethane, propane, and group of butane, respectively. The value of Ktr is quite closely related to the age of the gas-bearing reservoir and indicates not only the degree of methane homolog conversion but also the time of formation and duration of HCG presence in the trap (Gresov, 2011; Gresov A. I. and Yatsuk A. V., 2020).

The Abrams coefficient ("wet" of hydrocarbon gases) (Abrams, 2005; Abrams, 2017) is widely used in world practice of gas-geochemical studies as an indicator of the enrichment degree of "heavy" hydrocarbon fractions. The value of *Kwet* represented by the ratio is as follows:

$$Kwet = \left(\sum C2 - C5 \Big/ \sum C1 - C5\right) \bullet 100\%, \quad [3]$$

where C_1–C_5 are the weighted concentrations of hydrocarbons (in the author's version, instead of vol% in Abrams, 2005). *Kwet* values are a rather informative indicator of the degree of maturity of selected gas sources (geological formations) and the genesis of HCGs of the continental margin and the southeastern part of the ESS shelf (Gresov A. I. and Yatsuk A. V., 2020; Gresov and Yatsuk, 2021).

The informative base of gas-geochemical studies is presented by materials of studied natural gases from the bottom sediments of the inner shelf of the ESS (Gresov et al., 2016; Gresov et al., 2017; Gresov A. I. and Yatsuk A. V., 2020; Gresov A. I. and Yatsuk A. V., 2020; Gresov and Yatsuk, 2021).

An additional indicator for determining the genesis of HCGs is the "Bernard coefficient"—C_1/C_{2+} (Bernard et al., 1976) and the "Bernard plot"—C_1/C_{2+} versus δ^{13}C-CH_4 (Bernard et al., 1976; Whiticar, 1999). It is generally accepted that for gases of thermogenic genesis, the Bernard coefficient is less than 100 (Bernard et al., 1976; Whiticar, 1999) and for typical microbial gases, it exceeds 1000 (Bernard et al., 1976; Whiticar, 1999; Milkov et al., 2005; Kim et al., 2020; Pape et al., 2020). Secondary microbial gases from oil degradation generally have C_1/C_{2+} ratios between 10 and 1000. The isotopic composition δ^{13}C-CH_4 of primary microbial genesis is respectively less than −55‰ or −60‰ (Milkov et al., 2005; Kim et al., 2020; Pape et al., 2020), while for secondary microbial gases δ^{13}C-CH_4, it is between −50‰ and −30‰.

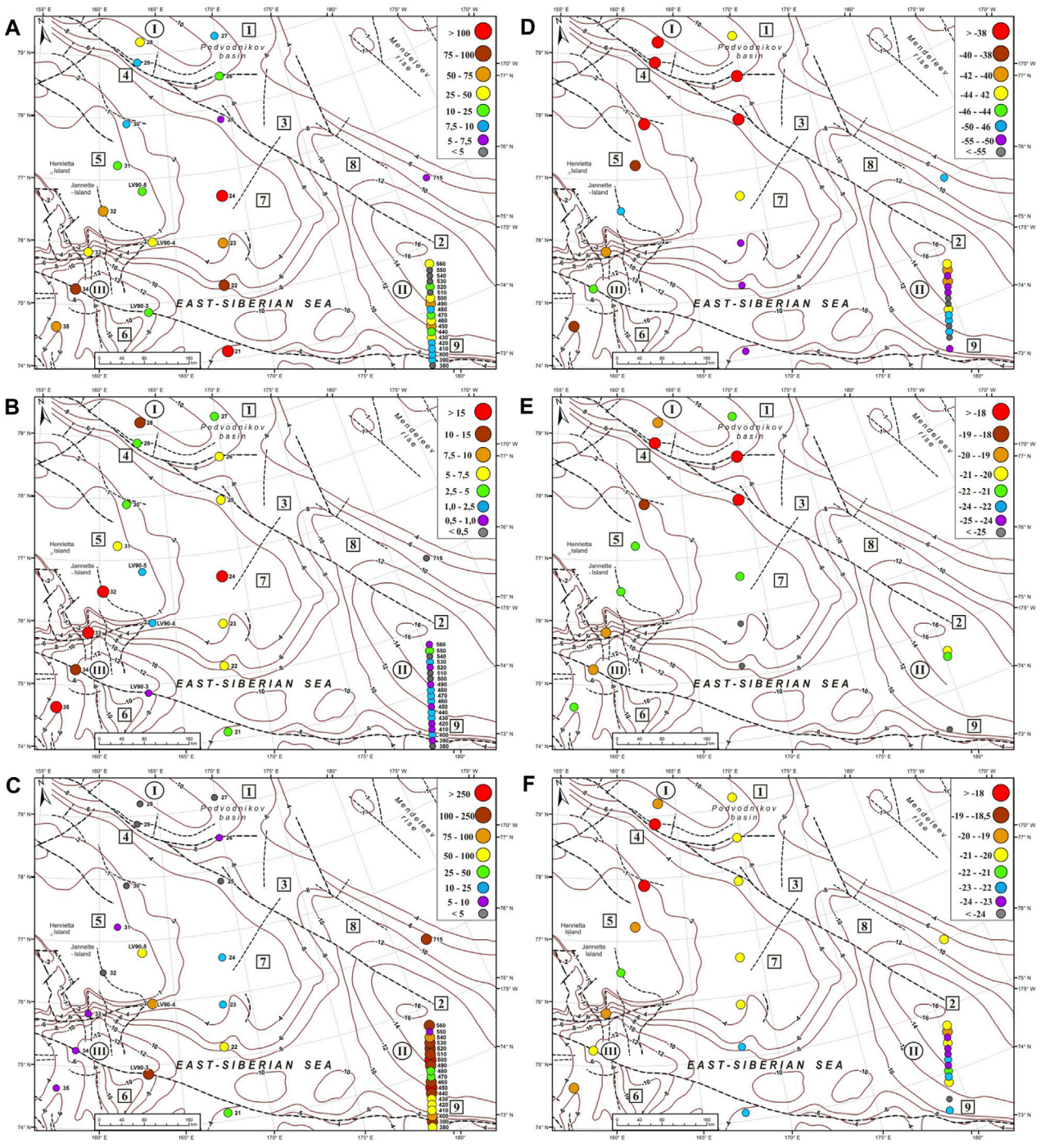

FIGURE 3 | Distribution plot of the concentration of CH_4 in ppm **(A)**, C_2–C_5 in ppm **(B)**, gas ratio C_1/C_{2+} **(C)**, and carbon isotope data of $\delta^{13}C\text{-}CH_4$ **(D)**, $\delta^{13}C\text{-}C_2H_6$ **(E)**, and $\delta^{13}C\text{-}CO_2$ **(F)**.

The plot $\delta^{13}C\text{-}CH_4$ versus $\delta^{13}C\text{-}CO_2$ has been used to distinguish between gases of different source origin: abiotic, thermogenic, primary microbial (Milkov and Etiope, 2018), and secondary microbial (Head et al., 2003; Milkov, 2011). In addition, the same plot has been used for the interpretation of fluid compositions ranging from high-temperature hydrothermal and geothermal systems to lower-temperature natural gas discharges based on the temperature-dependent isotopic equilibrium between CH_4 and CO_2 (Giggenbach, 1997; Horita, 2001; Hulston, 2004).

The plot $\delta^{13}C\text{-}CH_4$ versus $\delta^{13}C\text{-}C_2H_6$ has been used for isotope/maturity forecast between organic

precursors—huminitic vs. exinitic (Berner and Faber, 1996; Milkov, 2021). This ratio is very useful if data about regional carbon isotope values and maturity (vitrinite reflectance) of the sources of kerogen are available.

4 RESULTS

4.1 Total Carbon Content

The total carbon content (TC) of the lowest part of sediment cores from the study area ranges from 0.16 to 1.17% (average = 0.71%) (**Table 1**). The maximum TC is found within the Kolyuchinsky graben-rift and the North Chukchi and Novosibirsk sedimentary basins (**Table 1**). Such features of the distribution are mostly due to the influence of river runoff and morphological and hydrodynamic features of the study area. The results are in good agreement with data on surface sediment composition by the CASCADE project (Martens et al., 2021).

4.2 Gas Composition

The gas composition of the sorbed HCGs is presented in **Table 2**. The concentrations are given in parts per million (ppm, 10^{-4} vol %) and show a wide range of variability. Methane is the dominant component in HCGs. The CH_4 concentrations range from 2.90 to 121.34 ppm (median = 17.53 ppm). There is a weak correlation between CH_4 and C_3H_8 along with butane groups ($r^2 = 0.35$ and 0.31). The maximum concentrations of methane in seafloor sediments are found within the Novosibirsk sedimentary basin and the North structural terrace. The minimum concentrations of methane are typical for stations in the Cis-East Siberian and North Chukchi sedimentary basins (**Figure 3A**).

Saturated HCGs are represented by ethane, propane, butane (sum of i-C_4 and n-C_4), and pentane (sum of i-C_5 and n-C_5). Ethane and propane were detected in all samples, ranging from 0.01 to 8.30 ppm (median: 0.22 ppm) and from 0.001 to 5.10 ppm (median: 0.08 ppm), respectively. The butane group concentrations range from 0.001 to 4.15 ppm (100% of samples, median = 0.43 ppm) and the pentane group from 0.01 to 0.48 (79% of samples, median: 0.09 ppm). In the ethane–propane–butane group, a good correlation was identified: ethane–propane ($r^2 = 0.85$), ethane–butane ($r^2 = 0.79$), and propane–butane ($r^2 = 0.90$). Unsaturated hydrocarbons (ethene and propene) exceed saturated homologs (ethane and propane) in most samples from the eastern part; the opposite picture is observed in the western part of the study area (**Table 2**). Ethylene concentration ranges from 0.01 to 6.38 (100%; median: 0.38) and propylene from 0.01 to 0.87 (58%; median: 0.13). In general, the total content of C_2–C_5 hydrocarbons is higher in the western part of the study area (maximum concentrations are found within the North structural terrace, De Long uplift, and Novosibirsk basin) than in the eastern part (minimum in the Kolyuchinsky graben-rift and the North Chukchi basin) (**Figure 3B**).

The C_1/C_{2+} ratio ranges from 2 to 463 (**Table 2**), lower values are observed in western part of the study area (Cis-East Siberian basins, De Long uplift, and Novosibirsk basin), and higher values in the east (North Chukchi basin) (**Figure 3C**).

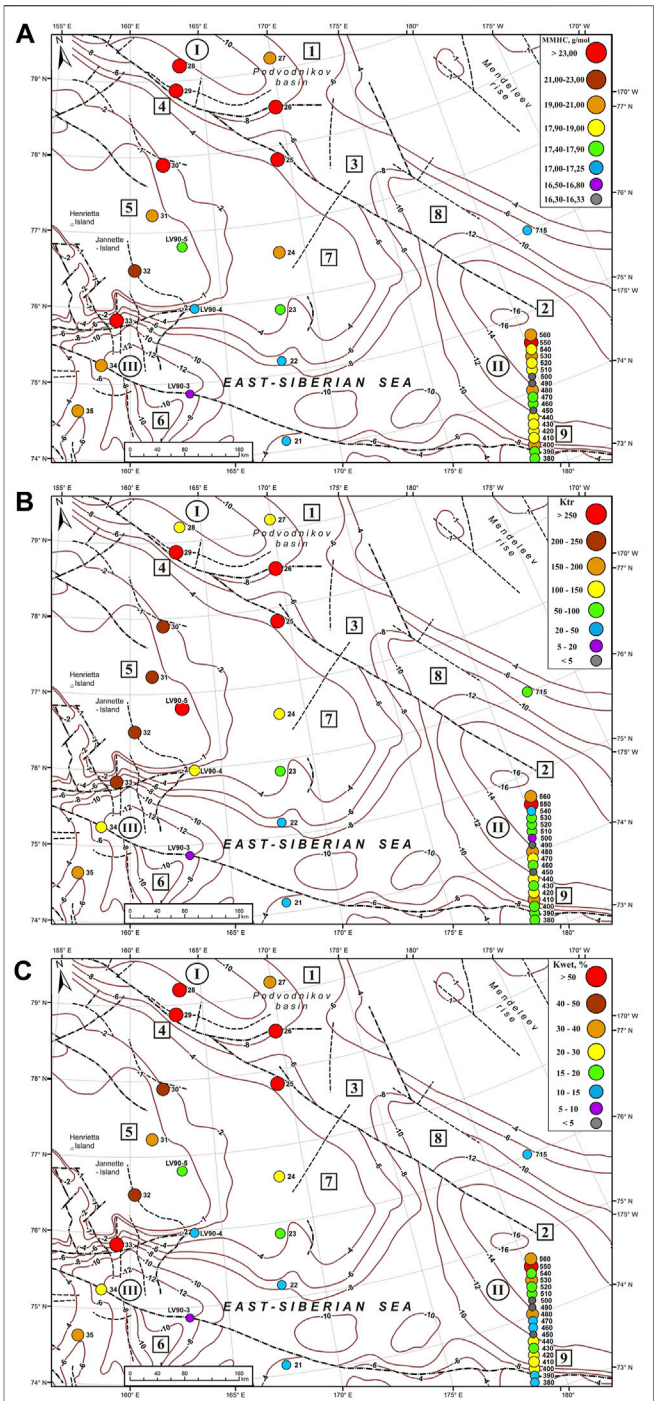

FIGURE 4 | Distribution plot of the gas-geochemical parameters of sorbed HCGs of bottom sediments: MM_{HC} **(A)**, Ktr **(B)**, and Kwet **(C)**.

Since our research has not found active gas seepage, the predominant type of gas migration in the near-surface sediments is upward diffusion of deeply derived thermogenic HCGs coupled with shallow contributions of microbial gas formed *in situ*. Methane concentrations are significantly lower than those of other regions which have been shown to

TABLE 3 | Average values of geochemical indicators of bottom sediment hydrocarbon gases of the inner shelf of the East Siberian Sea.

Gas source	Weight concentration (fraction of unit per 1000)					MM_{HC} g/mol	Geochemical parameters		
	C_1	C_2	C_3	C_4	C_5		Ktr	Kwet %	$\delta^{13}C\text{-}CH_4$‰
Modern sediments (31)	**998**	**1**	**tr**	**tr**	**0**	**16.05**	**0.3**	**0.1**	**–83.2**
Gas hydrates (6)?	**993**	**5**	**1**	**tr**	**0**	**16.10**	**1.8**	**0.6**	**–61.8**
Peat deposits (12)	**991**	**7**	**2**	**tr**	**0**	**16.12**	**1.5**	**0.9**	**–67.4**
Coal fields (55)	**977**	**13**	**5**	**3**	**tr**	**16.25**	**8.0**	**2.3**	**–58.4**
a. Lignite (10)	984	9	6	1	0	16.17	1.7	1.4	–61.2
b. Brown coal (30)	981	13	4	2	tr	16.22	6.4	1.8	–59.8
c. Black coal (15)	974	15	7	4	tr	16.29	9.2	2.6	–55.4
Gas deposits (30)	**976**	**14**	**6**	**3**	**1**	**16.23**	**7.0**	**2.3**	**–58.9**
a. Cenozoic age (20)	987	7	4	1	tr	16.15	1.8	1.2	–62.0
b. Mesozoic age (10)*	955	29	9	4	2	16.40	12.8	4.4	–52.8
Igneous rocks (18)*	**944**	**30**	**16**	**10**	**0**	**16.60**	**17.5**	**5.6**	**–25.3**
Solid bitumen (6)*	**844**	**58**	**41**	**56**	**1**	**17.64**	**79.2**	**15.5**	**–46.8**
Condensate-gas deposits (22)*	**884**	**59**	**23**	**18**	**16**	**17.19**	**46.2**	**11.5**	**–51.4**
Gas-condensate deposits (10)*	**797**	**82**	**47**	**54**	**21**	**18.24**	**94.2**	**20.2**	**–51.0**
Oil gas deposits (21)*	**718**	**83**	**59**	**68**	**72**	**19.57**	**96.7**	**28.1**	**–42.2**
Gas oil deposits (19)*	**549**	**147**	**100**	**85**	**119**	**22.44**	**125.0**	**44.8**	**–41.8**
Oil deposits (9)*	**480**	**196**	**103**	**116**	**105**	**24.34**	**220.7**	**51.4**	**–37.7**

*Data from Gresov et al., 2016; Gresov et al., 2017; Gresov and Yatsuk. 2020a; Gresov and Yatsuk. 2020b; Gresov and Yatsuk. 2021. *—supposed deposits (31)—number of samples. tr—trace.*

host gas hydrates, such as the northern part of the Chukchi Sea (Kim et al., 2020). Previous studies in ESS have also noted low concentrations of methane in pore water (Miller et al., 2017). Unfortunately, the work of Miller et al. (2017) does not provide any information about real concentration values of methane and its homologs. The study does indicate that the sulfate–methane transition (SMT) zone is deep, ranging from 23 to 64 meters. We did not measure sulfate in our study. Given our depth range of gravity coring, we assume that that all our samples were collected within the sulfate reduction zone, shallower than the methanogenic zone. This may explain such small concentration range of methane. Despite this, the concentrations of HCGs in our work is an order of magnitude higher than those observed in both the Barents Sea (Knies et al., 2004; Blumenberg et al., 2016; Weniger et al., 2019) and the Laptev Sea (Cramer and Franke, 2005), but lower than in the Kara Sea (Serov et al., 2015) and the Chukchi Sea (Kim et al., 2020). These differences can possibly be associated with regional features of the distribution of HCGs or they may be associated to differences in station selection strategy and methodological approaches (headspace technique, TVD, and acid extraction).

4.3 Gas Isotopic Properties and Gas Genesis Parameters

The carbon isotopic signatures of the sorbed hydrocarbon gases ($\delta^{13}C\text{-}CH_4$ and $\delta^{13}C\text{-}C_2H_6$) and carbon dioxide ($\delta^{13}C\text{-}CO_2$) are shown in **Table 2**. The isotope composition of methane carbon ($\delta^{13}C$) varied from −59.3 to −36.0‰, ethane from −26.4 to −16.8‰, and carbon dioxide from −24.3 to −18.0‰. Good correlation was identified for $\delta^{13}C\text{-}CH_4$–$\delta^{13}C\text{-}C_2H_6$ ($r^2 = 0.76$) and $\delta^{13}C\text{-}CH_4$–$\delta^{13}C\text{-}CO_2$ ($r^2 = 0.70$) and weak correlation for $\delta^{13}C\text{-}CO_2$–$\delta^{13}C\text{-}C_2H_6$ ($r^2 = 0.37$). The spatial distribution of carbon isotopic signatures is shown in plots (**Figures 3D–F**). The maximum values for all three components were obtained in the northwestern part of the study area (Cis-East Siberian sedimentary basins and Lomonosov–Mendeleev flexure-fault zone).

The values of the MM_{HC} vary in the range from 16.31 g/mol to 27.53 g/mol, Ktr from 4.0 to 354.2, and Kwet from 2.5 to 69.7%. Within this group of parameters, there is a good and moderate correlation: MM_{HC}–Kwet ($r^2 = 0.97$), Ktr—Kwet ($r^2 = 0.67$), and MM_{HC}–Ktr ($r^2 = 0.65$). In addition to this, a wide relationship with carbon isotope data was found ($r^2 = 0.42$–0.78). The spatial distribution of gas genesis parameters is shown in plots (**Figures 4A–C**).

Based on previous experience and interpretation of gas-geochemical parameters in continental sedimentary basins of the Balkan region, Northern Bulgaria (Velev, 1974; Velev, 1981), Far East of Russia (Gresov, 2011), and subaqueous sedimentary basins ESS (Gresov et al., 2016; Gresov et al., 2017; Gresov A. I. and Yatsuk A. V., 2020; Gresov A. I. and Yatsuk A. V., 2020; Gresov and Yatsuk, 2021), we have compiled a generalized summary of the geochemical indicators for the southeastern part internal shelf of the ESS (**Table 3**). This made it possible to perform similar work for the external shelf of the ESS and adjacent part of the AO.

Thus, we have determined eight main genetic groups of epigenetic HCGs in sediments of the edge shelf zone of the East Siberian Sea and adjacent part of the Arctic Ocean (**Table 4**). We assumed that these gases emanated from the supposed underlying deep sources in the process of natural diffusion and migration along the fault zones and lineaments of the study area. Relatively low values of total carbon content in sediments, probably from the Pleistocene age, appear to be responsible for the low levels of microbial gas formation in modern sediments. These gases are quite complicated to identify due to their mixing with the underlying migration gases of geological formations.

TABLE 4 | Average values of geochemical indicators of bottom sediment HCGs of the edge shelf zone of the East Siberian Sea and adjacent part of the Arctic Ocean.

Gas source (bottom stations)	Weight concentration (fraction of unit per 1000)					MM_{HC} g/mol	Geochemical parameters		
	C_1	C_2	C_3	C_4	C_5		Ktr	Kwet%	$\delta^{13}C\text{-}CH_4$‰
1. Coal gas deposits (450, 490, and 500)	974	7	8	4	8	**16.32**	9.1	2.6	–58.7
2. Magmatic formation (LV90-3)	920	37	29	14	0	**16.79**	18.0	8.4	–
3. Condensate-gas deposits (21, 22, 715, and LV90-4)	893	40	26	39	2	**17.13**	61.1	10.6	–52.2
4. Solid bitumen (380, 390, 460, 470, 23, and LV90-5)	851	53	27	57	12	**17.65**	114.1	14.9	–48.0
5. Gas-condensate deposits (410, 420, 430, 440, 510, 520, and 540)	811	43	31	75	40	**18.30**	98,1	18.9	–51.9
6. Oil gas deposits (400, 480, 530, 560, 24, 27, 31, 34, and 35)	675	111	97	82	34	**20.01**	139.9	32.5	–42.3
7. Gas oil deposits (30 and 32)	531	205	119	135	11	**22.17**	232.0	46.9	–42.8
8. Oil deposits (25, 26, 28, 29, and 550)	431	251	146	154	18	**24.04**	276.4	56.9	–37.3

TABLE 5 | Correlation (r^2) between gas genetic indicators of the study area.

Parameters	MM_{HC}	Ktr	Kwet	$\delta^{13}CH_4$	$\delta^{13}C_2H_6$	$\delta^{13}CO_2$
MM_{HC}						
Ktr	0.65					
Kwet	0.97	0.67				
$\delta^{13}CH_4$	0.71	0.63	0.78			
$\delta^{13}C_2H_6$	0.64	0.45	0.67	0.76		
$\delta^{13}CO_2$	0.45	0.42	0.53	0.70	0.37	

4.3.1 Coal Gas Sources

The first genetic group of HGCs is associated with black coal. The group is poorly represented in the study area (**Table 4**). The group is characterized by the values of the coefficients: MM_{HC}: 16.29–16.33 g/mol, Ktr: 4–19, Kwet: 2.5–2.7, and $\delta^{13}C\text{-}CH_4$ and CO_2: −58 ... −59.3 and −23.4 ... −22.4‰, respectively. In contrast to the areas of the inner shelf (Gresov A. I. and Yatsuk A. V., 2020; Gresov and Yatsuk, 2021), this source is not predominant in the study area and occurs locally in the southern slope of the North Chukchi sedimentary basin (**Figure 4A**). The complexity of the formation of the first group determines the mixed polygenic composition of biochemical, thermogenic-transformed, and possibly magmatic gases formed in the upper part of the sedimentary cover. This is also confirmed by rather high values of the C_1/C_{2+} ratio from 189 to 463, which is typical for gases of mixed genesis.

4.3.2 Igneous Rock Sources

The second group of HCGs is also represented quite locally. Igneous HCGs are assumed for station LV90-3 with the following coefficient values: MM_{HC}: 16.79 g/mol, Ktr: 18, and Kwet: 8.4. The values are close to those of the established gases of the Cretaceous igneous rocks of the southeastern part of the ESS. According to limited data, the isotopic composition of $\delta^{13}C\text{-}CH_4$ varies from −29 to −25‰ (Gresov A. I. and Yatsuk A. V., 2020; Gresov A. I. and Yatsuk A. V., 2020).

4.3.3 Condensate-Gas Sources

The migration gases of the supposed condensate-gas deposits represent the third genetic group of HCGs of bottom sediments. The groups were characterized by the average value of MM_{HC}: 17.13 g/mol, Ktr: 61.1, and Kwet: 10.6%. The C_1/C_{2+} ratio ranges from 34 to 153. The average value of $\delta^{13}C\text{-}CH_4$, C_2H_6, and CO_2 is −50.2, −26.4, and −21.7‰, respectively. The location of this group is mainly in Novosibirsk sedimentary basin (**Figure 4A**).

4.3.4 Solid Bitumen Sources

The fourth genetic group of hydrocarbon gases presented gas-geochemical parameters of solid bitumen of the continental-island framing and the internal shelf of the ESS (**Table 3**, **Table 4**). A specific feature of the gases in the eastern sector of the study area (stations 460, 470, 380, and 390) is their intermediate position between the sites of the first group and supposed oil gas deposits (**Figure 4A**) and in the western sector (station 23 and LV90-3) between station condensate-gas and oil gas deposit groups (**Figure 4A**). HCGs of the group are characterized by MM_{HC}: 17.43–17.87 g/mol, Ktr: 72.9–257.0, and Kwet: 14.2–16.4%. The average value of $\delta^{13}C\text{-}CH_4$, C_2H_6, and CO_2 is −48.0, −25.1, and −21.1‰, respectively. The C_1/C_{2+} ratio is 71 in average. The formation of HCGs of solid bitumen is associated with the thermogenetic transformation of organic matter and in some cases with thermal influences of magmatic processes (anthraxolites) (Klubov, 1983; Borukaev, 2017; Gresov A. I. and Yatsuk A. V., 2020; Gresov A. I. and Yatsuk A. V., 2020). In general, the poorly studied issue of gas formation in solid bitumen in the East Arctic region requires more complicated research.

4.3.5 Gas-Condensate Sources

Migration gases of the supposed gas-condensate deposits represent the fifth genetic group of HCGs in sediments (**Table 3**, **Table 4**). This group has a value of MM_{HC} ranging from 17.91 g/mol to 18.63 g/mol, Ktr: 42.3–151.0, and Kwet: 15.5–22.8%. The average value of $\delta^{13}C\text{-}CH_4$, C_2H_6, and CO_2 is −51.9, −23.5, and −23.3‰, respectively. The C_1/C_{2+} ratio is 102 in average. This group is most prevalent in the North Chukchi sedimentary basin (**Figure 4A**). Based on the gas-geochemical parameters, in the bottom sediments of the study area, there are probably two HCG subgroups of the supposed gas-condensate deposits with the values of Ktr 42.3–78.8 and 117.5–151.0. It has been established that HCGs of this group in most cases is a natural gas-geochemical "fringe" of oil and gas deposits.

4.3.6 Oil Gas, Gas Oil, and Oil Sources

Migration HCGs of the supposed oil gas, gas oil, and oil deposits represent the sixth, seventh, and eighth genetic

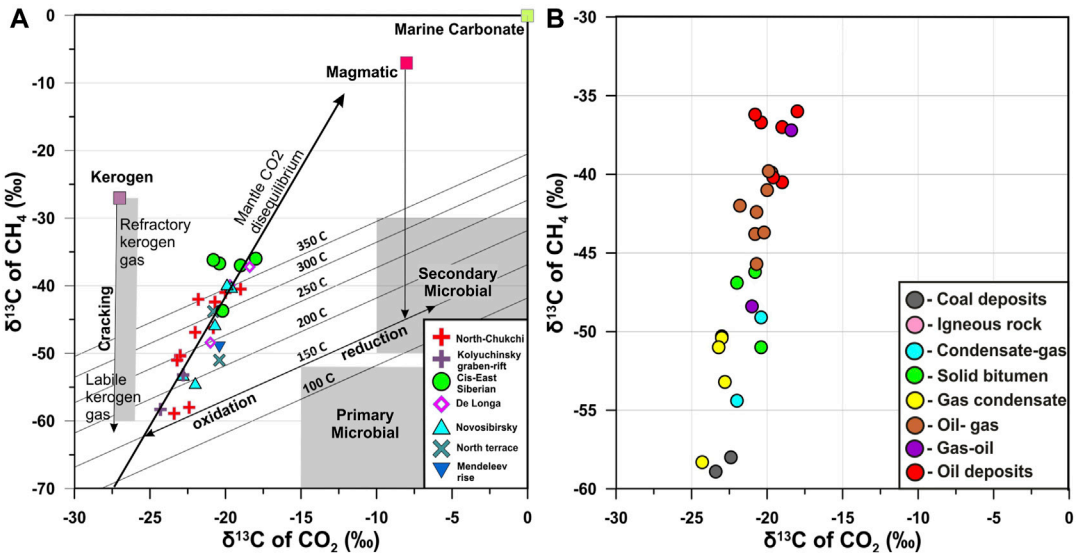

FIGURE 5 | Plot of values of δ^{13}C-CH_4 vs. δ^{13}C-CO_2 after Giggenbach (1997) **(A)**. Thin solid lines represent compositions expected for attainment of isotopic equilibrium as a function of temperature. Solid dashed lines correspond to compositions expected for formation of CH_4 and CO_2 from a common C source, such as a kerogen with δ^{13}C of total C of –27‰, or magmatic C with δ^{13}C of –7‰, as a function of the percentage of CO_2 in the gas mixture formed. Plot of values of δ^{13}C-CH_4 vs. δ^{13}C-CO_2 with author's gas genetic groups **(B)**: 1) coal and gas deposits, 2) igneous rock, 3) condensate-gas, 4) solid bitumen, 5) gas condensate, 6) oil gas, 7) gas oil, and 8) oil deposits.

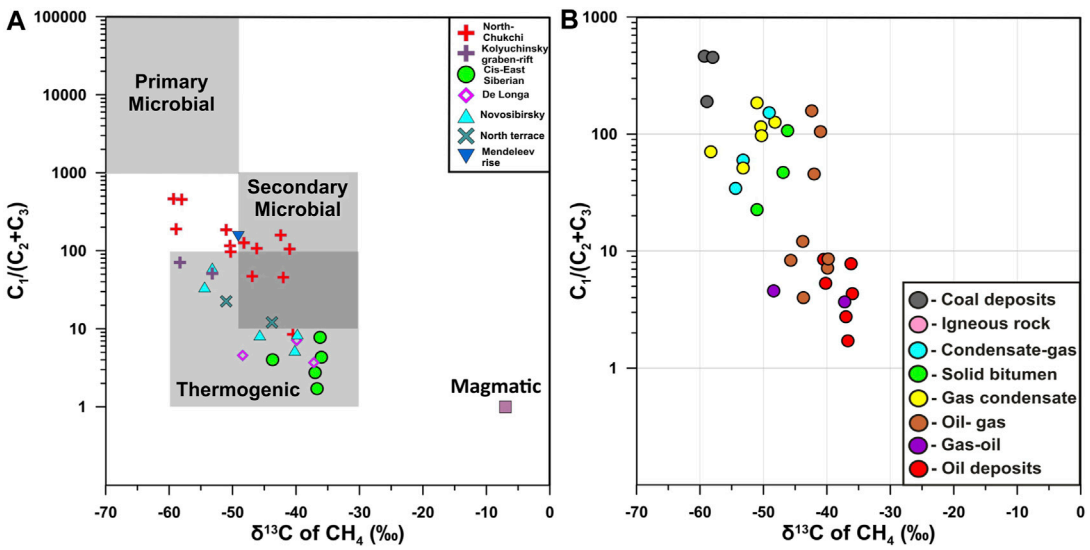

FIGURE 6 | Bernard diagram (after Bernard et al., 1976). **(A)** Bernard diagram versus author's gas genetic groups **(B)**. Genetic groups are the same such as in **Figure 5**.

groups of epigenetic gases of bottom sediments in the study area (**Table 3**, **Table 4**). The gas-geochemical parameters presented by MM_{HC}: 19.35–20.71, 21.5–22.79, and 22.61–27.53 g/mol; Ktr: 64.8–236.8, 221.3–242.7, and 136.3–354.2; and Kwet: 25.8–37.3, 44.1–49.8, and 50.8–69.7% (**Figures 4A–C**). The isotope parameter range for δ^{13}C-CH_4, C_2H_6, and CO_2 is –45.7 to –39.9, –21.8 to –19.8, and –21.8 to –19.9‰; –42.8 to –37.2, –21.7 to –18.2, and –21.0 to –18.4‰; and –40.5 to –36.0, –20.0 to –16.8, and –20.8 to –18.0‰, respectively (**Figures 3D–F**). Previously, we have found similar parameters for oil gas deposits in the southeastern part of the ESS (**Table 3**) and continental deposits of Far East of Russia (Gresov, 2011). These groups of HCGs are located in the bottom sediments

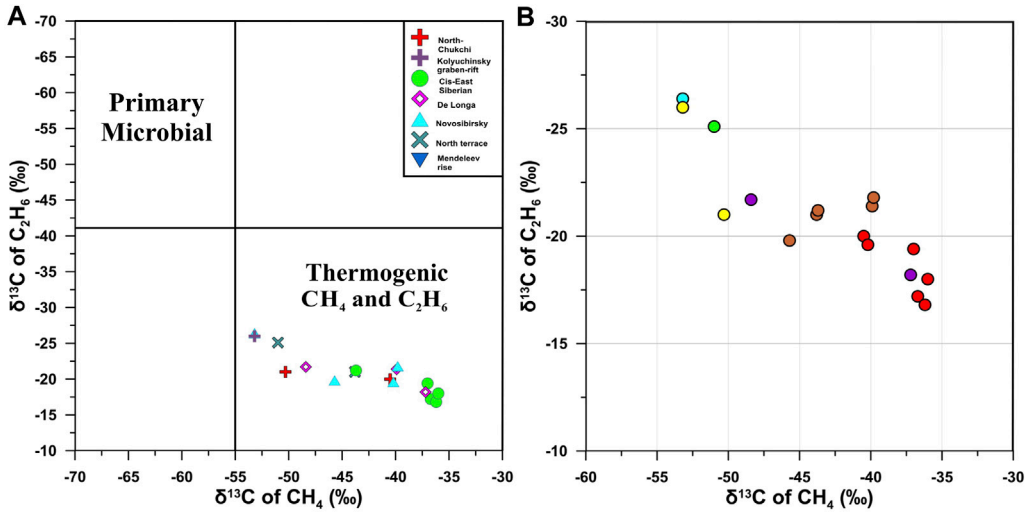

FIGURE 7 | Plot of values of $\delta^{13}C\text{-}C_2H_6$ versus $\delta^{13}C\text{-}CH_4$ after Milkov et al., 2005. Plot of values of $\delta^{13}C\text{-}C_2H_6$ versus $\delta^{13}C\text{-}CH_4$ with author's gas genetic groups **(B)**. Genetic groups are the same such as in **Figure 5**.

of North Chukchi, Cis-East-Siberian, Novosibirsk sedimentary basin, Longa uplift, Northern Terrace, and Lomonosov–Mendeleev flexure-fault zone.

Thus, the use of a complex of isotope and gas-geochemical indicators is a rather informative method for identifying various regional and stratigraphic gas sources of hydrocarbons in bottom sediments. It was found that all the isotope and gas-geochemical parameters of HCGs are closely associated with each other by wide correlation (r^2 = 0.37–0.97) (**Table 5**).

5 DISCUSSION

In the context of global climate change processes, great attention is paid to the current state of the Arctic region. At the same time, a number of studies have provided differing estimates as to the potentially catastrophic climatological impact resulting from the destruction of marine permafrost and massive greenhouse gas emissions (Shakhova et al., 2010; Shakhova et al., 2017). Most of these estimates are given for the water area of the inner ESS shelf. At the same time, a number of other studies indicate a rather limited or local distribution of these processes in the outer ESS shelf and adjacent part of the Arctic Ocean (Thornton et al., 2016; Miller et al., 2017; Sparrow et al., 2018; Thornton et al., 2020). In addition, it is important to emphasize that the study of the processes of migration of methane in the aquatic environment and at the water–atmosphere boundary should always be accompanied by a direct study of its bottom sources. In this regard, the ability to separate surface and deep sources of methane formation is especially important. It should be noted that the existing estimates of geological methane emissions are far from complete (Sherwood et al., 2017; Etiope et al., 2019), and the available global estimates have a large uncertainty in the values of natural methane emissions (Saunois et al., 2020).

Gas geochemistry is widely used to obtain information about the origin and sources of gas in geological systems. In this work, we used a complex technique for the determination and interpretation of isotope and gas-geochemical parameters to identify and determine the genesis of bottom sediment sorbed gases. The representativeness of our methodology has been confirmed by approbation of the results at continental and subaqueous areas with proven oil and gas-bearing sedimentary basins of the Northeast of Russia (Gresov, 2011; Gresov et al., 2012; Gresov et al., 2016; Gresov et al., 2017; Gresov A. I. and Yatsuk A. V., 2020), Balkan region, and Northern Bulgaria (Velev, 1974; Velev, 1981).

Undoubtedly, we understand that the sample and analysis of HCGs of surface sediments and samples from the source itself (natural gas seepage, commercial gas drilling, and oil- and gas-bearing rock) are slightly different factors. The thermogenic gases can have a long migration history to the surface and have possibly undergone various changes over time. There are works that show that it is possible to predict gas sources directly on a sufficiently large statistical scale (Schoell, 1983; Faber et al., 2015; Abrams, 2017; Weniger et al., 2019; Milkov, 2021). To check an important question: how does our proposed methodology correlate with existing classifications and approaches to assessing the genesis of gases, we used three famous diagrams: plot of values of $\delta^{13}C\text{-}CH_4$ versus $\delta^{13}C\text{-}CO_2$ after Giggenbach 1997 (**Figure 5A**), Bernard diagram (Bernard et al., 1976) (**Figure 6A**), and plot of values of $\delta^{13}C\text{-}C_2H_6$ versus $\delta^{13}C\text{-}CH_4$ after Milkov et al., 2005 (**Figure 7A**). Thus, based on a comparison with the main classification diagrams, we see that the distribution of thermogenic-sorbed gases prevails in the studied area. The influence of the processes of microbial formation, secondary microbial formation, and biodegradation (Etiope et al., 2009; Milkov, 2011) in the studied area of the ESS was not recorded.

The plot of $\delta^{13}C\text{-}CH_4$ versus $\delta^{13}C\text{-}CO_2$ shows us values for both components in the thermogenic field (**Figure 5A**).

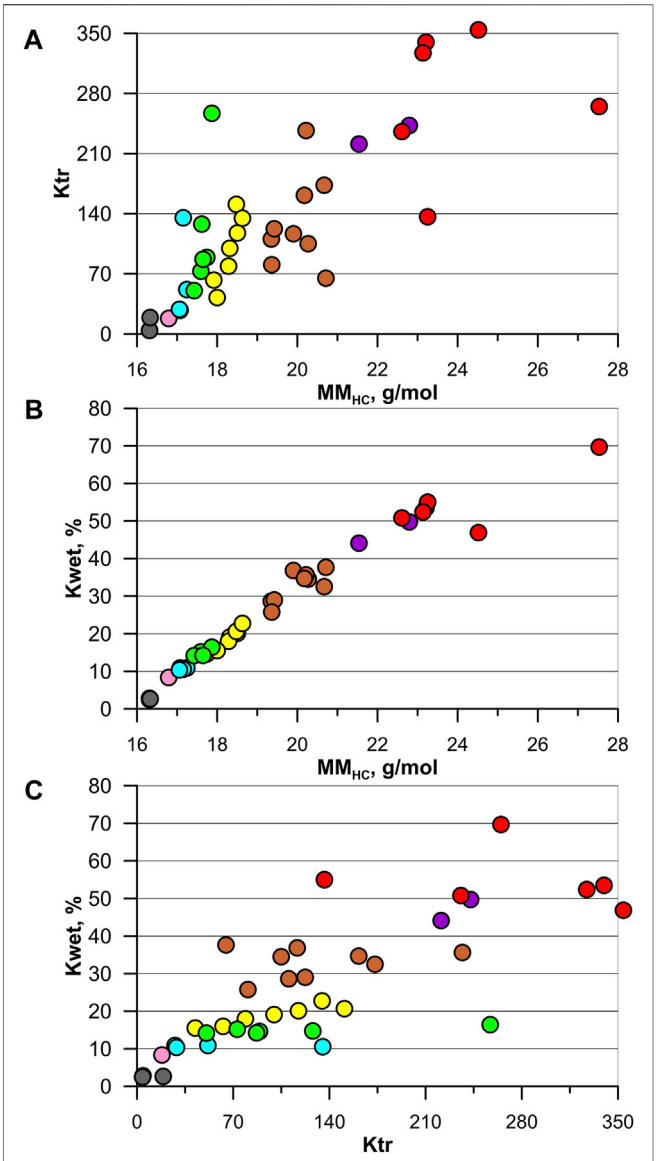

FIGURE 8 | Paragenetic variability of gas-geochemical parameters MM_{HC}-Ktr **(A)**, MM_{HC}-Kwet **(B)**, and Kwet-Ktr **(C)**. Genetic groups are the same such as in **Figure 5**.

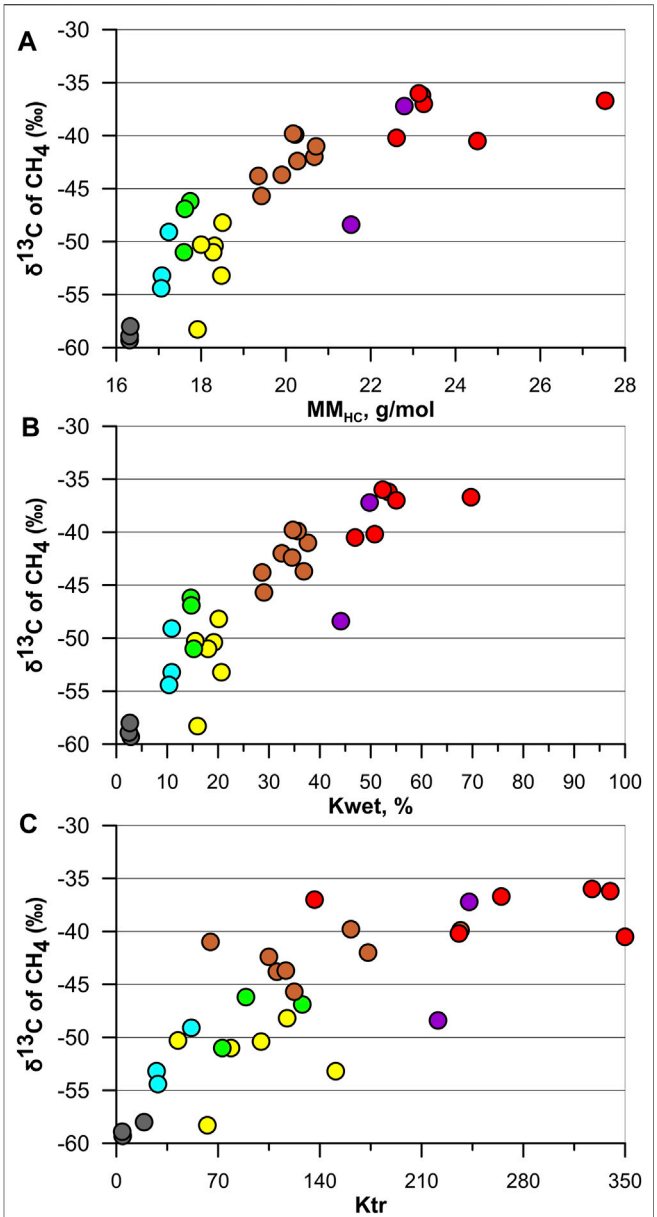

FIGURE 9 | Paragenetic variability of gas-geochemical and carbon isotopic data $\delta^{13}C$-CH_4 with MM_{HC} **(A)**, Kwet **(B)**, and Ktr **(C)**. Genetic groups are the same such as in **Figure 5**.

Isotherms from 100 to 350 °C show a starting gas characteristic of thermogenic gas from early-stage cracking of the more labile components of kerogen (Giggenbach, 1997), which becomes progressively more enriched in ^{13}C in both CH_4 and CO_2. The highest equilibrium reservoir temperatures derived from Hulston (2004) on the high end of what would be expected for methane-rich hydrocarbons. The progressively heavier ^{13}C values do not appear to represent the mixing between a secondary microbial gas source, similar to values indicated in previous studies (Head et al., 2003; Milkov, 2011), with a labile kerogen thermogenic gas as indicated by Giggenbach (1997). Instead, the gases trend toward a high-temperature magmatic end-member as has been observed in deep high-temperature geothermal systems (Giggenbach, 1997). Such values for magmatic gases seem to be influenced by subduction recycling of carbonates into the mantle. In any case, the Cis-East Siberian sedimentary basin has a sedimentary cover depth up to 10 km and De Long uplift up to 4 (**Figure 1**, **Figure 2B**). In our opinion, the most enriched ^{13}C samples shown in **Figure 5A** reflect the admixture deeply sourced of magmatic gas with a more labile kerogen source, predominantly in the western part of the study area. The source of the magmatic fluid may be Cretaceous basalts and intrusions, which are widespread at the base of the basement of the De Long uplift (Nikishin et al., 2021). Migration of fluids to the upper part of the sedimentary cover is possible along a network of tectonic faults that are deep (>5–6 km) and

represent an extended Lomonosov–Mendeleev flexure-fault zone (**Figure 1**, **Figure 2B**). The localization of such fluids in the course of vertical and lateral diffusion is possible in the zone of anticlinal uplifts and wedging out traps in the presence of seals. Promising areas of oil and gas deposits in the area of the De Long uplift were discovered according to MAGE data. There are 20 local anticlinal dome-shaped structures mapped, in the arch of which anomalies of the "bright spot" type were found (Kazanin et al., 2017a). The largest anomaly was found in the area of the Demidov saddle (length 39.5 km). Station 25 is located in the region of the dome-shaped uplift of the Demidov saddle and has typical parameter HCGs of oil fields: MM_{HC}: 27,5, Ktr: 265, Kwet: 70% and "heavy" isotopic composition of sorbed gases (**Table 2**). The average value of the geothermal coefficient in the outer ESS shelf is 57 °C/km (O'Regan et al., 2016). According to the roughest estimates, then the source of the origin of the gas maybe lies at a depth of approximately 6 km. This fully coincides with the geological features of the region, and the existing structure of tectonic faults is a channel for migration to the surface.

In the eastern part of the study area, the influence of magmatism is not so noticeable; perhaps the very large depth of the sedimentary layer (more than 16 km in the depocenter) has an effect (**Figure 2A**). However, there is also a tendency toward an increase in the gas–genetic parameters of oil and gas potential toward the Lomonosov–Mendeleev flexure-fault zone (**Figure 3**, **Figure 4**). In the eastern part of the study area, the predominant sources of HCGs are gas-condensate sources and coal-bearing formations.

As with the previous figure, a plot of $\delta^{13}C\text{-}CH_4$ vs. C_1/C_{2+} (**Figure 6**) shows that the same most thermogenic gases in the trend toward a magmatic gas end-member as indicated by Giggenbach (1997). The presence of higher C_1/C_{2+} values, particularly the North Chukchi area gases, indicates some involvement of both primary microbial and secondary microbial gases. Likewise, a plot of $\delta^{13}C\text{-}CH_4$ vs. $\delta^{13}C\text{-}C_2H_6$ (**Figure 7**) shows mixing of a thermogenic end-member where both C_2H_6 and CH_4 are relatively more enriched in ^{13}C, with an end-member containing both microbial CH_4 and thermogenic C_2H_6.

All of the isotopic diagrams indicate similar patterns in regard to the separation of potential sources in the series coal, condensate-gas, bitumen, gas condensate, and oil and gas (**Figure 5B**, **Figure 6B**, and **Figure 7B**). In addition to this, we create diagrams of the dependence of the three main gas genetic indicators (MM_{HC}, Ktr, and Kwet) among themselves (**Figure 8**) and between carbon isotopes of $\delta^{13}C\text{-}CH_4$ (**Figure 9**). In this case, the source categorization schema turns out to be quite good as all parameters have a good cross-correlation. In our opinion, the additional use of these three coefficients derived from weighted concentrations of hydrocarbon gases significantly expands the possibilities of interpreting gas data for hydrocarbon prospecting.

Next, a major feature of the distribution of thermogenic hydrocarbon gases is the mutual distribution of weight concentrations of hydrocarbons fractions. So, for HCGs of coal gas deposits is the steeply descending distribution of the weight concentrations of particular hydrocarbons toward high molecular mass members. Concentrations naturally decreases and the rule $C_n > C_{n+1}$ is completed with an increase in the sequence number of homologs. This feature is interpreted as a sign of a genetic relationship between members of the hydrocarbon fraction. Based on the validity of this assumption, one can consider HCGs of the first group as a set of interrelated and arranged elements of some integral gas-geochemical formation of the upper part of the Cenozoic–Cretaceous sedimentary cover. HCGs of the other genetic groups are characterized by an irregular distribution of weight concentrations of hydrocarbons in the form of $C_n = C_{n+1}$, $C_n > C_{n+1}$, and $C_n < C_{n+1}$ (**Table 3**, **Table 4**). This specific feature is typical for HCGs of gas oil and oil deposits of coal oil- and gas-bearing sedimentary basins in the Northeast of Russia (Gresov, 2011; Gresov et al., 2012).

Thus, the proposed methodology for determining HCG sources can be used quite organically with known classification schemes, mutually complementing and checking each other. We suggest several important points for conducting future studies which will improve on the qualitative analysis of hydrocarbon genesis:

- Carrying out a complete analysis of the content of HCGs C1–C5, especially at the level of trace concentrations.
- Information about regional geology, geophysical knowledge, and objects analogous to the industrial development of hydrocarbons is very important.
- The use of a large number of gas genetic parameters and classifications and sufficient statistics.

The solution of these issues in the future will significantly enhance the predictive assessment of oil and gas prospects and our fundamental knowledge about the processes of migration and accumulation of natural gases in the sedimentary cover of the Earth

6 CONCLUSION

As a result of the studies, the distribution of hydrocarbon gases was established, which are of great practical importance in the search and forecast of hydrocarbon deposits of the ESS marginal-shelf zone, the continental slope, and geological structures of the Arctic Ocean.

In the process of research in the bottom sediments, eight main genetic groups of epigenetic HCGs were identified, originating from supposed underlying gas sources in the process of natural diffusion and migration. Relatively low TC values determine the formation of insignificant volumes of syngenetic gases of modern sediments, which are difficult to identify due to their mixing with the migration gases of underlying geological formations. In general, the formation of the bottom sediment gas composition of the marginal-shelf zone of the ESS and AO is subject to the rules of additivity, that is, sequential spatiotemporal accumulation of migration gases in sediments with the

dominance of the gas phase and gas-geochemical parameters of a more gas-saturated source.

Based on the data of gas geochemical studies, the areas of the southeastern part of the Cis-East Siberian sedimentary basin (Vilkitsky depression), Lomonosov–Mendeleev structural tectonic zone, and northwestern part of the Novosibirsk basin are among the most highly promising oil-bearing forecast areas in the western sector of the study area. Similar territories in the eastern part of the study area include the southern flank and the central part of the North Chukchi basin.

The study of these inaccessible areas of the Arctic Ocean is important not only from the standpoint of resource hydrocarbon potential but also important from the point of view of climate change and the study of natural sources of greenhouse gases into the environment.

DATA AVAILABILITY STATEMENT

The raw data supporting the conclusion of this article will be made available by the authors, without undue reservation.

AUTHOR CONTRIBUTIONS

AG provided funding to conduct the research. AY, AG, and GS have contributed to the design of the study. AG analyzed the geological structure of the region. AG and AY participated in sea cruises and collected sediment samples. AY performed geochemical processing and gas analysis. GS performed isotope data processing and visualization of the genetic characteristics of HCGs. AY, AG, and GS contributed to the interpretation of the results. AY majorly contributed to writing the manuscript. All authors helped shape the research, analysis, and manuscript.

FUNDING

Gas-geochemical studies were carried out with the financial support of the State Assignment No. 0211-2021-0006 (121021500055-0). Marine expeditionary operations (cruises LV77 and LV90) were carried out with the financial support of the Ministry of Education and Science of the Russian Federation, the National Natural Science Foundation of the Republic of China NSFC-Shandong (Grant Nos. U1606401 and 41420104005), and grant from the Marine S&T Fund of Shandong Province (No. 2018SDKJ0104-3).

ACKNOWLEDGMENTS

We are grateful to the management of "Sevmorgeo" and POI FEB RAS. We greatly appreciate the head of cruises Renat Shakirov (LV45), Anatoly Astakhov (LV77), and Yuri Vasilenko (LV90) for their support in marine gas-geochemical studies. We are grateful to Viktor Kalinchuk (POI FEB RAS) for help with sediment sampling and Elena Maltseva and Dmitry Shvalov for gas analytic support. We are also very grateful to the editor and three reviewers for their constructive comments and help in improving this work.

REFERENCES

Abrams, M. A. (2005). Significance of Hydrocarbon Seepage Relative to Petroleum Generation and Entrapment. *Mar. Petroleum Geol.* 22, 457–477. doi:10.1016/j.marpetgeo.2004.08.003

Abrams, M. (2017). Evaluation of Near-Surface Gases in Marine Sediments to Assess Subsurface Petroleum Gas Generation and Entrapment. *Geosciences* 7 (2), 35. doi:10.3390/geosciences7020035

Baranov, B., Galkin, S., Vedenin, A., Dozorova, K., Gebruk, A., and Flint, M. (2020). Methane Seeps on the Outer Shelf of the Laptev Sea: Characteristic Features, Structural Control, and Benthic Fauna. *Geo-Mar Lett.* 40, 541–557. doi:10.1007/s00367-020-00655-7

Bernard, B. B., Brooks, J. M., and Sackett, W. M. (1976). Natural Gas Seepage in the Gulf of Mexico. *Earth Planet. Sci. Lett.* 31 (1), 48–54. doi:10.1016/0012-821X(76)90095-9

Berner, U., and Faber, E. (1996). Empirical Carbon Isotope/maturity Relationships for Gases from Algal Kerogens and Terrigenous Organic Matter, Based on Dry, Open-System Pyrolysis. *Org. Geochem.* 24 (10-11), 947–955. doi:10.1016/s0146-6380(96)00090-3

Bird, K. J., and Houseknecht, D. W. (2011). Chapter 32 Geology and Petroleum Potential of the Arctic Alaska Petroleum Province. *Geol. Soc. Lond. Memoirs* 35 (1), 485–499. doi:10.1144/m35.32

Blumenberg, M., Lutz, R., Schlömer, S., Krüger, M., Scheeder, G., Berglar, K., et al. (2016). Hydrocarbons from Near-Surface Sediments of the Barents Sea North of Svalbard - Indication of Subsurface Hydrocarbon Generation? *Mar. Petroleum Geol.* 76, 432–443. doi:10.1016/j.marpetgeo.2016.05.031

Borukaev, G. C. (2017). Organic Geochemistry of Paleosoic-Triassic Sediments of Wrangel Island. *Oil Gas Geol.* 4, 79–89. https://cyberleninka.ru/article/n/organicheskaya-geohimiya-paleozoy-triasovyh-otlozheniy-ostrova-vrangelya/pdf (in Russian).

Claypool, G. E., and Kaplan, I. R. (1974). "The Origin and Distribution of Methane in Marine Sediments," in *Natural Gases in Marine Sediments*. Editor I. R. Kaplan (Boston: Springer), 3, 99–139. Marine science. doi:10.1007/978-1-4684-2757-8_8

Claypool, G. E., and Kvenvolden, K. A. (1983). Methane and Other Hydrocarbon Gases in Marine Sediment. *Annu. Rev. Earth Planet. Sci.* 11, 299–327. doi:10.1146/annurev.ea.11.050183.001503

Cramer, B., and Franke, D. (2005). Indications for an Active Petroleum System in the Laptev Sea, NE Siberia. *J. Pet. Geol.* 28, 369–384. doi:10.1111/J.1747-5457.2005.TB00088.X

Etiope, G., Ciotoli, G., Schwietzke, S., and Schoell, M. (2019). Gridded Maps of Geological Methane Emissions and Their Isotopic Signature. *Earth Syst. Sci. Data* 11, 1–22. doi:10.5194/essd-11-1-2019

Etiope, G., Feyzullayev, A., Milkov, A. V., Waseda, A., Mizobe, K., and Sun, C. H. (2009). Evidence of Subsurface Anaerobic Biodegradation of Hydrocarbons and Potential Secondary Methanogenesis in Terrestrial Mud Volcanoes. *Mar. Petroleum Geol.* 26 (9), 1692–1703. doi:10.1016/j.marpetgeo.2008.12.002

Etiope, G., and Sherwood Lollar, B. (2013). Abiotic Methane on Earth. *Rev. Geophys.* 51, 276–299. doi:10.1002/rog.20011

Faber, E., Schmidt, M., and Feyzullayev, A. A. (2015). Geochemical Hydrocarbon Exploration - Insight from Stable Isotope Models. *Oil Gas. J.* 41, 93–98. https://www.researchgate.net/publication/282273227_Geochemical_Hydrocarbon_Exploration_-_Insights_from_Stable_Isotope_Models.

Franke, D., and Hinz, K. (2012). "Geology of the Shelves Surrounding the New Siberian Islands from Seismic Images," in *Regional Geology and Tectonics: Phanerozoic Rift Systems and Sedimentary Basins* (Oxford, UK: Elsevier), 37, 279–297. doi:10.1016/b978-0-444-56356-9.00011-0

Galimov, E. M. (2006). Isotope Organic Geochemistry. *Org. Geochem.* 37 (10), 1200–1262. doi:10.1016/j.orggeochem.2006.04.009

Geological Map of Russian Federation and Adjacent Waters (2016). *Geological Map of Russia and Adjacent Water Areas 1:2 500 000*. St. Petersburg: A. P. Karpinsky Russian Geological Research Institute. http://www.vsegei.com/ru/info/atlas/geol/(in Russian).

Geological Map (2015). *Ser. Laptevo-Sibiromorskaya, Okeanskaya. Sheet No. T-57-60 – Henrietta Island. 1:1 000 000. Explanatory Note*. St. Petersburg, A. P.: Karpinsky Russian Geological Research Institute. https://webftp.vsegei.ru/GGK1000/T-57-60/T-57-60_ObZap.pdf (in Russian).

Giggenbach, W. F. (1997). Relative Importance of Thermodynamic and Kinetic Processes in Governing the Chemical and Isotopic Composition of Carbon Gases in High-Heatflow Sedimentary Basins. *Geochimica Cosmochimica Acta* 61 (17), 3763–3785. doi:10.1016/s0016-7037(97)00171-3

Graves, C. A., James, R. H., Sapart, C. J., Stott, A. W., Wright, I. C., Berndt, C., et al. (2017). Methane in Shallow Subsurface Sediments at the Landward Limit of the Gas Hydrate Stability Zone Offshore Western Svalbard. *Geochimica Cosmochimica Acta* 198, 419–438. doi:10.1016/j.gca.2016.11.015

Gresov, A. I. (2011). Geochemical Classification of Hydrocarbon Gases of the Coal Basins of East Russia. *Russ. J. Pac. Geol.* 5 (2), 164–179. doi:10.1134/s1819714011020047

Gresov, A. I., Obzhirov, A. I., Yatsuk, A. V., Mazurov, A. K., and Ruban, A. S. (2017). Gas Content of Bottom Sediments and Geochemical Indicators of Oil and Gas on the Shelf of the East Siberian Sea. *Russ. J. Pac. Geol.* 11, 308–314. doi:10.1134/S1819714017040030

Gresov, A. I., Shakhova, N. E., Sergiyenko, V. I., Yatsuk, A. V., and Semiletov, I. P. (2016). Isotope and Geochemical Parameters of Hydrocarbon Gases in Bottom Sediments of the Shelf of the East Siberian Sea. *Dokl. Earth Sc.* 469 (2), 864–866. doi:10.1134/S1028334X16080225

Gresov, A. I., and Yatsuk, A. V. (2020a). Gas Geochemical Indicators of Oil and Gas Occurrence in South-Eastern Part of East Siberian Sea. *Geol. Oil Gas* 4, 83–96. doi:10.31087/0016-7894-2020-4-83-96

Gresov, A. I., and Yatsuk, A. V. (2020b). Geochemistry and Genesis of Hydrocarbon Gases of the Chaun Depression and Ayon Sedimentary Basin of the East Siberian Sea. *Russ. J. Pac. Geol.* 14, 87–96. doi:10.1134/S1819714020010042

Gresov, A. I., and Yatsuk, A. V. (2021). Geological Implications for Gas Saturation of Bottom Sediments in Sedimentary Basins in the Southeastern Sector of the East Siberian Sea. *Russ. Geol. Geophys.* 62 (2), 157–172. doi:10.2113/RGG20194075

Gresov, A. I., Yatsuk, A. V., Obzhirov, A. I., Razvozzhaeva, E. P., and Kirillova, G. L. (2012). Gas-geochemical Evaluation of the the Petroleum Potential of the Birofeld Graben of the Middle Amur Sedimentary Basin (Russian Far East). *Russ. J. Pac. Geol.* 6 (2), 143–157. doi:10.1134/s1819714012020030

Head, I. M., Jones, D. M., and Larter, S. R. (2003). Biological Activity in the Deep Subsurface and the Origin of Heavy Oil. *Nature* 426, 344–352. doi:10.1038/nature02134

Horita, J. (2001). Carbon Isotope Exchange in the System CO2-CH4 at Elevated Temperatures. *Geochimica Cosmochimica Acta* 65, 1907–1919. –1919. doi:10.1016/S0016-7037(01)00570-1

Horvitz, L. (1985). Geochemical Exploration for Petroleum. *Science* 229, 821–827. doi:10.1126/science.229.4716.821

Houseknecht, D. W., Bird, K. J., and Garrity, C. (2019). Geology and Assessment of Undiscovered Oil and Gas Resources of the Arctic Alaska Province, 2008, T. E. E of Moore and D. L. Gautier, eds., *The 2008 Circum-Arctic Resource Appraisal*: Reston, VA: U.S. Geological Survey, 25. doi:10.3133/pp1824EProfessional Paper 1824 [Supersedes USGS Scientific Investigations Report 2012–5147]

Hulston, J. R. (2004). Factors Controlling the Carbon Isotopic Composition of Methane and Carbon Dioxide in New Zealand Geothermal and Natural Gases. *Geochem. Soc. Spec. Publ.* 9, 67–83. A Tribute to Isaac R. Kaplan. doi:10.1016/S1873-9881(04)80008-7

Hunt, J. M., Philp, R. P., and Kvenvolden, K. A. (2002). Early Developments in Petroleum Geochemistry. *Org. Geochem.* 33 (9), 1025–1052. doi:10.1016/s0146-6380(02)00056-6

IGD'Skochinsky (1977). *Instructions for Determining and Predicting the Gas Content of Coal Seams and Enclosing Rocks during Exploration*. Moscow: Nedra. https://pdf.standartgost.ru/catalog/Data2/1/4293730/4293730660.pdf.

Jakobsson, M., Mayer, L., Coakley, B., Dowdeswell, J. A., Forbes, S., Fridman, B., et al. (2012). The International Bathymetric Chart of the Arctic Ocean (IBCAO) Version 3.0. *Geophys. Res. Lett.* 39, L12609. doi:10.1029/2012gl052219

Kazanin, G. S., Barabanova, Y. B., Kirillova-Pokrovskaya, T. A., Chernikov, S. F., Pavlov, S. P., and Ivanov, G. I. (2017a). Continental Margin of the East Siberia Sea: Geological Structure and Hydrocarbon Potential. *Razved. Okhrana Nedr* 10, 51–55. http://rion-journal.com/2017/11/02/10-2017/(in Russian).

Kazanin, G. S., Poselov, V. A., Zayats, I. V., Ivanov, G. I., Makarov, E. S., Vasil'ev, A. S., et al. (2017b). Complex Geophysical Studies of the Central Deep-Water Part of the Arctic Ocean. *Razved. Okhrana Nedr* 10, P25–30. http://rion-journal.com/2017/11/02/10-2017/(in Russian).

Kazanin, G. S., Verba, M. L., Ivanov, G. I., Kirillova-Pokrovskaya, T. A., and Smirnov, O. E. (2017c). Tectonic Map of the East Siberian Sea: the Role of the Paleozoic Complex of the Sedimentary Cover (According to Seismic Data from MAGE). *Razved. Okhrana Nedr* 10, 61–67. http://rion-journal.com/2017/11/02/10-2017/(in Russian).

Khain, V. E., Polyakova, I. D., and Filatova, N. I. (2009). Tectonics and Petroleum Potential of the East Arctic Province. *Russ. Geol. Geophys.* 50 (4), 334–345. doi:10.1016/j.rgg.2009.03.006

Kim, B. I., Evdokimova, N. K., and Kharitonova, L. I. (2016). Structure, Oil and Gas Potential, Oil-Geological Zonation of Russian West-Arctic Shelf. *Oil Gas Geol.* 1, 2–15. https://www.oilandgasgeology.ru/_files/ugd/19d8ab_8f8b1279dee840f8a4659c1aba4b5d9f.pdf (in Russian).

Kim, B. I., Evdokimova, N. K., Suprunenko, O. I., and Yashin, D. S. (2007). Oil Geological Zoning of Offshore Areas of the East-Arctic Seas of Russia and Their Oil and Gas Potential Prospects. *Oil Gas Geol.* 2, 49–59. https://drive.google.com/open?id=0B_bCwpRhYduYdlpRMldIRERtWlE (in Russian).

Kim, J.-H., Hachikubo, A., Kida, M., Minami, H., Lee, D.-H., Jin, Y. K., et al. (2020). Upwarding Gas Source and Postgenetic Processes in the Shallow Sediments from the ARAON Mounds, Chukchi Sea. *J. Nat. Gas Sci. Eng.* 76, 103223. doi:10.1016/j.jngse.2020.103223

Klubov, B. A. (1983). *Natural Bitumens of the North. Prirodnyye Bitumy Severa*. Moscow Nedra. https://www.osti.gov/etdeweb/biblio/5289125 (in Russian).

Knies, J., Damm, E., Gutt, J., Mann, U., and Pinturier, L. (2004). Near-surface Hydrocarbon Anomalies in Shelf Sediments off Spitsbergen: Evidences for Past Seepages. *Geochem. Geophys. Geosyst.* 5 (6). doi:10.1029/2003gc000687

Kus, J., Tolmacheva, T., Dolezych, M., Gaedicke, C., Franke, D., Brandes, C., et al. (2015). Organic Matter Type, Origin and Thermal Maturity of Paleozoic, Mesozoic and Cenozoic Successions of the New Siberian Islands, Eastern Russian Arctic. *Int. J. Coal Geol.* 152, 125–146. doi:10.1016/j.coal.2015.11.003

Lorenson, T. D., Collett, T. S., and Hunter, R. B. (2011). Gas Geochemistry of the Mount Elbert Gas Hydrate Stratigraphic Test Well, Alaska North Slope: Implications for Gas Hydrate Exploration in the Arctic. *Mar. Petroleum Geol.* 28, 343–360. doi:10.1016/j.marpetgeo.2010.02.007

Lorenson, T. D., Grienert, J., and Coffin, R. B. (2016). Dissolved Methane in the Beaufort Sea and the Arctic Ocean, 1992-2009; Sources and Atmospheric Flux. *Limnol. Oceanogr.* 61, S300–S323. doi:10.1002/lno.10457

Martens, J., Romankevich, E., Semiletov, I., Wild, B., van Dongen, B., Vonk, J., et al. (2021). CASCADE - the Circum-Arctic Sediment CArbon DatabasE. *Earth Syst. Sci. Data* 13, 2561–2572. doi:10.5194/essd-13-2561-2021

Martin Schoell, M. (1983). Genetic Characterization of Natural Gases. *Bulletin* 67, 2225–2238. doi:10.1306/ad46094a-16f7-11d7-8645000102c1865d

Matveeva, T., Savvichev, A., Semenova, A., Logvina, E., Kolesnik, A., and Bosin, A. (2015). Source, Origin, and Spatial Distribution of Shallow Sediment Methane in the Chukchi Sea. *Oceanography* 28, 202–217. doi:10.5670/oceanog.2015.66

Mau, S., Römer, M., Torres, M. E., Bussmann, I., Pape, T., Damm, E., et al. (2017). Widespread Methane Seepage along the Continental Margin off Svalbard - from Bjørnøya to Kongsfjorden. *Sci. Rep.* 7, 42997. doi:10.1038/srep42997

Milkov, A. V., Claypool, G. E., Lee, Y.-J., and Sassen, R. (2005). Gas Hydrate Systems at Hydrate Ridge Offshore Oregon Inferred from Molecular and Isotopic Properties of Hydrate-Bound and Void Gases. *Geochimica Cosmochimica Acta* 69, 1007–1026. doi:10.1016/j.gca.2004.08.021

Milkov, A. V., and Etiope, G. (2018). Revised Genetic Diagrams for Natural Gases Based on a Global Dataset of >20,000 Samples. *Org. Geochem.* 125, 109–120. doi:10.1016/j.orggeochem.2018.09.002

Milkov, A. V. (2021). New Approaches to Distinguish Shale-Sourced and Coal-Sourced Gases in Petroleum Systems. *Org. Geochem.* 158, 104271. doi:10.1016/j.orggeochem.2021.104271

Milkov, A. V. (2011). Worldwide Distribution and Significance of Secondary Microbial Methane Formed during Petroleum Biodegradation in Conventional Reservoirs. *Org. Geochem.* 42 (2), 184–207. doi:10.1016/j.orggeochem.2010.12.003

Miller, C. M., Dickens, G. R., Jakobsson, M., Johansson, C., Koshurnikov, A., O'Regan, M., et al. (2017). Pore Water Geochemistry along Continental Slopes North of the East Siberian Sea: Inference of Low Methane Concentrations. *Biogeosciences* 14 (12), 2929–2953. doi:10.5194/bg-14-2929-2017

Nikishin, A. M., Petrov, E. I., Cloetingh, S., Malyshev, N. A., Morozov, A. F., Posamentier, H. W., et al. (2021). Arctic Ocean Mega Project: Paper 2 - Arctic Stratigraphy and Regional Tectonic Structure. *Earth-Science Rev.* 217, 103581. doi:10.1016/j.earscirev.2021.103581

O'Regan, M., Backman, J., Barrientos, N., Cronin, T. M., Gemery, L., Kirchner, N., et al. (2017). The De Long Trough: a Newly Discovered Glacial Trough on the East Siberian Continental Margin. *Clim. Past.* 13, 1269–1284. doi:10.5194/cp-13-1269-2017

O'Regan, M., Preto, P., Stranne, C., Jakobsson, M., and Koshurnikov, A. (2016). Surface Heat Flow Measurements from the East Siberian Continental Slope and Southern Lomonosov Ridge, Arctic Ocean. *Geochem. Geophys. Geosyst.* 17, 1608–1622. doi:10.1002/2016GC006284

Pape, T., Bünz, S., Hong, W. L., Torres, M. E., Riedel, M., Panieri, G., et al. (2020). Origin and Transformation of Light Hydrocarbons Ascending at an Active Pockmark on Vestnesa Ridge, Arctic Ocean. *J. Geophys. Res. Solid Earth* 125. doi:10.1029/2018JB016679

Pohlman, J. W., Greinert, J., Ruppel, C., Silyakova, A., Vielstädte, L., Casso, M., et al. (2017). Enhanced CO 2 Uptake at a Shallow Arctic Ocean Seep Field Overwhelms the Positive Warming Potential of Emitted Methane. *Proc. Natl. Acad. Sci. U.S.A.* 114, 5355–5360. doi:10.1073/pnas.1618926114

Portnov, A., Smith, A. J., Mienert, J., Cherkashov, G., Rekant, P., Semenov, P., et al. (2013). Offshore Permafrost Decay and Massive Seabed Methane Escape in Water Depths >20 M at the South Kara Sea Shelf. *Geophys. Res. Lett.* 40 (15), 3962–3967. doi:10.1002/grl.50735

Poselov, V. A., Butsenko, V. V., Zholondz, S. M., Zholondz, A. S., and Kireev, A. A. (2017). Seismic Stratigraphy of Sedimentary Cover in the Podvodnikov Basin and North Chukchi Trough. *Dokl. Earth Sc.* 474 (2), 688–691. doi:10.1134/S1028334X17060137

Sakulina, T. S., Verba, M. L., Kashubina, T. V., Krupnova, N. A., Tabyrtsa, S. N., and Ivanov, G. I. (2011). Complex Geological and Geophysical Researches on the 5-AR Profile in the East-Siberian Sea. *Razved. Okhrana Nedr* 10, 17–23. http://docplayer.com/38712759-Kompleksnye-geologo-geofizicheskie-issledovaniya-na-opor-nom-profile-5-ar-v-vostochno-sibirskom-more.html (in Russian).

Sapart, C. J., Shakhova, N., Semiletov, I., Jansen, J., Szidat, S., Kosmach, D., et al. (2017). The Origin of Methane in the East Siberian Arctic Shelf Unraveled with Triple Isotope Analysis. *Biogeosciences* 14, 2283–2292. doi:10.5194/bg-14-2283-2017

Saunois, M., Stavert, A. R., Poulter, B., Bousquet, P., Canadell, J. G., Jackson, R. B., et al. (2020). The Global Methane Budget 2000-2017. *Earth Syst. Sci. Data* 12, 1561–1623. doi:10.5194/essd-12-1561-2020

Schoell, M. (1988). Multiple Origins of Methane in the Earth. *Chem. Geol.* 71, 1–10. doi:10.1016/0009-2541(88)90101-5

Serov, P., Portnov, A., Mienert, J., Semenov, P., and Ilatovskaya, P. (2015). Methane Release from Pingo-like Features across the South Kara Sea Shelf, an Area of Thawing Offshore Permafrost. *J. Geophys. Res. Earth Surf.* 120, 1515–1529. doi:10.1002/2015JF003467

Sevastyanov, V. S., Fedulov, V. S., Fedulova, V. Y., Kuznetsova, O. V., Dushenko, N. V., Naimushin, S. G., et al. (2019). Isotopic and Geochemical Study of Organic Matter in Marine Sediments from the Indigirka Delta to the Ice Shelf Border of the East-Siberian Sea. *Geochem. Int.* 57 (5), 489–498. doi:10.1134/S0016702919050100

Shakhova, N., Semiletov, I., Gustafsson, O., Sergienko, V., Lobkovsky, L., Dudarev, O., et al. (2017). Current Rates and Mechanisms of Subsea Permafrost Degradation in the East Siberian Arctic Shelf. *Nat. Commun.* 8, 15872. doi:10.1038/ncomms15872

Shakhova, N., Semiletov, I., Salyuk, A., Yusupov, V., Kosmach, D., and Gustafsson, Ö. (2010). Extensive Methane Venting to the Atmosphere from Sediments of the East Siberian Arctic Shelf. *Science* 327 (5970), 1246–1250. doi:10.1126/science.1182221

Shakirov, R. B., Sorochinskaya, A. V., and Obzhirov, A. I. (2013). Gas Geochemical Anomalies in Sediments of the East Siberian Sea. *KRAUNZ. Earth Sci.* 21 (1), 231–243. http://www.kscnet.ru/journal/kraesc/article/viewFile/350/pdf (in Russian).

Sherwood, K. W. (1998). "Undiscovered Oil and Gas Resources," in *Alaska Federal Offshore*. Editors K. W. Sherwood, J. D. Craig, and L. W. Cook (Department of the Interior Minerals Management Service), 531. As of January 1995Alaska OCS Monograph, MMS 980054. Anchorage, AK.

Sherwood, O. A., Schwietzke, S., Arling, V. A., and Etiope, G. (2017). Global Inventory of Gas Geochemistry Data from Fossil Fuel, Microbial and Burning Sources, Version 2017. *Earth Syst. Sci. Data* 9, 639–656. doi:10.5194/essd-9-639-2017

Sparrow, K. J., Kessler, J. D., Southon, J. R., Garcia-Tigreros, F., Schreiner, K. M., Ruppel, C. D., et al. (2018). Limited Contribution of Ancient Methane to Surface Waters of the U.S. Beaufort Sea Shelf. *Sci. Adv.* 4 (1), eaao4842. doi:10.1126/sciadv.aao4842

Steinbach, J., Holmstrand, H., Shcherbakova, K., Kosmach, D., Brüchert, V., Shakhova, N., et al. (2021). Source Apportionment of Methane Escaping the Subsea Permafrost System in the Outer Eurasian Arctic Shelf. *Proc. Natl. Acad. Sci. U.S.A.* 118 (10), e2019672118. doi:10.1073/pnas.2019672118

Stolper, D. A., Lawson, M., Davis, C. L., Ferreira, A. A., NetoSantos, E. V. S., Ellis, G. S., et al. (2014). Formation Temperatures of Thermogenic and Biogenic Methane. *Science* 344, 1500–1503. doi:10.1126/science.1254509

Thornton, B. F., Geibel, M. C., Crill, P. M., Humborg, C., and Mörth, C.-M. (2016). Methane Fluxes from the Sea to the Atmosphere across the Siberian Shelf Seas. *Geophys. Res. Lett.* 43 (11), 5869–5877. doi:10.1002/2016GL068977

Thornton, B. F., Prytherch, J., Andersson, K., Brooks, I. M., Salisbury, D., Tjernström, M., et al. (2020). Shipborne Eddy Covariance Observations of Methane Fluxes Constrain Arctic Sea Emissions. *Sci. Adv.* 6, eaay7934. doi:10.1126/sciadv.aay7934

Velev, V. K. (1981). Molecular Mass of Hydrocarbon Fraction and Weight Distribution of C_1–C_5 Components in Natural Gases of Different Genetic Types. *Precambrian Org. Geochem. Oils, Gases Org. Matter*, 22–28. Moscow: Nauka (in Russian).

Velev, V. K. (1974). Molecular Weight of the Hydrocarbon Fraction of Natural Gas Systems as a Classification Feature and as an Indicator in the Search for Oil and Gas. *Rep. Bulg. Acad. Sci.* 27 (3), 379–382. (in Russian).

Velivetskaya, T. A., Ignatev, A., and Kiyashko, S. (2015). "Universal Method for Preparation of Liquid, Solid and Gaseous Samples for Determining the Isotopic Composition of Carbon," in *Isotope Ratio Mass Spectrometry of Light Gas-Forming Elements*. Editor V. S. Sevastyanov (UK: CRC Press), 119–134.

Verba, M. L. (2016). Paleozoic Section of the Sedimentary Cover of the East Siberian Sea's Northern Outskirts and its Importance to Petroleum Potential Assessment. *Neftegazov. Geol. Teor. I Prakt.* 11 (4), 17. doi:10.17353/2070-5379/46_2016

VNIIGRIugol (1988). *A Manual for Determining the Gas Content of the Host Rocks of Coal Deposits during Geological Exploration*. Moscow: Nedra. https://pdf.standartgost.ru/catalog/Data2/1/4293741/4293741104.pdf (in Russian).

Wen, H.-Y., Sano, Y., Takahata, N., Tomonaga, Y., Ishida, A., Tanaka, K., et al. (2016). Helium and Methane Sources and Fluxes of Shallow Submarine Hydrothermal Plumes Near the Tokara Islands, Southern Japan. *Sci. Rep.* 6, 34126. doi:10.1038/srep34126

Weniger, P., Blumenberg, M., Berglar, K., Ehrhardt, A., Klitzke, P., Krüger, M., et al. (2019). Origin of Near-Surface Hydrocarbon Gases Bound in Northern Barents Sea Sediments. *Mar. Petroleum Geol.* 102, 455–476. doi:10.1016/j.marpetgeo.2018.12.036

Westbrook, G. K., Thatcher, K. E., Rohling, E. J., Piotrowski, A. M., Pälike, H., Osborne, A. H., et al. (2009). Escape of Methane Gas from the Seabed along the West Spitsbergen Continental Margin. *Geophys. Res. Lett.* 36, 1–5. doi:10.1029/2009gl039191

Whiticar, M. J. (1999). Carbon and Hydrogen Isotope Systematics of Bacterial Formation and Oxidation of Methane. *Chem. Geol.* 161, 291–314. doi:10.1016/s0009-2541(99)00092-3

Whiticar, M. J., Faber, E., and Schoell, M. (1986). Biogenic Methane Formation in Marine and Freshwater Environments: CO2 Reduction vs. Acetate Fermentation-Isotope Evidence. *Geochimica Cosmochimica Acta* 50, 693–709. doi:10.1016/0016-7037(86)90346-7

Whiticar, M. J. (1996). Stable Isotope Geochemistry of Coals, Humic Kerogens and Related Natural Gases. *Int. J. Coal Geol.* 32, 191–215. doi:10.1016/S0166-5162(96)00042-0

Conflict of Interest: The authors declare that the research was conducted in the absence of any commercial or financial relationships that could be construed as a potential conflict of interest.

Publisher's Note: All claims expressed in this article are solely those of the authors and do not necessarily represent those of their affiliated organizations, or those of the publisher, the editors, and the reviewers. Any product that may be evaluated in this article, or claim that may be made by its manufacturer, is not guaranteed or endorsed by the publisher.

frontiers | Frontiers in Earth Science

ORIGINAL RESEARCH
published: 01 June 2022
doi: 10.3389/feart.2022.850652

Ebullition Regulated by Pressure Variations in a Boreal Pit Lake

Kai Zhao, Edmund W. Tedford and Gregory A. Lawrence*

Department of Civil Engineering, University of British Columbia, Vancouver, BC, Canada

Methane ebullition from lakes is an important contributor to atmospheric greenhouse gases. However, ebullition is typically sampled at intervals greater than the duration of ebullition events, limiting our understanding of the factors controlling this flux. Here, we present high-frequency ebullition data from a single site in a boreal pit lake during the open-water season between June 24 and 21 October 2018. We record ebullition every 30 min for the first 2 months, and then every minute for the next 2 months. During the 4-month period, 24 ebullition events were recorded. These events generally lasted 2–4 days in response to low atmospheric pressure systems. The peaks in ebullition corresponded to troughs in atmospheric pressure. We provide empirical equations that incorporate a pressure threshold to model the time-series of ebullition events. Minor and gradual variations in mud temperature had no apparent effect on the observed ebullition events.

Keywords: methane ebullition, atmospheric pressure, temperature, timescales, high-frequency sampling, water level, lakes

OPEN ACCESS

Edited by:
Andreas Lorke,
University of Koblenz and Landau, Germany

Reviewed by:
Ingeborg Bussmann,
Alfred Wegener Institute Helmholtz Centre for Polar and Marine Research, Germany
Annika Linkhorst,
Bundesanstalt für Gewässerkunde, Germany

****Correspondence:***
Kai Zhao
zhaok1@student.ubc.ca

Specialty section:
This article was submitted to Marine Geoscience, a section of the journal Frontiers in Earth Science

Received: *08 January 2022*
Accepted: *16 May 2022*
Published: *01 June 2022*

Citation:
Zhao K, Tedford EW and Lawrence GA (2022) Ebullition Regulated by Pressure Variations in a Boreal Pit Lake. Front. Earth Sci. 10:850652. doi: 10.3389/feart.2022.850652

1 INTRODUCTION

Methane ebullition (bubbling) from lakes is an important contributor to atmospheric greenhouse gases (Bastviken et al., 2004; DelSontro et al., 2016; Rosentreter et al., 2021). However, ebullition is not often measured, adding uncertainty to estimated global lake emissions (DelSontro et al., 2018). Furthermore, given that ebullition is highly heterogenous in space and time, measurements of ebullition are not always representative (Ostrovsky, 2003). Ebullition events typically have a duration of 4 days or less (Varadharajan and Hemond, 2012; Zhao et al., 2021). However, longer sampling intervals have often been used, e.g., bi-weekly (Praetzel et al., 2021) or monthly (DelSontro et al., 2016), introducing uncertainties in the estimated ebullitive flux and our understanding of the driving factors (Varadharajan et al., 2010).

Methane ebullition from sediments is controlled by a complex sequence of processes. Biological and thermogenic processes generate methane (Etiope and Klusman, 2002). When methane concentrations exceed pore water solubility, bubbles form (Judd et al., 2002). Once these bubbles grow sufficiently large, they can migrate through the sediments by creating fracture paths, or making use of existing paths (Boudreau, 2012). Sediment temperature changes can affect methane production, solubility and bubble volume, and consequently affect ebullition (Fechner-Levy and Hemond, 1996; DelSontro et al., 2016). Ebullition can also be affected by pressure variations, which influence porewater solubility, bubble volume and bubble rise (Tokida et al., 2007; Boudreau, 2012).

In lakes, temperature variations (Wik et al., 2013; Natchimuthu et al., 2016; Praetzel et al., 2021), atmospheric pressure fluctuations (Mattson and Likens, 1990; Zhao et al., 2021), water level changes (Chanton et al., 1989; Harrison et al., 2017) or the combined effects of atmospheric pressure and water level (Varadharajan and Hemond, 2012; Delwiche and Hemond, 2017) have been shown to affect ebullition. However, the impact of these factors on ebullition varies from lake to lake. For example, Praetzel et al. (2021) studied ebullition in a small and shallow temperate lake (maximum

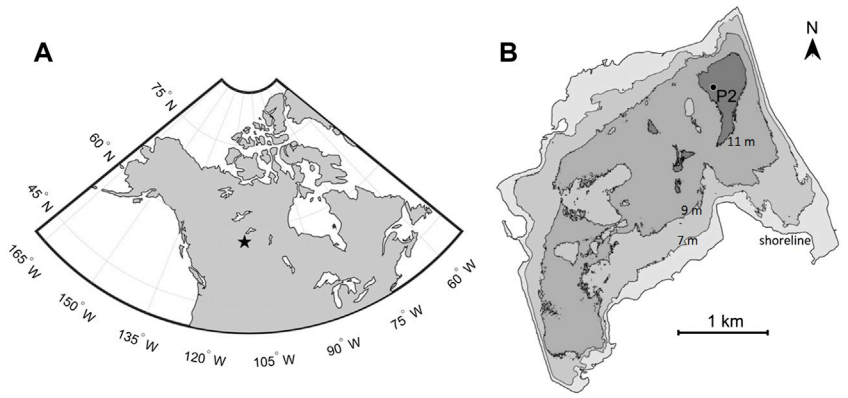

FIGURE 1 | Base Mine Lake **(A)** location, **(B)** bathymetry. Water temperature, mud temperature, and acoustic ebullition data are collected at Platform P2.

depth 1.5 m). They concluded that temporal changes in ebullition were controlled by sediment temperature, and did not find a relationship between ebullition and pressure variations. Varadharajan and Hemond (2012) investigated ebullition in a dimictic lake (mean depth 15 m) and reported that ebullition was mostly regulated by hydrostatic pressure changes.

The impacts of different environmental factors on ebullition can be different in the open-water season from the ice-cover season. During open-water, changes in water and sediment temperature, wind speed, water level, and atmospheric pressure can simultaneously affect ebullition (McClure et al., 2020), whereas during ice-cover, the impacts of temperature, water-level, and wind speed are minimal. Zhao et al. (2021) have shown that during ice cover in Base Mine Lake, a boreal pit lake in Alberta, Canada, ebullition occurred almost exclusively when atmospheric pressure dropped below a pressure threshold; and when the pressure rose above the threshold, ebullition ceased.

The focus of the present study is ebullition during the open water season in Base Mine Lake. In **Section 2**, we describe the study site and our data collection methods. In **Section 3**, we show the time series of atmospheric pressure, water level, ebullition, water and mud temperature. We also present a pressure-driven ebullition model. In **Section 4**, we discuss the effect of pressure and mud temperature on ebullition in Base Mine Lake. We give our conclusions in **Section 5**.

2 METHODS

2.1 Study Site

Base Mine Lake is located at 57°1′N, 111°37′W, in Alberta, Canada (**Figure 1**). The lake is 10 m deep on average and has a surface area of 7.8 km^2. The lake was formed by backfilling a mined-out pit with tailings, which were capped with water in 2012. The tailings have similar density, mean particle size, and clay fraction as the fine-grained sediments in natural lakes and estuaries (Dompierre and Barbour 2016). The open-water season of the lake normally starts around the beginning of May and lasts until mid-November. The lake exhibits the same seasonal stratification and mixing as natural northern lakes (Tedford et al., 2019).

The degeneration of residual hydrocarbon inside the tailings (mud) layer produces methane. Clark et al. (2021) measured a median methane flux of 10 mg m^{-2} h^{-1} between 2017 and 2019 using an eddy covariance system. Francis et al. (2022) have measured dissolved methane concentration inside the porewater that reaches 90–110% saturation 1–3 m below the mud-water interface. Bubbles have been observed to rise through the water column using echo sounding (Lawrence et al., 2016; Zhao et al., 2021). In their modelling of methane dynamics in Base Mine Lake, Slater et al. (2021) have assumed that the rising bubbles were: "composed either entirely of methane, or of 75% methane and 25% nitrogen (by volume), based on the results of the preliminary gas analyses (unpublished data)".

2.2 Data Collection

2.2.1 Ebullition Data

Ebullition was measured using a downward facing, single beam 400 kHz echosounder (Echologger EA400), which is capable of autonomously logging high-frequency acoustic data over an extended period. We deployed the echosounder three times during the open-water season between June 24 and October 21. The settings for these deployments were a burst of 100 pings over 50 s once every 30 min between June 24 and August 15, a burst of 50 pings over 25 s once every minute between August 16 and September 18 and between September 20 and 21 October 2018.

Rising bubbles emerged from pockmarks at the lakebed (**Figures 2A,B**). These rising bubbles were recorded by an echosounder, that was attached to Platform P2 and was suspended 8.5 m above the lakebed. With a 5° beam angle, the echosounder monitored an area of 0.7 m radius if it stays stationary. However, the platform can drift under the impacts of wind and waves. Therefore, the area monitored by the echosounder shifted with the movement of the platform.

A sample echogram is shown in **Figure 2C**. The diagonal lines show the backscatter intensity of rising bubbles, whereas the nearly horizontal lines are the result of unknown reflectors. The backscatter intensity is a unitless measure equivalent to the strength of the reflected signals. To estimate ebullition intensity, the nearly horizontal lines are filtered out, and then the backscatter intensity between 6.8 and 10.7 m depth is averaged over each 25-s burst. The

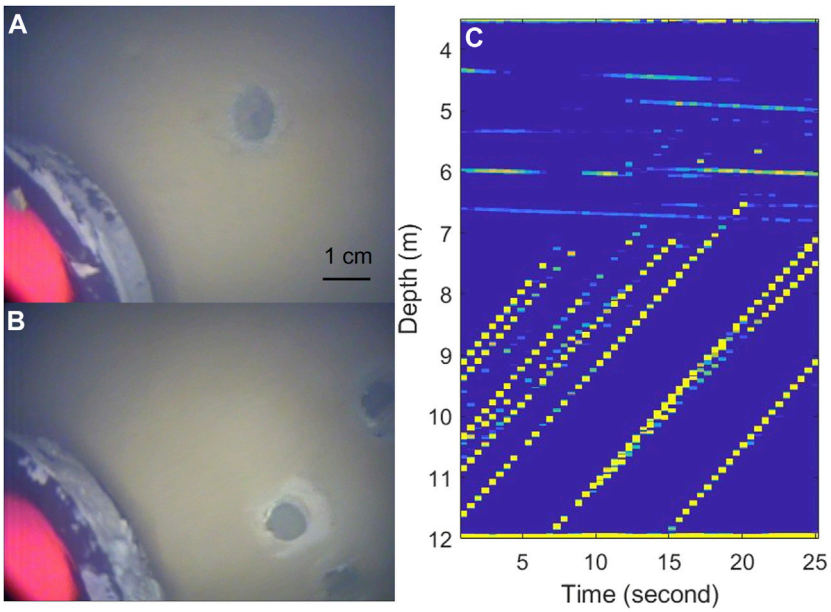

FIGURE 2 | Pockmarks and rising bubbles. **(A,B)** show two images of pockmarks in the lakebed. Bubbles emerge from these pockmarks. The red and black instrument on the left bottom corner of each image is a RBR Concerto data logger, which is partially covered by mud. **(C)** shows a sample echogram obtained by the echosounder over a 25-s burst at 13:25, 11 October 2018 (Mountain Standard Time). The diagonal lines are bubbles rising at a speed of approximately 25 cm/s.

ebullition intensity represented by **Figure 2C** is marked as a red dot in **Figure 3A**.

Compared to manually examined bubble traps or acoustic instruments that require external power, the advantage of our echosounder (Echologger EA400) is that it continuously monitors ebullition at a high frequency. Low ebullition intensity indicates low volumetric flux, and stronger ebullition intensity indicates higher volumetric flux. The single-beam echosounder provides the opportunity to directly observe ebullition at high-frequency over extended periods.

2.2.2 Other Data

To analyze the physical factors that affect ebullition, water level, atmospheric pressure, water temperature and mud temperature data were collected. The atmospheric pressure data were collected at nearby Fort McMurray Airport (47 km away). The variations in atmospheric pressure at the lake and the airport are almost identical (Zhao et al., 2021).

Water temperature and mud temperature were measured at Platform P2. Bottom-water temperature was measured at 11 m depth using an RBRsolo logger. Note, the lake was 12 m deep at Platform P2. The mud temperature was also measured at 0.5, 1, and 5 m depths beneath the lakebed by Francis et al. (2022) using 3001 L T Levelogger Edge M30 and HOBO Water Temperature Pro V2 sensors.

3 RESULTS

3.1 Field Observations

Variations in atmospheric pressure, water level, total hydrostatic pressure (atmospheric pressure plus water level) and ebullition intensity are presented in **Figures 3A–C**. Over the 4-month period, 24 ebullition events were identified. These ebullition events were caused by hydrostatic pressure variations and had a duration of 2–4 days. Of the 24 observed ebullition events, 22 peaked when hydrostatic pressure was at a local trough. The other 2 events (9 and 14) peaked while the pressure was decreasing. Even though the water level varied by 0.36 m (corresponding to 3.5 kPa) during the period of record, the rate of pressure change caused by water level fluctuations was generally much less than the rate of change in atmospheric pressure (**Figures 3A,C**). Consequently, the ebullition events were primarily caused by the passage of low atmospheric pressure systems of duration of 2–4 days.

3.2 Empirical Ebullition Model

The close correspondence between ebullition peaks and pressure troughs suggests that pressure variations are strong predictors for ebullition events. However, assuming a linear relationship between ebullition intensity and hydrostatic pressure over our 4-month study period yields a low correlation coefficient (R^2 = 0.13). Varadharajan and Hemond (2012) and Zhao et al. (2021) observed that ebullition generally occurred when pressure dropped below a threshold. Zhao et al. (2021) proposed that during ice cover ebullition could be modelled using

$$\hat{E} = \begin{cases} k * (P_{th} - P), & \text{if } P < P_{th} \\ 0, & \text{otherwise} \end{cases} \quad (1)$$

where, $\hat{E}$ is the modelled ebullition intensity; k is a proportionality constant; P_{th} is the pressure threshold; and P is the total hydrostatic pressure.

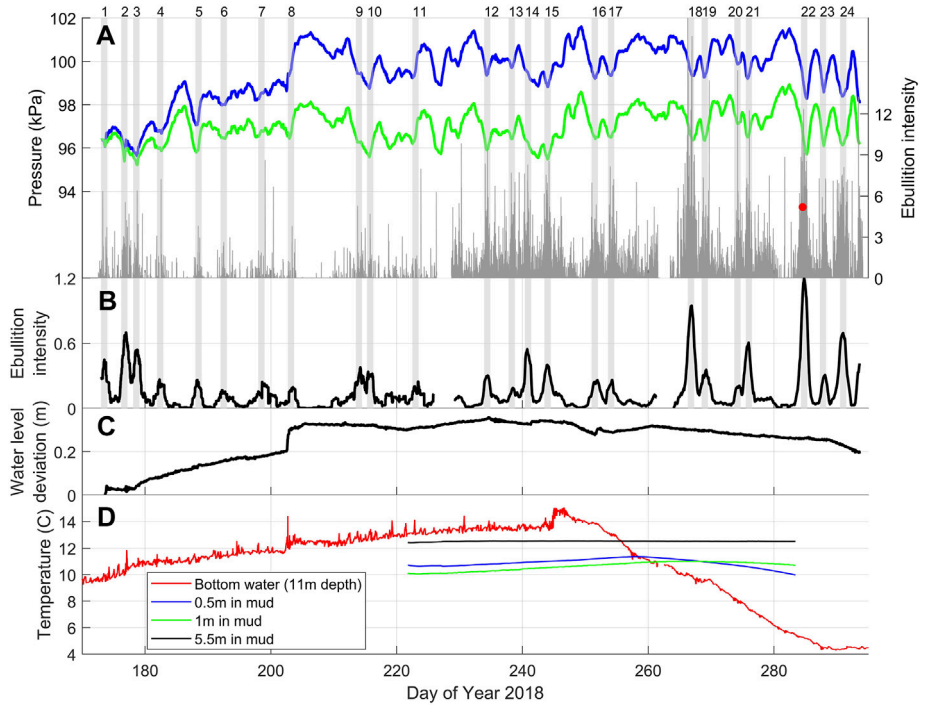

FIGURE 3 | (A) atmospheric pressure variations (green line), total pressure variations (blue line) and ebullition intensity (grey lines). The total pressure variation is the atmospheric pressure plus the pressure variation caused by water level changes. The vertical grey lines show the instantaneous ebullition intensity, obtained from each burst of echo-sounding. The red dot represents the instantaneous ebullition intensity obtained from **Figure 2C**. The width of each shaded area is 1 day. **(B)** shows the smoothed ebullition intensity, which is obtained by applying a 24-h moving average to the instantaneous ebullition intensity. **(C)** shows the water level variations, where a 0.1 m change in water level is equivalent to a 0.98 kPa pressure change. **(D)** shows the temperature measured at the 11 m depth in the water column, 0.5 m into the mud beneath lakebed, 1 m into the mud and 5.5 m into the mud. The lake is around 12 m deep at the location (Platform P2) of temperature measurements.

Applying **Equation 1** with a constant pressure threshold, Zhao et al. (2021) were able to model the magnitude and timing of major ebullition events in Base Mine Lake during ice cover. However, the history of ebullition events can affect the pressure threshold. For example, when a low-pressure event causes a significant ebullition event, the storage of methane in the mud decreases. In order to trigger the next ebullition event a lower pressure needs to be reached, i.e., the pressure threshold is reduced. On the other hand, when the pressure remains high, the storage of methane in the mud increases. Consequently, the next ebullition event is triggered at a higher pressure, i.e., the pressure threshold is increased. In the present study, this is the case between Day 204 and Day 209 after a sudden increase in water level and atmospheric pressure (**Figures 3A,C**). To model the effects of the past pressure on methane storage, we use a varying pressure threshold

$$P_{th}(t) = \frac{1}{\tau}\int_{t-\tau}^{t} P(t)dt \tag{2}$$

where τ is an empirically determined site-dependent parameter.

Despite the simplicity of the above model, the timing and magnitude of major ebullition events are well captured, as shown in **Figure 4**. The model parameters are obtained by minimizing the root mean square error (RMSE) between the observations and predictions:

$$RMSE = \sqrt{\frac{\sum_{i=1}^{N}\left(E_i - \widehat{E}_i\right)^2}{N}} \tag{3}$$

where E_i is the observed ebullition intensity and N = 2,751 is the total number of observations at hourly intervals. This yields k = 0.39 kPa^{-1} and τ = 8.5 days, and a correlation coefficient R^2 = 0.56.

Although the model performs well, it has limitations. Firstly, the amount of methane that is stored within the mud layer and released during ebullition events is likely to be affected by the *in-situ* mud characteristics. Therefore, τ and k should be site-dependent parameters. Secondly, we use the parameter τ to capture the changes in the pressure threshold, which reflects the variations in the methane storage compared to the total storage capacity. However, we cannot expect it to capture these effects with great accuracy using a single parameter.

4 DISCUSSION

4.1 Sampling Frequency and Pressure Effects on Ebullition

The close correspondence between ebullition and pressure observed during ice cover in Base Mine Lake (Zhao et al.,

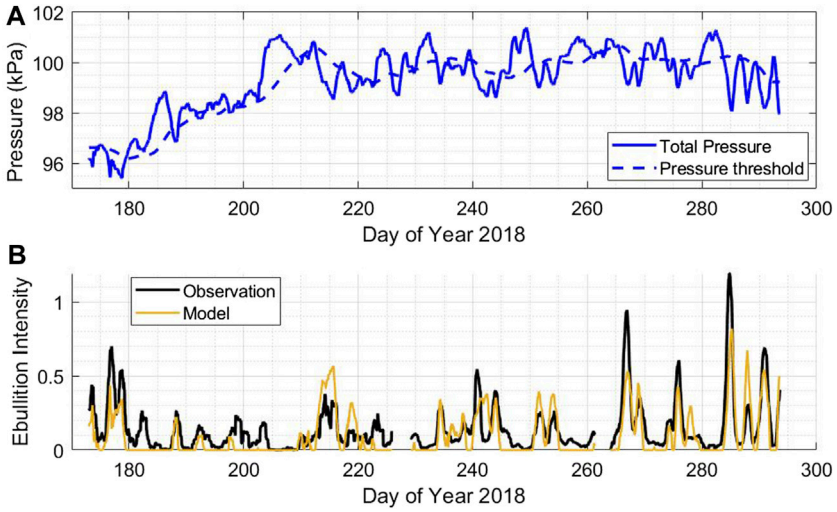

FIGURE 4 | Comparisons between model results and field observations. **(A)** shows the total pressure variations and the varying pressure threshold. **(B)** shows the comparison between model results and field observations.

2021) is also observed during the open-water season (**Figure 3**). Using a simple relationship (**Eq. 1**), where ebullition internsity is proportional to the pressure deficit below a threshold, we find that the predicted ebullition agrees well with our field observations (**Figure 4**). Our results are consistent with the observations in Upper Mystic Lake in Massachusetts by Varadharajan and Hemond (2012). In these studies, ebullition was sampled at high frequency (1–30 min samping intervals), sufficient to capture the response of ebullition to rapid atmospheric pressure variations.

However, when sampling intervals increase to weekly (Casper et al., 2000; Matthews et al., 2005), bi-weekly (Praetzel et al., 2021; Natchimuthu et al., 2016) or monthly (DelSontro et al., 2016; Descloux et al., 2017), the chances of omitting ebullition peaks increase. For example, Natchimuthu et al. (2016) who sampled ebullition once every 2 weeks state: "Importantly, although this study is extensive in its temporal coverage, compared with most previous studies, the measurements still just covered 7% of the time during the 2 yr study period. Thereby many low pressure induced flux events were likely missed . . .". Note that, if the objective of any field campaign is to better understand the response of ebullition to low atmospheric pressure events (typically 2–4 days), then ebullition needs to be sampled at least once per day.

4.2 Temperature Effects on Ebullition in Base Mine Lake

Increased sediment temperature decreases methane solubility, increases bubble volume, and enhances the methane production rate; all of which can lead to increased ebullitive flux (Fechner-Levy and Hemond, 1996). In shallow lakes, temperature variations have been shown to affect ebullition by Wik et al. (2013), Natchimuthu et al. (2016), and Praetzel et al. (2021). Praetzel et al. (2021) measured sediment temperatures between 3.5 and 23.2 C over an 18-month period in a shallow temperate lake (Lake Windsborn), and concluded that temporal variations in ebullition were strongly controlled by these sediment temperature variations.

In Base Mine Lake, during the period of our record (Day 222–283, August 10th - October 10th), the mud temperature varied by less than 1.5 C (**Figure 3D**). These fluctuations in mud temperature had no apparent effect on ebullition. The correlation coefficient (linear regression) between ebullition intensity and mud temperature is R^2 = 0.01 at 0.5 m, R^2 = 0.02 at 1 m, and R^2 = 0.00 at 5.5 m. An important difference between Base Mine Lake and Lake Windsborn is that the average depth of Base Mine Lake is 10 m (12 m deep at measurement site), whereas the maximum depth of Lake Windsborn is 1.5 m. Base Mine Lake is sufficiently deep that it is strongly thermally stratified in summer (Tedford et al., 2019) such that the bottom water temperature is nearly constant and the heat flux into the sediments is minimal. Also, in fall the water column in Base Mine Lake cools less than Lake Windsborn, as do the sediments.

5 CONCLUSION

Using continuous high-frequency acoustic data, we show the strong effects of atmospheric pressure variations on ebullition in Base Mine Lake. Over a 4-month period, 24 peaks in ebullition were observed, of which 22 peaks corresponded to local troughs in atmospheric pressure. These intense ebullition events generally

had a duration of 2–4 days, corresponding to the passage of low atmospheric pressure systems. Despite the strong correspondence between ebullition peaks and pressure troughs, a simple linear correlation does not yield high correlation coefficients ($R^2 = 0.13$) between pressure and ebullition. Incorporating the concept of a pressure threshold, we developed a two-parameter model of the time-series of ebullition events. This model yields $R^2 = 0.56$ for our 4-month dataset.

DATA AVAILABILITY STATEMENT

The raw data supporting the conclusions of this article will be made available by the authors, without undue reservation.

AUTHOR CONTRIBUTIONS

KZ analyzed the data and wrote the manuscript. ET led the field data collection. GL and ET made extensive revisions to the manuscript.

ACKNOWLEDGMENTS

The authors thank the support of a Collaborative Research and Development Grant from the Natural Sciences and Engineering Research Council of Canada [CRDPJ 484628 - 15] and Syncrude Canada Ltd. The authors also thank Daniel Francis, Lee Barbour, and Matthew Lindsay for providing the mud temperature data.

REFERENCES

Bastviken, D., Cole, J., Pace, M., and Tranvik, L. (2004). Methane Emissions from Lakes: Dependence of Lake Characteristics, Two Regional Assessments, and a Global Estimate. *Glob. Biogeochem. Cycles* 18 (4), 238. doi:10.1029/2004gb002238

Boudreau, B. P. (2012). The Physics of Bubbles in Surficial, Soft, Cohesive Sediments. *Mar. Petroleum Geol.* 38 (1), 1–18. doi:10.1016/j.marpetgeo.2012.07.002

Casper, P., Maberly, S. C., Hall, G. H., and Finlay, B. J. (2000). Fluxes of Methane and Carbon Dioxide from a Small Productive Lake to the Atmosphere. *Biogeochemistry* 49 (1), 1–19. doi:10.1023/a:1006269900174

Chanton, J. P., Martens, C. S., and Kelley, C. A. (1989). Gas Transport from Methane-Saturated, Tidal Freshwater and Wetland Sediments. *Limnol. Oceanogr.* 34 (5), 807–819. doi:10.4319/lo.1989.34.5.0807

Clark, M. G., Drewitt, G. B., and Carey, S. K. (2021). Energy and Carbon Fluxes from an Oil Sands Pit Lake. *Sci. Total Environ.* 752, 141966. doi:10.1016/j.scitotenv.2020.141966

DelSontro, T., Beaulieu, J. J., and Downing, J. A. (2018). Greenhouse Gas Emissions from Lakes and Impoundments: Upscaling in the Face of Global Change. *Limnol. Oceanogr. Lett.* 3 (3), 64–75. doi:10.1002/lol2.10073

DelSontro, T., Boutet, L., St-Pierre, A., del Giorgio, P. A., and Prairie, Y. T. (2016). Methane Ebullition and Diffusion from Northern Ponds and Lakes Regulated by the Interaction between Temperature and System Productivity. *Limnol. Oceanogr.* 61 (S1), S62–S77. doi:10.1002/lno.10335

Delwiche, K. B., and Hemond, H. F. (2017). Methane Bubble Size Distributions, Flux, and Dissolution in a Freshwater Lake. *Environ. Sci. Technol.* 51 (23), 13733–13739. doi:10.1021/acs.est.7b04243

Descloux, S., Chanudet, V., Serça, D., and Guérin, F. (2017). Methane and Nitrous Oxide Annual Emissions from an Old Eutrophic Temperate Reservoir. *Sci. Total Environ.* 598, 959–972. doi:10.1016/j.scitotenv.2017.04.066

Dompierre, K. A., and Barbour, S. L. (2016). Characterization of Physical Mass Transport through Oil Sands Fluid Fine Tailings in an End Pit Lake: a Multi-Tracer Study. *J. Contam. Hydrology* 189, 12–26. doi:10.1016/j.jconhyd.2016.03.006

Etiope, G., and Klusman, R. W. (2002). Geologic Emissions of Methane to the Atmosphere. *Chemosphere* 49 (8), 777–789. doi:10.1016/s0045-6535(02)00380-6

Fechner-Levy, E. J., and Hemond, H. F. (1996). Trapped Methane Volume and Potential Effects on Methane Ebullition in a Northern Peatland. *Limnol. Oceanogr.* 41 (7), 1375–1383. doi:10.4319/lo.1996.41.7.1375

Francis, D. J., Barbour, S. L., and Lindsay, M. B. (2022). Ebullition Enhances Chemical Mass Transport across the Tailings-Water Interface of Oil Sands Pit Lakes. *J. Contam. Hydrology* 245, 103938. doi:10.1016/j.jconhyd.2021.103938

Harrison, J. A., Deemer, B. R., Birchfield, M. K., and O'Malley, M. T. (2017). Reservoir Water-Level Drawdowns Accelerate and Amplify Methane Emission. *Environ. Sci. Technol.* 51 (3), 1267–1277. doi:10.1021/acs.est.6b03185

Judd, A. G., Hovland, M., Dimitrov, L. I., Garcia Gil, S., and Jukes, V. (2002). The Geological Methane Budget at Continental Margins and its Influence on Climate Change. *Geofluids* 2 (2), 109–126. doi:10.1046/j.1468-8123.2002.00027.x

Lawrence, G. A., Tedford, E. W., and Pieters, R. (2016). Suspended Solids in an End Pit Lake: Potential Mixing Mechanisms. *Can. J. Civ. Eng.* 43 (3), 211–217. doi:10.1139/cjce-2015-0381

Matthews, C. J. D., Joyce, E. M., Louis, V. L. S., Schiff, S. L., Venkiteswaran, J. J., Hall, B. D., et al. (2005). Carbon Dioxide and Methane Production in Small Reservoirs Flooding Upland Boreal Forest. *Ecosystems* 8 (3), 267–285. doi:10.1007/s10021-005-0005-x

Mattson, M. D., and Likens, G. E. (1990). Air Pressure and Methane Fluxes. *Nature* 347 (6295), 718–719. doi:10.1038/347718b0

McClure, R. P., Lofton, M. E., Chen, S., Krueger, K. M., Little, J. C., and Carey, C. C. (2020). The Magnitude and Drivers of Methane Ebullition and Diffusion Vary on a Longitudinal Gradient in a Small Freshwater Reservoir. *J. Geophys. Res. Biogeosciences* 125 (3), e2019JG005205. doi:10.1029/2019jg005205

Natchimuthu, S., Sundgren, I., Gålfalk, M., Klemedtsson, L., Crill, P., Danielsson, Å., et al. (2016). Spatio-temporal Variability of Lake CH4 Fluxes and its Influence on Annual Whole Lake Emission Estimates. *Limnol. Oceanogr.* 61 (S1), S13–S26. doi:10.1002/lno.10222

Ostrovsky, I. (2003). Methane Bubbles in Lake Kinneret: Quantification and Temporal and Spatial Heterogeneity. *Limnol. Oceanogr.* 48 (3), 1030–1036. doi:10.4319/lo.2003.48.3.1030

Praetzel, L. S. E., Schmiedeskamp, M., and Knorr, K. H. (2021). Temperature and Sediment Properties Drive Spatiotemporal Variability of Methane Ebullition in a Small and Shallow Temperate Lake. *Limnol. Oceanogr.* 66, 2598–2610. doi:10.1002/lno.11775

Rosentreter, J. A., Borges, A. V., Deemer, B. R., Holgerson, M. A., Liu, S., Song, C., et al. (2021). Half of Global Methane Emissions Come from Highly Variable Aquatic Ecosystem Sources. *Nat. Geosci.* 14 (4), 225–230. doi:10.1038/s41561-021-00715-2

Slater, G. F., Goad, C. A., Lindsay, M. B. J., Mumford, K. G., Colenbrander Nelson, T. E., Brady, A. L., et al. (2021). Isotopic and Chemical Assessment of the Dynamics of Methane Sources and Microbial Cycling during Early Development of an Oil Sands Pit Lake. *Microorganisms* 9 (12), 2509. doi:10.3390/microorganisms9122509

Tedford, E., Halferdahl, G., Pieters, R., and Lawrence, G. A. (2019). Temporal Variations in Turbidity in an Oil Sands Pit Lake. *Environ. Fluid Mech.* 19 (2), 457–473. doi:10.1007/s10652-018-9632-6

Tokida, T., Miyazaki, T., Mizoguchi, M., Nagata, O., Takakai, F., Kagemoto, A., et al. (2007). Falling Atmospheric Pressure as a Trigger for Methane Ebullition from Peatland. *Glob. Biogeochem. Cycles* 21 (2). doi:10.1029/2006gb002790

Varadharajan, C., and Hemond, H. F. (2012). Time-series Analysis of High-resolution Ebullition Fluxes from a Stratified, Freshwater Lake. *J. Geophys. Res. Biogeosciences* 117 (G2). doi:10.1029/2011jg001866

Varadharajan, C., Hermosillo, R., and Hemond, H. F. (2010). A Low-Cost Automated Trap to Measure Bubbling Gas Fluxes. *Limnol. Oceanogr. Methods* 8 (7), 363–375. doi:10.4319/lom.2010.8.363

Wik, M., Crill, P. M., Varner, R. K., and Bastviken, D. (2013). Multiyear Measurements of Ebullitive Methane Flux from Three Subarctic Lakes. *J. Geophys. Res. Biogeosci.* 118 (3), 1307–1321. doi:10.1002/jgrg.20103

Zhao, K., Tedford, E. W., Zare, M., and Lawrence, G. A. (2021). Impact of Atmospheric Pressure Variations on Methane Ebullition and Lake Turbidity during Ice-cover. *Limnol. Oceanogr. Lett.* 6, 253–261. doi:10.1002/lol2.10201

Conflict of Interest: The authors declare that the research was conducted in the absence of any commercial or financial relationships that could be construed as a potential conflict of interest.

frontiers | Frontiers in Earth Science

ORIGINAL RESEARCH
published: 08 June 2022
doi: 10.3389/feart.2022.877641

Gas Bubble Dynamics During Methane Hydrate Formation and its Influence on Geophysical Properties of Sediment Using High-Resolution Synchrotron Imaging and Rock Physics Modeling

B. N. Madhusudhan[1†], *S. K. Sahoo*[2*†], *F. Alvarez-Borges*[1,3†], *S. Ahmed*[3], *L. J. North*[2] and *A. I. Best*[2]

[1]Faculty of Engineering and Physical Sciences, University of Southampton, Southampton, United Kingdom, [2]National Oceanography Centre, Southampton, United Kingdom, [3]Diamond Light Source, Didcot, United Kingdom

OPEN ACCESS

Edited by:
Beatriz Quintal,
University of Lausanne, Switzerland

Reviewed by:
Yanhui Dong,
Institute of Geology and Geophysics (CAS), China
Hemin Yuan,
China University of Geosciences, China

***Correspondence:**
S. K. Sahoo
s.sahoo@noc.ac.uk

†ORCID:
B. N. Madhusudhan
orcid.org/0000-0002-2570-5934
F. Alvarez-Borges
orcid.org/0000-0002-6940-9918
S. K. Sahoo
orcid.org/0000-0001-9644-8878

Specialty section:
This article was submitted to Solid Earth Geophysics, a section of the journal Frontiers in Earth Science

Received: 18 February 2022
Accepted: 19 April 2022
Published: 08 June 2022

Citation:
Madhusudhan BN, Sahoo SK, Alvarez-Borges F, Ahmed S, North LJ and Best AI (2022) Gas Bubble Dynamics During Methane Hydrate Formation and its Influence on Geophysical Properties of Sediment Using High-Resolution Synchrotron Imaging and Rock Physics Modeling. Front. Earth Sci. 10:877641. doi: 10.3389/feart.2022.877641

Gas bubble in aquatic sediments has a significant effect on its geophysical and geomechanical properties. Recent studies have shown that methane gas and hydrate can coexist in gas hydrate–bearing sediments. Accurate calibration and understanding of the fundamental processes regarding such coexisting gas bubble dynamics is essential for geophysical characterization and hazard mitigation. We conducted high-resolution synchrotron imaging of methane hydrate formation from methane gas in water-saturated sand. While previous hydrate synchrotron imaging has focused on hydrate evolution, here we focus on the gas bubble dynamics. We used a novel semantic segmentation technique based on convolutional neural networks to observe bubble dynamics before and during hydrate formation. Our results show that bubbles change shape and size even before hydrate formation. Hydrate forms on the outer surface of the bubbles, leading to reduction in bubble size, connectivity of bubbles, and the development of nano-to micro-sized bubbles. Interestingly, methane gas bubble size does not monotonously decrease with hydrate formation; rather, we observe some bubbles being completely used up during hydrate formation, while bubbles originate from hydrates in other parts. This indicates the dynamic nature of gas and hydrate formation. We also used an effective medium model including gas bubble resonance effects to study how these bubble sizes affect the geophysical properties. Gas bubble resonance modeling for field or experimental data generally considers an average or equivalent bubble size. We use synchrotron imaging data to extract individual gas bubble volumes and equivalent spherical radii from the segmented images and implement this into the rock physics model. Our modeling results show that using actual bubble size distribution has a different effect on the geophysical properties compared to the using mean and median bubble size distributions. Our imaging and modeling studies show that the existence of these small gas bubbles of a specific size range, compared to a bigger

bubble of equivalent volume, may give rise to significant uncertainties in the geophysical inversion of gas quantification.

Keywords: gas bubble, gas hydrate, wave velocity, synchrotron X-ray imaging, rock physics model

INTRODUCTION

The presence of gas bubbles in aquatic (underwater) sediment pores affects both geomechanical and geophysical properties of the sediment (Sills et al., 1991; Best et al., 2004; Lee, 2004; Zheng et al., 2017). The presence of gas bubbles in pore space considerably reduces the sound speed (Sills et al., 1991; Kumar and Madhusudhan, 2012) and increases the attenuation (Best et al., 2004), in comparison to a fully water-saturated sediment state.

Hydrate is an ice-like solid comprising a hydrogen-bonded water lattice with trapped gas molecules that occurs within a pressure–temperature stability zone in seafloor sediments (Kvenvolden, 1993). Remote geophysics is used to quantify seafloor methane hydrates over large (km^2) areas. Typically, these methods use models where the seismic velocity (e.g., Schnurle et al., 2004; Lee and Collett, 2006; Fohrmann and Pecher, 2012) and electrical resistivity (e.g., Weitemeyer et al., 2006; Schwalenberg et al., 2010; Hsu et al., 2014) increase in relation to hydrate replacement within saline water in sediment pore space. However, accurate quantification of methane hydrate saturation is hindered by uncertainties in the relationship between geophysical parameters and hydrate content (e.g., Schnurle et al., 2004; Lee and Collett, 2008; Hsu et al., 2014; Goswami et al., 2015). Hence, the estimates from geophysical data result in uncertainty of the carbon inventory stored in hydrate and resulting assessments of well stability and methane production from hydrate reservoirs (Sahoo et al., 2018a).

The hydrate content is estimated by correlating the electrical resistivity increase in the hydrate stability zone in comparison to background sediments with no hydrates (e.g., Weitemeyer et al., 2006; Lee and Collett, 2008; Schwalenberg et al., 2010; Hsu et al., 2014). This method would not differentiate between hydrate and gas, although they both have greater resistivity in comparison to saline pore fluid (Lee and Collet, 2008). An increase in gas content reduces sound speed, whereas an increase in hydrate content increases sound speed (Sills et al., 1991; Guerin et al., 1999; Fohrmann and Pecher, 2012). Due to the strong effect of gas presence on sound speed, even small amounts of gas hinder the p-wave-hydrate content estimation models.

The co-existence of gas can also be under two-phase water-hydrate stability conditions, as identified in field studies on characterizing gas hydrate–bearing sediments such as Guerin et al. (1999) from Blake Ridge and Paganoni et al. (2016) from NW Borneo. Two types of co-existing gas with hydrate and water in pore space have been identified by many research works (Suess et al., 2001; Milkov et al., 2004; Schicks et al., 2006; Chaouachi et al., 2015; Yang et al., 2016; Sahoo et al., 2018b), which are 1) connected (pore network) and 2) disconnected (individual bubbles) within the pore space. The disconnected bubbles may remain in the hydrate or could have been still present, where hydrate formation is not yet completed (Schicks et al., 2006). On the other hand, hydrate formation can block contacts between gas and water within sediment pores and form pockets of gas (which could include several pores, e.g., Chaouachi et al., 2015; Yang et al., 2016). The trapped gas bubbles may be consumed by the surrounding pore fluid over time by diffusion; however, in a dynamic pore fluid system with gas production, diffusion is unlikely to dominate due to its relatively slow rate (Suesset al., 2001; Milkov et al., 2004). Studies on kinetic modeling of hydrate

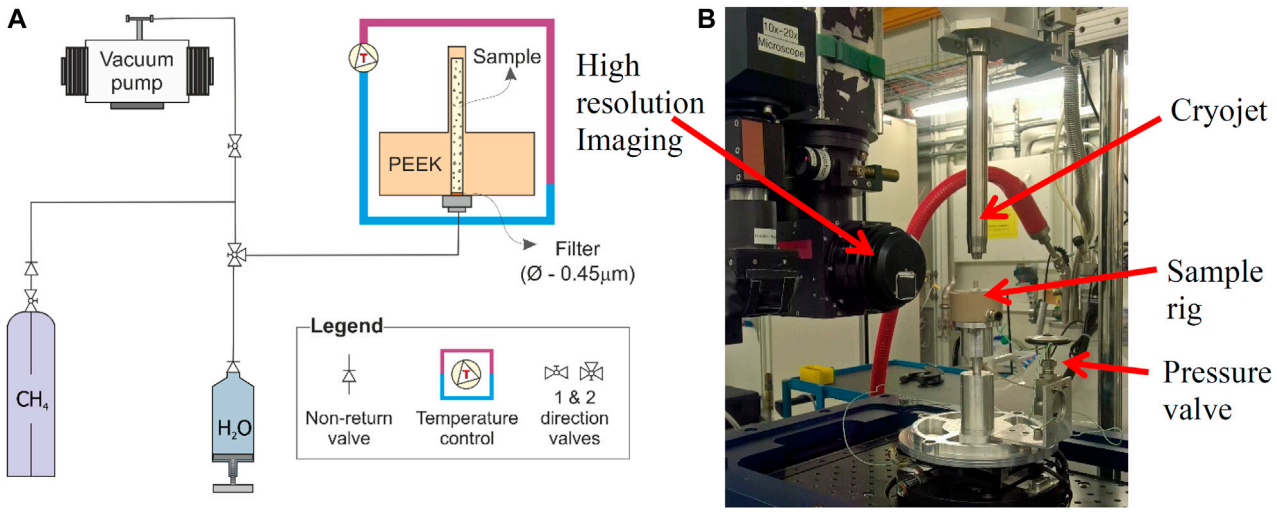

FIGURE 1 | (A) Schematic of the experimental setup; **(B)** Photograph of the experimental setup at Diamond Light Source, United Kingdom.

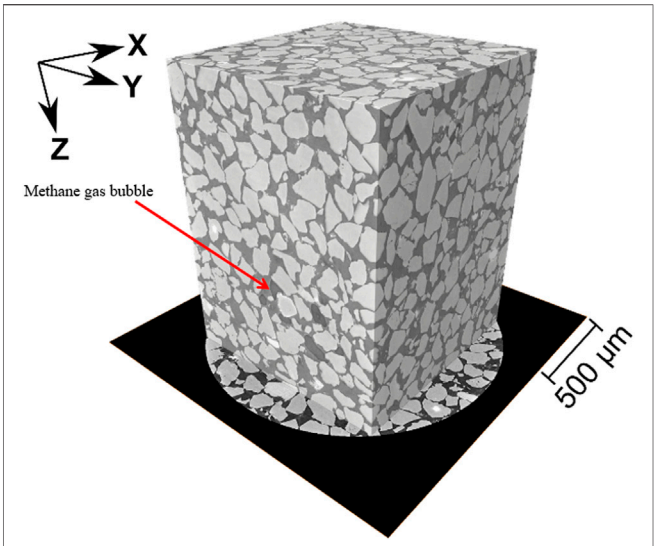

FIGURE 2 | 3D reconstructed CT scan image of sand with pore space filled with brine and methane gas after 3 h of initiating hydrate formation.

formation and dissociation in porous media conclude that the hydrate may never achieve equilibrium due to the three-phase system (e.g., Vafaei et al., 2014). Accurate calibration and understanding of the fundamental processes regarding such coexisting gas bubble dynamics is, thus, essential for geophysical characterization and hazard mitigation. This study presents the results from high-resolution synchrotron imaging of methane hydrate formation and dissociation experiments in porous media. Here, we imaged and analyzed the gas, hydrate, and brine phase changes with the specimen. Particular attention was given to gas bubble dynamics, in terms of its shape and distribution during hydrate formation and dissociation stages. We used an effective medium rock physics model (Marín-Moreno et al., 2017) to study the gas bubble size and distribution effect on the geophysical properties during hydrate formation and dissociation stages.

METHODOLOGY

We conducted high-resolution synchrotron imaging to capture gas bubble dynamics during methane hydrate formation, using a miniature cylindrical hydrate rig (Sahoo et al., 2018b). The rig dimensions were 2 mm internal diameter, 0.8 mm wall thickness, and 10 mm sample scan height (23 mm total height). The pore pressure port at the bottom was used to apply methane/brine pore pressure (**Figure 1A**). The process of formation and dissociation of gas hydrate in sand was imaged using synchrotron X-ray computed tomography (XCT) at beamline I13-2, Diamond Light Source, United Kingdom. The distance between the specimen and detector, exposure time, and beam energy were optimized initially by trial scans. It was found that beam energy of 30 keV and exposure periods between 30 and 200 ms were optimum for the scans. We used x4 and x10 optical objectives after trial runs to obtain images at 0.650 and 0.325 µm resolution, respectively. The schematic of the rig is presented in **Figure 1A** along with the temperature control and measurement system (**Figure 1B**).

Leighton Buzzard E sand (d50 = 100 µm) was weighed and tamped directly into a cylindrical hydrate rig (2 mm diameter and 23 mm height) to obtain a sample of 35% porosity. A vacuum of 1 Pa was applied to the sample to remove as much air as possible from the pore space. Brine (3.5 wt% NaCl solution in deionized and de-aerated water) was injected to partially fill the sample pore space, following the method of Waite et al. (2009), with a high (>83%) initial brine saturation. This method allows excess water condition (Ellis, 2008; Priest et al., 2009). The sample was left for 3 days so that the pore fluids could re-distribute throughout the sample by capillary action. The remaining pore space (~17%), which was previously under vacuum, may have been occupied by water vapor and/or remaining air. Our hydrate formation method and experimental setup represent gas hydrate systems with localized gas flow, such as the base of the GHSZ or near gas chimneys. Methane gas of 10 MPa was then applied to the bottom of the rig, and the valve was closed before the start of the hydrate formation stage. Hydrate was formed by reducing the temperature to 1°C using a cryojet stream applied at the top of the rig (**Figure 1B**) and a thermistor at the bottom of the specimen. The synchrotron rig was scanned every 2–3 h to image the hydrate formation in the pore space. Hydrate dissociation was then performed by initially reducing the temperature to −2.0°C and then slowly increasing the temperature to 3.0°C till the specimen is out of the hydrate pressure–temperature boundary. The scans were performed every 15–20 min during the dissociation stage. After the trial scans, the *in situ* XCT data were collected using a polychromatic "pink beam" at 30 keV peak energy. The detector system used was a scintillator-coupled pco.edge 5.5 camera fitted with a x4 optic magnification lens, resulting in an effective pixel size of 0.8125 µm. The detector was placed at 6.5 mm behind the

TABLE 1 | Details of scans analyzed from the hydrate formation experiment.

Time since initiation of hydrate formation (h)	Porosity (%)	CH4 content (%)	Temperature (°C)
0.00	35.9	6.2	1.0
10.72	35.1	2.0	1.0
20.77	34.9	1.9	1.1
30.02	34.4	1.2	1.0
36.52	34.5	0.9	1.0

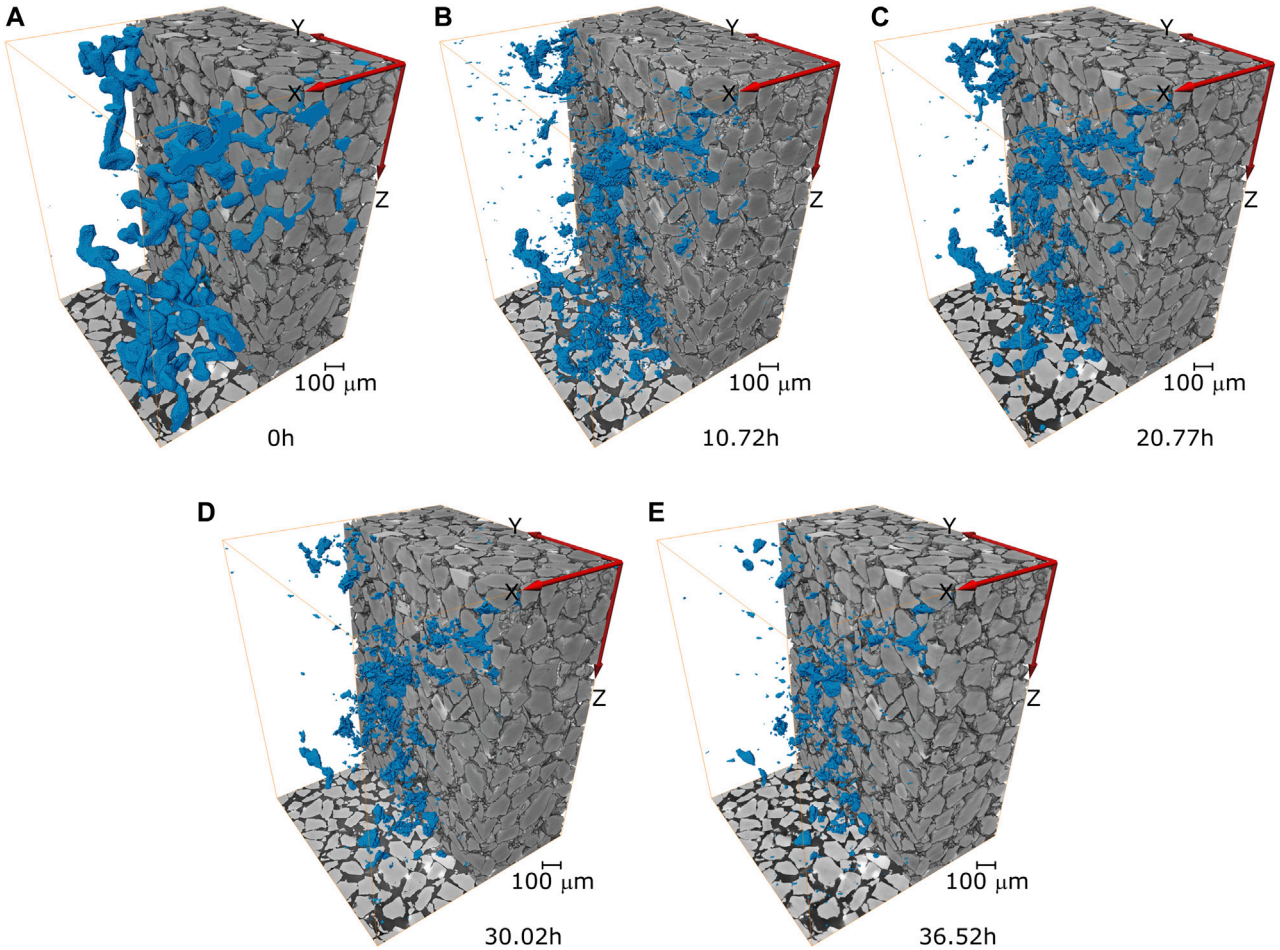

FIGURE 3 | Segmented 3D reconstructed CT scan of the specimen showing the gas bubble distribution within the pore space during hydrate formation **(A)** 0 h, **(B)** 10.2 h, **(C)** 20.77 h, **(D)** 30.02 h, and **(E)** 36.25 h after initiating the hydrate formation process.

sample. The X-ray projection size was 2560 wide by 2160 pixels high. Reconstruction, segmentation, and isolation of gas bubbles were observed during methane hydrate formation.

Reconstruction of CT Scans

X-ray projections were reconstructed using Savu 2.4 (Atwood et al., 2015; Wadeson and Basham, 2016). The reconstruction resulted in 3D volumes consisting of 2650 × 2560 × 2000 voxels, as 80 slices each from the top and bottom were discarded due to the presence of distortion artifacts produced by reduced beam intensity in these regions. **Figure 2** shows a 3D reconstructed image of the specimen after 3 h after initiation of hydrate formation.

Segmentation of CT Scans

As seen in **Figure 2**, it is important to identify the grayscale contrast between the four phases of the specimen, that is, methane gas, sand, brine, and gas hydrates. We used a novel semantic segmentation technique based on convolutional neural networks (CNNs) to observe bubble dynamics before and during hydrate formation (Alvarez-Borges et al., 2021). This methodology involved training U-Nets, a class of CNNs, to create models that could classify the synchrotron XCT data into three different phases: 1) sand, 2) brine + hydrates, and 3) methane gas. We used RootPainter (Smith et al., 2020) to perform this.

RootPainter is a client-server application that uses a graphical user interface (GUI) and interactive corrections to train a binary 2D U-Net model. The procedure involved, for each XCT volume, is the hand-annotation of 50 random XY slices using the GUI. From these, the software used 40 slices to train the model and 10 slices as the validation dataset to assess model accuracy at the end of each training cycle (or 'epoch') using the F-score parameter (F_1). At the conclusion of each training epoch, the F_1 number for the current and previous epochs was compared, and the associated model with the highest F_1 was saved. This was repeated until 60 consecutive epochs were completed without improvements in F_1. This led to minimum F_1 values of approximately 0.98 and a single U-Net segmentation model per scan.

F_1 is defined as (Smith et al., 2020) as follows:

TABLE 2 | Details of scans analyzed from the hydrate dissociation experiment.

Time since initiation of hydrate dissociation (h)	Porosity (%)	CH_4 content (%)	Temperature (°C)
0.00	34.5	0.9	−2.0
0.72	34.5	1.1	−1.6
1.93	34.6	2.2	−1.0
2.83	34.2	2.9	0.0
3.71	34.2	6.6	3.5

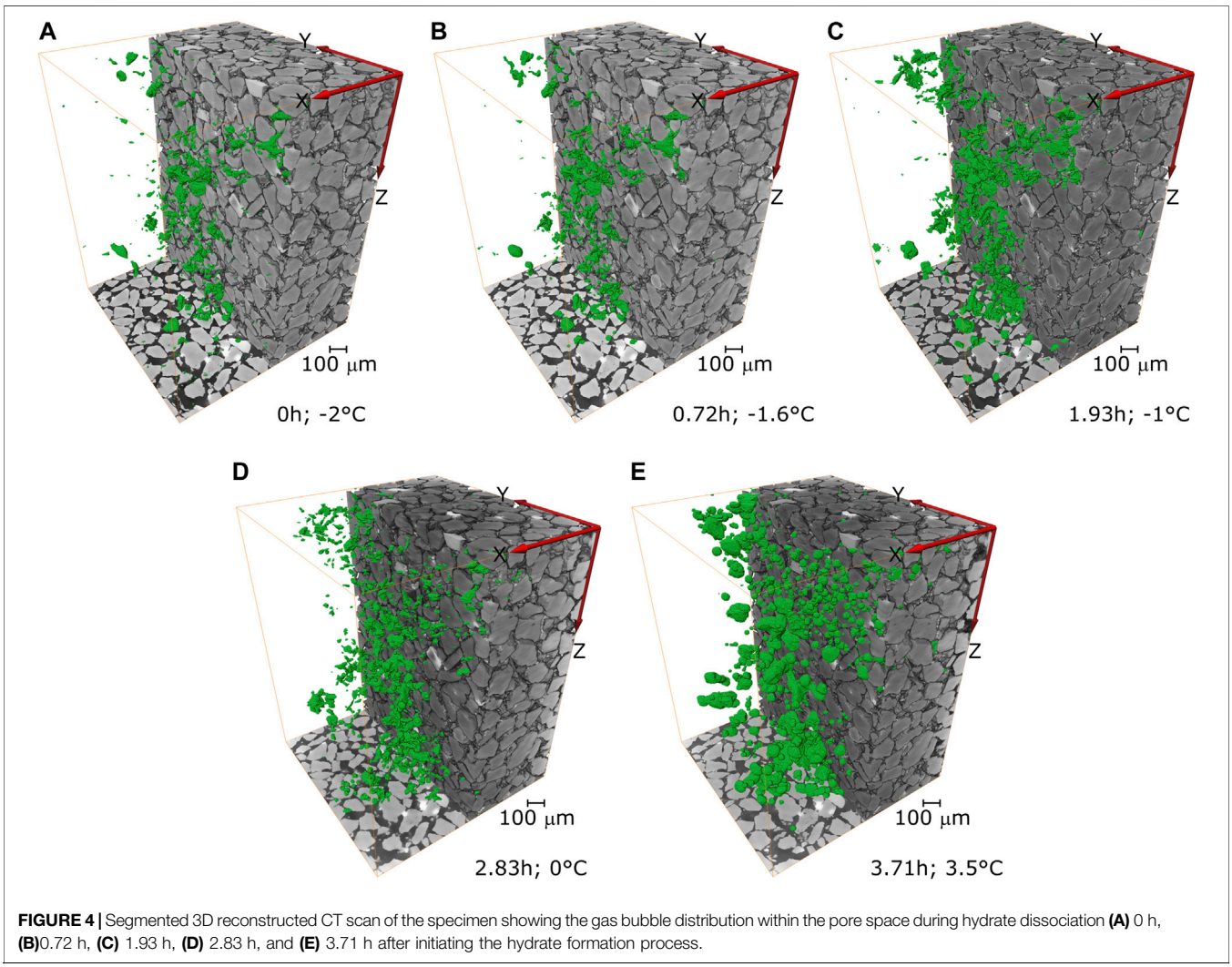

FIGURE 4 | Segmented 3D reconstructed CT scan of the specimen showing the gas bubble distribution within the pore space during hydrate dissociation **(A)** 0 h, **(B)**0.72 h, **(C)** 1.93 h, **(D)** 2.83 h, and **(E)** 3.71 h after initiating the hydrate formation process.

$$F_1 = \frac{TP}{TP + 0.5(FP + FN)} \quad (1)$$

where TP, FP, and FN are the number of true positive, false positive, and false negative pixel U-Net predictions, respectively, in each case.

The U-Net models were then used to segment a 1554 × 1554 × 2000 region of the original reconstructed volumes, therefore isolating the sand, brine + hydrate, and methane gas present in the image. This region was inscribed within the cylindrical field of view of the original volumes and omitted the dark black background generated during reconstruction. This was carried out to optimize computing time by reducing both the size of the 3D image and the number of labels required for annotation and prediction.

Table 1 presents the selected scans from the start of the hydrate formation stage that was processed to isolate the gas bubbles within the pore space. The temperature was maintained

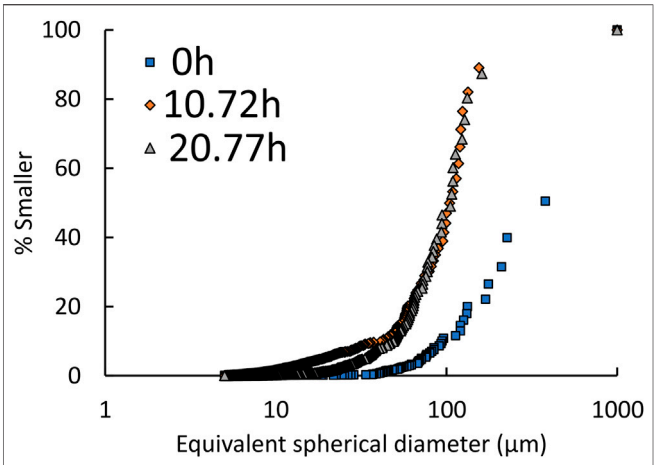

FIGURE 5 | Evolution of bubble size distribution within the pore space of the specimen during the hydrate formation stage.

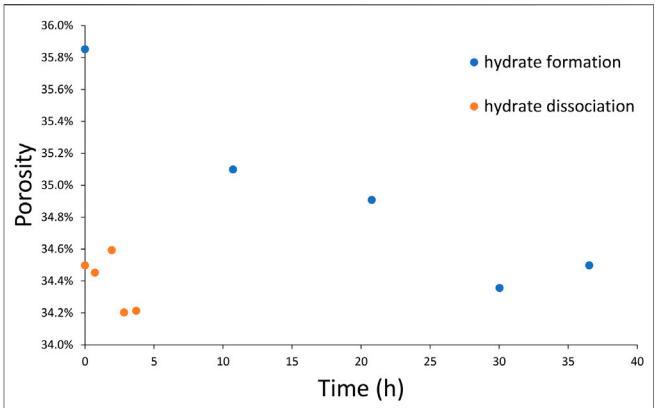

FIGURE 6 | Result of porosity from the analyzed scans during hydrate formation and dissociation stages. Irrecoverable densification of the specimen was observed due to methane gas consumption for hydrate formation.

constant at 1°C throughout the hydrate formation stage. The porosity and the methane (CH_4) gas content were calculated using the pore size distribution and methane gas in the specimen from the segmented volumes using **Eqs. 1**, **2**, respectively.

$$\text{Porosity } (\%) = \frac{volume\ of\ pores}{total\ volume} \times 100. \quad (2)$$

$$CH_4 \text{ saturation } (\%) = \frac{volume\ of\ CH_4}{volume\ of\ pores} \times 100. \quad (3)$$

Alvarez-Borges et al. (2021) found that the mean absolute errors for porosity and methane gas saturation measurements derived from these same XCT volumes segmented using this approach were below 1% and 0.05%, respectively. A detailed description of the implementation of this technique is given by these authors.

The segmented gas bubbles rendered using Avizo software during each selected time stamp of the hydrate formation stage are presented in **Figure 3**. Initially the gas within the pore space appears as a pipe-like structure, which may be due to an initial interconnected gas network that might have formed during the high pressure (10 MPa) gas injection before the hydrate formation process was initiated. As the hydrate begins to form in the pore space, the methane gas is consumed and the bubble size reduces from millimeter scale to micron and nano scale. Also, at the end of the hydrate formation, which was determined from our previous work by Sahoo et al. (2018b), methane gas still exists in the pore space, which is trapped within the newly formed hydrate pore structure. The coexistence of hydrate, brine, and gas in hydrate structure has been reported by many research works and our own work (Suess et al., 2001; Milkov et al., 2004; Schicks et al., 2006; Chaouachi et al., 2015; Yang et al., 2016; Sahoo et al., 2018b).

Table 2 similarly presents the selected scans during the process of the hydrate dissociation stage that was processed to isolate the gas bubbles within the pore space. **Figure 4** presents the segmented gas bubbles rendered using Avizo software during each selected time stamp of the hydrate dissociation stage. Initially, the volume of the gas trapped in the hydrate structure, which was never consumed during the hydrate formation stage, appears to be well-distributed within the

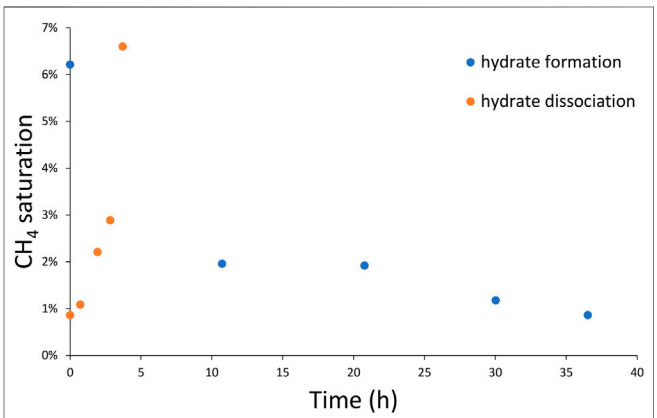

FIGURE 7 | Methane gas consumption and expulsion with time during hydrate formation and dissociation stage.

specimen. Thereafter, as temperature increases and hydrates begin to dissociate within the pore space, the methane bubble increases in size very quickly. At the final scan, where the dissociation was complete, the methane bubbles seem to be well-distributed in the specimen. In comparison to the gas bubble size and distribution before formation, the gas bubble seems to be well-distributed and consistent after the completion of the gas hydrate dissociation.

ANALYSIS OF GAS BUBBLE DYNAMICS DURING HYDRATE FORMATION AND DISSOCIATION STAGES

The shape of the individual methane gas bubble within the pore space was analyzed by calculating spheres of the same volume as that of each bubble and thereafter determining the diameter of said spheres. In this way, an equivalent spherical diameter was derived for each individual bubble. This enabled the quantification of the gas bubble size distribution in each specimen and the observation of

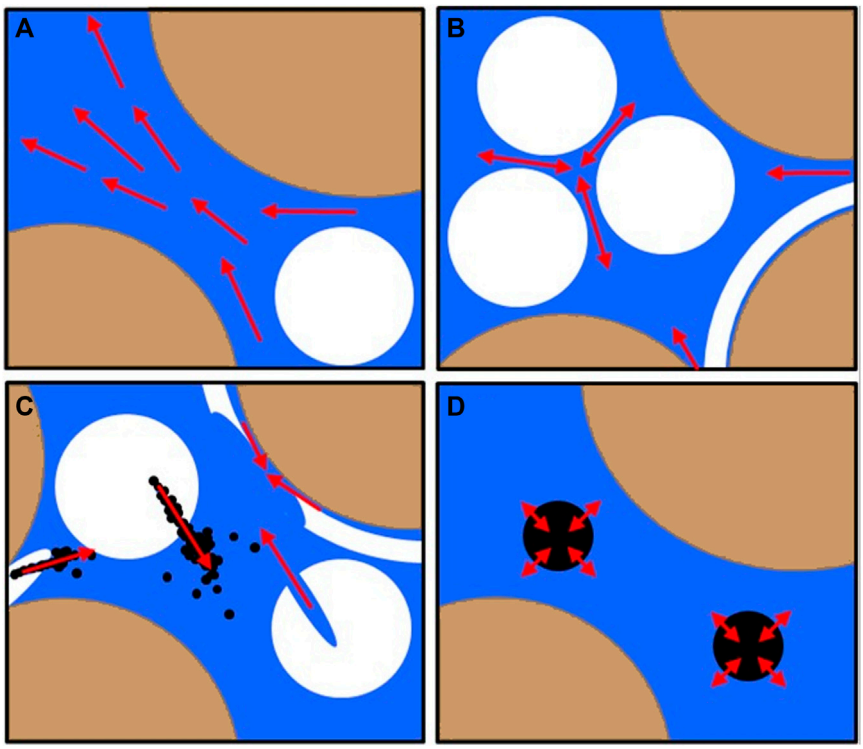

FIGURE 8 | Conceptual model (Marín-Moreno et al., 2017) to examine the effect of methane hydrate (white) and gas (black) on the geophysical properties of brine (blue)-saturated sediment (yellow). **(A)** Biot's type inertial fluid flow, **(B)** micro squirt flow, **(C)** sub-micro squirt flow due to inclusions of gas and water in hydrates, and **(D)** gas bubble resonance. Marín-Moreno et al. (2017).

changes in bubble size during hydrate formation and dissociation. **Figure 5** shows the bubble size distribution within the specimen pore space during the hydrate formation stage at time stamp 0, 10.72,, and 20.77 h. Initially, at the start of hydrate formation (0 h), due to the presence of large pipe-shaped bubbles (see **Figure 3A**), 60% of the bubbles are greater than 300 μm average size. Due to the formation of the hydrate, a large amount of gas is consumed, and hence less than 5% bubbles are greater than 300 μm. As hydrate formation continues, the bubble size analysis of t = 10.72 h shows good distribution from sizes 100 to 6 μm. This further evolves into a reduction in bubble size variability (homogenization of bubble size distribution) as seen from the analysis of specimen from scan after t-20.77 h.

The porosity, methane gas saturation, and average bubble size of the specimen during hydrate formation and dissociation are obtained from the analysis of pores and methane bubbles from the scans. The porosity of the specimen reduces significantly at the initial hydrate formation stage, probably due to particle rearrangement as a result of the consumption of large volumes of methane as shown in **Figure 6**. This slightly densifies the specimen and is an irrecoverable change as the analysis from the dissociation stage indicates no change in porosity as methane gas is released back into the pore space. As expected, methane saturation reduces with the hydrate formation (**Figure 7**), but even after complete formation (t > 30 h), at least 1% methane is still trapped within the hydrate structure. The average bubble size (d50) dramatically drops at the initial hydrate formation stage; thereafter, there is a small change in average bubble size till completion of hydrate formation.

EFFECTIVE MEDIUM ROCK PHYSICS MODEL USING BUBBLE RESONANCE

The presence of gas bubbles affects the geophysical properties of sediments. The extent or magnitude of this effect on the velocity of P and S waves depends on the gas bubble size and concentration (e.g., Marín-Moreno et al., 2017). We used an effective medium rock physics model to observe how the gas bubble size affects the geophysical properties. We used the hydrate-bearing effective sediment (HBES) model (Marín-Moreno et al., 2017) which is a development from the (Hydrate Effective Grain) model of Best et al. (2013). Our model accounts for the inertial fluid flow between different components of the system and gas bubble resonance (**Figure 8**). HBES also considers the effect of squirt flow in 1) inclusions in hydrates and 2) different aspect ratio pores created by hydrates. The over-reaching idea in this model is that hydrate-bearing porous medium is an effective medium of porous media (sediment) with solid hydrate and fluid in the pore space. The pore fluid comprises gas and liquid. The gas bubbles can give rise to resonance, modeled according to Smeulders and van Dongen

TABLE 3 | Values used in the HBES model runs (Marín-Moreno et al., 2017).

Parameter	Value	Units	References
Hydrate bulk modulus	7.9×10^9	Pa	Best et al. (2013)
Hydrate shear modulus	3.3×10^9	Pa	Best et al. (2013)
Hydrate Poisson's ratio	0.32		
Methane bulk modulus	KCH4 (Pp, T)	Pa	Millero et al. (1980)
Methane density	ρCH4 (Pp, T)	kg m^{-3}	Millero et al. (1980)
Methane viscosity	μCH4 (Pp, T)	Pa s	Millero et al. (1980)
Methane irreducible saturation	0.02		Reagan and Moridis (2008)
Sand/quartz grain bulk modulus	36×10^9	Pa	Ecker et al. (2000)
Sand/quartz grain shear modulus	45×10^9	Pa	Ecker et al. (2000)
Sand/quartz grain Poisson's ratio	0.062		
Sand/quartz grain density	2650	kg m^{-3}	Ecker et al. (2000)
Sand/quartz grain diameter	1×10^{-4}	m	Best et al. (2013)
Sand/quartz grain coordination number	8.5		Ecker et al. (2000)
Water bulk modulus	KW (Pp, T)	Pa	Setzmann and Wagner (1991)
Water density	ρW (Pp, T)	kg m^{-3}	Setzmann and Wagner (1991)
Water viscosity	μW (Pp, T)	Pa s	Setzmann and Wagner (1991)
Water irreducible saturation	0.2		Reagan and Moridis (2008)
Intrinsic permeability without hydrate	10^{-13}	$_m2$	Daigle et al. (2015)
Intrinsic permeability exponent for cementing hydrate	3		
Intrinsic permeability exponent for pore-filling hydrate	2		
Tortuosity	3		based on Mavko et al. (2009)
van Genuchten's (1980) capillary	0.45		Reagan and Moridis (2008)
pressure fitting parameter			
van Genuchten's (1980) capillary	2000	Pa	Reagan and Moridis (2008)
pressure gas entry parameter			
Critical porosity	0.36		Mavko et al. (2009)
K Feldspar bulk modulus	37.5×10^9	Pa	Mavko et al. (2009)
K Feldspar shear modulus	15×10^9	Pa	Mavko et al, (2009)
Illite bulk modulus	62.21×10^9	Pa	Mavko et al, (2009)
Illite shear modulus	25.70×10^9	Pa	Mavko et al. (2009)

(1997). Hydrate can have gas or liquid inclusions that can give rise to viscous (squirt) flow between these inclusions and pore fluid when an elastic wave passes through this effective medium, creating a pressure gradient. The hydrate formation in the pore space changes the aspect ratio of the pores, and squirt flow can occur between these newly formed hydrate and pore fluid. The squirt flow element is embedded in the Biot–Stoll global fluid flow model (Biot, 1956b; 1956a). This model uses different hydrate morphologies (cementing, pore-floating, and pore-bridging) as described by Ecker et al. (1998) and Helgerud et al. (1999), using model concepts developed by Leurer and Brown (2008) and Leurer (1997) for clay-squirt flow attenuation in marine sediments. We have used pore-bridging or load-bearing hydrate morphology as it is the most commonly occurring hydrate morphology in nature (e.g., Waite et al., 2009; Spangenberg et al., 2015). We have not used squirt flow due to inclusions in this study as we are interested in looking at the effect of gas bubbles. So, we have plotted the results as a change in velocity instead of absolute velocity, helping us to see how changes in gas bubble size affect the velocity. This model is explained in detail in Sahoo et al. (2018b). The input parameters used in the model are listed in **Table 3**.

Simulations were carried out to examine the effect of bubble size and distribution based on the results from the 3D image analysis of gas bubbles imaged during hydrate formation. The hydrate content increase with hydrate formation time was obtained from the synchrotron scans as described by Sahoo et al. (2018b). Using the hydrate content, the initial run was carried out assuming no gas was present in the hydrate structure. Thereafter, gas bubbles were introduced in the simulations in the following five different cases, and these were as follows: 1) uniform bubble size = 10 μm; 2) uniform bubble size = 100 μm; 3) uniform bubble size = d50 from **Figure 9** for each hydrate content. 4) Uniform mean (or average) bubble size = dA from bubble size distribution plots as shown in **Figure 5**; 5) bubble size distribution from **Figure 5** obtained for each hydrate content. The model runs on uniform bubble sizes 10 and 100 μm are carried out to cover the upper and lower bound limits of bubble sizes, whereas the d50 and dA use the mid-size and the average (or mean) size from bubble distribution. However, the 'distribution' run considered all the bubble sizes and distribution for the simulation. We grouped bubbles in bin size of 5 μm. We then calculated how much volume each of these bin-sized bubbles occupies. We used the mean bubble size of each bin (2.5 μm for a bin of 0–5 μm) and saturation of this bin (volume of this bin size bubbles/total pore volume) in the rock physics model to calculate velocity. Thereafter, we plot relative velocity for each bin size, defined as velocity with calculated hydrate saturation with no gas velocity with same hydrate saturation and gas saturation of this bin. We then added these relative velocities for each bin size to obtain the total effect of all the gas bubbles. **Figures 10**, **11** present comparative relative velocity change of P and S waves when gas bubbles of a given size are present compared to when no gas is present. We plot ΔV_p and ΔV_s, that is, V at a given gas

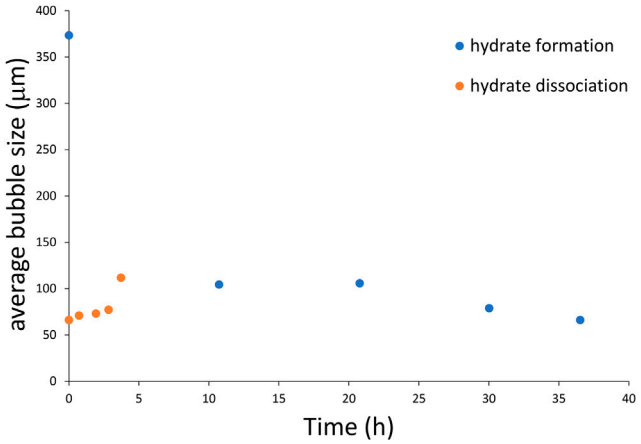

FIGURE 9 | Average bubble size (d50) evolution with hydrate formation and dissociation. The large average bubble size before formation is observed, which is irrecoverable after the dissociation stage.

saturation minus V at zero gas saturation. The bubble size and distribution play a significant role in the accurate determination of wave velocities. Variation of bubble size (uniform) from 100 to 10 μm has a significant effect on the wave velocities.

In the case of effect on P wave velocity, introducing a uniform bubble in the model results in significant reduction in P wave velocity for hydrate saturations <20%. However, beyond 20% hydrate saturation, the uniform d50 and uniform mean bubble size (DA) seem to predict the P wave velocities closer to reality. Simulations using actual bubble size distribution indicate less effect at low hydrate saturation (<10%), whereas the greatest reduction is found at 25% hydrate saturation, which might be due to the evolution of bubble sizes from well-distributed to more uniformly distributed bubble sizes (see **Figure 5**). In general, the relative change in S wave velocity might be smaller (**Figure 11**), but this is due to the assumed pore-filling hydrate morphology (Sahoo et al., 2018b) of the

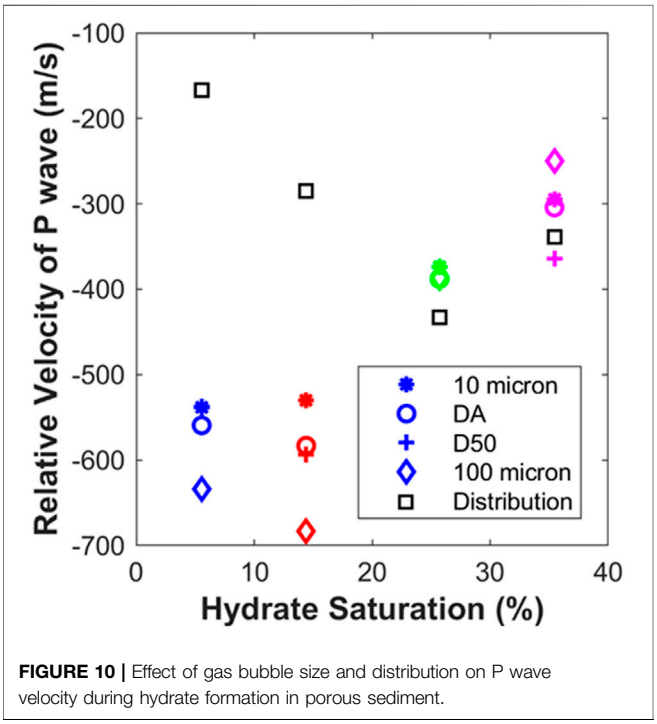

FIGURE 10 | Effect of gas bubble size and distribution on P wave velocity during hydrate formation in porous sediment.

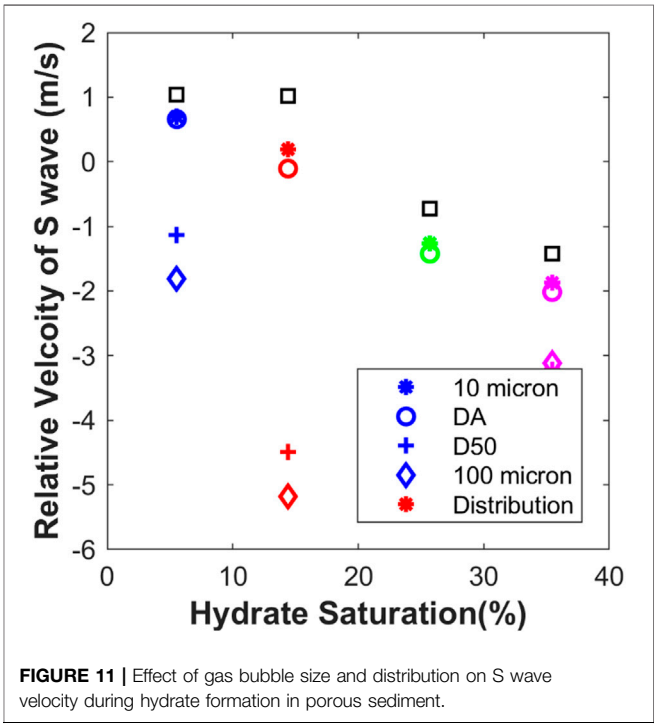

FIGURE 11 | Effect of gas bubble size and distribution on S wave velocity during hydrate formation in porous sediment.

hydrates. The uniform average bubble size and 10 μm bubble produce a similar effect on S wave propagation, but 100 μm and d50 bubble size reduce S wave velocity. Simulations using actual bubble size distribution show less effect on S wave propagation in general, but they seem to coincide with simulations of 100 μm and d50 bubble size.

DISCUSSION AND CONCLUSION

We show 4D time-lapse, high-resolution synchrotron imaging of methane gas evolution during methane hydrate formation and dissociation in brine-saturated sand. To our knowledge, this is the first imaging of bubble dynamics during the formation and dissociation of hydrates in brine-saturated sand. Initially, before hydrate formation, methane gas shows pipe-like structures, spread across several pores. These pipe structures either separate or get interconnected as hydrate formation starts and thereafter becomes disconnected as methane is consumed to form more hydrates. The initial bubble size distribution is well-graded, covering bubble sizes as big as 1,000 μm–50 μm (before hydrate formation). As hydrate begins to form, the bubble size variation reduces to poorly graded, varying from 200 to 10 μm, and further tending toward uniformly graded bubble size (**Figure 5**). The methane gas may not be fully consumed even after maximum hydrate formation as hydrate formed on the gas bubble surface and prevented further contact between gas and water. This phenomenon has been observed in our previous work (Sahoo et al., 2018b) and also from field samples in the Hydrate Ridge, (Suess et al., 2001). Hydrate formation in the unconsolidated porous material leads to densification (**Figure 6**), initially as the bubble size reduces and then as the solid hydrate replaces the fluid hydrate.

The dissociation of methane hydrate releases the methane gas with uniform bubble size and these bubble sizes increase with hydrate dissociation. However, hydrate formation and dissociation lead to more uniformity in gas bubble distribution. There are no interconnected bubbles upon full hydrate dissociation compared to those observed before hydrate formation (**Figures 3**, **4**).

Modeling the effect of bubble size and distribution using an effective medium rock physics model shows the actual bubble size distribution from the synchrotron data producing a very different effect on P wave propagation in comparison to representative uniform bubble size (either with an average diameter or D50), even though the actual average bubble size was used for comparative simulation. Our previous work by Sahoo et al. (2018b) on correlating hydrate morphology to geophysical properties, the hydrate morphology evolves from pore filling to pore bridging at hydrate saturation between 20%–30%, which is evidenced by the geophysical measurements. A similar observation about the transition from pore filling to pore bridging was also made by Priest et al. (2009) at hydrate saturations between 20% and 30%. Our simulations indicate uncertainty in predicting wave velocity because the presence of gas is higher when hydrate saturation is lower than 20%, which could be attributed to the pore filling nature of the hydrate structure. Hence, for pore filling hydrate morphology, the use of bubble size distribution can produce more accurate estimates of wave velocities. Pore bridging hydrate morphology is observed for >30% hydrate saturation and bubble size distribution is uniform; however, the size of the bubble becomes important in accurately predicting the wave velocities. The effect of bubble size and distribution plays a role in S wave velocity also, but the effect might be less for pore filling–type hydrate structure and further, this effect might be masked in pore bridging type hydrate structure due to an increase of the cementing effect as hydrate bridges with each other. This work clearly shows the significance of bubble size and distribution in predicting the geophysical properties of hydrate-bearing porous media.

DATA AVAILABILITY STATEMENT

The datasets presented in this study can be found in online repositories. The names of the repository/repositories and accession number(s) can be found in the article/ **Supplementary Material**.

AUTHOR CONTRIBUTIONS

The conceptualization for synchrotron CT imaging and major writing was carried out by BM. SS developed and analyzed the results using an effective medium rock physics model using bubble resonance and contributed to writing the manuscript. FA-B contributed toward analyzing the synchrotron data and developed the necessary methodology and scripts to segment, reconstruct, and analyze the 3D CT scan data from Diamond Light Source, United Kingdom. SA was instrumental in carrying out and reconstructing the images, while also assisting FA-B to develop necessary scripts at Diamond Light Source, United Kingdom. LN was instrumental in developing the rig to image gas hydrate formation along with BM and SS. AB was the key to securing funding for this work, both experiments and numerical modeling, and also participated in the discussions about the results of the analyses.

FUNDING

We acknowledge funding from the United Kingdom Natural Environment Research Council (Grant NE/J020753/1 and NE/R000123/1). BNM was supported by the SMMI HIEF internal grant from the University of Southampton. The experimental data are available at the National Geoscience Data Centre, United Kingdom under the Grant NE/J020753/1.

ACKNOWLEDGMENTS

The authors are grateful to the Diamond Light Source, United Kingdom synchrotron CT facility for access to the I-13 beamline (proposal MT16205-1) and for the assistance of Shashidhara Marathe (Beamline Scientist) Kaz Wanelik

(Data Acquisition and Scientific Computing). We thank the μ-VIS facility at the University of Southampton for image analysis capability and particularly Prof. Ian Sinclair for his help with the proposal to Diamond Light Source, United Kingdom.

SUPPLEMENTARY MATERIAL

The Supplementary Material for this article can be found online at: https://www.frontiersin.org/articles/10.3389/feart.2022.877641/full#supplementary-material

REFERENCES

Alvarez-Borges, F. J., King, O. N., Madhusudhan, B., Connolley, T., Basham, M., and Ahmed, S. I. (2021). *U-net Segmentation Methods for Variable-Contrast XCT Images of Methane-Bearing Sand*. Earth and Space Science Open Archive. [Preprint]. doi:10.1002/essoar.10506807.1

Atwood, R. C., Bodey, A. J., Price, S. W., Basham, M., and Drakopoulos, M. (2015). A High-Throughput System for High-Quality Tomographic Reconstruction of Large Datasets at Diamond Light Source. *Philos. Trans. A Math. Phys. Eng. Sci.* 373, 2369–2393. doi:10.1098/rsta.2014.0398

Best, A. I., Priest, J. A., Clayton, C. R. I., and Rees, E. V. L. (2013). The Effect of Methane Hydrate Morphology and Water Saturation on Seismic Wave Attenuation in Sand under Shallow Sub-seafloor Conditions. *Earth Planet. Sci. Lett.* 368, 78–87. doi:10.1016/j.epsl.2013.02.033

Best, A. I., Tuffin, M. D., Dix, J. K., and Bull, J. M. (2004). Tidal Height and Frequency Dependence of Acoustic Velocity and Attenuation in Shallow Gassy Marine Sediments. *J. Geophys. Res.* 109 (B8), B08101. doi:10.1029/2003jb002748

Biot, M. A. (1956a). Theory of Propagation of Elastic Waves in a Fluid-Saturated Porous Solid I Low-Frequency Range. *J. Acoust. Soc. Am.* 28 (2), 168–178. doi:10.1121/1.1908239

Biot, M. A. (1956b). Theory of Propagation of Elastic Waves in a Fluid-Saturated Porous Solid. II. Higher Frequency Range. *J. Acoust. Soc. Am.* 28 (2), 179–191. doi:10.1121/1.1908241

Chaouachi, M., Falenty, A., Sell, K., Enzmann, F., Kersten, M., Haberthür, D., et al. (2015). Microstructural Evolution of Gas Hydrates in Sedimentary Matrices Observed with Synchrotron X-Ray Computed Tomographic Microscopy. *Geochem. Geophys. Geosyst.* 16, 1711–1722. doi:10.1002/2015gc005811

Ecker, C., Dvorkin, J., and Nur, A. (1998). Sediments with Gas Hydrates: Internal Structure from Seismic AVO. *Geophysics* 63 (5), 1659–1669. doi:10.1190/1.1444462

Ellis, M. H (2008). Joint Seismic and Electrical Measurements of Gas Hydrates in Continental Margin Sediments. Doctoral Thesis. Southampton (England): University of Southampton, School of Ocean and Earth Science.

Fohrmann, M., and Pecher, I. A. (2012). Analysing Sand-Dominated Channel Systems for Potential Gas-Hydrate-Reservoirs Using an AVO Seismic Inversion Technique on the Southern Hikurangi Margin, New Zealand. *Mar. Petroleum Geol.* 38 (1), 19–34. doi:10.1016/j.marpetgeo.2012.08.001

Goswami, B. K., Weitemeyer, K. A., Minshull, T. A., Sinha, M. C., Westbrook, G. K., Chabert, A., et al. (2015). A Joint Electromagnetic and Seismic Study of an Active Pockmark within the Hydrate Stability Field at the Vestnesa Ridge, West Svalbard Margin. *J. Geophys. Res. Solid Earth* 120, 6797–6822. doi:10.1002/2015jb012344

Guerin, G., Goldberg, D., and Melser, A. (1999). Characterization of *In Situ* Elastic Properties of Gas Hydrate-Bearing Sediments on the Blake Ridge. *J. Geophys. Res.* 104 (817), 17781–17795. doi:10.1029/1999jb900127

Hsu, S.-K., Chiang, C.-W., Evans, R. L., Chen, C.-S., Chiu, S.-D., Ma, Y.-F., et al. (2014). Marine Controlled Source Electromagnetic Method Used for the Gas Hydrate Investigation in the Offshore Area of SW Taiwan. *J. Asian Earth Sci.* 92, 224–232. doi:10.1016/j.jseaes.2013.12.001

Kumar, J., and Madhusudhan, B. N. (2012). Dynamic Properties of Sand from Dry to Fully Saturated States. *Géotechnique* 62 (1), 45–54. doi:10.1680/geot.10.p.042

Kvenvolden, K. A. (1993). Gas Hydrates-Geological Perspective and Global Change. *Rev. Geophys.* 31 (2), 173–187. doi:10.1029/93rg00268

Lee, M. W., and Collett, T. S. (2006). "Gas Hydrate and Free Gas Saturations Estimated from Velocity Logs on Hydrate Ridge, Offshore Oregon, U.S. A, " in *Proceedings of the Ocean Drilling Program, 199 Scientific Results*(College Station, TX: Ocean Drilling Program), 1–25. doi:10.2973/odp.proc.sr.204.103.2006

Lee, M. W., and Collett, T. S. (2008). Integrated Analysis of Well Logs and Seismic Data to Estimate Gas Hydrate Concentrations at Keathley Canyon, Gulf of Mexico. *Mar. Petroleum Geol.* 25 (9), 924–931. doi:10.1016/j.marpetgeo.2007.09.002

Lee, M. W. (2004). Elastic Velocities of Partially Gas-Saturated Unconsolidated Sediments. *Mar. Petroleum Geol.* 21, 641–650. doi:10.1016/j.marpetgeo.2003.12.004

Leurer, K. C. (1997). Attenuation in Fine-grained Marine Sediments: Extension of the Biot-Stoll Model by the "effective Grain Model" (EGM). *Geophysics* 62 (5), 1465–1479. doi:10.1190/1.1444250

Leurer, K. C., and Brown, C. (2008). Acoustics of Marine Sediment under Compaction: Binary Grain-Size Model and Viscoelastic Extension of Biot's Theory. *J. Acoust. Soc. Am.* 123 (4), 1941–1951. doi:10.1121/1.2871839

Marín-Moreno, H., Sahoo, S. K., and Best, A. I. (2017). Theoretical Modeling Insights into Elastic Wave Attenuation Mechanisms in Marine Sediments with Pore-Filling Methane Hydrate. *J. Geophys. Res. Solid Earth* 122, 1835–1847. doi:10.1002/2016JB013577

Milkov, A. V., Dickens, G. R., Claypool, G. E., Lee, Y. J., Borowski, W. S., Torres, M. E., et al. (2004). Co-existence of Gas Hydrate, Free Gas, and Brine within the Regional Gas Hydrate Stability Zone at Hydrate Ridge (Oregon Margin): Evidence from Prolonged Degassing of a Pressurized Core. *Earth Planet. Sci. Lett.* 222 (3–4), 829–843. doi:10.1016/s0012-821x(04)00212-2

Paganoni, M., Cartwright, J. A., Foschi, M., Shipp, R. C., and Van Rensbergen, P. (2016). Structure II Gas Hydrates Found below the Bottom-Simulating Reflector. *Geophys. Res. Lett.* 43, 5696–5706. doi:10.1002/2016GL069452

Priest, J. A., Rees, E. V., and Clayton, C. R. I. (2009). Influence of Gas Hydrate Morphology on the Seismic Velocities of Sands. *J. Geophys. Res.* 114 (B11205), B11205. doi:10.1029/2009jb006284

Sahoo, S. K., Madhusudhan, B. N., Marín-Moreno, H., North, L. J., Ahmed, S., Falcon-Suarez, I. H., et al. (2018b). Laboratory Insights into the Effect of Sediment-Hosted Methane Hydrate Morphology on Elastic Wave Velocity from Time-Lapse 4-D Synchrotron X-Ray Computed Tomography. *Geochem. Geophys. Geosyst.* 19, 4502–4521. doi:10.1029/2018gc007710

Sahoo, S. K., Marín-Moreno, H., North, L. J., Falcon-Suarez, I., Madhusudhan, B. N., Best, A. I., et al. (2018a). Presence and Consequences of Coexisting Methane Gas with Hydrate under Two Phase Water-Hydrate Stability Conditions. *J. Geophys. Res. Solid Earth* 123, 3377–3390. doi:10.1029/2018jb015598

Schicks, J. M., Naumann, R., Erzinger, J., Hester, K. C., Koh, C. A., and Sloan, E. D. (2006). Phase Transitions in Mixed Gas Hydrates: Experimental Observations versus Calculated Data. *J. Phys. Chem. B* 110 (23), 11468468474–74. doi:10.1021/jp0612580

Schnurle, P., Liu, C.-S., Hsiuan, T.-H., and Wang, T.-K. (2004). Characteristics of Gas Hydrate and Free Gas Offshore Southwestern Taiwan from a Combined MCS/OBS Data Analysis. *Mar. Geophys. Res.* 25 (1–2), 157–180. doi:10.1007/s11001-005-0740-6

Schwalenberg, K., Haeckel, M., Poort, J., and Jegen, M. (2010). Evaluation of Gas Hydrate Deposits in an Active Seep Area Using Marine Controlled Source Electromagnetics: Results from Opouawe Bank, Hikurangi Margin, New Zealand. *Mar. Geol.* 272 (1–4), 79–88. doi:10.1016/j.margeo.2009.07.006

Sills, G. C., Wheeler, S. J., Thomas, S. D., and Gardner, T. N. (1991). Behaviour of Offshore Soils Containing Gas Bubbles. *Géotechnique* 41 (2), 227–241. doi:10.1680/geot.1991.41.2.227

Smith, A. G., Han, E., Petersen, J., Olsen, N. A. F., Giese, C., Athmann, M., et al. (2020). *RootPainter: Deep Learning Segmentation of Biological Images with Corrective Annotation*. [Preprint]. doi:10.1101/2020.04.16.044461

Spangenberg, E., Priegnitz, M., Heeschen, K., and Schicks, J. M. (2015). Are Laboratory-Formed Hydrate-Bearing Systems Analogous to Those in Nature? *J. Chem. Eng. Data* 60, 258–268. doi:10.1021/je5005609

Suess, E., Torres, M. E., Bohrmann, G., Collier, R. W., Rickert, D., Goldfinger, C., et al. (2001). "Sea Floor Methane Hydrates at Hydrate Ridge, Cascadia Margin," in *Natural Gas Hydrates—Occurrence, Distribution and Detection* (Washington, DC: American Geophysical Union), 87–98. doi:10.1029/GM124p0087

Vafaei, M. T., Kvamme, B., Chejara, A., and Jemai, K. (2014). A New Reservoir Simulator for Studying Hydrate Dynamics in Reservoir. *Int. J. Greenh. Gas Control* 23, 12–21. doi:10.1016/j.ijggc.2014.02.001

Wadeson, N., and Basham, M. (2016). *Savu: A Python-Based, MPI Framework for Simultaneous Processing of Multiple, N-Dimensional, Large Tomography Datasets*. arXiv:1610.08015 [Preprint].

Waite, W. F., Santamarina, J. C., Cortes, D. D., Dugan, B., Espinoza, D. N., Germaine, J., et al. (2009). Physical Properties of Hydrate-Bearing Sediments. *Rev. Geophys.* 47, RG4003. doi:10.1029/2008RG000279

Weitemeyer, K. A., Constable, S. C., Key, K. W., and Behrens, J. P. (2006). First Results from a Marine Controlled-Source Electromagnetic Survey to Detect Gas Hydrates Offshore Oregon. *Geophys. Res. Lett.* 33, L03304. doi:10.1029/2005gl024896

Yang, L., Falenty, A., Chaouachi, M., Haberthür, D., and Kuhs, W. F. (2016). Synchrotron X-Ray Computed Microtomography Study on Gas Hydrate Decomposition in a Sedimentary Matrix. *Geochem. Geophys. Geosyst.* 17, 3717–3732. doi:10.1002/2016gc006521

Zheng, G., Huang, Y., and Hua, J. (2017). Sound Speed, Attenuation, and Reflection in Gassy Sediments. *J. Acoust. Soc. Am.* 142, 530–539. doi:10.1121/1.4996440

Conflict of Interest: FA-B and SA are employed by Diamond Light Source Ltd. Diamond Light Source Ltd ("Diamond"), is UK's national synchrotron facility and is a not-for-profit limited company funded as a joint venture by the UK Government as part of UK Research and Innovation (UKRI) through the Science & Technology Facilities Council (STFC) in collaboration with the Wellcome Trust.

The remaining authors declare that the research was conducted in the absence of any commercial or financial relationships that could be construed as a potential conflict of interest.

frontiers | Frontiers in Earth Science

ORIGINAL RESEARCH
published: 13 July 2022
doi: 10.3389/feart.2022.825679

Ocean Dynamics and Methane Plume Activity in Tatar Strait, Far Eastern Federal District, Russia as Revealed by Seawater Chemistry, Hydroacoustics, and Noble Gas Isotopes

Glen Tritch Snyder[1,2], Andrey Yatsuk[3], Naoto Takahata[1], Renat Shakirov[3], Hitoshi Tomaru[4], Kentaro Tanaka[1], Anatoly Obzhirov[3], Aleksandr Salomatin[3], Shinsuke Aoki[5], Elena Khazanova[3], Evgeniya Maryina[3], Yuji Sano[6] and Ryo Matsumoto[2]*

[1]Atmosphere and Ocean Research Institute, University of Tokyo, Kashiwa Campus, Chiba, Japan, [2]Gas Hydrate Research Laboratory, Meiji University, Ikuta Campus, Kanagawa, Japan, [3]Department Geology, V. I. Il'ichev Pacific Oceanological Institute, Vladivostok, Russia, [4]Department Earth Sciences, Chiba University, Chiba, Japan, [5]Fuel Resource Geology Group, Research Institute for Geo-Resources and Environment, National Institute of Advanced Industrial Science and Technology, Tsukuba, Japan, [6]Center for Advanced Marine Core Research, Kochi University, Kochi, Japan

OPEN ACCESS

Edited by:
Miriam Römer,
University of Bremen, Germany

Reviewed by:
Laura Lapham,
University of Maryland, United States
Tamara Baumberger,
Oregon State University, United States

***Correspondence:**
Glen Tritch Snyder
glen@aori.u-tokyo.ac.jp

Specialty section:
This article was submitted to Geochemistry, a section of the journal Frontiers in Earth Science

Received: *30 November 2021*
Accepted: *16 June 2022*
Published: *13 July 2022*

Citation:
Snyder GT, Yatsuk A, Takahata N, Shakirov R, Tomaru H, Tanaka K, Obzhirov A, Salomatin A, Aoki S, Khazanova E, Maryina E, Sano Y and Matsumoto R (2022) Ocean Dynamics and Methane Plume Activity in Tatar Strait, Far Eastern Federal District, Russia as Revealed by Seawater Chemistry, Hydroacoustics, and Noble Gas Isotopes. Front. Earth Sci. 10:825679. doi: 10.3389/feart.2022.825679

This investigation presents methane, noble gas isotopes, CTD, and stable isotopic data for water samples collected in Niskin bottles at Tatar Strait during the spring seasons of 2015 and 2019 onboard the Russian R/V Akademik M.A. Lavrentyev. The results are compared to previous research carried out in 1999 in a nearby portion of the Strait and demonstrate that salinity and temperature can change appreciably. The CTD data from 1999 shows warm surface waters underlain by cold subsurface waters. In contrast, the 2015 data show the CTD data that show warm temperatures and high salinity extending down from the surface well into intermediate waters, while the 2019 data show cold surface waters underlain by even colder subsurface waters. CTD data collected above active gas plume sites along Sakhalin Island's western shore show no substantial difference in temperature or salinity from the non-plume sites, and the methane concentrations at all of the measured sites are significantly above saturation, even in the shallow waters. Hydroacoustic data also suggest the presence of free gas and gas hydrate–coated methane bubbles from the seafloor at least to the base of upper intermediate waters. All of the intermediate and deep Japan Sea Proper waters in Tatar Strait still retain tritiogenic ^{3}He, similar to that observed throughout much of the Japan Sea, indicating limited vertical exchange between these layers and surface waters. An analysis of the δ^{13}C of dissolved inorganic carbon in the seawater shows that positive values are limited to surface waters and that the waters become progressively more depleted in ^{13}C with depth. The results are consistent with research over the past several decades which has shown that ventilation of intermediate and deep Japan Sea Proper water is somewhat limited, while both the temperature and salinity of surface and subsurface water layers within the strait are sensitive to the balance between cold,

less saline waters contributed by the Amur River/Primorye Current from the north and warm, saline waters contributed by the Tsushima Current from the south.

Keywords: methane seep, Tatar Strait, ocean circulation, helium isotopic ratios, stable carbon isotopes, hydroacoustics, salinity, Japan Sea

INTRODUCTION

Background

Recent research at Tatar Strait, located in the northernmost Japan Sea, has indicated that surface water circulation patterns may change significantly from one year to the next, influencing not only the thermal structure of the strait but also potentially influencing the distribution of zooplankton well as the abundance and migration patterns of a variety of macrofaunal species (Tarasyuk et al., 2002; Kobayashi et al., 2009; Velikanov, 2016; Dulenina et al., 2020). To provide a preliminary assessment of the potential for changes in Tatar Strait circulation, we present CTD (conductivity, temperature, and depth) results and gas chemistry obtained on research cruises during the late spring of 2015 and 2019 onboard the Russian R/V Akademik M.A. Lavrentyev (cruises LV-70 and LV-85, respectively). The data is compared to that obtained in 1999 (Postlethwaite et al., 2005) to see if measurable changes have occurred over the past two decades.

For the gas plume sites in eastern Tatar Strait, hydroacoustic data are presented showing the active release of methane from seafloor seeps at the time of sampling. We also present noble gas isotopic data and compare this with earlier noble gas isotopic determinations carried out in non-plume sites of the strait (Postlethwaite et al., 2005). There are several reasons why the noble gas isotopic analysis is a compelling procedure to elucidate ocean circulation in general, as well as the behavior of gases at both hydrothermal and cold seep sites. Mantle-derived gases are more abundant in ^{3}He, whereas radiogenic ^{4}He is generated in uranium- and thorium-rich crustal rocks such as granite. As such, ^{3}He/^{4}He ratios have been used to determine, for example, whether mantle helium is present in methane hydrates located in gas chimneys in the eastern margin of the Japan Sea (Snyder et al., 2020). Adjacent to Tatar Strait, seeps and hydrocarbon wells on Sakhalin Island have shown consistent mantle helium signatures in the southern part of the island with crustal signatures being predominant in the northern part of the island (Lavrushin et al., 1996). Some helium anomalies have been noted in seawater and sediment gas around the plume sites (Shakirov et al., 2016) yet no previous noble gas isotopic studies have determined whether this helium is derived from mantle gases relating to rifting during the opening of the Tatar Trough, or whether the helium is related to sedimentary and granitic rocks of late Cretaceous to early Eocene which were subsequently uplifted during the formation of Sakhalin Island (Glorie et al., 2017) and which by now would have accumulated measurable amounts of ^{4}He.

Anaerobic oxidation of methane (AOM) has been shown to influence the isotopic composition of dissolved inorganic carbon in the pore waters of shallow sediments associated with gas seep sites as has been the well documented in the Japan Sea. Sediment pore waters associated with AOM at gas chimney sites in Umitaka Spur, for example, yield δ^{13}C values of around −40‰ (Hiruta et al., 2015). The fate of methane in the water column is not well understood, although the implications are important given it is the potential of methane as a greenhouse gas. We look at the δ^{13}C

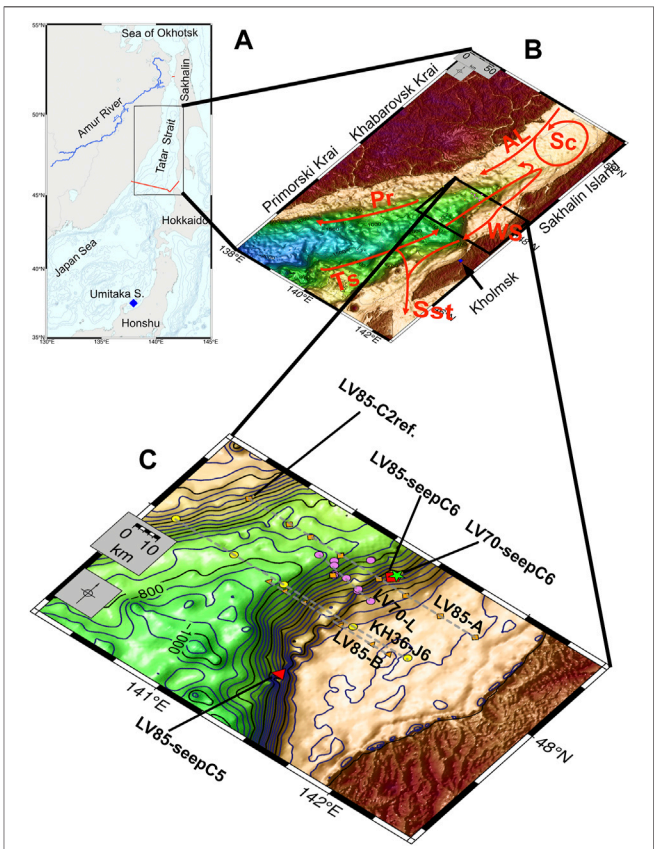

FIGURE 1 | (A) Map of Tatar Strait and the Amur River, relative to the Russian island of Sakhalin and the Japanese islands of Hokkaido and Honshu. The red line shows the current geographical boundary for Tatar Strait. The reference seep samples in this study are from Umitaka Spur in Japan Sea to the south. **(B)** Map of southern Tatar Strait with principal surface currents (After: Andreev, 2020; Pishchal'nik et al., 2010). Pr, Primorye Current; Sst, Soya Strait; WS, West Sakhalin Current; AL, Amur Liman Current; Sc, Schenk Current; Ts, Tsushima Current. Shelf areas (<500 m) of the strait are shaded in light brown. Deeper areas of the strait comprising Tatar Trough (>500 m) are shaded in green and blue. **(C)** Study area is located between 47°30′N and 48°30′N, near the Trough transitions from intermediate to shallow depths. Orange represents transects LV85 A&B sampled in 5/2019 and Violet represents LV70-L transect sampled in 6/2015. Yellow represents sites from KH36 sampled in 7/1999 and reported previously (Postlethwaite et al., 2005). Red represents Plume seep-C5 and seep-C6 from LV85. Green star represents Plume seep-C6 from LV70.

values of dissolved inorganic carbon (DIC) in one plume site in Tatar Strait, to see if methane oxidation in the water column is significantly large to influence the dissolved carbon pool within the water column. In addition, we calculate methane oversaturation in the shallow waters at the sampled plume sites and compare it with a reference site to see if it is significantly higher.

Study Area

Tatar Strait is situated at the northernmost part of the Japan Sea, between Sakhalin Island and the Russian Far Eastern districts of Primorski Krai and Khabarovsk Krai (**Figure 1A**). The northernmost extent of Tatar Strait comprises the 7.2 m deep Amur Estuary at 53.7°N which is located to the south of the Amur River mouth. The southern geographical boundary of Tatar Strait begins at the tip of Sakhalin Island at 45.9°N, extends just south of the Japanese Islands of Rebun and Rishiri, and then continues back up to 45.9°N in Primorski Krai (red line on **Figure 1A**) (Danchenkov, 2004). This boundary is for the most part geopolitical, in that there are no bathymetric features which either distinguish or isolate the southern extent of Tatar Strait from the rest of the Japan Sea. Water depths in the central southern portion of the strait are just over 2000 m, forming the Tatar Trough (blue- and green-shaded areas in **Figure 1B**), whereas north of 48.5° the Tatar Strait narrows and the waters are all shallower than 500 m (tan-shaded areas in **Figure 1B**).

Water circulation into the strait is limited to the Tsushima Current, which flows northward along the length of the Japan Sea, and to the Amur Liman Current, which flows from the mouth of the Amur River into the northern reaches of Tatar Strait (**Figure 1B**). The outflow of waters from the strait is either back into the Japan Sea along the western margin by means of the Primorye Current, or through Soya Strait and into the Okhotsk Sea, between the islands of Sakhalin and Hokkaido by means of the West Sakhalin Current. Internal circulation within the strait is quite variable but includes the West Sakhalin and the Schrenk currents (Andreev, 2018; Pishchal'nik et al., 2010). As will be discussed, the vertical structure of water masses in Tatar Strait can also be influenced by the variable influx of waters from either the Amur Liman Current, or from the Tsushima Current. This influence can extend through the shallow surface and subsurface waters, all the way down to the upper intermediate waters (Danchenkov, 2004).

Our study area is located between 47.5°N and 48.5°N in Tatar Strait (**Figure 1C**), including the eastern margin of the strait where abundant gas seep plumes are located, deeper central portion of the trough, and seep-free portion of the trough on the eastern margin (Shakirov et al., 2019; Yatsuk et al., 2020). The water depth is sufficient in the study areas to preserve the vertical water mass structure (Danchenkov, 2004), and the study area also includes the northern portion of the deep Tatar Trough. There are four sampling transects (**Figure 1C**) running roughly parallel from north to south: LV85-A sampled from 5/21 to 5/22, 2019; LV70-L sampled from 6/21 to 6/24, 2015; KH36-J6 sampled from 7/28 to 7/29, 1999; and LV85-B sampled in 5/23, 2019. A number of areas off the transects but above active gas plumes from the eastern margin of the strait were sampled around the same time as the transects, including LV85-seepsC5, LV85-seepC6, and LV70-seepC6. To provide a non-seep reference for comparison, site LV85-C2ref., located on the farthest west on the northernmost transect was selected for more detailed study.

SAMPLING AND ANALYSES

Hydroacoustic observations were carried out during both the June 2015 (LV70) and May 2019 (LV85) cruises using the sonar system of the R/V Akademik M.A. Lavrentyev, which consists of echo sounders Sargan-EM and ELAC, sonar Sargan-GM, a multichannel digital registration system, and a GPS system. The hydroacoustic system provides simultaneous registration of echo signals up to four independent channels with frequencies of 12, 20, and 135 kHz (Salomatin et al., 2014). At a time of acoustic measurements, accurate vessel's coordinates were determined with GPS and using the operating frequencies of 20 kHz with a beam width of 10°.

During both the LV70 and LV85 cruises, a Sea-Bird SBE-9 CTD and Niskin Rosette system were deployed. Water column salinity, temperature, and depth data were recorded over 1 s intervals and processed using Seasave ver. 7.26.2.13 (**Supplementary Data**). Seawater turbidity was also determined using a SeaPoint Turbidity Meter which operates with an 880 nm light source at scattering angles between 15° and 150°, with peak sensitivity covering approximately 90°. Turbidity measurements are reported in Formazin Turbidity Units (FTU). Upon shipboard recovery, water from the Niskin bottles was immediately transferred into 68 ml glass sample bottles which were hermetically sealed. The samples were then analyzed onboard the R/V Akademik M.A. Lavrentyev for dissolved gases (methane, hydrocarbon gases, carbon dioxide, nitrogen, and oxygen) using shipboard gas chromatographic instrumentation as described in Vereshchagina et al. (2013) and Shakirov et al. (2019). In order to create headspace gas in the 68 ml bottles, 12 ml high-purity helium was injected through the rubber septum. After this, samples were shaken on a LS-110 mixing device to reach equilibrium between the liquid and the gas phases. After mixing, an aliquot of the gas phase (4 ml) was taken up by a syringe for a gas chromatographic analysis. Onboard gas analysis was performed with a "KRISTALLUX-4000M" gas chromatograph ("Meta-Chrom", Yoshkar-Ola, Russia). The chromatograph has three detectors: two thermal conductivity (TCD) and one flame ionization (FID) detectors. FID allows one to study the quantitative content of hydrocarbon composition (C_1–C_6) with a sensitivity of 10^{-6}%. Inorganic gases such as nitrogen, oxygen, and carbon dioxide, as well as methane with a concentration of more than 1%, are analyzed on a TCD, the sensitivity of which is 0.01%. The gas chromatograph had two packed columns: HayeSep R column, 2.5 m length, 2.5 mm i.d., 80/100, "Meta-Chrome"; NaA column, 3 m length, 3 mm i.d., 60/80. The temperature program of the chromatographic column was isothermal—50 °C, 5 min hold. Temperature detectors were set at 195 °C for the evaporator and 160 °C for the carrier gas

which was ultrapure helium. The carrier gas flow rate was set at 20 ml/min for helium, 30 ml/min for hydrogen, and 250 ml/min for air. Calibration gas mixtures of methane were manufactured by PGS Service (1, 10, 20, 100, and 1000 ppm and 1%). The relative error of measurements did not exceed 5%. The laboratory gas geochemistry, POI FEB RAS is certified for measurements by Rosstandart (Federal Agency on Technical Regulating and Metrology, Russia). The concentrations of methane dissolved in seawater were calculated by technique described by Yamamoto et al. (1976) and modified by Wiesenburg and Guinasso (1979), using the solubility constants of the gases and are reported in nmol/L (**Table 2**). Oxygen concentrations were used to determine if the samples were subject to air contamination, and in one case (**Table 2**, LV85-5–150 m) the sample results were discarded and not considered in the figures or data analysis.

In addition to the aforementioned sampling and analyses, two additional sample splits were collected during LV85 from seepC6 and seepC5 (**Figure 1C**). Seawater samples were transferred directly from the Niskin bottles to copper tubing for later noble gas analysis using the procedures described in Takahata et al. (2008). In addition, for seepC5, 100 ml of seawater aliquots were filtered and introduced into evacuated flasks which each contained 100 mg sulfamic acid using a method adapted from Atekwana and Krishnamurthy (1998) and also employed at submarine seep sites by Hiruta et al. (2015) for later determination of the $\delta^{13}C$ values for dissolved inorganic carbon (DIC). Solid, reagent-grade sulfamic acid (HOS_2NH_2) was used, rather than phosphoric acid employed in the method of Atekwana and Krisnamurthy (1998), due to its ease in handling under shipboard conditions (Kawagucci et al., 2013). In addition, during cruise LV-85, the atmospheric methane concentrations were determined using a Picarro gas concentration analyzer so that the flux of methane from shallow water to the atmosphere could later be calculated above the two sites LV85-seepC6 and LV85-seepC5 as well as above a reference site (LV85-C2ref.) shown in **Figure 1C**.

At the end of the cruise, both the sealed copper tubes and the glass flasks for the DIC analysis were shipped from Vladivostok to the Atmosphere and Ocean Research Institute (AORI), University of Tokyo, Japan for analysis at the Noble Gas Isotope Laboratory. For noble gas isotopic composition, the dissolved gas in the seawater was transferred from the copper tubing using methods described in Takahata et al. (2008). The procedures for the noble gas isotopic analysis are described in Sano and Nakjima, (2008) and Park et al.(2006). Helium and neon were separated from the gas using a combination of charcoal traps kept at liquid nitrogen temperature as well as hot titanium getters. The ratios of $^{20}Ne/^{4}He$ were determined using a Pfeiffer Vacuum Prisma quadrupole mass spectrometer. Helium was separated from neon using a 40K charcoal trap. Helium isotopic composition was determined using a GV Instruments Helix SFT noble gas mass spectrometer, and the ratios of $^{3}He/^{4}He$ were normalized to the air ratio (R_A=1.4 x 10^{-6}). Precision of the $^{3}He/^{4}He$ ratios is ± 0.01 R_A. The results are listed in **Table 2**. Of the 18 samples analyzed from the gas plumes, two samples showed signs of atmospheric contamination with $^{20}Ne/^{4}He$ similar to the air ratio of 3.14. The noble gas isotopic composition was not further considered for the two air-contaminated samples which were LV85-seepC5–12 (0 m water depth) and LV85-seepC6–2 (316 m water depth) due to air contamination.

For the stable isotopic composition of DIC, the gas sample in the headspace of the sampling bottle (5–10 ml), including CO_2 liberated from DIC, was transferred to a glass vial, which was pre-filled with pure helium. The carbon isotope ratio of samples was then measured with a conventional continuous flow mass spectrometer (Delta V plus, Thermo Fisher Scientific). The carbon isotope ratio is expressed as conventional delta notation ($\delta^{13}C$) with respect to Pee Dee Belemnite (PDB). NBS-19 ($\delta^{13}C$=1.95‰) served as the standard material to determine $\delta^{13}C$ of the sample. Repeated analyses of NBS-19 yielded the reproducibility of $\delta^{13}C$ measurement better than ± 0.2‰. After measuring the reference CO_2 gas three times, the sample CO_2 gas was analyzed six times. The standard deviation for sample gas varied from 0.02‰ to 0.1‰, depending on the intensity.

RESULTS

In order to provide a consistent depth reference, the results are presented in the context of the eight recognizable water masses, as described by Danchenkov (2004), which provide the vertical seawater structure found in Tatar Strait (**Figure 2**) and are consistent with water layers found in the Japan Sea in general. The water masses have been numbered in the figures and discussion as follows: a surface water mass (I) which generally extends down to around 40 m. In areas where the Tsushima Current is present, surface water (I) may be subtropical and saline (>34.1 Practical Saline Units, PSU). In other areas where the surface water is influenced more by the Amur and Primorye currents, surface water (I) is subarctic, cold, and has low salinity. A subsurface water mass (II) is generally restricted to the upper 75 m and may consist of either subtropical or subarctic water and depending on which is denser than the prevailing surface waters. Below the surface (I) and subsurface (II) waters are intermediate waters (III). Just as the Japan Sea in general may be characterized by intermediate and central waters (Jenkins, 2008), Tatar Strait intermediate waters are subdivided into upper (IIIa) and lower (IIIb) water masses. The upper (IIIa) is slightly warmer with low-salinity (33.96–34.04 PSU, 3–4 °C), while the lower (IIIb) is colder and with high-salinity (>34.06 PSU, 1–2 °C). The relative thickness of IIIa and IIIb is variable, but the combined intermediate water mass extends from 75 to 300 m. Below 300 m is the deep Japan Sea Proper water mass (IV) with temperatures indistinguishable from those of the rest of the Japan Sea deep waters at 0.12–1.2 °C and salinities of 34.05–34.08 PSU. Finally, a slightly warmer bottom water mass (V) can be present just above the seafloor, but it is found only in the deepest parts of the Tatar Trough located to the south of our study area and need not be considered in this study.

Hydroacoustic Flares at Methane Seep Sites

Methane seeps from the eastern margin of Tatar Strait are readily identified by hydroacoustic flares, or areas of high reflection intensity in the echograms which are shown plotted against time (**Figure 3**), and are situated at depths of 300–350 m. The hydroacoustic flare at the site LV85-seepC6 was observed in 2019 (**Figure 3A**) and is from the same gas chimney structure as the site LV70-seepC6 in 2015 (**Figure 3B**), while the site LV85-seepC5 is situated along the same margin, but to the south (**Figure 3C**). The reference site LV85-C2ref. is situated 64 km to the west of plume LV85-seepC6, (**Figure 1C**) along transect LV85-A and does not show any evidence of flaring at all (**Figure 3D**). Where flares are apparent, the highest reflection intensity is in deep Japan Sea Proper water (IV) and attenuates as the gas rises through lower intermediate water (IIIb), disappearing completely toward the top of upper intermediate water (IIIa) and subsurface water (II).

In addition, all of the echograms in this study reveal a number of reflective areas or sound scattering layers (SSL), including the reference site, (**Figure 3D**) which do not appear to be related to gas seep activity or rising gas bubbles. The SSL are most intense in the Surface (I) and Subsurface (II), although similar layering is observed in lower intermediate (IIIb) water.

Salinity and Temperature Trends Along the Transects Crossing the Strait

Depth profiles were constructed with salinity (in Practical Salinity Units, PSU) and temperature (^{o}C) as well as turbidity (in Nephelometric Turbidity Units, NTU). The data from the 2015 and 2019 cruises in this study (**Supplementary Data**), as well as those of those of the 1999 cruise, (Postlethwaite et al., 2005) are plotted against depth (**Figures 4A,B**). Turbidity was not available from the 1999 study, so the depth profile for turbidity only considers data from 2015 to 2019.

As can be observed with the temperature depth profiles (**Figure 4A**), samples show a strong temperature minimum at the boundary between surface (I) and sub-surface (II) waters in 1999 (KH36) and 2019 (LV85). This boundary appears to be missing in 2015 (LV70). In addition, with the 2015 sites, there is an inflection at or just above the boundary between upper (IIIa) and lower (IIIb) water masses. Both 1999 (KH36) and 2015 (LV70) waters show higher temperatures in the surface and subsurface waters than that observed in 2019 (LV85). These differences decrease with depth, but do extend all the way to the base of the lower intermediate waters (IIIb). For each of the given years, there are no apparent differences between the different cross-basin transects, nor is there an apparent difference between seep temperatures and the temperatures of non-seep transect sites.

Salinity increases rapidly with depth in the surface waters (**Figure 4B**). For both 1999 (KH36) and 2015 (LV70), the salinities largely coincide as opposed to the less saline 2019 (LV85) samples. For both KH36 and LV70, salinities reach maximum values in the shallow subsurface (II), as opposed to the LV85 sites where salinity continues to increase until the base of the upper intermediate (IIIa) waters. Turbidity is, in all cases, greatest in the deepest waters of all sites, regardless of what depth that actually is (**Figure 4C**). The 2015 LV70 transect-C sites show an increase in turbidity with depth in surface waters (I), followed by a decrease in the sub-surface (II), followed by fairly constant turbidity until the waters near the bottom. This increase coincides with the area of SSL in the hydroacoustic data associated with the nearby plume (**Figure 3C**), which will be further discussed.

A cross-plot of salinity versus temperature (**Figure 4D**) clearly shows how the water compositions converge in the deeper Japan Sea Proper waters (IV), but diverge greatly in the shallow subsurface (II) and surface waters (I). In addition to the CTD data, isopycnal lines were calculated using the UNESCO formula (Massel, 2015) and plotted in the same figure. The most recent waters from 5/2019 (LV85) trend toward low-salinity, low-temperature sub-arctic waters. The next most recent waters from 6/2015 (LV70) show the greatest influence of shallow, high-salinity subtropical waters. Waters from two decades previous, in 7/1999 (KH36), are situated in-between those of the two most recent cruises. It is interesting that shallow and intermediate waters can vary greatly from year to year, but the overall density trend with depth remains constant with low-salinity and cold shallow and intermediate water masses having nearly the same density as high-salinity warm waters from the same water masses.

In order to visually evaluate the spatial distribution of temperature and salinity in the water column, Generic Mapping Tools (Wessel et al., 2019) was used to interpolate between the CTD sites for transects in 2019, 2015, and 1999 (**Figures 5**, **6**; **Supplementary Figures S1, S2**). The seafloor position was mapped according to Gebco's Bathymetry Data (IOC, IHO and BODC, 2003). The transects studied include the northernmost deep portion of the trough (**Figure 1C**).

Cross-basin temperature profiles (**Figure 5**) clearly show layering consistent with that of the depth profile in **Figure 4A**. Both 2019 (LV85) sections (**Figures 5A,B**) show a warm surface water mass underlain by cold sub-surface waters and slightly warmer intermediate waters underlain by colder deep waters. The 1999 section (**Figure 5C**) shows surprisingly little difference when compared to the corresponding nearby 2019 section (**Figure 5B**), despite two decades having elapsed between the two cruises. The surface waters are warmer for 1999 (as seen in **Figure 4B**), perhaps since they were sampled in July rather than in May, but temperatures in the sub-surface waters and deeper are not discernible from 2019. Very striking differences are observed in 2015, however, where there are high temperatures which extend from the surface through the subsurface, and even somewhat into the intermediate waters (**Figures 4A**, **5D**). Data from the 2019 transects were combined with the data from the two plume sites of that year to see anomalies in surface and bottom waters (**Supplementary Figure S1**). In general, a plume of somewhat cooler waters (by about 2 $^{\circ}$C) seems to extend over the surface waters from north to south, just west of the slope on the Sakhalin Island side of the trough. Bottom waters are uniformly cold at near-

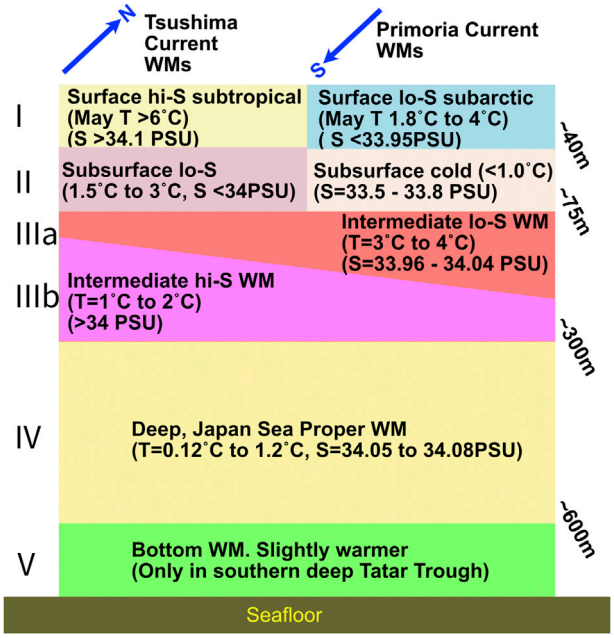

FIGURE 2 | Vertical structure of in Tatar Strait seawater showing eight discernible water masses (after Danchenkov, 2004). Surface (I), subsurface (II), and intermediate (IIIa, b) water masses are influenced by changes in the relative amounts of water from the southbound Primorye Current and the northward migrating Tsushima Current. Japan Sea Proper water (IV) is generally found below 300 m and shows less variation. Slightly warmer bottom waters (V) are found only in the part of Tatar Trough to the south of our study area.

zero temperatures throughout the sampled area, with only slightly warm bottom waters in the shallowest site which is closest to the Sakhalin coast.

Cross-basin profiles of salinity also demonstrate how different the 2015 data is. Both of the 2019 profiles (**Figures 6A,B**) show very dilute surface waters, underlain by somewhat more saline subsurface waters, and intermediate waters that are slightly less saline than the deep waters. Once again, the 1999 waters from Postlethwaite et al. (2005) are not appreciably different (**Figure 5C**) from those of 2019. In contrast, the 2015 profile (**Figure 5D**) shows saline surface waters, very saline subsurface waters, slightly less saline intermediate waters, and finally saline deep waters. The most striking feature in the 2015 profile is the highly saline subsurface waters, clearly influenced by the subtropical Tsushima Current. As with temperature, the interpolated salinity values from 2019 were also mapped for surface and bottom waters (**Supplementary Figure S2**). On the surface, areas of slightly greater salinity are observed both to the west and to the east of the low-temperature surface waters (shown in **Supplementary Figure S1A**); however, a clearly-lineated low-salinity plume is not observed. Bottom waters are uniformly more saline (**Supplementary Figure S2B**), with the exception of slightly less saline waters on the margins of Sakhalin Island. Still, in 2019, surface waters are less saline than bottom waters, even along the coastal margin.

Plume Site Depth Trends and Methane Concentrations

One point of interest with submarine gas seeps is the depth of hydrate stability within the water column in the area where the gas is ascending. The phase boundary between pure methane hydrate and methane gas in seawater was calculated using the following simplified relationship (Dickens and Quinby-Hunt, 1994):

$$T^{-1} = 3.79 \times 10^{-3} - 2.83 \times 10^{-4} (logP), \quad [1]$$

where T is temperature in K, P is pressure in MPa, and the pressure gradient is assumed to be 1 x 10^{-2} MPa/m.

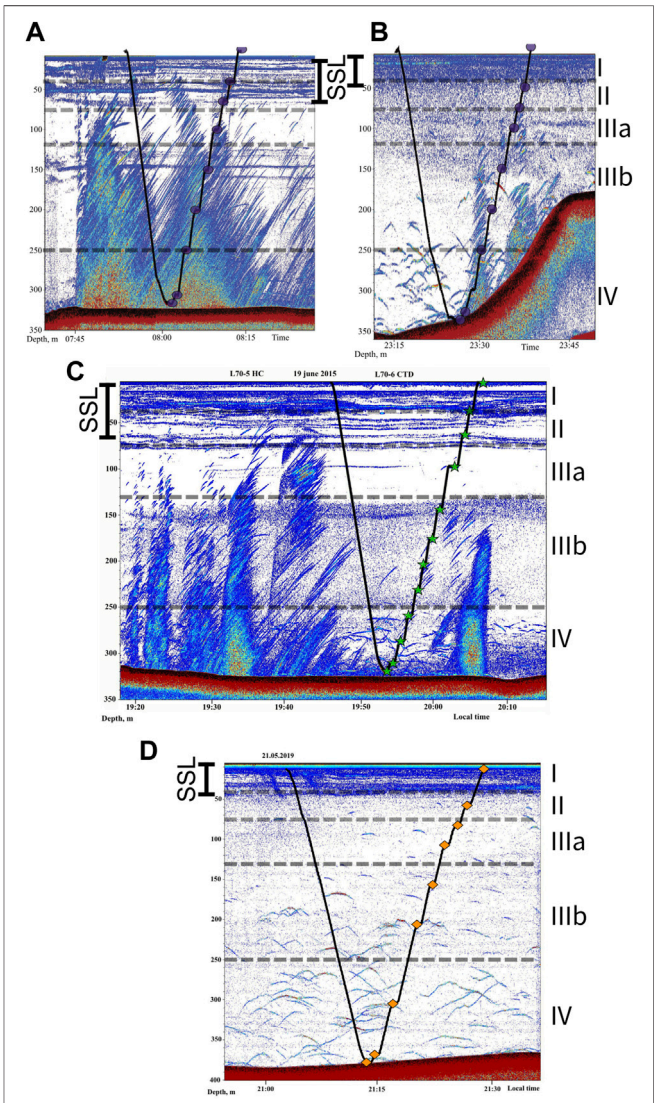

FIGURE 3 | (A) Hydroacoustic data, depth versus time, for LV85-seepC6, showing the gas plume position as well as the position of the CTD during sampling during 5/2019. Sound scattering layers (SSL) infer the presence of zooplankton in the upper 50–70 m and possibly deeper. **(B)** Hydroacoustic data for LV85-seepC5 sampled during 5/2019. **(C)** Hydroacoustic data for LV70-seepC6, sampled during 6/2015 adjacent to the same location as LV85-seepC6. **(D)** Hydroacoustic data for reference site LV85-C2ref., located on the western margin where there are no gas plumes.

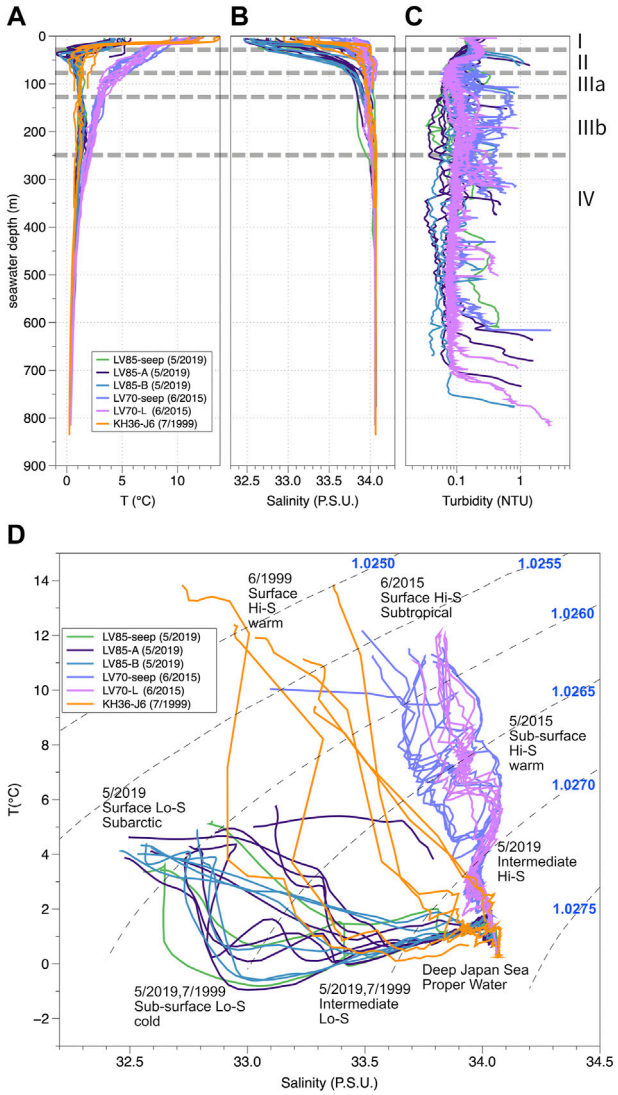

FIGURE 4 | Water column salinity and temperature profiles determined from CTD data. Isopycnal lines (g/cm^3) calculated from the UNESCO formula (Massel, 2015). Appreciable changes have occurred from between the three sampling years in shallow to upper intermediate waters. **(A)** Temperature profiles show warm surface waters (I) in 1999 and 2015. Cold subsurface waters (II) are observed in both 1999 and 2019. Temperatures from each sampling year converge in the Deep Japan Sea Proper water mass (IV). In both 2015 and 2019, there is no appreciable difference in the temperatures was observed for seep and non-seep sites. **(B)** Salinity profiles show the highest values in lower surface (I) and subsurface waters (II) collected in 2015 and 1999. As with temperature, there is that are largely coincident in lower intermediate (IIIb) and Japan Sea proper (IV) waters. **(C)** Turbidity is generally greatest in samples closest to the seafloor; however, some inflections occur between water layers. **(D)** Temperature-salinity plot showing that while samples from 1999, 2015, and 2019 diverge in surface (I) and sub-surface water masses (II), they still fall into similar density fields for any give depth. The samples from all three years converge with depth in the Japan Sea Proper water mass (IV).

The CTD data is matched with intervals where the Niskin bottle water was sampled (**Table 1**), in order to provide a direct comparison with gas chemistry and isotopic composition (**Table 2**). In order to compare seawater above the plume sites (LV70-seepC6, LV85-seepC6, and LV85-seepC5), the reference site located at a similar depth on the western margin of Tatar Strait is also included (LV85-C2ref., **Figure 1C**), as well as the non-plume sites with noble gas data sampled in 1999 (Postlethwaite et al., 2005). Also presented for comparison are data from a major plume site Umitaka Spur (Saegusa et al., 2007; Takahata et al., 2008), which is located in the Japan Sea just offshore Niigata Prefecture and 1200 km to the southeast of our study area (**Figure 1A**), collected in 5/2005. As can be observed (**Figure 7A**), the temperatures for all of the sites converge near the top of the Japan Sea Proper water mass (IV), between 250 and 300 m. It is also apparent that waters in the deep Japan Sea Proper waters (IV) can host stable gas hydrate, including at the base of plume sites LV70-seepC6, LV85-seepC5, and LV85-seepC6 as well as through much of the water column in the central portion of Tatar Trough and in Umitaka Spur. At depths of ~900 m, as observed in Umitaka Spur, hydrate can be stable in seawater at temperatures below 10 °C. This is much warmer than the deep Japan Sea Proper (IV) waters at ~0.4 °C, which could host rising gas hydrate bubbles to depths shallow as 313 m.

Both temperature (**Figure 7A**) and salinity (**Figure 7B**) were combined with pressure to calculate water density in g/cm^3 (**Figure 7C**) using the UNESCO formula (Massel, 2015). Unlike temperature and salinity which can vary significantly in surface (I) and subsurface (II) between sampling years and localities, density largely coincides between the different sampling years and localities. From surface (I) to subsurface (II) there is a rapid increase in density followed by a gradual, nearly linear increase in density from subsurface (II) to deep Japan Sea Proper waters (IV).

Methane concentrations for the plume and reference sites are shown plotted against depth (**Figure 7D**). Many of the LV85 plume samples are not appreciably different from the reference site (LV85-C2Ref.), with the exception of some elevated values near the top of the deep Japan Sea Proper waters (IV) and a few high values in the upper intermediate (IIIa) and lower intermediate (IIIb) waters. Water sampled in 2015 at the site LV70-C6, however, shows uniformly higher values than the LV85 plumes and reference site, with one extremely high methane concentration in the subsurface (II).

As has been documented previously (Shakirov et al., 2019), methane concentrations can exceed saturation around the Tatar Strait plume sites. To determine to what degree oversaturation is present, the oversaturation ratio (SR) for methane (Kudo et al., 2018) was determined as follows:

$$SR(\%) = ([[CH4]_w/[CH4]_a] - 1) \times 100\%, \quad [2]$$

where $[CH4]_w$ and $[CH_4]_a$ are the observed concentration in seawater and the calculated saturation concentration of dissolved atmospheric methane in seawater, respectively. The value of $[CH_4]_a$ in nmol/L is calculated as follows:

$$ln[CH_4]_a = ln f_G + A_1 + A_2(100/T) + A_3 ln(T/100) + A_4(T/100) + S[B + B(T/100) + B(T/100)^2], \quad [3]$$

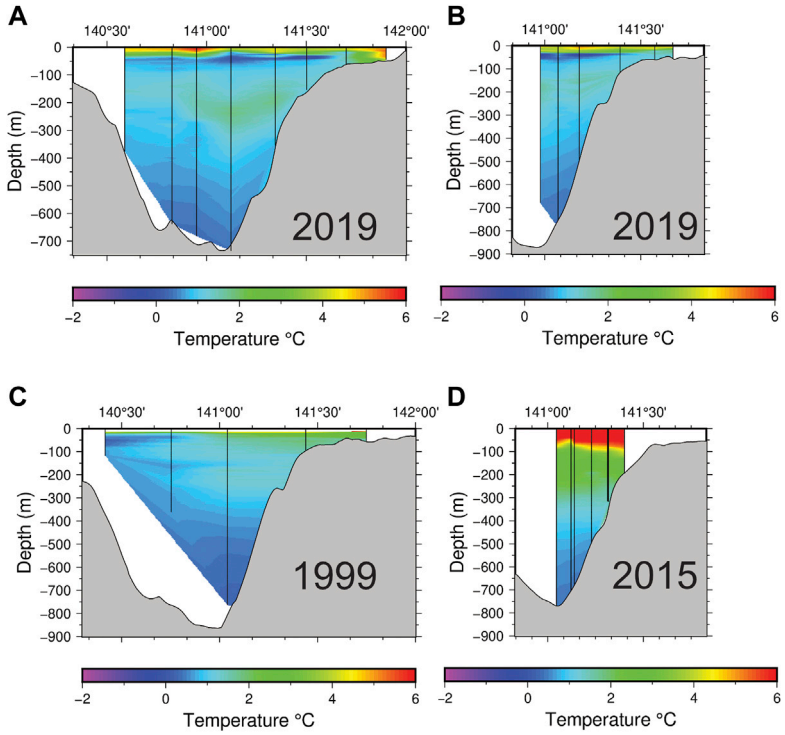

FIGURE 5 | (A) Cross-basin temperature transect in 5/2019, showing shallow warm surface waters underlain by cold subsurface, slightly warmer intermediate and cold deep waters. **(B)** Shorter transect to the south, showing similar thermal layering. **(C)** Similar cross-basin transect from 7/1999, shows cooler waters in the shallow western portion of the basin, along the Primorye coast and warmer along the Sakhalin coast. **(D)** Extremely warm shallow and intermediate waters in 6/2015.

where f_G is the concentration of atmospheric CH_4 in ppmv, T is seawater temperature in K, S is salinity in PSU, and the coefficients for solubility concentration in nmol/L are (Wiesenburg and Guinasso, 1979) A_1 = −415.2807, A_2 = 596.8104, A_3 = 379.2599, A_4 = −62.0764, B_1 = −0.05916, B_2 = 0.032174, and B_3 = −0.0048198. The atmospheric f_G is generally around 2 ppmv. Actual atmospheric values were measured onboard the R/V Akademik M.A. Lavrentyev during cruise LV85 at the time of Niskin bottle sampling (**Supplementary Table S3**) and range from 1.89 ppmv to 2.02 ppmv. For LV70-seepC6, we assume the same atmospheric concentration for LV85-seepC6 of 1.97 ppmv. For Umitaka Spur, we assume an atmospheric f_G = 1.89 ppmv (Kudo et al., 2018). Both methane concentrations in nmol/L and the derived SR are reported in **Supplementary Table S1**. Methane gas concentrations were not measured for the 1999 KH-76 cruise (Postlethwaite et al., 2005).

It is worth noting that this approach, as applied to this study and others (e.g., Kudo et al., 2018) does not contain a pressure term and only calculates the percent saturation relative to surface conditions. Nonetheless, it does provide a means of comparison over time and between sites which integrates measured headspace gas, seawater temperature, and salinity. Using this approach, the waters above the gas plumes as well as the reference sites show positive oversaturation ratios throughout the range of measurement depths (**Figure 7E**), meaning gas would exsolve from such water when brought to the surface. In some cases, a shallow maximum oversaturation occurs at 50–75 m depth, either in the subsurface (II) or the top of the upper intermediate (IIIa) waters. For the 2019 reference site LV85-C2ref., the maximum is 205% at 50 m. For the 2015 plume gas sample LV70-seepC6, the corresponding shallow maximum oversaturation value is 5212% at 60 m. Other sites have deeper maximum saturation ratios, either near the seafloor or at the boundary between upper and lower intermediate (IIIb) waters, or between lower intermediate (IIIb) waters and Japan Sea Proper (IV) waters. For example, at 305 m depth LV85-seepC6 reaches a methane oversaturation ratio of 2386%, while at 200 m LV85-seepC5 reaches an oversaturation ratio of 3740% (**Table 2**).

Noble Gas Isotopic Composition in Seawater Above plumes and Reference Sites

The noble gas isotopic composition was determined for two plume sites in Tatar Strait from cruise LV85 (**Table 2**), which we compared with the previously mentioned Umitaka Spur plume site (Saegusa et al., 2007; Takahata et al., 2008). Because the availability of noble gas sampling materials was somewhat limited on cruise LV85, we did not sample the reference site but instead compared our results with the 1999 noble gas determinations from non-plume sites (Postlethwaite et al., 2005).

Seawater in the Japan Sea generally does not show measurable amounts of mantle helium (Postlethwaite et al., 2005; Takahata

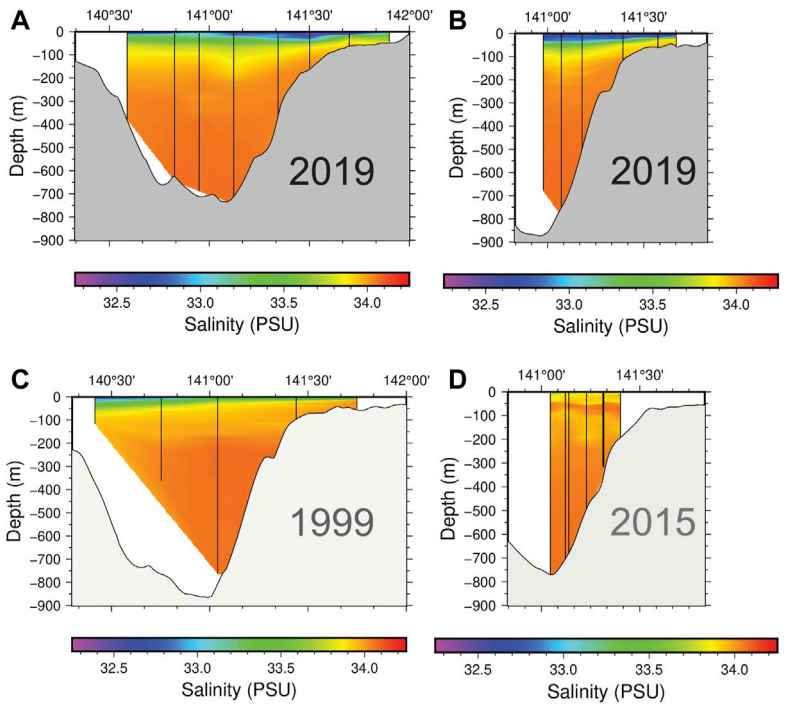

FIGURE 6 | Salinity values in southern Tatar Trough. **(A)** Cross-basin profile in 5/2019 show less saline surface, sub-surface, and upper intermediate waters. **(B)** Transect to the south from 5/2019 shows similar layering. **(C)** Profile from 7/1999 shows the less saline surface water mass and subsurface low salinity water mass are thicker on the Primorye side of the basin than the Sakhalin Side. **(D)** Short transect from 6/2015 shows predominantly high salinity waters, particularly in the subsurface.

et al., 2008) and the samples in this study are no exception. Since the changes in $^3He/^4He$ ratios are small, it is convenient to refer to the helium isotopic composition using delta notation.

$$\delta^3He = \frac{\left[\frac{^3He}{^4He}\right]_{samp.} - \left[\frac{^3He}{^4He}\right]_{air}}{\left[\frac{^3He}{^4He}\right]_{air}} X\ 100\%, \qquad [4]$$

where $R_{air} = {}^3He/{}^4He_{air} = 1.4 \times 10^{-6}$.

We report both air-normalized $^3He/^4He$ ratios and δ^3He values for the plumes and reference sites. Depth profiles (**Figure 7F**) show a near-linear increase in δ^3He which is observed for both the Umitaka Spur and Tatar Strait samples, starting at air-saturated seawater values ($\delta^3He = -1.5\%$) in surface (I) waters to 5%–7% in the upper portions of Japan Sea Proper (IV) waters. The δ^3He values for Tatar Strait waters increase more rapidly with depth than the Umitaka Spur values, reaching maximum values at 200–300 m above the seafloor. These increases are fairly typical of Japan Sea and elsewhere and are not due to the admixture of relatively ^3He-enriched mantle gas from the seafloor, but rather contributions of tritiogenic ^3He produced during the surface nuclear weapons testing in the mid-1960's. The presence of tritiogenic ^3He provides some indication of the limited exchange of water masses between shallow surface (I) and subsurface (II) waters, with the older, deeper intermediate (III) and Japan Sea Proper (IV) water masses (Postlethwaite et al., 2005; Jenkins, 2008; Takahata et al., 2008; Gamo et al., 2014). Tritium undergoes β-decay producing both a β electron (e−) and an antineutrino ($\bar{\nu}$):

$$^3H \rightarrow {}^3He + e^- + \bar{\nu}, \qquad t_{\frac{1}{2}} = 12.43yr. \qquad [5]$$

Given the short half-life, practically all of the anthropogenic tritium from the 1960's has decayed to ^3He. Although tritium analyses were not measured in this study, previous studies have shown the correlation between ^3H and δ^3He values in intermediate and deep waters which are similar to those found in this study (Postlethwaite et al., 2005; Takahata et al., 2008).

The ratios of $^{20}Ne/^4H$ also give some indication of the amount of helium added to air-saturated seawater from sources such as mantle gases and radiogenic sources. As will be shown, however, the ratios are also temperature dependent and at lower temperatures, the solubility of helium increases more relative to neon. Salinity also has an influence, although in the conditions of this study, much less than temperature. A useful method for discussing the relative amount of neon and helium is a deviation from the equilibrium solubility ratio under the observed temperature and solubility conditions (after Nicholson et al., 2011).

$$\Delta\frac{^{20}Ne}{^4He} = \frac{\left[\frac{^{20}Ne}{^4He}\right]_{samp.} - \left[\frac{^{20}Ne}{^4He}\right]_{eq.}}{\left[\frac{^{20}Ne}{^4He}\right]_{eq.}} X\ 100\%. \qquad [6]$$

The equilibrium solubility ratios $\left[\frac{^{20}Ne}{^4He}\right]_{eq.}$ were calculated using the Bunsen solubilities for each gas using experimentally

TABLE 1 | Location and depth of samples collected with Niskin bottles, as well as corresponding temperature and salinity from CTD. Density is calculated from pressure, temperature, and salinity (Massel, 2015).

Cruise	Site	Date	Long.	Lat.	Depth	Temperature	Salinity	Density (ρ)
			(E)	(N)	(m)	(˚C)	(PSU)	(g/cm^3)
Tatar Strait Slope Seeps [1]								
LV-85	C5	05/23/2019	141.367	47.722	0	4.331	32.593	1.025990
LV-85	C5	05/23/2019	141.367	47.722	50	1.064	33.875	1.027290
LV-85	C5	05/23/2019	141.367	47.722	75	1.165	33.933	1.027330
LV-85	C5	05/23/2019	141.367	47.722	100	1.582	34.035	1.027383
LV-85	C5	05/23/2019	141.367	47.722	150	1.356	34.051	1.027412
LV-85	C5	05/23/2019	141.367	47.722	200	0.969	34.057	1.027432
LV-85	C5	05/23/2019	141.367	47.722	250	0.969	34.057	1.027442
LV-85	C5	05/23/2019	141.367	47.722	326	0.885	34.058	1.027448
LV-85	C5	05/23/2019	141.367	47.722	336	0.885	34.058	1.027448
LV-85	C6	05/23/2019	141.392	47.982	0.15	3.382	32.556	1.026053
LV-85	C6	05/23/2019	141.392	47.982	40	−0.708	33.128	1.026781
LV-85	C6	05/23/2019	141.392	47.982	75	0.303	33.585	1.027103
LV-85	C6	05/23/2019	141.392	47.982	100	1.079	33.868	1.027284
LV-85	C6	05/23/2019	141.392	47.982	150	1.622	33.993	1.027346
LV-85	C6	05/23/2019	141.392	47.982	200	1.658	34.035	1.027377
LV-85	C6	05/23/2019	141.392	47.982	250	1.233	34.033	1.027405
LV-85	C6	05/23/2019	141.392	47.982	306	0.841	34.000	1.027404
LV-85	C6	05/23/2019	141.392	47.982	316	0.839	34.038	1.027435
LV-70	C6	06/19/2015	141.392	48.246	0	10.731	33.617	1.025903
LV-70	C6	06/19/2015	141.392	48.246	34	7.335	33.826	1.026598
LV-70	C6	06/19/2015	141.392	48.246	60	4.461	33.879	1.026998
LV-70	C6	06/19/2015	141.392	48.246	95	3.874	33.999	1.027154
LV-70	C6	06/19/2015	141.392	48.246	142	3.001	33.991	1.027232
LV-70	C6	06/19/2015	141.392	48.246	174	2.373	33.990	1.027286
LV-70	C6	06/19/2015	141.392	48.246	202	2.307	34.019	1.027314
LV-70	C6	06/19/2015	141.392	48.246	230	2.157	34.025	1.027331
LV-70	C6	06/19/2015	141.392	48.246	258	2.070	34.027	1.027339
LV-70	C6	06/19/2015	141.392	48.246	286	1.553	34.037	1.027387
LV-70	C6	06/19/2015	141.392	48.246	310	1.359	34.041	1.027404
LV-70	C6	06/19/2015	141.392	48.246	319	1.267	34.042	1.027411
Tatar Strait W. Slope References Site [1]								
LV85	C2	5/21/19	140.5895	48.20316	0	4.644	32.498	1.025882
LV85	C2	5/21/19	140.5895	48.20316	50	0.630	33.671	1.027154
LV85	C2	5/21/19	140.5895	48.20316	75	0.942	33.823	1.027257
LV85	C2	5/21/19	140.5895	48.20316	100	1.043	33.874	1.027291
LV85	C2	5/21/19	140.5895	48.20316	150	1.190	33.936	1.027331
LV85	C2	5/21/19	140.5895	48.20316	200	1.059	33.988	1.027381
LV85	C2	5/21/19	140.5895	48.20316	300	0.820	34.040	1.027439
LV85	C2	5/21/19	140.5895	48.20316	364	0.781	34.040	1.027441
LV85	C2	5/21/19	140.5895	48.20316	374	0.781	34.040	1.027441
Tatar Strait Slope and Trough [2]								
KH-35	124	07/28/1999	141.4400	48.0000	3.2	11.105	33.243	1.025548
KH-35	124	07/28/1999	141.4400	48.0000	66.3	2.2516	34.038	1.027334
KH-35	124	07/28/1999	141.4400	48.0000	111.7	1.8835	34.031	1.027358
KH-35	125	07/28/1999	141.0400	48.0000	4.2	11.793	33.089	1.025307
KH-35	125	07/28/1999	141.0400	48.0000	21.6	2.903	33.688	1.026999
KH-35	125	07/28/1999	141.0400	48.0000	40.0	1.289	33.825	1.027235
KH-35	125	07/28/1999	141.0400	48.0000	139.6	1.214	33.981	1.027366
KH-35	125	07/28/1999	141.0400	48.0000	254.4	1.251	34.076	1.027439
KH-35	125	07/28/1999	141.0400	48.0000	348.4	0.835	34.071	1.027463
KH-35	125	07/28/1999	141.0400	48.0000	441.9	0.606	34.070	1.027476
KH-35	125	07/28/1999	141.0400	48.0000	648.6	0.327	34.067	1.027490
KH-35	125	07/28/1999	141.0400	48.0000	801.0	0.233	34.065	1.027493
KH-35	125	07/28/1999	141.0400	48.0000	838.4	0.235	34.065	1.027493
KH-35	127	07/29/1999	140.7533	48.0000	3.6	12.100	32.945	1.025141
KH-35	127	07/29/1999	140.7533	48.0000	69.5	1.273	33.924	1.027316
KH-35	127	07/29/1999	140.7533	48.0000	160.5	0.669	33.968	1.027390
KH-35	127	07/29/1999	140.7533	48.0000	219	0.833	34.022	1.027424
KH-35	127	07/29/1999	140.7533	48.0000	268.5	0.718	34.042	1.027447
KH-35	127	07/29/1999	140.7533	48.0000	362.4	0.652	34.048	1.027456
KH-35	128	07/29/1999	140.4150	48.0017	28.9	1.0184	33.280	1.026815
KH-35	128	07/29/1999	140.4150	48.0017	59	0.2819	33.762	1.027246
KH-35	128	07/29/1999	140.4150	48.0017	116.9	0.6764	33.938	1.027365
Umitaka Spur, Niigata Prefecture [3]								
KT05-11	1D1-12	05/19/2005	137.33	41.35	300.63	1.3965	34.1551	1.027492
KT05-11	1D1-11	05/19/2005	137.33	41.35	499.63	0.6234	34.1704	1.027555
KT05-11	1D1-9	05/19/2005	137.33	41.35	720.3	0.3476	34.1707	1.027571
KT05-11	1D1-1	05/19/2005	137.33	41.35	911.29	0.2521	34.1689	1.027574

[1] This study, [2] Postlethwaite et al., 2005, and [3] Takahata et al., 2008; Saegusa et al., 2007.

TABLE 2 | Noble gas, methane, and dissolved inorganic carbon stable isotopic data for samples collected in Niskin bottles.

Cruise	Site	Depth (m)	$^3He/^4He$ (R/R_{air})	δ^3He (%)	$^{20}Ne/^4He$	$\Delta^{20}Ne/^4He$ (%)	CH_4 (nmol/L)	CH_4 SR (%)	$\delta^{13}C_{DIC}$ (‰)
Tatar Strait Slope Seeps [1]									
LV-85	C5	0	a.c.	a.c.	a.c.	a.c.	5.7	63.0	0.02
LV-85	C5	50	0.982 ± 0.01	−1.8	3.81	−3.48	13.2	245.6	−0.66
LV-85	C5	75	0.979 ± 0.01	−2.1	3.71	−6.14	31.4	728.8	−0.74
LV-85	C5	100	0.997 ± 0.01	−0.3	3.67	−6.93	31.5	740.6	−0.87
LV-85	C5	150	1.007 ± 0.01	0.7	3.58	−9.24	a.c.	a.c.	−0.86
LV-85	C5	200	1.001 ± 0.01	0.1	3.51	−11.16	145.8	3740.5	−0.86
LV-85	C5	250	1.023 ± 0.01	2.3	3.93	−0.61	42.7	1020.1	−0.96
LV-85	C5	326	1.035 ± 0.01	3.5	3.79	−4.22	35.7	834.8	−0.93
LV-85	C5	336	1.039 ± 0.01	3.9	3.75	−5.25	34.4	801.4	−1.05
LV-85	C6	0.15	0.984 ± 0.01	−1.6	3.72	−5.04	5.3	50.8	n.d.
LV-85	C6	40	0.988 ± 0.01	−1.2	3.96	−0.81	7.7	96.4	n.d.
LV-85	C6	75	0.991 ± 0.01	−0.9	3.94	−0.63	8.3	118.7	n.d.
LV-85	C6	100	0.989 ± 0.01	−1.1	4.00	1.30	8.4	126.2	n.d.
LV-85	C6	150	0.984 ± 0.01	−1.6	3.94	0.05	7.6	109.1	n.d.
LV-85	C6	200	0.97 ± 0.01	−3	3.67	−6.90	8.3	127.8	n.d.
LV-85	C6	250	1.022 ± 0.01	2.2	3.76	−4.76	14.7	299.0	n.d.
LV-85	C6	306	1.033 ± 0.01	3.3	3.76	−4.94	92.9	2386.2	n.d.
LV-85	C6	316	a.c.	a.c.	a.c.	a.c.	46.1	1134.6	n.d.
LV-70	6	0	n.d.	n.d.	n.d.	n.d.	11.1	301.1	n.d.
LV-70	6	34	n.d.	n.d.	n.d.	n.d.	29.4	879.3	n.d.
LV-70	6	60	n.d.	n.d.	n.d.	n.d.	172.0	5212.0	n.d.
LV-70	6	95	n.d.	n.d.	n.d.	n.d.	46.1	1303.6	n.d.
LV-70	6	142	n.d.	n.d.	n.d.	n.d.	26.5	687.3	n.d.
LV-70	6	174	n.d.	n.d.	n.d.	n.d.	17.0	396.7	n.d.
LV-70	6	202	n.d.	n.d.	n.d.	n.d.	29.4	758.3	n.d.
LV-70	6	230	n.d.	n.d.	n.d.	n.d.	24.0	596.4	n.d.
LV-70	6	258	n.d.	n.d.	n.d.	n.d.	24.1	597.9	n.d.
LV-70	6	286	n.d.	n.d.	n.d.	n.d.	30.8	777.6	n.d.
LV-70	6	310	n.d.	n.d.	n.d.	n.d.	23.9	577.8	n.d.
LV-70	6	319	n.d.	n.d.	n.d.	n.d.	121.5	3340.8	n.d.
Tatar Strait W. Slope References Site [1]									
LV85	C2	0	n.d.	n.d.	n.d.	n.d.	5.3	64.3	n.d.
LV85	C2	50	n.d.	n.d.	n.d.	n.d.	11.0	205.2	n.d.
LV85	C2	75	n.d.	n.d.	n.d.	n.d.	9.8	174.1	n.d.
LV85	C2	100	n.d.	n.d.	n.d.	n.d.	9.2	159.3	n.d.
LV85	C2	150	n.d.	n.d.	n.d.	n.d.	7.6	113.5	n.d.
LV85	C2	200	n.d.	n.d.	n.d.	n.d.	8.9	150.3	n.d.
LV85	C2	300	n.d.	n.d.	n.d.	n.d.	12.0	235.6	n.d.
LV85	C2	364	n.d.	n.d.	n.d.	n.d.	13.0	263.2	n.d.
LV85	C2	374	n.d.	n.d.	n.d.	n.d.	12.8	256.4	n.d.
Tatar Strait Slope and Trough [2]									
KH-35	125	4.2	0.9863	−1.4	a.c.	a.c.	n.d.	n.d.	n.d.
KH-35	125	21.6	0.9831	−1.7	4.02	2.53	n.d.	n.d.	n.d.
KH-35	125	40.0	n.d.	n.d.	n.d.	n.d.	n.d.	n.d.	n.d.
KH-35	125	139.6	0.9947	−0.5	4.03	2.05	n.d.	n.d.	n.d.
KH-35	125	254.4	1.0213	2.13	4.02	1.85	n.d.	n.d.	n.d.
KH-35	125	348.4	1.0443	4.43	4.03	1.76	n.d.	n.d.	n.d.
KH-35	125	441.9	1.07	7	4.05	2.10	n.d.	n.d.	n.d.
KH-35	125	648.6	n.d.	n.d.	n.d.	n.d.	n.d.	n.d.	n.d.
KH-35	125	801.0	1.0721	7.21	4.02	1.27	n.d.	n.d.	n.d.
KH-35	125	838.4	n.d.	n.d.	n.d.	n.d.	n.d.	n.d.	n.d.
KH-35	127	3.6	0.981	−1.9	3.71	−1.76	n.d.	n.d.	n.d.
KH-35	127	69.5	n.d.	n.d.	n.d.	n.d.	n.d.	n.d.	n.d.
KH-35	127	160.5	n.d.	nd.	n.d.	n.d.	n.d.	n.d.	n.d.
KH-35	127	219	1.0101	1.01	4.02	1.54	n.d.	n.d.	n.d.
KH-35	127	268.5	1.0261	2.61	4.02	1.40	n.d.	n.d.	n.d.
KH-35	127	362.4	1.0353	3.53	4.01	1.14	n.d.	n.d.	n.d.
Umitaka Spur, Niigata Prefecture [3]									
KT05-11	1D1-12	300.63	1.003	0.3	3.72	−5.84	6.3	79.1	n.d.
KT05-11	1D1-11	499.63	1.023	2.3	3.78	−4.47	23.1	543.3	n.d.
KT05-11	1D1-9	720.3	1.054	5.4	3.86	−2.77	3.5	−3.4	n.d.
KT05-11	1D1-1	911.29	1.045	4.5	3.86	−2.72	5.6	54.1	n.d.

[1] This study, [2] Postlethwaite et al., 2005, and [3] Takahata et al., 2008; Saegusa et al., 2007. n.d.= not determined, a.c.= air-contaminated sample split.

determined coefficients (Smith and Kennedy, 1983; Sano and Takahata, 2005) as well as with the temperatures and salinity shown in **Figures 7A,B** along with the $^{20}Ne/^{4}He$ ratio measured from waters collected from the Niskin bottles (**Table 2**).

Using this approach, it can be seen (**Figure 7G**) that for the Tatar Strait samples collected in 1999 (KR125 and KR127), only surface waters present negative $\Delta^{20}Ne/^{4}He$ values, meaning that the waters are undersaturated in ^{20}Ne relative to ^{4}He, at the given temperature and salinity conditions. All of the other samples collected in 1999 are above saturation for neon relative to helium. In contrast, during 2019, the $\Delta^{20}Ne/^{4}He$ values for plume LV85-seepC5 are negative for both surface (I) and subsurface (II) waters, decreasing almost linearly with depth to the base of the lower intermediate waters (IIIb) and then increasing somewhat for deeper Japan Sea Proper (IV) samples. The $\Delta^{20}Ne/^{4}He$ profile for 2019 plume LV85-seepC6 similar to the 1999 profile, in that values are negative in the surface (I), then around saturation down to the base of lower intermediate (IIIb), with the exception of one negative value at the boundary between water layers IIIb and IV. At the depths of Japan Sea Proper (IV) water, the 2019 samples are not appreciably different from the Umitaka Spur samples from offshore Niigata Prefecture which also have negative $\Delta^{20}Ne/^{4}He$ values and only approach solubility near the seafloor. The very gradual changes in Umitaka Spur may be since the Umitaka Spur is in deeper water (>900 m), compared with the Tatar Strait plumes (<400 m). In the central portions of Japan Sea, the relative amount of neon the helium appears to increase more gradually as the transition between water masses is also deeper (Postlethwaite et al., 2005; Takahata et al., 2008).

Stable Isotopic Composition of DIC in Seawater at a Plume Site

The $\delta^{13}C$ of DIC was determined in seawater that was recovered and transferred from Niskin bottles above site LV85-seepC5 in 2019 (**Table 2**). The measured values begin slightly positive at +0.02‰ in the shallowest waters and become increasingly more depleted in ^{13}C with depth, with the deepest sample (336 m) having the most negative $\delta^{13}C$ value at −1.16‰. Although at 200 m depth, LV85-seepC5 has an anomalously low $\Delta^{20}Ne/^{4}He$ value (−11.6%) coupled with a very high methane oversaturation ratio (3740%), the $\delta^{13}C$ of DIC at this depth shows no such anomaly and is consistent with adjacent water samples at −0.86‰.

DISCUSSION

Presence and Fate of Methane at Plume Sites

Although to date there have not been ROV deployments to directly observe the seafloor seeps in Tatar Strait, the flares themselves (**Figure 3)** are thought to be comprised of free gas, free gas enclosed in a gas hydrate shell, or gas hydrate flakes similar to those observed elsewhere in related studies including at Umitaka Spur (Aoyama et al., 2007). In these cases, it has been shown that the ascending gas hydrate melts and gas bubbles disperse within the water column before reaching the subsurface (II) and surface (I) waters (e.g., Greinert et al., 2006; Salomatin et al., 2014). Gravity coring during both LV70 and LV85 as well as the previous cruises has revealed thin laminar gas hydrate layers in the shallow sediments beneath the plumes (Jin et al., 2013; Shakirov et al., 2019), while no sediment-hosted gas hydrate has been recovered from the western margin of Tatar Strait where the reference site LV85-C2ref. is located.

The Tatar Strait plumes differ from plumes situated offshore of NE Sakhalin (Salomatin et al., 2014) and Umitaka Spur (Aoyama et al., 2007) in that the location of gas venting in Tatar Strait is significantly shallower. Plumes at Umitaka Spur, Sea of Japan (**Figure 1A**) are at 900 m or more (Aoyama et al., 2007; Hiruta et al., 2015), while numerous plumes situated in the Okhotsk Sea to the northeast of Sakhalin Island are mostly found between 500 and 1000 m (Jin et al., 2011). Any gas hydrate forming at 350 m at the base of the Tatar Strait Plumes, would travel a much shorter distance before dissociating and dissipating into the water column. The speed of ascending bubbles decreases as the diameter of the bubbles becomes smaller until they eventually reach neutral buoyancy and dissipate in the water column (Yapa et al., 2001; Greinert et al., 2006; Salomatin et al., 2014). Assuming an average vertical velocity of 15 cm/s (Salomatin et al., 2014) bubbles could presumably travel up to 100 m depth in as little as 28 min. On the other hand, at such shallow depths, the water pressure is less at the top of upper intermediate waters (IIIa), which leads to more rapid dissociation of gas hydrate and dissipation into the water column. In any case, the echograms would suggest that most of what is free gas has dissipated into the water column in the intermediate waters (IIIa and IIIb) or at least reached a bubble diameter so small that it cannot be detected through hydroacoustic methods.

If the most intense red and orange areas within the hydroacoustic flares (**Figure 3)** do in fact represent such gas hydrate which forms layers around rising gas bubbles as has been observed elsewhere in the Japan Sea (Aoyama et al., 2007), it is clear that the gas hydrate bubbles could extend into lower intermediate (IIIb) and even upper intermediate (IIIa) water masses, above the predicted range of gas hydrate stability (**Figure 7A**) as calculated from the equation of Dickens and Quinby-Hunt (1994). Shakirov et al. (2019) interpreted some of the shallower gas anomalies as being due to the dissociation gas hydrate bubbles, based on observations by Yapa et al. (2001), whereby gas hydrate from seeps which are relatively rich in ethane and propane, with $C_1/(C_2+C_3)<6$, can remain stable at higher temperatures and shallower depths, even shallower than intermediate waters (IIIa and IIIb) found in Tatar Strait. Recovered shallow seafloor sediments near the plume sites in Tatar Strait yield headspace gases which are primarily thermogenic with measured $C_1/(C_2+C_3)$ ratios <10 and as low as 2.8 (Yatsuk et al., 2020), so the upper limit of hydrate stability could potentially be shallower than the ~300 m depth indicated by pure methane, although the rising gas bubbles would have to be collected and analyzed to directly confirm this. It is apparent, however, that the presence of gas bubbles in the plume sites does not seem to have a detectible net effect on salinity or temperature

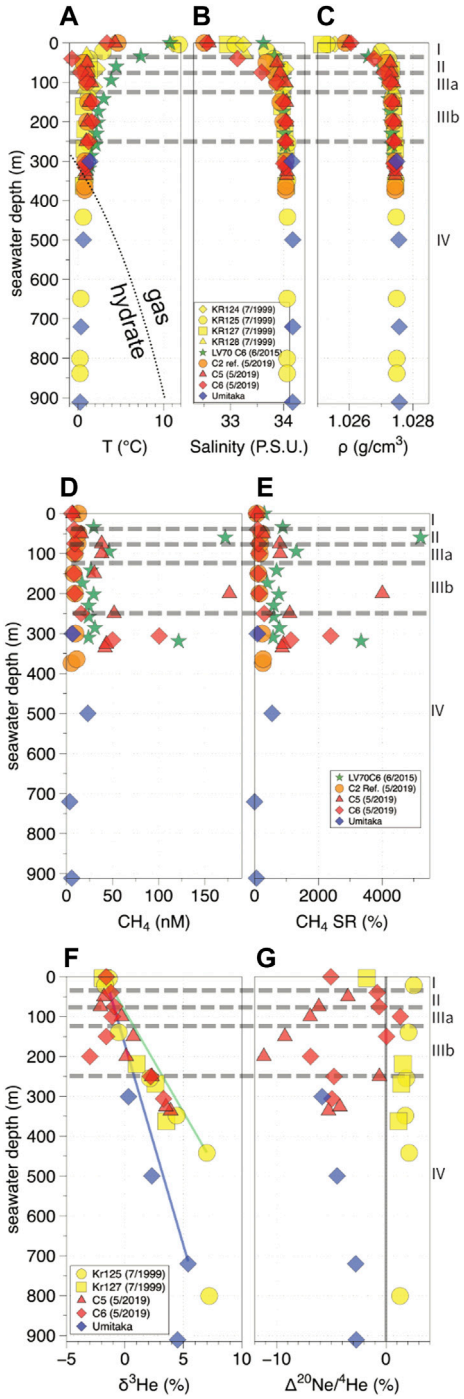

FIGURE 7 | (A,B) Depth profiles for temperature and salinity in seawater, respectively, from CTD data. Red represents plume samples from LV85-seepC5 and LC85-seepC6 in 2019, green stars represents plume LV70-seepC6 in 2015, yellow represents Tatar Strait sites from Cruise KH76 in 1999 (Postlethwaite et al., 2005), blue represents Umitaka Spur seep, offshore Niigata from Cruise KT05-11 in 2005 (Takahata et al., 2008). The dotted line shows gas hydrate stability for pure methane in seawater (Dickens and Quinby-Hunt, 1994) **(C)** Seater density calculated from temperature, salinity, and pressure (after UNESCO, 1981). **(D)** Dissolved methane. **(E)** Dissolved methane expressed as the oversaturation ratio (SR) calculated from

(*Continued*)

FIGURE 7 | concentration, temperature, and salinity. **(F)** Tritiogenic ^{3}He should increase somewhat linearly down to the base of intermediate waters (Postlethwaite et al., 2005). The slope is greater in Tatar Strait (green line) than that in Umitaka Spur due to Tatar Strait's shallower seafloor depth. Introduction of radiogenic ^{4}He in the plume sites at ~200 m water depth may be the cause of the apparent negative excursion in δ^{3}He. **(G)** Depth profile for Δ^{20}Ne/^{4}He calculated from the observed ratios, temperature, and salinity.

that influences the density (**Figure 7C**), as the profile from the reference site LV85-C2ref. is indistinguishable from the plume sites, nor are the Tatar Strait density profiles from the 1999 Tatar Strait transect sites observably different from the 2015 and 2019 plume sites.

In terms of CH_4 saturation in the water column, water collected from site LV85-C2ref. has the highest oversaturation in the deep Japan Sea Proper water (IV), decreasing only gradually until the base of surface water (I). The plume sites have high methane anomalies in the subsurface (II) and in lower intermediate water (IIIb). Such anomalies could potentially be from dissolved gas or from finely suspended gas bubbles entrained in the Niskin bottle at the time of sampling since the Niskin Rosette system passed directly into the plume during sampling (**Figure 3**). It is worth noting that, although accumulation of small gas bubbles at water mass boundaries is not impossible, the SSL observed in the hydrograms are probably not directly related to the gas seeps themselves, especially since similar SSL are also observed in the reference site (**Figure 3D**). Such SSL are frequently associated with the presence of zooplankton and micronekton in the water column (Liao et al., 1999) and, in such cases, position of the SSL often ascends during night time as these organisms tend to migrate closer to the surface (Evans and Hopkins, 1981; Baliño and Aksnes, 1993; Iida et al., 1996). Both the LV85-seepC6 (**Figure 3A**) and LV70-seepC6 (**Figure 3C**) were sampled during daylight hours (from 8:53 to 9:14 and from 6:47 to 7:09 local Sakhalin Time, respectively). During these hours, it seems that the SSL is most intense in surface (I) and subsurface (II) water layers, with hardly any reflection in the upper intermediate waters (IIIa) and a more broadly dispersed SSL in the lower intermediate waters (IIIb). In contrast, the CTD sampling and hydroacoustic measurements above plume LV85-seepC5 (**Figure 3B**) occurred at night (from 00:15 to 00:38). At the night time, the strong SSL is in the upper surface waters (I), while the more disperse SSL has migrated up from its position in the lower intermediate waters during daylight hours to upper intermediate (IIIa) and subsurface (II) waters. The reference site LV85-C2ref. was also sampled in the earlier night hours (from 21:02 to 21:34), yet with the exception of the surface waters (I), any deeper SSL is either absent for far more disperse than near the plume sites. While finely dispersed gas bubbles could potentially produce SSLs, these layers appear to change position between day and night and are likely entirely due to biotic activity.

Hydroacoustic data suggest that by the time the plume gas reaches the subsurface waters, the bubbles are dispersed enough that either the bubble diameter is too small for them to be

detected or they have dissolved into the surrounding water. Despite the disappearance from the hydrograms (**Figure 3**), the seawater methane in Tatar Strait is not completely oxidized; however, as shown by oversaturation ratios in surface (I) and subsurface (II) waters above both plumes and in the reference site (**Figure 3D**). If the gas dispersed from the plumes is effectively oxidized within the water column before reaching the air–water interface, it is possible that the oxidized methane would influence the carbon pool, at least around the plumes.

Unfortunately, with the exception of this plume study, there have not been other investigations of the $\delta^{13}C$ of DIC in the water column in Tatar Strait, or even in the Japan Sea to compare with at the time of this study. It is obvious from the data, however, that the more negative trend in $\delta^{13}C_{DIC}$ with depth observed at the Tatar Strait plume site is not caused by deep-water ventilation of sub-arctic, less saline Amur River water, even though rivers in other Arctic marginal sea settings have been shown to impart negative $\delta^{13}C_{DIC}$ values (Bauch et al., 2015; Dubinina et al., 2020). Such ventilation would require the Tatar Strait intermediate (IIIa, IIIb) and deep (IV) waters to be much less saline, less dense, and would have lower $\delta^{3}He$ values than those which are observed. To provide some comparison, the LV85-seepC5 results are plotted alongside with two reference sites where waters were also collected during late spring and early summer months along ocean margins where the water depth is similar, Skagerrak between the North Sea and the Baltic Sea (sampled in 5/19/2006) (Filipsson et al., 2017) and a shallow portion of the South China Sea (site-n, sampled during 6/1995) (Lin et al., 1999). For LV85-seepC5, the values generally become more negative with depth and with water density (**Figure 8A**). The largest difference is between surface (0 m, $\delta^{13}C_{DIC}$=+0.02‰) and subsurface (50 m, $\delta^{13}C_{DIC}$ = −0.66‰), and the most negative value is near the seafloor (336 m, $\delta^{13}C_{DIC}$ = −1.05‰). The waters of South China Sea (Lin et al., 1999) show a similar trend; however, the waters there show more positive $\delta^{13}C_{DIC}$ values and the water is significantly warmer (26.76 ˚C at 10 m to 34.46 ˚C at 301 m), leading to lower water density. Skagerrak samples show a more complex pattern since sub-surface waters are much shallower at <20 m consist of colder, less saline Baltic Sea waters which transition abruptly to more saline, warmer intermediate waters at only 50 m (Filipsson et al., 2017). That said, all of the Skagerrak waters have more positive $\delta^{13}C_{DIC}$ values than those of the Tatar Strait plume. There are some marine settings where the range of $\delta^{13}C_{DIC}$ values overlaps with those of the Tatar Strait site. A number of sites in the South China Sea (Lin et al., 1999) have $\delta^{13}C_{DIC}$ values which extend from around +1‰ in surface waters to just less than −1‰ in the deep waters; however, the more negative values are generally much deeper, at 500–1500 m depth. Bornholm Basin, Baltic Sea, has $\delta^{13}C_{DIC}$ values ranging from as high as +1.3‰ in surface waters to as low as −3.3‰ at 90 m (Filipsson et al., 2017); but the waters are less saline and less dense than those of Tatar Strait.

Depending on gas flux, the deep Japan Sea Proper (IV) water above the Tatar Strait gas plumes can possibly be influenced by the expulsion of fluids from gas vents. Sediment pore waters associated with seafloor gas chimneys have been shown to have quite negative $\delta^{13}C_{DIC}$ values of around −40‰ due primarily to anaerobic methane oxidation (Hiruta et al., 2015). We can see for example, that the deepest waters in plume LV85-seepC5 which are least influenced by tritiogenic ^{3}He are also those that have the

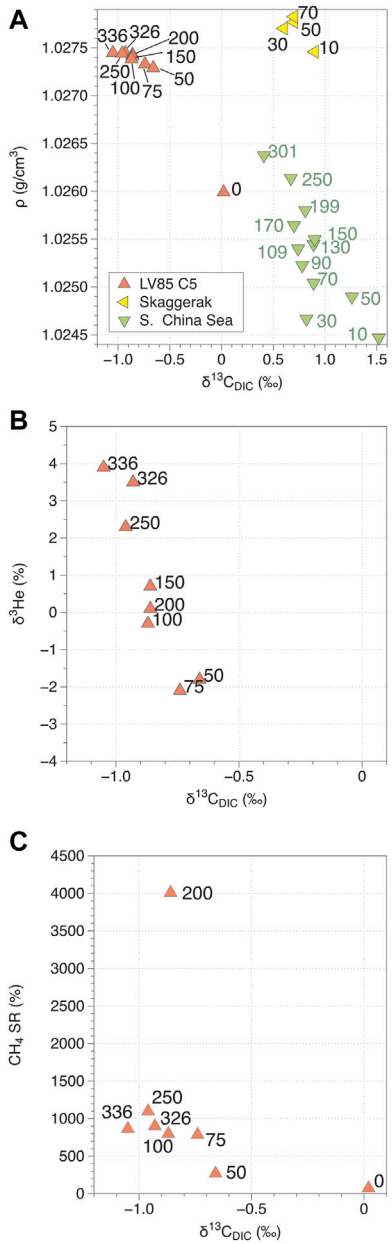

FIGURE 8 | Stable isotopic composition of dissolved inorganic carbon (DIC) versus gas composition at the LV85-seepC5 sampled in 5/2019. Depth indicated in meters beside each data point. **(A)** Deeper, dense waters generally have the most negative $\delta^{13}C$ values for DIC, compared to the South China Sea (Lin et al., 1999) and Skagerrak (Filipsson et al., 2017). **(B)** Most positive $\delta^{3}He$ values for LV85-seepC5 sampled in 2019 generally correspond with the deeper waters due to past tritiogenic production of ^{3}He in the waters, which also show an influence of DIC production from methane oxidation near the seafloor. **(C)** With the exception of the extremely high methane concentration at 200 m, there is generally more negative $\delta^{13}C$ with greater methane concentration in waters closer to the seafloor.

most negative $\delta^{13}C_{DIC}$ values (**Figure 8B**) and also that, with the deep Japan Sea Proper (IV) water with more negative $\delta^{13}C_{DIC}$ values also has a methane saturation ratio which is greater than the shallower surface (I) and subsurface (II) waters (**Figure 8C**). The problem is that contributions of DIC produced through mineralization of particulate organic matter as it settles on the seafloor can also impart negative $\delta^{13}C_{DIC}$ values similar to those observed. As such, the present data from the Tatar Strait plume is insufficient to determine whether the trend towards more negative values in the deep waters is influenced at all by the localized expulsion of water from a single gas chimney or even from fluids expelled by multiple gas seeps on a more regional scale. Future studies of the $\delta^{13}C_{DIC}$ in this area are merited. In a recent study, Na et al. (2022) found that the DIC concentrations in deep Japan Sea waters have increased significantly between 1999 and 2019, due to the slowing of ventilation of shallow waters coupled with an increasing contribution of DIC from oxidation of detrital material. Since an increase in dissolved CO_2 from oxidation of particulate organic carbon can lead to deep water acidification, clearly more research is needed to see if this is occurring in Tatar Strait.

Another environmental concern in light of the global warming potential of methane gas is the transfer of methane from shallow surface waters (I) to the atmosphere. The methane flux into the atmosphere from the shallow ocean can be calculated as follows (Kudo et al., 2018):

$$F_{CH4} = K_w \text{ x } ([CH_4]_{w(0-10m)} - [CH4]_a), \quad [7]$$

where F_{CH4} is the flux in μmol/m^2/day (also reported in some studies as mol/km^2/day), K_w is the gas transfer coefficient in cm/hr, $[CH_4]_{w(0-10m)}$ is the concentration of methane in μmol/L in the upper 10 m of water depth, and $[CH_4]_a$ is the saturation concentration of atmospheric methane in water from **Eq. 3.** The gas transfer coefficient (K_w) is calculated as follows:

$$K_w = 0.31v^2 (Sc/660)^{-1/2}, \quad [8]$$

where v is the wind speed in m/s and S_c is the Schmidt number for CH_4 in seawater. The Schmidt number which is dimensionless is calculated as follows:

$$Sc = 2039.2 - 120.31T + 3.4029T^2 - 0.040437T^3, \quad [9]$$

where T in this case is temperature in °C. As can be appreciated in **Eq. 8**, changes in wind speed have a strong influence on the gas transfer coefficient which is directly proportional to the flux of methane to the atmosphere, more than air temperature change. The range of wind velocities measured during sampling of the plumes and the reference site during cruise LV85 ranged from 1.1 to 7.7 m/s, while air temperature varied from 5.2 to 7.9 °C. In another study, wind velocities measured during a sampling in the southernmost portion of Tatar Strait in August, 2010 yielded a range from 2 to 10 m/s (Vereschchagina et al., 2013). In order to provide a meaningful comparison of methane flux between the plume sites and the reference site regardless of changes in weather, we assume a constant air speed of 7 m/s and an air temperature of 6 °C, yielding a Schmidt number (S_c) of 1431 and a gas transfer coefficient (K_w) of 10.32 cm/h. The gas transfer coefficient is then applied to the difference in measured concentrations of methane observed in shallow waters versus the calculated air saturation values yielding flux values for the plume sites and the reference site (**Supplementary Table S1**). The 2019 reference site LV85-C2ref has a methane flux of 5.16 μmol/m^2/day. Despite having much higher methane concentrations in the intermediate waters, the two plume sites from the same year, LV85-seepC6 and LV85-seepC5 have essentially the same flux to the atmosphere at 4.41 μmol/m^2/day and 5.18 μmol/m^2/day, respectively. The 2015 site LV70-seepC6 has an atmospheric methane flux which is significantly greater, at 20.68 μmol/m^2/day. It is also possible that sporadic gas emissions can result in even greater methane emissions, as noted with an anomalously high methane profile for 2015 site LV70-20, which has near-surface concentrations of 115 nmol/L and yields an atmospheric flux of 482 μmol/m^2/day (Shakirov et al., 2019). It could be that some the methane fluxes are variable from year to year as noted by Mishukova et al. (2015), in part as a result of sporadic releases of gas following local seismic activity (Shakirov et al., 2020). Although there was no significant difference between plume and reference sites in sampled during LV85 in 2019, all of the calculated fluxes are higher than those of non-plume sites to the south of Tatar Strait which were shown to range from 0.1 μmol/m^2/day to 0.6 μmol/m^2/day using a similar method of calculation (Vereshchagina et al., 2013). Aoki et al. (2020) demonstrated that methane concentrations in the air just above the sea surface in Umitaka Spur were significantly greater than background atmospheric values in other parts of Japan Sea. It could be that the calculated plume values for Tatar Strait are an underestimate, if plume gases dispersing and entering over a larger area, or if the plume gas is moving laterally beyond our sampling area before reaching the surface.

Mixing of Water Masses and Temporal Changes

In general, combining the observed chemical and isotopic results suggest three different groups based on mixing trends between the described water masses (**Figure 2**) as shown by on cross plots with the water depth noted alongside the data (**Figure 9**). The theoretical $^{20}Ne/^4He$ ratios (calculated form Sano and Takahata, 2005; Smith and Kennedy, 1983) are only slightly influenced by the observed range of salinities (green lines), with predicted ratios for 0 °C representing the coldest waters versus 15 °C representing the warmest summer temperatures in southern Tatar Strait (Andreev, 2018). Group-a comprises all the samples deeper than 150 m from July, 1999 (Postlethwaite et al., 2005) from lower intermediate waters (IIIb), as well as possibly one of the deeper 2019 samples. This group represents mixing of the lower intermediate waters (IIIb) with cold deep Japan Sea Proper waters (IV), all with salinities all between 34.0 and 34.1 PSU. Group-b occurs at <150 m deep and represents mixing between less saline surface waters (I) and subarctic subsurface water masses (II) and as well as the upper portion of Intermediate low-salinity water

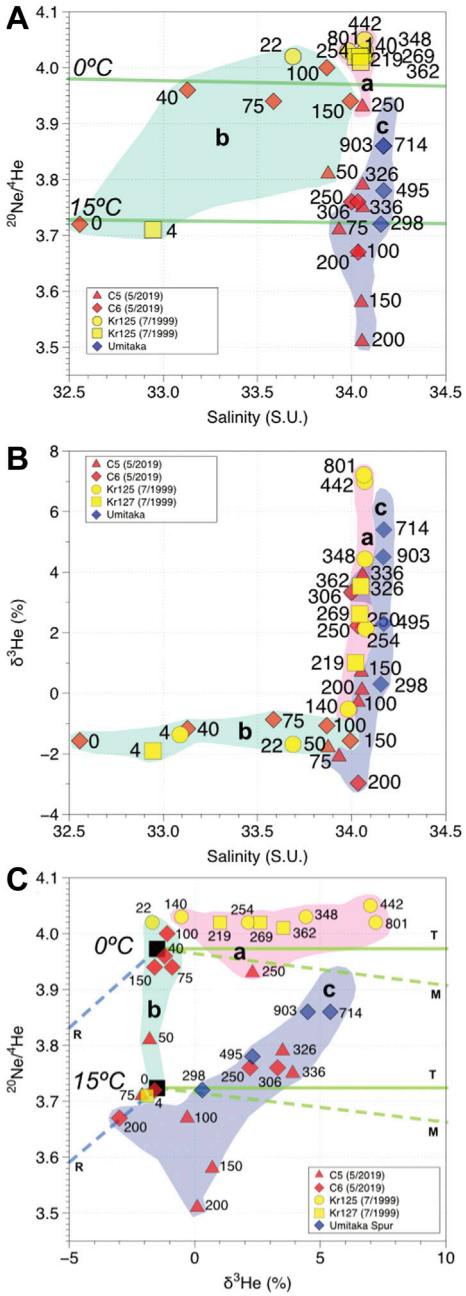

FIGURE 9 | Mixing trends observed in Tatar Strait and Umitaka Spur water masses. Seawater depth indicated in meters. **Group-a:** Mixing between subarctic intermediate and deep waters. **Group-b:** Mixing between less saline surface waters and subarctic subsurface waters **Group-c:** Mixing slightly more saline subtropical intermediate and deep waters. **(A)** Observed salinities have only a modest effect on $^{20}Ne/^{4}He$ ratios, as shown by the solubility lines (green) at 0 and 15 °C. As shown, low salinity values are mostly shallow waters. Extremely low values for $^{20}Ne/^{4}He$ can be produced either by air injection or by the addition of radiogenic ^{4}He. **(B)** Salinity versus $\delta^{3}He$. Low salinity values are primarily from surface and subsurface Group-b. **(C)** Addition of mantle gas (M) appear to be minimal, and mixing of tritiogenic (T) ^{3}He in intermediate and deep waters seems to be the source of the observed variation. Points below and to the left of the 15 °C seawater end-member indicate some modification of group III by the addition of radiogenic

(*Continued*)

FIGURE 9 | helium, particularly in intermediate waters at around 200 m. The 1999 waters tend to trend between intermediate and deep sub-arctic values in Group-a while the Umitaka Spur and Tatar 2019 waters show an influence form the Tsushima Current sub-tropical waters, particularly in the intermediate water masses.

masses (IIIa). Members of this group are represented by samples from both July, 1999 and May, 2019. The warmer, less saline portion of Group-b is restricted to <4 m and may represent low-salinity subarctic waters that have warmed during the spring to mid-summer months. Finally, Group-c represents the mixing between more-saline subtropical intermediate waters (IIIb) with anomalously low $^{20}Ne/^{4}He$ ratios and deep Japan Sea Proper waters (IV). This group includes seawater sampled in May, 2019 as well as the Umitaka Spur samples. Roughly half of the samples in this group have anomalous $^{20}Ne/^{4}He$ ratios which cannot be accounted for by air saturation even at temperatures above the warmest water temperatures of 15 °C, especially since the actual water temperatures are much lower.

Looking at the $\delta^{3}He$ values for the same samples involved in the aforementioned groups (**Figure 9B**) reveals some more details. While Group-a does not very much in $^{20}Ne/^{4}He$ ratios, it spans a wide range of $\delta^{3}He$ values which increase predictably with water depth. Group-b, however, has a limited range of $\delta^{3}He$ values, since these surface and subsurface waters are not influenced by tritiogenic ^{3}He from the early to mid-1960's. Group-c waters are more saline than Group-a, but also have increasing $\delta^{3}He$ values with depth. Some of the $\delta^{3}He$ values for waters involved in Group-c are even lower than those of the shallow waters.

Finally, combining the $\delta^{3}He$ values with $^{20}Ne/^{4}He$ values (after Takahata et al., 2005), we can also consider mixing of warm and cold waters with several other gas sources (**Figure 9C**). Addition of tritiogenic helium (T) would increase the $\delta^{3}He$ values while having no effect on $^{20}Ne/^{4}He$ (solid green lines). Addition of even minor amounts of mantle helium (M) would cause a large increase in $\delta^{3}He$ with a corresponding drop in $^{20}Ne/^{4}He$ (dashed green lines). Addition of a radiogenic ^{4}He component (R) would cause both $\delta^{3}He$ values and $^{20}Ne/^{4}He$ ratios to drop (dashed blue lines). Considering this, Group-a consists of cold waters with varying degrees of tritiogenic ^{3}He addition which increases with depth. It is not entirely clear why the $^{20}Ne/^{4}He$ ratios are above seawater saturation, though. The formation of ice during the winter months could possibly increase the relative amount of He sequestered in ice bubbles, with injection of cold dense brines produced by the freezing of seawater resulting in intermediate and deep waters with higher $^{20}Ne/^{4}He$ ratios (Hamme and Emerson, 2002; Hamme et al., 2019). Group-b consists of shallow waters which are free of tritiogenic ^{3}He.

This group covers a large range of salinities depending on the relative amount of water from the Tsushima and Amur River currents. While there is a large amount of variation in $^{20}Ne/^{4}He$ ratios, this could also be the result of changes in the

relative solubility of neon and helium entirely due to temperature differences. Group-c includes intermediate to deep waters which are enriched, in varying degrees, with tritiogenic ^{3}He, but which have lower ^{20}Ne/^{4}He ratios than Group-a. Only two samples from May 2019, at 75 and 200 m, have negative δ^{3}He values, suggesting potential mixing between shallow warm waters and a crustal radiogenic ^{4}He source that could have originated from the gas plume. While gas associated with methane hydrate in Umitaka Spur has mantle helium (^{3}He/^{4}He >2 R_a), radiogenic helium (^{3}He/^{4}He<0.1 R_a) has been found associated with gas hydrate in Lake Baikal, Russia (Matveeva et al., 2003) The other samples in this group at 100 m, 150 m, and 200 m do not fall on the radiogenic mixing trend, have atmospheric δ^{3}He values and could represent deeply advected air bubbles produced during ice formation and salt exclusion. This is not likely due to a problem during sample recovery, since the LV85-seepC5 samples appear to show a systematic decrease in ^{20}Ne/^{4}He with increasing depth between 50 and 200 m (**Figure 7G**). Hahm et al. (2004) observed a similar situation at Knipovich Ridge and proposed that such helium and neon anomalies are a combined effect of air bubble inclusions and brine injection caused by the process of salt exclusion which occurs during winter sea-ice formation. The phenomenon of deep convection of brines has been observed elsewhere in Japan, in particular in the southern Tatar Strait and offshore Primorye (Talley et al., 2003). In the case of Group-c waters, the ^{20}Ne/^{4}He ratios are lower than could reasonably be assumed through seawater saturation, yet are not as low as that of air (^{20}Ne/^{4}He$_{air}$= 3.14, Sakamoto et al., 1992). This would suggest brine injection into deep waters with air bubbles which have preferentially lost some of their helium due to ice formation. The most helium-depleted of Group-c waters are all >200 m depth and have both δ^{3}He values and ^{20}Ne/^{4}He ratios which approach the deeper waters observed in Group-a, while the least helium-depleted waters are <200 m and have δ^{3}He and ^{20}Ne/^{4}He ratios approaching those of air bubbles.

Potential for Climatic Fluctuations to Produce Significant Temporal Changes in Tatar Strait circulation

There are concerns that a decrease in deep water ventilation over the past two decades has already resulted in an increase in deep water acidification in the Japan Sea (Na et al., 2022) and it is also worrisome that changes in circulation may also decrease the upwelling of nutrient-rich waters (Jenkins, 2008) as well as changes in marine species distribution. Tatar Strait is relatively shallow when compared to the Japan Sea as a whole so the potential for significant change is even greater. Annual fluctuations in circulation appear to be intimately associated with the rate at which the Amur River discharges into the Okhotsk Sea across from the northernmost part of Sakhalin Island, and then spills over into Tatar Strait, thus influencing the northward migration of the Tsushima Current, and impacting both the thermohaline structure and circulation of water in the strait (Andreev, 2018; Ponomarev et al., 2018). As the Amur River is one of the largest rivers in East Asia, it has been hypothesized that increased water usage by humans as it courses through Mongolia, China, and Russia might lead to unintended changes in the thermohaline structure of Tatar Strait (Shevchenko et al., 2011).

To assess the degree to which riverine discharge may have varied over time, we looked hydrological data provided by the Russian Federal Water Resources agency for Brodgoroskoye, located at the mouth of the Amur River (**Figure 10**, **Supplementary Table S2**). The data shows average seasonal discharge during the period of Spring thaw each year (March, April, May) and the period of Fall monsoons (September, October, November). The data represents averages each season between 1990 and 2019, except for 2005–2007 where no data is available. With only one exception, the Spring discharge is less than that of the Fall discharge of the preceding year. The Spring discharge has increased only in the past decade but interannual variability has not changed appreciably. From 1990–1999, the mean and standard deviation of Spring discharge was 17,790 ± 3,500 m^3/s compared to the period of 2010–2019 where it was at 23,870 ± 3,800 m^3/s, representing an increase of 25%. If we compare Fall monsoonal discharge, both the mean and variability have increased from 33,200 ± 7,240 m^3/s from 1990–1999 to 52,990 ± 21,540 m^3/s, up by 37%. In general, we do not see a decreasing trend over time which would be attributable to increased water consumption through human activities as proposed by Shevchenko et al. (2011) and if water usage is increasing, it is more than offset by other factors which increase discharge. As far as possible changes in discharge related to intense weather activities, the most extreme seasonal discharge during this period (Fall, 2013: 97,300 m^3/s) is more than double that of the most extreme from 1990–1999 (Fall, 1994: 45,700 m^3/s).

The Fall monsoonal season of 2014, followed by the Spring thaw season of 2015 both preceded our sampling cruise in 2015 (LV70) and, compared with all of the other annual measurements of Amur River discharge, is unusual in that the Fall discharge is the second lowest for the decade (Shaded area in **Figure 10**) while the Spring discharge is the highest, resulting in the only year in which the Spring discharge is greater than that of the preceding Fall over a span of 30 years. This low Fall monsoonal discharge may have resulted in a decline in the intensity of the Amur Leeman and Primorye Currents (**Figure 1B**) and a northward encroachment of the warm saline Tsushima Current as described by Andreev (2018). In contrast, fall of 2018 marked the fourth highest monsoonal discharge for the decade, followed by the second lowest Spring discharge. The data for 1998–1999 and is in-between the extremes experienced in 2014–2015 and 2018–2019. These fluctuations in Amur River discharge could explain our CTD data for Tatar Strat shallow and subsurface water in 2015 is quite different from that 2019, and why the CTD data for 1999 is between the two (**Figure 4D**).

Regarding the influence of Amur River discharge on the Okhotsk Sea to the north, Ogi et al. (2001) found that the amount of ice cover in the Winter months was anticorrelated with the discharge rate recorded in the Fall monsoonal months of the previous year, presumably because of the transport of heat from the river water into the shallow surface layers of the Okhotsk. Subsequent research has further shown that annual

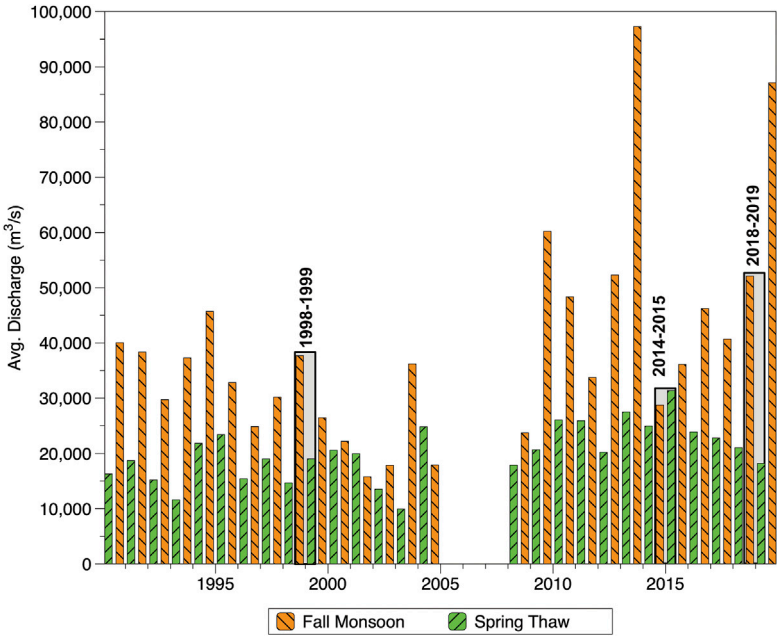

FIGURE 10 | Average seasonal discharge near the mouth of the Amur River in Brodgoroskoye. In general, between 2009 and 2018 the discharge is greater for both the spring thaw and the fall monsoonal months than between 1998 and 2005. The discharge was significantly lower during the fall of 2014 followed by only a slightly greater spring thaw discharge in 2015. (Data courtesy of the Russian Federal Water Resources Agency).

changes in Arctic Oscillation (AO) drive the fluctuations in humidity and Amur River Discharge which, in turn, influence shallow seawater temperatures and the extent of ice cover in the Okhotsk (Ogi and Tachibana, 2006).

Since the two extreme years of our study are 2015 and 2019, we compare Sentinel 1A Satellite imagery of the sea ice extent in Tatar Strait during the month of February in which we have shaded the thicker ice cover for greater visibility (**Supplementary Figure S3**). The rectangle indicating our study area in **Figure 1B** is also indicated in the supplementary figures and even though the images from the two years do not overlap exactly, the study area is present in both. In 2015, a year of low monsoonal input, the waters of the Amur are seen reducing the ice cover in the northern portions of the Strait (**Supplementary Figure S3A**) but their passage southward is blocked by ice restricting the circulation of shallow cold, freshwater southward by the Primorye Current along the western margin of Tatar Strait. At the same time, ice cover is reduced on eastern margin of the strait, along the shore of Sakhalin Island, due to the unimpeded northward flow of the Tsushima Current. With an ice-free area established in our study area in February, it is not surprising that the shallow waters observed in June were much warmer than other years. In contrast, during 2019, following high Fall monsoonal discharge, the western margin is in large part open to southward circulation of the Primorye Current, consistent with the anticorrelation between Amur River Discharge and ice extent in the Okhotsk Sea (Ogi et al., 2001; Ogi and Tachibana, 2006) yet impeding the northward migration of warm saline Tsushima Current waters to the east as described by Shevchenko et al., 2011, resulting in ice cover across most of our study area and along the coast of Sakhalin Island.

CONCLUSION

Our data is consistent with previous investigations which show that Amur River discharge appears to be a key factor in determining shallow, subsurface and even to some extent intermediate water circulation in the Tatar Strait since waters related to river discharge limit the extent to which the Tsushima Current can migrate northward along the coast of Sakhalin Island. Our noble gas results suggest that vertical migration of water masses is somewhat limited, since tritiogenic ^{3}He from the 1960's is still present in intermediate and deep waters. One concern has been that global warming has caused a slowing or even stopping of deep ventilation in the Tatar Strait since the 1960's and even more so in the past 20 years (Riser et al., 1999; Jenkins, 2008; Na et al., 2022), which would have profound implications regarding nutrient cycling and oxygen availability in parts of the water column. The presence of saline waters with low ^{20}Ne/^{4}He ratios and atmospheric δ^{3}He at depths of 100–250 m in 2019 would suggest that that is not entirely the case, and that deep convection as described by Talley et al. (2003), does still occur, perhaps even more so than the data of 1999 (Postlethwaite et al., 2005) when all the waters showed very high ^{20}Ne/^{4}He ratios. Unfortunately, our data is too limited in geographic distribution to tell if this is a localized phenomenon or whether it occurs more broadly. Since the Satellite images from the winters preceding the 2015 and 2019 sampling seasons show substantial changes in ice cover, one would expect that deep convection of air bubbles and brine also varies significantly from year to year depending on whether ice has accumulated more on the Primorye side of the Strait or on the Sakhalin Island side of the Strait.

Gas plumes, consisting primarily of methane gas, have been observed in deep and intermediate waters but are not visible in subsurface and surface waters. As has been noted by others (Shakirov et al., 2019, 2020), methane is still present in the water column in shallow water. The atmospheric flux observed in 2019 for plumes LV85-seepC5 and LV85-seepC6 (4.41 and 5.18 μmol/m^2/day, respectively) is essentially the same as that of the reference site LV85-C2ref. located on the opposite side of Tatar Trough (5.18 μmol/m^2/day), yet is significantly higher than values previously measured in the southernmost part of Tatar Strait (0.1–0.6 μmol/m^2/day Vereshchagina et al., 2013). The atmospheric flux that accompanied warm, saline surface and subsurface waters above the plumes in 2015 was greater at between 20.68 μmol/m^2/day observed at LV70-seepC6 (this study) and 684 μmol/m^2/day at LV70-20 (Shakirov et al., 2020). These flux values above the plumes may be underestimated due to lateral migration or more disperse transfer of the methane to the atmosphere.

As indicated by sites with similar depth profiles that are not associated with seeps, the stable isotopic composition of deep DIC seems to be affected in large degree by scavenging of CO_2 during shallow photosynthesis and by degradation of particulate organic matter in deep water. That said, more work should be done to monitor changes in DIC concentrations, $\delta^{13}C_{DIC}$, and as well as dissolved oxygen throughout the basin, in order to assess changes in water chemistry over the coming years.

While the noble gas isotopic data is limited to two seep sites from LV85 in 2019 as well as comparison with the published 1999 results from KH-36 (Postlethwaite et al., 2005), the observed depth profiles and notable differences in both δ^3He and Δ^{20}Ne/^{4}He from the two sampled years highlight the utility of noble isotope isotopic analysis in delimiting the interactions between water masses, and illustrate the necessity for more research which should be done in Tatar Strait, perhaps including tritium analyses of seawater in future cruises. In particular, future studies of air bubble injection due to brine rejection in winter months can indicate which parts of Tartar Strait undergo convection and whether the overall degree of deep ventilation in the strait is waning over time. Finally, ongoing research into marine seep sites should continue to focus on how methane plumes interact with local water masses and the degree to which plume activity contributes to greenhouse gas emissions.

DATA AVAILABILITY STATEMENT

The original contributions presented in the study are included in the article/**Supplementary Material**; further inquiries can be directed to the corresponding author.

AUTHOR CONTRIBUTIONS

GS: lead author, sample collection for noble gas analysis, data processing, and manuscript writing. AY: Niskin sample collection and gas concentration analysis. NT: noble gas isotopic analysis and manuscript revision. RS: research cruise lead investigator, site selection, and equipment planning. HT: equipment and sample shipping logistics and shipboard water chemistry. KT: analysis of stable isotopic composition of DIC. AO: research senior investigator, logistic planning, and site selection. AS: shipboard collection and analysis of hydroacoustic data. SA: shipboard sample preparation for land-based isotopic analysis and manuscript revision. EK: ice-cover analysis and interpretation of satellite data. EM: collection and analysis of CTD data. YS: noble gas analysis and manuscript revision. RM: lead investigator and organization of international research collaboration.

FUNDING

This research was carried out as part of a joint research program established between the Meiji University Gas Hydrate Research Laboratory (GHRL) and the Pacific Oceanological Institute Far Eastern Branch of Russian Academy of Sciences (POI FEB RAS). Marine expeditionary work was supported by the State Assignment of POI FEB RAS No. 0211-2021-0006 (121021500055-0) and approved by the Ministry of Science and Education of the Russian Federation.

ACKNOWLEDGMENTS

The authors would like to thank C. Postlethwaite for providing research data from the 1998–1999 study, the crew and researchers onboard the R/V Akademik M.A. Lavrentyev for their assistance in making the research cruise a success, and the reviewers who provided useful suggestions leading to the improvement of this manuscript.

SUPPLEMENTARY MATERIAL

The Supplementary Material for this article can be found online at: https://www.frontiersin.org/articles/10.3389/feart.2022.825679/full#supplementary-material

REFERENCES

Andreev, A. G. (2020). Impact of the Amur Discharge and Coastal Upwelling on the Water Circulation in the Northern Tartar Strait (Japan Sea). *Vestnik Far East Branch Russ. Acad. Sci.* 1, 120–126. (in Russian) http://www.vestnikdvo.ru/index.php/vestnikdvo/article/view/527.

Andreev, A. G. (2018). Peculiarities of Water Circulation in the Southern Tatar Strait. *Izv. Atmos. Ocean. Phys.* 54, 1050–1056. doi:10.1134/S0001433818090037

Aoki, S., Komiya, S., Oi, T., Noborio, K., and Matsumoto, R. (2020). Relationship between Atmospheric CH4 Concentration above Sea Surface and Gas Plumes from Seafloor along the Eastern Margin of Japan Sea and Around Hokkaido. *J. Jpn. Assoc. Petroleum Technol.* 85 (6), 309–314.

Aoyama, C., Matsumoto, R., Hiruta, A., Ishizaki, O., Machiyama, H., Numanami, H., et al. (2007). "Acoustical Surveys of Methane Plumes Using the Quantitative Echo Sounder in Japan Sea," in *Symposium on Underwater Technology and Workshop on Scientific Use of Submarine Cables and Related Technologie* (IEEE), 249–255. doi:10.1109/UT.2007.370804*s*

Atekwana, E. A., and Krishnamurthy, R. V. (1998). Seasonal Variations of Dissolved Inorganic Carbon and $\delta^{13}C$ of Surface Waters: Application of a Modified Gas Evolution Technique. *J. Hydrology* 205 (3–4), 265–278. doi:10.1016/S0022-1694(98)00080-8

Balino, B., and Aksnes, D. (1993). Winter Distribution and Migration of the Sound Scattering Layers, Zooplankton and Micronekton in Masfjorden, Western Norway. *Mar. Ecol. Prog. Ser.* 102, 35–50. doi:10.3354/meps102035

Bauch, D., Polyak, L., and Ortiz, J. D. (2015). A Baseline for the Vertical Distribution of the Stable Carbon Isotopes of Dissolved Inorganic Carbon (δ13CDIC) in the Arctic Ocean. *Arktos* 1 (1), 15. doi:10.1007/s41063-015-0001-0

Danchenkov, M. A. (2004). "Vladivostok: FERHRI)," in *Spatial Structure of the Tatar Strait Waters" in* Pacific Oceanography. Editor Y. N. Volkov, 2, 20–43.

Dickens, G. R., and Quinby-Hunt, M. S. (1994). Methane Hydrate Stability in Seawater. *Geophys. Res. Lett.* 21, 2115–2118. doi:10.1029/94GL01858

Dubinina, E. O., Kossova, S. A., Miroshnikov, A. Y., Avdeenko, A. S., and Chizhova, Y. N. (2020). Dissolved Inorganic Carbon ([DIC], δ13C(DIC)) in Waters of the Eastern East Siberian Sea. *Geochem. Int.* 58 (8), 867–886. doi:10.1134/S0016702920080054

Dulenina, P. A., Ustinova, E. I., and Dulenin, A. A. (2020). Current State of Resources for Japanese Flying Squid Todarodes Pacificus in the Northwestern Tatar Strait (Japan Sea). *Izv. Tihookean. Naučno-issled. Rybohoz. Cent.* 200 (3), 586–604. doi:10.26428/1606-9919-2020-200-586-604

Evans, R. A., and Hopkins, C. C. E. (1981). Distribution and Standing Stock of Zooplankton Sound-Scattering Layers along the North Norwegian Coast in February-March, 1978. *Sarsia* 66 (2), 147–160. doi:10.1080/00364827.1981.10414532

Filipsson, H. L., McCorkle, D. C., Mackensen, A., BernhardAndersson, J. M. L. S., Andersson, L. S., Naustvoll, L.-J., et al. (2017). Seasonal Variability of Stable Carbon Isotopes (δ13CDIC) in the Skagerrak and the Baltic Sea: Distinguishing between Mixing and Biological Productivity. *Palaeogeogr. Palaeoclimatol. Palaeoecol.* 483, 15–30. doi:10.1016/j.palaeo.2016.11.031

Gamo, T., Nakayama, N., Takahata, N., Sano, Y., Zhang, J., Yamazaki, E., et al. (2014). The Sea of Japan and its Unique Chemistry Revealed by Time-Series Observations over the Last 30 Years. *Monogr. Environ. Earth Planets* 2 (1), 1–22. doi:10.5047/meep.2014.00201.0001

Glorie, S., Alexandrov, I., Nixon, A., Jepson, G., Gillespie, J., and Jahn, B.-M. (2017). Thermal and Exhumation History of Sakhalin Island (Russia) Constrained by Apatite U-Pb and Fission Track Thermochronology. *J. Asian Earth Sci.* 143, 326–342. doi:10.1016/j.jseaes.2017.05.011

Greinert, J., Artemov, Y., Egorov, V., Debatist, M., and McGinnis, D. (2006). 1300-m-high Rising Bubbles from Mud Volcanoes at 2080m in the Black Sea: Hydroacoustic Characteristics and Temporal Variability. *Earth Planet. Sci. Lett.* 244 (1–2), 1–15. doi:10.1016/j.epsl.2006.02.011

Hahm, D., Postlethwaite, C. F., Tamaki, K., and Kim, K.-R. (2004). Mechanisms Controlling the Distribution of Helium and Neon in the Arctic Seas: the Case of the Knipovich Ridge. *Earth Planet. Sci. Lett.* 229 (1-2), 125–139. doi:10.1016/j.epsl.2004.10.028

Hamme, R. C., and Emerson, S. R. (2002). Mechanisms Controlling the Global Oceanic Distribution of the Inert Gases Argon, Nitrogen and Neon. *Geophys. Res. Lett.* 29 (23), 35-1–35-4. doi:10.1029/2002GL015273

Hamme, R. C., Nicholson, D. P., Jenkins, W. J., and Emerson, S. R. (2019). Using Noble Gases to Assess the Ocean's Carbon Pumps. *Annu. Rev. Mar. Sci.* 11 (1), 75–103. doi:10.1146/annurev-marine-121916-063604

Hiruta, A., Ishizaki, O., Tuchinaga, K., Snyder, G. T., and Matsumoto, R. (2015). Influence of the Carbon Isotopic Composition of Methane and the Proportion of Methane-Derived Bicarbonate on the 13C/12C Ratio of Dissolved Inorganic Carbon at the Sulfate-Methane Transition in the Joetsu Basin Area, Eastern Margin of the Sea of Japan. *Mar. Petroleum Geol.* 67, 468–480. doi:10.1016/j.marpetgeo.2015.05.004

Iida, K., Mukai, T., and DooJin, H. (1996). Relationship between Acoustic Backscattering Strength and Density of Zooplankton in the Sound-Scattering Layer. *ICES J. Mar. Sci.* 53 (2), 507–512. doi:10.1006/jmsc.1996.0073

IOC, IHOBODC (2003). "Centenary Edition of the GEBCO Digital Atlas," in *CD-ROM on Behalf of the Intergovernmental Oceanographic Commission and the International Hydrographic Organization* (Liverpool: British Oceanographic Data Centre). Published on www.gebco.net.

Jenkins, W. J. (2008). The Biogeochemical Consequences of Changing Ventilation in the Japan/East Sea. *Mar. Chem.* 108 (3-4), 137–147. doi:10.1016/j.marchem.2007.11.003

Jin, Y. K., Kim, Y.-G., Baranov, B., Shoji, H., and Obzhirov, A. (2011). Distribution and Expression of Gas Seeps in a Gas Hydrate Province of the Northeastern Sakhalin Continental Slope, Sea of Okhotsk. *Mar. Petroleum Geol.* 28 (10), 1844–1855. doi:10.1016/j.marpetgeo.2011.03.007

Jin, Y. K., Shoji, H., Obzhirov, A., Baranov, B., and R/V Akademik, M. A. (2013). "Operation Report of Sakhalin Gas Hydrate Project," in *Lavrentyev Cruise 59" Proceedings of SSGH-12* (Incheon: Korea Polar Research Institute).

Kawagucci, S., Ueno, Y., Takai, K., Toki, T., Ito, M., Inoue, K., et al. (2013). Geochemical Origin of Hydrothermal Fluid Methane in Sediment-Associated Fields and its Relevance to the Geographical Distribution of Whole Hydrothermal Circulation. *Chem. Geol.* 339, 213–225. doi:10.1016/j.chemgeo.2012.05.003

Kobayashi, M., Kouno, Y., Ito, M., Nishina, M., Fujimoto, Y., and Kato, K. (2009). "Seasonal Change in Number and Movement Pattern of Spotted Seals (*Phoca largha*) Migrating Around the Sea of Japan and Adjacent Areas," in *Paper Presented at Proceedings of the Fourth Workshop on the Okhotsk Sea and Adjacent Areas, Abashiri, Japan, August, 2008*. Editors M. Kashiwai and G. A. Kantakov (PICES Scientific Report No. 36), 76–81.

Kudo, K., Yamada, K., Toyoda, S., Yoshida, N., Sasano, D., Kosugi, N., et al. (2018). Spatial Distribution of Dissolved Methane and its Source in the Western Arctic Ocean. *J. Oceanogr.* 74, 305–317. doi:10.1007/s10872-017-0460-y

Lavrushin, V. Y., Polyak, B. G., Pyrazolo, R. M., and Kaminski, I. L. (1996). Sources of Material in Mud Volcano Products (Based on Isotopic, Hadrochemical, and Geological Data). *Lithology Mineral Resour.* 316, 557–578.

Liao, C., Lee, K. -T., Lee, M. -A., and Lu, H. -J. (1999). Biomass Distribution and Zooplankton Composition of the Sound-Scattering Layer in the Waters of Southern East China Sea. *ICES J. Mar. Sci.* 56, 766–778. doi:10.1006/jmsc.1999.0497

Lin, H.-L., Wang, L.-W., Wang, C.-H., and Gong, G.-C. (1999). Vertical Distribution of δ13C of Dissolved Inorganic Carbon in the Northeastern South China Sea. *Deep Sea Res. Part I Oceanogr. Res. Pap.* 46 (5), 757–775. doi:10.1016/S0967-0637(98)00091-0

Matveeva, T. V., Mazurenko, L. L., Soloviev, V. A., Klerkx, J., Kaulio, V. V., and Prasolov, E. M. (2003). Gas Hydrate Accumulation in the Subsurface Sediments of Lake Baikal (Eastern Siberia). *Geo-Marine Lett.* 23 (3-4), 289–299. doi:10.1007/s00367-003-0144-z

Mishukova, G. I., Mishukov, V. F., Obzhirov, A. I., Pestrikova, N. L., and Vereshchagina, O. F. (2015). Peculiarities of the Distribution of Methane Concentration and Methane Fluxes at the Water-Air Interface in the Tatar Strait of the Sea of Japan. *Russ. Meteorol. Hydrol.* 40, 427–433. doi:10.3103/S1068373915060096

Na, T., Hwang, J., Kim, S.-Y., Jeong, S., Rho, T., and Lee, T. (2022). Large Increase in Dissolved Inorganic Carbon in the East Sea (Japan Sea) from 1999 to 2019. *Front. Mar. Sci.* 9. doi:10.3389/fmars.2022.825206

Nicholson, D. P., Emerson, S. R., Khatiwala, S., and Hamme, R. C. (2011). "An Inverse Approach to Estimate Bubble-Mediated Air-Sea Gas Flux from Inert Gas Measurements," in *Proceedings on the 6th International Symposium on Gas Transfer at Water Surfaces*, 223–327. Available at: https://www.ldeo.columbia.edu/~spk/Papers/Nicholsonetal_InverseAirSeaFlux_11.pdf.

Ogi, M., and Tachibana, Y. (2006). Influence of the Annual Arctic Oscillation on the Negative Correlation between Okhotsk Sea Ice and Amur River Discharge. *Geophys. Res. Lett.* 33 (8). doi:10.1029/2006GL025838

Ogi, M., Tachibana, Y., Nishio, F., and Danchenkov, M. A. (2001). Does the Fresh Water Supply from the Amur River Flowing into the Sea of Okhotsk Affect Sea Ice Formation? *J. Meteorological Soc. Jpn.* 79 (1), 123–129. doi:10.2151/jmsj.79.123

Ogi, M., Taguchi, B., Honda, M., Barber, D. G., and Rysgaard, S. (2015). Summer-to-Winter Sea-Ice Linkage between the Arctic Ocean and the Okhotsk Sea through Atmospheric Circulation. *J. Clim.* 28 (12), 4971–4979. doi:10.1175/JCLI-D-14-00297.1

Park, K.-A., Kim, K., Cornillon, P. C., and Chung, J. Y. (2006). Relationship between Satellite-Observed Cold Water along the Primorye Coast and Sea Ice in the East Sea (The Sea of Japan). *Geophys. Res. Lett.* 33 (10), a–n. doi:10.1029/2005GL025611

Pishchal'nik, V. M., Arkhipkin, V. S., and Leonov, A. V. (2010). On Water Circulation in Tatar Strait. *Water Resour.* 37 (6), 759–772. doi:10.1134/S0097807810060035

Ponomarev, V. I., Fayman, P. A., Prants, S. V., Budyansky, M. V., and Uleysky, M. Y. (2018). Simulation of Mesoscale Circulation in the Tatar Strait of the Japan Sea. *Ocean. Model.* 126, 43–55. doi:10.1016/j.ocemod.2018.04.006

Postlethwaite, C. F., Rohling, E. J., Jenkins, W. J., and Walker, C. F. (2005). A Tracer Study of Ventilation in the Japan/East Sea. *Deep Sea Res. Part II Top. Stud. Oceanogr.* 52 (11-13), 1684–1704. doi:10.1016/j.dsr2.2004.07.032

Riser, S. C., Warner, M. J., and Yurasov, G. I. (1999). Circulation and Mixing of Water Masses of Tatar Strait and the Northwestern Boundary Region of the Japan Sea. *J. Oceanogr.* 55 (2), 133–156. doi:10.1023/A:1007881727369

R. Massel, S. (2015). "Internal Gravity Waves in the Shallow Seas," in *Internal Gravity Waves in the Shallow SeasGeoPlanet: Earth and Planetary Sciences*, 153–156. doi:10.1007/978-3-319-18908-6

Saegusa, S., Tsunogai, U., Nakagawa, F., Gamo, T., Zhang, J., Takeushi, A., et al. (2007). *Methane Anomalies in the Water Columns above Pockmarks, Offshore Sado Island*. Tokyo: Geochemical Society of Japan. Paper presented at Annual Meeting of the Geochemical Society of Japan 2005.

Sakamoto, M., Sano, Y., and Wakita, H. (1992). 3He/4He Ratio Distribution in and Around the Hakone Volcano. *Geochem. J.* 26 (4), 189–195. doi:10.2343/geochemj.26.189

Salomatin, A. S., Yusupov, V. I., Vereshchagina, O. F., and Chernykh, D. V. (2014). An Acoustic Estimate of Methane Concentration in a Water Column in Regions of Methane Bubble Release. *Acoust. Phys.* 60 (6), 671–677. doi:10.1134/S1063771014050133

Sano, Y., and Nakajima, J. (2008). Geographical Distribution of 3He/4He Ratios and Seismic Tomography in Japan. *Geochem. J.* 42 (1), 51–60. doi:10.2343/geochemj.42.51

Sano, Y., and Takahata, N. (2005). Measurement of Noble Gas Solubility in Seawater Using a Quadrupole Mass Spectrometer. *J. Oceanogr.* 61 (3), 465–473. doi:10.1007/s10872-005-0055-x

Shakirov, R. B., Syrbu, N. S., and Obzhirov, A. I. (2016). Distribution of Helium and Hydrogen in Sediments and Water on the Sakhalin Slope. *Lithol. Min. Resour.* 51 (1), 61–73. doi:10.1134/S0024490216010065

Shakirov, R. B., Valitov, M. G., Obzhirov, A. I., Mishukov, V. F., Yatsuk, A. V., Syrbu, N. S., et al. (2019). Methane Anomalies, its Flux on the Sea-Atmosphere Interface and Their Relations to the Geological Structure of the South-Tatar Sedimentary Basin (Tatar Strait, the Sea of Japan). *Mar. Geophys Res.* 40, 581–600. doi:10.1007/s11001-019-09389-3

Shakirov, R. B., Valitov, M. G., Syrbu, N. S., Yatsuk, A. V., Obzhirov, A. I., Mishukov, V. F., et al. (2020). Methane Fluxes at the Water-Atmosphere Interface in the Southern Tatar Strait of the Sea of Japan: Distribution and Variation. *Russ. Geol. Geophys.* 61 (9), 994–1006. doi:10.15372/RGG2019184

Shevchenko, G. V., Vilyanskaya, E. A., and Chastikov, V. N. (2011). Seasonal Variability of Oceanological Conditions in the Northern Part of the Tatar Strait. *Russ. Meteorol. Hydrol.* 36 (1), 55–64. doi:10.3103/S1068373911010080

Smith, S. P., and Kennedy, B. M. (1983). The Solubility of Noble Gases in Water and in NaCl Brine. *Geochimica Cosmochimica Acta* 47 (3), 503–515. doi:10.1016/0016-7037(83)90273-9

Snyder, G. T., Sano, Y., Takahata, N., Matsumoto, R., Kakizaki, Y., and Tomaru, H. (2020). Magmatic Fluids Play a Role in the Development of Active Gas Chimneys and Massive Gas Hydrates in the Japan Sea. *Chem. Geol.* 535, 119462. doi:10.1016/j.chemgeo.2020.119462

Takahata, N., Agarwal, M., Nishizawa, M., Shirai, K., Inoue, Y., and Sano, Y. (2005). Helium-3 Plume over the East Pacific Rise at 25°S. *Geophys. Res. Lett.* 32 (11). doi:10.1029/2005GL023076

Takahata, N., Sano, Y., Horiguchi, K., Shirai, K., and Gamo, T. (2008). Helium Isotopes of Seawater in the Japan Sea. *J. Oceanogr.* 64 (2), 293–301. doi:10.1007/s10872-008-0023-3

Talley, L. D., Lobanov, V., Ponomarev, V., Salyuk, A., Tishchenko, P., Zhabin, I., et al. (2003). Deep Convection and Brine Rejection in the Japan Sea. *Geophys. Res. Lett.* 30 (4). doi:10.1029/2002GL016451

Tarasyuk, S. N. (2002). "Survival of Yellowfin Sole (*Limanda aspera* Pallas) in the Northern Part of the Tatar Strait (Sea of Japan) during the Second Half of the 20th Century," in *Paper Presented at PICES-GLOBEC International Program on Climate Change and Carrying Capacity*. Editors B. C. Sidney and H. P. Batchelder (Canada, PICES Scientific Report No.).

Velikanov, A. Y. (2016). Pacific Sardine (Sardinops Melanostictus) Migrations to the Shores of Sakhalin Island in the 20th-Early 21st Centuries. *J. Ichthyol.* 56 (5), 715–727. doi:10.1134/S0032945216040147

Vereshchagina, O. F., Korovitskaya, E. V., and Mishukova, G. I. (2013). Methane in Water Columns and Sediments of the North Western Sea of Japan. *Deep Sea Res. Part II Top. Stud. Oceanogr.* 86-87, 25–33. doi:10.1016/j.dsr2.2012.08.017

Wessel, P., Luis, J. F., Uieda, L., Scharroo, R., Wobbe, F., Smith, W. H. F., et al. (2019). The Generic Mapping Tools Version 6. *Geochem. Geophys. Geosyst.* 20 (11), 5556–5564. doi:10.1029/2019GC008515

Wiesenburg, D. A., and Guinasso, N. L. (1979). Equilibrium Solubilities of Methane, Carbon Monoxide, and Hydrogen in Water and Sea Water. *J. Chem. Eng. Data* 24 (4), 356–360. doi:10.1021/je60083a006

Yamamoto, S., Alcauskas, J. B., and Crozier, T. E. (1976). Solubility of Methane in Distilled Water and Seawater. *J. Chem. Eng. Data* 21 (1), 78–80. doi:10.1021/je60068a029

Yapa, P. D., Zheng, L., and Chen, F. (2001). A Model for Deepwater Oil/Gas Blowouts. *Mar. Pollut. Bull.* 43 (7–12), 234–241. doi:10.1016/S0025-326X(01)00086-8

Yatsuk, A., Shakirov, R., Gresov, A., and Obzhirov, A. (2020). Hydrocarbon Gases in Seafloor Sediments of the Tatar Strait, the Northern Sea of Japan. *Geo-Mar. Lett.* 40, 481–490. doi:10.1007/s00367-019-00628-5

Conflict of Interest: The authors declare that the research was conducted in the absence of any commercial or financial relationships that could be construed as a potential conflict of interest.

frontiers | Frontiers in Earth Science

ORIGINAL RESEARCH
published: 22 July 2022
doi: 10.3389/feart.2022.858992

Quantitatively Monitoring Bubble-Flow at a Seep Site Offshore Oregon: Field Trials and Methodological Advances for Parallel Optical and Hydroacoustical Measurements

Mario E. Veloso-Alarcón[1], Peter Urban[1,2], Tim Weiss[1], Kevin Köser[1], Mengkun She[1] and Jens Greinert[1,3]*

[1]GEOMAR Helmholtz Centre for Ocean Research Kiel, Kiel, Germany, [2]Department of Geology and Department Data Analysis and Mathematical Modeling, Ghent University, Ghent, Belgium, [3]Institute of Geosciences, Christian-Albrechts University Kiel, Kiel, Germany

OPEN ACCESS

Edited by:
Andreas Lorke, University of Koblenz and Landau, Germany

Reviewed by:
Binbin Wang, University of Missouri, United States
Ian MacDonald, Florida State University, United States

***Correspondence:**
Mario E. Veloso-Alarcón
mveloso@geomar.de

Specialty section:
This article was submitted to Marine Geoscience, a section of the journal Frontiers in Earth Science

Received: *20 January 2022*
Accepted: *10 June 2022*
Published: *22 July 2022*

Citation:
Veloso-Alarcón ME, Urban P, Weiss T, Köser K, She M and Greinert J (2022) Quantitatively Monitoring Bubble-Flow at a Seep Site Offshore Oregon: Field Trials and Methodological Advances for Parallel Optical and Hydroacoustical Measurements. Front. Earth Sci. 10:858992. doi: 10.3389/feart.2022.858992

Two lander-based devices, the Bubble-Box and GasQuant-II, were used to investigate the spatial and temporal variability and total gas flow rates of a seep area offshore Oregon, United States. The Bubble-Box is a stereo camera–equipped lander that records bubbles inside a rising corridor with 80 Hz, allowing for automated image analyses of bubble size distributions and rising speeds. GasQuant is a hydroacoustic lander using a horizontally oriented multibeam swath to record the backscatter intensity of bubble streams passing the swath plain. The experimental set up at the Astoria Canyon site at a water depth of about 500 m aimed at calibrating the hydroacoustic GasQuant data with the visual Bubble-Box data for a spatial and temporal flow rate quantification of the site. For about 90 h in total, both systems were deployed simultaneously and pressure and temperature data were recorded using a CTD as well. Detailed image analyses show a Gaussian-like bubble size distribution of bubbles with a radius of 0.6–6 mm (mean 2.5 mm, std. dev. 0.25 mm); this is very similar to other measurements reported in the literature. Rising speeds ranged from 15 to 37 cm/s between 1- and 5-mm bubble sizes and are thus, in parts, slightly faster than reported elsewhere. Bubble sizes and calculated flow rates are rather constant over time at the two monitored bubble streams. Flow rates of these individual bubble streams are in the range of 544–1,278 mm^3/s. One Bubble-Box data set was used to calibrate the acoustic backscatter response of the GasQuant data, enabling us to calculate a flow rate of the ensonified seep area (~1,700 m^2) that ranged from 4.98 to 8.33 L/min (5.38×10^6 to 9.01×10^6 CH_4 mol/year). Such flow rates are common for seep areas of similar size, and as such, this location is classified as a normally active seep area. For deriving these acoustically based flow rates, the detailed data pre-processing considered echogram gridding methods of the swath data and bubble responses at the respective water depth. The described method uses the inverse gas flow quantification approach and gives an in-depth example of the benefits of using acoustic and optical methods in tandem.

Keywords: methane seeps, bubbles, hydroacoustic quantification, GasQuant-II, optical bubble measurements, Bubble-Box, Astoria Canyon

1 INTRODUCTION

1.1 Methane Seepage

For almost 40 years, scientists have studied the global phenomena of natural methane release from underwater seepage areas at different geological settings (see overview in Suess, 2014). This research has covered different aspects of methane seepage, including their ability to sustain chemoautotrophic ecosystems and microbial communities (Boetius et al., 2000; Sahling et al., 2002; Levin et al., 2016), their geological past and their manifestation in methane derived carbonates (Greinert et al., 2001; Campbell, 2006; Liebetrau et al., 2010), their link to gas hydrates and hydrocarbon reservoirs (Westbrook et al., 2008; Smith et al., 2014; Ruppel and Kessler, 2017), or the potential transport of methane into the atmosphere and its relevance to global atmospheric methane concentrations (Etiope, 2009; Shakhova et al., 2010; Kirschke et al., 2013; Pohlman et al., 2017; Römer et al., 2017; Weber et al., 2019). To answer these questions, scientists have tried to elucidate in detail the mechanism of bubble seepage and its triggers including internal forcing (source depletion and refilling and clogging of pathways) or external forcing (pressure changes, e.g., due to tides, tectonic activity, or sea-level changes) (Westbrook et al., 2009; Berndt et al., 2014; Shakhova et al., 2014; Wallmann et al., 2018).

In all these studies, the key aspects for properly interpreting the spatio-temporal modulations of a bubble seepage area are their quantitative assessment and their accurate geo-reference. For more than a decade, the quantification and positioning of seepage occurrences have been performed using independent or combinations of optical and remote hydroacoustic methods as well as direct sampling techniques (Sauter et al., 2006; Nikolovska et al., 2008; Sahling et al., 2009; Weber et al., 2014). In most cases, only local measurements could be undertaken when, for example, ROVs performed the direct measurement. Others allowed for longer, lander-based, studies at a single release location, seep area (e.g., Leifer and Boles, 2005; Greinert, 2008; Schneider von Deimling et al., 2011; Kannberg et al., 2013), or entire margins (Skarke et al., 2014; Leifer et al., 2017; Riedel et al., 2018); yet another set of studies revisited the same area several times to investigate seep activity and location changes over days (Jerram et al., 2015) to years (Römer et al., 2017; Urban et al., 2017; Veloso-Alarcón et al., 2019). Only few studies allowed for a quasi-continuous evaluation of temporal variability, for example, at the monitoring site Barkley Canyon of the Ocean Networks Canada cable observatory for seep-related biological activity or gas hydrate and seepage dynamics (Römer et al., 2016; Doya et al., 2017; De Leo et al., 2018).

1.2 Investigation Methodologies

Optical observatories employing simple (only a camera and scale) or more sophisticated devices (back-illuminated bubble chambers with high-speed cameras) are commonly deployed and positioned by ROV or divers (Leifer et al., 2000; Rehder et al., 2002; Rehder et al., 2009; Leifer and Culling 2010). These techniques are rather straightforward in theory and very precise in determining bubble sizes and rising speeds, once the hurdle of fast enough acquisition of high-resolution images and subsequent processing of high amounts of data is overcome. Recent improvements include stereoscopic imaging techniques for characterizing bubble release that have been successfully tested under controlled conditions (Wang and Socolofsky, 2015; She et al., 2022) as well as *in situ* (Wang et al., 2016; Razaz et al., 2020; Wang et al., 2020). These are, however, limited (by the range of visual observation) to a distance of a few meters, making active acoustic approaches in combination with optical observatories the method of choice for the quantification of bubble emissions of large areas. Alternatively, passive acoustics has emerged as a new supporting technique for quantitative monitoring of seep areas, including CO_2 CCS areas (Bergès et al., 2015; Li et al., 2020a; Longo et al., 2021; Caudron et al., 2022). Moreover, the combination of hydroacoustics and optical techniques has also been used for studying the dissolution of bubbles within the water column, including the validation of models for mass transfer and bubble transport for natural bubble seepage (Wang et al., 2020).

In contrast to optics, active and passive hydroacoustic systems do not provide direct measurements of the bubble amount and sizes, and quantification is achieved by the sonar signal inversion. Subsequently, a robust method for quantitative assessment of bubble flow rates relies on a very good understanding of the used hydroacoustic technology and the theoretical background of the acoustical backscattering response of bubbles. Particularly, over the last decade, active hydroacoustic systems have been employed during research cruises for mapping bubbling seep areas and quantitative assessments using single beam echosounder systems (SBES; Kannberg et al., 2013; Weber et al., 2014; Veloso et al., 2015; Turco et al., 2022) or multibeam echosounder systems (MBES; Römer et al., 2017; Higgs et al., 2019). Most published quantification methods used hydroacoustic inversion techniques of calibrated SBES parameters as target strength and volume backscattering strength, including the input of optically or acoustically derived bubble size distributions; fewer attempts have been made only using MBES data (e.g., Scandella et al., 2016). The inversion of the MBES signal is still challenging since most of the commercially available echosounder systems, with a few exceptions (e.g., Kongsberg ME70 and iXblue SeapiX), are un-calibrated systems. Compared to the calibration effort for SBESs, calibrating MBESs is more complicated and not yet a standard procedure. Additionally, a very good knowledge about the internal processing steps from signal detection to data recording is important for correctly processing MBES data for gas flow quantifications. As the knowledge about the exact processing is often proprietary information, it is sometimes difficult to get.

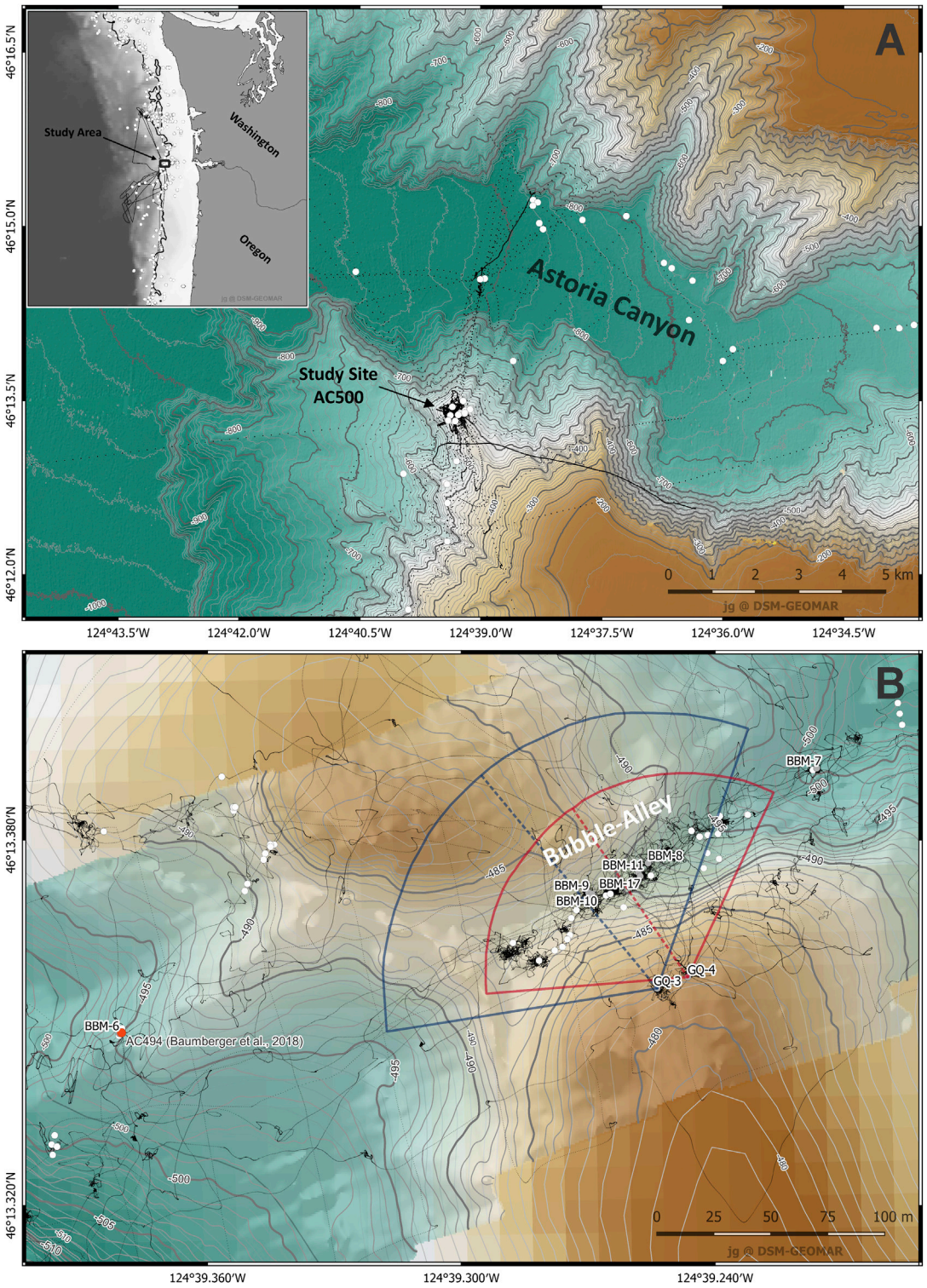

FIGURE 1 | (A) Bathymetric map of the Astoria Canyon area, with the Study Site AC500 on the ridge crest as part of the southern canyon flank. White circles indicate active seep sites detected during MBES surveys from several cruises. Small black spots indicate the cruise track of RV FALKOR. Previously sample seep locations by Baumberger et al. (2018) are given (bathymetric data courtesy of the USGS). **(B)** Detailed map of the AC500 site; bathymetric data have been acquired using the GasQuant Imagenex MBES mounted on the ROV during a mapping survey (Dive 272). All BBM sites are indicated; BBM-11 and BBM-17 locations were close to each other in the middle of the Bubble-Alley. **(A,B)** White dots indicate bubble locations that were annotated during the dives (not all locations are shown), and small black dots are ship **(A)** and ROV tracks **(B)**.

1.3 Data and Scope of the Article

This article describes and analyzes optical and hydroacoustic data from an active seep site offshore Oregon well above the methane hydrate stability zone. The systems used were the lander-based hydroacoustic multibeam system GasQuant-II and the stereo camera–equipped system Bubble-Box (BBox; She et al., 2022), both developed at GEOMAR. The deployments of the systems took place as part of cruise FK190612 with RV FALKOR from the Schmidt-Ocean Institute in June 2019. The cruise was led by the USGS with the aim of investigating gas release above and below the hydrate stability zone at known and new seep sites along the Cascadia continental margin. During the cruise, several sites were investigated during ROV dives and also with GasQuant and BBox deployments, but the data set presented here is only from the Astoria Canyon site AC500 at a water depth of about 500 m (**Figure 1**). Both systems were simultaneously deployed to measure bubble release activity of individual streams (BBox and GasQuant) and an entire seepage area (GasQuant). The measurements were planned as an *in situ* experiment to 1) monitor and quantify gas bubble release at the site for several days and identify potential internal and external forcing on the release; 2) test and verify an approach for parallel deployment of optical and acoustic systems in which bubble parameters are derived from optical information and then used in the inverse hydroacoustic method for temporally and spatially high-resolution quantifications; and 3) highlight system-dependent and general pitfalls of the acoustic quantification caused by the intricacies during acoustic bubble observations.

In detail, we report on the undertaken processing steps to measure bubble size distributions and flow rates over time from both systems. We highlight the difficulties of acquiring good data and particularly of understanding what the received multibeam signals actually represent. In a final step, we merge bubble size distributions, rising speeds, and backscatter intensity to derive bubble flow rates and the variability from the ~1,700-m^2 large seep area. We further discuss bubble flow changes with respect to pressure/tidal, small bubble size variations, and shifts of the bubble location when crossing the acoustic MBES swath. The presented work thus not only presents "another" high-resolution data set about flow rate and temporal variability of gas bubbles at a seep site but also highlights a number of methodological processes that greatly influence the analyses, but are rarely or not considered in many other publications. Furthermore, the presented work provides new insightful information regarding *in situ* MBES calibration using simultaneous optical information, as well as indicating the challenges, the problems, and their possible solutions toward advancing the technique.

1.4 Study Area

The study area lies in a gully-like depression on a ridge crest belonging to the southern slope of the Astoria Canyon system (**Figure 1A**). As such, the area is part of the accretionary prism of the Cascadia margin formed due to the subduction of the Juan de Fuca plate beneath North America. Due to this accretion and the proximity to land and therefore high organic and terrestrial sediment input, the entire region of Cascadia is characterized by the widespread occurrence of active and past methane seepage that make this region one of the most renowned methane seep areas in the world. Locations like Hydrate Ridge (Suess et al., 1999; Torres et al., 2002; Kannberg et al., 2013) or Coil Oil Point (Leifer and Culling, 2010; Schmale et al., 2015) further to the south or Barkley Canyon to the north (Römer et al., 2016; Doya et al., 2017) are part of this larger seep region. **Figure 1B** shows the detailed location of our study and seep site AC500. During cruise FK190612, the wider area of the canyon was studied during several ROV dives and hydroacoustic surveys, showing that a number of already known seep sites were still active whereas new sites, for example, at the edge of the flat canyon infill to the northern canyon slope, were newly discovered. The AC500 sites was known before the cruise through investigations in 2016 during expedition NA072 with E/VNautilus where visual inspections and gas sampling indicated several seep locations with secondarily oxidized biogenic methane being expelled (Baumberger et al., 2018). To repeat gas analyses at site AC494 from the study by Baumberger et al. (2018), the area was revisited with ROV SuBastian during dive 262 and the "Bubble-Alley" within an ENE striking gully-like valley about 150 m east of site AC494 was discovered and inspected more closely (**Figure 1B**). Over a distance of about 150 m, many bubble release sites occur in the sandy seafloor, and more than 100 isolated bubble streams or clusters of them were encountered during live annotation of bubble occurrences as well as during subsequent re-annotation of the video footage. A total of seven ROV dives, including dive 262, were performed at site AC500 (other SuBastian dives were 263, 264, 266, 272, 273, and 276), during which the Bubble-Alley was sampled repeatedly with the BBox and visually inspected for seep-related features such as bubble release, chemoautotrophic fauna, and methane-derived authigenic carbonates.

2 DATA, EQUIPMENT, AND METHODS

2.1 Data Sets

Of the seven ROV dives at the AC500 site, three were used to deploy GasQuant and the BBox in parallel for several days; a total of seven BBox measurements (BBM) and three GasQuant measurements (GQM) were undertaken. In this study, we only present and discuss data from BBM-11 and GQM-3 (dives 264–266) and BBM-17 and GQM-4 (dives 272–276) as these have the needed spatial and temporal overlap for reaching our measurements goals (details see **Table 1**). Both systems were placed accurately by the ROV on the ground, and the transducer head of the GasQuant system was oriented toward the direction of the bubble source, using the compass and manipulator of the ROV to rotate and tilt the transducer head accordingly. The general system parts and functions are briefly described below, followed by a more detailed data processing section.

2.2 Bubble-Box System

The Bubble-Box System (BBox, **Figure 2A–C**) is a compact, ROV-deployable photogrammetric system designed to acquire black and white images for an automatic analysis of bubbles larger than 0.5 mm in diameter. The purpose of the system is to derive

TABLE 1 | Deployment details of the BBox and GasQuant measurements at the AC500 site.

Deployment	ROV dive	Start (2019; UTC)	Stop (2019; UTC)	Depth (m)	Latitude and longitude	System settings
BBM-11	264	19 June, 16:35	21 June, 09:44	490	46.22291153 N 124.65430253 W	1 min recording, 14 min off, 80 images per second
GQM-3	264	19 June, 15:13	21 June, 21:13	482	46.22261273 N 124.65422939 W	120° swath, 80 m range, 480 µs pulse length, 500 samples for entire range, view direction toward ~320°
BBM-17	272	27 June, 16:21	29 June, 19:34	490	46.22290054 N 124.65429503 W	1 min recording, 14 min off, 80 images per second
GQM-4	273	28 June, 13:40	30 June, 06:40	482	46.2226344 N 124.65410701 W	120° swath, 60 m range, 360 µs pulse length, 500 samples for entire range, view direction toward ~325°

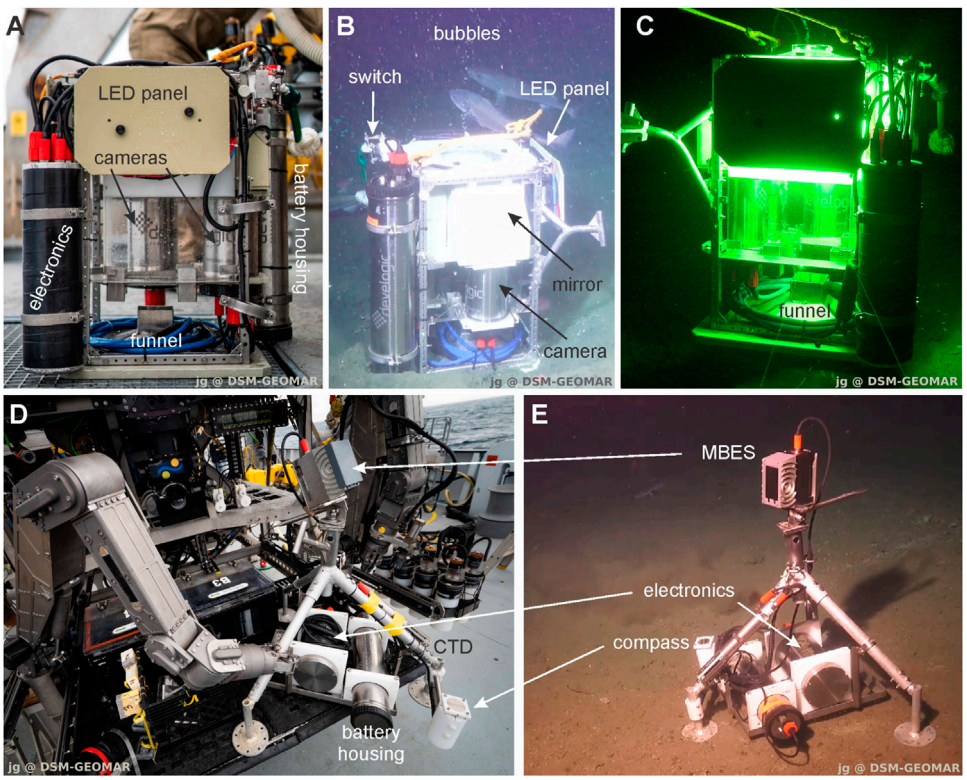

FIGURE 2 | BBox on deck **(A)**, on the seafloor **(B)**, and turned on with flushing LEDs **(C)**. Shown are the different components. In **(B,C)**, bubbles can be seen escaping the BBox on the top; C also shows bubble within the BBox. GasQuant II lander system before deployment on the ROV **(D)** and located on the seafloor **(E)** with main parts of the system indicated.

bubble size distributions (BSD), bubble rising speeds (BRS), and the shape and number of the bubbles per time (**Figure 2**; She et al., 2022). This can be used to directly quantify free gas flow rates and get important input parameters such as size and rising speed for hydroacoustic gas flow quantifications. Two synchronized and photogrammetrically calibrated machine vision cameras take images with a back-illuminated setting (bright-field), where each bubble is photographed from two perspectives of 90° difference. With each image pair, individual bubble positions and shapes can be measured precisely (1% diameter uncertainty) and bubble rising speeds can be determined over time. The upward installed cameras in their 6,000-m pressure-resistant housings look through a 45° tilted mirror at a bubble rise corridor to keep a compact size of the instrument. The lenses are carefully centered within the dome ports to minimize refraction at the air–glass–water interfaces (She et al., 2019). To maximize bubble contrast, a set of four green LEDs (550 nm) is mounted behind acrylic diffusor plates opposite to each camera. The LEDs flash at 80 or 100 Hz to save energy, and a microcontroller triggers the camera at each flash to acquire two synchronized images exposed for 1 ms. Power for the complete system is provided by a container for exchangeable batteries (**Figure 2B**). An additional pressure housing contains the electronics for distributing the power and synchronizing

signals. It further contains the driver circuits for the LEDs. The BBox has a mechanic switch which allows for turning the system on and off by the ROV when in the water.

ROV SuBastian deployed the BBox by placing it as straightly as possible onto the selected bubble release source (e.g., youtube-video-FK-Dive264, video time: ~min 37). The open structure on one side of the box allows for monitoring the rising bubbles through the box and their escape through an opening at the top. A funnel at the bottom of the box ensures that bubbles enter the 8 cm by 8 cm wide rise corridor in the center of the box, where they are recorded by the two cameras. Once the BBox was in position, the measurement was started, using the switch to turn power on. A much more detailed description of the BBox, its technical specifications, and processing steps are given in the study by She et al. (2022).

Prior to deployment, the computer times were synchronized to UTC time and the setting parameters were set (**Table 1**). Upon recovery of the system, data were downloaded and visually inspected to check data quality. In general, bubbles were successfully captured by the two cameras with the exception of some time-intervals when the camera dome ports were blocked by sediment and/or animals (sea urchins) or when the observed bubble stream moved out of the camera field of view. The latter happened in two deployments when the BBox sank into the sediment and lost its upright orientation. Example images are provided as **Supplementary Figure S4**. Prior to and after the cruise, the two cameras were photogrammetrically calibrated in the laboratory (She et al., 2022), but re-calibration was necessary for the *in situ* acquired images because slight movements of the mirrors and camera housings occurred due to the increased pressure and lower temperature at depth. Thus, slight adjustments of the *in situ* calibration were derived by manually selecting a subset of images from the entire observation time; it was verified that the same re-calibration parameters can be used for all deployments. The BBox data were processed as discussed in the study by She et al. (2022) and results include individual bubble sizes (mm radius of the volume equivalent sphere) and rising speeds (cm/s), the number of bubbles per time (n/s), and the respective volume flow rates (ml/s). Three data sets could be derived, one for each camera individually (camera 1 and 2) as well as the stereo matching result. The automated recording was set to one minute of recording every 15 min which results in about 3,600–4,000 images per interval used for bubble analyses. The data of the two BBox deployments are published on PANGAEA (Veloso-Alarcón et al., all BBox related post-processed data will be submitted soon; the DOI will be added in the final article).

2.3 GasQuant II System

The GasQuant II system is a hydroacoustic lander with a horizontally oriented multibeam swath for performing long-term observations of bubble release activity of an entire seep area. In contrast to a vertically oriented swath, which needs to be mechanically rotated (e.g., Römer et al., 2017), a vertically oriented swath enables us to monitor the target area continuously without spatial or temporal gaps for the entire 120°-wide swath. GasQuant II (**Figures 2D,E**) was built as the successor of the original, much larger GasQuant system (Greinert, 2008), which has been successfully used for tempo-spatial variability measurements of gas releases in the Black Sea and North Sea (Greinert, 2008; Schneider von Deimling et al., 2011). GasQuant II uses an Imagenex 837B Delta T multibeam as its primary sensor (similar to the work of Scandella et al., 2016 and Römer et al., 2017). The transducer has a maximum opening angle of 120°, comprises 120 beams, and transmits at 260 kHz. The beam opening angles as given by the manufacturer are 3° by 3°; no details are given about the suppression level of the side lobes. The measurement range extends from 5 to 100 m and can be set at nine different discrete levels of the maximum recording range. The Imagenex provides 500 data values (independent of the range) for each beam that represents voltage levels proportional to the backscattered acoustic pressure, the applied time-varying gain, and a constant gain (the start and display gains of the system). The time-varying gain compensates the propagation loss for volume backscattering (named extended target by the manufacturer). These values can be converted to un-calibrated amplitudes proportional to backscatter volume strength values as described in **Supplementary Section 1**. It needs to be noted that these un-calibrated amplitudes are possibly angle dependent (where in the swath, the backscatter target exists) as shown by Scandella et al. (2016). Thus, an angular correction of the backscatter amplitudes of the echogram might be required. The multibeam is installed on top of a tripod at a height of 1.25 m (**Figures 2D,E**). A Sea and Sun CTD is attached to the tripod to record pressure, temperature, and conductivity, used for investigating pressure changes over time and to derive the ambient sound velocity in real time and feed it into the Imagenex for sound velocity adaptations. A magnetic compass provides information about the orientation of the lander general view direction of the transducer. Electric power of 3 kWh is provided by lithium battery cells installed in a housing for exchangeable batteries. The power is distributed to the different sensors through the additional electronics housing that holds the control computer and logging unit for the multibeam and CTD. The system is preprogrammed to start at a certain time, and it is stopped manually upon recovery. The system was deployed with the ROV and placed on the seafloor using its manipulator (e.g., youtube-video-FK-Dive264, video time ~min 16). In total, five deployments were conducted during FK190612, but only GQM-3 and GQM-4 are used in this study. **Table 1** summarizes settings, date–time information, and position of the GasQuant deployments. The data of the two GasQuant deployments presented here are published on PANGAEA (Veloso-Alarcón et al., all BBox related post-processed data will be submitted soon; the DOI will be added in the final article). A detailed description about data quality is given in **Supplementary Section 2**. Because the processing of the acoustic data is essential for correct interpretation of the data, the different processing steps are explained in more detail here.

2.4 GasQuant Data Processing

2.4.1 MBES Data Correction

The first step in processing was correcting the Imagenex MBES data for transmission loss due to sound absorption. The original absorption of 0.1 dB/km was replaced by new values calculated using the recorded CTD data and applying the empirical relation of Francois and Garrison (1982). Absorption values and ambient parameters used for the deployments GQM-3 and GQM-4 are presented in **Supplementary Table S1**. Un-calibrated volume backscattering values (A_V) along each beam were calculated using the recorded amplitude/voltage values A_{rec} of the system

(**Supplementary Equation S.1**). Due to lack of our own experimental calibration, the angular correction of A_V was not applied.

2.4.2 MBES Data Gridding and Interpolation

For quantitative analysis of MBES water column imaging data (WCI), it must be acknowledged that volumes of neighboring acoustic samples from adjacent beams physically overlap. Summing up measurements of neighboring beams to a combined value would therefore lead to an overestimation of the measured gas flow depending on the exact beam overlap. To overcome this problem, we applied the gridding method presented by Urban et al. (2022), in which un-calibrated volume backscattering values A_V (proportional to volume backscattering) of the ping-based WCI data were gridded onto a two-dimensional voxel grid by calculating an average acoustic value from all samples in the vicinity of each voxel (voxel weighted mean method from the study by Urban et al., 2022). Voxel volumes were set to 0.7 m by 0.7 m horizontal and 1 m vertical (Δx, Δy, and Δz). A horizontal size of 0.7 m was determined as a lower limit before the voxel-grid started to have empty voxels because of the sample spacing between beams at a larger range. Temporarily, pings were averaged over 60 s although the ping rate was set to 6.3 and 7.6 pings per second for GQM-3 and -4, respectively. The gridded un-calibrated volume backscattering values $A_{V(i,j)}$ are multiplied by their voxel volume to obtain un-calibrated acoustical cross-section values $A_{bs(i,j)}$ that are proportional to the total backscattering cross-section within each voxel (**Eq. 1**):

$$A_{bs(i,j)} = A_{V(i,j)} \Delta x \Delta y \Delta z \tag{1}$$

Due to the limited acoustic resolution (wide beam opening angle of 3°), gridded amplitudes may include backscatter signals from other targets in the water column which are physically not located in the respective grid voxels. Urban et al. (2022) showed that the summation of the gridded voxels $A_{bs(i,j)}$ (**Figure 3**) approximates to a value proportional to the total backscattering cross-section of the targets within the ensonified volumetric section of the total backscattering cross-section σ_{bsT}. In this case, σ_{bsT} can be written as follows:

$$\sigma_{bsT} = kA_{bsT} \tag{2}$$

where k is a constant representing the proportionality between the real and the un-calibrated total backscattering cross-section. The value k was approximated through theoretical considerations as indicated in **Supplementary Section 1** (**Supplementary Eq. S.6**).

2.4.3 Seep-Anomalies Tracking and Amplitude Determination

The interactive display of consecutive echogram voxel grids allowed for visual identification of acoustic anomalies potentially related to gas seepage in the monitored area (e.g., **Supplementary Figure S5**; **Supplementary Videos 1 and 2**). Since bubbles move laterally with currents, their acoustic signals change position within the echogram. Two algorithms were applied for tracking these locations over time (**Supplementary Section 3**). None of the algorithms always worked successfully, especially in areas where acoustic artifacts, noise, and reverberation occasionally masked the bubble seepage signal. In such cases, an interactive method implemented in MATLAB was used which allows for a 3D visualization of the data around the potential seep location with time as the z-axis (**Supplementary Figure S5**). Signals outside of a continuous signal trend can be interactively deleted before the cell with the maximum backscatter value for each ping is detected and determines the central position of the seep spot. This interactive approach was performed when the automated tracking failed (about 30% of the seep spot locations needed manual interaction).

A representative (un-calibrated) backscatter amplitude of the respective seep-anomaly A_{bsT} was calculated by the exponential summation of all $A_{bs(i,j)}$ values within a 5 by 5 voxel area around the tracked central seep-anomaly voxel (i.e., $10\log\sum_{5x5Area}10^{Abs_i/10}$). Alternatively, the overall amplitude of the entire echogram fan (OVA) was calculated by integrating the gridded-voxels (i.e., $10\log\sum_{FAN}10^{Abs_i/10}$). This was done for performing activity analysis assuming that the total amplitude modulation was only affected by mobile targets (e.g., bubbles) and backscatter from static reflectors such as the seafloor remained constant. Additionally, the fan was spatially masked where the seafloor was clearly identified. Subsequently, the overall amplitude of the echogram fan excluding the masked region (OVA-masked) was calculated in the same way as explained for the OVA time-series. Both OVA and OVA-masked time series were obtained for GQM-3 and GQM-4 deployments.

2.5 Acoustic Bubble-Flow Rate Quantification

2.5.1 Calibrating GasQuant Acoustic Data With BBox Measurements

The approach of our trials is to use verified bubble-flow rates from the BBox to derive a scaling factor for correlating the acoustic seep-anomaly signals seen in the GasQuant MBES echogram data. Thus, at least one BBox-observed bubble stream needs to be matched with one of the acoustic anomalies within the echogram of the corresponding GQM. To find the BBox location in the MBES-echogram, first, the navigational data of the GasQuant and BBox locations were used and the echograms corresponding to the time when the BBox was placed on the seep-spot were investigated (youtube-video-FK-Dive264, video time ~16 min). As GasQuant was deployed before, the BBox placement reflections of the ROV itself pinpointed the approximated BBox position in the MBES-echogram.

The selection criteria for the BBox bubble stream include that it should be rather isolated (no other bubble stream in the direct proximity) and that it should consist of one vent that could be completely covered with the BBox funnel. As such, the selected bubble stream was not very strong, and finding an isolated bubble stream was difficult in the Bubble-Alley. Two acoustic anomalies (control acoustic anomalies) were identified and used separately to derive the scaling factor value. Only one set of deployments

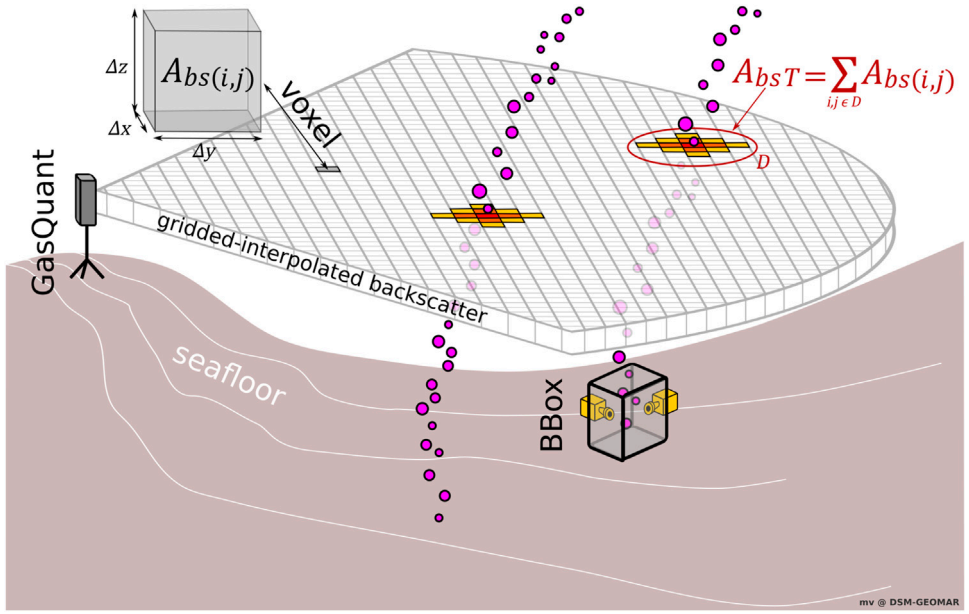

FIGURE 3 | Schematic of experimental setup for parallel GasQuant and BBox measurements at the study area. The image includes the idealized gridded-interpolated echo-fan used for the calculation of the representative un-calibrated amplitudes A_{bsT} of a single bubble-stream. The graph indicates that each voxel has its specific un-calibrated backscatter value $A_{bs(i,j)}$.

(GQM-3 and BBM-11) reached the selection criteria and was used for deriving the MBES scaling factor for all GasQuant-based flow-rate quantifications.

2.5.2 Scaling Factor

Within a horizontal-oriented MBES ensonifying a bubble stream with separation between bubbles comparable to the wavelength, the summation of the acoustic backscatter cross-section of gridded voxels σ_{bsT} (**Eq. 2**) can be approximated by the summation of the theoretical backscatter of the single bubbles (incoherent backscattering; e.g., see Sarkar and Prosperetti, 1993) located within the ensonified parcel of water (**Eq. 3**).

$$\sigma_{bsT} = \Delta z \sum_{r_i}^{r_f} \frac{N_r}{\Delta t U_r} \sigma_{bs}(r) \tag{3}$$

where

$\sigma_{bs}(r)$: Theoretical backscattering cross-section of a single bubble in the function of bubble radius r [m^2]
N_r: Number of bubbles of radius r measured in a Δt interval of time [n.° bubbles]
U_r: Average bubble rising speed of bubbles of radius r [m/s]
Δt: Time interval of measurement [s]
r_i, r_f: Initial and final radius size of the bubble size distribution [m]
Δz: Voxel depth [m]

Equation 3 allows us to calculate the total acoustical cross-section per unit of vertical distance (in this case the voxel depth), based on bubble numbers (N_r) per unit of time (Δ_t) and binned according to their size, their associated bubble rising speeds (U_r) and the theoretical response of single bubbles. If N_r/Δ_t and U_r are obtained from the ground-truthed BBox measurement and the associated total amplitude A_{bsTG} from the gridded echogram data is known the value of proportionality k from **Eq. 2** can be obtained by replacing σ_{bsT} in **Eq. 3** with **Eq. 2**:

$$k = \frac{\Delta z \sum_{r_i}^{r_f} \frac{N_r}{\Delta t U_r} \sigma_{bs}(r)}{A_{bsTG}} \tag{4}$$

where

$$A_{bsTG} = \sum_{i,j \epsilon D_G} A_{bs(i,j)} \tag{5}$$

D_G is the spatial domain (grid cells) containing the voxels of the control acoustic anomaly. If a probability density function of f_r not changing in time is assumed, **Eq. 4** can be expressed as follows:

$$k = k_0 \Delta z \sum_{r_i}^{r_f} \frac{f_r}{U_r} \sigma_{bs}(r) \tag{6}$$

Where

$$k_0 = \frac{N_0}{\Delta t A_{bsTG}} \tag{7}$$

$$f_r = \frac{N_r}{N_{TOT}} \tag{8}$$

and

$$\sum_{r_i}^{r_f} f_r = 1 \tag{9}$$

N_r: Total number of bubbles of radius r in the entire data series (binned data).
N_{TOT}: Total number of bubbles counted in the entire data series.
N_0: Number of bubbles counted at each 1-min data-package analysis.

The value k_0 is defined as the scaling factor which is a constant value used to calibrate the MBES echosounder under the assumption that f_r does not change in time.

2.5.3 Frequency-Dependent Hydroacoustic Bubble Response

We derived the acoustic response of the ensonified section of the bubble stream under the specific ambient pressure conditions by using the theoretical model of Thuraisingham, (1997) with improvements for the damping (Ainslie and Leighton, 2009; Ainslie and Leighton, 2011) as considered by Li et al. (2020b). Values for the ambient conditions and other constants used to perform the model calculations are listed in **Supplementary Table S2**. The resulting acoustical response of single spherical bubbles ranging from 0.05 to 20 mm in radius and ensonified by a monochromatic acoustic signal of 260 kHz is shown in **Supplementary Figure S6**. From this response, it can be seen that the backscatter cross-section TS significantly varies repeatedly for small-size changes. This highlights that bubble size changes of only 0.5 mm could theoretically increase/decrease the backscatter response by up to 40 dB.

2.5.4 Flow Rate Quantification Using the Inverse Method

For deriving the inverse mathematical expression, the flow rate calculation is defined as in **Eq. 10**:

$$\Phi = \frac{N_0}{\Delta t} \sum_{r_i}^{r_f} f_r V_r \tag{10}$$

This expression is multiplied by the ratio (~1) between the measured backscatter (**Eq. 2**) and the theoretically predicted backscatter (**Eq. 3**). Considering that the probability density function f_r is non-variant in time and each bubble size has an associated bubble volume V_r and rising velocity U_r), **Eq. 10** can be written as follows:

$$\Phi = kA_{bsT} \frac{\frac{1}{\Delta t}\sum_{r_i}^{r_f} f_r V_r}{\frac{\Delta z}{\Delta t}\sum_{r_i}^{r_f} \frac{f_r}{U_r}\sigma_{bs}(r)} \tag{11}$$

Replacing k with **Eq. 6** in **Eq. 11** results in the simplified flow rate of **Eq 12**:

$$\Phi = k_0 A_{bsT} \sum_{r_i}^{r_f} f_r V_r \tag{12}$$

Note that **Eq. 12** is independent of the backscattering acoustic response when f_r, U_r, and V_r are considered constant through time.

3 RESULTS

3.1 Bubble Sizes and Rising Speeds in BBox Data

The two BBox deployments, BBM-11 and BBM-17, are analyzed in this study. As previously mentioned, the data were occasionally affected by view obstructions (BBM-17) through sediment or sea urchins or the incomplete coverage of the bubble stream (BBM-11) in both cameras, preventing a stereo evaluation. Bubbles could still be counted "manually" assuming the bubble position and 3D shape (monocular approximation). However, we experienced some discrepancies in monocular evaluation when compared to the stereo evaluation, and due to the lower confidence of these intervals, they were excluded from later analysis. In summary, the presented bubble-size–related time series only contain those times where bubble numbers varied by less than 100 between camera 1 and camera 2 and where a stereo matching could be achieved. The final results for the two BBox data sets are shown in **Figure 4** and **Supplementary Table S3**.

In general, the results show no significant variability in bubble sizes within one and between the two measurements. Similarly, the amount of bubbles per time does not vary significantly within each measurement, but they are about twice as high in BBM-17, with ~19 bubbles/s compared to only ~9 bubbles/s in BBM-11. Thus, the calculated flow rate of BBM-17 is approximately double the one from BBM-11 (6.55 cm^3/s compared to 12.28 cm^3/s). This indicates that the initial bubble size at release is not changing between different seep spots, but the number of bubbles changes and therefore modulates the flow rate.

For bubble number analyses of any individual 1-min data sets, we considered results from the individual camera observations and excluded the ones from the stereo matching. This is because the number of bubbles analyzed through the stereo matching is lower due to the difficulties in the actual matching. Single bubbles can be measured better using the stereo matching method, but when many bubbles form a bubble stream, some bubbles are occluded by others and leave the observation corridor unnoticed. Conversely, bubble size and rising speed analyses were performed using results from the stereo matching approach since they provide higher confidence. For deriving an average bubble size distribution (BSD), bubbles were binned according to their size in 0.25-mm intervals between 0.5 and 15 mm for both BBM data sets. **Figure 5A** shows the average normalized BSDs from the stereo matching and their combination of both BBM data sets. Similarly, bubble rising speeds (BRSs) from the stereo matching results were binned according to their size. **Figure 5B** shows BRSs for the two deployments together with their combination.

The BSDs of both deployments are roughly Gaussian distributed with a center at about 2.6 mm in radius for similar bubble sizes (BSD BBM-11: ~2.6 mm and BSD BBM-17: ~2.4 mm). Most of the bubble sizes range from 1 to 4 mm in radii and BRSs vary from 10 to 47 cm/s and are slightly faster for BBM-17 than for BBM-11 (**Figure 5B**). BRS distributions for the two deployments have a local maximum radius around ~1 mm, after which the rising speed decreases slightly with increasing bubble size until a bubble radius of 3.5 mm. BRSs of bubbles

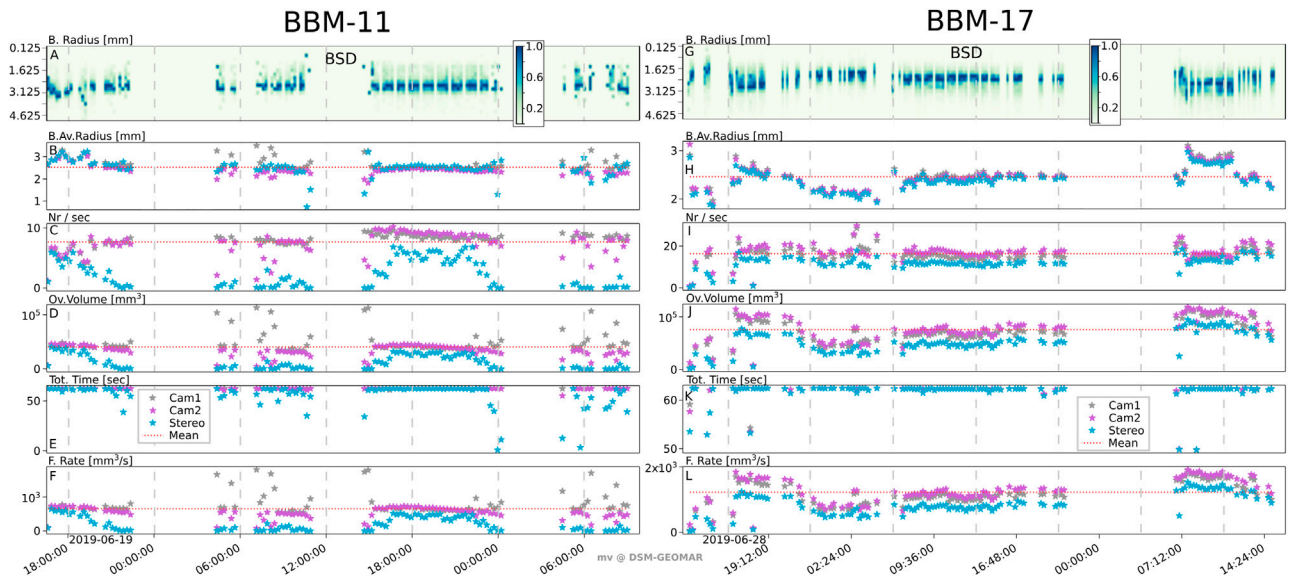

FIGURE 4 | Bubble-Box results versus time including BSD, average sizes, number per time, overall volume, time period of bubble analyses, and flow rates. **(A–F)** Results for BBM-11. **(G–L)** Results for BBM-17.

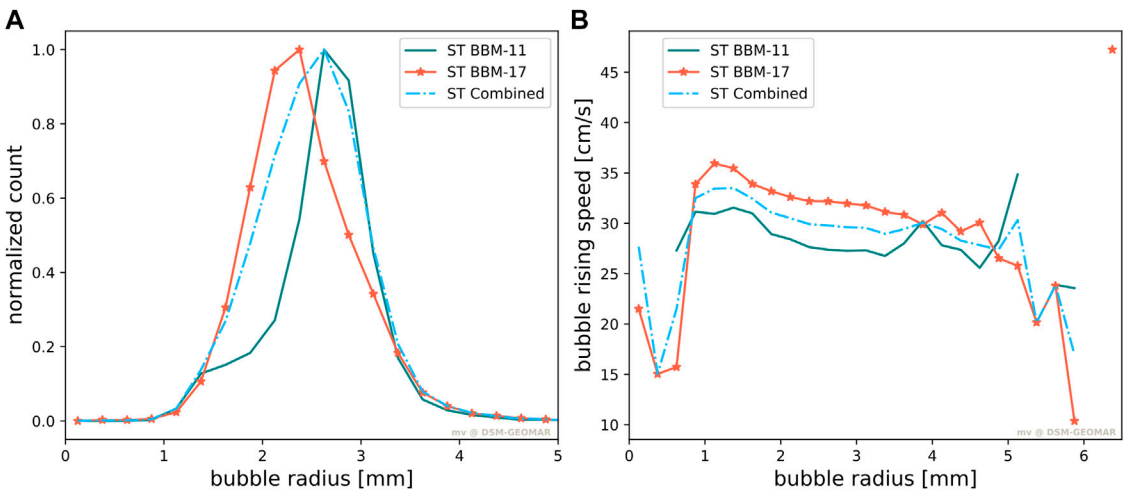

FIGURE 5 | (A) Normalized bubble size distributions (BSDs) obtained from results of the stereo-matching approach at each BBM deployment (ST BBM-11 and ST BBM-17) and the average between them (ST Combined). **(B)** Bubble rising speeds in function of the radius generated from the results of the stereo-matching approach (ST BBM-11 and ST BBM-17) and the average between them (ST Combined).

larger than 4 mm in radius scatter wider than the rising speeds of bubbles smaller than 4 mm. Rising speeds between 25 cm/s and 40 cm/s are rather rapid compared to data presented, for example, in the study by McGinnis et al. (2006), but the size distribution is very similar to many other observations from different seep locations (see discussion).

3.2 GasQuant Results

Tracking of potential seep-related acoustic anomalies in the MBES swath data resulted in eight locations for GQM-3 and 10 locations for GQM-4 (**Figure 6**; **Supplementary Excel file F1**; **Supplementary Videos 3, 4**). The time-series of the tracked position for each acoustic anomaly were created using the difference to the transducer position in UTM coordinates (UTM zone 11; x = easting, y = northing). The tracked seep anomaly positions were later geo-referenced using the absolute coordinate of each GasQuant deployment (**Table 1**) to link them accurately to the bathymetry of the study area and to each other (**Figure 6**). Amplitudes of each single acoustic anomaly were calculated as described in **Section 2.4** (**Supplementary Figures**

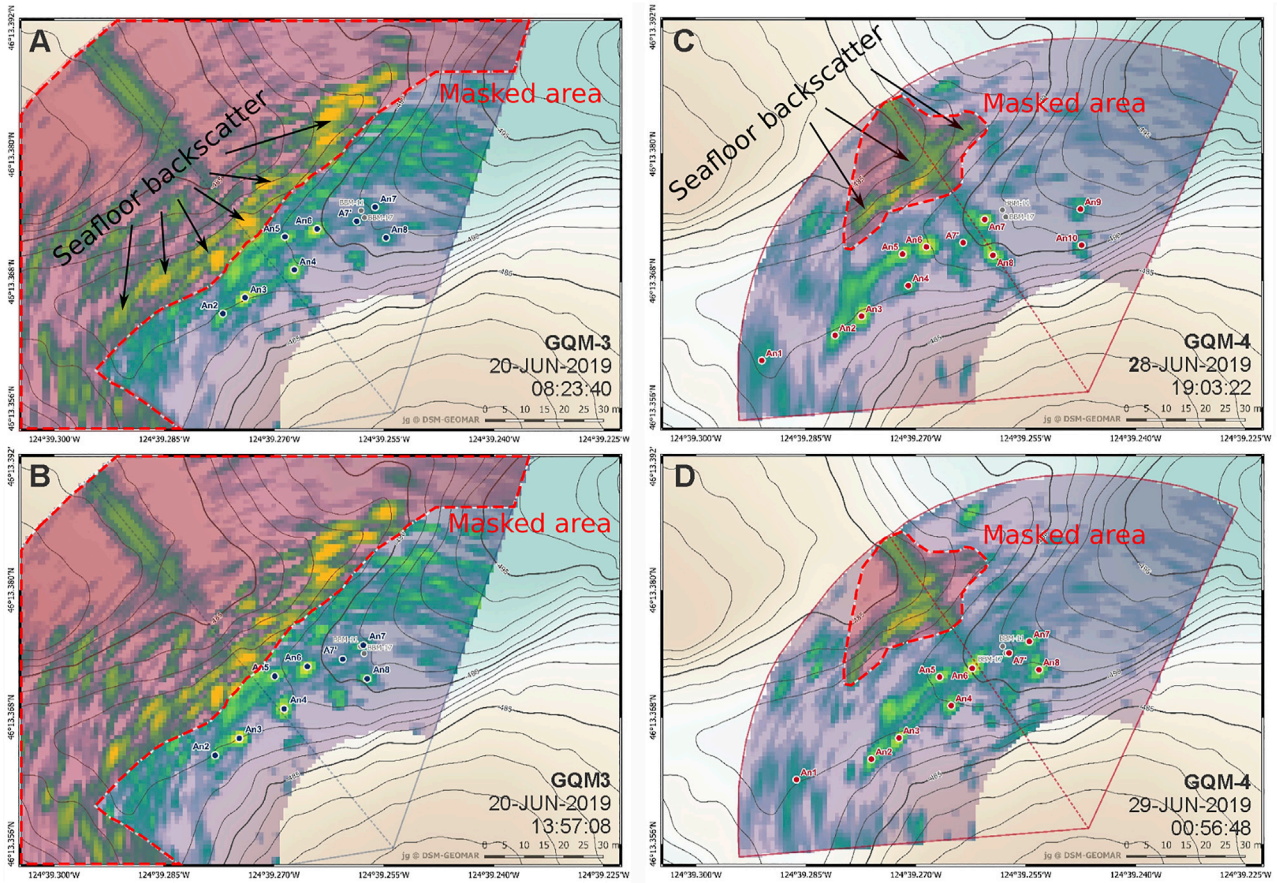

FIGURE 6 | Bathymetric maps of the study area including GQM echogram-fan at different times for the two deplyments. The maps include the average position at different times of the tracked anomalies related to gas seepage, the position of the Bubble-Box lander from the different BBM deployments, the upper view of the areal coverage of each GQM deployment, and the eliminated masked regions for calculating the OVA-masked amplitude time-series. Additionally, **(A,B)** echograms related to times when anomalies were at their maximum displacement to the east and west, respectively, are shown for deployments GQM-3 **(A,B)** and GQM-4 **(C,D)**. The image also indicates the acoustic anomalies related to seafloor-backscattering.

S7, S8; **Supplementary Excel file F1**). Additional strong anomalies were identified but associated to seafloor returns since they perfectly matched with the geomorphology and did not show any spatial modulation (**Figure 6**). Our observations indicate that GQM-3 echograms were more contaminated by seafloor backscattering than GQM-4 echograms. OVA and OVA-masked time series were calculated as indicated in **Section 2.4**. Masked regions containing seafloor backscattering that were excluded for the calculation of OVA-masked time series are indicated in **Figure 6**. Finally, the overall contribution of single anomalies was also derived for both deployments using their exponential summation (i.e., $ASA = 10\log\sum_i 10^{AbsTi/10}$). **Figure 7** shows ASA, OVA, and OVA-masked time series (**Figures 7B,E**) together with hydrostatic pressure and ambient temperature (**Figures 7A,D**), and BBox results (**Figures 7C,F**; i.e., bubble sizes and number of bubbles per time) for comparison. For evaluating any angular dependency of the recorded backscattering, we calculated time-series of the weighted arithmetic mean of angles from the nadir of single acoustic anomalies (WAN) as indicated in **Eq. 13**. WAN time-series are included in **Figure 7**.

$$WAN(t) = \frac{\sum_{i=1}^{N} |\varphi_i(t)| Abs_{Si}(t)}{\sum_{i=1}^{N} Abs_{Si}(t)} \quad (13)$$

$|\varphi_i(t)|$: Absolute angle from the nadir of each acoustic anomaly (degrees); Abs_{Si}: un-calibrated acoustical cross-section single acoustic anomaly (m^2).

3.3 Variability of Seep-Related Acoustic Anomalies

For qualitatively analyzing the bubble release variation, data were processed in the time and frequency domain. First, amplitude and position time-series were plotted jointly with the pressure time-series to visually inspect potential relationships to the tidal regimes (**Figure 7**; **Supplementary Figures S7, S8**). Seep anomaly data show a clear tide-induced lateral shift in easting

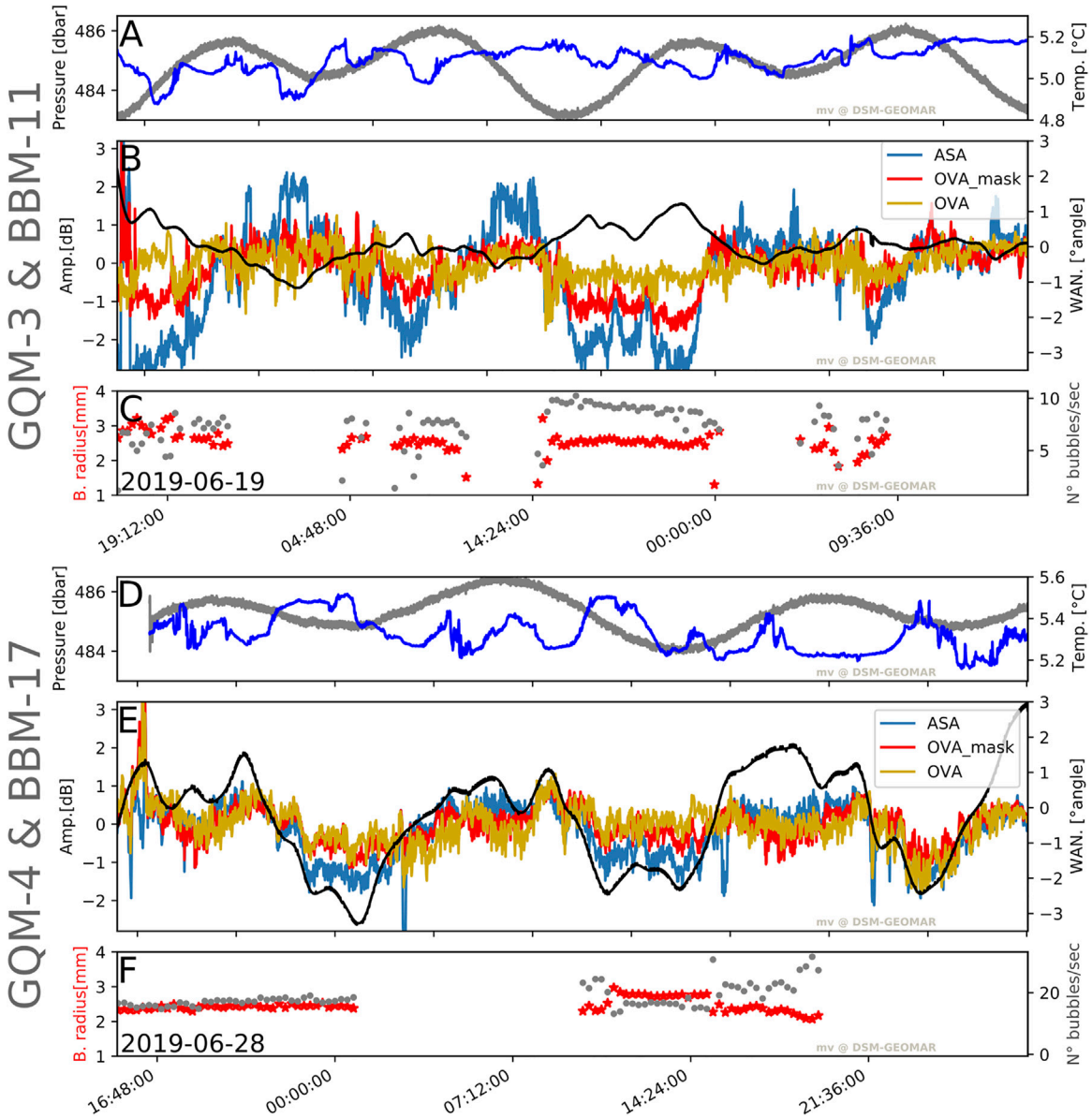

FIGURE 7 | (A–C) from BBM-11 & GQM-3; **(E,F)** from BBM-17 & GQM-4. Time series of **(A,D)** static pressure and water temperature; **(B,E)** show the overall acoustic amplitudes of the gridded-echogram sub-regions (OVA and OVA masked), the sum of all single seep spot anomalies (ASA), and the WAN time-series for GQM-3 **(B)** and GQM-4 **(E)**. Mean values of each amplitude time series were subtracted to be display time-series together (median OVA: 57.77 [dB], median OVA-masked: 48.02 [dB] and median ASA: 45.88 [dB] for deployment GQM-3; median OVA: 49.05 [dB], median OVA-masked: 47.15 [dB] and median ASA: 45.80 [dB] for deployment GQM-4). Figures **(C,F)** show average bubble radius and number of bubbles per time from BBox data BBM-11 and BBM-17, respectively.

and northing of sometimes several meters with changes of the same period for most of the tracked anomalies in both deployments (from An2-An8 in GQM-3 and all the anomalies in GQM-4). Similarly, time-series from amplitudes of the total contribution of single anomalies (ASA) as well as the total amplitudes from the gridded-echogram of GQM-4 (OVA and OVA-masked) vary with a similar period as the pressure data.

For quantitatively evaluating the correlation between the acoustic amplitudes (i.e., ASA, OVA, and OVA-masked time series) and the gradient of pressure (derivative), a lagged Pearson correlation (LPC) was performed for time legs ranging from −6 to 6 h (**Figures 8A,B,D,E**). Additionally, a simple Pearson correlation was applied between the acoustic amplitudes and the angle from the anomaly to the nadir to detect any correlation with the MBES angular response (**Figures 8C,F**). Results from the LPC show that for GQM-3 (**Figure 8A**), ASA and OVA-masked time-series have a moderate negative correlation with the pressure gradient (i.e., coefficients ≤ −0.5) whereas OVA time-series have a low negative correlation (≥ −0.5) with a small lag applied (~ −40 min for ASA and OVA-masked and ~90 min for

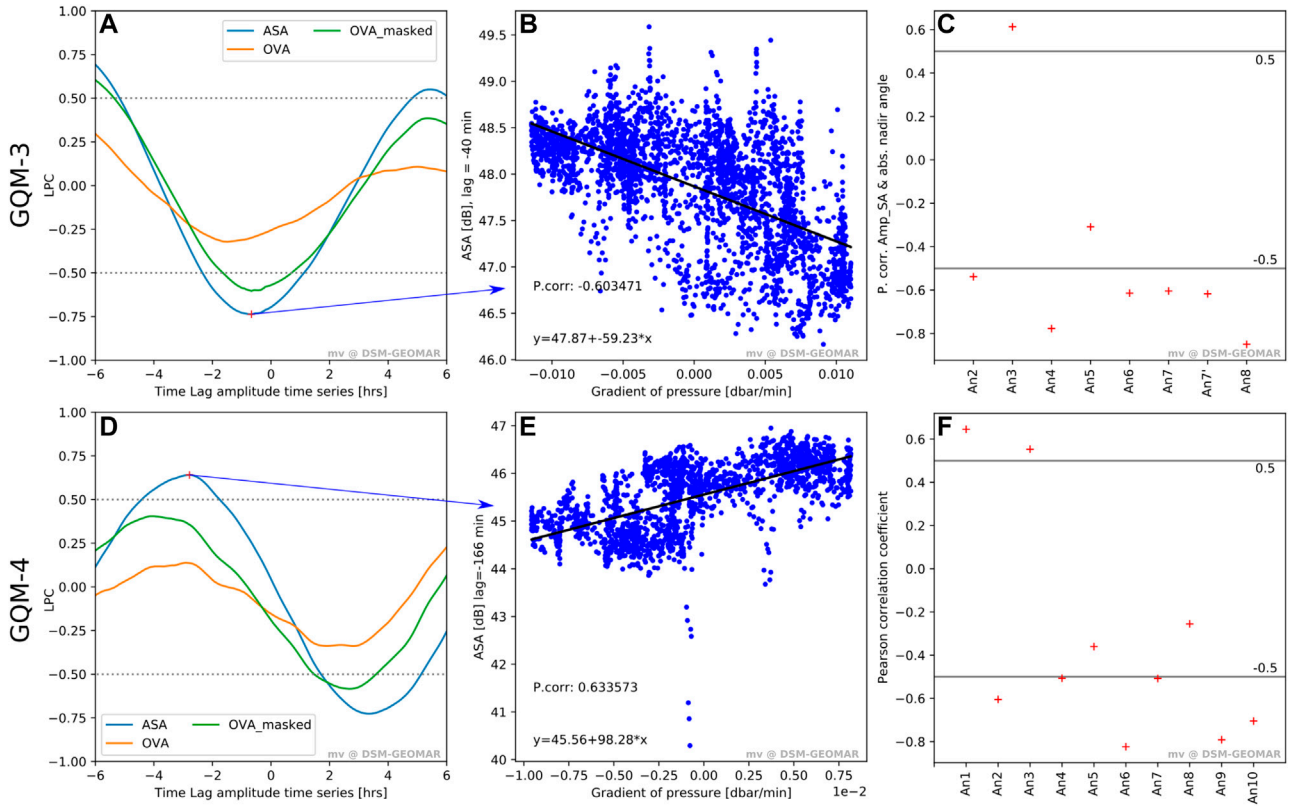

FIGURE 8 | Correlation analyses for overall amplitudes and acoustic anomalies detected in GQM-3 and GQM-4. **(A,D)** are results from the lagged Pearson correlation (LPC) between time-series of the gradient of the static pressure and overall amplitudes (OVA, OVA-masked, and ASA) associated with bubble release for GQM-3 and GQM-4, respectively. **(B,E)** are examples of the negative and positive lagged correlation maxima for ASA time-series for GQM-3 and GQM-4, respectively. **(C,F)** is the Pearson correlation between each single anomaly related to gas seepage and their angle from the MBES-nadir for GQM-3 and GQM-4, respectively.

OVA). Assuming that flow rates are proportional to amplitudes, this can be interpreted as evidence of maximum flow rates increasing with the strong hydrostatic pressure decay for most of the ensonified seeps during the GQM-3 deployment. The latter has been explained in other studies to be the result of the pressure release on the fluid conduit network and surface near gas reservoirs/pockets in the sediment (e.g., Schneider von Deimlig et al., 2010; Scandella et al., 2011; Römer et al., 2016). Furthermore, the low negative correlation between the OVA-time series and the pressure gradient can be attributed to a stronger influence of seafloor backscatter on its calculation.

LPC results for GQM-4 (**Figure 9**) show that the time-series amplitudes have a moderate positive correlation with pressure changes when the time lag is between ~−3 to −2 h. This suggests that the flow rate of the overall seepage site, assuming flow rate is proportional to the amplitude, modulates in a similar way to the hydrostatic pressure. Differently than GQM-3, these results are in contradiction to the π/2 phase lag between maximum pressure and flow rate rising regimes commonly observed in other studies (Schneider von Deimlig et al., 2010).

An alternative explanation of the amplitude modulation is indicated when calculating the Pearson correlation between amplitudes of single anomalies and their relative nadir angle (C and F in **Figure 8**). Results show a moderate-to-strong correlation for most of the seepage-related anomalies detected in GQM-3 (7 of 8) and GQM-4 (8 of 10). This good correlation can be interpreted as an effect of the MBES angular response or influences of additional backscattering (e.g., seafloor backscatter) captured by the main or side lobes. The latter is supported by the strong positive correlation between amplitudes (ASA, OVA, and OVA-masked) and WAN time-series observed in **Figure 7E**.

A Fast Fourier Transform (FFT) was applied to all amplitude and tracked position time-series to identify the main periodic components in the frequency domain (**Supplementary Figure S9**). Results show that for both GasQuant deployments, tracked position and amplitude time-series contain a dominant component at ~0,023 mHz (~12 h) as well as at 0,046 (~6 h) and 0,015 (~18.5 h). The latter two are recognized as harmonics; no important spectral components are recognized at higher frequencies.

3.4 Bubble-Flow Rate Strength and Variability

To obtain bubble flow rates, the scaling factor k_0, as derived through **Eq. 7**, was calculated for the total contribution of

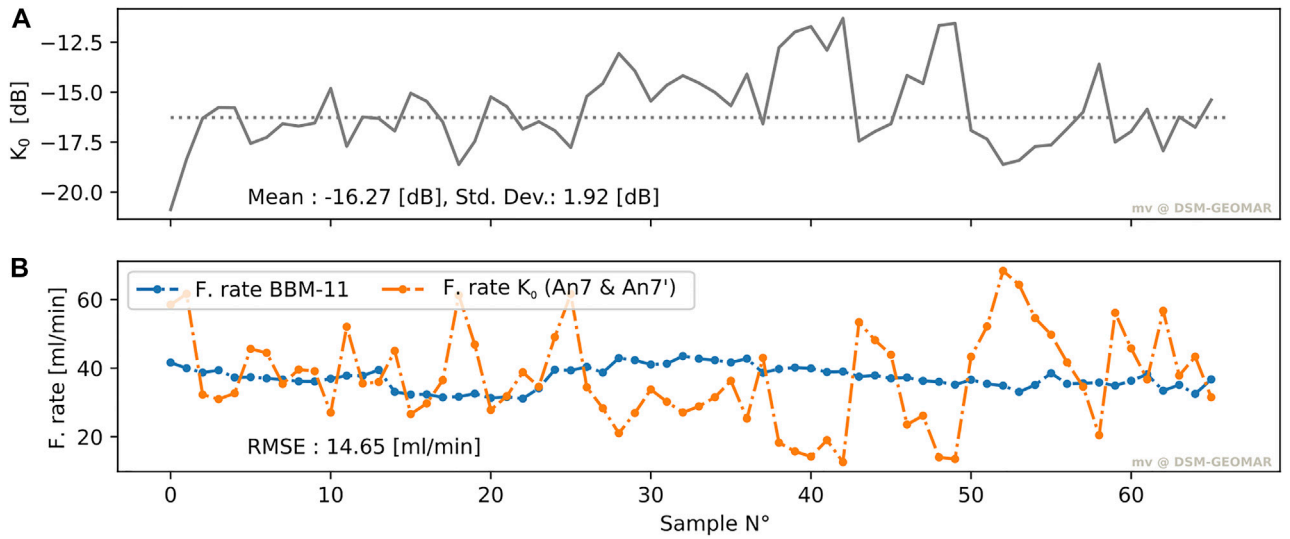

FIGURE 9 | (A) Calculated K_0 value using the contribution of representative amplitudes of the two acoustic anomalies (i.e., An7 & A7′). The image includes the average value (dotted lines) of the calculation of K_0.value (i.e., $\bar{K}_0$). **(B)** Flow rates of control acoustic sample derived by their hydroacoustic information and its respective $\bar{K}_0$ value compared to flow rate optically obtained with the BBox system.

acoustic anomalies An7 and An7′ of the GQM-3 deployment (**Supplementary Figure S7**), as these were identified to jointly represent the bubble stream observed during BBM-11. This was concluded since both anomalies spatially oscillated around the reported BBox position (**Figure 6**) and it was hypothesized that these anomalies were formed by common-source bubbles horizontally separated by their sizes due to near-bottom currents when rising (see *Discussion*). As such, the k_0 value was calculated using the A_{bsTG} time-series represented by the sum of both anomalies and therefore calculated as the decibel value of their exponential summation ($A_{bsTG} = 10\log[10^{A_{bsAN7}/10} + 10^{A_{bsAN7'}/10}]$).

The k_0 value was calculated using the optically measured numbers of bubbles N_0 per unit of time Δt for each 1-min BBox data sub-set. Subsequently, an amplitude value A_{bsTG} from the data series closest in time to each BBox observation was used for each k_0 calculation. A total of 65 data pairs could be achieved (**Figure 9A**). For finally calculating flow rates, a mean $\bar{K}_0$ value of -16.27 dB ($\bar{K}_0 = 10\log\bar{k}_0$) was considered. Since bubble size variations were not significant (**Figures 4**, **5**), a constant, non-modulating probability density function f_r and its associated bubble volume distribution V_r were used for deriving flow rates. A comparison between the BBox determined real flow rate (F. rate real BB) and the hydroacoustically derived ones (FC_{K0}; **Eq. 12** and **Figure 9B**) indicates a root mean square error (RMSE) of 14.65 ml/min. For this comparison, real flow rates were calculated using the discrete functions f_r and V_r derived from results of BBM-11 deployment (mean flow rate: ~39 ml/min; **Figure 4**).

Flow rates of the entire ensonified area for each deployment were calculated using the total backscatter contribution (ASA and OVA-masked time-series). OVA time-series was not used for flow rate estimates due to the strong influence of seafloor backscatter. Flow rates were calculated using one discrete function of f_r and V_r derived as the average from the two BBox deployments (**Figure 4**). Since the pulse length of the GasQuant was different between GQM-3 and GQM-4, it is expected that the constant of proportionality k and the scaling factor k_0 values also change. According to the definition of k in **Supplementary Eq. S.6**, the scaling factor should be theoretically multiplied by the reciprocal value of the ratio between the different pulse lengths for correction. To obtain flow rates using hydroacoustic data from GQM-4, the k_0 value was thus multiplied by 480 µs/360 µs (pulse length GQM-3/pulse length GQM-4). It is uncertain if other effects occur when changing the pulse-length values of the Imagenex system. Final flow rate results are presented in **Figure 10** and average values are summarized in **Table 2**. Flow rates of the single bubble streams measured at the two different BBox deployments are included in **Figure 10** for comparison.

Since flow rates derived from the hydroacoustic data are proportional to the total acoustical backscattering cross-sections (**Eq. 12**), the flow rate variation over time is similar to the one visualized in the direct hydroacoustic information (**Figures 7B,E**). Thus, flow rates vary with the static pressures for all results in the same way as the backscattering amplitudes do. In general, we observed that flow rates derived from the OVA-masked time-series are stronger than the ones obtained from the summed contribution of the single anomalies (ASA flow rates). Mean flow results and standard deviations are similar for both deployments, including the pulse length correction. It should be noted that applying the pulse length correction amplifies the standard deviation of GQM-4 flow rate results. Small differences between flow rates of both deployments can be attributed to several possibilities that are discussed in the next section.

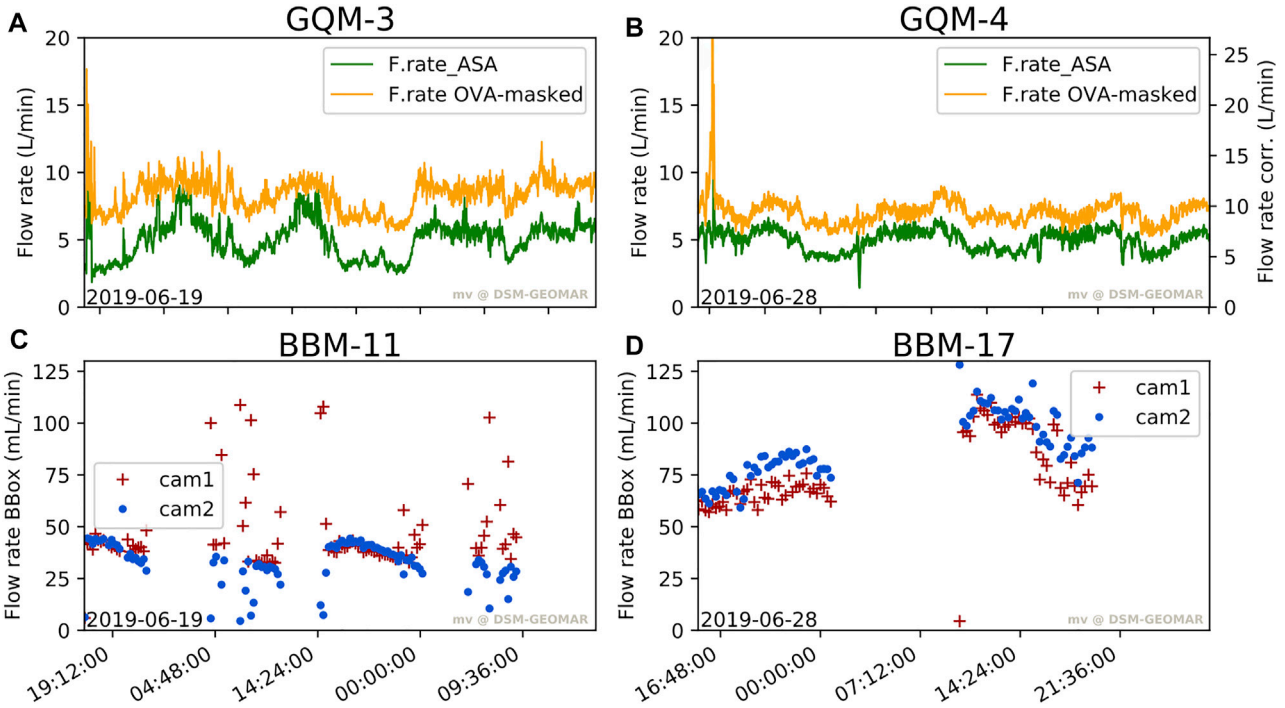

FIGURE 10 | (A,B) Flow rates as derived from ASA and OVA-masked amplitude data-series and $\bar{K}_0$ value for the two deployments. Results also show flow rates for deployment GQM-4 using the pulse length correction **(B)**. Flow rate of bubble streams optically measured by each camera in the two BBox deployments are shown **(C,D)** for visually comparing their behavior with total flow rates. No similarities were found.

TABLE 2 | Average flow rates for deployments GQM-3 and -4 using ASA and OVA-masked time-series. The table includes flow rate values for deployment GQM-4 considering pulse length correction. Values are given in l/min, CH_4 T/yr, and CH_4 mol/yr. Standard deviation of each flow rate estimate is included.

		GQM-3			GQM-4			GQM-4 corr		
		l/min	CH_4 T/yr (*)	$\times 10^6$ CH_4 mol/yr (*)	l/min	CH_4 T/yr (*)	$\times 10^6$ CH_4 mol/yr (*)	l/min	CH_4 T/yr (*)	$\times 10^6$ CH_4 mol/yr (*)
ASA	M. flow rate	5.04	87.46	5.45	4.982	86.41	5.39	6.642	115.21	7.18
	Std. dev.	1.44	24.90	1.55	0.799	13.85	0.86	1.065	18.47	1.15
OVA-masked	M. flow rate	8.33	144.56	9.01	7.055	122.37	7.63	9.406	163.15	10.17
	Std. dev.	1.18	20.46	1.28	1.334	23.13	1.44	1.778	30.84	1.92

(*) CH_4 density ρ_{490}: ~33 kg/m^3 at 490 m water depth, considering CH_4 atmospheric density ρ_0: ~0.66 kg/m^3; Equation 17, from Veloso et al. (2015).

4 DISCUSSION

4.1 Technological Challenges and Recommendations

4.1.1 Optical Data and Processing

The described BBox lander qualifies among the accurately measuring optical lander systems for observing submarine bubble seepage as of today, due to its high sampling rate and its stereo matching approach. Its deployment imposes challenges with regard to a proper positioning of the box over the observed bubble stream (well centered and upright). If the BBox is used to provide ground-truth information for calibrating a hydroacoustic system, the challenge increases even more because the optical bubble measurements must be linked to an identifiable acoustic location in the sonar echogram. Unlike an optical system, sonar systems are not able to differentiate bubble streams too close to each other due to the fixed beam angle and side lobes (i.e., Imagenex Delta-T system ~3° beam aperture), and therefore, an acoustic anomaly could be produced by the backscatter contribution of several bubble streams in the beam footprint (youtube-video-FK-Dive273; time video ~3:56:30; **Supplementary Figure S10**).

BBox measurements will not be ideal ground-truth information for an acoustic anomaly if the system is placed at

a location where too many bubble streams are close to each other. For calibration purposes, the BBox, or similar systems, should be deployed on isolated bubble streams. This is not always possible and a very good knowledge of the area prior the deployment is necessary. The repeated deployments of the BBox during FK190612 showed that the camera calibration must be adapted to the *in situ* conditions since the physical configuration of the BBox components did change under different temperature and pressure conditions causing slight frame deformation (see She et al., 2021). A limitation of the current BBox version is the confinement of the bubble stream within a narrow corridor and the consequences of eliminating the action of currents on bubbles in comparison to normal release. As tested by Wang and Socolofsky (2015), eliminating the interaction between bubbles and currents enhances bubble rising velocities as a result of bubble wake. Another difficulty is that the field of view can be obstructed, for example, by settling sediment or animal activity, which causes loss of information. Both difficulties are hard to prevent because the top sediment in the deep sea is typically muddy and will be stirred up when the BBox is placed on the sediment, and motile fauna will use the elevated spot of the BBox as hiding or feeding ground. Future system improvements may consider a periodical cleaning of the glass domes with a water jet to prevent sediment and animals from settling.

Observations showed that even with optimal placement of the BBox, a bubble stream drifted out of the field of view for one of the cameras. Reasons are that either the BBox tilts by slowly sinking into the sediment on one side or that the vent location below the BBox funnel changed. Future system improvements should consider increasing the field of view, adding a third camera for measurements. Additionally, the design needs to prevent the size distribution of bubbles exiting the BBox from changing due to bubble coalescence. Evidence of such coalescence was witnessed in some of the other BBox deployments, where bubbles accumulated at the top part of the box before finally leaving the box (**Supplementary Figure S4**). This will change the bubble size distribution significantly and makes the use of such data unfit for hydroacoustic calibration purposes, as these strongly depend on correct bubble size information.

4.1.2 Hydroacoustic Data and Processing

Through our hydroacoustic studies, we gained additional insight for using horizontal-looking MBESs and the Imagenex Delta-T system in particular for bubble monitoring. Since GasQuant uses a horizontal-looking MBES placed rather close to the seafloor, part of the backscattering received can be a result of the main beam and/or vertical side lobes interacting with the seafloor (**Figure 6** and **Supplementary Figure S3**), particularly if the seafloor is not flat. In the present work, a time-stacked echogram of the sonar swath was compared with the bathymetry to detect potential anomalies related to seafloor backscattering and differentiate them from seep-related anomalies that change position due to tide-dependent current changes. Results from this comparison show perfect matching between geomorphology and strong static anomalies indicating that echograms were partly contaminated by unwanted backscattering (**Figure 6**). Researchers of future surveys might also consider vertically mapping the water column for bubble locations as, for example, Urban et al. (2022) did, using a ship-based system and then placing the GasQuant system on the seafloor to map a well-defined seep area.

As mentioned in the data quality section given in **Supplementary Section 2**, the acoustic long-term time-series relied on the *.83b files (output file Imagenex Delta-T) that contain fixed gain settings with a limited dynamic range for the amplitude. The dynamic range limitation could cause clipping of strong backscatter signals which therefore result in non-representative values of the real backscatter produced by targets (i.e., strong bubble stream). Since our approach associates acoustic backscatter with flow rates (**Eq. 12**), signal clipping would result in underestimating these flow rates. Future long-term measurements must consider storing raw data (output file from Imagenex Delta-T with extension *.837) even during long deployments to enable re-processing these data and increase the dynamic range. However, flow rate results presented here are considered to not be affected by amplitude clipping since only few percentages of the total voxel cells in gridded echograms were found to reach a common maximum (e.g., **Supplementary Figure S2**).

Finally, the two GQM deployments presented here used different pulse lengths. Theoretically, a change in pulse lengths will modify the sample volume and therefore change the amplitudes obtained from the Imagenex Delta-T since they are proportional to volume backscattering. As stated above, a theoretical correction was applied by multiplying k_0 values (scaling factor used for calculating flow rates) by the ratio between different pulse lengths. Results show that flow rates from different deployments are in agreement, including the pulse length correction (**Table 2**). However, a further investigation is needed to prove that our pulse length correction is valid to exclude additional effects when changing the pulse length parameter in the sonar settings.

4.2 Seepage-Related Results

4.2.1 Bubble Observations

Our data of 91 h of BBox observation time show, in general, no strong fluctuations in average bubble radius, the BSDs, or the amount of bubbles per time of the two individual seep spots measured. Small variation in bubble size occurs for BBM-17 (1.96 mm–3.11 mm, std. dev.: 0.23 mm), but no clear correlation to pressure changes is observed. We are convinced that the 15-min observation interval with each 1-min measuring time is sufficient to detect tide-dependent bubble size and bubble amount variations. This also holds true for the complete data set in which post-processing–related data gaps occur. In general, the 15-min measurement interval potentially can miss short-term bursts as described, for example, by Greinert (2008). Nevertheless, we think that based on the BBox data and the ROV-based observations during FK190612 that irregular and burst-like bubble release is not common in the Bubble-Alley. We are confident that the very homogenous individual observations of BBM-11 and -17 (**Figure 4**) and their almost identical bubble

size distribution (**Figure 5**) allow for deriving a general BSD probability density function, although the flow rate of the BBM-17 bubble stream is almost twice as high as that for BBM-11. Based on the rather similar and homogenous bubble size distribution (also seen during ROV-based bubble size measurements), we assume that the observed BSD can be extrapolated to calculate realistic total flow rates of the hydroacoustically investigated areas during GQM-3 and -4. For comparison, **Supplementary Figure S11** shows our BSD data together with other experimental and observational data. Even compared to other data, our measurements are rather similar (with the exception to Muyakshin and Sauter, 2010) pointing at the fact that the sediment properties and fluid pressure conditions at seep sites are rather similar, creating a more or less common BSD.

Bubble rising speeds show similar behavior between the two BBM deployments, although values are slightly higher in BBM-17 than BBM-11. Rising speeds between 25 cm/s and 40 cm/s (bubble radii from 1 to 5 mm; **Figure 5**) are slightly higher compared to data and models presented in other studies (e.g., McGinnis et al., 2006; Park et al., 2017). These results may be realistic for this seep site, although they might as well suffer from the rising speed enhancement related to bubble wake as a result of the bubble stream confinement within the BBox (Wang and Socolofsky, 2015). Since BRSs are directly related to our flow rate estimation, rising speed enhancement must be considered as a possible source of error in our estimates. Above a bubble radius of 4 mm, BRSs scatter wider in our measurements. This might be explainable because larger bubbles can vary more in shape and, therefore, can have different rising speeds (e.g., Park et al., 2017). Future analysis of BBox data could thus include shape classification (e.g., sphericity and curvature) to determine the impact of these characteristics on the bubble rising speed.

4.2.3 Spatial Distribution and Spatio-Temporal Variation of Seepage

The integration of bathymetry with geo-referenced positions of seepage occurrences identified in ROV videos (**Figure 1B**) and anomalies identified in echograms (**Figure 6**) reveals that bubble venting is concentrated along a topographic depression. The latter may be indicative of gas venting using faults as pathways before reaching the water column as suggested in other studies (e.g., Riedel et al., 2021). Currently, little is known about the sediment-column characteristics of the study area. Future surveys may include equipment to perform sub-bottom and seismic profiling for scanning the sediment-column and proving this hypothesis.

Acoustic results from GasQuant deployments show that spatial shifts of tracked acoustic anomalies are correlated with tide-dependent current variations (**Supplementary Figures S7, S8**), as also seen by Crone et al. (2010) and Tsai et al. (2019). Spatial changes during GQM-4 cover larger distances which we explain by the higher swath altitude in which the GasQuant system recorded the bubbles when deployed relatively higher above the Bubble-Alley floor (see profile in **Figure 6**). The latter is strongly supported by seafloor-related anomalies in echograms that are less present in GQM-4 but also detected further upslope when comparing their position in echograms (**Figure 6**). The absolute shift of the bubbles in 8 (GQM-3) and 11 m (GQM-4) above the seafloor is following the ENE-orientation direction of the gully, highlighting the influence of the seafloor morphology on near-bottom currents.

As suggested in **Section 3.3** (LPC analysis), the correlation between hydrostatic pressure and overall amplitude modulation (ASA and OVA-masked) provides different results for the two deployments, and the amplitude rise related to bubble flow as a result of hydrostatic pressure drops (falling tides) can only be associated to GQM-3 results. An interesting finding was that amplitudes of single acoustic anomalies and their overall contribution (ASA and OVA-masked) modulated parallel with their relative position within the echogram (**Figure 7**; **Supplementary Figures S7, S8**), which could be indicative of sensitivity changes of the system related to the direction (relative to the nadir) of the target. The latter is supported by the WAN time series, which can be interpreted as the relative shift from the nadir of the overall contribution of tracked single anomalies associated to bubble seepage. **Figure 7** shows that strongest fluctuations of WAN time-series are found in deployment GQM-4, and they are correlated with the overall amplitudes. From this, it is assumed that the influence of target spatial modulation is stronger in data from deployment GQM-4 than for deployment GQM-3. The angular dependency is confirmed by the experiments of Scandella et al. (2016) using a calibration sphere of a known acoustical backscatter cross-section, where a directional pattern was found for the Imagenex Delta-T system. This observation suggests that amplitudes collected by the sonar must be corrected by this angular dependency in order to make information from different parts of the swath comparable. Our MBES lacks proper calibration, and therefore, no angular correction was applied. Thus, the latter can be considered as a potential error in the final flux calculations.

An alternative explanation for the correlation between amplitude and anomalies' relative positions could be attributed to side-lobe effects. Because of the irregular geomorphology of the seafloor, the spatially modulated anomalies may have been differently affected by side-lobe backscatter coming from the seafloor as they move within the echogram. Unfortunately, this hypothesis cannot be tested with the data of the presented work. Future research related to quantification of bubble emissions using MBES must consider the study of MBES angular sensitivity and the overlapping of side-lobe backscattering of multiple targets in controlled environments for answering these questions. In general, our results show that amplitude correlation with hydrostatic pressure, relative position of targets, or their combination is possible. Although the reason for the amplitude variations is still not completely clear, we suggest that average values do provide a reasonable level of confidence for calculating the overall amount of gas expelled into the water column.

4.2.3 Flow Rate Quantification

One reason why stationary multibeam systems are not used regularly for quantifying gas flow rates is the difficulty of proper calibration. One approach is the experimental

calibration in a tank or ship dock as undertaken by Greinert and Nützel (2004) or Shakhova et al. (2014). Problems here lie in the generation of bubbles, the layout of the experiment, and finding the needed space to artificially generate bubbles and perform measurements without disturbing acoustic backscatter from walls and the bottom. To overcome these problems, we decided on an *in situ* calibration using a natural bubble vent, facing the challenge of finding an isolated bubble stream in the chosen AC500 seep area.

As outlined above, the two anomalies, An7 and An7′, in the GQM-3 data set are most likely correlating with the bubble stream measured during BBM-11. Our best explanation is that anomalies An7 and An7′ are produced by ensonifying differently sized bubbles (the BSD of BBM-11 shows more small bubbles) that come from the same vent outlet but are horizontally separated by the near-bottom currents because of their different bubble rising speeds (**Figure 11A**). Considering that the optically calculated average flow rate in BBM-11 is 0.037 L/min, a number ranging from ~135 to ~243 of such bubble streams would be needed to generate the flow rate as calculated from $\bar{K}_0$ (i.e., between ~5 to ~9 L/min, **Table 2**). From ROV video observations and the number of anomalies detected on the echogram, it is suggested that this scenario is plausible.

For evaluating our hypothesis, we considered common near-bottom current speeds ranging from 5 to 40 cm/s (Korgen et al., 1970), a BRS ranging from 15 to 37 cm/s (**Figure 5B**), and an observation/rise height of 8 m above the seafloor (**Figures 11A,B**). The horizontal displacement of fast and slow bubbles can be up to ~10 m (**Figure 11C**). Compared to the distance between anomalies An7 and An7′ of 3–6 m (**Figure 11D**), the hypothesis of bubble separation while rising seems feasible. Alternatively, the BBM-11 measurement, if associated with a single anomaly, could only be related to An7 which is the strongest anomaly that spatially oscillates in the neighborhood of the BBox position. Mean flow rates derived from An7 are rather similar to the derived by the contribution of An7 and An7′ with differences up to ~2 L/min (**Supplementary Table S4**). The rejection of An7′ to be the only anomaly related to the BBox measurements is because its use for calibration would imply the obtaining of considerable large mean flow rates (up to ~63 L/min; **Supplementary Table S4**) which is something not supported by the ROV visual observations. As expected, results of the flow rates calculated from OVA-masked time-series are higher than the ones calculated from the ASA time-series since the calculation accounts for the amplitude signals of all voxels within the gridded-echogram (**Figure 10**; **Table 2**). Based on a simulation approach, Urban et al. (2022) suggested that the correct way of deriving the total backscatter from MBES ensonified bubbles in the water column is to use a voxel weighted mean method of all voxels in the grid area, rather than adding only the backscatter from seep-related acoustic anomalies delimited by a specific spatial domain/threshold. The latter is related to the backscattering spreading around a target voxel-neighborhood when the gridding/interpolation is applied. As such, differences between OVA-masked and ASA flow rates could be related to the use of the complete and more correct voxel-information when the OVA-masked flow rate is calculated. On the other hand, applying this approach in real measurements with a horizontal swath close to the seafloor involves including the contribution of unwanted targets (e.g., seafloor backscatter) and noise that will influence the final flow rate result. In order to eliminate the seafloor backscatter and therefore avoid flow rate overestimation, the echogram was masked where we clearly found anomalies associated with the seafloor. Although the elimination of the main part of the unwanted backscattering is reflected in the final flow rate estimates, it is not possible to evaluate whether this effect was totally removed. Thus, the latter is an alternative explanation for the differences, although not significant (up to ~3 L/min; **Table 2**), between OVA-masked and ASA flow rates. Here, we assume that seafloor backscatter may still have an influence on the OVA-masked–based flow rate calculation, though to what extent we cannot say.

The comparison between average flow rate estimates of different deployments shows that they are similar (**Table 2**), indicating no significant release changes in time between them. Small differences, mostly reflected in OVA-masked, can be attributed to 1) a truly different flow rate fluctuation at the different times of measurements, 2) small differences of MBES areal coverage between deployments, 3) small bubble size differences between the deployments that change the backscatter response of bubbles even though real flow rates do not considerably change (**Figure 12**; **Supplementary Figure S6**), 4) a different deployment (i.e., GQM-3) was more affected by unwanted seafloor backscatter, or 5) the same seepage area captured by different sectors of a MBES with angular sensitivity variations. Answering which of these possibilities or a combination of some caused backscatter differences is still not possible in this study.

Using one constant BSD for obtaining flow rates over longer time from an area might always introduce an error on acoustically derived flow rate estimates as small bubble size variations over time and between bubble-vents need to be assumed. **Figure 12** illustrates how sensitive the used hydroacoustic inversion method (**Eq. 11**) is to BSD shifts. Flow rate changes considerably even for small shifts of the mode of the BSD (flow rate increases almost 10 times when the BSD mode shifts from a radius of 2 mm to 3 mm). For a more stable acoustical response associated with bubble sizes, a system that operates at a lower frequency (e.g., 38 kHz) would have been the better choice for the observed bubble size distribution and water depth. However, using a lower frequency demands a larger transducer to keep the same beam resolution which increases the weight and power consumption of the system, making it harder to be deployed by an ROV in the undertaken agile and simple way.

In general, flow rate results of the Bubble-Alley of the AC500 site (in l/min and CH4 tones/year) are similar to others reported in the literature, for example, from the Black Sea, the Cascadia Margin, or the North Sea (**Supplementary Table S5**) and stands for a well active, natural seep area. The remaining uncertainties of our quantification are well within the range of other uncertainties, particularly when considering spatial assumptions and the extrapolation of a few directly measured seep vents, which are then extrapolated to entire areas (e.g., Römer et al., 2012).

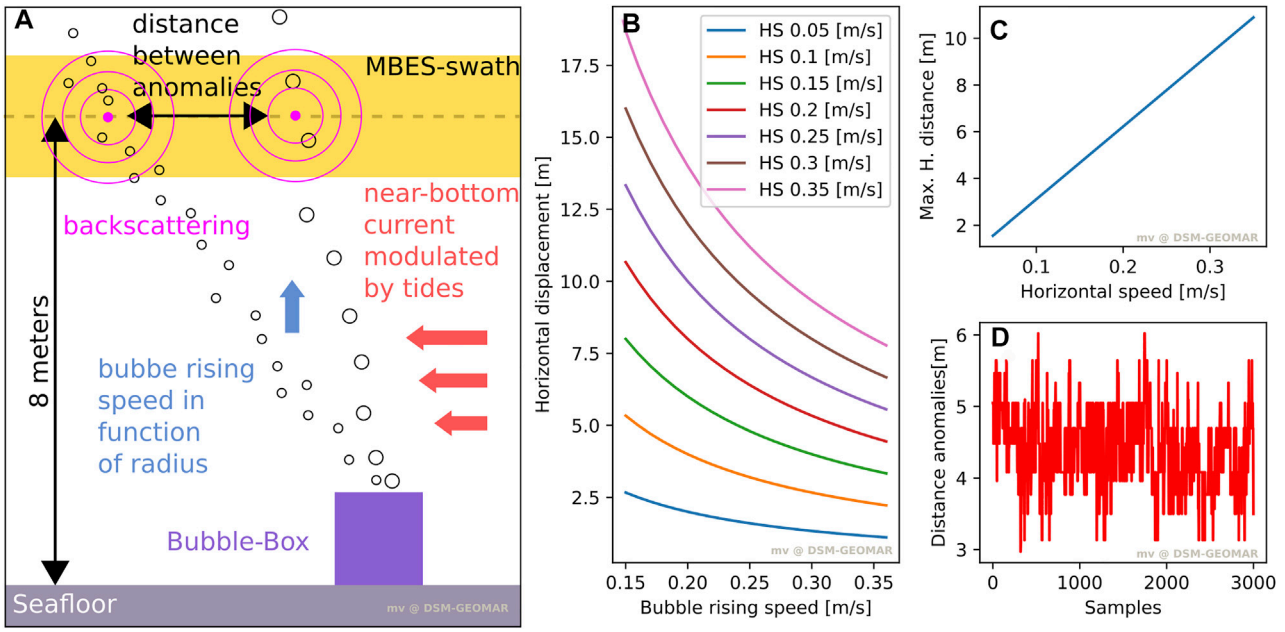

FIGURE 11 | (A) Schematic of hypothesis of separation of ascending bubbles by different sizes under the effect of near-bottom currents. The image includes the MBES-swath (yellow rectangle) ensonifying two bubble streams with differently sized bubbles coming from the same bubble outlet at the seafloor. **(B)** Horizontal displacement of bubbles with different rising speeds (between 15 and 37 cm/s) The calculation is done for near-bottom currents (HS) ranging from 0.05 to 0.35 m/s and a rise height of 8 m. **(C)** Linear relationship between horizontal current speeds and maximum displacement (slowest bubbles) at a height of 8 m above the seafloor. **(D)** Distance between the acoustic anomalies An7 and An7′ over time (mean value ~4.4 m).

5 SUMMARY AND CONCLUSION

In this study, we evaluated an *in situ* experimental setup which consisted of an acoustic multibeam system (GasQuant-II) and a stereo camera system (Bubble-Box) deployed in tandem. This sensor configuration was chosen for 1) calibrating the hydroacoustic system using optical information for estimating bubble flow-rates and 2) quantitatively assessing the temporal and spatial release activity of the seepage site. To achieve 1) and 2), we first proposed a method for bubble flow rate quantification using echo-grid integration of seepage-related MBES backscatter and simultaneous optical information of bubble release. This method was applied on a dataset acquired during the cruise FK190612 with RV FALKOR at the Astoria Canyon site AC500 (Bubble-Alley).

From a technical perspective, we concluded that using BBox measurements for *in situ* calibration of a horizontal-looking MBES is possible but imposes challenges regarding the box positioning over an isolated bubble-stream that at the same time can be individually detected in acoustic images. The selected bubble stream used for calibration in this experiment was partially influenced by acoustic returns from close-by bubble streams. Future surveys that attempt to use a similar sensor setup are advised to gain prior knowledge regarding the spatial distribution of the seeps, for example, using AUV-based high-resolution down-looking MBES surveys. These surveys could help with identifying and eliminating seafloor-related backscatter which was surprisingly difficult to differentiate from bubble-related backscattering in this experiment. Our results show that eliminating strong seafloor-related backscatter is crucial to avoid flow rate overestimation using the presented inverse method.

Our evaluation exposes a number of limitations of the current measurement design, therefore providing directions for future improvements of this system. One of them is the dynamic range limitation associated with the recorded 0.83b files. Future improvement of the system must take care that the 0.837 raw data files are also properly stored even when data acquisition is performed during longer periods of time. Additionally, our results suggest a possible relationship between backscatter amplitudes and relative positions of acoustic anomalies. A calibration experiment is necessary to equalize the sensitivity for the different beam angles (relative calibration). Additionally, we hypothesize that correlation of amplitude with anomalies' relative position could also be caused by seafloor-backscatter (from main and side lobes) that overlaps differently with the tracked-acoustic anomaly as it moves within the echogram-fan. Furthermore, we cannot exclude that the measured acoustic backscattering strength was influenced by modifying the MBES range setting between dives which influenced the acoustic pulse length of our measurements. Future investigations using the GasQuant II system should either take more care to use the same setup or calibrate different settings against each other using the exact same target.

From a scientific point of view, our BBox results do not show strong fluctuations of bubble size, BRSs, and flow rates, suggesting that emissions are relatively stable and constant at the study area. BSDs are similar between the two observed bubble streams, and

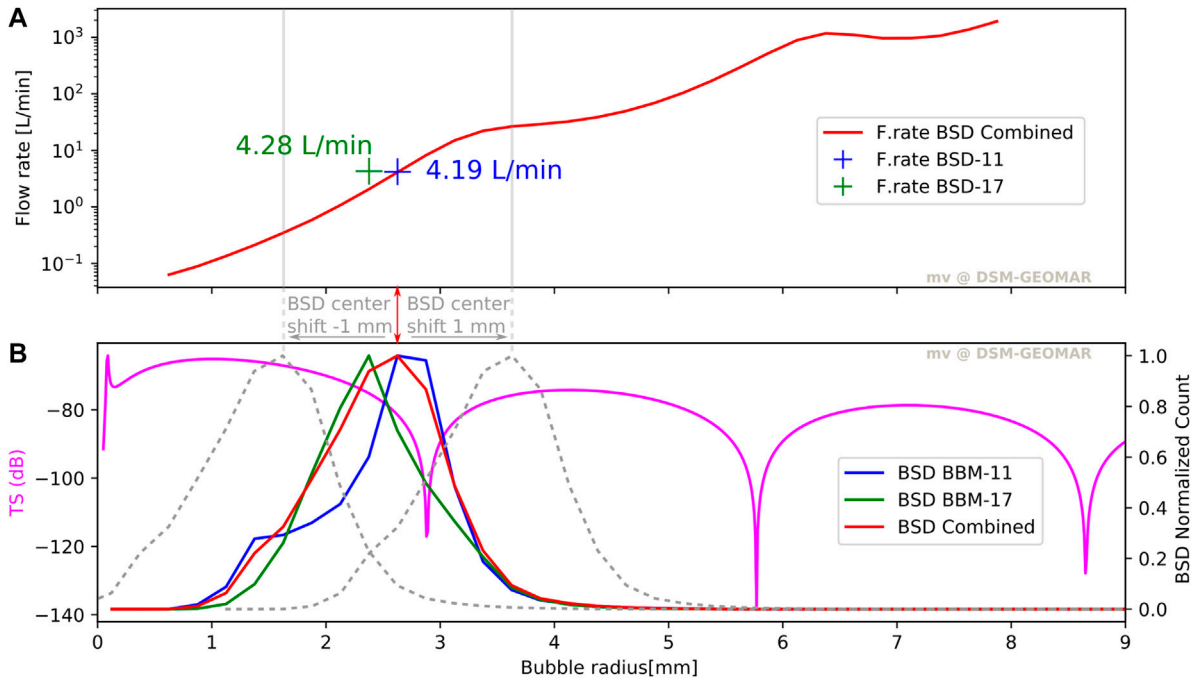

FIGURE 12 | Sensitivity of the inverse method to BSD. **(A)** Flow rates using a BSD shifted by size obtained with **Eq. 11** for a constant amplitude value A_{bsT} = 53 dB. The calculation used the combined BSD obtained from BBox observations (**Figure 5A**). The figure also depicts the results of the flow rate based on BBM-11 and BBM-17 bubble size distribution (4.19 and 4.28 L/min, respectively). **(B)** Theoretical acoustical backscattering response of single spherical bubble versus bubble radius and BSDs from deployments BBM-11 and BBM-17 and their combination.

therefore, we assume a general BSD for the entire area. Additionally, BSD is similar to published data from other areas pointing out that the sediment properties and fluid pressure conditions at seep sites are rather similar. The measured BRSs for the study area are slightly higher compared to values from published data and models. BRS values might be realistic for the study area but could alternatively be explained to be the result of the elimination of the interaction between currents and bubbles, which is produced by the bubble stream confinement within the BBox. This thus represents a possible source of error in our flow rate estimates.

The analysis of the spatial seep distribution shows that seeps are clustered along a topographic depression, which may suggest that faults are used as gas-migrating pathways. Sediment-column profiles are required to prove this hypothesis.

The spatiotemporal analysis of acoustic anomalies tracked in the echograms of the two deployments reveal that bubble streams are spatially modulated by near-bottom currents associated with the tidal regime. On the other hand, only overall backscattering amplitudes from GQM-3 can be associated with the rise in bubble-flow resulting from falling tides as observed in other studies. Due to the uncertainty caused by the MBES angular sensitivity, it was not possible to establish a precise amplitude–tide relationship. Despite this relative calibration error, the average flow rate results can be used to represent a realistic amount of gas expelled into the water column. In comparison with other studies, our results indicate that the flow rates presented in this work ranging from 5.38×10^6 to 9.01×10^6 CH_4 mol/year can be categorized as a well active natural seep area.

It has to be noted that the presented work is one of the few existing attempts of calibrating MBES using simultaneous optical measurements. We believe that the results presented here provide insightful information regarding the method for calibrating MBES with simultaneous optical information *in situ*, as well as indicating the challenges, the problems, and their possible solutions. Future studies related to MBES-optical sensor configuration using the presented method must address the issues and consider the recommendations presented in this work for improving the precision of gas flow evaluations.

DATA AVAILABILITY STATEMENT

The original contributions presented in the study are included in the article/**Supplementary Material**; further inquiries can be directed to the corresponding author.

AUTHOR CONTRIBUTIONS

The present work can be subdivided in different contributions related to 1) the development of the GasQuant-II and Bubble Box system, 2) their use during cruise FK190612, 3) planning the

research in the field and supplying financial support, 4) elaboration of methodology for GasQuant data post-processing, 5) GasQuant data post-processing, 6) elaboration of methodology for BBox data post-processing, 7) BBox data post-processing, 8) data analysis and elaboration of hypotheses, and 9) interpretation and discussion of results. In detail, MV-A contributed to 4, 5, 7, 8, and 9; PU contributed to 1, 4, 8, and 9; TW contributed to 1, 2, and 3; KK contributed to 1, 6, and 9; MS contributed to 6, 7, 8, and 9; and JG contributed to 1, 2, 3, 4, 6, 8, and 9. The manuscript was written by MV-A and JG with contributions of all authors.

FUNDING

Cruise FK190612 was funded by the Schmidt Ocean Institute as part of the "Observing seafloor methane seepage at the edge of hydrate stability," based on a proposal formulated under the leadership of the Gas Hydrates and Benthic Ecology projects at the United States Geological Survey (USGS). Funding for cruise preparations, travel, and article writing for TW, JG, and MV-A came through GEOMAR internal funds from the Deep Sea Monitoring group. Incidental cruise support was provided through interagency agreement DE-FE0023495 between the USGS and the United States Department of Energy for gas hydrate research.

ACKNOWLEDGMENTS

We thank the Schmidt Ocean Institute (SOI) for providing access to the *R/V Falkor* and are grateful to SOI's staff, the ship's crew, and the operators of *ROV* SuBastian for their professionalism and support that made this cruise a success. Our gratitude to C. Ruppel (USGS) for the opportunity to participate in the cruise and to A. Demopoulos for her outstanding at-sea leadership. E. Suess, B. Collier, and Jonathan Fram from Oregon State, as well as H. Mendlovitz (UNC), provided support for peripherals and logistics necessary for GasQuant and the BBox. We further want to thank the rest of the scientific party and ship's crew for the relaxed and professional work environment during the cruise. Special thanks go to B. Scandella for kindly discussing results of his publications with us. Finally, we would like to thank the reviewers for their comments and suggestions, which helped us to improve the quality of the manuscript. This is publication 56 of the DeepSea Monitoring group at GEOMAR.

SUPPLEMENTARY MATERIAL

The Supplementary Material for this article can be found online at: https://www.frontiersin.org/articles/10.3389/feart.2022.858992/full#supplementary-material

REFERENCES

Ainslie, M. A., and Leighton, T. G. (2009). Near Resonant Bubble Acoustic Cross-Section Corrections, Including Examples from Oceanography, Volcanology, and Biomedical Ultrasound. *J. Acoust. Soc. Am.* 126, 2163–2175. doi:10.1121/1.3180130

Ainslie, M. A., and Leighton, T. G. (2011). Review of Scattering and Extinction Cross-Sections, Damping Factors, and Resonance Frequencies of a Spherical Gas Bubble. *J. Acoust. Soc. Am.* 130, 3184–3208. doi:10.1121/1.3628321

Baumberger, T., Embley, R. W., Merle, S. G., Lilley, M. D., Raineault, N. A., and Lupton, J. E. (2018). Mantle-Derived Helium and Multiple Methane Sources in Gas Bubbles of Cold Seeps along the Cascadia Continental Margin. *Geochem. Geophys. Geosyst.* 19, 4476–4486. doi:10.1029/2018GC007859

Bergès, B. J. P., Leighton, T. G., and White, P. R. (2015). Passive Acoustic Quantification of Gas Fluxes during Controlled Gas Release Experiments. *Int. J. Greenh. Gas Control* 38, 64–79. doi:10.1016/j.ijggc.2015.02.008

Berndt, C., Feseker, T., Treude, T., Krastel, S., Liebetrau, V., Niemann, H., et al. (2014). Temporal Constraints on Hydrate-Controlled Methane Seepage off Svalbard. *Science* 343, 284–287. doi:10.1126/science.1246298

Boetius, A., Ravenschlag, K., Schubert, C. J., Rickert, D., Widdel, F., Gieseke, A., et al. (2000). A Marine Microbial Consortium Apparently Mediating Anaerobic Oxidation of Methane. *Nature* 407, 623–626. doi:10.1038/35036572

Campbell, K. A. (2006). Hydrocarbon Seep and Hydrothermal Vent Paleoenvironments and Paleontology: Past Developments and Future Research Directions. *Palaeogeogr. Palaeoclimatol. Palaeoecol.* 232, 362–407. doi:10.1016/j.palaeo.2005.06.018

Caudron, C., Vandemeulebrouck, J., and Sohn, R. A. (2022). Turbulence-induced Bubble Nucleation in Hydrothermal Fluids beneath Yellowstone Lake. *Commun. Earth Environ.* 3, 1–6. doi:10.1038/s43247-022-00417-6

Crone, T. J., Wilcock, W. S. D., and Mcduff, R. E. (2010). Flow Rate Perturbations in a Black Smoker Hydrothermal Vent in Response to a Mid-ocean Ridge Earthquake Swarm. *Geochem. Geophys. Geosyst.* 11, 13. doi:10.1029/2009GC002926

De Leo, F. C., Ogata, B., Sastri, A. R., Heesemann, M., Mihály, S., Galbraith, M., et al. (2018). High-frequency Observations from a Deep-Sea Cabled Observatory Reveal Seasonal Overwintering of Neocalanus Spp. In Barkley Canyon, NE Pacific: Insights into Particulate Organic Carbon Flux. *Prog. Oceanogr.* 169, 120–137. doi:10.1016/j.pocean.2018.06.001

Doya, C., Chatzievangelou, D., Bahamon, N., Purser, A., De Leo, F. C., Juniper, S. K., et al. (2017). Seasonal Monitoring of Deep-Sea Megabenthos in Barkley Canyon Cold Seep by Internet Operated Vehicle (IOV). *PLOS ONE* 12, e0176917. doi:10.1371/journal.pone.0176917

Etiope, G. (2009). Natural Emissions of Methane from Geological Seepage in Europe. *Atmos. Environ.* 43, 1430–1443. doi:10.1016/j.atmosenv.2008.03.014

Francois, R. E., and Garrison, G. R. (1982). Sound Absorption Based on Ocean Measurements. Part II: Boric Acid Contribution and Equation for Total Absorption. *J. Acoust. Soc. Am.* 72, 1879–1890. doi:10.1121/1.388673

Greinert, J., Bohrmann, G., and Suess, E. (2001). "Gas Hydrate-Associated Carbonates and Methane-Venting at Hydrate Ridge: Classification, Distribution, and Origin of Authigenic Lithologies," in *Natural Gas Hydrates: Occurrence, Distribution, and Detection* (Washington, DC: American Geophysical Union AGU), 99–113. doi:10.1029/GM124p0099

Greinert, J. (2008). Monitoring Temporal Variability of Bubble Release at Seeps: The Hydroacoustic Swath System GasQuant. *J. Geophys. Res.* 113, 7048. doi:10.1029/2007JC004704

Greinert, J., and Nützel, B. (2004). Hydroacoustic Experiments to Establish a Method for the Determination of Methane Bubble Fluxes at Cold Seeps. *Geo-Marine Lett.* 24, 75–85. doi:10.1007/s00367-003-0165-7

Higgs, B., Mountjoy, J. J., Crutchley, G. J., Townend, J., Ladroit, Y., Greinert, J., et al. (2019). Seep-bubble Characteristics and Gas Flow Rates from a Shallow-Water, High-Density Seep Field on the Shelf-To-Slope Transition of the Hikurangi Subduction Margin. *Mar. Geol.* 417, 105985. doi:10.1016/j.margeo.2019.105985

Jerram, K., Weber, T. C., and Beaudoin, J. (2015). Split-beam Echo Sounder Observations of Natural Methane Seep Variability in the Northern Gulf of Mexico. *Geochem. Geophys. Geosyst.* 16, 736–750. doi:10.1002/2014GC005429

Kannberg, P. K., Tréhu, A. M., Pierce, S. D., Paull, C. K., and Caress, D. W. (2013). Temporal Variation of Methane Flares in the Ocean above Hydrate Ridge, Oregon. *Earth Planet. Sci. Lett.* 368, 33–42. doi:10.1016/j.epsl.2013.02.030

Kirschke, S., Bousquet, P., Ciais, P., Saunois, M., Canadell, J. G., Dlugokencky, E. J., et al. (2013). Three Decades of Global Methane Sources and Sinks. *Nat. Geosci.* 6, 813–823. doi:10.1038/ngeo1955

Korgen, B. J., Bodvarsson, G., and Kulm, L. D. (1970). Current Speeds Near the Ocean Floor West of Oregon. *Deep Sea Res. Oceanogr. Abstr.* 17, 353–357. doi:10.1016/0011-7471(70)90026-4

Leifer, I., and Boles, J. (2005). Turbine Tent Measurements of Marine Hydrocarbon Seeps on Subhourly Timescales. *J. Geophys. Res.* 110, 12. doi:10.1029/2003JC002207

Leifer, I., Chernykh, D., Shakhova, N., and Semiletov, I. (2017). Sonar Gas Flux Estimation by Bubble Insonification: Application to Methane Bubble Flux from Seep Areas in the Outer Laptev Sea. *Cryosphere* 11, 1333–1350. doi:10.5194/tc-11-1333-2017

Leifer, I., and Culling, D. (2010). Formation of Seep Bubble Plumes in the Coal Oil Point Seep Field. *Geo-Mar Lett.* 30, 339–353. doi:10.1007/s00367-010-0187-x

Leifer, I., Patro, R. K., and Bowyer, P. (2000). A Study on the Temperature Variation of Rise Velocity for Large Clean Bubbles. *J. Atmos. Ocean. Technol.* 17, 1392–1402. doi:10.1175/1520-0426(2000)017<1392:asottv>2.0.co;2

Levin, L. A., Baco, A. R., Bowden, D. A., Colaco, A., Cordes, E. E., Cunha, M. R., et al. (2016). Hydrothermal Vents and Methane Seeps: Rethinking the Sphere of Influence. *Front. Mar. Sci.* 3, 72. doi:10.3389/fmars.2016.00072

Li, J., Roche, B., Bull, J. M., White, P. R., Davis, J. W., Deponte, M., et al. (2020a). Passive Acoustic Monitoring of a Natural CO_2 Seep Site - Implications for Carbon Capture and Storage. *Int. J. Greenh. Gas Control* 93, 102899. doi:10.1016/j.ijggc.2019.102899

Li, J., Roche, B., Bull, J. M., White, P. R., Leighton, T. G., Provenzano, G., et al. (2020b). Broadband Acoustic Inversion for Gas Flux Quantification-Application to a Methane Plume at Scanner Pockmark, Central North Sea. *J. Geophys. Res. Oceans* 125, 21. e2020JC016360. doi:10.1029/2020JC016360

Liebetrau, V., Eisenhauer, A., and Linke, P. (2010). Cold Seep Carbonates and Associated Cold-Water Corals at the Hikurangi Margin, New Zealand: New Insights into Fluid Pathways, Growth Structures and Geochronology. *Mar. Geol.* 272, 307–318. doi:10.1016/j.margeo.2010.01.003

Longo, M., Lazzaro, G., Caruso, C. G., Radulescu, V., Radulescu, R., Sciré Scappuzzo, S. S., et al. (2021). Black Sea Methane Flares from the Seafloor: Tracking Outgassing by Using Passive Acoustics. *Front. Earth Sci.* 9, 678834. doi:10.3389/feart.2021.678834

McGinnis, D. F., Greinert, J., Artemov, Y., Beaubien, S. E., and Wüest, A. (2006). Fate of Rising Methane Bubbles in Stratified Waters: How Much Methane Reaches the Atmosphere? *J. Geophys. Res.* 111, C09007. doi:10.1029/2005JC003183

Muyakshin, S. I., and Sauter, E. (2010). The Hydroacoustic Method for the Quantification of the Gas Flux from a Submersed Bubble Plume. *Oceanol.* 50 (6), 1001. doi:10.1134/S0001437010060202

Nikolovska, A., Sahling, H., and Bohrmann, G. (2008). Hydroacoustic Methodology for Detection, Localization, and Quantification of Gas Bubbles Rising from the Seafloor at Gas Seeps from the Eastern Black Sea. *Geochem. Geophys. Geosyst.* 9, 10010. doi:10.1029/2008GC002118

Park, S. H., Park, C., Lee, J., and Lee, B. (2017). A Simple Parameterization for the Rising Velocity of Bubbles in a Liquid Pool. *Nucl. Eng. Technol.* 49, 692–699. doi:10.1016/j.net.2016.12.006

Pohlman, J. W., Greinert, J., Ruppel, C., Silyakova, A., Vielstädte, L., Casso, M., et al. (2017). Enhanced CO_2 Uptake at a Shallow Arctic Ocean Seep Field Overwhelms the Positive Warming Potential of Emitted Methane. *Proc. Natl. Acad. Sci. U.S.A.* 114, 5355–5360. doi:10.1073/pnas.1618926114

Razaz, M., Di Iorio, D., Wang, B., and MacDonald, I. (2020). Temporal Variations of a Natural Hydrocarbon Seep Using a Deep-Sea Camera System. *J. Atmos. Ocean. Technol.* 37, 1737–1751. doi:10.1175/JTECH-D-19-0137.1

Rehder, G., Brewer, P. W., Peltzer, E. T., and Friederich, G. (2002). Enhanced Lifetime of Methane Bubble Streams within the Deep Ocean. *Geophys. Res. Lett.* 29, 21-1–21-4. doi:10.1029/2001GL013966

Rehder, G., Leifer, I., Brewer, P., Friederich, G., and Peltzer, E. T. (2009). Controls On Methane Bubble Dissolution Inside And Outside The Hydrate Stability Field From Open Ocean Field Experiments And Numerical Modeling. *Marine Chem.* 114 (1-2), 19–30. doi:10.1016/j.marchem.2009.03.004

Riedel, M., Hähnel, L., Bialas, J., Bachmann, A. K., Gaide, S., Wintersteller, P., et al. (2021). Controls on Gas Emission Distribution on the Continental Slope of the Western Black Sea. *Front. Earth Sci.* 8, 601254. doi:10.3389/feart.2020.601254

Riedel, M., Scherwath, M., Römer, M., Veloso, M., Heesemann, M., and Spence, G. D. (2018). Distributed Natural Gas Venting Offshore along the Cascadia Margin. *Nat. Commun.* 9, 3264. doi:10.1038/s41467-018-05736-x

Römer, M., Riedel, M., Scherwath, M., Heesemann, M., and Spence, G. D. (2016). Tidally Controlled Gas Bubble Emissions: A Comprehensive Study Using Long-Term Monitoring Data from the NEPTUNE Cabled Observatory Offshore Vancouver Island. *Geochem. Geophys. Geosyst.* 17, 3797–3814. doi:10.1002/2016GC006528

Römer, M., Sahling, H., Pape, T., Bahr, A., Feseker, T., Wintersteller, P., et al. (2012). Geological Control and Magnitude of Methane Ebullition from a High-Flux Seep Area in the Black Sea-The Kerch Seep Area. *Mar. Geol.* 319-322, 57–74. doi:10.1016/j.margeo.2012.07.005

Römer, M., Wenau, S., Mau, S., Veloso, M., Greinert, J., Schlüter, M., et al. (2017). Assessing Marine Gas Emission Activity and Contribution to the Atmospheric Methane Inventory: A Multidisciplinary Approach from the Dutch Dogger Bank Seep Area (North Sea). *Geochem. Geophys. Geosyst.* 18, 2617–2633. doi:10.1002/2017GC006995

Ruppel, C. D., and Kessler, J. D. (2017). The Interaction of Climate Change and Methane Hydrates. *Rev. Geophys.* 55, 126–168. doi:10.1002/2016RG000534

Sahling, H., Bohrmann, G., Artemov, Y. G., Bahr, A., Brüning, M., Klapp, S. A., et al. (2009). Vodyanitskii Mud Volcano, Sorokin Trough, Black Sea: Geological Characterization and Quantification of Gas Bubble Streams. *Mar. Petroleum Geol.* 26, 1799–1811. doi:10.1016/j.marpetgeo.2009.01.010

Sahling, H., Rickert, D., Lee, R., Linke, P., and Suess, E. (2002). Macrofaunal Community Structure and Sulfide Flux at Gas Hydrate Deposits from the Cascadia Convergent Margin, NE Pacific. *Mar. Ecol. Prog. Ser.* 231, 121–138. doi:10.3354/meps231121

Sarkar, K., and Prosperetti, A. (1993). Coherent and Incoherent Scattering from Oceanic Bubbles. *J. Acoust. Soc. Am.* 93, 2379. doi:10.1121/1.406101

Sauter, E. J., Muyakshin, S. I., Charlou, J.-L., Schlüter, M., Boetius, A., Jerosch, K., et al. (2006). Methane Discharge from a Deep-Sea Submarine Mud Volcano into the Upper Water Column by Gas Hydrate-Coated Methane Bubbles. *Earth Planet. Sci. Lett.* 243, 354–365. doi:10.1016/j.epsl.2006.01.041

Scandella, B. P., Pillsbury, L., Weber, T., Ruppel, C., Hemond, H. F., and Juanes, R. (2016). Ephemerality of Discrete Methane Vents in Lake Sediments. *Geophys. Res. Lett.* 43, 4374–4381. doi:10.1002/2016GL068668

Scandella, B. P., Varadharajan, C., Hemond, H. F., Ruppel, C., and Juanes, R. (2011). A Conduit Dilation Model of Methane Venting from Lake Sediments. *Geophys. Res. Lett.* 38, 6. doi:10.1029/2011GL046768

Schmale, O., Leifer, I., Deimling, J. S. v., Stolle, C., Krause, S., Kießlich, K., et al. (2015). Bubble Transport Mechanism: Indications for a Gas Bubble-Mediated Inoculation of Benthic Methanotrophs into the Water Column. *Cont. Shelf Res.* 103, 70–78. doi:10.1016/j.csr.2015.04.022

Schneider von Deimling, J., Greinert, J., Chapman, N. R., Rabbel, W., and Linke, P. (2010). Acoustic Imaging of Natural Gas Seepage in the North Sea: Sensing Bubbles Controlled by Variable Currents. *Limnol. Oceanogr. Methods* 8, 155–171. doi:10.4319/lom.2010.8.155

Schneider von Deimling, J., Rehder, G., Greinert, J., McGinnnis, D. F., Boetius, A., and Linke, P. (2011). Quantification of Seep-Related Methane Gas Emissions at Tommeliten, North Sea. *Cont. Shelf Res.* 31, 867–878. doi:10.1016/j.csr.2011.02.012

Shakhova, N., Semiletov, I., Leifer, I., Sergienko, V., Salyuk, A., Kosmach, D., et al. (2014). Ebullition and Storm-Induced Methane Release from the East Siberian Arctic Shelf. *Nat. Geosci.* 7, 64–70. doi:10.1038/ngeo2007

Shakhova, N., Semiletov, I., Salyuk, A., Yusupov, V., Kosmach, D., and Gustafsson, Ö. (2010). Extensive Methane Venting to the Atmosphere from Sediments of the East Siberian Arctic Shelf. *Science* 327, 1246–1250. doi:10.1126/science.1182221

She, M., Song, Y., Mohrmann, J., and Köser, K. (2019). "Adjustment and Calibration of Dome Port Camera Systems for Underwater Vision," in *Pattern RecognitionLecture Notes in Computer Science*. Editors G. A. Fink, S. Frintrop, and X. Jiang (Cham: Springer International Publishing), 79–92. doi:10.1007/978-3-030-33676-9_6

She, M., Weiß, T., Song, Y., Urban, P., Greinert, J., and Köser, K. (2022). Marine Bubble Flow Quantification Using Wide-Baseline Stereo Photogrammetry. *ISPRS J. Photogrammet. Remo. Sens.*

Skarke, A., Ruppel, C., Kodis, M., Brothers, D., and Lobecker, E. (2014). Widespread Methane Leakage from the Sea Floor on the Northern US Atlantic Margin. *Nat. Geosci.* 7, 657–661. doi:10.1038/ngeo2232

Smith, A. J., Mienert, J., Bünz, S., and Greinert, J. (2014). Thermogenic Methane Injection via Bubble Transport into the Upper Arctic Ocean from the Hydrate-

Charged Vestnesa Ridge, Svalbard. *Geochem. Geophys. Geosyst.* 15, 1945–1959. doi:10.1002/2013GC005179

Suess, E. (2014). Marine Cold Seeps and Their Manifestations: Geological Control, Biogeochemical Criteria and Environmental Conditions. *Int. J. Earth Sci. Geol. Rundsch)* 103, 1889–1916. doi:10.1007/s00531-014-1010-0

Suess, E., Torres, M. E., Bohrmann, G., Collier, R. W., Greinert, J., Linke, P., et al. (1999). Gas Hydrate Destabilization: Enhanced Dewatering, Benthic Material Turnover and Large Methane Plumes at the Cascadia Convergent Margin. *Earth Planet. Sci. Lett.* 170, 1–15. doi:10.1016/S0012-821X(99)00092-8

Thuraisingham, R. A. (1997). New Expressions of Acoustic Cross-Sections of a Single Bubble in the Monopole Bubble Theory. *Ultrasonics* 35, 407–409. doi:10.1016/S0041-624X(97)00021-8

Torres, M. E., McManus, J., Hammond, D. E., de Angelis, M. A., Heeschen, K. U., Colbert, S. L., et al. (2002). Fluid and Chemical Fluxes in and Out of Sediments Hosting Methane Hydrate Deposits on Hydrate Ridge, OR, I: Hydrological Provinces. *Earth Planet. Sci. Lett.* 201, 525–540. doi:10.1016/S0012-821X(02)00733-1

Tsai, C.-H., Hsu, S.-K., Chen, Y.-F., Lin, H.-S., Wang, S.-Y., Chen, S.-C., et al. (2019). Gas Plumes and Near-Seafloor Bottom Current Speeds of the Southernmost Okinawa Trough Determined from Echo Sounders. *Terr. Atmos. Ocean. Sci.* 30, 649–674. doi:10.3319/TAO.2019.07.07.01

Turco, F., Ladroit, Y., Watson, S. J., Seabrook, S., Law, C. S., Crutchley, G. J., et al. (2022). Estimates of Methane Release from Gas Seeps at the Southern Hikurangi Margin, New Zealand. *Front. Earth Sci.* 10, 834047. doi:10.3389/feart.2022.834047

Urban, P., Köser, K., and Greinert, J. (2017). Processing of Multibeam Water Column Image Data for Automated Bubble/seep Detection and Repeated Mapping. *Limnol. Oceanogr. Methods* 15, 1–21. doi:10.1002/lom3.10138

Urban, P., Veloso-Alarcón, M., and Greinert, J. 2022 Echo Grid-Integration: A Novel Approach for Preprocessing Multibeam Water Column Data to Quantify Underwater Gas Bubble Emissions. Submitted to *L&O Methods*.

Veloso, M., Greinert, J., Mienert, J., and De Batist, M. (2015). A New Methodology for Quantifying Bubble Flow Rates in Deep Water Using Splitbeam Echosounders: Examples from the A Rctic Offshore NW-S Valbard. *Limnol. Oceanogr. Methods* 13, 267–287. doi:10.1002/lom3.10024

Veloso-Alarcón, M. E., Jansson, P., De Batist, M., Minshull, T. A., Westbrook, G. K., Pälike, H., et al. (2019). Variability of Acoustically Evidenced Methane Bubble Emissions Offshore Western Svalbard. *Geophys. Res. Lett.* 46, 9072–9081. doi:10.1029/2019GL082750

Wallmann, K., Riedel, M., Hong, W. L., Patton, H., Hubbard, A., Pape, T., et al. (2018). Gas Hydrate Dissociation off Svalbard Induced by Isostatic Rebound rather Than Global Warming. *Nat. Commun.* 9, 83. doi:10.1038/s41467-017-02550-9

Wang, B., Jun, I., Socolofsky, S. A., DiMarco, S. F., and Kessler, J. D. (2020). Dynamics of Gas Bubbles from a Submarine Hydrocarbon Seep within the Hydrate Stability Zone. *Geophys. Res. Lett.* 47, 9. e2020GL089256. doi:10.1029/2020GL089256

Wang, B., Socolofsky, S. A., Breier, J. A., and Seewald, J. S. (2016). Observations of Bubbles in Natural Seep Flares at MC 118 and GC 600 Using *In Situ* Quantitative Imaging. *J. Geophys. Res. Oceans* 121, 2203–2230. doi:10.1002/2015JC011452

Wang, B., and Socolofsky, S. A. (2015). On the Bubble Rise Velocity of a Continually Released Bubble Chain in Still Water and with Crossflow. *Phys. Fluids* 27, 103301. doi:10.1063/1.4932176

Weber, T. C., Mayer, L., Jerram, K., Beaudoin, J., Rzhanov, Y., and Lovalvo, D. (2014). Acoustic Estimates of Methane Gas Flux from the Seabed in a 6000 Km2region in the Northern Gulf of Mexico. *Geochem. Geophys. Geosyst.* 15, 1911–1925. doi:10.1002/2014GC005271

Weber, T., Wiseman, N. A., and Kock, A. (2019). Global Ocean Methane Emissions Dominated by Shallow Coastal Waters. *Nat. Commun.* 10, 4584. doi:10.1038/s41467-019-12541-7

Westbrook, G. K., Chand, S., Rossi, G., Long, C., Bünz, S., Camerlenghi, A., et al. (2008). Estimation of Gas Hydrate Concentration from Multi-Component Seismic Data at Sites on the Continental Margins of NW Svalbard and the Storegga Region of Norway. *Mar. Petroleum Geol.* 25, 744–758. doi:10.1016/j.marpetgeo.2008.02.003

Westbrook, G. K., Thatcher, K. E., Rohling, E. J., Piotrowski, A. M., Pälike, H., Osborne, A. H., et al. (2009). Escape of Methane Gas from the Seabed along the West Spitsbergen Continental Margin. *Geophys. Res. Lett.* 36, 5. doi:10.1029/2009GL039191

Conflict of Interest: The authors declare that the research was conducted in the absence of any commercial or financial relationships that could be construed as a potential conflict of interest.

Publisher's Note: All claims expressed in this article are solely those of the authors and do not necessarily represent those of their affiliated organizations, or those of the publisher, the editors, and the reviewers. Any product that may be evaluated in this article, or claim that may be made by its manufacturer, is not guaranteed or endorsed by the publisher.

Advantages of publishing in Frontiers

OPEN ACCESS
Articles are free to read for greatest visibility and readership

FAST PUBLICATION
Around 90 days from submission to decision

HIGH QUALITY PEER-REVIEW
Rigorous, collaborative, and constructive peer-review

TRANSPARENT PEER-REVIEW
Editors and reviewers acknowledged by name on published articles

Frontiers
Avenue du Tribunal-Fédéral 34
1005 Lausanne | Switzerland

Visit us: www.frontiersin.org
Contact us: frontiersin.org/about/contact

REPRODUCIBILITY OF RESEARCH
Support open data and methods to enhance research reproducibility

DIGITAL PUBLISHING
Articles designed for optimal readership across devices

FOLLOW US
@frontiersin

IMPACT METRICS
Advanced article metrics track visibility across digital media

EXTENSIVE PROMOTION
Marketing and promotion of impactful research

LOOP RESEARCH NETWORK
Our network increases your article's readership